Development of Numerical Tools For the Evaluation of Pile Response to Laterally Spreading Soil

Alborz Ghofrani

A dissertation
submitted in partial fulfillment of the
requirements for the degree of

Doctor of Philosophy

University of Washington

2018

Reading Committee:

Pedro Arduino, Chair

Steven, L. Kramer

Peter Mackenzie-Helnwein

Program Authorized to Offer Degree:
Civil and Environmental Engineering

University of Washington

Abstract

Development of Numerical Tools For the Evaluation of Pile Response to Laterally Spreading Soil

Alborz Ghofrani

Chair of the Supervisory Committee:
Professor Pedro Arduino
Civil and Environmental Engineering

Problems in geotechnical earthquake engineering often involve complex geometries and boundary conditions prohibiting the use of simple models. Although very useful, empirical models are sometimes not applicable to the problem at hand and performing experimental tests is costly and difficult. Improvements in computer technology have made advanced numerical modeling an essential tool for analysis and design of systems in the field of geotechnical earthquake engineering. In this context, there is a need for a robust numerical framework capable of handling different aspects of the engineering problems in this field. In this study, several of these aspects for 3D dynamic finite element analysis of such engineering problems are addressed. Particularly, constitutive modeling of granular soil to capture liquefaction, and soil-pile interaction are considered and tools are developed and implemented in OpenSees to address the problem of bridge foundations subjected to liquefaction induced lateral spreading loads. Several 3D static, quasi-static and dynamic examples are included for verification and validation of the tools implemented as part of this research.

"سبب علوّ وجود و سموّ آن علوم و فنون و صنائع است. علم بمنزلهٔ جناحست از

برای وجود و مرقاتست از برای صعود.

فی‌الحقیقه کنز حقیقی از برای انسان علم اوست

و اوست علّت عزّت و نعمت و فرح و نشاط و بهجت و انبساط. "

حضرت بهاءالله

"Arts, crafts and sciences uplift the world of being, and are conducive to its exaltation. Knowledge is as wings to man's life, and a ladder for his ascent.

In truth, knowledge is a veritable treasure for man, and a source of glory, of bounty, of joy, of exaltation, of cheer and gladness unto him."

Bahá'u'lláh

TABLE OF CONTENTS

LIST OF FIGURES

LIST OF TABLES

ACKNOWLEDGMENTS

The completion of this dissertation would not have been possible without the assistance, support and guidance of Prof. Pedro Arduino who patiently advised me during all the years behind this work. His high standards drove me towards higher quality both professionally and in life. I would like to give my gratitude to Prof. Steven L. Kramer and Prof. Peter Mackenzie-Helnwein for reading this dissertation. I absolutely enjoyed their consult and the quality of this writing is indebted to their valuable comments and suggestions. I owe a big share of my knowledge to these three men along with Prof. Robert D. Holtz and Prof. Joseph Wartman, and for that I'm eternally thankful to them.

My friends and colleagues were a big part of this effort. My special thanks goes to Long Chen, Kamal Ahmed, Krishnendu Shekhar, Abbas Ganji, Farnaz Asl and many other who were always there for me. I appreciate the funding support from Washington State Department of Transportation for a portion of my Ph.D. studies.

Above all, my family is the solid rock on which I stand. I enjoyed endless support from my parents, Aziz and Shahla, my aunt and uncle, Shahin and Mehrdad, my sisters and brother, Gelareh, Asareh and Arsalan and my cousins, Arya and Tara. I am grateful for having such a wonderful family.

Chapter 1

INTRODUCTION

Geotechnical engineering has a long history developing and using empirical and semi-empirical methods. Empiricism has been a big player in this field due to the complexity found in modeling soil and rock behavior. In parallel to empiricism, theories have been developed to provide a better physical basis for such empirical models. Although very useful, finding a closed-form solution for theoretical models is only possible for very simple and idealized problems with boundary conditions that may not completely represent real cases. As a result, simulations based on sound theories and verified using empirical methods are of interest to examine situations outside the range of applicability of empirical solutions. These capabilities are continuously enhanced with advances in computing power that comes with computational software equipped with parallel processing. This is of importance in geotechnical engineering and in particular geotechnical earthquake engineering.

Problems in geotechnical earthquake engineering often involve complex geometries and boundary conditions. Moreover, soils are made of three phases and interaction between these phases play an important role in the global response, making theories even more complicated. Materials comprising the medium over which geotechnical problems are described behave almost always in a nonlinear fashion. Natural material inhomogeneity caused by the way soils are deposited, as well as human influence, bring other complexities to the problem. In addition, the dynamic nature of earthquakes and their effects can rarely be considered in simplified models while preserving all their important aspects.

Interaction of structural foundations (e.g. bridges, abutments or buildings) with the surrounding soil is also a major aspect to consider in geotechnical earthquake analysis and design. Foundation geometry and site soil topography (being natural or man-made) play

an important role in this matter. Among other geotechnical problems, of importance in seismically active regions is the design of bridge foundations considering different aspects of seismic and co-seismic events happening during and after earthquake shaking. One of such events is lateral spreading. In this research the term *lateral spreading* is used to indicate large displacements of a soil mass caused by liquefaction of the underlying cohesionless soil due to ground excitation. River-crossing bridge foundations built on loosely placed cohesionless fluvial deposits are often subject to lateral spreading. In such areas, soil layers are usually mildly sloped towards the river where liquefaction of an underlying soil layer can lead to large deformations near the ground surface. As a result, a large mass of dry soil crust can be pushed into the bridge foundation exerting passive pressures and consequently increasing structural demands, leading to a hefty and expensive design.

Soil constitutive behavior and soil-structure interaction are two of the most important aspects in numerical analysis of bridge foundations under seismic loading. This research aims to expand, develop and implement tools and methods in these two subject areas to enhance geotechnical earthquake engineering capabilities in 3D numerical models of dynamic problems.

1.1 3D Analysis of Bridge Foundations Subject to Lateral Spreading

The main objective of this dissertation is to introduce new tools for the analysis of dynamic geotechnical phenomena such as liquefaction and interaction of deep foundations with the surrounding soil. These tools will provide the ingredients for better 3D dynamic analysis of such problems. A specific problem considered in this work is the analysis of bridge pile foundations subject to loads from lateral spreading of the soil.

Current methodologies for design of pile foundations subject to lateral spreading are mostly based on plane-strain models. Although some 3D effects can be considered in plane-strain models by using simplifying strategies, there are situations where plane-strain assumptions are not adequate to capture 3D geometrical/behavioral effects and can lead to over-conservative and expensive solutions. Case histories have exhibited very different de-

formation patterns in the near field of bridge foundations and structures, when compared to corresponding free field displacements [1]. These effects are more pronounced when the approach embankment out-of-plane dimension is relatively small. In this case the embankment slumps and flows around the bridge foundation resulting in less passive pressures compared to the case where the out-of-plane dimension of the surrounding soil is greater. The resistance provided by the bridge foundation is part of the reason the deformation of the near-field soil is impeded; which in turn leads to reduced demands to the bridge foundation. Foundation geometry is another important aspect to consider when evaluating the response of a structural system to lateral spreading. In many cases the foundation system can be simply modeled using plane-strain models. However if 3D aspects are important in the foundation geometry, plane-strain assumptions no longer hold and the three dimensionality of the foundation system must be considered in the analysis and modeling approach. In this context, there is a need to model 3D effects (soil and structure) both qualitatively and quantitatively well, to improve current design methodologies, hoping for more efficient and cost-effective solutions.

Effects of site geometry on foundation demands and abutment displacements under lateral spreading kinematic demands were addressed by McGann (2013). A 3D quasi-static finite element method was used in his work to evaluate loads on bridge foundations due to lateral spreading. Part I of this dissertation follows the same line of investigation on a different bridge that eventually requires a more complete 3D dynamic model. As an additional parameter to McGann's studies, effects of bridge foundation geometry are included in this study (in contrast to site geometry). Further, the same simplified 1D analysis procedure, introduced by McGann (2013), is validated against results from this 3D model. For completeness a summary of the simplified method used by Washington State Department of Transportation, WSDOT, is presented in part I. In performing comparisons with 3D simulations, both McGann (2013) and this part of the dissertation introduce simplifications

[1] In the literature, this is typically referred as *pinning effect*.

in terms of constitutive models, soil-structure interaction methods and application of the dynamic loads using a quasi-static approach.

Performing a dynamic analysis of such 3D models under actual earthquake excitation requires additional considerations. To name a few: 1) a fully coupled formulation is required to consider the interaction of different material phases in the soil mass; 2) suitable constitutive models are needed to capture cyclic aspects of soil behavior; 3) efficient and reliable formulations for dynamic interaction between soil and the buried structure is needed to mimic a realistic behavior; and 4) appropriate boundary conditions must be imposed in the model representing the actual dynamic excitation on these boundaries. McGann (2013) developed and implemented a stabilized single integration point element with u-P formulation to address the first issue. This element proved to be very efficient and practical. In his analyses, McGann used existing tools to capture the soil nonlinearity and soil-pile interaction effects. Constitutive modeling and soil structure interaction are two topics considered in this dissertation. Imposed boundary conditions for dynamic 3D numerical models is an on-going research topic that requires further development for 3D cases and it is not included in this work.

1.2 Constitutive Modeling

Solid mechanics requires satisfaction of three conditions in the absence of thermal effects. These conditions are:

- equilibrium of the system (balance of linear and angular momentum or Newton's law of motion),
- compatibility conditions relating displacements to strains,
- and constitutive laws linking strains to stresses.

In the case of iso-static (statically determined) systems, internal forces can be calculated directly from the external forces and kinematic boundary conditions. The deformation of

iso-static systems however, cannot be calculated directly from the equilibrium equations. Material models (constitutive laws) and compatibility conditions provide the additional necessary equations for calculating the system's deformation.

The role of constitutive models become even more apparent in the case of hyper-static (statically indeterminate) systems. Most real mechanical systems, especially engineering systems, are hyper-static meaning the internal forces and stresses not only depend on the externally applied forces and kinematic boundary conditions, but also on the behavior of the material itself. In terms of numerical models, equilibrium conditions provide fewer equations than existing unknowns making the system undetermined. The constitutive laws provide the additional equations needed to solve the system of equations for such systems.

In this context, stress-strain relationships (constitutive models) are of fundamental importance in numerical modeling. These models should be advanced enough to capture fundamental characteristics of the material behavior, in particular under cyclic loads, and yet simple enough not to increase the computation cost of the whole numerical model. A constitutive law is a simplified mathematical description of material behavior and is an inherent characteristic of the material. In that sense constitutive laws are independent of the configuration of the model and its boundary conditions.

Material behavior can be categorized in many different forms such as linear vs. nonlinear, elastic vs. plastic vs. viscous, rate-dependent vs. rate-independent, monotonic vs. cyclic, etc. The real material behavior is a hybrid combination of all these behaviors. In geotechnical engineering, experiments have shown that there are many factors affecting soil behavior such as soil type (i.e. cohesive vs cohesionless), consistency and density, loading path, etc. Therefore, there is a need for developing and implementing advanced constitutive models capable of capturing various aspects of soil behavior in an accurate and efficient manner. During recent years, several constitutive models have been proposed to simulate liquefaction of sands under monotonic and cyclic excitation. In this work, a multi-yield-surface plasticity model is used in the quasi-static analyses presented in part I. This model can reasonably capture nonlinearity of soil behavior specifically under monotonic loading cases. For dynamic

analyses, part II of this dissertation introduces the formulation and implementation of an advanced constitutive model for dynamic analyses of granular soils capable of capturing liquefaction of such materials. This model has shown promising results in capturing granular soil behavior under cyclic loading, e.g., Khosrojerdi and Pak (2015).

1.3 Soil-Structure Interaction

Interaction of structural components with the surrounding soil is another major concern of geotechnical engineering. This issue arises in many geotechnical problems whether related to retaining soil mass, foundation engineering, underground construction or even soil improvement systems; and is one of the most important and challenging aspects of geotechnical numerical modeling since it is inherently nonlinear and complicated. Among all possible structural components in contact with the soil, pile foundations are of special importance due to their vast use in many applications. Different approaches have been proposed in the past 20 years that range from simple interaction springs to methods based on contact mechanics. Simplified models rely heavily on empirical methods and extrapolating these methods to more complicated and general cases requires extreme scrutiny of the problem at hand and method used. The more advanced the methods for modeling soil-structure interaction are, the more complex and costly they become in terms of computations. For example, although computationally intensive, contact mechanics has shown to be very effective in geotechnical engineering problems.

Soil-Structure Interaction (SSI) modeling methods include but are not limited to 1D decoupled p-y, t-z and Q-z springs (McClelland and Focht, 1958; Reese and Matlock, 1956), joint (Goodman et al., 1968) and thin layer (Zienkiewicz et al., 1970) interface elements and finally contact mechanics formulations. Contact mechanics is extensively discussed in Wriggers (2002) and Laursen (2002).

A p-y spring simulates the interaction between a pile and the behavior of its surrounding soil through nonlinear response. The response is generally empirically based and it is calibrated using load test data. Following the same methodology, the axial interaction between

the pile and the surrounding soil is evaluated using t-z springs along the side of the pile in contact with soil and using Q-z spring to represent end-bearing at the tip of the pile. Other 1D springs exist that combine frictional behavior with drag and gap formation (Taciroglu et al., 2006; Boulanger et al., 1999). The main drawback in using these methods is that the response is decoupled in each direction and between springs.

Zero-thickness and thin layer joint finite elements have also been used in various rock and soil mechanics applications. The zero-thickness element uses relative displacements as nodal degrees of freedom in an isoparametric formulation. In contrast, thin layer elements are regular continuum elements for which a specific constitutive model representing the interface behavior is defined. Although proven to be effective in the numerical simulation of many geotechnical problems, both these types of finite elements suffer from certain drawbacks; zero-thickness elements require definition of large stiffness parameters to avoid interpenetrations, which are usually physically meaningless, and the thickness of thin layer interface elements is of high importance for numerical stability of the simulations.

A different approach in modeling soil-structure interaction is to use standard contact elements. In this approach a gap function is defined which represents the geometric distance between two bodies in contact and a geometric constraint is applied to this function so that when the gap is closed no penetration is allowed between these bodies. Different contact (gap) element types include node-to-node, node-to-segment and node-to-surface elements. When using these elements, geometric constraints can be handled using standard mathematical approaches from optimization theory. The method of Lagrange Multipliers, Penalty method and the Augmented Lagrange Multipliers method are commonly used in contact mechanics. The advantage of these formulations is that they describe the actual geometric interaction between bodies and consideration of different interface behaviors are allowed. Recently, the so-called *mortar* methods have been developed to enforce contact constraints in non-matching discretization of contacting bodies (Bernardi, 1994). In this method an intermediate *mortar* surface is added between two contacting bodies over which the con-

tact interaction is defined. This allows for continuity of stresses at the contact interface maintaining force and moment equilibrium.

Implementation of two- and three dimensional node-to-segment and node-to-surface contact elements in OpenSees are described in Petek (2006). These elements were further developed to enforce contact conditions between a one dimensional beam element and a two- or three dimensional solid element. Although these elements are very effective in capturing different aspects of the interface behavior specially in geotechnical engineering problems, setting up the model for use of these elements during pre-processing requires significant effort. Part III of this dissertation introduces new numerical techniques to represent this interaction by developing new embedded interface elements that can be used to represent the interaction between soil and a pile structure.

1.4 Thesis Organization

The work presented in this thesis is organized in 15 chapters divided in 4 parts. Part I includes a brief literature review on numerical finite element analysis and state-of-the-art methods for the analysis of piles subject to lateral spreading and presents results from a 3D quasi-static finite element analysis of a bridge bent subject to lateral spreading. Part II concentrates on the constitutive modeling aspect of the problem. Part III pertains to the soil structure interaction aspect and finally part IV presents a few static and dynamic examples of typical geotechnical engineering problems that can be used to validate and verify the tools developed in this dissertation.

1.4.1 Part I

This part consists of two chapters:

- **Chapter 2** presents a literature review on numerical modeling of foundations subjected to lateral spreading. The design methodology used by the Washington State Department of Transportation (WSDOT) is described in this chapter.

- **Chapter 3** presents details of a case study bridge in Chile which was subject to lateral spreading loads during the 2010 Maule earthquake. This chapter also presents results from a quasi-static 3D finite element analysis of the bridge's northeast approach that is used to further validate the simplified Caltrans design methodology currently adopted by WSDOT.

1.4.2 Part II

This part considers constitutive modeling aspects of granular materials under earthquake excitation and consists of three chapters:

- **Chapter 4** presents a brief review of general constitutive modeling theories and presents an advanced bounding surface plasticity model for granular soils capable of capturing liquefaction and cyclic mobility.

- **Chapter 5** presents different methods for integrating the constitutive equations and provides details on different implementation aspects of these integration schemes in a finite element analysis framework.

- **Chapter 6** presents several examples verifying and validating the material model introduced in Chapter 4 and its implementation in the finite element analysis framework, OpenSees.

1.4.3 Part III

This part addresses soil-structure interaction aspects of geotechnical earthquake engineering and consists of six chapters:

- **Chapter 7** introduces a fiber overlay finite element to motivate the idea of an overlay formulation to account for the interaction of different material domains.

- **Chapter 8** presents a theory to represent the interaction of a deep foundation with its surrounding soil. This chapter states the problem and explains the notation being used in the following chapters.

- **Chapter 9** introduces a interaction overlay finite element that enforces the interaction conditions between a pile and soil in a strong sense.

- **Chapter 10** introduces a interaction mortar overlay finite element that enforces the interaction conditions between a pile and soil in a weak sense.

- **Chapter 11** expands the concept of a mortar finite element by augmenting the interaction with an elastoplastic behavior.

- **Chapter 12** provides examples for verification of the elements introduced in Chapters 7, 8, 9, 10 and 11.

1.4.4 Part IV

This part presents several static and dynamic examples that brings together the different concepts presented in the previous parts. It consists of three chapters:

- **Chapter 13** presents several static and quasi-static validation examples including reinforced soil, batter pile, and single pile and group of piles subjected to lateral spreading.

- **Chapter 14** presents several dynamic examples relating all concepts presented in the previous chapters. The element developed in part III is used to briefly evaluate kinematic soil-structure interaction effects. A simple bridge bent is modeled next. Finally the material model presented in part II and the element described in part III are used to model a simple pile foundation subject to lateral spreading induced by dynamic loading.

- **Chapter 15** presents a summary of research outcomes, conclusions and suggestions for future studies.

Part I

STATE-OF-THE-ART METHODS IN NUMERICAL MODELING OF LATERAL SPREADING EFFECTS ON PILE FOUNDATIONS

The first part of the dissertation summarizes state of the art methodologies used for the analyses and design of bridge foundations subject to lateral spreading. Motivation for this part of the research comes from a project recently completed by the author for the Washington State Department of Transportation (WSDOT). The project included validation of a simplified method to estimate lateral forces on bridge foundations due to lateral spreading using a 3D finite element model of the bridge bent that was subject to this form of loading. This part also includes a brief literature review of pile design procedures and details of the mentioned WSDOT 3D analysis project.

Journal papers and reports published by the author and coworkers as a result of this part of the research include:

1. **Ghofrani**, A., McGann, C. R., and Arduino, P. (2016). "Influence of modeling decisions on three-dimensional finite element analysis of two existing highway bridges subjected to lateral spreading." *Transportation Research Record: Journal of the Transportation Research Board*, 2592, 143–150

2. Arduino, P., McGann, C., **Ghofrani**, A., et al. (2017a). "Numerical evaluation of forces on piled bridge foundations in laterally spreading soil." *Report No. WA-RD 874.1*, Washington (State) Dept. of Transportation. Research Office

3. Arduino, P., McGann, C. R., and **Ghofrani**, A. (2017b). "Design procedure for bridge foundations subject to liquefaction-induced lateral spreading." *Report No. WA-RD 874.2*, Washington (State) Dept. of Transportation. Research Office

Chapter 2

DESIGN OF PILE FOUNDATIONS IN LATERALLY SPREADING GROUND - A BRIEF REVIEW

Extensive research has been done in the field of seismic design and analysis of deep foundations subject to liquefaction and lateral spreading. Terms like "liquefaction" and "lateral spreading" have been used in the literature to indicate different phenomena. In this document, the word *liquefaction* is used to indicate the condition where the strength and stiffness of saturated cohesionless soil is substantially reduced due to pore water pressure build-up often resulting from rapid shaking (Kramer, 1996). The term *lateral spreading* is used to indicate the global movement of soil due to liquefaction of the underlying cohesionless soil. This embodies the case of "flow liquefaction" [1] as well (After Ashford et al. (2011)). Furthermore, the word *pile* is used to indicate general deep foundations including all kinds of displacement and non-displacement deep foundations, i.e. driven piles and drilled shafts.

In practice, engineers seek balance between engineering rigor and economic efficiency by deciding which type of analysis to use and how much uncertainty (i.e. risk) to accept. As stated in Ashford et al. (2011), there are three steps in the design (also in the performance evaluation process) of pile foundations for bridges. The first step involves designing piles for inertial loads that would occur without liquefaction happening. The second step involves estimating the susceptibility to liquefaction of the surrounding soil and quantifying any ground displacement due to liquefaction. The kinematic demands can be high in liquefiable

[1] In flow liquefaction, the residual strength of the soil, i.e. the strength of the soil in its liquefied state, is less than the shear stress required for static equilibrium. Therefore as the soil liquefies, a large amount of soil is displaced due to instability under static conditions. On the other hand, in cases where the residual strength is greater than the static shear stresses, ground lurching and ratcheting due to cyclic mobility of the liquefied soil can cause large ground deformation which is identified as lateral spreading by some researchers. Here the term lateral spreading encompasses both of these phenomena.

soil deposits even when lateral spreading does not occur, i.e. in level ground. The third and last step involves designing the piles accounting for lateral spreading and inertial demands if liquefaction is triggered.

For the first step, an estimation of pile capacity and stiffness under axial and lateral loads can be achieved using conventional approaches; based on general soil conditions, pile type and local industry experience. For estimating axial and lateral stiffness, and capacity of piles, standard methods can be used including empirical correlations to in-situ tests such as V_s measurements, Standard Penetration Test (SPT) or Cone Penetration Test (CPT) and back-calculations from dynamic monitoring during pile-driving or pile re-strikes. Additionally, full scale physical tests on actual piles can significantly reduce uncertainties.

For the second step, the susceptibility of the site to liquefaction is estimated using information from site characterization and available empirical relationships. The amount of ground deformation due to liquefaction is also estimated in this step. There is a vast amount of research regarding this process and ample number of empirical relationships have been proposed for evaluation of liquefaction susceptibility and estimation of ground deformation as a result of lateral spreading.

The third step focuses on the *evaluation of deep foundation elements subject to lateral spreading and inertial demands in case of liquefaction* and is the main objective of part I of this dissertation. There is significant amount of research dedicated to investigating this matter. These investigations utilize different types of numerical modeling and experimental testing to understand the response of bridge foundations to liquefaction and laterally spreading soil. In addition, case histories are commonly used to evaluate the real response of an existing bridge to a real earthquake event. These case histories are also used to verify and validate the predictions from numerical and experimental analysis.

In this chapter a review of recent relevant literature comes first. Due to the nature of this research, the focus of this part is mainly on numerical analysis. A brief review of recent Washington state bridge design procedures for piles subject to lateral spreading follows afterwards.

2.1 Literature Review

A vast amount of research has been performed on design and analysis of piles in laterally spreading ground. Researchers have taken different approaches towards this subject. These include study of case histories, experimental testing and numerical analyses. The numerical analyses have been performed using 1D, 2D and 3D models. A brief literature review of each of these subjects follows next.

2.1.1 Case Histories

Damage to piles during earthquakes due to liquefaction and lateral spreading has been documented in many case histories (e.g. Karube and Kimura, 1996; Hamada, 1996; Matsui and Oda, 1996; Matsui et al., 1997; Tokimatsu et al., 1996, 1997; Tokimatsu and Asaka, 1998; Oh-Oka et al., 1997, 1998). Boulanger et al. (2003) summarized 19 different case histories providing information on pile type, soil type and shaking parameters for each case. In several of these cases, the occurrence of liquefaction resulted in large transient and permanent ground deformation both vertically and laterally. Ground deformations impose kinematic demands on the pile structure. The situation is worsened by reduction in the capacity of the pile due to loss of strength in the surrounding soil as a result of liquefaction. In areas where strong non-liquefiable crustal layers exist, kinematic loads become even more important. As an example, a common damage pattern was identified in piles extending from a non-liquefiable crustal layer through a liquefiable layer, ending in a competent soil (e.g. Matsui et al., 1997; Fujii et al., 1998b; Tokimatsu et al., 1997; Tokimatsu and Asaka, 1998; Oh-Oka et al., 1997, 1998; Ramos et al., 1999). The observed damage in these piles was concentrated at the interface of the liquefiable layer both at the top and bottom.

Pile failure has also been observed as a result of transient ground lurching even without large permanent ground deformations. This effect was observed in Port Island after the 1995 Kobe earthquake (Fujii et al., 1998a) and was confirmed by centrifuge tests performed at the University of California at Davis (Robins et al., 1999). Another important consideration in

evaluating pile damage is the effect of inertial loads. Contribution of inertial loads to pile damage has been studied by Yoshida and Hamada (1990); Matsui (1993); Matsui and Oda (1996); Tokimatsu et al. (1996); Fujii et al. (1998a); Nishizawa et al. (1998) and in model tests by Adachi et al. (1998); Taji (1998).

2.1.2 Recent Work Using Experimental Testing

Interaction of pile foundations with the surrounding soil during seismic events has been studied experimentally using different test strategies with different levels of complexity. In this context, Knappett et al. (2010) used a modified direct shear box device to study the effects of lateral spreading on a foundation element by applying a relative displacement between the soil and the structure. Full size and scaled shake table tests were employed to assess the effects of lateral kinematic loads on piles (e.g. Suzuki et al., 2006; Dungca et al., 2006; Cubrinovski et al., 2006; Tokimatsu et al., 2005). Centrifuge tests have been widely used by researchers in order to study different aspects of soil and structure interaction (e.g. Armstrong et al., 2008; Tobita et al., 2006; Bhattacharya et al., 2005; Brandenberg et al., 2005; Boulanger et al., 2003; Kondoh and Tamura, 2003; Abdoun and Dobry, 2002). Full scale field tests (e.g. Lemitzer et al., 2009, 2010; Bozorgzadeh et al., 2008; Stewart et al., 2007; Rollins et al., 2005; Wallace et al., 2001; Romstad et al., 1995) and other miscellaneous experiments have been conducted on isolated or grouped piles or piled bridge abutments for the purpose of studying their behavior under lateral spreading loading conditions.

Besides the general response of piles and pile groups to liquefaction and lateral spreading, various other phenomena have been identified and studied in these experiments, including:

- pile pinning effects during lateral spreading (Armstrong et al., 2008),
- pile buckling in liquefied soils (Bhattacharya et al., 2005),
- lateral behavior of bridge abutments and backfill soils (Lemitzer et al., 2009; Bozorgzadeh et al., 2008; Romstad et al., 1995),

- induced earth pressures on bridge abutments during lateral spreading (Kondoh and Tamura, 2003), and

- interaction of piles and crustal layers during lateral spreading (Knappett et al., 2010; Brandenberg et al., 2007a).

2.1.3 Recent Research Using Numerical Modeling

With the advancement of computing power numerical methods have become a viable tool for the analysis and design of engineering problems. Currently, many of these methods are being evaluated against experiments and field observations. The spectrum of available numerical tools ranges from simplified and easy-to-use methods to complex and sophisticated approaches. Usually the more complex the methods are, the more aspects of the engineering problem that can be captured. However, this comes with higher computational costs and resources, more engineering time for identifying problem inputs and interpretation of the results, and also the need for sound mechanics and numerical methods knowledge. In geotechnical engineering there are three major numerical approaches commonly used for the analysis of soil-pile interaction: The *Beam on Nonlinear Winkler Foundation (BNWF) method* , *two-dimensional finite element (2D-FE) and finite difference (2D-FD) methods* using plane-strain assumptions and *three-dimensional finite element (3D-FE) and finite difference (3D-FD) methods*. Certain considerations are worth mentioning for each case.

Beam on Nonlinear Winkler Foundation (BNWF) Method

In this method, the pile is modeled using a beam-column element – a structural element that is much longer in one dimension than the other two and that carries the lateral load mostly by bending – and the soil mass is represented by a series of nonlinear springs. The soil response in the lateral direction is represented by nonlinear force density vs. displacement springs which are generally referred to as p-y springs (e.g., Reese and Van Impe, 2001; API, 2007). The frictional side resistance is also modeled using springs known as t-z springs (e.g.,

Seed and Reese, 1957; Kraft et al., 1981; Reese et al., 2006), and Q-z springs are used to capture the pile end bearing behavior (e.g., Meyerhof, 1976; Vijayvergiya, 1977).

Numerous studies have compared and validated results of BNWF analyses, for both single piles and pile groups, against experimental data and case histories. In general, acceptable agreement has been observed between BNWF analyses and experimental results including pseudo-static pushover tests (e.g., Boulanger et al., 2003; Tokimatsu et al., 2005; Brandenberg et al., 2007b; Takahashi et al., 2006; Ashford and Juirnarongrit, 2006; Khalili-Tehrani et al., 2007) and dynamic analyses (e.g., Miwa et al., 2006; Boulanger et al., 2003). The most important component of BNWF analyses is in the definition of the nonlinear springs representing the interface and surrounding soil behavior. Available correlations for definition of these springs has increased the viability of the BNWF method in industry.

This method has also been employed to study soil-structure interaction in 2D and 3D models of single isolated piles, pile groups and complete bridge systems (e.g., Silva and Manzari, 2008; Dicleli, 2005). Dicleli (2005) examined effects of live load distributions on integral bridge abutments, Faraji et al. (2001) investigated thermal loads on bridges and Ates and Constantinou (2011) analyzed a base isolated curved bridge using nonlinear dynamic 3D-FEA, all by incorporating the BNWF approach. Arduino et al. (2006) used the BNWF approach to assess the stiffness of piles subjected to dynamic loading in liquefiable soils.

Currently, many of the simplified design and analysis approaches used in industry are based on the BNWF representation of soil-foundation interaction. Ashour and Ardalan (2011) proposed an analytical method for estimating demands on piles subject to lateral spreading considering strain wedge effects and accounting for the response of crustal soil, liquefied soil and non-liquefied soil. Bradley et al. (2011) and Valsamis et al. (2011) proposed simplified approaches for piles subject to lateral spreading. The former proposed a probabilistic framework for the analysis of such cases and the latter proposed a design procedure based on parametric analysis of the problem and presented design charts for maximum bending moment and displacement in the pile. The BNWF method has also been used in performance-based engineering studies. Brandenberg et al. (2011) developed demand

fragility curves for such cases with input sampled using Monte Carlo simulations. Cubrinovski and Ishihara (2004) employed an equivalent linear approach to develop a simplified analysis procedure for piles in laterally spreading soils using a closed-form solution to the elastic beam on elastic foundation equation. They further developed this method to consider pile groups (Cubrinovski and Ishihara, 2006). A finite difference solution was presented for the BNWF method by Meera et al. (2007) and Chang et al. (2008) for the analysis of piles subject to lateral spreading.

2D Plane Strain Finite Element and Finite Difference Models

Two dimensional plane strain finite elements (2D-FE) can be used to analyze bridge foundation-soil systems more effectively than BNWF. These models provide a tool to consider the continuum soil which can be extended to consider effective stress analysis and interaction of solid-fluid phases. The advantage of 2D-FE analysis over fully 3D-FE method is the drastically lower computational cost. However, although plane strain assumptions are perfectly applicable to many geotechnical engineering problems, deep foundations are difficult to model properly using this simplification; hence making it less common in practice. Pile foundations have a small out-of-plane dimension resulting in a three dimensional behavior inherent to their response when interacting with the surrounding soil that is difficult to capture using 2D models.

Nevertheless, researchers have used this method to analyze pile group behavior subject to lateral spreading (Chang et al., 2006) and to simulate the response of bridge abutments to lateral loads and seismic shaking (Hara et al., 2004; Shamsabadi et al., 2010; Ooi et al., 2010). This method has also been used to model the dynamic response of bridge-foundation-soil systems to seismic loads using an effective stress approach (Shin et al., 2008; Bradley et al., 2010). One of the several ways to overcome the problem related to the out-of-plane dimension is to use *p-y* springs connecting the beam-column elements (representing the piles) to the continuum solid elements used to represent the soil domain (Shin et al., 2008; Chang et al., 2006). In this case, the *p-y* springs account for the three dimensional interaction of

the pile-soil system. In this approach the soil behavior is captured by both the nonlinear *p-y* springs and the solid elements; with the solid elements representing the far-field soil behavior while the *p-y* springs representing the near-field soil behavior. Although not completely accurate, the stiffness of the *p-y* springs can be modified such that the combined behavior of the spring and solid element represent the target behavior (Armstrong, 2010). An alternative approach is to model each row of the pile group as a plane strain wall sometimes modeled with equivalent beam-column elements (Hara et al., 2004; Ooi et al., 2010; Bradley et al., 2009, 2010). The downside of this method is that it is not applicable to all pile spacings and cannot consider the response of an isolated single pile.

3D Finite Element and Finite Difference Models

The most comprehensive approach for modeling soil-foundation systems is to use 3D-FE models. Full behavior of the soil-foundation system can be captured using this method although it requires the greatest computational resources. Recent advances in computing technology makes this restriction less prohibitive and the use of 3D-FE more viable.

Early work in 3D numerical analysis of soil-foundation systems showed that this method is viable in capturing realistic response of single and grouped pile foundations, especially if nonlinear constitutive behavior, geometric nonlinearity, nonlinear interface behavior and other influential factors are incorporated in the model (Desai and Appel, 1976; Faruque and Desai, 1982; Muqtadir and Desai, 1986; Brown et al., 1989; Brown and Shie, 1990, 1991).

The research presented in this dissertation aims to use 3D-FE to numerically analyze bridge foundations subject to lateral spreading kinematic demands. McGann et al. (2015) used this method to analyze a bridge abutment and foundation system subject to lateral spreading and used the corresponding results to validate and improve a simplified design method. The constitutive model proposed by Elgamal et al. (2003) was used in McGann's research and the interface behavior was modeled using the beam-solid contact elements developed by Petek (2006). Three dimensional effects inherent to the geometry of the bridge embankment was the subject of investigation in the research carried out by McGann et al.

(2015). Along the same line of thought, the research presented in this part of the dissertation will add the consideration of three dimensional effects due to the geometry of the foundation. For validation purposes, the Llacolén bridge case history in Chile will be used. This bridge suffered little damage during the 2010 Maule earthquake and except for a span that fell due to lateral spreading, other parts of the bridge performed relatively well.

2.1.4 Other Methodologies

There are various numerical methods that do not necessarily fit into the categories described above. For instance, Boulanger et al. (2006) used a slope stability approach to examine pile pinning effects. Shamsabadi et al. (2005, 2007) used the same methodology to assess the behavior of bridge abutments, Basha and Babu (2009) examined displacements of bridge abutments and Zha (2006) used the same method to estimate forces on bridge piles due to lateral spreading. Using a different approach, Sextos and Taskari (2008) proposed a multi-platform analysis approach for the seismic analysis of bridge-foundation-soil systems. Kotsoglou and Pantazopoulou (2009) used an equivalent single degree-of-freedom system to analyze a bridge-foundation-soil system.

2.2 Washington State Department of Transportation Procedure

Since December 2013, WSDOT design guidelines have followed the Caltrans methodology which is based on the works of Martin et al. (2002); Zha (2004); Boulanger et al. (2006); Ashford et al. (2011). In this methodology, lateral spreading problems are divided into two cases, "restrained" and "unrestrained" ground displacement cases. In the restrained ground displacement case it is assumed that the failure soil mass has limited width and its flow is somewhat impeded by the foundation system. In contrast, it is assumed that in the unrestrained case the foundation system does not provide significant resistance to the soil flow due to the large and massive failure mass.

Current WSDOT design and analysis methodology is primarily based on Beam on Nonlinear Winkler Foundation (BNWF) and one- or two-dimensional FE techniques. Although

3D-FE analysis is allowed, its use is uncommon and is typically restricted to special situations. The design process follows the Load and Resistance Factor Design (LRFD) methodology and the design guidelines are specified in the current WSDOT bridge and geotechnical design manuals (WSDOT, 2011a,b). American Association of State Highway and Transportation Officials (AASHTO) specifications for bridge design (AASHTO, 2010b) and seismic design (AASHTO, 2010a) are used to estimate the design loads for which all the substructure elements are designed. Several alternative analysis procedures are made available to the designer to choose based on applicability to particular site conditions, foundation and structure.

In both cases, the first step is to assess the liquefaction potential. Then the residual strength of the liquefied soil is estimated. A simplified 1D foundation model is developed next for BNWF analysis. To account for reduced stiffness and strength of the liquefied layer, the soil-foundation interaction (p-y, t-z and Q-z) curves representing the liquefied soil must be modified using the p-multiplier approach of Brandenberg (2005) or using the undrained shear strength parameters obtained from laboratory tests or available from empirical relationships. The resistances and stiffnesses of the other nonliquefiable soil layers are estimated from field exploration, in-situ testing and lab testing. Group effects are accounted for by multiplying the appropriate group factors in 2D analysis. Group effects for curves in fully liquefied soil layers are neglected after Rollins et al. (2005).

In order to estimate the kinematic demand of laterally spread soil on the pile, different approaches for each case are adopted. For the unrestrained case, since the foundation provides insignificant resistance to the soil flow, displacement estimation does not consider the stiffness of the foundation system at all. In this case the slope stability factor of safety is estimated. If FS $\leq$ 1.05 a flow-type failure is assumed and a typical displacement of 5 ft is applied to the BNWF analysis model. This amount of displacement is assumed to fully mobilize soil strength. If otherwise (FS $>$ 1.05), methods for estimating ground movement - e.g. Bray and Travasarou (2007) or Faris et al. (2006) - are used. For this purpose, the estimated ground displacement is used to perform a lateral spreading pushover analysis.

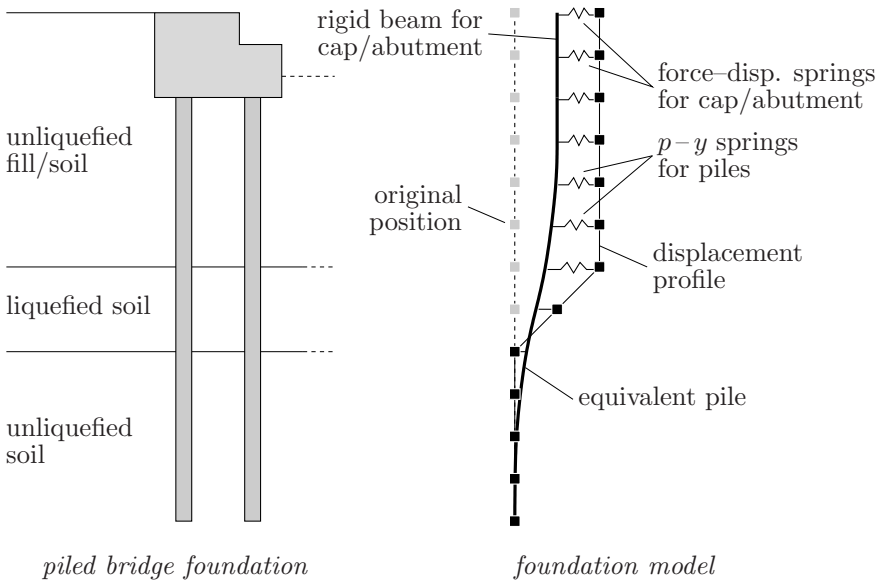

Figure 2.1: Schematic of the BNWF model used to analyze lateral spreading pushover analysis. The axial pile response is considered using t-z and Q-z springs not depicted in the figure (after McGann (2013)).

The imposed displacement profile shown in Figure 2.1 is applied to the foundation model developed previously.

The restrained ground displacement case involves additional steps to estimate the crustal movement. In this case a series of pushover analysis with increasing displacements are performed. For each displacement a running average of the shear force at the center of the liquefiable soil layer is recorded to obtain the lateral spreading pushover curve for the foundation system under consideration. To find a compatible displacement with the shear force in the foundation element, a pseudo-static slope stability model is developed and used to determine the force at the center of liquefiable layer for a series of horizontal accelerations k_h applied as a constant inertial force. The resisting force for which the factor of safety reaches 1.0 is recorded for each applied k_h. Using a Newmark rigid sliding block analysis, displacements of the slope corresponding to each k_h value is determined. Given the resisting force and the slope displacement a force-displacement curve is obtained that together with

the force-displacement curve of the foundation model provide a compatible point at which the displacement and resisting force are equal in both the foundation and the soil mass. This compatible displacement obtained as shown in Figure 2.2 is used to perform the BNWF lateral spreading pushover analysis.

Inertial effects of superstructure elements for the bridge bent are considered by applying an equivalent moment and force pair. This pair is determined based on the design of the bridge columns; considering whether the column is designed to yield and develop plastic hinges before the onset of yielding in foundation elements or otherwise. A more complete description of the Caltrans design guidelines for deep foundations subject to lateral spreading loading conditions can be found in Arduino et al. (2017a).

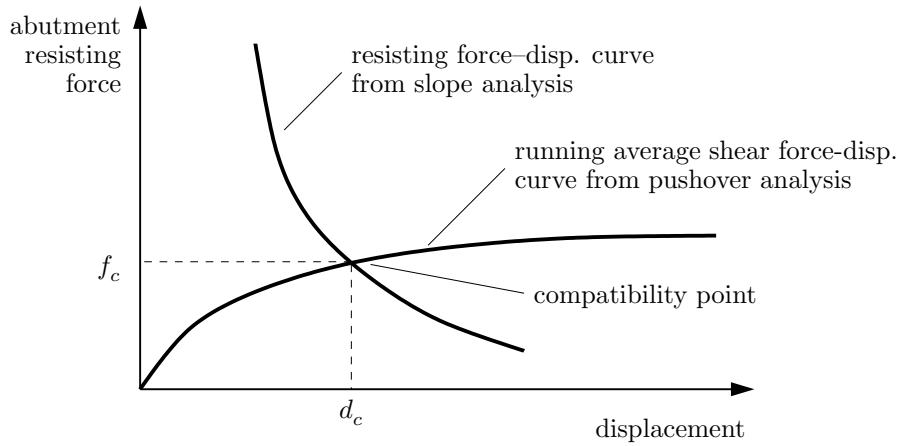

Figure 2.2: Determination of compatible force-displacement state (after McGann (2013))

Chapter 3

SIMPLIFIED 3D NUMERICAL MODEL FOR EVALUATING LATERAL FORCES ON FOUNDATIONS SUBJECT TO LATERAL SPREADING - WSDOT PROJECT

3.1 Introduction

Evaluation of lateral spreading demands on bridge foundations involves several different aspects of structural and soil mechanics. Besides the nonlinear behavior of the foundation structural elements and difficulties in capturing their response, the surrounding soil behavior and soil-pile interaction effects introduce additional complex and nonlinear aspects to the problem. 3D-FE models using appropriate numerical representation of the structure, soil and interface behavior, can be used to simulate lateral spreading induced forces on pile foundations.

Although 3D dynamic analysis of such situations would be ideal for capturing different aspects of lateral spreading, it is an extremely time-consuming and complicated task. Recently, high performance computing and parallel processing have increased the capacity for performing computation intensive tasks like 3D dynamic FE analysis. However the implementation of FE frameworks with parallel processing capabilities is difficult. The parallel version of OpenSees to this date, still suffers from minor problems which impede performing large scale numerical analysis. Moreover, new aspects of boundary conditions, such as absorbing and quiet boundary conditions, become important in dynamic analysis of geotechnical problems. As a result, it is often convenient and practical to perform pseudo-static analysis which are capable of capturing some of the dynamic aspects relatively well. In this chapter, a case study bridge foundation is introduced for performing lateral spreading analysis. The objective of this exercise is to explore the possibility of running simplified pseudo-static analysis

and validate the WSDOT method presented in the previous chapter for an unrestrained case. Later in parts II and III we will explore the possibility of performing dynamic analysis. The idea is to develop tools that can handle both types of analyses.

Similarities between geological conditions along the Pacific ocean in the Northwestern parts of the United States and the Maule region in Chile make post-event site observations of the M_w8.8 offshore Maule earthquake highly valuable. Seismic design of bridges and construction methods in Chile are comparable to the ones currently used in the United States. Therefore site exploration after the Maule earthquake has provided informative observations based on which, recommendations can be proposed to modify the current design codes in the US in order for a safer and more cost-effective design.

The Llacolén bridge was among 7250 highway bridges in Chile subjected to shaking from the Maule earthquake. Except for the collapsed northeastern span, the bridge suffered only minor damage during and after the earthquake. Extensive evidence of liquefaction was seen at the bridge site, especially on the eastern bank of the river which was typical at other locations.

Bridge pier geometry at the northeastern approach of the bridge (where the deck was unseated) makes the study of this pier attractive. Inherent three-dimensional effects due to the pier geometry cannot be captured using simplified methods currently used in design practice. Also, as evidence of liquefaction was seen at the bridge site, lateral spreading of the bank towards the river was suspected to be a major cause of the span unseating. In this study, numerical models are developed to evaluate the effects of three-dimensional geometry of the bridge structure on the response of the foundation to lateral spreading of the surrounding soil. These models are used to assess the validity of state-of-practice design methods currently used for deep foundations subject to lateral spreading with three-dimensional geometric complexities and complement similar studies performed by McGann (2013) on a bridge where 3D site effects were important.

A vast amount of the information used in this study is taken from the reconnaissance report from the *Geotechnical Extreme Events Reconnaissance (GEER)* team who investigated

the affected areas during the March of 2010, almost a week after the event (GEER, 2010). Another major resource for the information comes from the reconnaissance report by the *Transportation Infrastructure Reconnaissance Team (TIRT)* which was organized by the Federal Highway Administration (FHWA) during the April of 2010 (FHWA, 2011). These two teams along with many other reconnaissance efforts provided very valuable post-earthquake information.

3.1.1 Maule Earthquake

On February 27th, 2010 at 03:34 a.m. local time, a M_w 8.8 earthquake hit the coast of Chile as a result of thrust faulting. This was due to steady eastward subduction of the Nazca tectonic plate (also known as the oceanic plate) underneath the South American plate (also known as the continental plate) with a slip rate of about 70 millimeters per year. This situation is very similar to the Cascadia subduction zone along the coasts of Washington and Oregon states in the United States, where the slip rate is about 35 millimeters per year. The difference in slip rate explains why more of these types of events occur in Chile than in the Pacific Northwest. The rupture surface of the fault was about 500 km long and about 100 km wide along the coast of Chile and about 100 km wide.

The earthquake was felt by more than eight million people in the urban areas of central south region of Chile -i.e. Santiago, Valparaíso Viña del Mar and Concepción. About 1.8 million people were affected with about 800,000 displaced (Moehle et al., 2010). Ruegg et al. (2009) estimated that at least 10 m of slip deficit had accrued on the boundary of these plates since the last time this part of the subduction zone ruptured in 1835. Therefore the earthquake was expected to happen. The PGA recorded by a station located on a relatively firm soil and about 3 km away from the Llacolén Bridge was 0.65 g in the North-South direction, 0.61 g in East-West direction and 0.58 g in vertical direction. Another station located on a relatively soft soil about 2 km away from the Llacolén bridge recorded a PGA of 0.40 g in the horizontal direction and 0.28 g in the vertical direction (Boroschek et al., 2012).

Figure 3.1: Lateral spreading and span collapse of northeast approach embankment of Llacolén Bridge (FHWA, 2011).

3.1.2 Llacolén Bridge

Figure 3.2 shows an aerial view of the bridge location. The 2160 m long Llacolén bridge spans the Bío Bío river between the cities Concepción and San Pedro de la Paz. The superstructure, consisting of four traffic lanes and pedestrian sidewalks, is supported by column bents with inverted-T cap beams, which in turn carry the loads from simply-seated, prestressed I-girders forming the deck of the bridge.

During the 2010 Maule earthquake, the Bío-Bío river eastern bank experienced extensive amount of lateral spreading. Although the approach span of the bridge was unseated as a result of lateral displacement (Figure 3.1), unlike many other bridges crossing the Bío-Bío river in the same region, this bridge did not suffer much damage, resulting in other parts of the bridge to remain operable. The bridge consists of 49 spans, not considering the entrance and exit ramps. Bridge bents, typically consisting of six 1.35 m diameter columns, carry the loads of the superstructure. The piers are founded on 1.5 m diameter reinforced concrete drilled shafts which are tied together at the top by a 1.75 m $\times$ 2.5 m rectangular cap beam (Figure 3.3a). This beam also provides the connection between the columns and the piles. Most of the piles are 20.0 m or longer and they extend into a very stiff and dense layer with SPT blow counts of more than 100. Series of precast, pre-stressed reinforced concrete I-girders, which are simply seated on column bents with inverted-T cap beams, form the bridge

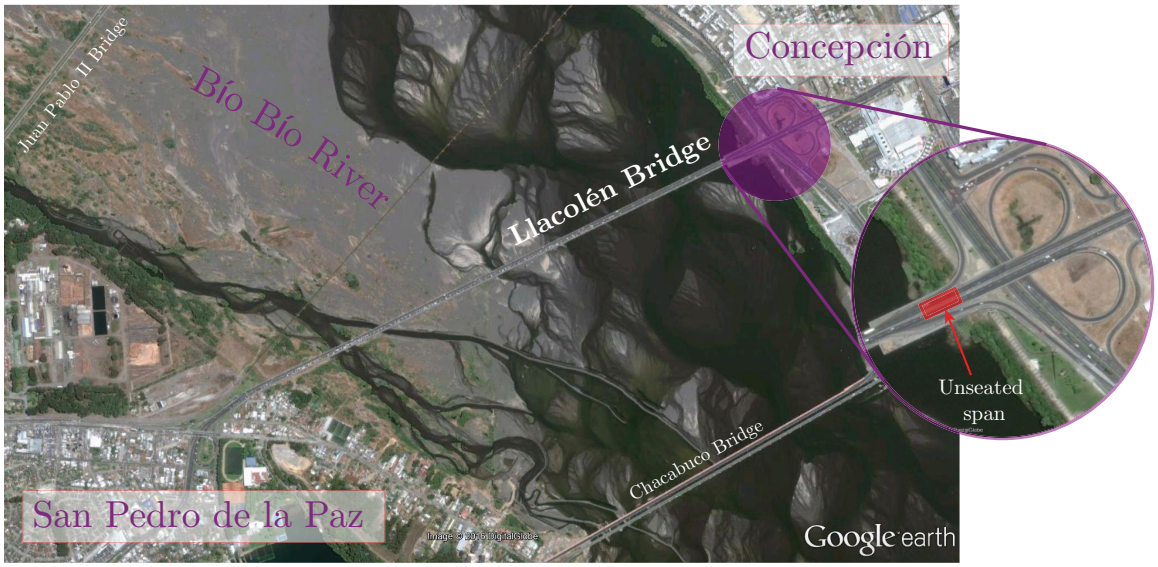

Figure 3.2: Location of Llacolén bridge site. (Latitude: 36°50′4.00″S, Longitude: 73°4′45.07″W) - Photo taken from Google Earth on 5/2/2016

deck. Figure 3.3b shows a schematic of the bridge pier transverse cross section. As shown in this figure, two seismic bars located between each pair of adjacent girders are supposed to provide integrity to the bridge during seismic loading. A 10 cm expansion joint was designed between the deck slab and the bent on each side. Figure 3.4 depicts a cross-sectional view of the bridge deck and the girders at interior spans. The 21 cm thick deck is covered with a 5 cm asphalt pavement for the traffic lanes. A 3.5 m wide pedestrian sidewalk located on the southern side of the bridge deck indicates a non-uniform live load distribution on the deck which is transmitted to the foundations.

Shown in the magnified section in Figure 3.2, the northeast approach of the bridge consists of geometrically complicated entrances and exits. Having all these structures with different stiffnesses converging in one location results in complex loading conditions on the approach pier foundation. This may be one of the reasons why the approach span collapsed, however, evidence of lateral spreading at the site strengthens the slope failure hypothesis.

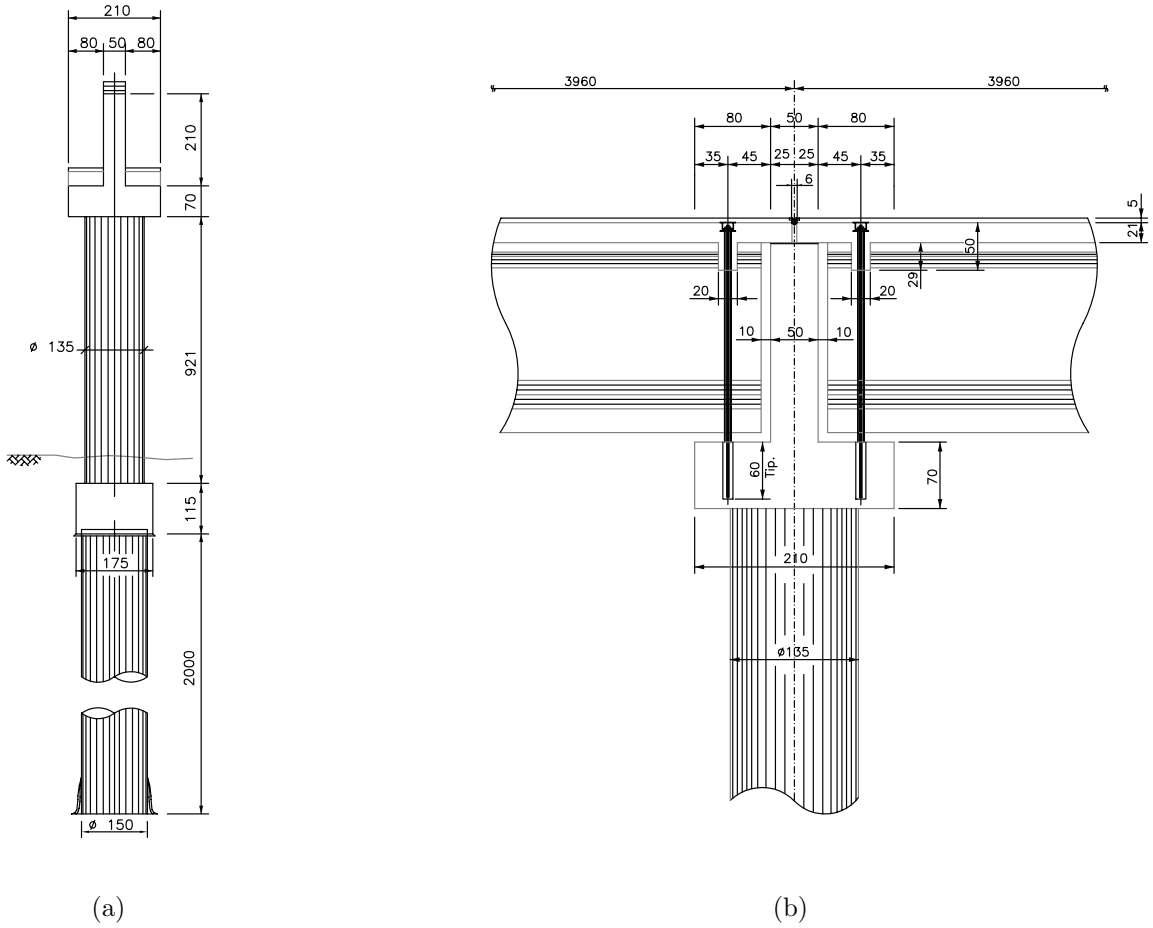

(a) (b)

Figure 3.3: Schematic of (a) bridge approach pier, (b) deck to pier connection. (courtesy Ministerio de Obras Públicas, Chile)

During the earthquake, the northeast approach span of the bridge collapsed. Views from the north and south of the collapsed span as well as the west-bound entrance - which was also nearly unseated - are shown in Figure 3.5. Site investigators observed many flexural cracks on the riverside of the columns which were subject to lateral spreading. These cracks were specifically seen on the pier columns holding the unseated span. These columns are located at the river shoreline and are embedded in the rip-rap. Flexural cracks were seen at the level of rip-rap as well as at the construction joints. A close-up view of these cracks is shown in Figure 3.5. Although unbalanced stiffness of different structures (entrance and exit ramps)

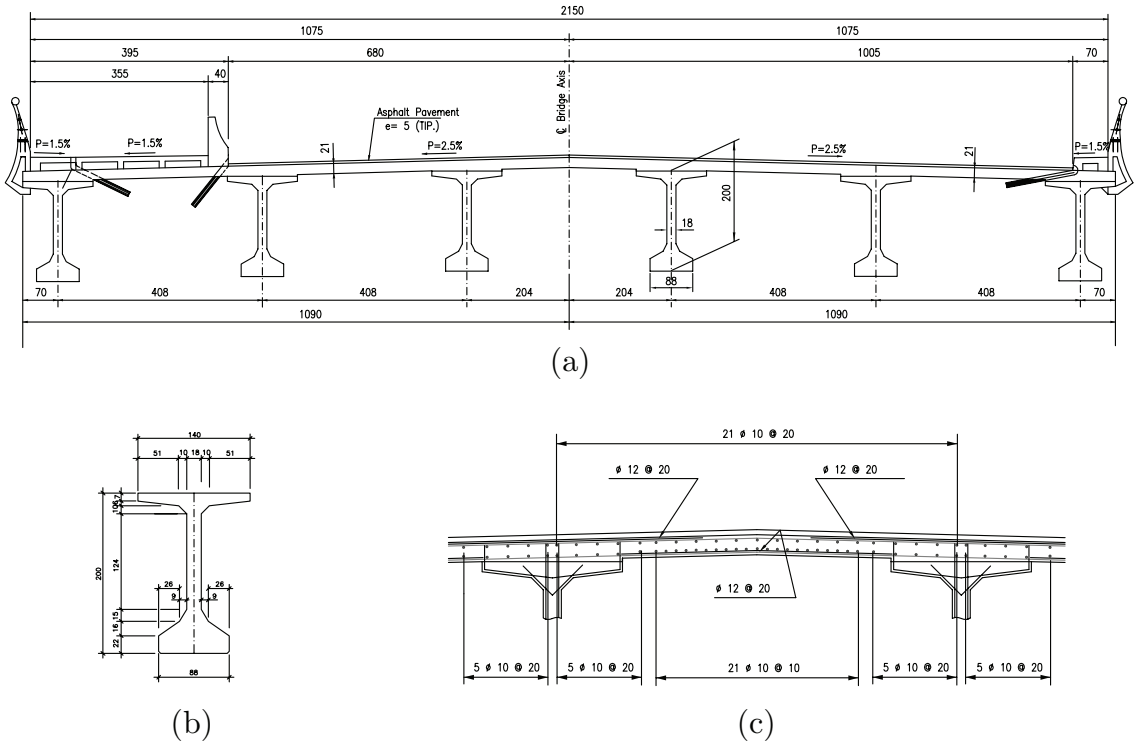

Figure 3.4: Schematic of (a) the bridge superstructure at interior spans, (b) deck girder beam, (c) reinforcement arrangement of deck slab. (courtesy Ministerio de Obras Públicas, Chile)

meeting at the approach span could be a major cause of failure, a liquefaction-induced lateral spreading or slope failure is the most probable cause.

Evidence of liquefaction such as sand boils, liquefaction-induced settlement and several lateral spreading cracks was seen on site after the earthquake. This evidence was wide-spread along the eastern bank of the Bío-Bío river. Liquefaction of the subterranean soil caused exhaustive damage to nearby bridges. As shown in Figure 3.6, the ground surrounding the approach bent settled up to 40 cm. Ground cracks were seen at the bridge site and many sand boils – important indicator of liquefaction – were also seen at the site. The pavement was detached from the approach columns and the resulting gaps were sized from 8 cm to 23 cm. The variation in amount of separation indicates either that the direction of the lateral spreading was not perpendicular to the axis of the bridge pier or that a rotational

View From North

View From South

Fallen Span

Westbound Entrance

River-Side View

Figure 3.5: Structural damage caused by lateral spreading. Different views of the fallen span, the almost unseated west-bound entrance and a view from the riverside of the approach pier.

component exists in the response of the bridge to lateral spreading. The latter deduction seems more reasonable and, as will be presented in the following sections, the 3D-FE model results confirm this observation to be due to the inherent 3D effects of the bridge geometry.

Figure 3.7 shows a LIDAR (Light Detection and Ranging) scan of the two northern-most in-river bridge piers. In this figure locations of the fallen span and the approach pier are marked. The scan shows an obvious outward tilting of the bent columns located in the river immediately next to the unseated span. Parts magnified in the image show the relative displacement of the column head to its visible base. As is symbolically shown on the side of the image, direction of the relative displacements are opposite for the approach pier and the in-river pier. This indicates that the imposed displacements on the subterranean parts of the pier due to lateral spreading was higher for the approach pier than the in-river pier. Another significant conclusion from this observation is that the existence of the bridge deck and the resistance it provides to the whole system is of paramount importance for the analysis.

3.1.3 Hypothetical Failure Mechanism

Based on the observations from post-event explorations and the information given by the LIDAR scan shown in Figure 3.7, a hypothetical failure mechanism that explains many aspects of the observations is proposed. Figure 3.8 shows details of the proposed failure mechanism. In Figure 3.8a the conditions of the pier and its foundation is shown before the loose sand layer liquefied. During ground shaking and liquefaction of the loose sand layer, the upper dry crust was displaced towards the river. As a result, large passive forces were exerted on the approach pier foundation. This resulted in movement of the superstructure and closure of the expansion gaps. The movement of the pier was enough for the deck to be unseated but further movement at the top of the columns was impeded because of the resistance provided by the bridge deck. However, the lower parts were still pushed by the dry crust, resulting in a negative relative displacement between the head and the base of the column. On the other hand, the interior span foundations were not subject to extensive lateral spreading and less lateral movement was induced in the foundation while the superstructure was pushed by the

Ground Cracks at the River Bank

Sand Boils

Settlement at Entrance Piers

Separation of the Pavement

Ground Cracks Extending to the Street

Figure 3.6: Manifestations of liquefaction and lateral spreading at the Llacolén bridge site

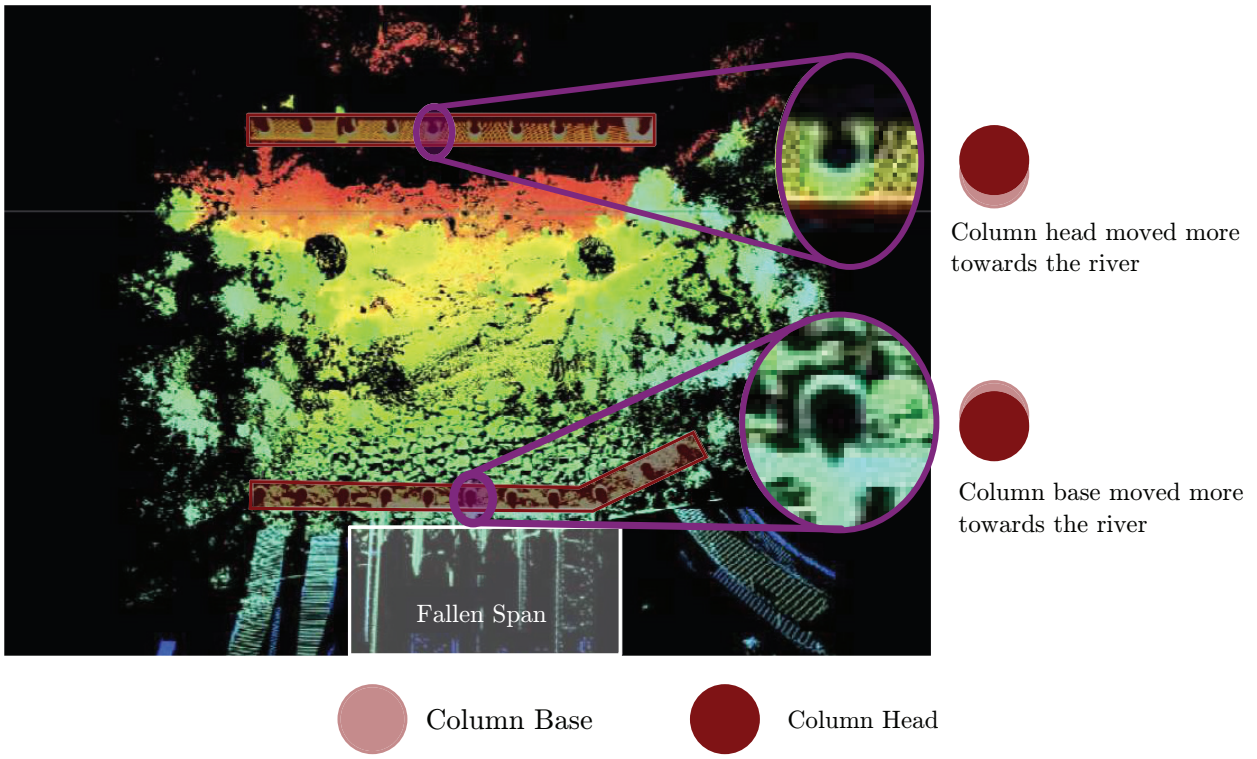

Figure 3.7: LIDAR scan at Llacolén bridge site. Relative movement of the pier columns to their observable base (The bridge deck is digitally removed)

adjacent span, creating a positive relative displacement between the column head and base. This hypothesis explains the observed opposite direction of relative movement between the columns' heads and their visible base in the approach pier and the in-river one. Collapse of the approach span is also justified if the amount of the lateral movement at the top of approach pier was higher than the length provided for the deck to be seated on the pier. The observed flexural cracks on the river-side of the pier columns at the approach pier can be easily explained by the curvature of the resulting lateral displacements in the pier columns.

3.2 Model Development for the Llacolén Bridge

In contrast to the research done by McGann et al. (2015) on the Mataquito river bridge, the Llacolén bridge was chosen as a representative case where soil embankment three-dimensional

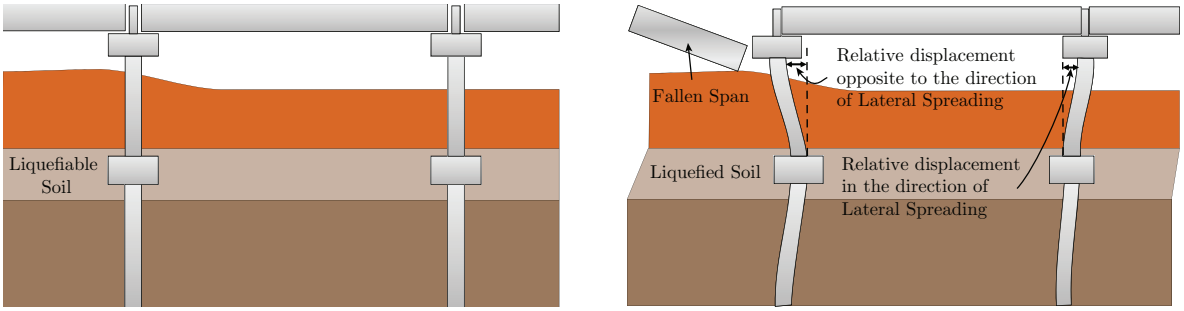

(a) Before (b) After

Figure 3.8: Hypothetical failure mechanism at Llacolén bridge

effects are not present. Instead, the geometry of the bridge approach introduces structural three-dimensional aspects to the response to lateral spreading. Numerical models are therefore developed to assess these three-dimensional effects. For this purpose beam on Nonlinear Winkler Foundation (BNWF) models are developed to test and compare simplified lateral spreading analysis procedures, and 3D finite element models of the northeast approach are used to simulate the local response to lateral spreading kinematic demands and assess potential 3D effects. Both of these models share certain aspects of model development which are described in this chapter. Specific considerations for development of each of these models are explained in Section 3.3.

3.2.1 Development of Idealized Soil Profile

Subsurface information available at the Llacolén bridge site are two series of pre-event Standard Penetration Test (SPT) blow counts and the information gathered after the event by reconnaissance teams and other institutes. First series of pre-event tests were conducted by the Japanese International Cooperation Agency (JICA) in 1993 at four locations along the bridge alignment. A consultant consortium of Systra-Sofretu/Cade Idepe performed six additional standard penetration tests in 1996. Figure 3.9 shows the location of these tests

Figure 3.9: Location of Standard Penetration Tests along the bridge axis. Picture taken from `www.maps.google.com`.

along the bridge axis. Figures 3.10a and 3.10c show the result profiles for these two series of standard penetration tests.

The GEER team conducted three Dynamic Cone Penetration Tests (DCPT) at the bridge site. They reported that the soil above 2 m deep was loose and the penetration was refused at a depth of 2.2-3.0 m. They also performed a LIDAR (Light Detection and Ranging, Terretrial Laser Scanning) scan of the bridge and an SASW (Spectral Analysis of Surface Waves) test. The GEER team categorized the soil at the site as relatively uniform, consisting of very dark gray to black, medium to coarse grained sand with traces of fine gravel. Figure 3.11 depicts the data from their explorations.

Requested by University of California at Berkeley, el Centro de Investigación Desarrollo e Innovación de Estructuras y Materiales, IDIEM (the Center for Research, Development and Innovation of Structures and Materials), performed an additional SPT and two CPT tests. Figure 3.10b shows the SPT resistance profile and Figure 3.13 shows CPT penetration

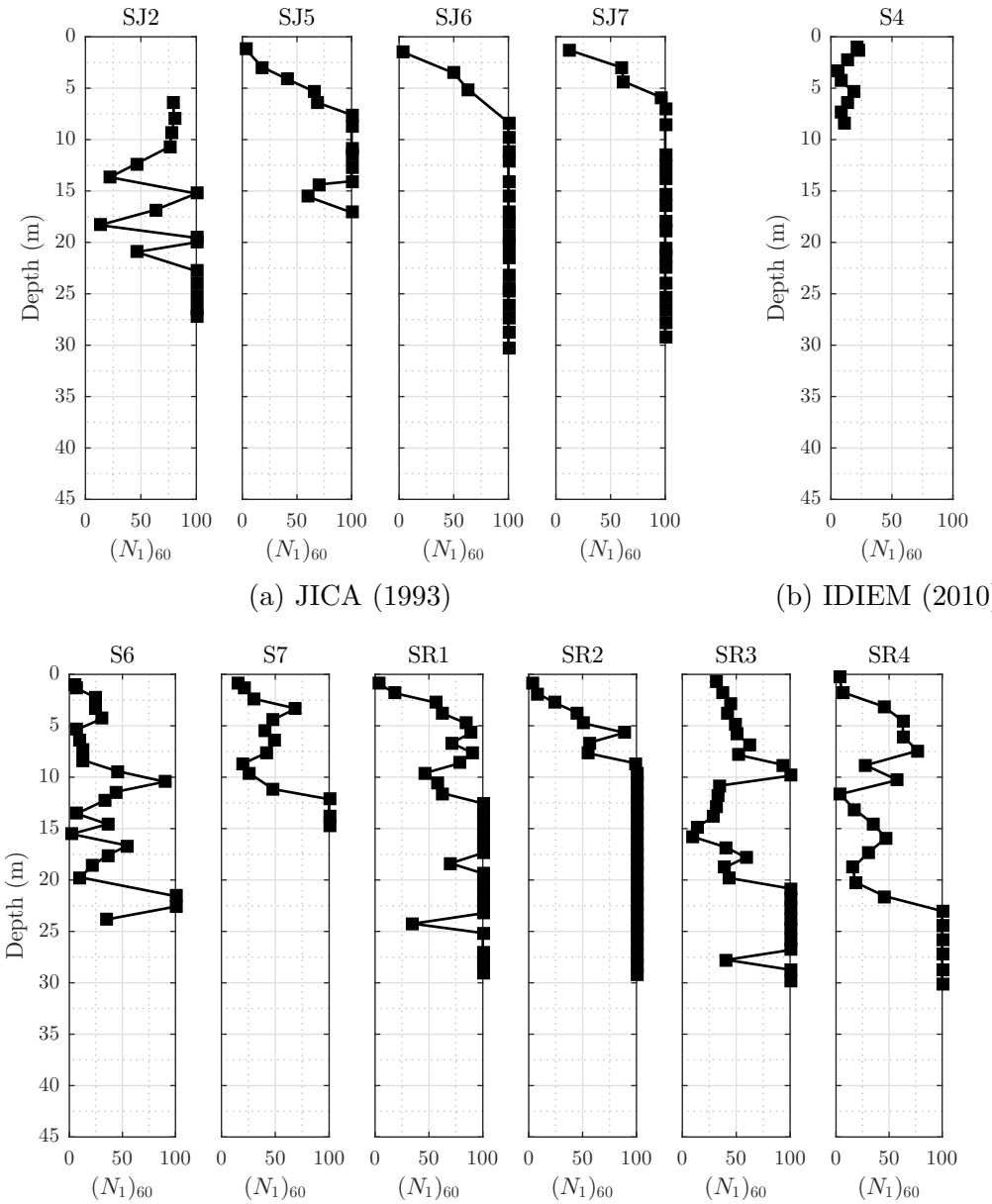

(a) JICA (1993)

(b) IDIEM (2010)

(c) Consultant consortium (1996)

Figure 3.10: SPT resistance profiles for subsurface explorations at Llacolén bridge site.

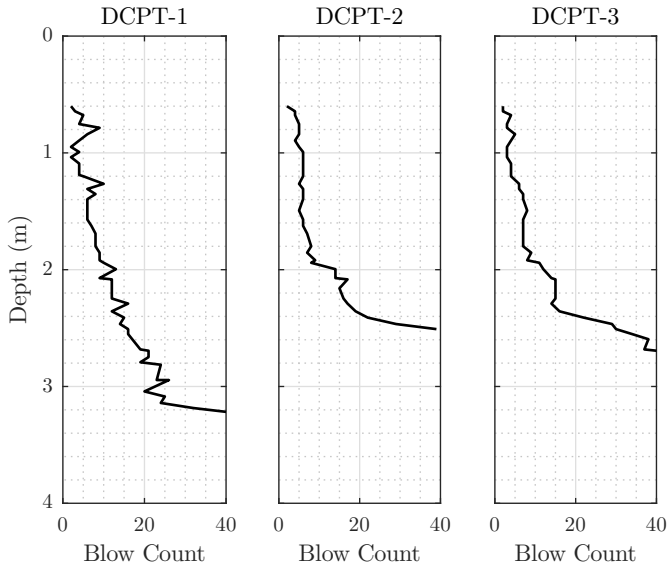

Figure 3.11: Dynamic Cone Penetration Test (DCPT) resistance profiles at Llacolén bridge site after the 2010 Maule earthquake.

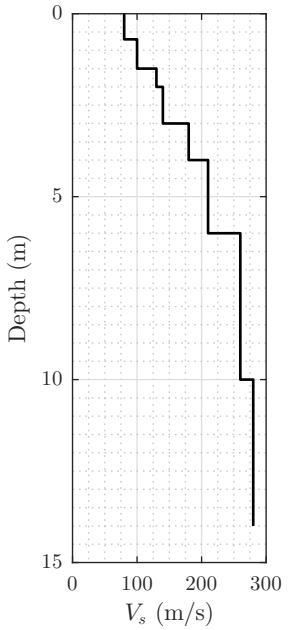

Figure 3.12: Shear wave velocity profile at Llacolén bridge site after the 2010 Maule earthquake obtained using SASW Method.

Table 3.1: Soil description at Llacolén bridge site (GEER, 2010).

Height		Description
Top (m)	Bottom (m)	
0.00	3.00	Gray medium sand, homogeneous structure, average compactness
3.00	5.00	Brown medium sand, homogeneous structure, brick particles are observed at 5.00 m
5.00	7.45	Gray medium sand, homogeneous structure, low compactness, no plasticity.

No water table detected.

Table 3.2: Grain size distribution of soil samples at Llacolén bridge site (GEER, 2010).

Sample Depth (m)	1.00-1.45	1.75-2.20	4.00-4.45	4.75-5.20	7.00-7.45
USCS Class	SP-SM	SP	SP-SM	SM	SM
D_{10} (mm)	1.03	0.93	-	-	-
D_{30} (mm)	0.40	0.37	0.35	-	0.37
D_{50} (mm)	0.61	0.58	0.61	0.33	0.59
D_{60} (mm)	0.72	0.71	0.74	0.46	0.68
C_u	0.70	0.76	-	-	-
C_c	0.22	0.21	-	-	-

resistance profiles obtained by IDIEM. In order to perform the CPT tests, IDIEM excavated the dense sand layers to allow for the penetration of the cone. This gave IDIEM an opportunity to get samples from the soil and perform grain size distribution analysis as well. It is worth mentioning that the CPT test at this site ended at a depth of 3.25 m because the cone resistance reached higher than 30.0 MPa indicating a granular material was encountered. Based on their observations, stratification of the soil layers are summarized in Table 3.1.

Using this information an idealized soil profile is obtained to be used in the development of the numerical models of the Llacolén bridge's northeast bent. Pre-event information is used

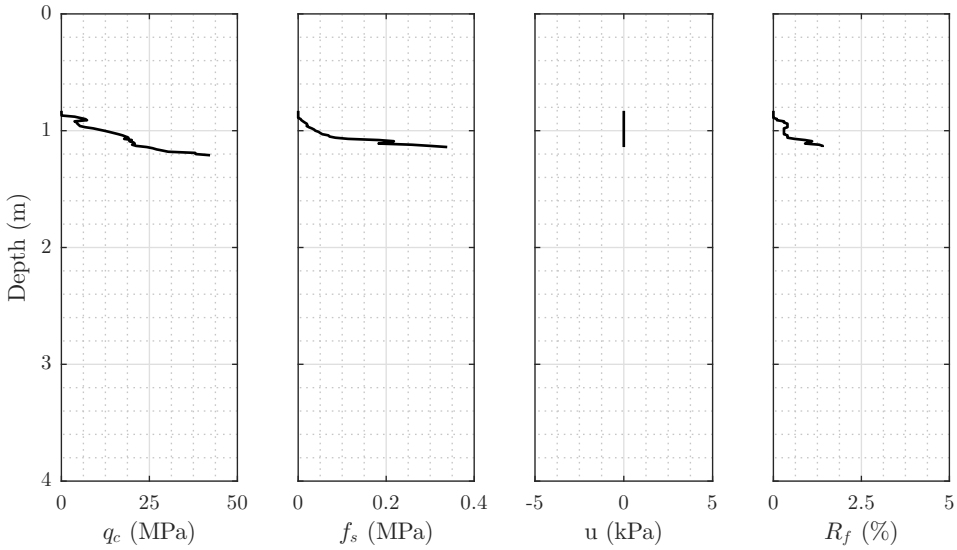

(a) CPT-9

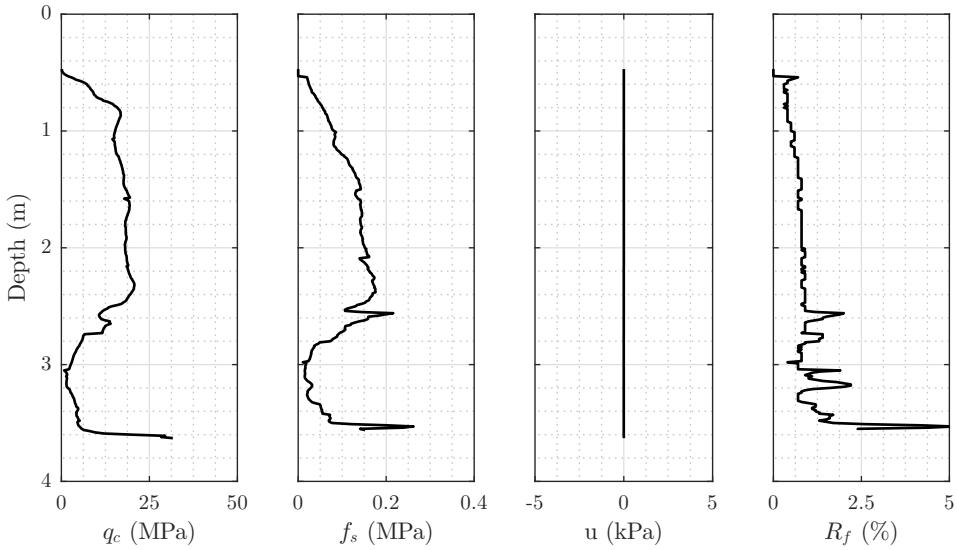

(b) CPT-10

Figure 3.13: Cone Penetration Test (CPT) resistance profiles at Llacolén bridge site obtained by IDIEM.

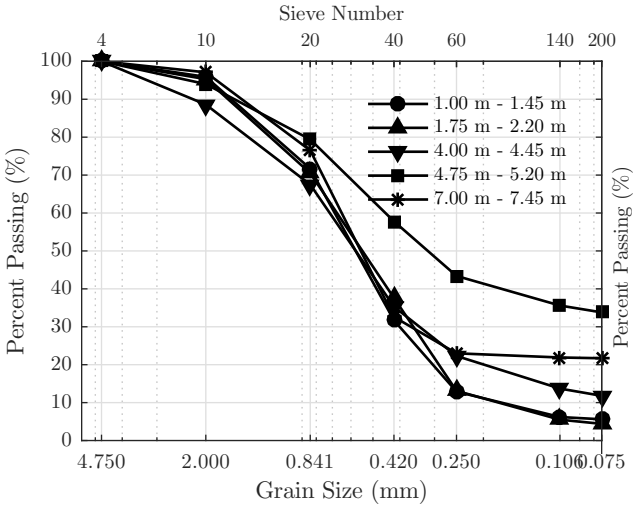

Figure 3.14: Grain size distribution of soil samples at Llacolén bridge site (GEER, 2010).

for soil profile generation to disregard any soil disturbance due to liquefaction densifications. Some of the post-event information is used in different aspects of parameter identification for the soil as well. Figure 3.3b shows a longitudinal profile of the subsurface strata along the bridge axis and the location of the pre-event SPT experiments. The corresponding SPT resistance profiles are shown in Figure 3.10. The soil description provided by IDIEM (Table 3.1) indicates that the shallower parts of the soil are predominantly cohesionless. Although boring logs are not available for deeper soils at the site, boring logs at the adjacent bridge, Puente Juan Pablo II, indicate that the soil profile is generally non-plastic and cohesionless. For the purposes of the numerical models, minor variations in the soil profile are ignored and all materials are assumed to be cohesionless. The groundwater table is assumed to be at the average annual level of the river flow and all of the soil below the groundwater table is assumed to be saturated.

Based on the available subsurface information, the profile can be divided roughly into four soil layers, an upper loose sand layer, a middle layer of denser sand over a layer of medium dense sand and an underlying dense gravel layer. A weighted average SPT resistance value is calculated for each layer from the data illustrated in Figure 3.10. Representative friction

angles, ϕ, for each layer are estimated from the SPT values using the correlation proposed by Kulhawy and Mayne (1990). Estimated properties for the site soils are summarized in Table 3.3.

Liquefaction Potential Assessment

Susceptibility of the soil to liquefaction at the Llacolén bridge site is assessed using the procedure proposed by Youd et al. (2002). The nearest available ground motion to the Llacolén bridge site recorded a peak ground acceleration (PGA) of 0.65 g (Boroschek et al., 2010). Based on the available grain size distribution data for the upper parts of the soil profile, fines content fall in the range of 5% to 33%. An SPT resistance of 26 is shown to be the threshold value indicating if a soil in this site liquefactied. Based on this analysis, the saturated portion of the upper loose sand layer is shown to be susceptible to liquefaction. The assessment procedure by Youd et al. is only valid up to depths of 15 meters. Therefore the points below 15 meters are not considered in this analysis although they might be subject to liquefaction. This assumption is not necessarily representative of actual conditions at the Llacolén bridge site but for the purposes of this research is acceptable.

Constitutive Modeling of Site Soils

In this part of the study, the constitutive models proposed by Elgamal et al. (2003) are used for the analysis of northeast approach of the Llacolén bridge. This family of constitutive models use nested yield surfaces to capture plasticity behavior and are available in pressure dependent (Drucker-Prager type), PDMY, and pressure independent (J2 type), PIMY, variants. The Pressure independent constitutive model is used for the liquefiable layer to represent an almost incompressible soil layer, and pressure dependent models are used to represent the behavior of all cohesionless soil. The input parameters for each soil type are summarized in Table 3.4.

Table 3.3: Model properties for soil layers in the idealized soil profile.

	Soil Type	ρ (Mg/m^3)	ϕ (°)	G_{max} (MPa)	K_{max} (MPa)	e	ϕ_{pt} (°)
	Loose sand	1.7	33	10.3	30.8	0.77	29
	Dense sand	2.0	35	20.5	44.4	0.65	26
	Med. dense sand	1.8	32	10.3	26.7	0.77	26
	Gravel	2.1	42	41.0	80.0	0.55	26

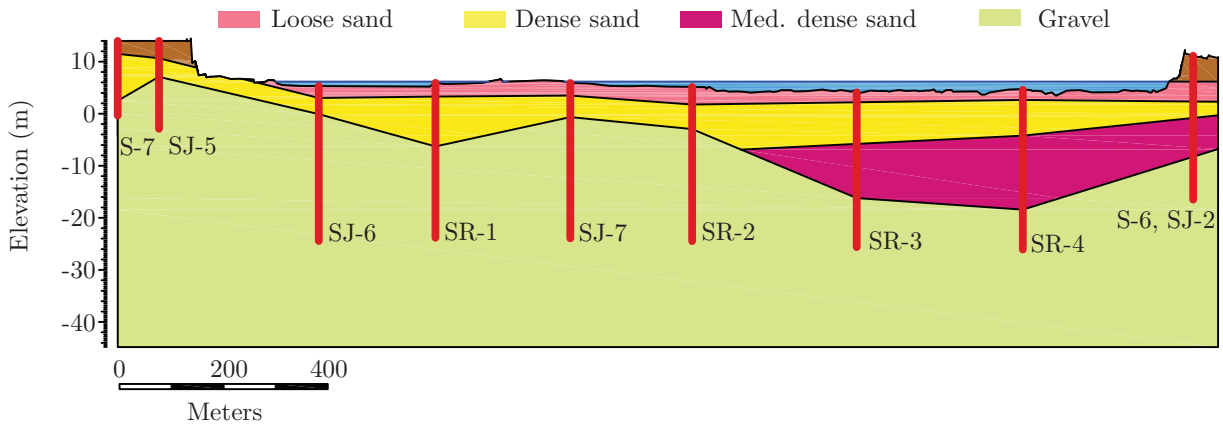

(a) Elevation view of idealized soil profile with location of SPT locations.

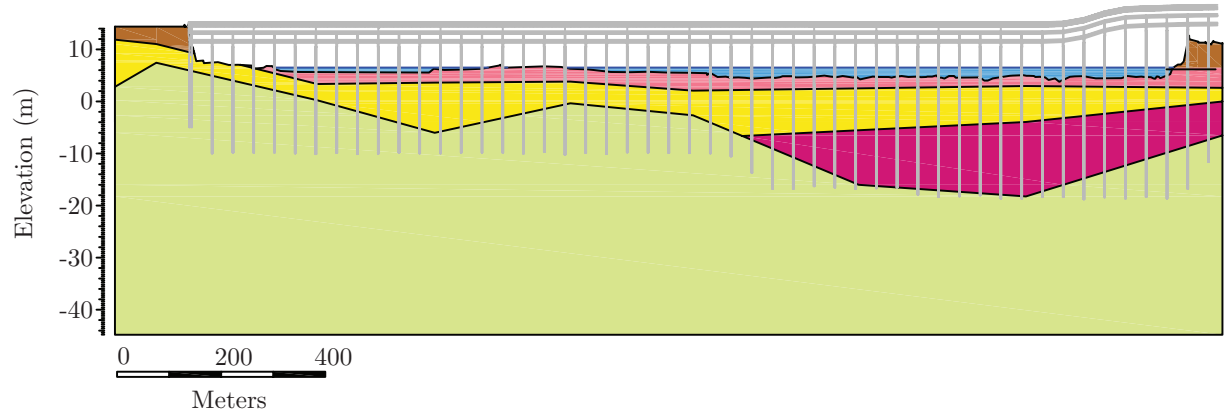

(b) Elevation view of the idealized soil profile with the longitudinal view of the bridge.

Figure 3.15: Elevation view of idealized soil profile along with location of SPT boreholes and longitudinal bridge profile at Llacolén bridge site (Vertical scale increased).

Table 3.4: Contraction and dilation input parameters used for PDMY constitutive model for each soil type.

Soil Type	c_1	c_2	c_3	d_1	d_2	d_3
Loose sand	0.067	5.0	0.23	0.06	0.0	0.27
Dense sand	0.028	5.0	0.05	0.1	0.0	0.05
Med. dense sand	0.067	5.0	0.23	0.06	0.0	0.27
Gravel	0.013	5.0	0.0	0.3	0.0	0.0

3.2.2 Foundation Modeling Approach

Fiber sections are used to incorporate the cross-sectional behavior of foundation elements in the finite element model. Uniaxial material models govern the behavior of these fiber sections. As shown in Figure 3.16, the pier consists of 11 columns and an inverted-T beam on which the girders are seated. This beam is modeled with displacement-based beam-column elements using properties that are calculated based on the geometry of the beam shown in Figure 3.3b. The same type of element is used to model the columns and foundation shafts. Pier columns are made of 1.35 m circular sections with two different reinforcement layout (Figure 3.17a). The moment-curvature behavior of these sections under the assumed axial force is shown in Figure 3.18a. The foundation shafts are 1.5 m diameter circular sections with four different types of reinforcement arrangement(Figure 3.17b). Figure 3.18b depicts the moment-curvature diagrams of each of these sections. An empty circular region along the columns and piles representing the area occupied by the these elements is incorporated into the 3D finite element models. The interface between these elements and the surrounding soil elements is modeled using beam-solid contact elements (Petek, 2006). The cap beam which connects the piles to the columns is modeled with solid elements and an elastic constitutive model is assigned to these elements.

The bridge deck geometry (Figure 3.4) is not explicitly modeled in the numerical models, instead a linear elastic spring is used to represent the effects of the presence of the bridge deck and expansion joints. The constitutive behavior of the spring considers the existence of a gap

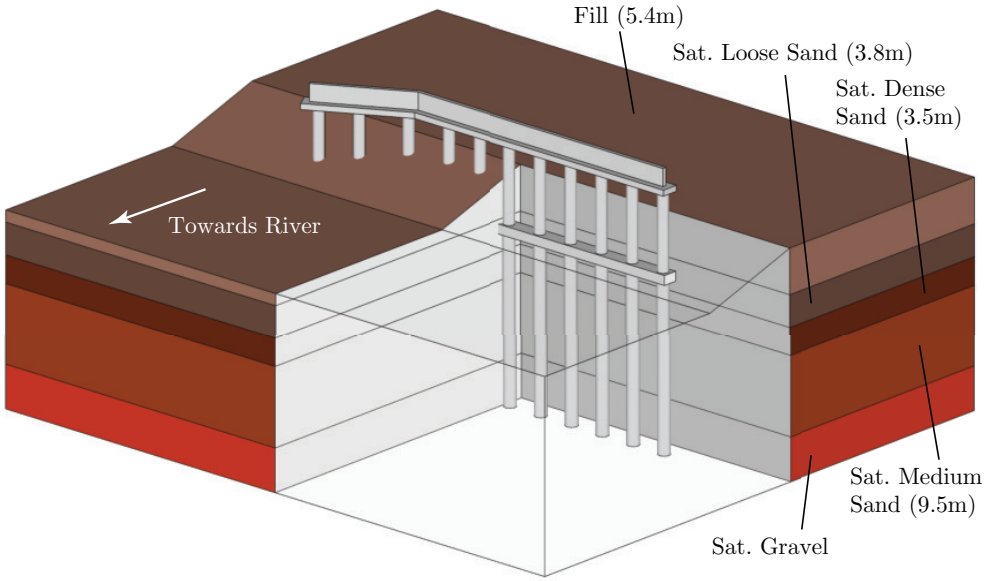

Figure 3.16: Schematic of the northeast approach of the Llacolén bridge with idealized soil profile.

which when closed acts in compression. The spring considers zero tensile and compressive stiffness if the gap is open. Based on the deck geometry and the reinforcement details of the deck shown in Figure 3.4, a gross cross-sectional area and a composite stiffness can be calculated for the bridge deck. Assuming a smeared reinforced concrete elastic modulus of $E_{deck} = 63.2$ GPa, and using the span length of 21 meters, a stiffness of $k = EA/L$ can be calculated for the deck spring. Assuming equal tributary area for each of the pier columns, the area A is divided by the number of columns and a spring is defined for each column. These springs are connected to the head of the columns on one side and are assumed fixed in the other side. The gap is assumed to be almost equal to the sum of the openings of the expansion joints on each side of the pier which is 10 cm.

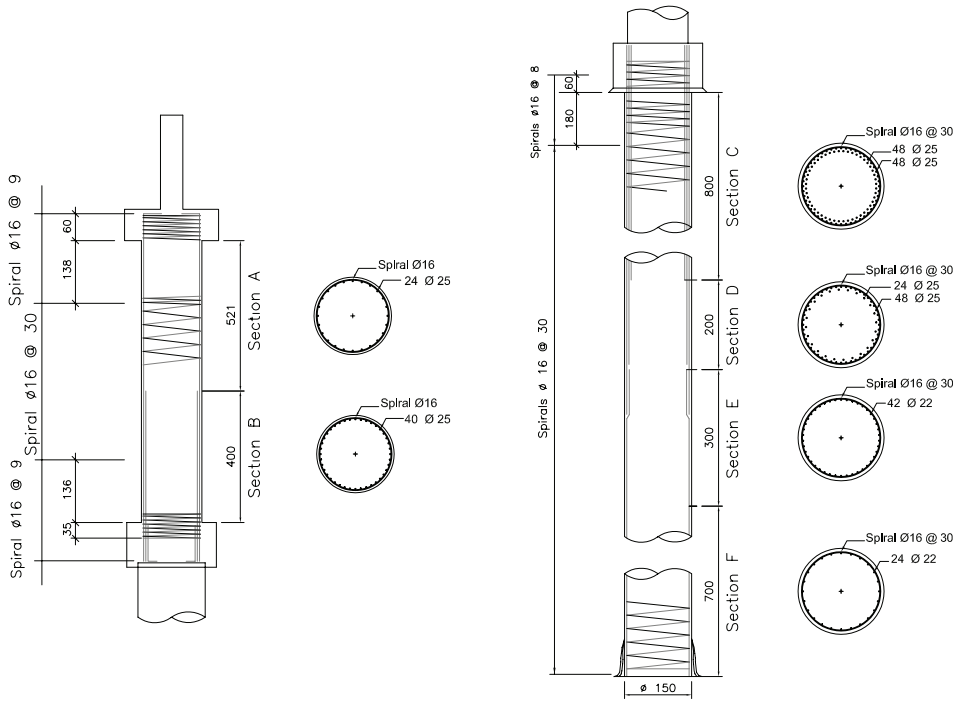

(a) (b)

Figure 3.17: Construction detail of the Llacolén bridge foundation shafts and pier columns.

3.3 Simulation and Assessment of Effects of Lateral Spreading on Northeast approach to Llacolén Bridge

As discussed in Section 3.1.2 extensive evidence of liquefaction and lateral spreading was observed on the eastern bank of the Bío Bío river in the vicinity of Llacolén bridge. Moreover, the shape of the northeast approach provides an opportunity to assess three-dimensional structural effects on the response of the bridge approach to lateral spreading. For this purpose, two types of numerical models are used: (1) the pile pinning analysis procedure involving a BNWF model of the foundation system, and (2) a 3D finite element model of the bridge approach. The following sections discuss details on the development of these models and presents results from the numerical simulations. Analysis and comparison of the results from the simplified and 3D numerical simulations are also included at the end of the chapter.

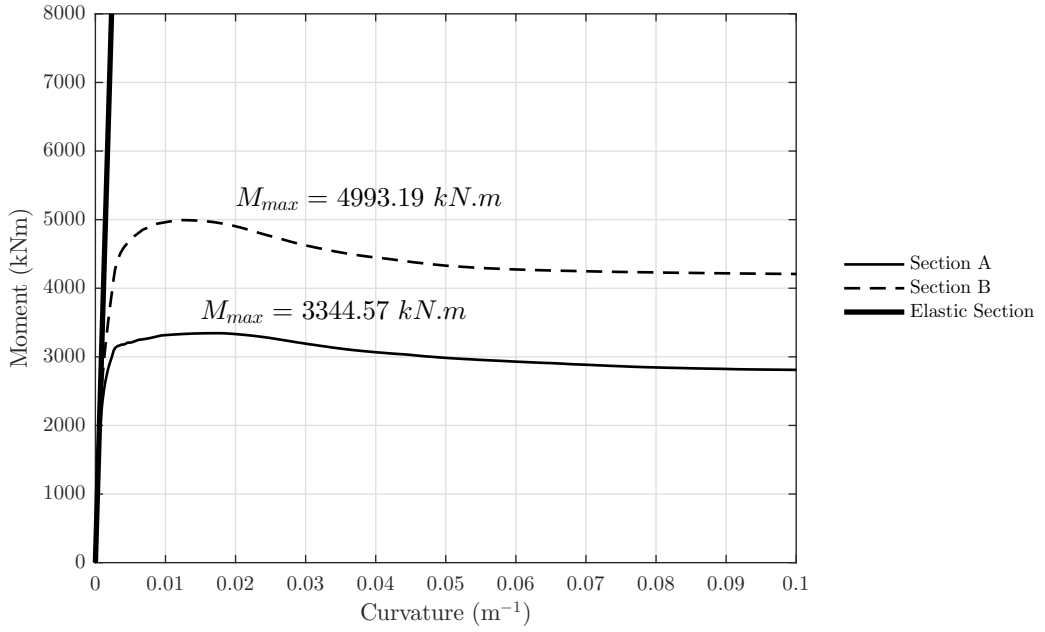

(a) Pier column sections A and B.

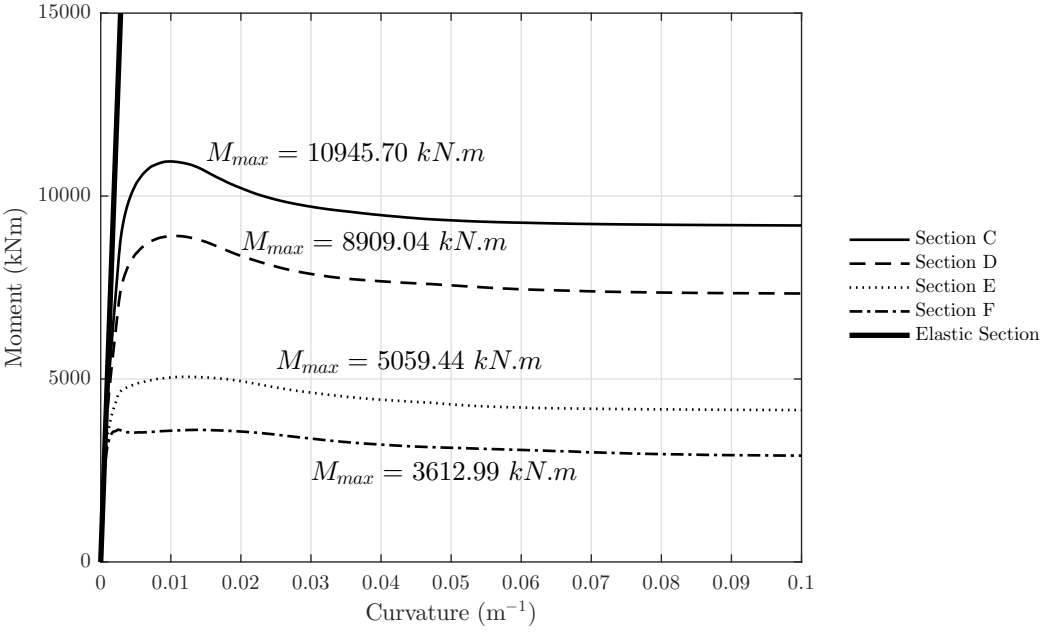

(b) Foundation pile sections C, D, E and F.

Figure 3.18: Model moment-curvature curves for different sections of the Llacolén bridge foundation pile and pier column at design axial force. Equivalent elastic section stiffness is shown as the initial tangent to moment-curvature response.

Due to the length of the bridge and the large number of bridge spans two-dimensional plane strain simulations are not included in this study.

3.3.1 Pile Pinning Model Development

As indicated before, the Llacolén bridge fits the case where three-dimensional soil effects are not applicable. Therefore, following the Caltrans (2011) procedure for unrestrained ground displacement cases presented in Section 2.2, the pile pinning model of the northeast approach is created. The purpose for development of this model is to assess the viability of this design procedure through comparison with the observations made at the bridge site and results from the 3D finite element models. Therefore a BNWF model of the foundation is developed using a representative shaft model and definition of *p-y* curves that appropriately capture the soil-shaft interaction for the idealized soil profile, liquefied layer and group effects.

Development of Foundation Model

The northeast approach pier foundation consists of 11 piles located side-by-side, three diameters apart and tied together with a cap beam. The cap beam is located in the liquefiable layer and is not likely to provide much resistance to lateral spreading. Each pile is made of reinforced concrete with four different reinforcement arrangements along their length resulting in four sections with different capacities and moment-curvature behavior. The approach bent is made of 11 pier columns which are partly embedded and each consist of two different sections (Figure 3.18). The moment-curvature diagrams of these sections are scaled per Caltrans recommendations to convert the foundation system into an equivalent shaft.

Both linear elastic shaft response and nonlinear inelastic shaft response are considered and a separate model is created for each case. The properties for the linear elastic shaft are determined using the initial bending stiffness seen in the moment-curvature plots of Figure 3.18, and geometry of the sections. For a single pier column section the initial bending stiffness is $EI = 3.473$ GN.m^2 which along with the gross second moment of area for a single shaft, $I_g = 0.163$ m^4, results in an elastic stiffness $E = 21.3$ GPa. Assuming a

Table 3.5: Properties of linear elastic equivalent beam model for grouped shaft foundation.

	Parameter	Single Shaft	Equivalent Shaft
Pier Columns	E	21.30 GPa	21.30 GPa
	I	0.16 m^4	1.79 m^4
	A	1.43 m^2	15.75 m^2
	G	8.52 GPa	8.52 GPa
Foundation Piles	E	19.00 GPa	19.00 GPa
	I	0.25 m^4	2.73 m^4
	A	1.77 m^2	19.44 m^2
	G	7.60 GPa	7.60 GPa

Poisson's ratio of 0.25, this elastic stiffness gives a shear modulus of $G = 8.52$ GPa. Similarly for the foundation piles $EI = 4.722$ GN.m^2, $I_g = 0.249$ m^4 resulting in $E = 19.0$ GPa and $G = 7.6$ GPa. Table 3.5 presents a summary of the linear elastic equivalent shaft properties. The moment-curvature diagrams for single nonlinear shaft sections are scaled by the number of piles in the group to provide equivalent single shaft properties.

Since the group of piles in the northeast approach of Llacolén bridge is a side-by-side arrangement except for the three northern piles that are located eccentric to the group axis, no rotational spring is considered in the BNWF analyses to represent the rotational stiffness due to group effects. Eccentricity of the northern three piles introduces some local rotational stiffness, however it is assumed that this stiffness is negligible compared to global response of the bridge bent.

A linear compressional spring is used at the column head to represent the existence of the bridge deck. This spring incorporates a gap, meaning it exerts no force to the foundation system before its closure. As the gap is closed, the spring acts in compression and simulates a linear elastic deck section. Stiffness of this spring is calculated using the elastic properties of the deck and its geometry.

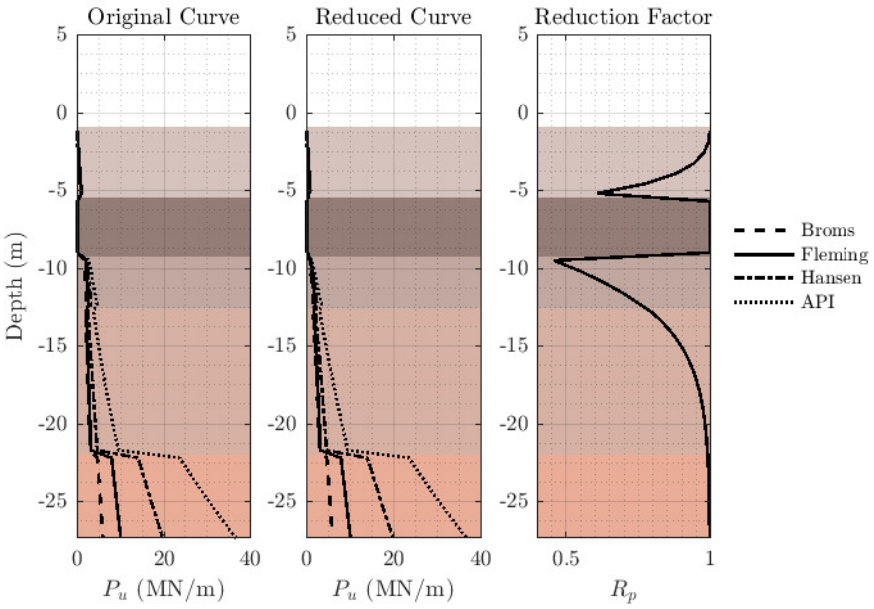

Figure 3.19: Calculated p_u for definition of p-y curves. Effects of liquefied soil layer on neighboring layers p_u applied based on procedure proposed by McGann et al. (2012).

Definition of p-y curves

Soil-pile interaction in BNWF analysis is represented through series of p-y curves defined based on the idealized soil profile. Necessary parameters to define these curves are the ultimate lateral resistance, p_u, and initial stiffness, k_T. Four distinct methods for calculation of p_u based on the idealized soil profile properties are used here: (1) method by Broms (1964), (2) method by Fleming et al. (1985), (3) method by Brinch Hansen (1961) and (4) method by API (1987). Figure 3.19 shows the calculated values of p_u for each of these methods along with the reduced values due to the presence of a liquefiable layer as recommended by McGann et al. (2012). Although there is a great discrepancy among the values of p_u calculated using each of these methods specially at depth, in this case the results are less impacted by the variance of p_u, since the liquefiable layer, where most of the deformations happens, is close to the surface.

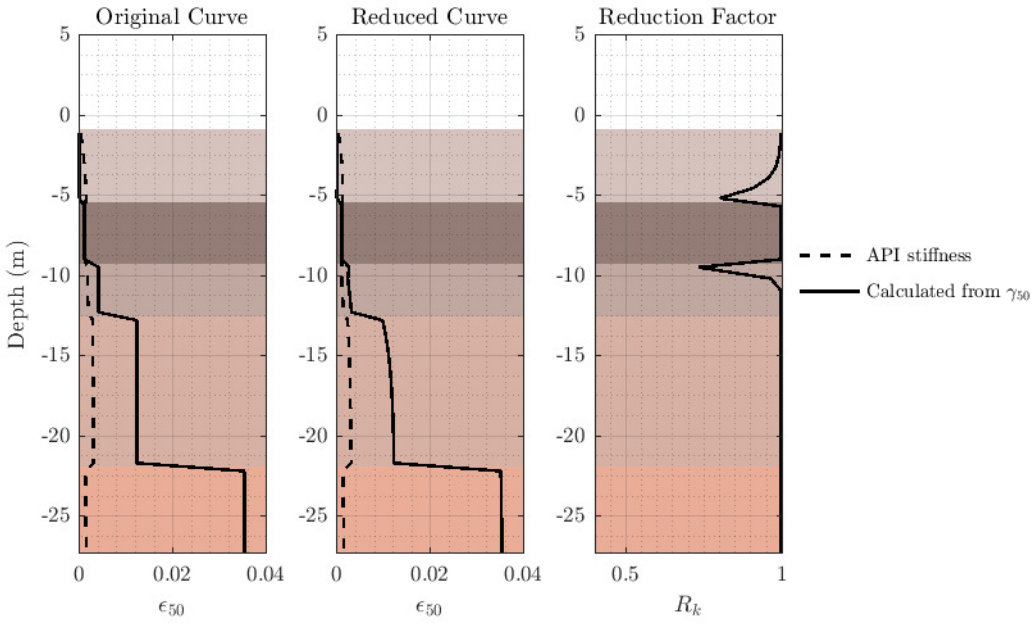

Figure 3.20: Comparison of ϵ_{50} values based on the stiffness proposed by API and calculated based on γ_{50}. Effects of liquefied soil layer on neighboring layers ϵ_{50} is applied based on the procedure proposed by McGann et al. (2012).

The API (1987) method recommends an empirical relationship for the initial stiffness, k_T, of $p - y$ curves. Another method for calculating this parameter is using the modulus reduction of the idealized soil material and relating the strain at which the shear stiffness is reduced to half the original value, γ_{50}, to ϵ_{50} which is the strain at which half the strength is mobilized in a conventional triaxial compression test. Then the initial stiffness is calculated using the semi-empirical equation $y_{50} = 2.5D\epsilon_{50}$ and the definition of the p-y curve, where y_{50} is the displacement at which half the p_u is mobilized and D is the pile diameter. Figure 3.20 illustrates the comparison between these two methods along with the reduced curves as proposed by McGann et al. (2012).

Caltrans (2011) recommends to use group efficiency factors, e.g. Mokwa and Duncan (2001), to incorporate the loss of efficiency of piles due to group effects. However this procedure is less applicable to side-by-side pile groups where only one row of piles exists. For

side-by-side pile groups, Reese and Van Impe (2010) suggests using an efficiency factor of

$$e = \begin{cases} 0.64\,(s/D)^{0.34} & 1 \leq s/D \leq 3.75 \\ 1.0 & s/D \geq 3.75 \end{cases} , \tag{3.1}$$

where s is the spacing between the piles. The group effect p-multiplier for the equivalent shaft model is computed as the product of number of piles with the group efficiency factor

$$p_{group} = 11 \times 0.93 = 10.23\,. \tag{3.2}$$

The residual strength of the liquefiable soil is computed using the undrained shear strength hybrid expression proposed by Kramer (2008) per Caltrans recommendation

$$S_{ur} = 2116 \exp\left(-8.444 + 0.109\,\overline{N} + 5.379\left(\frac{\sigma'_m}{2116}\right)^{0.1}\right) , \tag{3.3}$$

where S_{ur} is the undrained shear strength (in psf), σ'_m is the mean vertical effective stress (in psf), and $\overline{N}$ is the average $N_{1,60}$ which is the corrected SPT blow count. For $N_{1,60} = 10$ and $\sigma'_v = 106$ kPa, the undrained shear strength of the liquefiable layer is equal to $S_{ur} \approx 15$ kPa.

Deformation Analysis

Ground crust displacement due to liquefaction of the subterranean layers is needed to define the displacement profile resulting in lateral spreading. Caltrans (2011) recommends using either the Newmark-based method by Bray and Travasarou (2007) or the procedure by Faris et al. (2006) which is based on strain potential[1]. Estimated ground displacements, d (in cm),

[1]Bray recommends not using the method by Bray and Travasarou (2007) for estimating lateral spreading displacements (Kramer 2018, personal communication).

Table 3.6: Displacements estimated using Bray and Travasarou (2007) procedure.

k_y (g)	$d_{16\%}$ (cm)	d (cm)	$d_{84\%}$ (cm)
0.05	88.7	171.6	332.1
0.1	35.8	69.3	134.0
0.15	18.1	35.1	67.9
0.2	10.5	20.3	39.3
0.25	6.6	12.8	24.7
0.35	3.1	6.0	11.5
0.45	1.7	3.2	6.2
0.55	1.0	1.9	3.7
0.65	0.6	1.2	2.3

using the expression presented by Bray and Travasarou (2007)

$$\begin{aligned}\ln(d) = &- 0.22 - 2.83\ln(k_y) - 0.333(\ln(k_y))^2 + 0.566\ln(k_y)\ln(\text{PGA}) \\ &+ 3.04\ln(\text{PGA}) - 0.244(\ln(\text{PGA}))^2 + 0.278(M-7) \pm \epsilon\,, \end{aligned} \tag{3.4}$$

using a peak ground acceleration, PGA $= 0.65g$ and moment magnitude, $M_w = 8.8$ are summarized in Table 3.6 for different k_y values. The value of k_y needs to be estimated using some slope stability analysis method.

The second method by Faris et al. (2006) requires computation of the Displacement Potential Index (DPI) which is the integral of the strain potential within the liquefiable layer, that is $DPI = \int_{liq\ layer} \gamma_{max}\, dz$ where z is a depth measure. The amount of ground deformation is then estimated as

$$d_{max}(m) = [DPI(m)]^{1.07}\ . \tag{3.5}$$

Wu (2002) gives a relationship between $N_{1,60}$ and the estimated cyclic stress ratio, CSR, corrected for earthquake magnitude. Using a magnitude corrected CSR of 0.3 and a corrected SPT blow count of 10, this relationships results in a $\gamma_{max} = 0.36$. This results in a maximum ground displacement of $d = 140.0$ cm. Such large displacements mobilize the passive resistance of the soil completely and the structural demands become insensitive to the

amount of displacement. Therefore a displacement of 100 cm is considered for the BNWF analyses.

Assessment of Foundation Performance

The final stage in the pile-pinning analysis is applying the displacement profile to the equivalent BNWF model and assess the foundation performance under such loading conditions. Estimated p_u values using different methods result in slightly different foundation demands. Figure 3.21 shows the shaft displacement profile, shear force diagram and bending moment diagram resulting from lateral spreading BNWF pushover analysis using each of the methods for estimating p_u values. In this figure a deck spring with a 10 cm gap is considered and initial stiffness of p-y curves are calculated using γ_{50}. This figure shows that BNWF results are relatively insensitive to the method chosen for definition of the ultimate lateral resistance of the p-y curves. Figure 3.22 depicts the effects of choosing initial stiffness using any of the two methods described previously. In this case no deck spring is considered to emphasize the effect of the choice of stiffness on the results. Behavior of the shafts is assured to be linear elastic in this case to remove any side effects caused by the nonlinear behavior of the shafts. The effects are relatively small and are even smaller in the case a 10 cm gap deck spring is considered. From this point on, all reported results are based on p_u calculated using Brinch Hansen (1961) and initial stiffnesses calculated using γ_{50}.

Figure 3.23 compares BNWF results for linear elastic versus nonlinear cases and also cases with a 10 cm gap deck versus cases with no deck considered. The importance of considering nonlinear behavior of the shafts is obvious in the case with no deck where a plastic hinge is formed and the bending moments are redistributed. The shear force and bending moment diagrams are quite different in this case. However in the case where a deck spring is present, linearity of shaft behavior plays a less important role and there is no meaningful difference between them. In cases where a deck spring is considered the bending moment demands are different in nature. In these cases a negative moment demand is seen close to the surface due to the lateral force applied by the deck which also decreases the positive demands at depth.

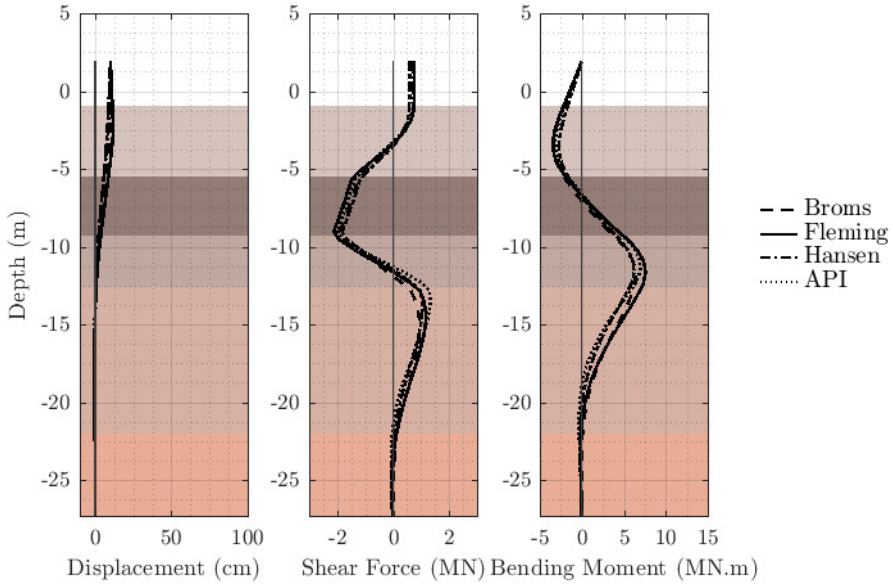

Figure 3.21: Effect of different p_u calculation methods on shaft shear and bending demands at the end of analysis for 1-D BNWF model with 10 cm gap using back-calculated stiffness from γ_{50}.

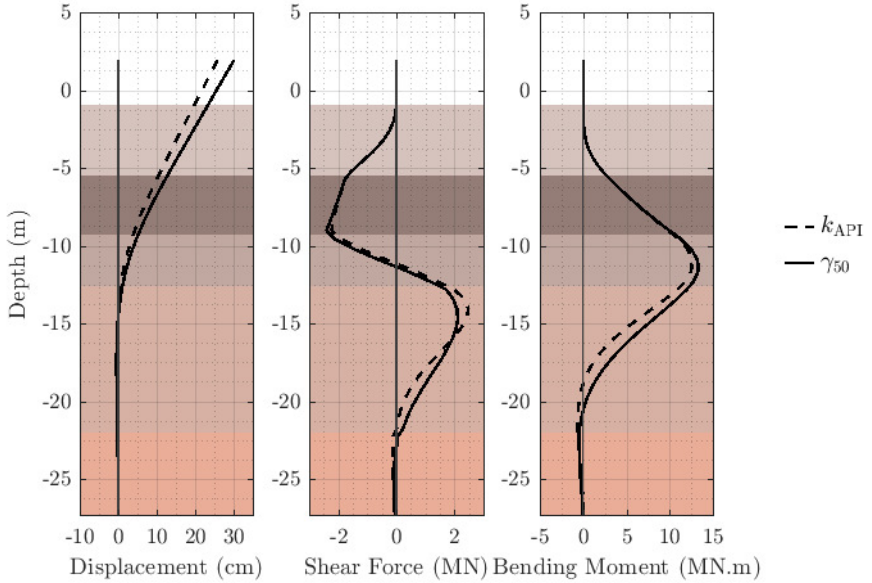

Figure 3.22: Effect of different initial stiffness calculation methods on shaft shear and bending demands at the end of analysis for 1-D BNWF model with no deck using Hansen formulation.

The amount of lateral spreading observed in the bridge site is reported to be about 25 cm. Figures 3.24 and 3.25 depict profiles of demand evolution with increasing free field displacement. It is obvious that at a 25 cm free field displacement the strength of the soil springs is fully mobilized close to the surface where most of the lateral spreading displacement profile exists. Comparing result profiles for the case with no deck for 25 cm and 100 cm ground displacements, it is apparent that formation of the plastic hinge results in redistribution of the bending moments. Figure 3.25, however, shows that as soon as the deck gap is closed, further application of free field displacement has minimal effect on the structural demands.

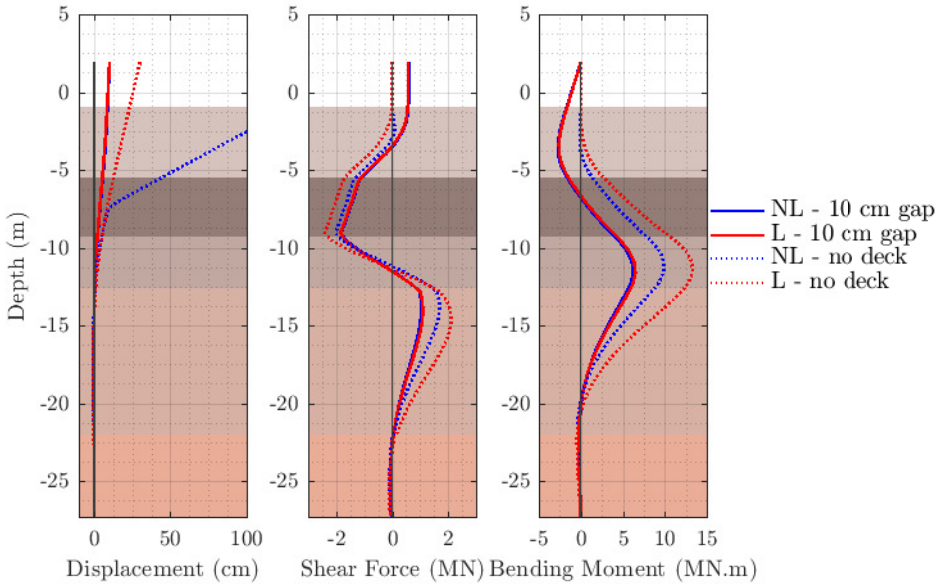

Figure 3.23: Effect of linear versus nonlinear structural response on shaft shear and bending demands at the end of analysis for 1-D BNWF model.

3.3.2 3D Finite Element Model Development

Figure 3.26a depicts the domain considered for finite element analysis of the Llacolén bridge northeast approach pier along with a simple representation of the bridge pier with its foundation system. The foundation structure consists of the 11 piles connected to each other

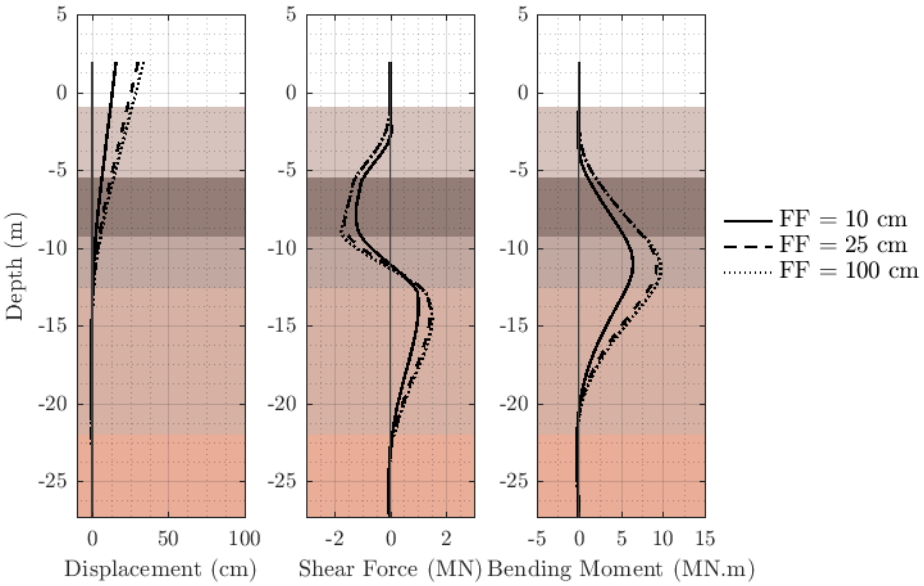

Figure 3.24: Effect of free field displacement on shaft shear and bending demands for 1-D BNWF model with no deck.

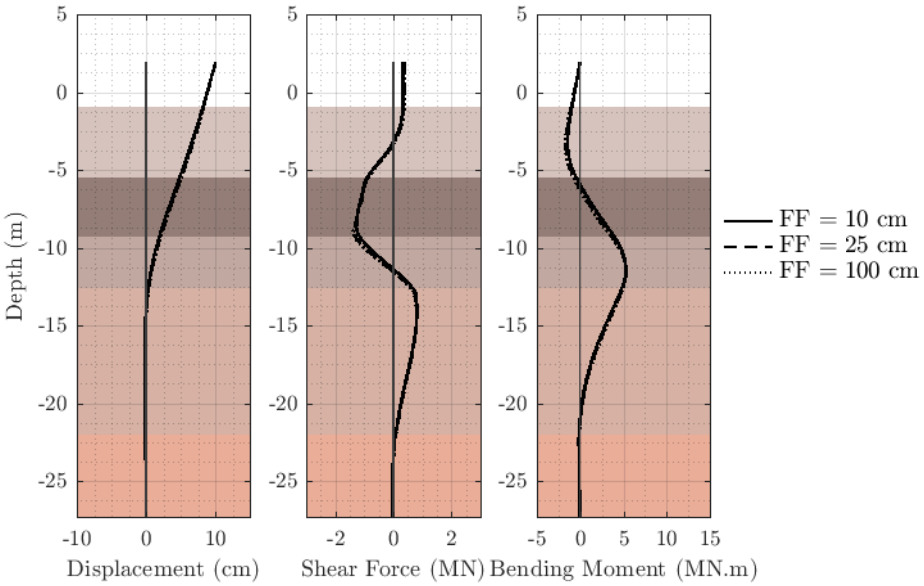

Figure 3.25: Effect of free field displacement on shaft shear and bending demands for 1-D BNWF model with 10 cm gap.

by means of a cap beam. The end of the 11 bridge pier columns embed into the cap beam to transfer the loads to the foundation. Bridge girders are simply seated on an inverted-T beam which transmits the loads of the superstructure to the pier. The bank slope is protected from erosion with a rock rip-rap. A 4V:13H slope is assumed based on the information available, and material properties of the upper dry sand layer are applied to this layer for simplicity. For the sake of simplicity, soil layering is assumed to be horizontal and extend to the boundaries of the model. Also, since the gravel layer in which the pile toes are embedded is very stiff ($N_{SPT} > 100$), it is assumed that this layer extends only to the bottom of the shaft foundations and, as explained in the following sections, pile toes are assumed to be fixed against translation in the vertical direction. A representative three-dimensional mesh is created for this domain to analyze the response of bridge piers to kinematic demands due to lateral spreading. As shown in Figure 3.27, the mesh is selectively refined near the foundation and element size becomes larger with increasing distance from the foundation.

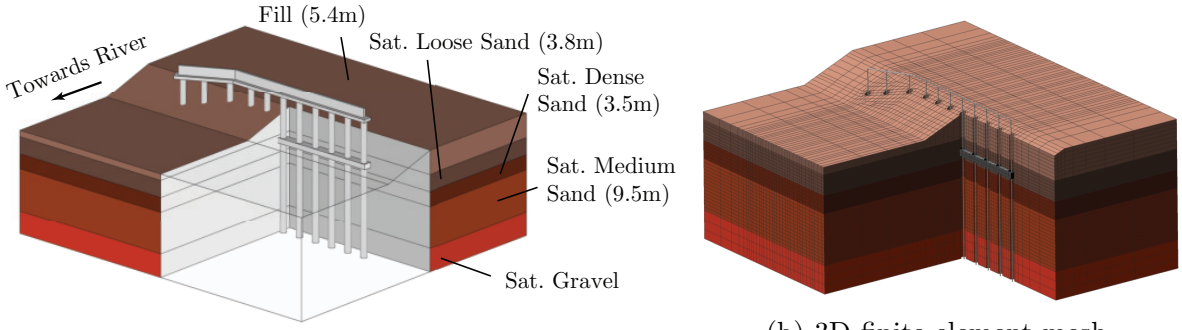

(a) Schematic of the bridge approach.

(b) 3D finite element mesh.

Figure 3.26: Schematic of the northeast approach of Llacolén bridge and generated 3D finite element mesh.

Stabilized single-point integration solid elements (McGann et al., 2015) are used to model the soil and the embedded cap beam. This type of element uses a stabilization technique to minimize the effects of hourglass locking with a single integration point and provides a

fast, and at the same time, reliable computational analysis. Constitutive models proposed by (Elgamal et al., 2003), i.e. PDMY and PIMY, are used to model the soil behavior. Total stress analysis assumptions are used for the purposes of this research and therefore no consideration for pore water pressure effects is made. Piles, columns and the inverted-T beam are all modeled using beam-column elements. The interface between the piles and the surrounding soil is modeled using beam-solid contact elements (Petek, 2006).

All numerical models are developed and analyzed using the OpenSees computational framework (McKenna, 1997; McKenna et al., 2010; OpenSees, 2007). OpenSees (Open system for Earthquake Engineering Simulations) is an open source, object-oriented finite element platform maintained by Pacific Earthquake Engineering Research (PEER).

Boundary and Loading Conditions

The size of the model and the proximity of the foundation to model boundaries are chosen to minimize boundary effects and to eliminate errors associated with modeling only a portion of a very large soil domain. All the nodes on the vertical boundary planes are fixed against out-of-plane translation. The gravel layer at the bottom of the model is a very stiff soil which is assumed to be almost incompressible below the foundation. Therefore all the nodes at the base of the model, including both solid and beam nodes are restrained in the vertical translation. As a result toe bearing effects on the piles are ignored.

The weight of the deck portion corresponding to the tributary area for each column and span is calculated and applied to the columns. Weight of the columns and shafts at different sections are calculated and applied along the elements in order to represent the actual axial loads in these elements. Application of these loads is necessary to account for the nonlinearity in the foundation elements.

Kinematic demands due to lateral spreading are accounted for using a gradually increasing displacement profile applied to the vertical boundaries as shown in Figure 3.28. This type of displacement profile represents the free-field kinematic demand on the soil system. It is assumed that layers above the liquefiable layer move a constant amount laterally with respect

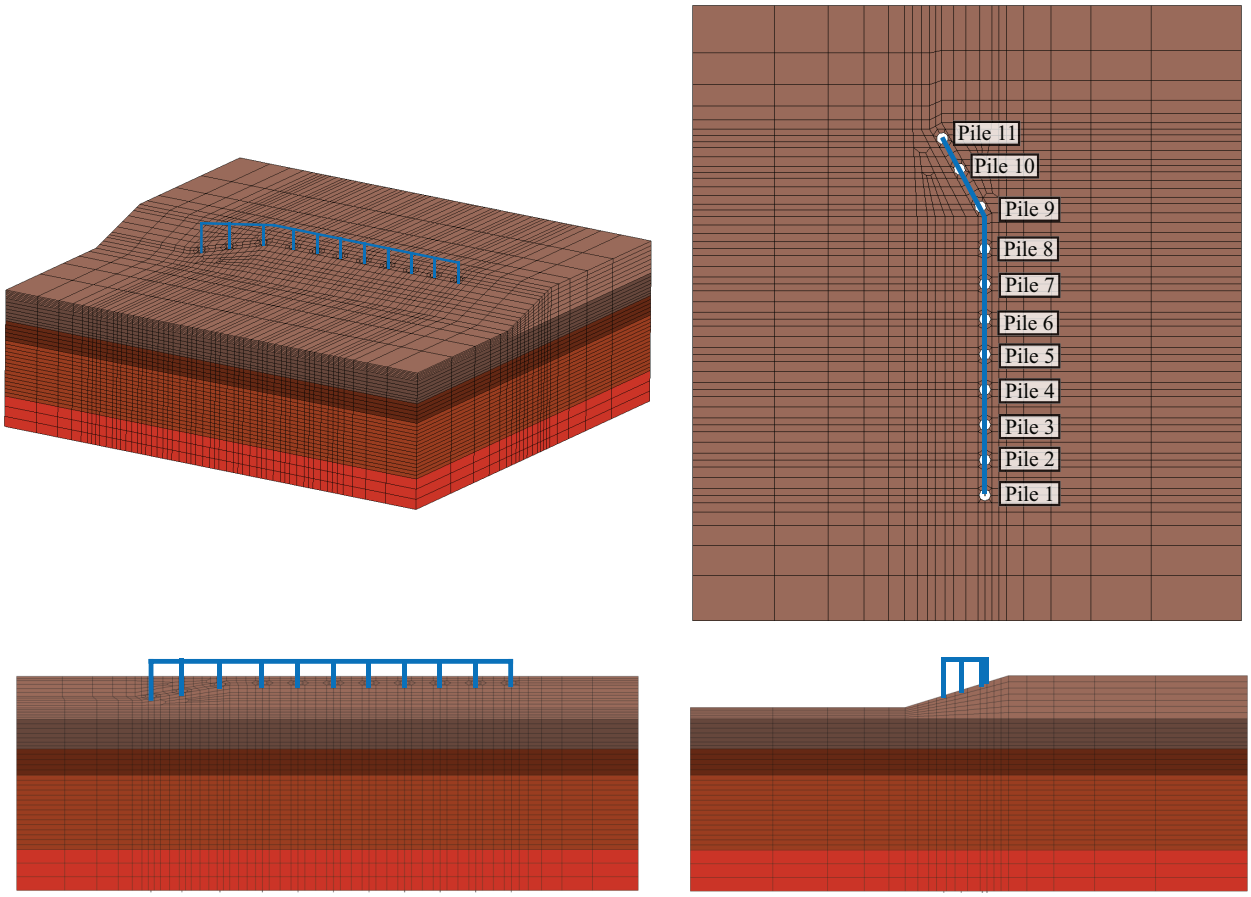

Figure 3.27: 3D finite element mesh for northeast approach of Llacolén bridge.

to the underlying material. The transition between the translation of above-liquefiable-soil layers and below-liquefiable-soil layers is assumed linear over the thickness of the liquefiable layer.

Modified Soil Properties

Modeling liquefaction initiation is not included in this part of the research. The goal here is to assess the foundation response to the kinematic demands of lateral spreading. Therefore, it is assumed that the kinematic demands are applied while the properties of the liquefied layer is modified such that this layer has a low shear stiffness and nearly incompressible

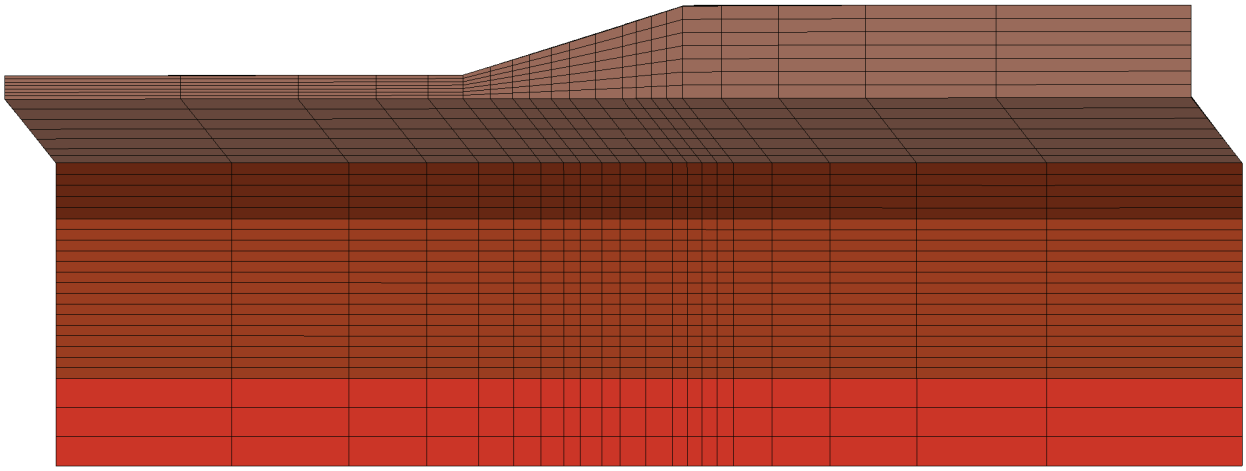

Figure 3.28: Displacement profile applied to mesh boundaries used to simulate kinematic demands of lateral spreading.

volumetric response associated with a liquefied state. Also an undrained strength value representing the ultimate residual strength of the liquefied soil is assumed for this layer. The properties of the remaining soil layers is kept the same as their assumed properties discussed in Section 3.2.1.

3D-FE Analysis of Northeast Approach with Applied Kinematic Model

As discussed in the previous section, the effects of lateral spreading on the bridge foundation is modeled using a kinematic displacement pattern applied to the boundaries of the model in a quasi-static manner. Reconnaissance teams estimated the amount of spreading to be around 25 cm based on their measurements done at the site. Given the extent of damage and structural deformation, it is probable that the amount of lateral spreading was more than the measured accumulation of ground cracks on the surface. In this study, a 1 m lateral spreading is applied and results are recorded at the end of analysis for every 5 cm of lateral spreading increments to account for a wide range of possible lateral spreading displacements. The results obtained from the numerical models are contrasted to the 25 cm observed lateral spreading response.

To evaluate the effects of the bridge deck on the foundation response, the deck is modeled using a compressional spring with an assigned gap. There is a 10 cm expansion gap between the bridge deck and the pier structure on each side. Models with different gap values (10, 20, 30 cm and ∞) are created and the results are compared in the following sections.

As an initial analysis, elastic behavior was assigned to the pier columns and the foundation structural elements. However, it turns out that the nonlinear response of these elements is important and in some cases may totally change the response mechanism. Effects of nonlinear material behavior of the columns and piles are assessed by contrasting the initial model results with linear material behavior to an additional model with nonlinear material behavior.

Global Model Response

Figures 3.29–3.31 show the deformed mesh with horizontal displacement contours for 10 cm and 20 cm gap and no deck conditions. Deformations are magnified 5 times for better visualization. In all these figures, nonlinear pile and column behavior is considered and the results correspond to the maximum applied kinematic boundary condition of 1 m. The horizontal displacement contours shown in these figures are the displacement component in the direction of lateral spreading. Figure 3.32 depicts the displacement component perpendicular to the direction of lateral spreading. Results shown in this figure are from the case with a 10 cm gap.

The effect of the bridge foundation resistance is obvious in all Figures 3.29–3.31. This effect is more pronounced in cases where a smaller gap is considered for the bridge deck. Figure 3.29 shows displacement results for the model with a 10 cm gap deck spring. In comparison, Figure 3.30 showing the results for a 20 cm gap model indicates that the near-field displacements are more affected since the bridge deck stiffness provides more resistance at earlier stages of the loading program, leading to more contrast in the near field displacements versus the free field displacements. Figure 3.31 shows the results for a case without bridge

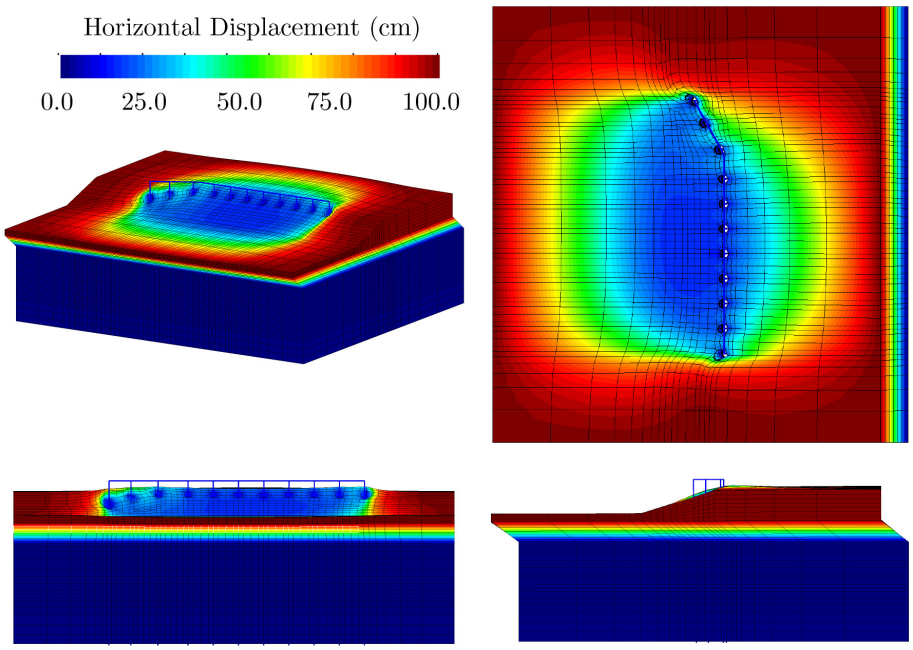

Figure 3.29: Deformed mesh (magnified 5 times) for 10 cm gap applied kinematic model with contours of river-ward horizontal displacement.

deck. In this case the resistance comes from the structural stiffness of the foundation system and the superstructure does not affect the response.

Contours of displacement in the transverse direction (perpendicular to the direction of lateral spreading) are shown in Figure 3.32. This figure shows that, due to the resistance of the bridge foundation, the soil mass is forced to flow around the bridge foundation, especially on the northern side. This higher concentration of displacement is due to the shape of the bridge pier near this location where the bridge pier is angled at about 29° relative to the pier axis. The three-dimensional effects resulting from the geometry of the bridge pier cannot be captured in 1D or 2D analysis methods and is of high importance. A closer look in the same region in this figure shows that near the piles located at the angled part of the bridge, the soil is forced to flow around the individual piles more than around any other pile in the straight part.

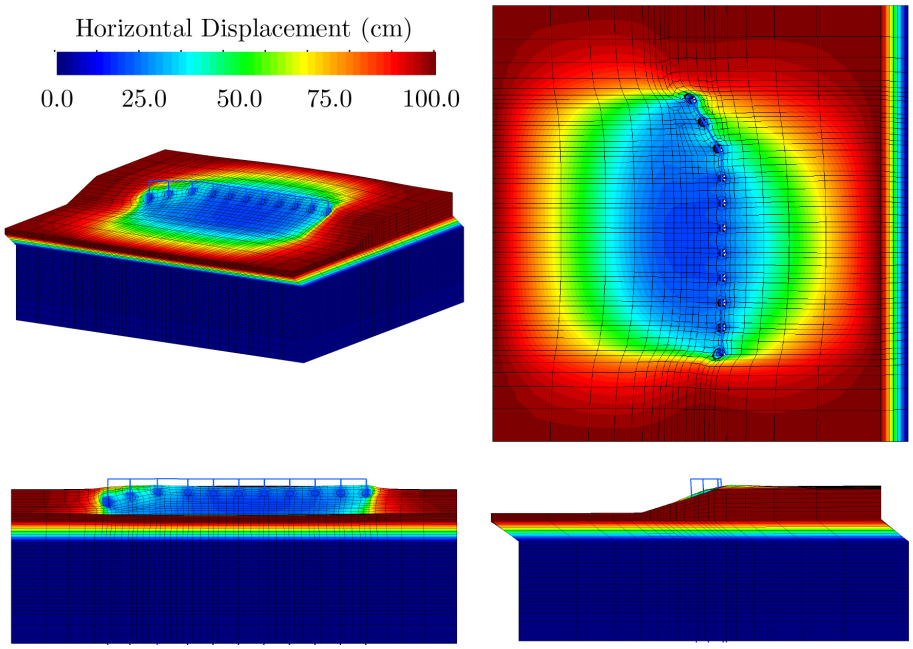

Figure 3.30: Deformed mesh (magnified 5 times) for 20 cm gap applied kinematic model with contours of river-ward horizontal displacement.

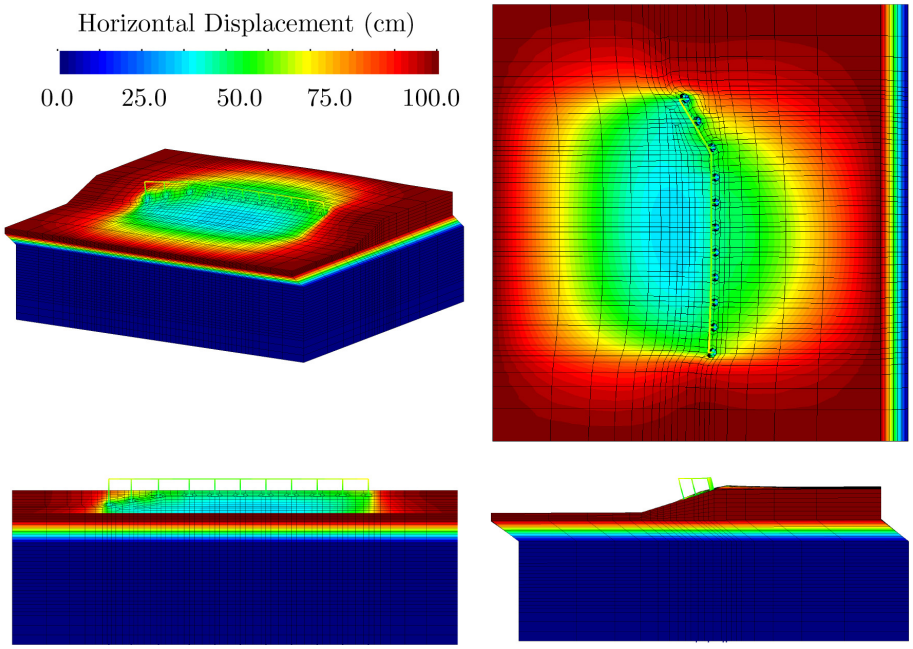

Figure 3.31: Deformed mesh (magnified 5 times) for no deck applied kinematic model with contours of river-ward horizontal displacement.

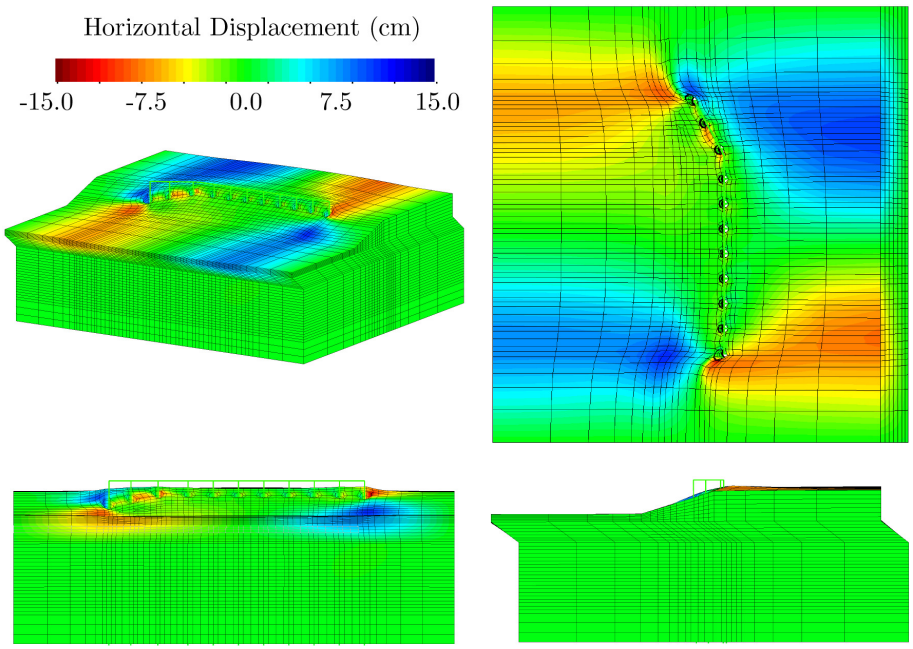

Figure 3.32: Deformed mesh (magnified 5 times) for 10 cm gap applied kinematic model with contours of transverse horizontal displacement.

Pier and Foundation Response

Figure 3.33 shows the displacement of the bridge pier at the top of the pier column 1 over the course of the free field displacement application from models with 10 cm, 20 cm and 30 cm gaps. Figure 3.33a shows the results when elastic behavior is assigned to the shafts and Figure 3.33b shows the results when elastoplastic behavior is considered for the shafts. The 1 : 1 bisection line is shown for reference. For all these cases, after the closure of the expansion gap, the displacement of the pier is effectively impeded by the stiffness provided by the bridge deck. Prior to closure of the gap, the pier movement is closer to the free field displacement indicating that the foundation provides much less resistance. In making this observation it is important to consider the rotation of the column as the location of the top of the bridge pier is several meters above the ground surface and small rotations at the ground surface elevation of the shafts result in larger displacements at the top of the column.

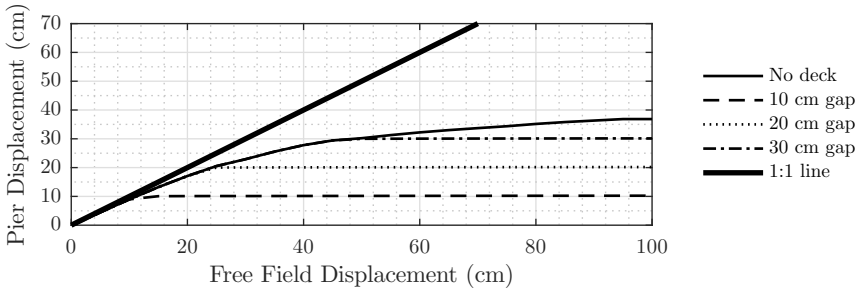

(a) Linear elastic beam elements.

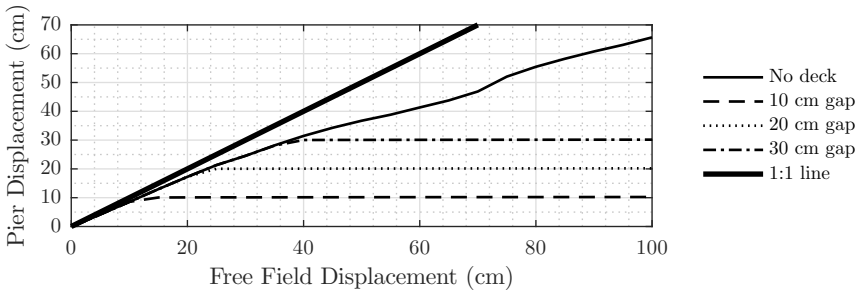

(b) Nonlinear beam elements.

Figure 3.33: Evolution of pier beam displacement in direction of lateral spreading for various gap sizes using (a) linear beam elements, and (b) nonlinear beam elements.

In cases where no deck spring is considered, the elastoplastic shafts show larger displacements due to their softer response. Specifically, the response shows a sudden increase in displacements at a free field displacements of around 75 cm. At this point, a plastic hinge forms along the shaft causing the formation of a response mechanism leading to larger displacements.

As mentioned before, the stiffness of the bridge deck spring is simply calculated based on the Young's modulus of the concrete, the cross-sectional area of the deck and length of the span. Calculation of the actual stiffness is more complicated. In order to consider the effect of the deck stiffness, models with deck spring stiffnesses based on different span lengths are created and the results are shown in Figure 3.34. Prior to closure of the gap these models are essentially the same and the responses are equal. Even after the gap is closed, the response

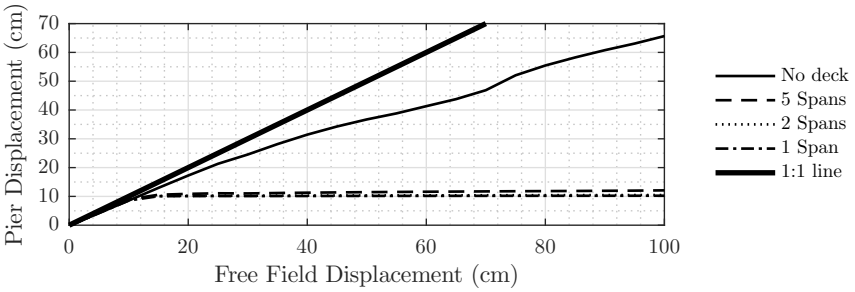

Figure 3.34: Evolution of pier beam displacement in direction of lateral spreading for 10 cm gap with various deck stiffnesses.

is not very sensitive to the stiffness of the deck. This is expected since axial stiffness of the deck is much higher than the lateral flexural stiffness of the pier.

Figure 3.35 compares the displacements of the piers at different locations. Also shown in this figure is the displacement of the pier in the transverse direction. Displacements in the direction perpendicular to the lateral spreading direction are much smaller compared to the other direction. This is expected due to the direction of the kinematic loading. Also, the stiffness of the pile group in the transverse direction is much greater. Complimentary to these results, Figures 3.36 and 3.37 show the displacement of the pier beam at the end of the application of 1 m free field displacement for a case with a 10 cm gap and a case with no bridge deck. Figure 3.36 shows relatively uniform displacements in both directions parallel and perpendicular to the direction of lateral spreading. Less uniform displacements at the distal locations are expected due to less structural stiffness at these locations. This effect is more pronounced in Figure 3.37 where the bridge deck is not accounted for. Transverse displacements are mostly uniform in the straight portion of the pier. However in the angled part of the pier an obvious hinge mechanism is formed.

Foundation Bending Demands

The shaft displacement, shear force and bending moment profiles for three shafts are shown in Figures 3.38 and 3.39 for free field displacements of 25 cm and 1 m respectively. Results

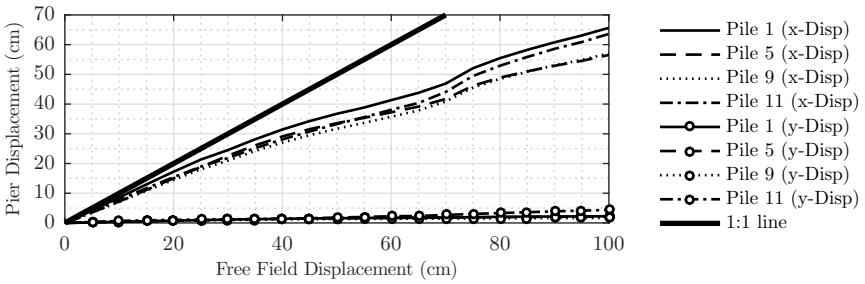

Figure 3.35: Evolution of pier beam displacement in direction of lateral spreading movement (x-disp) and perpendicular to the lateral spreading movement (y-disp) for no deck case. Refer to Figure 3.27 for pile numbering.

shown in these figures are from models with a 10 cm gap and elastoplastic shafts. Bending moment demands vary for each of the piles in both cases. This variability is more pronounced for larger displacements.

The rough irregularity seen in the shear force and bending moment diagrams at about 8 m deep is due to the stiffness provided by the cap beam connecting pile heads to each other. This beam resists a portion of the demands due to its high stiffness. Figure 3.40 shows the result profiles for a case in which the cap beam has been removed and the results are contrasted with the case which considers the existence of the cap beam. This figure shows that if the pile structure were to resist the soil passive forces alone, the result profile would be smooth as expected.

Figures 3.41 and 3.42 show the evolution of displacement, shear force and bending moment demands as the free field displacement increases. Results shown in these figures correspond to 10 cm, 25 cm and 1 m free field displacements. Figure 3.41 displays the results for the case with no deck while Figure 3.42 shows the results for a case with a 10 cm gap model. In the case with no deck spring, the demands increase to the point a plastic hinge is formed. The deformation mechanism is different when a deck spring is considered, and as a result the moment distribution along the shafts is different between these two cases.

Figure 3.43 compares the response of the system when linear and nonlinear shafts are used. As expected, since structural demands due to passive forces exerted on the shafts

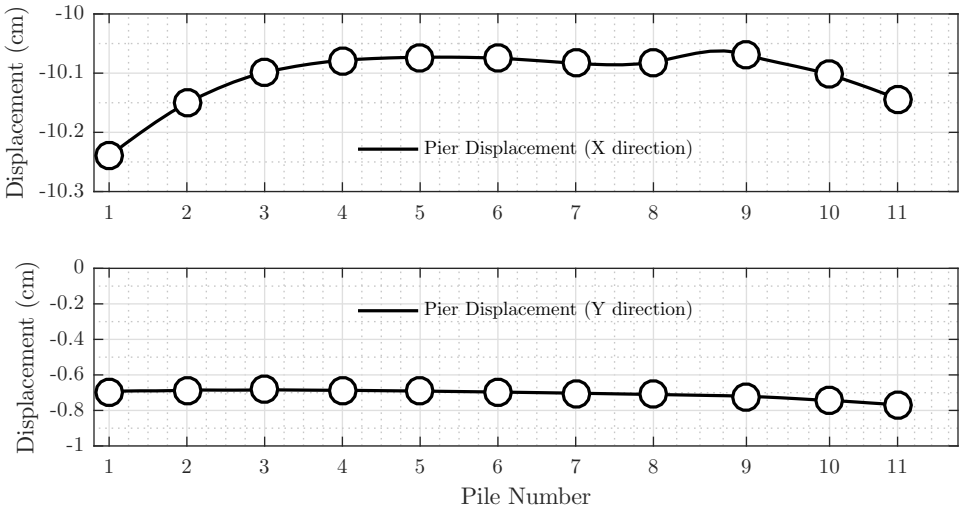

Figure 3.36: Pier displacements parallel (X) and perpendicular (Y) to the direction of lateral spreading for 10 cm gap case. Refer to Figure 3.27 for pile numbering.

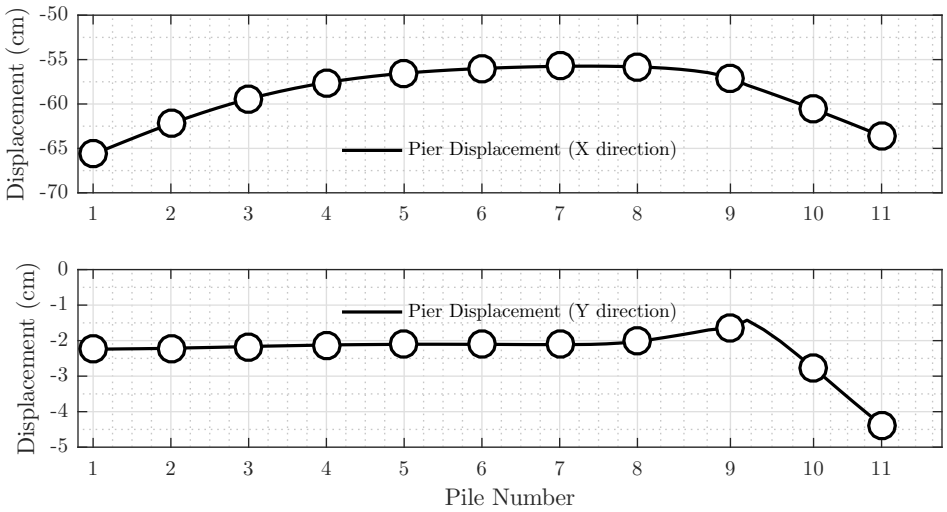

Figure 3.37: Pier displacements parallel (X) and perpendicular (Y) to the direction of lateral spreading for no deck case. Refer to Figure 3.27 for pile numbering.

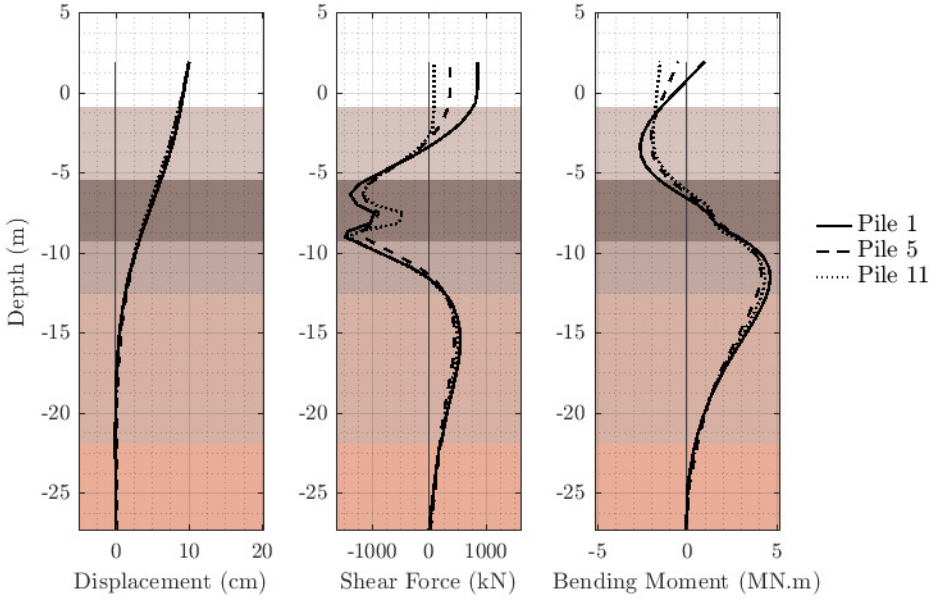

Figure 3.38: Shaft shear and bending demands at 25 cm free field displacement for 10 cm gap case for various piles. Refer to Figure 3.27 for pile numbering.

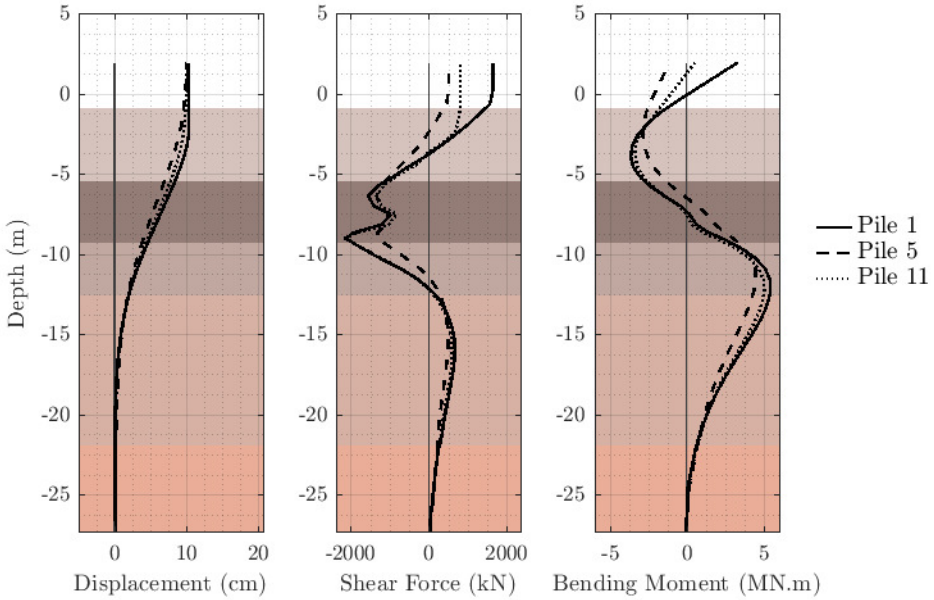

Figure 3.39: Shaft shear and bending demands at 100 cm free field displacement for 10 cm gap case for various piles. Refer to Figure 3.27 for pile numbering.

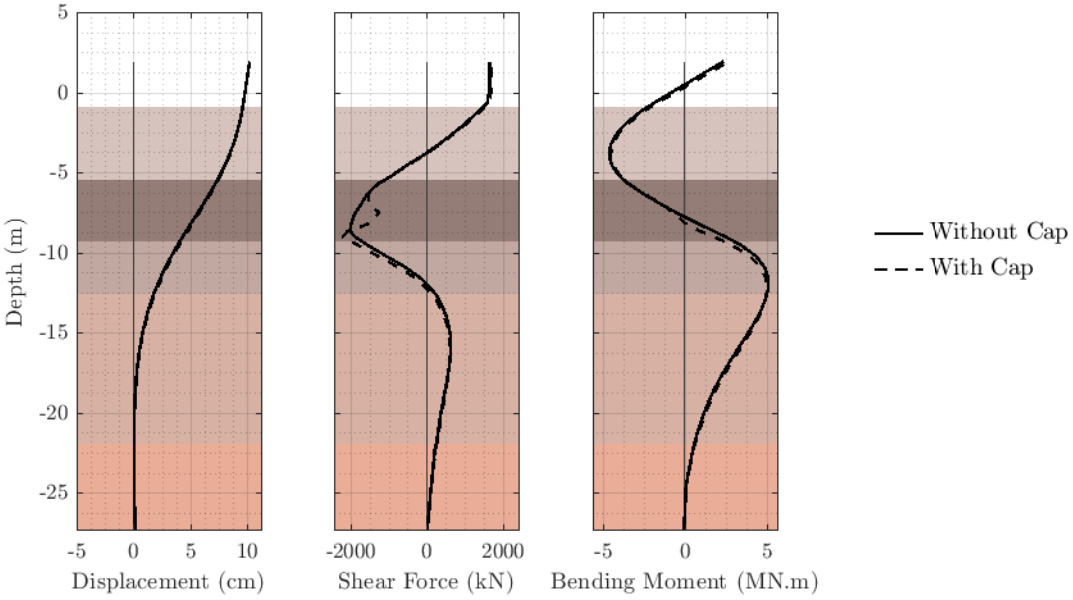

Figure 3.40: Effect of foundation cap on shaft shear and bending demands for 10 cm gap case.

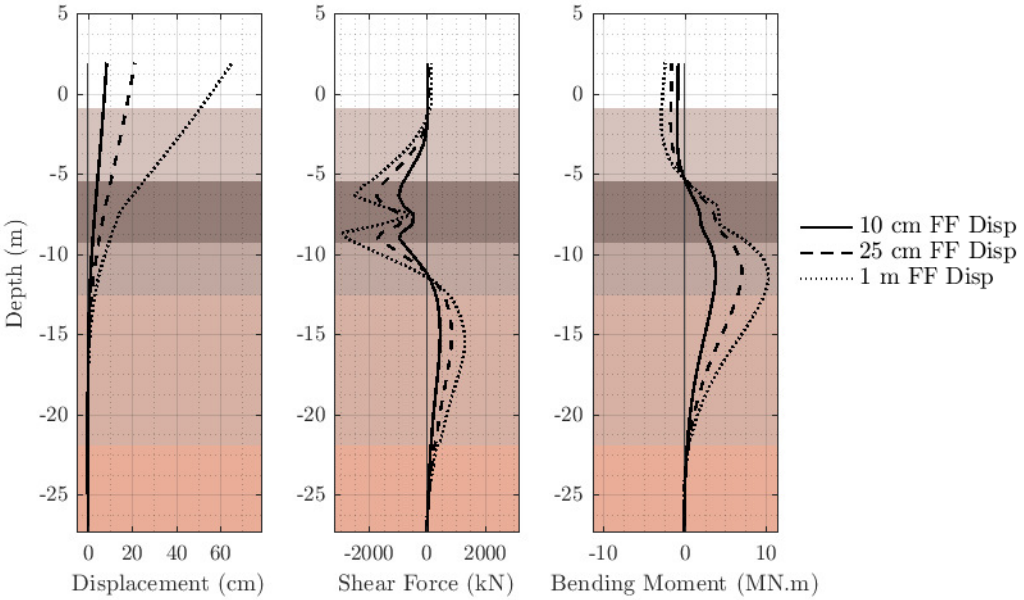

Figure 3.41: Effect of free field displacement on shaft shear and bending demands for no deck case.

are larger than the capacity of pile sections in the linear analysis, formation of a plastic hinge is clear in the nonlinear results at the corresponding location. This is consistent with the observations made in the field and shown in Figure 3.5. Figure 3.43 shows that the linear elastic shaft compares well with the elastoplastic shaft behavior prior to formation of a plastic hinge. For the case with a 20 cm gap, displacements and structural demands are reasonably close. However, for the no deck case, the response of a linear shaft deviates from the nonlinear shaft due to formation of a plastic hinge and redistribution of the bending moments and stresses.

The evolution of maximum shear force and maximum bending moment along three shafts for linear and nonlinear structural element behavior is shown in Figures 3.44 through 3.46. Bending capacity of these shafts changes during the kinematic loading due to change in axial forces. This change in axial force is discussed later, however, these figures show that the bending demands are generally higher when a linear elastic shaft is used. The reason being that for the nonlinear cases, the maximum moment capacity (as shown in Figure 3.18) is reached and further demands are redistributed along the shafts. For the linear cases on the other hand, the capacity of the shafts are not capped and therefore the response of the shaft is defined completely from the soil reaction demands.

The effect of considering the deck resistance manifests in changes in axial force in the shafts over the course of the loading. Figures 3.47 and 3.48 show the evolution of the change in maximum axial forces over the course of the application of the free field displacement. One of the non-intuitive three-dimensional effects seen in these figures is the evolution of the axial forces in shafts 9 and 11. These shafts are located with an offset with respect to the bridge pier axis and because of this, a group rotation effect is seen in their axial response. For the no-deck case (Figure 3.47) shaft 11 has additional compressional forces while Shaft 9 has additional tensile forces. Although the overall axial force in Shaft 9 remains in compression, the reduction in axial force increases the bending capacity of the shaft while the opposite is true for Shaft 11. This effect is something that cannot be captured by any simplified model of

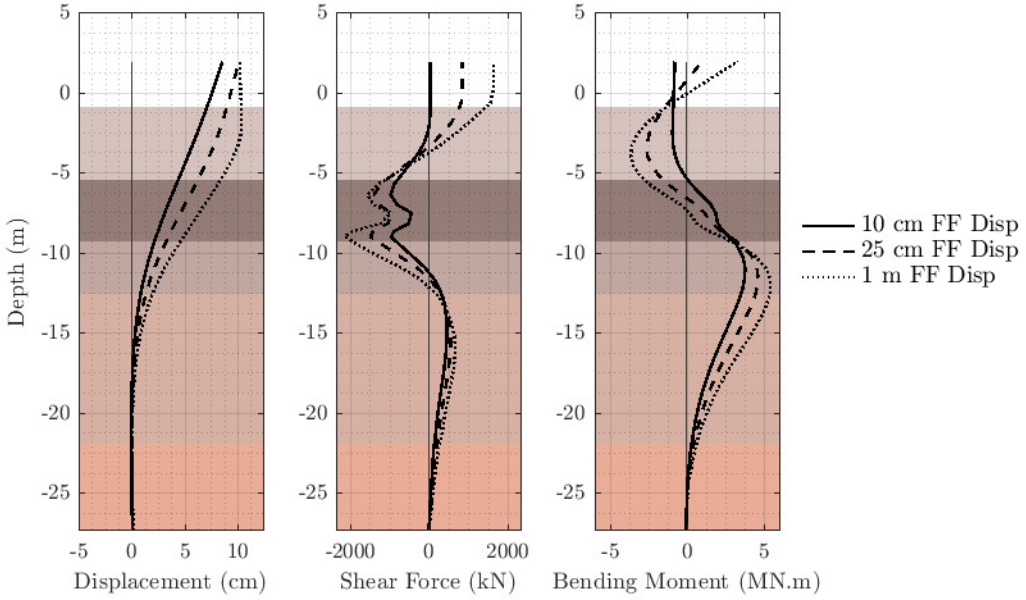

Figure 3.42: Effect of free field displacement on shaft shear and bending demands for 10 cm gap case.

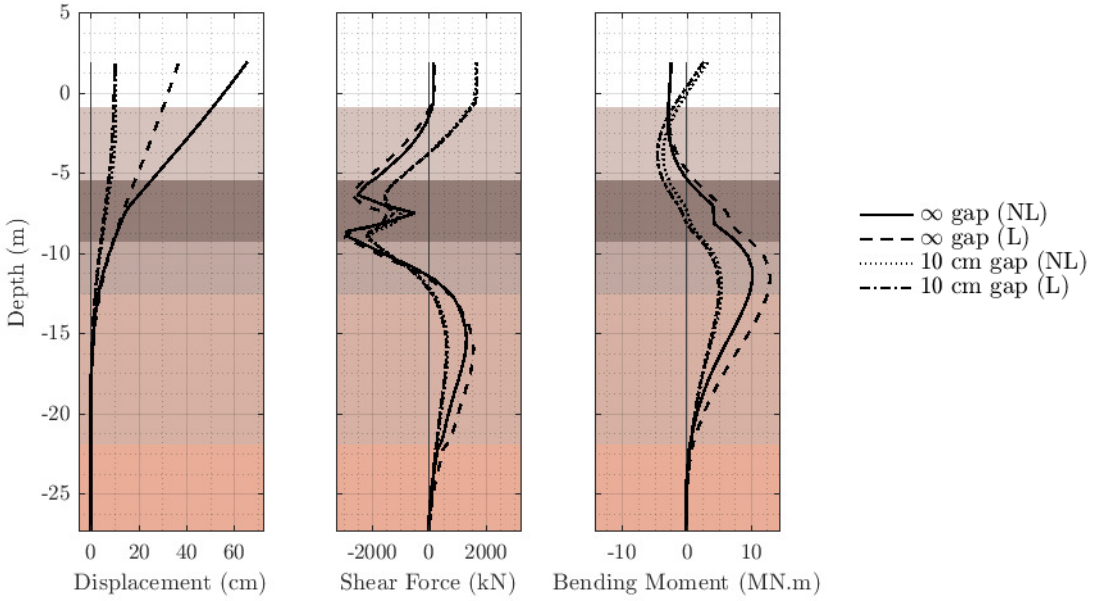

Figure 3.43: Effect of structural element nonlinearity on shaft shear and bending demands at the end of analysis.

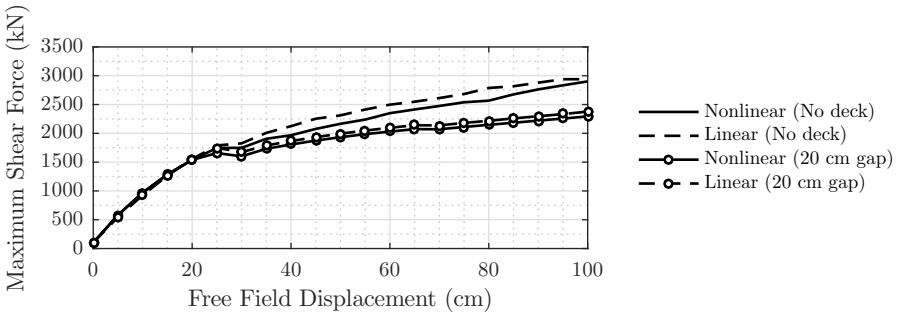

(a) Evolution of maximum shear force.

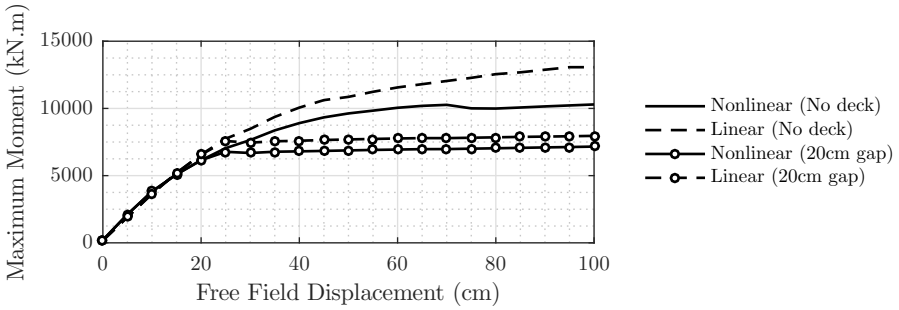

(b) Evolution of maximum bending moment.

Figure 3.44: Effect of structural element nonlinearity on evolution of structural demands (Pile 1).

a three-dimensional case like the Llacolén bridge pier. These effects are less pronounced when using a 10 cm gap deck (Figure 3.48) probably because of the impediment in displacement.

The 3D geometric effects can also be seen in Figure 3.49. In this figure the evolution of the maximum shear forces and bending moments along the shafts are shown for piles 1, 5, 9 and 11. For comparison, the same quantities in the transverse direction are also depicted. Demands in the transverse direction are generally ignored in simplified methods because they are based on either 1-D analysis or 2-D plane-strain simplifications; for which the strains in the transverse direction are assumed to be zero. However, Figure 3.49 shows that depending on the geometry of the problem, if 3D structural effects are present, not only these are not conservative assumptions but also the demands in the transverse direction can in some cases be in the same order of magnitude as the main direction.

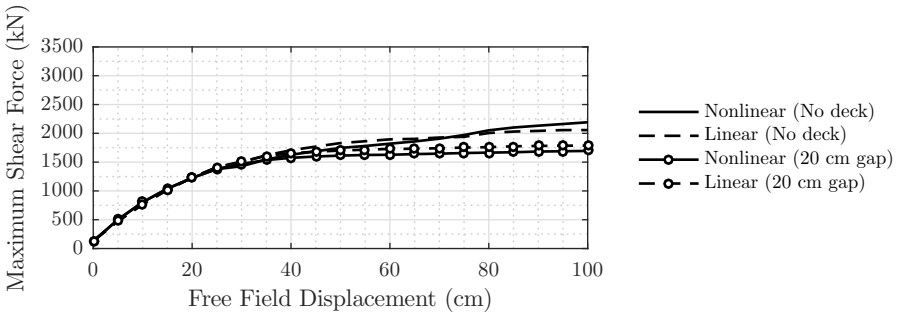

(a) Evolution of maximum shear force.

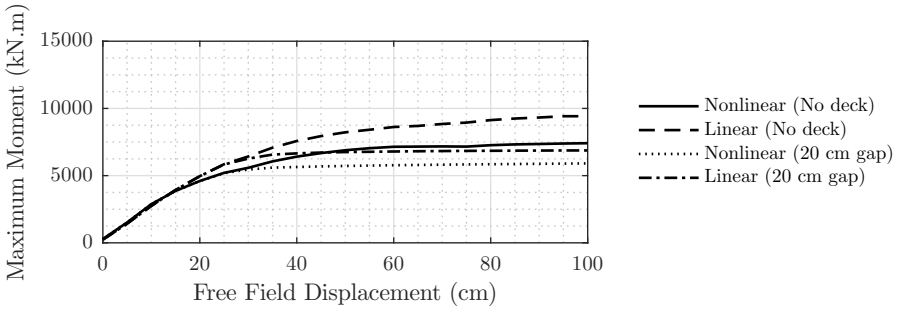

(b) Evolution of maximum bending moment.

Figure 3.45: Effect of linearity of structural elements on evolution of structural demands (Pile 9).

Figures 3.50 and 3.51 show the demand profiles for pile 1 at 25 cm free field displacement and 1 m free field displacement. The figures show that the response of the shafts in the transverse direction varies quite differently for each shaft. These demands remain relatively constant after the closure of the gap as is the case with the demands in the main direction as well.

The effect of gap size on structural demands are shown in Figures 3.52. The bending demands increase with gap size. This indicates that the resistance provided by the deck is an important component of the lateral resistance provided by the foundation system. For the no-deck case, the demands exceed the capacity of the pier column, and plastic hinges form at the connection between the column to the pile cap.

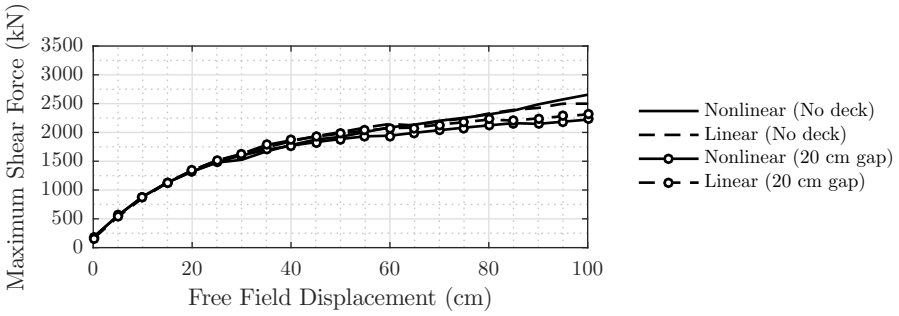

(a) Evolution of maximum shear force.

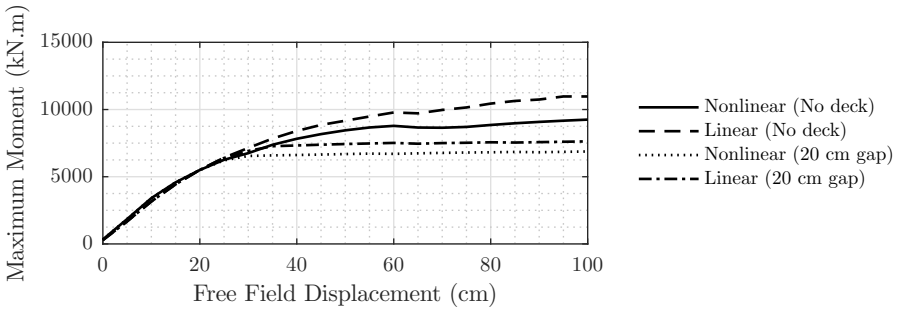

(b) Evolution of maximum bending moment.

Figure 3.46: Effect of linearity of structural elements on evolution of structural demands (Pile 11).

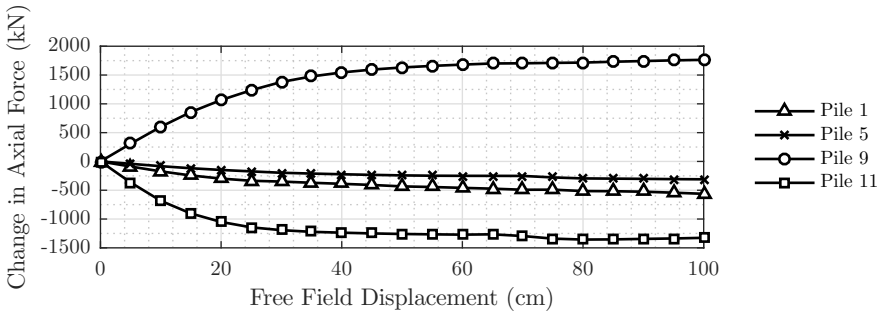

Figure 3.47: Evolution of change in axial force in structural elements for no deck case. Refer to Figure 3.27 for pile numbering.

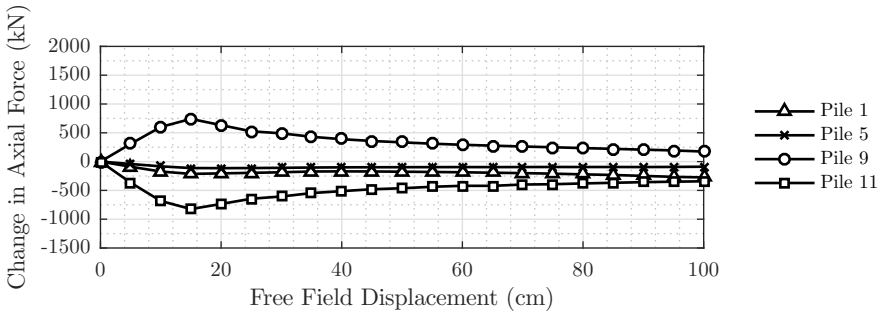

Figure 3.48: Evolution of change in axial force in structural elements for 10 cm gap case. Refer to Figure 3.27 for pile numbering.

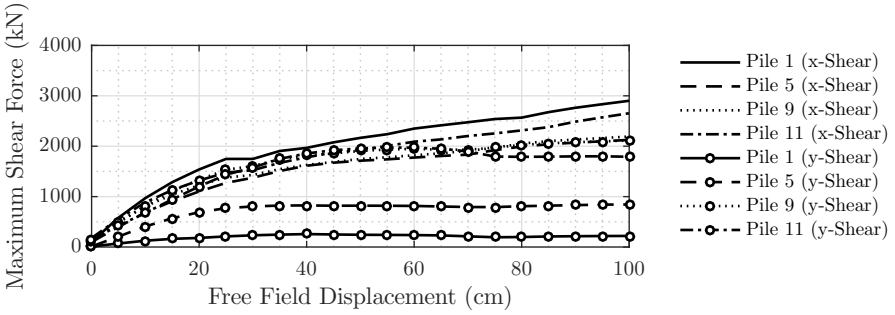

(a) Evolution of maximum shear force.

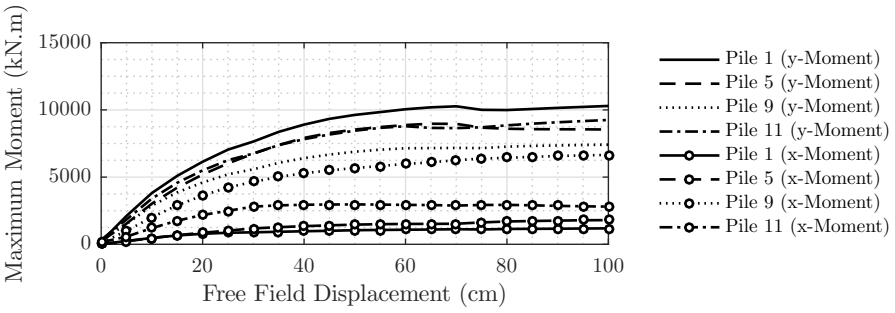

(b) Evolution of maximum bending moment.

Figure 3.49: Evolution of maximum shear force and maximum bending moment parallel (X) and perpendicular (Y) to the direction of lateral spreading for various piles for 10 cm gap case. Refer to Figure 3.27 for pile numbering.

Figure 3.53 shows the effect of gap size over the course of the kinematic loading. This figure shows that after the gap is closed, the demands remain essentially constant, emphasizing the influence of the gap size on shaft demand. Additionally the results show that given the resistance provided by the bridge deck is large, the structural demands are governed by the size of the gap to the point that the maximum demand observed when the gap size is 10 cm is about half the demand in a scenario where the gap is never closed and the deck resistance does not play a role.

3.3.3 Comparison of 3D-FE and Pile Pinning Analysis

The pile-pinning model described in Section 3.3.1 represents a simplified model to be used for the design of deep foundations against loads due to liquefaction-induced lateral spreading. A second distinct numerical technique using a 3D finite element model of the bridge approach was explained in Section 3.3.2 to account for some of the three-dimensionality which could not be captured in the first method. Results of these two models are compared to reveal their similarities and differences. Contrasting results of a simplified 1D model against a more complicated 3D model also demonstrates positive aspects and possible shortcomings of the simplified pile-pinning BNWF method.

Figures 3.54 and 3.55 show the evolution of maximum displacement, shear force and bending moment of the foundation elements over the course of the free field displacement application considering linear and nonlinear shaft behavior respectively. The shaded part of the plots represent the range of values obtained from the 3D model for all 11 shaft elements. The 3D geometry of the bridge bent causes piles at different locations to respond differently to the lateral spreading loads. As a result, a relatively wide range of values are obtained from the 3D models.

The difference in initial slopes observed in these curves is expected due to the nature of applied boundary conditions in each model. Free field displacements shown on the horizontal axis of these plots, are applied as a far-field displacement pattern to the boundaries of the 3D model. Due to pinning effects, the pile elements do not feel the same amount of displacement

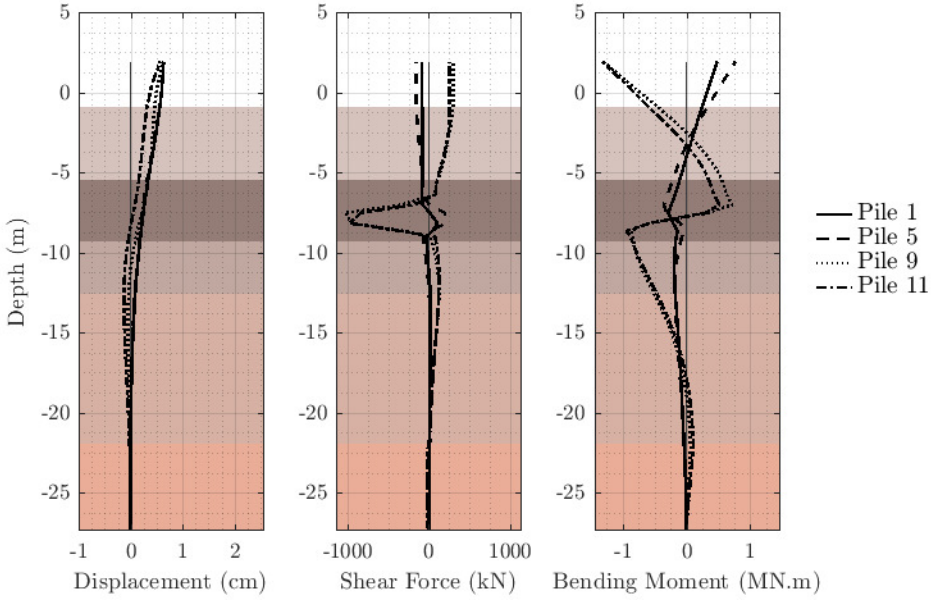

Figure 3.50: Transverse shaft shear and bending demands at 25 cm free field displacement for 10 cm gap case. Refer to Figure 3.27 for pile numbering.

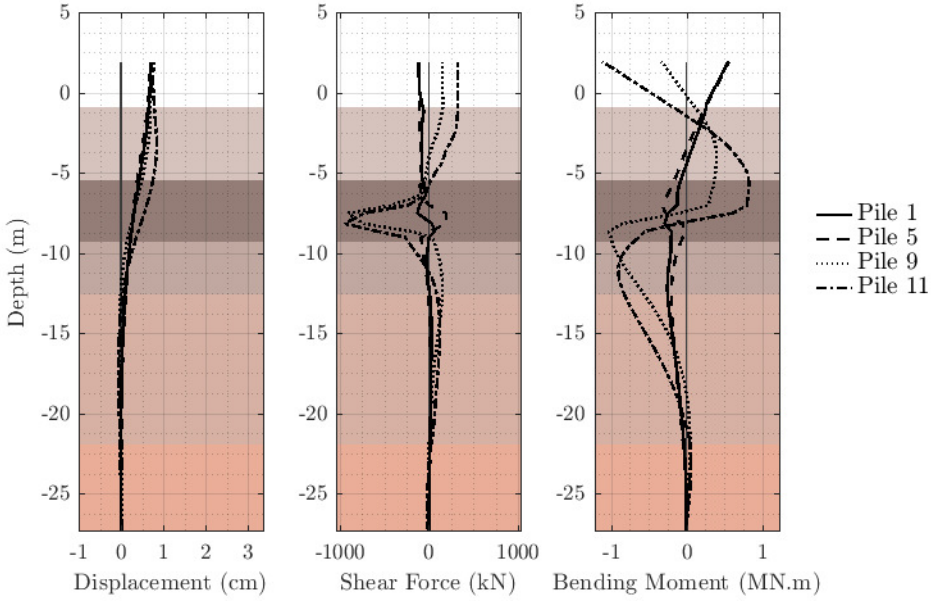

Figure 3.51: Transverse shaft shear and bending demands at 100 cm free field displacement for 10 cm gap case. Refer to Figure 3.27 for pile numbering.

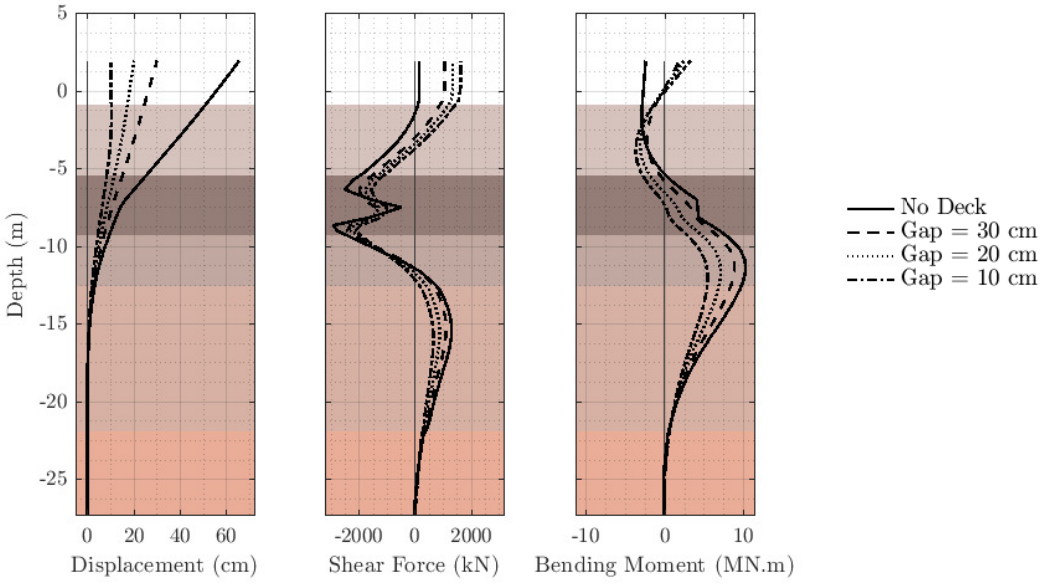

Figure 3.52: Effect of gap size on shaft shear and bending demands at the end of analysis.

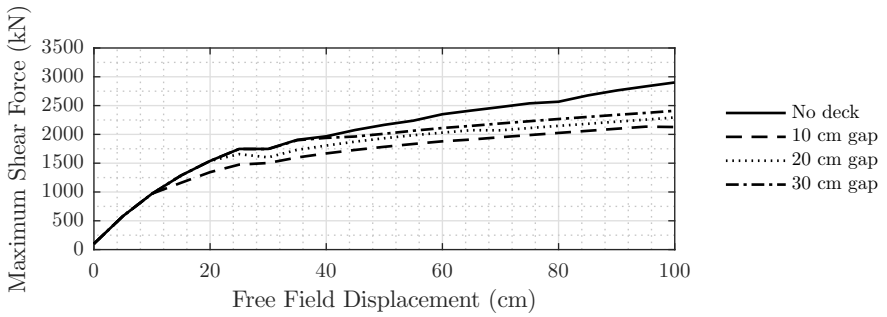

(a) Evolution of maximum shear force.

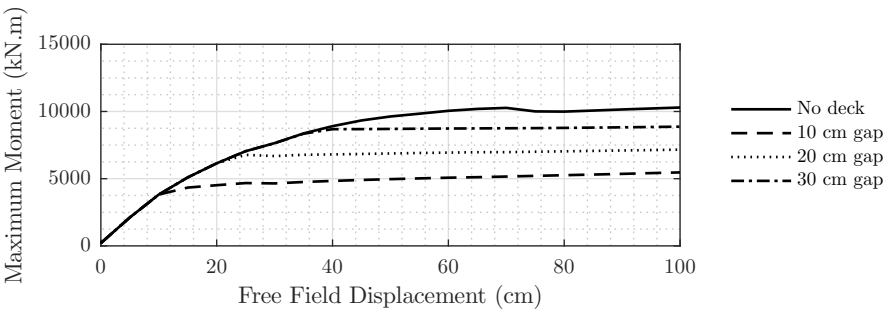

(b) Evolution of maximum bending moment.

Figure 3.53: Effect of gap size on evolution of structural demands.

in the local vicinity of themselves resulting in less demands on these elements. On the other hand, free field displacements are applied directly to the end of the p-y springs connected to the foundation elements, representing a near-field displacement. Therefore, the equivalent shaft in the 1D model feels the same free field displacements sooner than the elements in the 3D models.

The bending demands obtained from the BNWF analyses at the end of the free field displacement application fall within the range of 3D results, demonstrating the effectiveness of this analysis procedure for such problems. However if the estimated ground displacement does not mobilize the full passive resistance of the soils, the pile-pinning analysis results in conservative structural demands and probable over-design of the bridge foundation.

For the linear elastic case (Figure 3.54), after mobilization of the full passive resistance of the soils, the foundation response reaches a plateau state where any further ground lateral displacement has no additional effect on the foundation. However for the inelastic case (Figure 3.55) a plastic hinge is formed, hence unbounded displacement of the column head. The evolution of the maximum bending moment shows that around 25 cm, the moment demands redistribute and a deformation mechanism is formed. This phenomenon happens at about 70 cm in the 3D model suggesting that the near-field displacement is about 25 cm when a far-field displacement of 70 cm is applied.

Figure 3.56 shows results for the range of foundation responses observed in the 3D model and the BNWF model at an applied free field of 25 cm. As shown in the previous plots, it is not appropriate to compare the results of the 3D models with the BNWF model at the same ground displacement. The discrepancy between the results observed in Figure 3.56 is partly a result of this issue, therefore profiles of results at a ground displacement of 10 cm – which seems to be the corresponding near-field displacement for a 25 cm far-field displacement in Figure 3.55 – is also plotted in this figure. Results fall in the same range emphasizing the importance of estimating equivalent lateral ground displacements for cases where flow failure is not likely to occur. When full passive forces are mobilized and flow failure happens,

the results become insensitive to the ground displacement and as shown in Figure 3.57, a simplified BNWF analysis could be used for design purposes.

Results of cases considering a 10 cm gap deck spring are depicted in Figures 3.58 to 3.61. The results show that in the presence of a deck spring, if the deck provides enough resistance to the lateral movement of the bridge bent, the impediment causes demands to reach a plateau before bending capacity of the elements are reached making the nonlinear behavior of these elements less relevant to some degree. Consideration of the bridge deck and expansion gap proves to be an important aspect to be considered in simplified design methods.

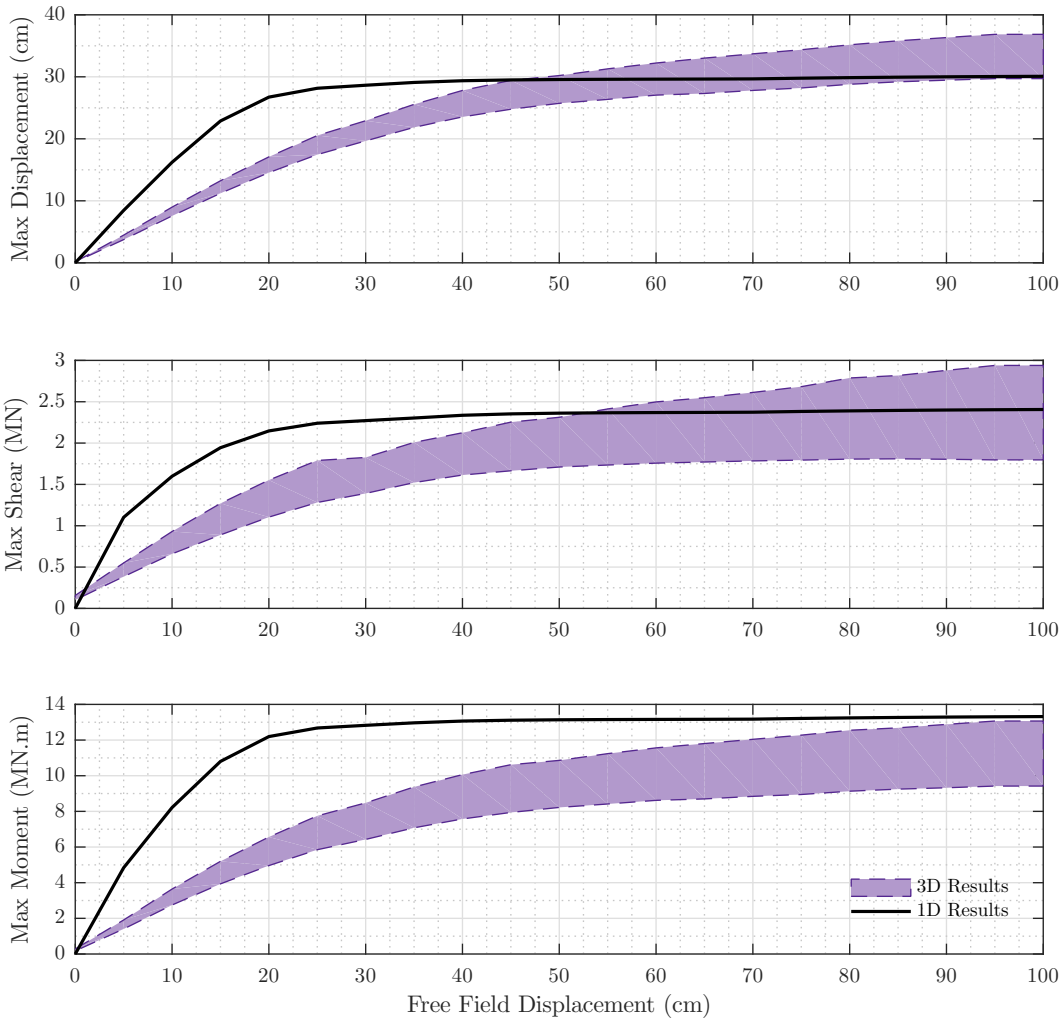

Figure 3.54: Evolution of maximum pier displacement, maximum shear force and maximum bending moment for no-deck case using linear structural elements. The shaded area represents the range of pile response recorded in 3D model.

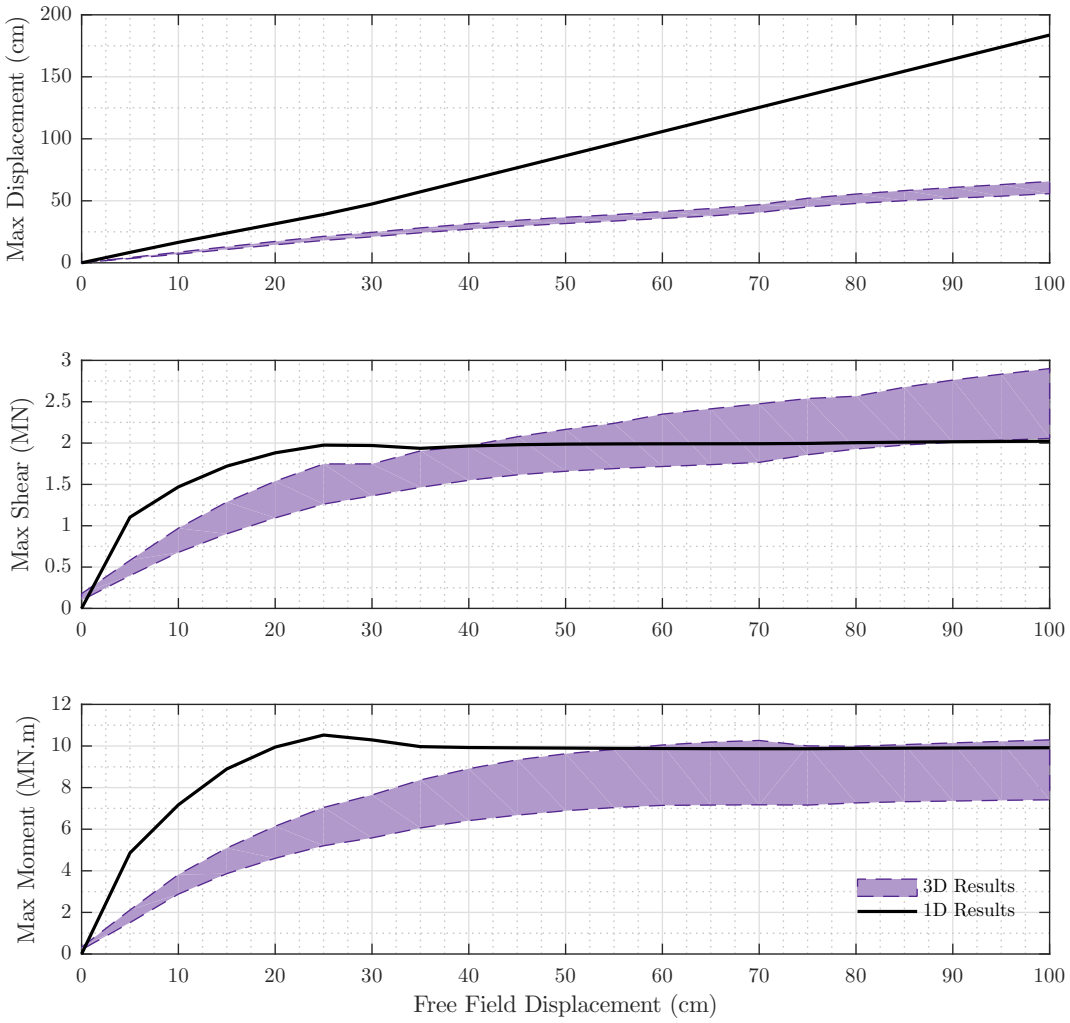

Figure 3.55: Evolution of maximum pier displacement, maximum shear force and maximum bending moment for no-deck case using nonlinear structural elements. The shaded area represents the range of pile response recorded by the 3D model.

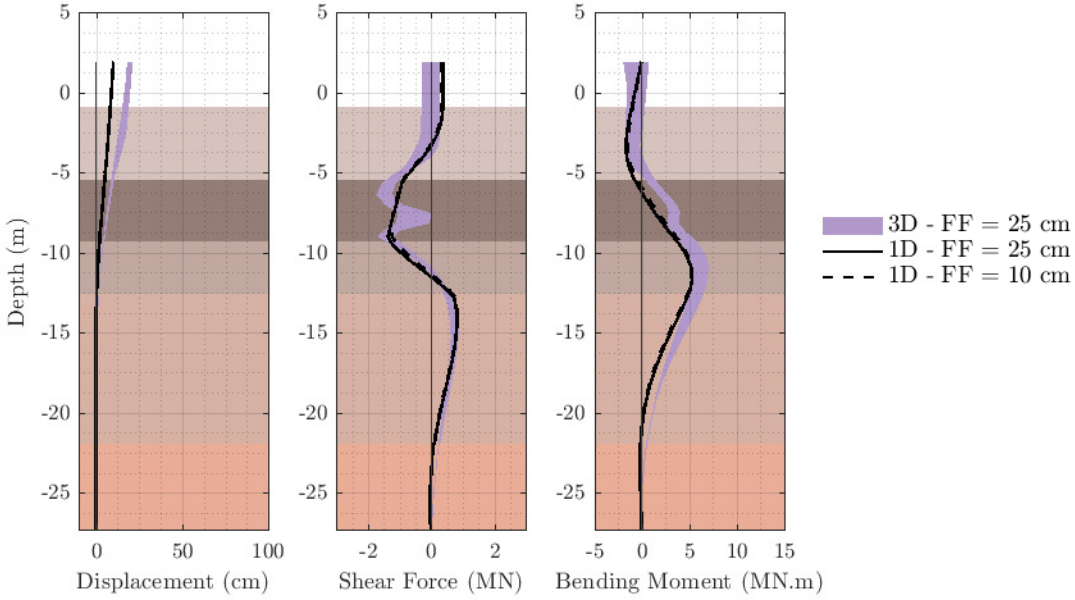

Figure 3.56: Shaft shear and bending demands at 25 cm free field displacement for no-deck case. The shaded area represents the range of pile response recorded by the 3D models.

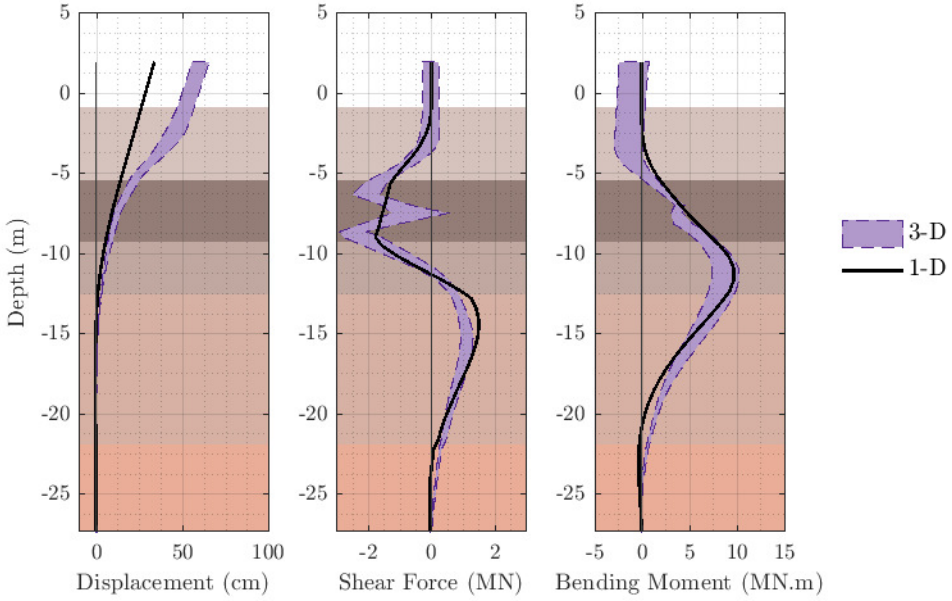

Figure 3.57: Shaft shear and bending demands at 100 cm free field displacement for no-deck case. The shaded area represents the range of pile response recorded by the 3D models.

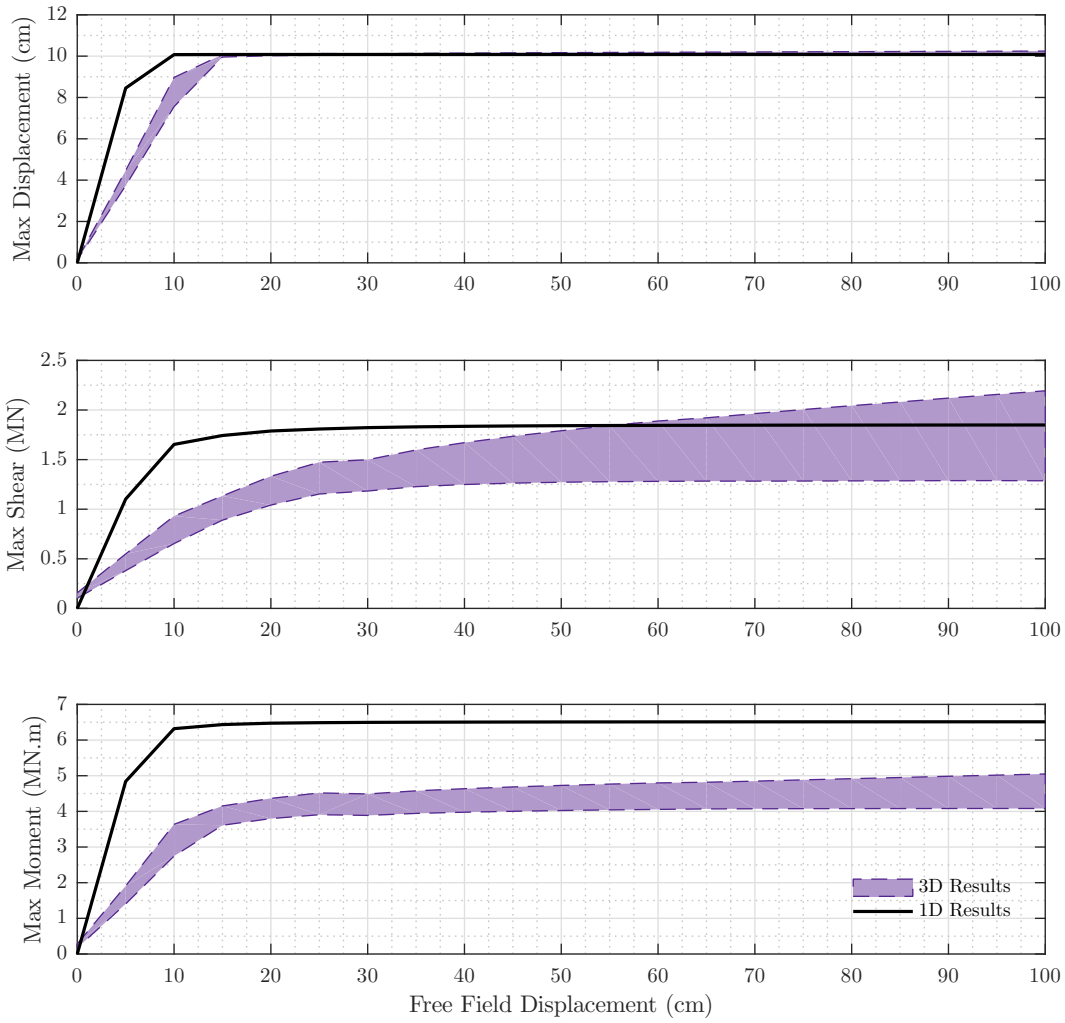

Figure 3.58: Evolution of maximum pier displacement, maximum shear force and maximum bending moment for 10 cm gap case using linear structural elements. The shaded area represents the range of pile responses recorded by the 3D model.

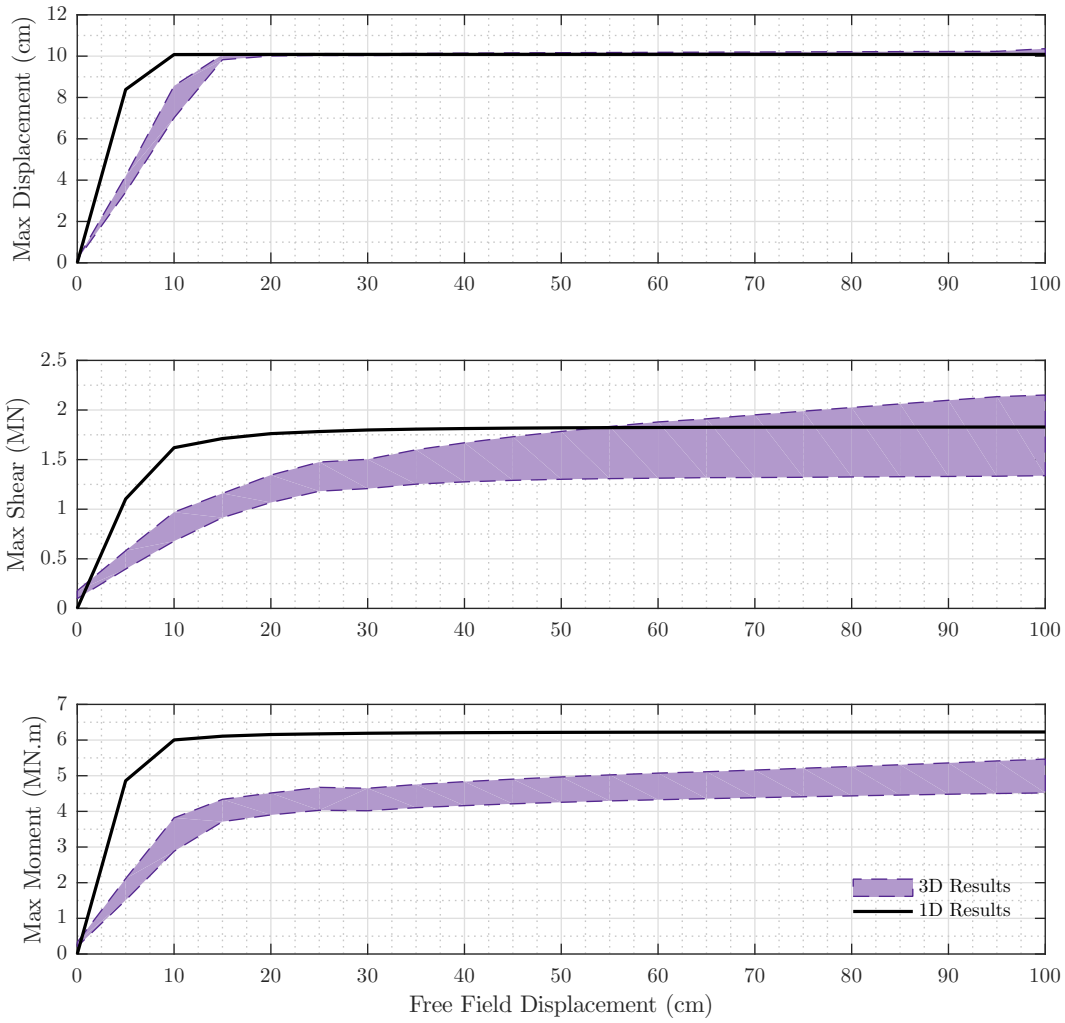

Figure 3.59: Evolution of maximum pier displacement, maximum shear force and maximum bending moment for a 10 cm gap case using nonlinear structural elements. The shaded area represents the range of pile response recorded by the 3D model.

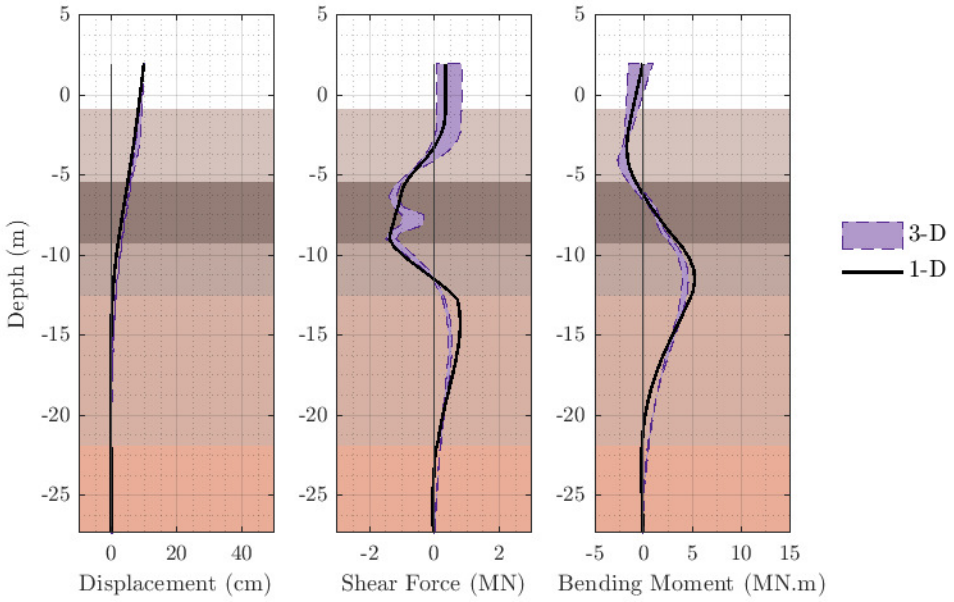

Figure 3.60: Shaft shear and bending demands at 25 cm free field displacement for 10 cm gap case. The shaded area represents the range of pile response recorded by the 3D model.

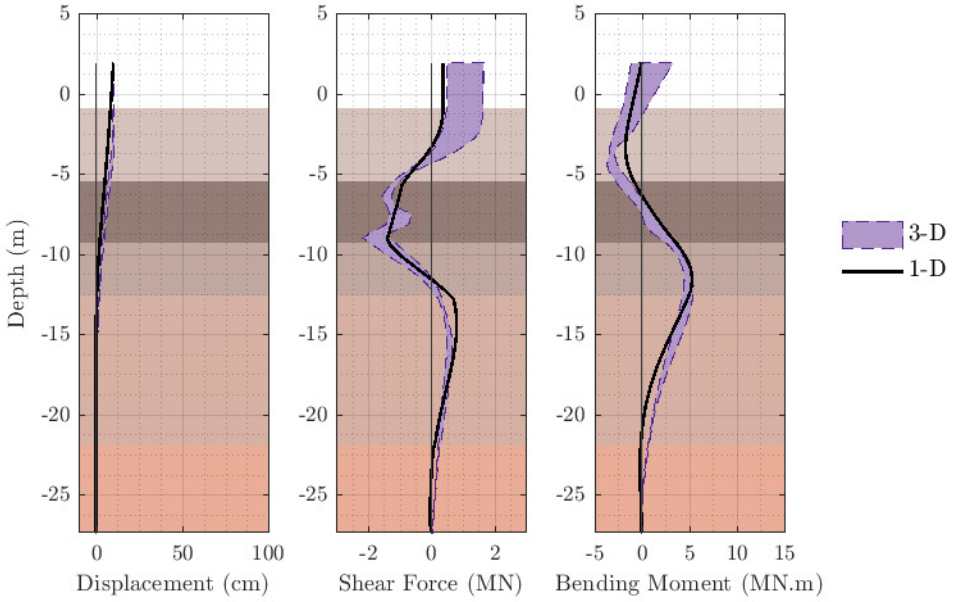

Figure 3.61: Shaft shear and bending demands at 100 cm free field displacement for 10 cm gap case. The shaded area represents the range pile response recorded by the 3D model.

Part II

CONSTITUTIVE MODELING OF GRANULAR SOILS

The second part of the dissertation addresses the topic of constitutive modeling of granular soils. In particular, advanced constitutive models capable of capturing liquefaction and cyclic mobility of sands is of interest. An advanced bounding surface plasticity model is introduced and implementation details are given. Methods for integrating the resulting constitutive equations are discussed and verification and validation of this constitutive model follows afterward.

Journal papers and reports published by the author and coworkers as a result of this part of the research include:

– *Liquefaction Experiment and Analysis Projects (LEAP)*

1. **Ghofrani**, A. and Arduino, P. (2017). "Prediction of leap centrifuge test results using a pressure-dependent bounding surface constitutive model." *Soil Dynamics and Earthquake Engineering*
2. Zeghal, M., Goswami, N., Kutter, B. L., Manzari, M. T., Abdoun, T., Arduino, P., Armstrong, R., Beaty, M., Chen, Y.-M., **Ghofrani**, A., Haigh, S., Hung, W.-Y., Iai, S., Kokkali, P., Lee, C.-J., Madabhushi, G., Tobita, T., Ueda, K., Zhou, Y.-G., and Ziotopoulou, K. (2017). "Stress-strain response of the LEAP-2015 centrifuge tests and numerical predictions." *Soil Dynamics and Earthquake Engineering*
3. Manzari, M. T., Ghoraiby, M. E., Kutter, B. L., Zeghal, M., Abdoun, T., Arduino, P., Armstrong, R. J., Beaty, M., Carey, T., Chen, Y., **Ghofrani**, A., Gutierrez, D., Goswami, N., Haigh, S. K., Hung, W.-Y., Iai, S., Kokkali, P., Lee, C.-J., Madabhushi, S. G., Mejia, L., Sharp, M., Tobita, T., Ueda, K., Zhou, Y., and

Ziotopoulou, K. (2017). "Liquefaction experiment and analysis projects (LEAP): Summary of observations from the planning phase." *Soil Dynamics and Earthquake Engineering*

4. Chen, L., **Ghofrani**, A., and Arduino, P. (under review). "Prediction of leap-ucd-2017 centrifuge test results using two advanced plasticity sand models." *Centrifuge Experiments and Numerical Simulations of Lateral Spreading due to Soil Liquefaction: Proceedings of the LEAP-UCD-2017 Workshop – 14-15 Dec 2017*, M. Zeghal, B. Kutter, and M. Manzari, eds., Davis, CA

– *Prediction of Nonlinear Soil Behavior (PRENOLIN)*

5. Rgnier, J., Bonilla, L., Bard, P., Bertrand, E., Hollender, F., Kawase, H., Sicilia, D., Arduino, P., Amorosi, A., Asimaki, D., Boldini, D., Chen, L., Chiaradonna, A., DeMartin, F., Ebrille, M., Elgamal, A., Falcone, G., Foerster, E., Foti, S., Garini, E., Gazetas, G., Glis, C., **Ghofrani**, A., Giannakou, A., Gingery, J. R., Glinsky, N., Harmon, J., Hashash, Y., Iai, S., Jeremi, B., Kramer, S., Kontoe, S., Kristek, J., Lanzo, G., Lernia, A. d., LopezCaballero, F., Marot, M., McAllister, G., Diego Mercerat, E., Moczo, P., MontoyaNoguera, S., Musgrove, M., NietoFerro, A., Pagliaroli, A., Pisan, F., Richterova, A., Sajana, S., Santisi d'Avila, M. P., Shi, J., Silvestri, F., Taiebat, M., Tropeano, G., Verrucci, L., and Watanabe, K. (2016). "International benchmark on numerical simulations for 1d, nonlinear site response (prenolin): Verification phase based on canonical casesinternational benchmark on numerical simulations for 1d, nonlinear site response (prenolin)." *Bulletin of the Seismological Society of America*, 106(5), 2112

6. Rgnier, J., Bonilla, L., Bard, P., Bertrand, E., Hollender, F., Kawase, H., Sicilia, D., Arduino, P., Amorosi, A., Asimaki, D., Boldini, D., Chen, L., Chiaradonna, A., DeMartin, F., Elgamal, A., Falcone, G., Foerster, E., Foti, S., Garini, E., Gazetas, G., Glis, C., **Ghofrani**, A., Giannakou, A., Gingery, J., Glinsky, N., Harmon,

J., Hashash, Y., Iai, S., Kramer, S., Kontoe, S., Kristek, J., Lanzo, G., Lernia, A. d., LopezCaballero, F., Marot, M., McAllister, G., Diego Mercerat, E., Moczo, P., MontoyaNoguera, S., Musgrove, M., NietoFerro, A., Pagliaroli, A., Passeri, F., Richterova, A., Sajana, S., Santisi dAvila, M. P., Shi, J., Silvestri, F., Taiebat, M., Tropeano, G., Vandeputte, D., and Verrucci, L. (2018). "Prenolin: International benchmark on 1d nonlinear siteresponse analysisvalidation phase exerciseprenolin: International benchmark on 1d nonlinear siteresponse analysisvalidation phase exercise." *Bulletin of the Seismological Society of America*, 108(2), 876

– *Miscellaneous Projects*

7. Ramirez, J., Barrero, A. R., Chen, L., **Ghofrani**, A., Dashti, S., Taiebat, M., and Arduino, P. (2018). "Capabilities and limitations of different numerical tools in capturing seismic site performance in a layered liquefiable site." *Geotechnical Earthquake Engineering and Soil Dynamics V, June 10-13, 2018 – Austin, Texas*

8. Ramirez, J., Barrero, A., Chen, L., Dashti, S., **Ghofrani**, A., Taiebat, M., and Arduino, P. (in press). "Site response in a layered liquefiable deposit: Evaluation of different numerical tools and methodologies with centrifuge experimental results." *Journal of Geotechnical and Geoenvironmental Engineering*

Chapter 4

AN ADVANCED RATE-INDEPENDENT BOUNDING SURFACE PLASTICITY MODEL FOR GRANULAR SOILS

4.1 Introduction

Various material behaviors such as yielding, plasticity, work (strain) hardening/softening, creep, stress relaxation etc. can be numerically modeled using basic combination of simple rheological models. Elasto-plastic, Visco-elastic and Visco-plastic material models are examples of formulations based on such combinations.

Rate-independent elasto-plastic theory is one of the most important and most common sub-categories of computational inelasticity in geotechnical engineering. Usually the behavior of sands is modeled using this type of inelastic formulation. A brief review of rate-independent elasto-plasticity follows in this chapter. An implicit assumption of small-deformations underlies the theory presented below. For a more extensive discussion on computational inelasticity, the reader may refer to the textbooks by Simo and Hughes (1998) and Anandarajah (2011).

An advanced constitutive model for granular soils proposed by Dafalias and Manzari (2004) is explained in this chapter. The following chapters discuss the integration of nonlinear constitutive equations specifically considering this constitutive model.

4.2 Rate-Independent Elastic-Plastic Theory

It is common practice in the implementation of Initial-Boundary Value Problem (IBVP) solution platforms for solid mechanics, to use the displacement field as the primary variable. Therefore, it is convenient to consider strains as the driving variable in constitutive model development and write the stress tensor and its evolution as a function of strain tensor.

Assuming small-deformations, the infinitesimal strain tensor, $\boldsymbol{\varepsilon}$, at a point $\mathbf{x}$ in the body domain is defined as the symmetric gradient (∇^s) of the displacement field, $\mathbf{u}$, at that point,

$$\boldsymbol{\varepsilon}(\mathbf{x}) = -\nabla^s \mathbf{u}(\mathbf{x}) = -\frac{1}{2}\left(\nabla \mathbf{u}(\mathbf{x}) + \nabla^{\mathsf{T}} \mathbf{u}(\mathbf{x})\right) , \tag{4.1}$$

where the superscript T denotes transpose. The negative sign is commomnly used in geotechnical engineering in order for the compressional strains to be positive. Throughout this section, the theory applies to $\mathbf{x}$, a point in the domain under consideration. For the sake of brevity and clarity the explicit notion of this dependence (dependence of parameters and variables on $\mathbf{x}$) is omitted in some equations.

4.2.1 Strain decomposition and hyperelastic/hypoelastic constitutive relation

In small-strain, rate-independent elastoplasticity, it is usually assumed that the strain tensor can be additively decomposed into a recoverable elastic part, $\boldsymbol{\varepsilon}^e$, and a non-recoverable plastic part, $\boldsymbol{\varepsilon}^p$, that is

$$\boldsymbol{\varepsilon} = \boldsymbol{\varepsilon}^e + \boldsymbol{\varepsilon}^p \, . \tag{4.2}$$

The evolution of the plastic strain is governed by the flow rule discussed later. Since the total strain tensor is an independent variable, it makes sense to write equation 4.2 as $\boldsymbol{\varepsilon}^e = \boldsymbol{\varepsilon} - \boldsymbol{\varepsilon}^p$.

The stress tensor, $\boldsymbol{\sigma}$, is related to the strain tensor (and therefore the displacement field) through a constitutive relationship. In classical rate-independent plasticity theory, a *hyperelastic* relationship can be used to define the stress response. Using a hyperelastic relationship, a stored energy function, W, of the system can be used to characterize the stress response as

$$\boldsymbol{\sigma} = \frac{\partial W(\boldsymbol{\varepsilon}^e)}{\partial \boldsymbol{\varepsilon}^e} \, . \tag{4.3}$$

The stress tensor can be written as $\boldsymbol{\sigma} = \mathbb{C} : \boldsymbol{\varepsilon}^e$. Here $\mathbb{C} = \frac{\partial^2 W}{\partial \boldsymbol{\varepsilon}^e \otimes \partial \boldsymbol{\varepsilon}^e}$ is the 4^{th} order elastic tangent tensor. The hyper-elastic response of the system can be nonlinear in nature, i.e., $\mathbb{C} \neq \text{const}$ but $\mathbb{C} = \hat{\mathbb{C}}(\boldsymbol{\varepsilon}^e)$. Therefore, it is more convenient to write this relationship in rate form as

$$\dot{\boldsymbol{\sigma}} = \hat{\mathbb{C}}(\boldsymbol{\varepsilon}^e) : \dot{\boldsymbol{\varepsilon}}^e = \hat{\mathbb{C}}(\boldsymbol{\varepsilon}^e) : (\dot{\boldsymbol{\varepsilon}} - \dot{\boldsymbol{\varepsilon}}^p)\,. \tag{4.4}$$

However, in advanced rate-independent plasticity certain conditions, described later, must hold in order for a stored energy function to exist. In the absence of these conditions the stress response is defined through *hypoelastic* rate constitutive relationships. In that case, the 4^{th} order elastic tangent tensor is not derived from a stored energy function and is explicitly defined. The stress response will still follow Equation 4.4.

In the rate-independent theory, Equation 4.4 is the main foundation through which the constitutive behavior is defined. Definitions of $\hat{\mathbb{C}}$ and $\dot{\boldsymbol{\varepsilon}}^p$, i.e., the elastic (material) stiffness tensor and an evolution for plastic strain, define the material constitutive behavior. The following sections define conditions and building blocks for the definition of these variables.

4.2.2 Yield surface and admissible stresses

A *yield surface* is a hyper-surface defined in the stress space. This surface divides the stress state into three regions: inside the yield surface, outside of it, and on the yield surface. The material behaves elastically inside the yield surface where its behavior is reversible. On the surface, material behavior is elastoplastic and a portion of its response is irreversible. The stress state cannot reside outside the yield surface. This means that the plastic response happens only when the stress state is located on the yield surface. The yield surface is expressed in mathematical terms by the yield function commonly defined implicitly as

$$f(\boldsymbol{\sigma}, \mathbf{q}) = 0\,, \tag{4.5}$$

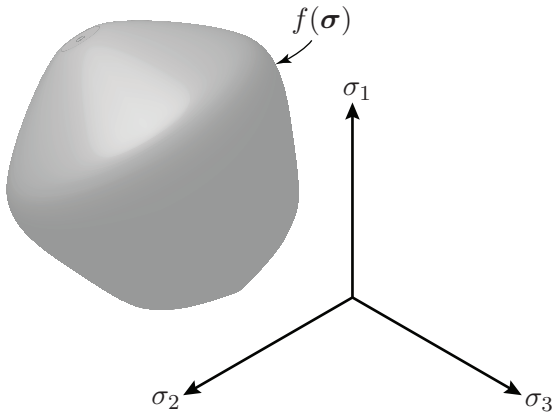

Figure 4.1: Yield Surface

where $\mathbf{q}$ represents a set of internal variables which define the current state of the material and hold its history as well. Since the plastic response happens only if a stress state is located on the yield surface, the post-yielding, *hardening/softening*, behavior of the constitutive model is defined through the evolution of the yield surface. If the yield surface does not evolve in stress space, the behavior of the model is perfectly plastic. In a perfectly plastic material, further application of strains does not induce any change in the stresses after yielding occurs.

There are three general forms of hardening behavior (i.e., evolution of the yield surface): isotropic hardening, kinematic hardening and rotational hardening. In the case of *isotropic hardening*, the size of the yield surface changes in stress space. In *kinematic hardening*, translation of the yield surface defines the hardening behavior. Lastly, rotation of the yield surface in stress space defines a form of hardening called *rotational hardening* (Sekiguchi, 1977; Dafalias and Taiebat, 2013). Most hardening behaviors can be defined through a combination of these different hardening rules.

4.2.3 Flow and hardening rule

During a plastic step, the material behavior is defined in terms of the *flow* and *hardening rules*. The flow rule defines the evolution of the plastic strain, $\dot{\boldsymbol{\varepsilon}}^p$, whereas hardening rule defines the evolution of internal parameters, $\dot{\mathbf{q}}$.

The flow rule describes the plastic strain rate by defining both its magnitude and direction. The direction of plastic strains may be defined through a potential function defined in stress space, $g(\boldsymbol{\sigma}, \mathbf{q})$, usually referred to as the *plastic potential*. In an *associative* flow rule, the plastic potential is the yield surface, otherwise, the flow rule is *non-associative*. The magnitude of the plastic strain rate is defined by a non-negative parameter, $\dot{\gamma}$, called the *consistency parameter*. In mathematical terms, the evolution of the plastic strain is expressed as

$$g(\boldsymbol{\sigma}, \mathbf{q}) = 0 \quad \text{and} \tag{4.6}$$

$$\dot{\boldsymbol{\varepsilon}}^p = \dot{\gamma} \, \frac{\partial g}{\partial \boldsymbol{\sigma}} \,, \tag{4.7}$$

where $\partial g / \partial \boldsymbol{\sigma}$ represents the gradient to the plastic potential.

Evolution of the internal parameters is governed by the *hardening rule*. A function $\mathbf{h}$ is commonly used to define the rate of change of the internal parameters, $\mathbf{q}$, using the current state of the model[1]. It is customary to write the hardening rule as

$$\dot{\mathbf{q}} = \dot{\gamma} \, \mathbf{h}(\boldsymbol{\sigma}, \mathbf{q}) \,. \tag{4.8}$$

4.2.4 Persistency / Consistency condition

As mentioned before, the yield function divides the stress state into three regions. The exterior of the yield surface where $f(\boldsymbol{\sigma}, \mathbf{q}) > 0$ is inadmissible for the stress state. Therefore, only the interior of the yield surface as well as the surface itself are admissible for a stress

[1] In a more rigorous mathematical terminology, the hardening rule is defined as $\dot{\boldsymbol{\beta}} = -\dot{\gamma} \partial g / \partial \mathbf{q}$, and $\dot{\mathbf{q}} = \mathbf{h}(\boldsymbol{\beta})$, where $\boldsymbol{\beta}$ is a strain-like hardening variable.

state. This translates mathematically to a non-positive yield function, i.e., $f(\boldsymbol{\sigma}, \mathbf{q}) \leq 0$. Additionally, plastic deformations happen only if the stress state is on the yield surface. As a result, elastic behavior can happen only inside the yield surface which means $\dot{\gamma} = 0$ when $f(\boldsymbol{\sigma}, \mathbf{q}) < 0$. Irreversible behavior can happen only if $f(\boldsymbol{\sigma}, \mathbf{q}) = 0$. Therefore, $\dot{\gamma} \geq 0$ when $f(\boldsymbol{\sigma}, \mathbf{q}) = 0$. These conditions can be combined and mathematically written using conventional Kuhn-Tucker complementarity conditions as

$$f \leq 0 \quad , \quad \dot{\gamma} \geq 0 \quad , \quad \dot{\gamma} f = 0 \,. \tag{4.9}$$

Clearly, $\dot{f} \leq 0$ whenever $f = 0$, otherwise $\dot{f} > 0$ leads to an inadmissible stress state. In other words plastic behavior happens when the stress state persists on being on the yield surface. Elastic unloading happens as soon as it moves inward. This condition is satisfied through the *persistency* or *consistency* condition defined as

$$\dot{\gamma}\, \dot{f} = 0 \,. \tag{4.10}$$

The persistency condition ensures the stress state remains inside or on the boundary of the yield surface during a plastic state.

It is noteworthy that the flow rule and the hardening rule are related through the persistency condition. From Equation 4.10 we get

$$\dot{f} = \frac{\partial f}{\partial \boldsymbol{\sigma}} : \dot{\boldsymbol{\sigma}} + \frac{\partial f}{\partial \mathbf{q}} : \dot{\mathbf{q}} = 0 \,. \tag{4.11}$$

Combining this equation with Equations 4.4, 4.7 and 4.8, and solving for the consistency parameter, $\dot{\gamma}$, results in

$$\dot{\gamma} = \frac{\partial f / \partial \boldsymbol{\sigma} : \mathbb{C} : \dot{\boldsymbol{\varepsilon}}}{\partial f / \partial \boldsymbol{\sigma} : \mathbb{C} : \partial g / \partial \boldsymbol{\sigma} - \partial f / \partial \mathbf{q} : \mathbf{h}} \,. \tag{4.12}$$

This equation is often written as

$$\dot{\gamma} = \frac{\partial f/\partial \boldsymbol{\sigma} : \mathbb{C} : \dot{\boldsymbol{\varepsilon}}}{\partial f/\partial \boldsymbol{\sigma} : \mathbb{C} : \partial g/\partial \boldsymbol{\sigma} + K_p}\,, \tag{4.13}$$

where

$$K_p = \frac{1}{\dot{\gamma}} \frac{\partial f}{\partial \boldsymbol{\sigma}} : \dot{\boldsymbol{\sigma}}\,. \tag{4.14}$$

is known as the *plastic modulus*. Using Equation 4.10, K_p can be written in terms of the internal variables, $\mathbf{q}$, as

$$\dot{f} = \dot{\gamma}\, K_p + \frac{\partial f}{\partial \mathbf{q}} : \dot{\mathbf{q}} = 0 \Rightarrow K_p = -\frac{1}{\dot{\gamma}} \frac{\partial f}{\partial \mathbf{q}} : \dot{\mathbf{q}}\,, \tag{4.15}$$

hence Equation 4.13.

Together, these rules and conditions form the basis of rate-independent elastoplastic constitutive models. There are many different constitutive models proposed in the literature based on this theory. They mainly differ in the definition of the yield condition, plastic potential function, flow rule and the hardening rules.

4.2.5 Material Tangent

It is usually required to calculate the rate of change of stress with respect to change in strain. This quantity is called the *material tangent* or simply the *elastoplastic tangent* denoted as $\mathbb{C}^{\text{ep}}$. Using Equations 4.4, 4.7 and 4.13 and expressing

$$\dot{\boldsymbol{\sigma}} = \mathbb{C} : (\dot{\boldsymbol{\varepsilon}} - \dot{\boldsymbol{\varepsilon}}^p) = \mathbb{C} : (\dot{\boldsymbol{\varepsilon}} - \dot{\gamma} \frac{\partial g}{\partial \boldsymbol{\sigma}}) \tag{4.16}$$

$$= \left(\mathbb{C} - \frac{\mathbb{C} : \partial g/\partial \boldsymbol{\sigma} \otimes \partial f/\partial \boldsymbol{\sigma} : \mathbb{C}}{\partial f/\partial \boldsymbol{\sigma} : \mathbb{C} : \partial g/\partial \boldsymbol{\sigma} + K_p} \right) : \dot{\boldsymbol{\varepsilon}} = \mathbb{C}^{\text{ep}} : \dot{\boldsymbol{\varepsilon}}\,, \tag{4.17}$$

with

$$\mathbb{C}^{\text{ep}} = \frac{d\boldsymbol{\sigma}}{d\boldsymbol{\varepsilon}} = \mathbb{C} - \frac{\mathbb{C} : \partial g/\partial \boldsymbol{\sigma} \otimes \partial f/\partial \boldsymbol{\sigma} : \mathbb{C}}{\partial f/\partial \boldsymbol{\sigma} : \mathbb{C} : \partial g/\partial \boldsymbol{\sigma} + K_p} \,. \tag{4.18}$$

4.3 Bounding Surface Plasticity

Bounding surface plasticity is a subclass of rate-independent plasticity in which a measure of the distance between the current stress state and a properly defined *image* stress state on a *bounding surface* is used to define the flow and hardening rules. Using a mapping strategy, a point on the *bounding surface*, called the *image stress state*, is associated to the current stress state. The mapping strategy assigns a unique image stress point for each stress state on or inside the bounding surface. The mapping cannot be invertible but it should be continuous. Continuity of the mapping guaranties that the image stress coincides with the stress state as it approaches the bounding surface. To ensure that the yield/loading surface does not intersect with the bounding surface, the gradient to these surfaces must point in the same direction. An elaborate description of "bounding surface plasticity" is given in Dafalias (1986).

4.4 Manzari-Dafalias Model Description

Using bounding surface plasticity, Manzari and Dafalias (1997) proposed an elastoplastic constitutive model based on "critical state soil mechanics" to capture the behavior of cohesionless soils (sands) . This model has laid the basis for several advanced constitutive models for sands and has proven to be effective in capturing many of the well-known behavior observed in sands at different densities and under different drainage and loading conditions. The relationship with critical state soil mechanics is made through the state parameter, ψ (Been and Jefferies, 1985) which enables the model to capture denser-than-critical and looser-than-critical stress-strain behavior. Later, Dafalias and Manzari (2004) improved the model by introducing the idea of a fabric tensor to facilitate a better representation of contraction

and dilation. A brief description of the model proposed in 2004 and its implementation in OpenSees (2007) is given below.

Yield surface and elastic response The constitutive behavior in this model is driven by the change in stress ratio ($\mathbf{s}/p$), where p is the mean confining effective pressure defined as $p = \frac{1}{3}\,\mathrm{tr}(\boldsymbol{\sigma})$ and $\mathbf{s}$ is the deviatoric portion of the stress tensor $\boldsymbol{\sigma}$ defined as $\mathbf{s} = \boldsymbol{\sigma} - p\mathbf{1}$, where $\mathbf{1}$ is the 2$^{\text{nd}}$ order identity tensor. The yield surface is represented by a cone in stress space as

$$f = \|\mathbf{s} - p\boldsymbol{\alpha}\| - \sqrt{\tfrac{2}{3}}mp = 0\,, \tag{4.19}$$

where m controls the size of the yield surface and $\boldsymbol{\alpha}$ is a back-stress ratio defining the center of the yield surface. The back-stress (here back-stress ratio) is a deviatoric tensor used in this constitutive model to control kinematic hardening behavior. Evolution of this parameter defines the hardening behavior and is described in the following sections. The trace of the yield surface (Equation 4.19) on a deviatoric plane with a hydrostatic stress p and parallel to the π-plane[2], is a circle with its center located at $p\boldsymbol{\alpha}$ and a radius equal to $\sqrt{\frac{2}{3}}mp$ (Figure 4.2).

The gradient of the yield function is calculated as

$$\frac{\partial f}{\partial \boldsymbol{\sigma}} = \boldsymbol{n} - \frac{1}{3}\left(\boldsymbol{n} : \boldsymbol{\alpha} + \sqrt{\frac{2}{3}}m\right)\mathbf{1}\,, \tag{4.20}$$

where

$$\mathbf{n} = \frac{\mathbf{s} - p\boldsymbol{\alpha}}{\|\mathbf{s} - p\boldsymbol{\alpha}\|}\,. \tag{4.21}$$

[2] π-plane is defined as the plane on which $\sigma_1 + \sigma_2 + \sigma_3 = 0$.

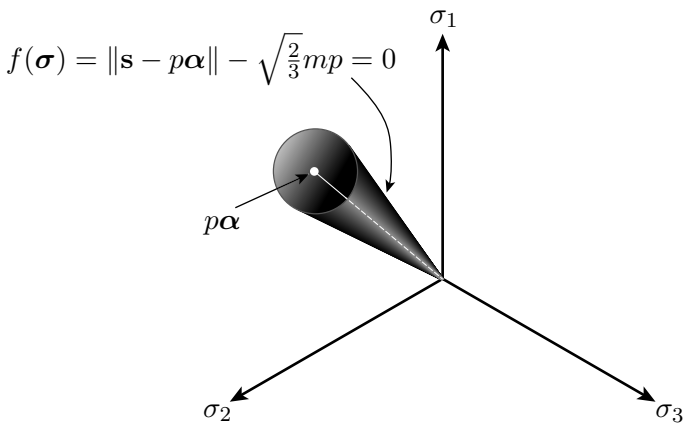

Figure 4.2: Manzari-Dafalias yield surface

It is clear that $\mathbf{n}$ is a deviatoric tensor, which means $\text{tr}(\mathbf{n}) = 0$. It further satisfies $\|\mathbf{n}\| = 1$. The normal tensor to the yield surface at any point on the yield surface is obtained as

$$\left.\frac{\partial f}{\partial \boldsymbol{\sigma}}\right|_{f=0} = \mathbf{n} - \frac{1}{3}\mathbf{n} : \frac{\mathbf{s}}{p}\mathbf{1}\,. \tag{4.22}$$

In deriving Equation 4.22, we use $f = 0$ and substitute $\sqrt{\frac{2}{3}}mp = \|\mathbf{s} - p\boldsymbol{\alpha}\|$ in the gradient of the yield surface as

$$\begin{aligned} -\frac{1}{3}\left(\boldsymbol{n} : \boldsymbol{\alpha} + \sqrt{\frac{2}{3}}m\right)\mathbf{1} &= -\frac{1}{3}\left(\frac{(\frac{\boldsymbol{s}}{p} - \boldsymbol{\alpha}) : \boldsymbol{\alpha} + (\frac{\boldsymbol{s}}{p} - \boldsymbol{\alpha}) : (\frac{\boldsymbol{s}}{p} - \boldsymbol{\alpha})}{\|\frac{\boldsymbol{s}}{p} - \boldsymbol{\alpha}\|}\right)\mathbf{1} \\ &= -\frac{1}{3}\left(\frac{(\frac{\boldsymbol{s}}{p} - \boldsymbol{\alpha}) : \frac{\boldsymbol{s}}{p}}{\|\frac{\boldsymbol{s}}{p} - \boldsymbol{\alpha}\|}\right)\mathbf{1} \\ &= -\frac{1}{3}\boldsymbol{n} : \frac{\boldsymbol{s}}{p}\,. \end{aligned} \tag{4.23}$$

For the elastic component of the model behavior a hyper-elastic formulation is used such that

$$\dot{\boldsymbol{\sigma}} = \mathbb{C} : \dot{\boldsymbol{\varepsilon}}^e\,. \tag{4.24}$$

The elastic tensor $\mathbb{C}$ can be expressed in terms of the shear modulus, G and the bulk modulus, K, such that

$$\mathbb{C} = K\mathbf{1} \otimes \mathbf{1} + 2G(\mathbb{1} - \frac{1}{3}\mathbf{1} \otimes \mathbf{1}) \,, \tag{4.25}$$

also known as Hooke's law. In this equation, $\mathbf{1}$ and $\mathbb{1}$ are respectively the 2^{nd} and 4^{th} order identity tensors. As a result, Equation 4.24 can be written in a different form by decomposing the strain and stress tensors in volumetric, ε_v and p, and deviatoric parts, $\mathbf{e}$ and $\mathbf{s}$, such that

$$\dot{p} = K \, \dot{\varepsilon}_v^e \,, \tag{4.26}$$

$$\dot{\mathbf{s}} = 2G \, \dot{\mathbf{e}}^e \,, \tag{4.27}$$

where the shear modulus, G, and bulk modulus, K are both functions of p and current void ratio e (Richard et al., 1970; Li and Dafalias, 2000) as follows.

$$G = G_0 p_{\text{atm}} \frac{(2.97 - e)^2}{1 + e} \sqrt{\frac{p}{p_{\text{atm}}}} \,, \tag{4.28}$$

$$K = \frac{2(1 + \nu)}{3(1 - 2\nu)} G \,. \tag{4.29}$$

In these equations, p_{atm} is the atmospheric pressure, and dimensionless G_0 and ν are model parameters defining the elastic properties of the material, with ν being the Poisson's ratio.

Critical state surface The critical state for a soil (Schofield and Wroth, 1968) is defined as a line in the $\langle p, q, e \rangle$ space, where

$$q = \sqrt{\tfrac{3}{2}\mathbf{s} : \mathbf{s}} \tag{4.30}$$

is a measure of the deviatoric stress. It is assumed that when a material reaches the critical state, it deforms continuously in shear with no change in volume. That is when $q = q_c$, $p = p_c$, $e = e_c$, where $q_c \,, p_c$ and e_c define a point on the critical state line (CSL), we have $\dot{\varepsilon}_v = 0$.

The CSL used in the Manzari-Dafalias model is defined using a power law as suggested by Li and Wang (1998),

$$e_c = e_0 - \lambda_c \left(\frac{p_c}{p_{\text{atm}}} \right)^{\xi} , \tag{4.31}$$

where e_0 is the critical state void ratio at $p_c = 0$. λ_c and ξ are material parameters; p_{atm} is the atmospheric pressure and is used as a non-dimentionalizing factor. The critical state stress ratio, M, is defined as

$$M = \frac{q_c}{p_c} , \tag{4.32}$$

and is closely related to the critical state friction angle, ϕ_c. Figure 4.3 shows the critical state line used in this model in the $\langle p, q, e \rangle$ space as well as its projections on the $\langle e, q \rangle$, $\langle q, p \rangle$ and $\langle e, p \rangle$ planes.

The state parameter, $\psi = e - e_c$, (Been and Jefferies, 1985) measures the distance from the current state to the corresponding critical state. The Manzari-Dafalias constitutive model further uses ψ to define the flow and hardening rules as a way to connect critical state mechanics to rate-independent plasticity theory.

Experiments have shown that the behavior of the soil is dependent on stress paths. In order to capture the effects of stress path in this constitutive model, an effective Lode angle[3] θ is used to locate the stress state which varies from 0 to $\pi/3$. This angle is used to interpolate the value of the critical stress state ratio at a given θ between its value in triaxial compression,

[3]Lode angle is defined as $\theta = \frac{J_3}{2} \left(\frac{3}{J_2} \right)^{3/2}$, where J_2 and J_3 are the second and third invariants of the deviatoric stress $\mathbf{s}$, defined as $J_2 = \frac{1}{2}\mathbf{s} : \mathbf{s}$, and $J_3 = \det \boldsymbol{\sigma}$.

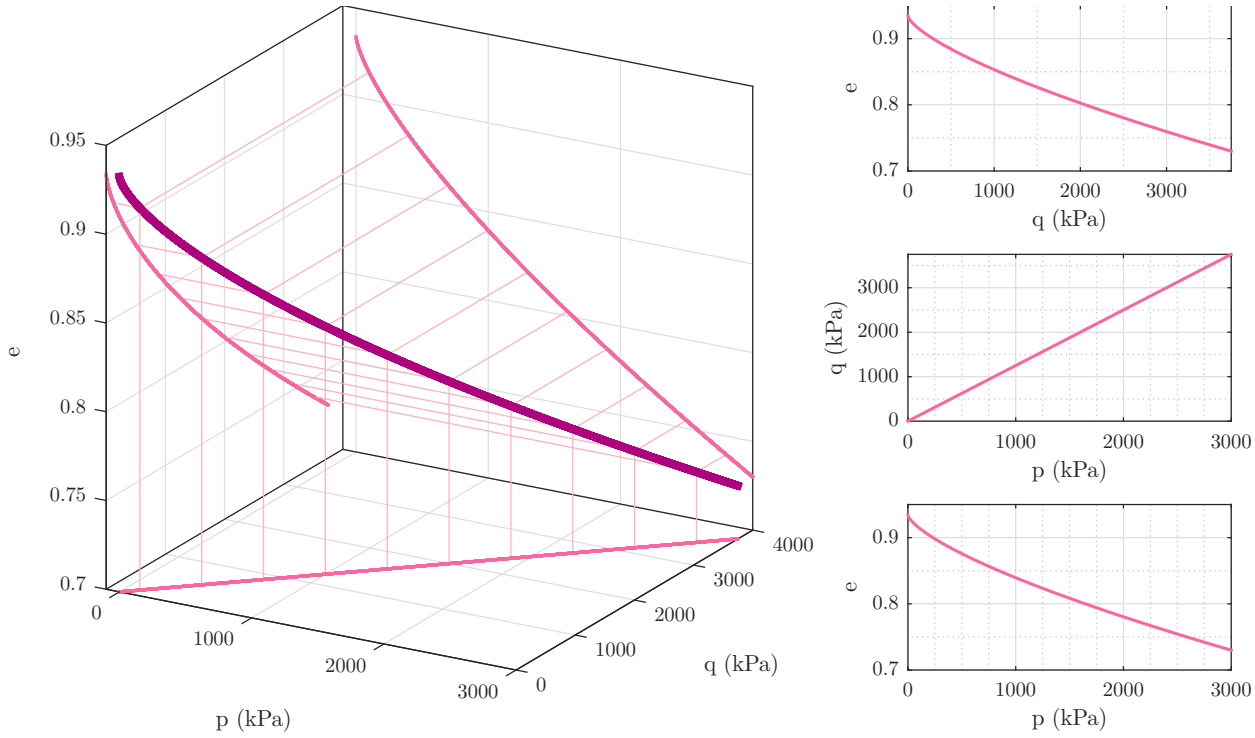

Figure 4.3: Critical State Line

$M_c = M$ $(\theta = 0)$, and its value in triaxial extension, M_e $(\theta = \pi/3)$, according to

$$M_\theta = g(\theta, c)M\,, \tag{4.33}$$

$$g(\theta, c) = \frac{2c}{(1+c) - (1-c)\cos 3\theta}\,, \tag{4.34}$$

where $c = M_e/M_c$ is a parameter of the model. The locus of critical state lines in principal stress space (principal stress ratio space) is a cone as illustrated in Figure 4.4.

Bounding surface In bounding surface plasticity, the plastic modulus is a function of the distance between a stress state to its image on a bounding surface. In the Manzari-Dafalias model, the bounding surface is defined in the stress-ratio space by scaling the critical state

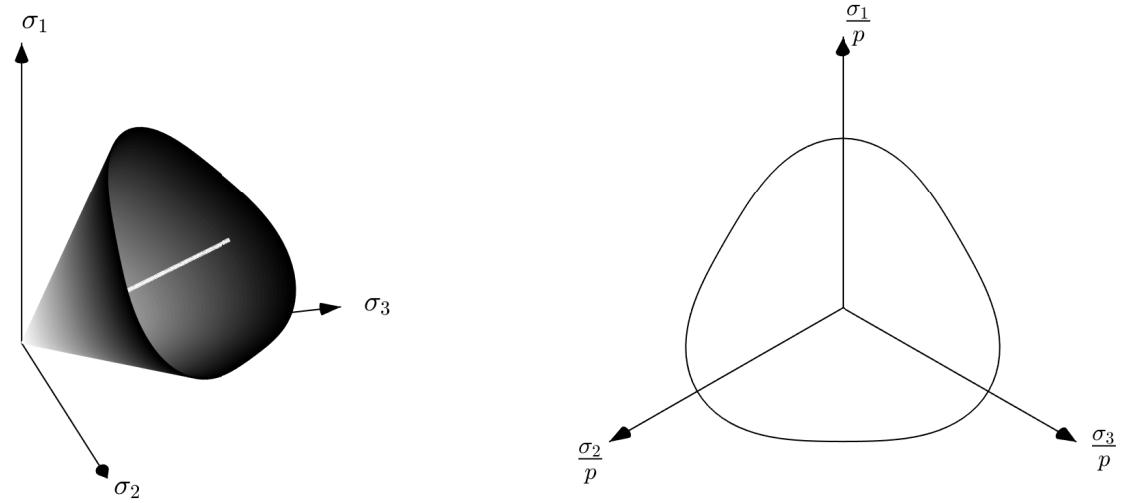

(a) (b)

Figure 4.4: Critical State Surface: a) Principal stress space, b) Deviatoric plane

surface. The scaling factor (M^b/M) is defined by an exponential function of the form

$$M^b = M \, \exp(-n^b \psi) \,, \tag{4.35}$$

where n^b is a model parameter and ψ is the state parameter. The stress state image on the bounding surface is mapped using the normal to the yield surface at the stress state in the deviatoric space, $\mathbf{n}$. Instead of defining the actual stress state image, it is convenient to use the image of the back stress ratio, $\boldsymbol{\alpha}_\theta^b$, to define the behavior of the material. This mapping can be expressed as

$$\boldsymbol{\alpha}_\theta^b = \sqrt{\frac{2}{3}} \alpha_\theta^b \mathbf{n} = \sqrt{\frac{2}{3}} \left(M_\theta^b - m \right) \mathbf{n} \,, \tag{4.36}$$

where $M_\theta^b = g(\theta, c)M^b$. Figure 4.5 illustrates the definition of the bounding surface and bounding stress image point.

Dilatancy surface Another important feature of the Manzari-Dafalias model is its ability to capture dilation/contraction behavior. For this purpose the model uses Rowe's dilatancy theory (Rowe, 1962) and defines a variable D as the ratio of plastic volumetric strain and plastic deviatoric strain. This variable, D, is made proportional to the distance between the back-stress ratio ($\boldsymbol{\alpha}$) and a dilatancy stress ratio image point defined on the so called phase transformation surface (Ishihara et al., 1975). Similar to the bounding surface, the dilatancy surface, shown in Figure 4.5, is defined by scaling the critical state surface by

$$M^d = M \, \exp(n^d \psi) \,, \tag{4.37}$$

where n^d is a model parameter. Similar to the image on the bounding surface, the image state on the dilatancy surface, $\boldsymbol{\alpha}_\theta^d$ is mapped using the normal to the yield surface at the stress state in the deviatoric space, $\mathbf{n}$, and the interpolation function $g(\theta, c)$ and is defined as

$$\boldsymbol{\alpha}_\theta^d = \sqrt{\frac{2}{3}} \alpha_\theta^d \mathbf{n} = \sqrt{\frac{2}{3}} \left(M_\theta^d - m \right) \mathbf{n} \,, \tag{4.38}$$

where $M_\theta^d = g(\theta, c)M^d$.

Whenever the material is at a denser-than-critical state ($\psi < 0$), we have $M^d < M < M^b$, meaning that the dilatancy surface is smaller than the critical surface while the bounding surface is larger. If $\psi > 0$, indicating a material at a looser-than-critical state, the opposite situation arises and $M^b < M < M^d$. Eventually, when the material reaches a critical state where $\psi = 0$, the three surfaces coincide. Implications of these inequalities become apparent in the following section.

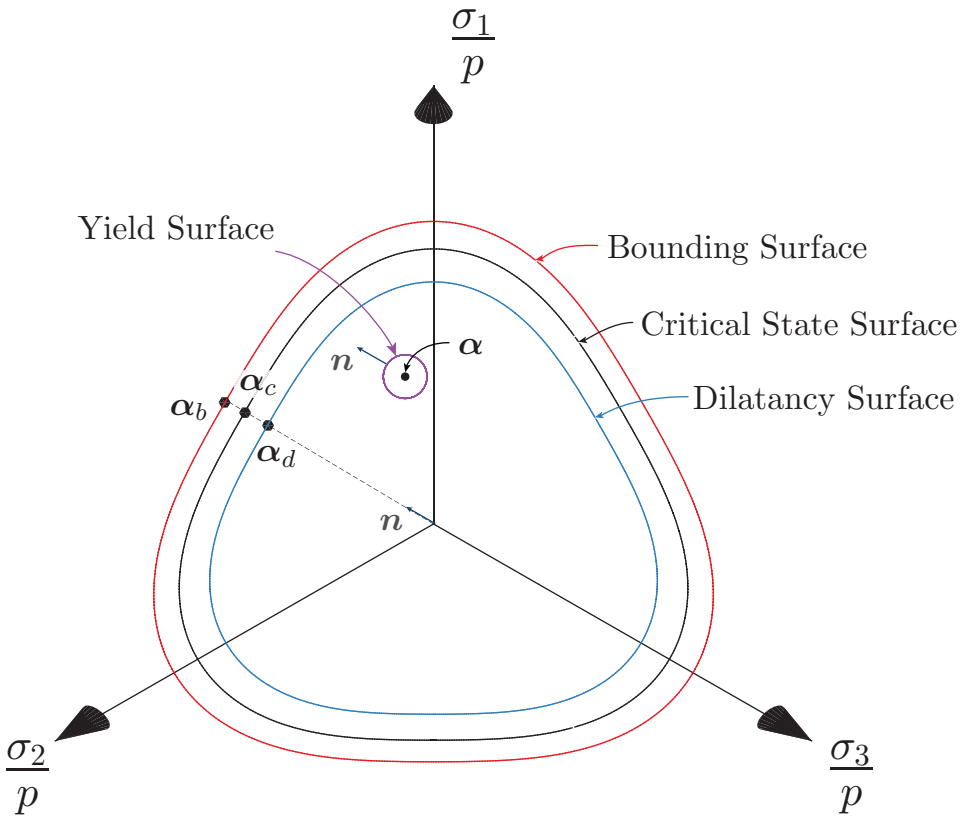

Figure 4.5: Bounding and Dilatancy Surfaces

Flow rule The flow rule in the Manzari-Dafalias model is defined by

$$\dot{\boldsymbol{\varepsilon}}^p = \dot{\gamma}\mathbf{R}\,, \tag{4.39}$$

where the direction of the plastic strain rate, $\mathbf{R}$, is decomposed into volumetric and deviatoric parts as

$$\mathbf{R} = \mathbf{R}' + \frac{1}{3}D\mathbf{1}\,, \tag{4.40}$$

with

$$\mathbf{R}' = B\mathbf{n} - C(\mathbf{n}^2 - \frac{1}{3}\mathbf{1})\,, \tag{4.41}$$

and D is Rowe's dilatancy variable (Rowe, 1962).

To satisfy continuity and avoid intersection of the yield surface with the bounding surface, $\mathbf{R}'$ is defined as the normal to critical state surface at the location of the image point $\boldsymbol{\alpha}_\theta^c$. Therefore, B and C are obtained as

$$B = 1 + \frac{3}{2}\frac{1-c}{c}g(\theta, c)\cos 3\theta\,, \tag{4.42}$$

$$C = 3\sqrt{\frac{3}{2}}\frac{1-c}{c}g(\theta, c)\,. \tag{4.43}$$

For $B \neq 1$ or $C \neq 0$, the flow rule is non-associative. It is important to observe that $\|\mathbf{R}\|$ is not necessarily equal to one. Therefore, $\dot{\gamma}$ alone does not define the magnitude of the incremental plastic strain.

As mentioned before, the dilatancy variable, D, follows Rowe's theory and depends on the distance between the back-stress ratio, $\boldsymbol{\alpha}$, and the image stress ratio on the dilatancy surface, $\boldsymbol{\alpha}_\theta^d$. This is done in the model by defining D as

$$D = A_d(\boldsymbol{\alpha}_\theta^d - \boldsymbol{\alpha}) : \mathbf{n}\,, \tag{4.44}$$

where A_d is a proportionality factor defined as

$$A_d = A_0(1 + \langle \mathbf{z} : \mathbf{n} \rangle)\,, \tag{4.45}$$

where A_0 is a model parameter and $\mathbf{z}$ is the fabric tensor. In this equation, the MacCauley bracket, $\langle \bullet \rangle$ (also known as Heaviside function) defined as

$$\langle x \rangle = \begin{cases} 0 & \text{if } x < 0 \\ x & \text{if } x \geq 0 \end{cases} , \tag{4.46}$$

is used. Introducing a fabric tensor in the definition of the dilatancy parameter is another feature of the Manzari-Dafalias model which helps stabilize cyclic mobility behavior at low confining pressures allowing the model to reproduce the well known "butterfly" orbits and prevent stagnation of stress path at higher confining pressures. The fabric tensor evolves according to

$$\dot{\mathbf{z}} = -c_z \langle -\dot{\varepsilon}_v^p \rangle (z_{\max} \mathbf{n} + \mathbf{z}) , \tag{4.47}$$

where c_z and $z_{\max}$ are model parameters. The fabric tensor starts from zero and accumulates when the material response is dilative, i.e., $\dot{\varepsilon}_v^p < 0$. The rate of plastic volumetric strain increases if the fabric tensor and the normal to yield surface are aligned (i.e., $\mathbf{z} : \mathbf{n} \geq 0$). Otherwise D evolves according to $D = A_0(\boldsymbol{\alpha}_\theta^d - \boldsymbol{\alpha}) : \mathbf{n}$.

Hardening rule The hardening rule in this model only consists of kinematic hardening (change in location of the yield surface in stress space). The isotropic hardening (change in size of the yield surface) used in earlier versions of the constitutive model is omitted ($\dot{m} = 0$). Kinematic hardening is defined in terms of the evolution of the back-stress ratio, $\boldsymbol{\alpha}$, as

$$\dot{\boldsymbol{\alpha}} = \dot{\gamma} \left(\frac{2}{3} \right) h(\boldsymbol{\alpha}_\theta^b - \boldsymbol{\alpha}) , \tag{4.48}$$

where h is a proportionality factor and is a function of the material state. In this version of the model, h is defined as

$$h = \frac{b_0}{(\boldsymbol{\alpha} - \boldsymbol{\alpha}_{in}) : \mathbf{n}} \,, \tag{4.49}$$

with

$$b_0 = G_0 h_0 (1 - c_h e) \left(\frac{p}{p_{\text{atm}}} \right)^{-\frac{1}{2}} \,, \tag{4.50}$$

where h_0 and c_h are material parameters and $\boldsymbol{\alpha}_{in}$ is the stress ratio at which load reversal occurs. To identify the loading reversal $(\boldsymbol{\alpha} - \boldsymbol{\alpha}_{in}) : \mathbf{n}$ is used. Bn is used as a measure of loading direction and $(\boldsymbol{\alpha} - \boldsymbol{\alpha}_{in})$ as a measure of loading history. $\boldsymbol{\alpha}_{in}$ is updated whenever $(\boldsymbol{\alpha} - \boldsymbol{\alpha}_{in}) : \mathbf{n} < 0$.

Chapter 5

INTEGRATION OF NONLINEAR CONSTITUTIVE EQUATIONS

5.1 Introduction

The model introduced in the previous chapter results in a system of differential equations that define the evolution of internal variables of the model as well as the change in stress knowing a strain rate. Except for very few cases, no analytical solutions can be obtained for these equations. Therefore, a numerical approach is necessary to integrate the evolution equations. There are many integration schemes available and the characteristics of them are well-known to mathematicians and engineers. These schemes are broadly divided into two classes: a) *Explicit methods* where the solution of the equation is an explicit function of the parameters for which the values are already known, and b) *Implicit methods* where the solution also depends on the parameters that are not yet known and some sort of iterative method is required to solve the often nonlinear equations.

In this section a general evolution equation

$$\dot{u} = f(u), \quad u(0) = 0\,, \tag{5.1}$$

is considered to introduce and discuss the different integration schemes. Here we use a pseudo-time variable t to represent the solution domain and for simplicity we discretize the domain in k pieces of size Δt. In general, Equation 5.1 can represent a system of ordinary differential equations as

$$\dot{\mathbf{u}} = \mathbf{f}(\mathbf{u}), \quad \mathbf{u}(\mathbf{0}) = \mathbf{0}\,, \tag{5.2}$$

where $\mathbf{u}$ can be a vector with s components $u_1, \cdots, u_s$ and $\mathbf{f}(\mathbf{u})$ representing a vector-valued function with components $f_1(\mathbf{u}), \cdots, f_s(\mathbf{u})$; each of which can be a nonlinear function of all components of $\mathbf{u}$. The discrepancy between the actual solution of the ODE and the one calculated using any numerical scheme is called *local truncation error*, which depends on the discretization of the solution domain. If, for example, the domain is divided into k pieces of size Δt and the local truncation error is of order $(\Delta t)^2$ we say the scheme is 1^{st} order accurate; however we cannot be certain that the global error will have the same behavior. In order for a scheme to be consistent, the local truncation error should vanish as $\Delta t \to 0$. So, basically any scheme with an order of accuracy greater than zero is consistent. Lax's theorem states that any integration scheme that is both consistent and stable is also convergent (Lax and Richtmyer, 1956). It is common practice to consider an integration scheme to be "unstable" if it generates a numerical solution error that grows faster than the true solution (Durran, 2013). An integration scheme is only useful if it is both consistent and stable.

In the following sections, the solution at step $n+1$ is sought knowing the solution at step n. A general description of several integration schemes is given and specific details regarding integration of Manzari-Dafalias constitutive model follows after each section.

5.2 Explicit Methods

In explicit methods, we move forward in time using the results and parameters that we already know. Therefore, implementation of these methods comprise of function evaluations and marching forward in time. However, in these methods the region of stability is usually small, requiring fine discretization of the solution domain, resulting in expensive computations. For the implementation of the Manzari-Dafalias model, three explicit integration schemes are considered: Forward Euler method, Modified (or two-step) Euler method and 4^{th} order Runge-Kutta method. Description of these methods follows.

5.2.1 Forward Euler

The simplest method for ODE integration is the *Forward Euler* method. In this method the differential of the function is approximated by:

$$\dot{u}(t_n) = \frac{du(t_n)}{dt} = f(u^n) \approx \frac{u^{n+1} - u^n}{\Delta t} \quad , \tag{5.3}$$

where $u^n = u(t_n)$. It is possible to solve this equation explicitly for u^{n+1},

$$u^{n+1} = u^n + \Delta t f(u^n) \quad . \tag{5.4}$$

The forward Euler method is very simple to implement and is very efficient in terms of function evaluations. This method is 1$^{\text{st}}$ order accurate and it has a very small region of stability. In terms of integrating constitutive equations this means that, if no error control strategy is used, the stress state drifts from the yield surface (i.e., violating the persistency/consistency rule); which in turn increases the accumulated amount of error. Although extremely small increments may delay the problem diverging.

5.2.2 Modified Euler

The modified or two-step Euler method (also known as a two-stage Runge-Kutta) is a 2$^{\text{nd}}$ order accurate explicit method. Although the region of stability is still small, what makes this method attractive is the availability of error measure. Using this idea, Sloan et al. (2001) developed an integration method for elastoplastic models with automatic sub-stepping error control. In this method the stress state may still drift away from the yield surface, however in their approach, Sloan et al. devised a correction step which returns the stress state back to the yield surface in case drift happens.

The integration steps in this scheme are

1. First step (Forward Euler) $$\hat{u}^{n+1/2} = u^n + \frac{\Delta t}{2} f(u^n) \quad . \tag{5.5}$$

2. Second step $$u^{n+1} = u^n + \Delta t f(\hat{u}^{n+1/2}) \quad . \tag{5.6}$$

Since the local truncation error in the first step is $O(\Delta t)$ while it is $O(\Delta t^2)$ for the whole two steps, the ratio of u^{n+1} and $\hat{u}^{n+1/2}$ can be used as a measure of error and to roughly estimate the length of a more appropriate time step.

5.2.3 4^{th} Order Runge-Kutta and Other Methods

Runge-Kutta methods are a family of explicit and implicit numerical integration schemes. The most popular explicit methods among the Runge-Kutta family is the four-stage 4^{th} order method. This method enjoys a bigger region of stability with 4^{th} order accuracy. However it is computationally intensive and it is not necessarily the first option to be used for numerical integration of constitutive models. The four stages of this method are summarized below:

1. $$\hat{u}^{n+\frac{1}{2}} = u^n + \frac{\Delta t}{2} f(u^n) \quad . \tag{5.7}$$

2. $$\tilde{u}^{n+\frac{1}{2}} = u^n + \frac{\Delta t}{2} f(\hat{u}^{n+1/2}) \quad . \tag{5.8}$$

3. $$\breve{u}^n = u^n + \Delta t f(\tilde{u}^{n+1/2}) \quad . \tag{5.9}$$

4. $$u^{n+1} = u^n + \frac{\Delta t}{6}\big(f(u^n) + 2f(\hat{u}^{n+\frac{1}{2}}) + 2f(\tilde{u}^{n+\frac{1}{2}}) + f(\breve{u}^n)\big) \quad . \tag{5.10}$$

5.3 Considerations for Explicit Methods

When these explicit integration methods are used for constitutive equations, the behavior inside and outside of the yield surface needs to be distinguished and treated accordingly. Therefore, an intersection detection strategy is required to be devised to find the portion of the stress path inside the yield surface (purely elastic response) and the portion outside

the yield surface (elastoplastic response). This results in finding the intersection of the yield function with the stress increment over the loading step. Any root-finding strategies such as bisection method, Regula-Falsi or even Newton iteration can be used. For the implementation of the Manzari-Dafalias model, a modified Regula-Falsi root-finding method is used in order to find the intersection of the loading step with the yield surface.

The other shortcoming of explicit methods is the drift of the stress state from the yield surface. There are different ways to overcome this problem. Different strategies are mentioned in the literature all of which come with their strengths and weaknesses. Potts and Gens (1985) make a critical assessment of five methods for correcting the stress state for drift from the yield surface. These methods include:

1. projecting the stress state back to the yield surface by keeping the confining pressure, p, constant and reducing the shear stress (i.e., the deviatoric part of the stress),

2. projecting the stress state back to the yield surface along the accumulated effective stress direction,

3. projecting the stress state back to the yield surface along the plastic flow direction (i.e., along $\dot{\boldsymbol{\varepsilon}}^p$),

4. projecting the stress state back to the yield surface along the total strain increment direction (i.e., $\dot{\boldsymbol{\varepsilon}}$), and finally,

5. projecting the stress state back to the yield surface considering the changes in the elastic strains (called the *correct* projecting back method).

The last method seems to be more promising than the other four methods specifically because it is mathematically consistent with the definition of any constitutive model and therefore it is used in this study.

Also, in pressure-dependent models negative mean pressures are not acceptable (mean pressures usually appear under a square root in the formulation). Therefore, during integration of such constitutive models, care should be taken to avoid mean pressures to go below a threshold value or otherwise the results might be contaminated with NaN (Not a Number) values or blow up. An approach toward solving this issue is to introduce an additional *tension cut-off* surface which acts as a second yield surface (Hofstetter and Taylor, 1990). The consistency (persistency) condition on this surface prevents stresses to reach states with negative mean pressures. This feature is added to the Manzari-Dafalias model, as this model is best suited for simulating liquefaction where the confining stresses are low and are susceptible to become negative.

Finally, if the nonlinear FE framework uses global implicit methods to step forward in time, usually Newton's method is used to solve the nonlinear system of equations. In these cases, it is well known that a consistent tangent operator is needed in order to maintain quadratic convergence rate near the solution.

5.4 Consistent Tangent for Explicit Methods

The nonlinear finite element method at the global level iterates over the vector of nodal displacements to satisfy equilibrium of the discretized system. During nonlinear iterations the equilibrium equations are linearized with respect to nodal displacements and in this process it is needed to know the rate of change in stresses at each integration (Gauss quadrature) point as the nodal displacements vary. Therefore the quantity $d\boldsymbol{\sigma}_{n+1}/d\Delta\boldsymbol{\varepsilon}$ (or similarly $d\boldsymbol{\sigma}_{n+1}/d\boldsymbol{\varepsilon}_{n+1}$) appears in the tangent matrix of the global level equations. Since we can rarely find a closed-form solution for $\boldsymbol{\sigma}_{n+1}$, different numerical integration schemes are being used. As a result, the 4^{th}-order tangent tensor $d\boldsymbol{\sigma}_{n+1}/d\Delta\boldsymbol{\varepsilon}$ depends on the integration method used. This tensor is commonly called "algorithmic tangent" or "consistent tangent" operator.

In the following sections we derive the consistent tangent operator for the presented explicit numerical integration schemes. The following evolution relationships for the plastic

strain tensor, $\boldsymbol{\varepsilon}^p$, and back-stress ratio tensor, $\boldsymbol{\alpha}$, are used for the purpose of this subject;

$$\begin{cases} \dot{\boldsymbol{\varepsilon}^p} = \dot{\gamma}\mathbf{R} & , \\ \dot{\boldsymbol{\alpha}} = \dot{\gamma}\bar{\boldsymbol{\alpha}} & , \end{cases} \tag{5.11}$$

where $\dot{\gamma}$ is the consistency parameter, $\mathbf{R}$ defines the direction of the plastic strain rate and $\bar{\boldsymbol{\alpha}}$ defines the direction of the hardening variable, back stress ratio. Using the consistency condition, $\dot{f} = 0$, the consistency parameter is obtained as

$$\dot{\gamma} = \frac{\partial f/\partial \boldsymbol{\sigma} : \mathbb{C} : \dot{\boldsymbol{\varepsilon}}}{K_p + \partial f/\partial \boldsymbol{\sigma} : \mathbb{C} : \mathbf{R}} \quad , \tag{5.12}$$

where K_p is the plastic modulus.

5.4.1 Consistent Tangent for Forward Euler Method

In the forward Euler method the evolution laws are converted to an incremental form by using the parameters and quantities from the current step to calculate the increment.

$$\begin{cases} \Delta\boldsymbol{\varepsilon}^p = \Delta\gamma_n \mathbf{R}_n \\ \Delta\boldsymbol{\alpha} = \Delta\gamma_n \bar{\boldsymbol{\alpha}}_n \end{cases} \Rightarrow \begin{cases} \boldsymbol{\varepsilon}^p_{n+1} = \boldsymbol{\varepsilon}^p_n + \Delta\gamma_n \mathbf{R}_n \\ \boldsymbol{\alpha}_{n+1} = \boldsymbol{\alpha}_n + \Delta\gamma_n \bar{\boldsymbol{\alpha}}_n \end{cases} . \tag{5.13}$$

In these equations the incremental consistency parameter, $\Delta\gamma_n$, is calculated as

$$\Delta\gamma_n = \underbrace{\frac{\partial f/\partial \boldsymbol{\sigma} : \mathbb{C}}{K_p + \partial f/\partial \boldsymbol{\sigma} : \mathbb{C} : \mathbf{R}}}_{\text{Calculated at step } n} : \Delta\boldsymbol{\varepsilon} \quad . \tag{5.14}$$

Therefore, the stress at step $n+1$ can be calculated as

$$\boldsymbol{\sigma}_{n+1} = \boldsymbol{\sigma}_n + \mathbb{C} : (\Delta\boldsymbol{\varepsilon} - \Delta\boldsymbol{\varepsilon}^p) = \boldsymbol{\sigma}_n + \mathbb{C} : \Delta\boldsymbol{\varepsilon} - \Delta\gamma_n \mathbb{C} : \mathbf{R}_n \quad . \tag{5.15}$$

Computing the differentials of both sides of Equation 5.15 and knowing that the differentials of known quantities at step n are zero, we end up with

$$\mathrm{d}\boldsymbol{\sigma}_{n+1} = \mathbb{C} : \mathrm{d}\Delta\boldsymbol{\varepsilon} - \mathrm{d}\Delta\gamma_n \mathbb{C} : \mathbf{R}_n \quad . \tag{5.16}$$

From Equation 5.14 we can get the differentials of the incremental consistency parameter as

$$\mathrm{d}\Delta\gamma_n = \left(\frac{\partial f/\partial\boldsymbol{\sigma} : \mathbb{C}}{K_p + \partial f/\partial\boldsymbol{\sigma} : \mathbb{C} : \mathbf{R}} \right)_n : \mathrm{d}\Delta\boldsymbol{\varepsilon} \quad . \tag{5.17}$$

Substituting Equation 5.17 into Equation 5.16 we get

$$\mathrm{d}\boldsymbol{\sigma}_{n+1} = \mathbb{C} : \mathrm{d}\Delta\boldsymbol{\varepsilon} - \left(\left(\frac{\partial f/\partial\boldsymbol{\sigma} : \mathbb{C}}{K_p + \partial f/\partial\boldsymbol{\sigma} : \mathbb{C} : \mathbf{R}} \right)_n : \mathrm{d}\Delta\boldsymbol{\varepsilon} \right) \mathbb{C} : \mathbf{R}_n \tag{5.18}$$

$$= \left(\mathbb{C} - \frac{\mathbb{C} : \mathbf{R} \otimes \partial f/\partial\boldsymbol{\sigma} : \mathbb{C}}{K_p + \partial f/\partial\boldsymbol{\sigma} : \mathbb{C} : \mathbf{R}} \right)_n : \mathrm{d}\Delta\boldsymbol{\varepsilon} \tag{5.19}$$

$$= \mathbb{C}_n^{ep} : \mathrm{d}\Delta\boldsymbol{\varepsilon} \quad . \tag{5.20}$$

Therefore, the consistent tangent operator for the forward Euler method is equal to the continuum tangent at step n defined in 4.18.

5.4.2 Consistent Tangent for Modified (2-step) Euler Method

In the modified Euler method, a forward Euler step is taken first to get incremental values at a temporary state, and then these values are used to calculate the evolution laws and get new increments. The values of parameters at the step $n+1$ are calculated using the average of these two sets of increments. The first step in the modified Euler method is basically a

forward Euler step, resulting in an intermediate state

$$\begin{cases} \widehat{\boldsymbol{\varepsilon}^p_{n+1}} = \boldsymbol{\varepsilon}^p_n + \Delta\gamma_n \mathbf{R}_n \\ \widehat{\boldsymbol{\alpha}_{n+1}} = \boldsymbol{\alpha}_n + \Delta\gamma_n \bar{\boldsymbol{\alpha}}_n \end{cases} . \tag{5.21}$$

In the second step, the information from the first step is used to calculate $\widehat{\Delta\gamma_{n+1}}$, $\widehat{\mathbf{R}_{n+1}}$ and $\widehat{\bar{\boldsymbol{\alpha}}_{n+1}}$, and eventually the variables are updated as

$$\begin{cases} \boldsymbol{\varepsilon}^p_{n+1} = \boldsymbol{\varepsilon}^p_n + \frac{1}{2}(\Delta\gamma_n \mathbf{R}_n + \widehat{\Delta\gamma_{n+1}}\widehat{\mathbf{R}_{n+1}}) \\ \boldsymbol{\alpha}_{n+1} = \boldsymbol{\alpha}_n + \frac{1}{2}(\Delta\gamma_n \bar{\boldsymbol{\alpha}}_n + \widehat{\Delta\gamma_{n+1}}\widehat{\bar{\boldsymbol{\alpha}}_{n+1}}) \end{cases} . \tag{5.22}$$

The stress at step $n+1$ then follows as

$$\boldsymbol{\sigma}_{n+1} = \boldsymbol{\sigma}_n + \mathbb{C} : \Delta\boldsymbol{\varepsilon} - \frac{1}{2}\Delta\gamma_n \mathbb{C} : \mathbf{R}_n - \frac{1}{2}\widehat{\Delta\gamma_{n+1}}\mathbb{C} : \widehat{\mathbf{R}_{n+1}} \quad . \tag{5.23}$$

The differential of Equation 5.23 is

$$\mathrm{d}\boldsymbol{\sigma}_{n+1} = \mathbb{C} : \mathrm{d}\Delta\boldsymbol{\varepsilon} - \frac{1}{2}\mathrm{d}\Delta\gamma_n \mathbb{C} : \mathbf{R}_n - \frac{1}{2}\mathrm{d}\widehat{\Delta\gamma_{n+1}}\mathbb{C} : \widehat{\mathbf{R}_{n+1}} - \frac{1}{2}\widehat{\Delta\gamma_{n+1}}\mathbb{C} : \mathrm{d}\widehat{\mathbf{R}_{n+1}} \tag{5.24}$$

$$= \mathbb{C}^{\mathrm{ep}}_{n+1} : \mathrm{d}\Delta\boldsymbol{\varepsilon} \quad . \tag{5.25}$$

where $\mathbb{C}^{\mathrm{ep}}_{n+1}$ is the consistent tangent for the Modified Euler scheme. Equation 5.17 can be used to get $\mathrm{d}\Delta\gamma_n$. Using Equation 5.14, $\widehat{\Delta\gamma_{n+1}}$ and its differential can be calculated as

$$\widehat{\Delta\gamma_{n+1}} = \left.\frac{\partial f/\partial \boldsymbol{\sigma} : \mathbb{C}}{K_p + \partial f/\partial \boldsymbol{\sigma} : \mathbb{C} : \mathbf{R}}\right|_{\widehat{n+1}} : \Delta\boldsymbol{\varepsilon} \tag{5.26}$$

$$\begin{aligned} \mathrm{d}\widehat{\Delta\gamma_{n+1}} = & \left.\frac{\partial f/\partial \boldsymbol{\sigma} : \mathbb{C}}{K_p + \partial f/\partial \boldsymbol{\sigma} : \mathbb{C} : \mathbf{R}}\right|_{\widehat{n+1}} : \mathrm{d}\Delta\boldsymbol{\varepsilon} \\ & + \left.\frac{\left(K_p + \partial f/\partial \boldsymbol{\sigma} : \mathbb{C} : \mathbf{R}\right)\left[\mathrm{d}(\partial f/\partial \boldsymbol{\sigma}) : \mathbb{C}\right]}{\left(K_p + \partial f/\partial \boldsymbol{\sigma} : \mathbb{C} : \mathbf{R}\right)^2}\right|_{\widehat{n+1}} \\ & - \left.\frac{\left(\partial f/\partial \boldsymbol{\sigma} : \mathbb{C}\right)\left[\mathrm{d}K_p + \mathrm{d}(\partial f/\partial \boldsymbol{\sigma}) : \mathbb{C} : \mathbf{R} + \partial f/\partial \boldsymbol{\sigma} : \mathbb{C} : \mathrm{d}\mathbf{R}\right]}{\left(K_p + \partial f/\partial \boldsymbol{\sigma} : \mathbb{C} : \mathbf{R}\right)^2}\right|_{\widehat{n+1}} . \end{aligned} \tag{5.27}$$

$\mathrm{d}K_p$, $\mathrm{d}\left(\partial f/\partial \boldsymbol{\sigma}\right)$ and $\mathrm{d}\mathbf{R}$ depend on the definition of the yield surface, hardening rule and the flow rule and can usually be calculated analytically for the intermediate step $\widehat{n+1}$. Therefore, the consistent tangent operator is calculated by substituting Equation 5.26 into Equation 5.24.

5.5 Implicit Methods

In contrast to explicit methods, implicit methods need prior knowledge of the solution, requiring iterative solution schemes. However, these methods provide some attractive features that make them desirable. In these methods we end up with a system of equations that are generally nonlinear. Therefore, some type of nonlinear system of equation solver is needed. Newton's method is the most popular one, but it requires calculation of the Jacobian (or Hessian) of the system of equations which is not always easy to obtain. There exist many implicit integration methods in the literature including Runge-Kutta implicit methods, but the backward Euler method is currently the most popular implicit method in the integration of constitutive models due to its simplicity and some of its unique features. These features are discussed next.

5.5.1 Backward Euler Method (Closest Point Projection Method)

The backward Euler method is one of the most popular integration methods for constitutive models. The method is given the name "Closest Point Projection Method", or simply CPPM, due to its geometrical interpretation in stress space. A trial state is defined by freezing the plastic parameters over the strain increment, thus calculating the stress increment assuming pure elastic response. The method is merely computing the closest point projection from the trial stress state onto the yield surface. The second reason is because the yield function is satisfied at the solution and therefore no drift from the yield surface occurs. In addition, the consistent tangent operator is obtained as a part of the Jacobian of the system of equations and no further calculations are needed.

Presented in terms of our simple problem, this method can be stated as

$$\mathbf{u}^{n+1} = \mathbf{u}^n + \Delta t\, \mathbf{f}(\mathbf{u}^{n+1}) \quad . \tag{5.28}$$

One of the drawbacks of implicit schemes is inherited from Newton's method used to solve the nonlinear system of implicit equations. Newton's method needs an appropriate starting point for iterations in order to converge. Also, it is only quadratically convergent if the iterations are sufficiently close to the solution. Convergence may be lost when the nonlinearities are large or the initial guess, used to initiate the Newton iterations, is too far from the solution.

5.5.2 Integration of Manzari-Dafalias using CPPM

The evolution equations for the Manzari-Dafalias model can be summarized as

$$\begin{cases} \dot{\boldsymbol{\sigma}} &= \mathbb{C} : (\dot{\boldsymbol{\varepsilon}} - \dot{\boldsymbol{\varepsilon}}^p) \\ \dot{\boldsymbol{\varepsilon}}^p &= \dot{\gamma}\mathbf{R} \\ \dot{\boldsymbol{\alpha}} &= \dot{\gamma}\bar{\boldsymbol{\alpha}} \\ \dot{\mathbf{z}} &= \dot{\gamma}\bar{\mathbf{z}} \\ f &= \|\mathbf{s} - p\boldsymbol{\alpha}\| - \sqrt{\tfrac{2}{3}}mp = 0 \\ \dot{\gamma} &> 0 \end{cases} . \tag{5.29}$$

where $\mathbf{R}$, $\bar{\boldsymbol{\alpha}}$ and $\bar{\mathbf{z}}$ are defined in Chapter 4. Using a Backward Euler integration scheme, the above equations can be written in an incremental form as

$$\begin{cases} \boldsymbol{\sigma}_{n+1} &= \boldsymbol{\sigma}_n + \mathbb{C} : (\Delta\boldsymbol{\varepsilon} - \Delta\gamma_{n+1}\mathbf{R}_{n+1}) \\ \boldsymbol{\varepsilon}^p_{n+1} &= \boldsymbol{\varepsilon}^p_n + \Delta\gamma_{n+1}\mathbf{R}_{n+1} \\ \boldsymbol{\alpha}_{n+1} &= \boldsymbol{\alpha}_n + \Delta\gamma_{n+1}\bar{\boldsymbol{\alpha}}_{n+1} \\ \mathbf{z}_{n+1} &= \mathbf{z}_n + \Delta\gamma_{n+1}\bar{\mathbf{z}}_{n+1} \\ f_{n+1} &= 0 \\ \Delta\gamma_{n+1} &> 0 \end{cases} . \tag{5.30}$$

Since the parameters of the model at step $n+1$ are not known a priori, Equations 5.30 require an iterative solution technique. Therefore, given a strain increment $\Delta\boldsymbol{\varepsilon}$ the following vector of residuals is formed and a Newton solution method is used to find the material state at which this residual vector is zero. A trial stress state is defined assuming the loading increment is fully elastic, i.e., $\boldsymbol{\sigma}^{\text{tr}}_{n+1} = \boldsymbol{\sigma}_n + \mathbb{C} : \Delta\boldsymbol{\varepsilon}$. Similarly, the trial elastic strain is defined as $\boldsymbol{\varepsilon}^{e,\text{tr}}_{n+1} = \boldsymbol{\varepsilon}^e_n + \Delta\boldsymbol{\varepsilon}$. If the yield function for the trial state is negative, material behavior is elastic and the trial state is the solution. Otherwise, the increment is a plastic

step and the trial state is used to initiate the Newton iterations.

$$\{\mathcal{R}_{n+1}\} = \left\{ \begin{array}{c} \boldsymbol{\varepsilon}^e_{n+1} + \Delta\gamma_{n+1}\mathbf{R}_{n+1} - \boldsymbol{\varepsilon}^{e,\mathrm{tr}}_{n+1} \\ \boldsymbol{\alpha}_{n+1} - \boldsymbol{\alpha}_n - \Delta\gamma_{n+1}\hat{\boldsymbol{\alpha}}_{n+1} \\ \mathbf{z}_{n+1} - \mathbf{z}_n - \Delta\gamma_{n+1}\hat{\mathbf{z}}_{n+1} \\ \|\mathbf{s}_{n+1} - p_{n+1}\boldsymbol{\alpha}_{n+1}\| - \sqrt{\frac{2}{3}}mp_{n+1} \end{array} \right\} = \left\{ \begin{array}{c} \mathbf{0} \\ \mathbf{0} \\ \mathbf{0} \\ 0 \end{array} \right\} \quad . \tag{5.31}$$

where $\boldsymbol{\varepsilon}^e_{n+1} = \boldsymbol{\varepsilon}_{n+1} - \boldsymbol{\varepsilon}^p_{n+1} = \boldsymbol{\varepsilon}^e_n + \mathbb{C}^{-1} : (\boldsymbol{\sigma}_{n+1} - \boldsymbol{\sigma}_n)$. The 2$^{\mathrm{nd}}$ order symmetric tensors, i.e., $\boldsymbol{\varepsilon}$, $\mathbf{R}$, $\boldsymbol{\alpha}$, $\hat{\boldsymbol{\alpha}}$, $\mathbf{z}$, $\hat{\mathbf{z}}$ and $\mathbf{s}$ are written in their corresponding vector form with 6 components[1]. The linearized equation of the residual vector with respect to the vector of unknowns, $\{q\}$, yields

$$\{\mathcal{R}\} + [J] \cdot \{\Delta q\} = \{0\} \ , \tag{5.32}$$

where

$$\{q\} = \{\boldsymbol{\sigma}_{n+1},\ \boldsymbol{\alpha}_{n+1},\ \mathbf{z}_{n+1},\ \Delta\gamma_{n+1}\}^{\mathrm{T}} \ , \tag{5.33}$$

and $\{\Delta q\} = \{q_{n+1}\} - \{q_n\}$. The Jacobian, $[J]$, follows from

$$\{\mathcal{R}_{n+1}\} + \underbrace{\frac{\partial\{\mathcal{R}_{n+1}\}}{\partial\{\boldsymbol{\sigma}_{n+1}, \boldsymbol{\alpha}_{n+1}, \mathbf{z}_{n+1}, \Delta\gamma_{n+1}\}^{\mathsf{T}}}}_{[J_{n+1}]} \cdot \left\{ \begin{array}{c} \Delta\boldsymbol{\sigma} \\ \Delta\boldsymbol{\alpha} \\ \Delta\mathbf{z} \\ \Delta(\Delta\gamma) \end{array} \right\} = \{0\} \quad . \tag{5.34}$$

---

[1]Here, a symmetric second order tensor $\boldsymbol{\beta}$ is represented in vector form as

$$\{\boldsymbol{\beta}\} = \{\beta_{xx} \quad \beta_{yy} \quad \beta_{zz} \quad \beta_{xy} \quad \beta_{yz} \quad \beta_{zx}\}^{\mathsf{T}} .$$

Note that $\Delta(\Delta\gamma)$ is the iterative change of the increment $\Delta\gamma = \dot{\gamma}\,\Delta t$. A Newton iterative solution method for Equation 5.31 using Equation 5.34 yields

$$\begin{Bmatrix} \boldsymbol{\sigma}_{n+1}^{k+1} \\ \boldsymbol{\alpha}_{n+1}^{k+1} \\ \mathbf{z}_{n+1}^{k+1} \\ \Delta\gamma_{n+1}^{k+1} \end{Bmatrix} = \begin{Bmatrix} \boldsymbol{\sigma}_{n+1}^{k} \\ \boldsymbol{\alpha}_{n+1}^{k} \\ \mathbf{z}_{n+1}^{k} \\ \Delta\gamma_{n+1}^{k} \end{Bmatrix} - [J_{n+1}^{k}]^{-1} \cdot \left\{ \mathcal{R}_{n+1}^{k} \right\} \quad , \tag{5.35}$$

where k represents the iteration counter. The Jacobian matrix for Equation 5.31 follows as

$$[J_{n+1}] = \begin{bmatrix} \mathbb{C}^{-1} + \Delta\gamma\partial\mathbf{R}/\partial\boldsymbol{\sigma} & \Delta\gamma\partial\mathbf{R}/\partial\boldsymbol{\alpha} & \Delta\gamma\partial\mathbf{R}/\partial\mathbf{z} & \mathbf{R} \\ -\Delta\gamma\partial\bar{\boldsymbol{\alpha}}/\partial\boldsymbol{\sigma} & \mathbb{1} - \Delta\gamma\partial\bar{\boldsymbol{\alpha}}/\partial\boldsymbol{\alpha} & \mathbf{0} & -\bar{\boldsymbol{\alpha}} \\ -\Delta\gamma\partial\bar{\mathbf{z}}/\partial\boldsymbol{\sigma} & -\Delta\gamma\partial\bar{\mathbf{z}}/\partial\boldsymbol{\alpha} & \mathbb{1} - \Delta\gamma\partial\bar{\mathbf{z}}/\partial\mathbf{z} & -\bar{\mathbf{z}} \\ \partial f/\partial\boldsymbol{\sigma} & \partial f/\partial\boldsymbol{\alpha} & \mathbf{0} & 0 \end{bmatrix} \quad , \tag{5.36}$$

where $\mathbf{1}$ is the 2^{nd} order identity tensor and $\mathbb{1}$ is the 4^{th} order identity tensor. Although the subscript $(\bullet)_{n+1}$ is omitted here for sake of brevity, all the quantities in the Jacobian are computed at step $n+1$.

Appropriate convergence criterion is used to stop the Newton iterative process. During each iteration step, inversion of the Jacobian matrix is needed, making the whole process computationally expensive. By performing the algebraic manipulation described next, the inversion of the 19×19 matrix reduces to inversion of a 6×6 matrix. That is the way this integration method is implemented in OpenSees. Substituting the Jacobian in Equation 5.34

we arrive at a linear system of equation as

$$\mathcal{R}_1 + (\mathbb{C}^{-1} + \Delta\gamma\frac{\partial \mathbf{R}}{\partial \boldsymbol{\sigma}}) : \Delta\boldsymbol{\sigma} + \Delta\gamma\frac{\partial \mathbf{R}}{\partial \boldsymbol{\alpha}} : \Delta\boldsymbol{\alpha} + \Delta\gamma\frac{\partial \mathbf{R}}{\partial \mathbf{z}} : \Delta\mathbf{z} + \Delta(\Delta\gamma)\mathbf{R} = \mathbf{0} \quad , \tag{5.37a}$$

$$\mathcal{R}_2 - \Delta\gamma\frac{\partial \bar{\boldsymbol{\alpha}}}{\partial \boldsymbol{\sigma}} : \Delta\boldsymbol{\sigma} + (\mathbb{1} - \Delta\gamma\frac{\partial \bar{\boldsymbol{\alpha}}}{\partial \boldsymbol{\alpha}}) : \Delta\boldsymbol{\alpha} - \Delta(\Delta\gamma)\bar{\boldsymbol{\alpha}} = \mathbf{0} \quad , \tag{5.37b}$$

$$\mathcal{R}_3 - \Delta\gamma\frac{\partial \bar{\mathbf{z}}}{\partial \boldsymbol{\sigma}} : \Delta\boldsymbol{\sigma} - \Delta\gamma\frac{\partial \bar{\mathbf{z}}}{\partial \boldsymbol{\alpha}} : \Delta\boldsymbol{\alpha} + (\mathbb{1} - \Delta\gamma\frac{\partial \bar{\mathbf{z}}}{\partial \mathbf{z}}) : \Delta\mathbf{z} - \Delta(\Delta\gamma)\bar{\mathbf{z}} = \mathbf{0} \quad , \tag{5.37c}$$

$$\mathcal{R}_4 + \frac{\partial f}{\partial \boldsymbol{\sigma}} : \Delta\boldsymbol{\sigma} + \frac{\partial f}{\partial \boldsymbol{\alpha}} : \Delta\boldsymbol{\alpha} = 0 \quad . \tag{5.37d}$$

From Equation 5.37b we calculate $\Delta\boldsymbol{\alpha}$ as

$$\Delta\boldsymbol{\alpha} = \underbrace{\left(\mathbb{1} - \Delta\gamma\frac{\partial \bar{\boldsymbol{\alpha}}}{\partial \boldsymbol{\alpha}}\right)^{-1}}_{\mathbf{C}^{\alpha}} : \left[\Delta\gamma\frac{\partial \bar{\boldsymbol{\alpha}}}{\partial \boldsymbol{\sigma}} : \Delta\boldsymbol{\sigma} + \Delta(\Delta\gamma)\bar{\boldsymbol{\alpha}} - \mathcal{R}_2\right] \tag{5.38}$$

$$= \underbrace{\Delta\gamma\mathbf{C}^{\alpha} : \frac{\partial \bar{\boldsymbol{\alpha}}}{\partial \boldsymbol{\sigma}}}_{\mathbf{A}^{\sigma}} : \Delta\boldsymbol{\sigma} + \Delta(\Delta\gamma)\underbrace{\mathbf{C}^{\alpha} : \bar{\boldsymbol{\alpha}}}_{\mathbf{A}^{\gamma}} - \underbrace{\mathbf{C}^{\alpha} : \mathcal{R}_2}_{\mathbf{A}^{c}} \tag{5.39}$$

$$= \mathbf{A}^{\sigma} : \Delta\boldsymbol{\sigma} + \mathbf{A}^{\gamma}\Delta(\Delta\gamma) - \mathbf{A}^{c} \quad . \tag{5.40}$$

Then using Equation 5.37c we calculate $\Delta\mathbf{z}$ as

$$\Delta\mathbf{z} = \underbrace{\left(\mathbb{1} - \Delta\gamma\frac{\partial\bar{\mathbf{z}}}{\partial\mathbf{z}}\right)^{-1}}_{\mathbf{C}^z} : \left[\Delta\gamma\frac{\partial\bar{\mathbf{z}}}{\partial\boldsymbol{\sigma}} : \Delta\boldsymbol{\sigma} + \Delta\gamma\frac{\partial\bar{\mathbf{z}}}{\partial\boldsymbol{\alpha}} : \Delta\boldsymbol{\alpha} + \Delta(\Delta\gamma)\bar{\mathbf{z}} - \mathcal{R}_3\right] \tag{5.41}$$

$$\begin{aligned}
&= \underbrace{\left(\Delta\gamma\mathbf{C}^z : \frac{\partial\bar{\mathbf{z}}}{\partial\boldsymbol{\sigma}} + \Delta\gamma\mathbf{C}^z : \frac{\partial\bar{\mathbf{z}}}{\partial\boldsymbol{\alpha}} : \mathbf{A}^\sigma\right)}_{\mathbf{Z}^\sigma} : \Delta\boldsymbol{\sigma} \\
&+ \underbrace{\left(\Delta\gamma\mathbf{C}^z : \frac{\partial\bar{\mathbf{z}}}{\partial\boldsymbol{\alpha}} : \mathbf{A}^\gamma + \mathbf{C}^z : \bar{\mathbf{z}}\right)}_{\mathbf{Z}^\gamma} \Delta(\Delta\gamma) \\
&+ \underbrace{\left(\Delta\gamma\mathbf{C}^z : \frac{\partial\bar{\mathbf{z}}}{\partial\boldsymbol{\alpha}} : \mathbf{A}^c + \mathbf{C}^z : \mathcal{R}_3\right)}_{\mathbf{Z}^c}
\end{aligned} \tag{5.42}$$

$$= \mathbf{Z}^\sigma : \Delta\boldsymbol{\sigma} + \mathbf{Z}^\gamma\Delta(\Delta\gamma) + \mathbf{Z}^c \quad . \tag{5.43}$$

Following the same path for Equation 5.37d we calculate $\Delta(\Delta\gamma)$ as

$$\Delta(\Delta\gamma) = \underbrace{-\frac{\partial f/\partial\boldsymbol{\sigma} + \partial f/\partial\boldsymbol{\alpha} : \mathbf{A}^\sigma}{\partial f/\partial\boldsymbol{\alpha} : \mathbf{A}^\gamma}}_{\boldsymbol{\Gamma}^\sigma} : \Delta\boldsymbol{\sigma} \underbrace{-\frac{\partial f/\partial\boldsymbol{\alpha} : \mathbf{A}^c + \mathcal{R}_4}{\partial f/\partial\boldsymbol{\alpha} : \mathbf{A}^\gamma}}_{\boldsymbol{\Gamma}^c} \tag{5.44}$$

$$= \boldsymbol{\Gamma}^\sigma : \Delta\boldsymbol{\sigma} + \boldsymbol{\Gamma}^c \quad . \tag{5.45}$$

Combining Equations 5.40, 5.43 and 5.45 and using Equation 5.37a in the residuals system of equations, we can calculate $\Delta\boldsymbol{\sigma}$ as

$$\left(\mathbb{C}^{-1} + \Delta\gamma\frac{\partial \mathbf{R}}{\partial \boldsymbol{\sigma}} + \Delta\gamma\frac{\partial \mathbf{R}}{\partial \boldsymbol{\alpha}} : \mathbf{A}^{\sigma} + \Delta\gamma\frac{\partial \mathbf{R}}{\partial \mathbf{z}} : \mathbf{Z}^{\sigma}\right) : \Delta\boldsymbol{\sigma} =$$

$$-\left(\Delta(\Delta\gamma)\underbrace{\left(\Delta\gamma\frac{\partial \mathbf{R}}{\partial \boldsymbol{\alpha}} : \mathbf{A}^{\gamma} + \Delta\gamma\frac{\partial \mathbf{R}}{\partial \mathbf{z}} : \mathbf{Z}^{\gamma} + \mathbf{R}\right)}_{\boldsymbol{\Sigma}^{\gamma}} + \Delta\gamma\frac{\partial \mathbf{R}}{\partial \boldsymbol{\alpha}} : \mathbf{A}^{c} + \Delta\gamma\frac{\partial \mathbf{R}}{\partial \mathbf{z}} : \mathbf{Z}^{c} + \mathcal{R}_1\right) \tag{5.46}$$

$$\Rightarrow \Delta\boldsymbol{\sigma} = -\underbrace{\left(\mathbb{C}^{-1} + \Delta\gamma\frac{\partial \mathbf{R}}{\partial \boldsymbol{\sigma}} + \Delta\gamma\frac{\partial \mathbf{R}}{\partial \boldsymbol{\alpha}} : \mathbf{A}^{\sigma} + \Delta\gamma\frac{\partial \mathbf{R}}{\partial \mathbf{z}} : \mathbf{Z}^{\sigma} + \boldsymbol{\Sigma}^{\gamma} \otimes \boldsymbol{\Gamma}^{\sigma}\right)^{-1}}_{\mathbf{C}^{\sigma}} :$$

$$\underbrace{\left(\boldsymbol{\Gamma}^{c}\boldsymbol{\Sigma}^{\gamma} + \Delta\gamma\frac{\partial \mathbf{R}}{\partial \boldsymbol{\alpha}} : \mathbf{A}^{c} + \Delta\gamma\frac{\partial \mathbf{R}}{\partial \mathbf{z}} : \mathbf{Z}^{c} + \mathcal{R}_1\right)}_{\boldsymbol{\Sigma}^{c}} \tag{5.47}$$

$$= -\mathbf{C}^{\sigma} : \boldsymbol{\Sigma}^{c} \quad . \tag{5.48}$$

Taking the differentials of Equation 5.31 with respect to $\Delta\boldsymbol{\varepsilon}$ and using $\boldsymbol{\varepsilon}^{e,\mathrm{tr}}_{n+1} = \boldsymbol{\varepsilon}^{e}_{n} + \Delta\boldsymbol{\varepsilon}$, gives

$$\frac{d\left\{\mathcal{R}_{n+1}\right\}}{d\Delta\boldsymbol{\varepsilon}} = \frac{d}{d\Delta\boldsymbol{\varepsilon}} \left\{ \begin{array}{c} \boldsymbol{\varepsilon}^{e}_{n+1} + \Delta\gamma_{n+1}\mathbf{R}_{n+1} - \boldsymbol{\varepsilon}^{e}_{n} - \Delta\boldsymbol{\varepsilon} \\ \boldsymbol{\alpha}_{n+1} - \boldsymbol{\alpha}_{n} - \Delta\gamma_{n+1}\hat{\boldsymbol{\alpha}}_{n+1} \\ \mathbf{z}_{n+1} - \mathbf{z}_{n} - \Delta\gamma_{n+1}\hat{\mathbf{z}}_{n+1} \\ \|\mathbf{s}_{n+1} - p_{n+1}\boldsymbol{\alpha}_{n+1}\| - \sqrt{\frac{2}{3}}mp_{n+1} \end{array} \right\} \tag{5.49}$$

$$= \underbrace{\frac{d}{d\Delta\boldsymbol{\varepsilon}} \left\{ \begin{array}{c} \boldsymbol{\varepsilon}^{e}_{n+1} + \Delta\gamma_{n+1}\mathbf{R}_{n+1} - \boldsymbol{\varepsilon}^{e}_{n} \\ \boldsymbol{\alpha}_{n+1} - \boldsymbol{\alpha}_{n} - \Delta\gamma_{n+1}\hat{\boldsymbol{\alpha}}_{n+1} \\ \mathbf{z}_{n+1} - \mathbf{z}_{n} - \Delta\gamma_{n+1}\hat{\mathbf{z}}_{n+1} \\ \|\mathbf{s}_{n+1} - p_{n+1}\boldsymbol{\alpha}_{n+1}\| - \sqrt{\frac{2}{3}}mp_{n+1} \end{array} \right\}}_{\hat{\mathcal{R}}_{n+1}} - \frac{d}{d\Delta\boldsymbol{\varepsilon}} \left\{ \begin{array}{c} \Delta\boldsymbol{\varepsilon} \\ \mathbf{0} \\ \mathbf{0} \\ 0 \end{array} \right\} \tag{5.50}$$

$$= \underbrace{\frac{d\left\{\hat{\mathcal{R}}_{n+1}\right\}}{d\left\{\boldsymbol{\sigma}_{n+1}, \boldsymbol{\alpha}_{n+1}, \mathbf{z}_{n+1}, \Delta\gamma_{n+1}\right\}^{\mathsf{T}}}}_{[J_{n+1}]} \cdot \left[\begin{array}{c} d\boldsymbol{\sigma}_{n+1}/d\Delta\boldsymbol{\varepsilon} \\ d\boldsymbol{\alpha}_{n+1}/d\Delta\boldsymbol{\varepsilon} \\ d\mathbf{z}_{n+1}/d\Delta\boldsymbol{\varepsilon} \\ d\Delta\gamma_{n+1}/d\Delta\boldsymbol{\varepsilon} \end{array} \right] - \left[\begin{array}{c} \mathbf{I} \\ \mathbf{0} \\ \mathbf{0} \\ 0 \end{array} \right] = \{0\}_{19\times 6} \quad . \tag{5.51}$$

Given that $\mathbb{C}^{\mathrm{ep}}_{n+1} = d\boldsymbol{\sigma}_{n+1}/d\Delta\boldsymbol{\varepsilon}$ and defining $\mathbb{P} = \left[\mathbf{I}_{6\times 6} \quad \mathbf{0}_{6\times 13}\right]^{\mathsf{T}}$, from Equation 5.51 we have

$$\mathbb{C}^{\mathrm{ep}}_{n+1} = \mathbb{P}^{\mathsf{T}} \; [J]^{-1} \; \mathbb{P} \quad . \tag{5.52}$$

Alternatively, a full linearization of Equation 5.34 gives

$$\{\mathcal{R}_{n+1}\} + \underbrace{\frac{\partial\{\mathcal{R}_{n+1}\}}{\partial\{\boldsymbol{\sigma}_{n+1}, \boldsymbol{\alpha}_{n+1}, \mathbf{z}_{n+1}, \Delta\gamma_{n+1}\}^{\mathsf{T}}}}_{[J_{n+1}]} \cdot \left\{ \begin{array}{c} d\boldsymbol{\sigma} \\ d\boldsymbol{\alpha} \\ d\mathbf{z} \\ d(\Delta\gamma) \end{array} \right\} + \frac{\partial\{\mathcal{R}_{n+1}\}}{\partial\Delta\boldsymbol{\varepsilon}} \cdot \{d\Delta\boldsymbol{\varepsilon}\} = \{0\} \quad . \tag{5.53}$$

At a converged step $\{\mathcal{R}_{n+1}\} = \{0\}$. Also we have

$$\frac{\partial\{\mathcal{R}_{n+1}\}}{\partial\Delta\boldsymbol{\varepsilon}} = \left[\begin{array}{c} \mathbf{I} \\ \mathbf{0} \\ \mathbf{0} \\ 0 \end{array} \right] \quad . \tag{5.54}$$

Following the same algebraic process described above and considering that the residuals at a converged step are equal to zero, we get

$$d\boldsymbol{\alpha} = \mathbf{A}^{\sigma} : d\boldsymbol{\sigma} + \mathbf{A}^{\gamma} d(\Delta\gamma) \quad , \tag{5.55}$$

$$d\mathbf{z} = \mathbf{Z}^{\sigma} : d\boldsymbol{\sigma} + \mathbf{Z}^{\gamma} d(\Delta\gamma) \quad , \tag{5.56}$$

$$d(\Delta\gamma) = \boldsymbol{\Gamma}^{\sigma} : d\boldsymbol{\sigma} \quad . \tag{5.57}$$

The first six equations from 5.53 yields

$$d\boldsymbol{\sigma} = -\left(\mathbb{C}^{-1} + \Delta\gamma \frac{\partial \mathbf{R}}{\partial \boldsymbol{\sigma}} + \Delta\gamma \frac{\partial \mathbf{R}}{\partial \boldsymbol{\alpha}} : \mathbf{A}^{\sigma} + \Delta\gamma \frac{\partial \mathbf{R}}{\partial \mathbf{z}} : \mathbf{Z}^{\sigma} + \boldsymbol{\Sigma}^{\gamma} \otimes \boldsymbol{\Gamma}^{\sigma} \right)^{-1} : d(\Delta\boldsymbol{\varepsilon}) \quad . \tag{5.58}$$

A comparison between Equation 5.58 and the definition of algorithmic tangent reveals that $\mathbb{C}^{\mathrm{ep}}_{n+1} = -\mathbf{C}^{\sigma}$.

5.6 Integration of the Manzari-Dafalias Model Augmented with a Tension Cut-off Surface Using CPPM

As many other pressure-dependent constitutive models in geotechnical engineering, tensile pressures are not tolerated in the Manzari-Dafalias model and the results are only valid if $p \geq 0$ assuming compression stresses are positive. In undrained situations where the behavior of the model is contractive and the confining pressure is very close to zero, the resulting stresses may have a negative volumetric part. One way to deal with such issue is to introduce a secondary yield surface that prevents the stress state to fall in the inadmissible region of negative pressures (Hofstetter and Taylor, 1990). For practical reasons, the secondary yield surface is put at a pressure $p_{\min}$ slightly greater than zero. A new plastic potential has to be defined for the new yield surface in order to satisfy the consistency condition. This plastic potential surface can coincide with the yield surface so that the flow rule corresponding to this potential surface follows the associative rule. In mathematical terms, the tension cut-off surface and its contribution to the flow rule is

$$\begin{cases} f_2 = p_{\min} - \mathbf{1} : \boldsymbol{\sigma} \leq 0 \\ \dot{\boldsymbol{\varepsilon}}^p = \dot{\gamma}\mathbf{R} - \dot{\lambda}\mathbf{1} \end{cases} , \tag{5.59}$$

where $\dot{\lambda}$ is the consistency parameter for the second tension cut-off yield surface. As a result, the consistency equation requires to satisfy the yield condition for both yield surfaces. Therefore, an equation is added to the system of nonlinear equations that needs to be solved for the backward Euler integration of the Manzari-Dafalias model. The new system of

equations now reads as

$$\begin{cases} \boldsymbol{\sigma}_{n+1} &= \boldsymbol{\sigma}_n + \mathbb{C} : (\Delta\boldsymbol{\varepsilon} - \Delta\gamma_{n+1}\mathbf{R}_{n+1}) \\ \boldsymbol{\varepsilon}^p_{n+1} &= \boldsymbol{\varepsilon}^p_n + \Delta\gamma_{n+1}\mathbf{R}_{n+1} \\ \boldsymbol{\alpha}_{n+1} &= \boldsymbol{\alpha}_n + \Delta\gamma_{n+1}\bar{\boldsymbol{\alpha}}_{n+1} \\ \mathbf{z}_{n+1} &= \mathbf{z}_n + \Delta\gamma_{n+1}\bar{\mathbf{z}}_{n+1} \\ f_{1,n+1} &\leq 0\,, \quad \Delta\gamma_{n+1} \geq 0\,, \quad f_{1,n+1}\,\Delta\gamma_{n+1} = 0 \\ f_{2,n+1} &\leq 0\,, \quad \Delta\lambda_{n+1} \geq 0\,, \quad f_{2,n+1}\,\Delta\lambda_{n+1} = 0 \end{cases} . \tag{5.60}$$

To find the correct solution a trial state is defined by freezing all the plastic (internal) parameters and assuming the strain increment is elastic. If both yield functions are negative at this state, the trial state is identified as the solution. If only one of the yield functions are negative, an iterative process is used to project the trial state to the other yield surface, keeping the consistency parameter related to the negative yield function zero. If both yield functions are non-negative, a new system of residual equations is formed, as explained below, and an iterative process is used to find the solution. At the end of step calculations, values of consistency parameters are checked to make sure the Karush-Kuhn-Tucker condition for the corresponding yield surface is satisfied.

The vector of residuals in Equation 5.31 is also augmented with an additional equation for the contribution of the tension cut-off surface. Also the first equation in the vector of residuals has to be modified in order to incorporate the alternative flow rule:

$$\{\mathcal{R}_{n+1}\} = \begin{Bmatrix} \boldsymbol{\varepsilon}^e_{n+1} + \Delta\gamma_{n+1}\mathbf{R}_{n+1} - \boldsymbol{\varepsilon}^{e,\mathrm{tr}}_{n+1} \\ \boldsymbol{\alpha}_{n+1} - \boldsymbol{\alpha}_n - \Delta\gamma_{n+1}\hat{\boldsymbol{\alpha}}_{n+1} \\ \mathbf{z}_{n+1} - \mathbf{z}_n - \Delta\gamma_{n+1}\hat{\mathbf{z}}_{n+1} \\ \|\mathbf{s}_{n+1} - p_{n+1}\boldsymbol{\alpha}_{n+1}\| - \sqrt{\frac{2}{3}}mp_{n+1} \\ p_{\min} - \mathbf{1} : \boldsymbol{\sigma}_{n+1} \end{Bmatrix} = \begin{Bmatrix} \mathbf{0} \\ \mathbf{0} \\ \mathbf{0} \\ 0 \\ 0 \end{Bmatrix} . \tag{5.61}$$

Defining residuals in this way requires little modification to the formulation described for the case where tension cut-off surface is not employed. Therefore, after linearizing system of equations 5.61, we can write the new Jacobian for this system of equations with $\{q\} = \{\boldsymbol{\sigma}_{n+1}, \boldsymbol{\alpha}_{n+1}, \mathbf{z}_{n+1}, \Delta\gamma_{n+1}, \Delta\lambda_{n+1}\}^{\mathsf{T}}$ being the vector of unknowns, as:

$$[J_{n+1}] = \begin{bmatrix} \mathbb{C}^{-1} + \Delta\gamma\partial\mathbf{R}/\partial\boldsymbol{\sigma} & \Delta\gamma\partial\mathbf{R}/\partial\boldsymbol{\alpha} & \Delta\gamma\partial\mathbf{R}/\partial\mathbf{z} & \mathbf{R} & -\mathbf{1} \\ -\Delta\gamma\partial\bar{\boldsymbol{\alpha}}/\partial\boldsymbol{\sigma} & \mathbb{1} - \Delta\gamma\partial\bar{\boldsymbol{\alpha}}/\partial\boldsymbol{\alpha} & \mathbf{0} & -\bar{\boldsymbol{\alpha}} & \mathbf{0} \\ -\Delta\gamma\partial\bar{\mathbf{z}}/\partial\boldsymbol{\sigma} & -\Delta\gamma\partial\bar{\mathbf{z}}/\partial\boldsymbol{\alpha} & \mathbb{1} - \Delta\gamma\partial\bar{\mathbf{z}}/\partial\mathbf{z} & -\bar{\mathbf{z}} & \mathbf{0} \\ \partial f/\partial\boldsymbol{\sigma} & \partial f/\partial\boldsymbol{\alpha} & \mathbf{0} & 0 & 0 \\ -\mathbf{1} & \mathbf{0} & \mathbf{0} & 0 & 0 \end{bmatrix} \quad , \tag{5.62}$$

The system of linear equations obtained from linearizing Equation 5.61 is

$$\mathcal{R}_1 + (\mathbb{C}^{-1} + \Delta\gamma\frac{\partial\mathbf{R}}{\partial\boldsymbol{\sigma}}) : \Delta\boldsymbol{\sigma} + \Delta\gamma\frac{\partial\mathbf{R}}{\partial\boldsymbol{\alpha}} : \Delta\boldsymbol{\alpha} + \Delta\gamma\frac{\partial\mathbf{R}}{\partial\mathbf{z}} : \Delta\mathbf{z} + \Delta(\Delta\gamma)\mathbf{R} = \mathbf{0} \quad , \tag{5.63a}$$

$$\mathcal{R}_2 - \Delta\gamma\frac{\partial\bar{\boldsymbol{\alpha}}}{\partial\boldsymbol{\sigma}} : \Delta\boldsymbol{\sigma} + (\mathbb{1} - \Delta\gamma\frac{\partial\bar{\boldsymbol{\alpha}}}{\partial\boldsymbol{\alpha}}) : \Delta\boldsymbol{\alpha} - \Delta(\Delta\gamma)\bar{\boldsymbol{\alpha}} = \mathbf{0} \quad , \tag{5.63b}$$

$$\mathcal{R}_3 - \Delta\gamma\frac{\partial\bar{\mathbf{z}}}{\partial\boldsymbol{\sigma}} : \Delta\boldsymbol{\sigma} - \Delta\gamma\frac{\partial\bar{\mathbf{z}}}{\partial\boldsymbol{\alpha}} : \Delta\boldsymbol{\alpha} + (\mathbb{1} - \Delta\gamma\frac{\partial\bar{\mathbf{z}}}{\partial\mathbf{z}}) : \Delta\mathbf{z} - \Delta(\Delta\gamma)\bar{\mathbf{z}} = \mathbf{0} \quad , \tag{5.63c}$$

$$\mathcal{R}_4 + \frac{\partial f}{\partial\boldsymbol{\sigma}} : \Delta\boldsymbol{\sigma} + \frac{\partial f}{\partial\boldsymbol{\alpha}} : \Delta\boldsymbol{\alpha} = 0 \quad , \tag{5.63d}$$

$$\mathcal{R}_5 - \mathbf{1} : \Delta\boldsymbol{\sigma} = 0 \quad . \tag{5.63e}$$

Following the same process described before for the case with no tension cut-off surface we can find that:

$$\begin{aligned}
\Delta\boldsymbol{\alpha} &= \mathbf{A}^{\sigma} : \Delta\boldsymbol{\sigma} + \mathbf{A}^{\gamma}\Delta\dot{\gamma} - \mathbf{A}^{c} \\
\Delta\mathbf{z} &= \mathbf{Z}^{\sigma} : \Delta\boldsymbol{\sigma} + \mathbf{Z}^{\gamma}\Delta\dot{\gamma} + \mathbf{Z}^{c} \\
\Delta\dot{\gamma} &= \boldsymbol{\Gamma}^{\sigma} : \Delta\boldsymbol{\sigma} + \boldsymbol{\Gamma}^{c} \\
\Delta\boldsymbol{\sigma} &= -\mathbf{C}^{\sigma} : \boldsymbol{\Sigma}^{c} - \Delta\dot{\lambda}\mathbf{C}^{\sigma} : \mathbf{1}
\end{aligned} \quad . \tag{5.64}$$

Using the Equation 5.63e we can find $\Delta\dot{\lambda}$ as:

$$\Delta\dot{\lambda} = \frac{\mathbf{1} : \mathbf{C}^{\sigma} : \boldsymbol{\Sigma}^{c} + \mathcal{R}_5}{\mathbf{1} : \mathbf{C}^{\sigma} : \mathbf{1}} \quad . \tag{5.65}$$

5.7 Implementation of Manzari-Dafalias Constitutive Model in OpenSees

In this study, the `ManzariDafalias` is added to OpenSees as a class derived from the `NDMaterial` class. Elements in OpenSees call material's `getStress()` and `getTangent()` to get the stress tensor and the tangent matrix associated with the material. If convergence is reached in the global iteration scheme, `commitstate()` member function is called in the material class. In order for different integration schemes to be implemented in the `ManzariDafalias` class, function pointers are used to point to the function performing the desired integration scheme. These functions get state variables at the current converged state (at time or pseudo-time t_n) and fill in the values for the integrated state values at t_{n+1}.

The subclasses `ManzariDafaliasPlaneStrain` and `ManzariDafalias3D` are derived from`ManzariDafalias` to perform 2D plane-strain analysis and full 3D analysis, respectively. In the plane strain subclass, out of plane components of the strain tensor are set to zero and stresses are calculated based on that.

Besides the Forward Euler integration method, The integration method proposed by Sloan et al. (2001) (Modified Euler method with sub-stepping error-control strategy), Closest Point Projection Method (CPPM or Backward Euler method) and the 4^{th} order Runge-Kutta in-

tegration methods are implemented in OpenSees. Several sub-stepping strategies are also implemented in case large strain increments are encountered. The "maximum strain increment" criterion is used when the users does not allow any strain component to be larger than a specific value. In this case the strain increment is divided into smallest number of sub-divisions, n_{sub}, to honor this criterion and integration is performed over n_{sub} sub-steps. In a different strategy, the energy increment is calculated from $\frac{1}{2}\Delta\boldsymbol{\sigma} : \Delta\boldsymbol{\epsilon}$, and the user can set a limit on how large this quantity can be for each time step. In this method, the number of sub-divisions on the strain increment, n_{sub}, is calculated from the energy increment and the integration is performed over n_{sub} sub-steps. A sub-stepping strategy specific to the CPPM integration method is devised to overcome the problems with the nonlinear equation solving method. In this approach, a recursive function is created which checks if a solution is found and if it's valid. In the case the solver does not converge or the solution is invalid, the function divides the strain increment into two equal parts and calls itself over each of these increments. The recursion continues until a specific sub-stepping depth, 10 in the case of our implementation.

Three choices of tangent matrix are implemented in OpenSees for the `ManzariDafalias` class: elastic tangent, continuum elastoplastic tangent or the algorithm consistent tangent matrix to be used in the global system iteration scheme. The algorithm consistent tangents described in the previous sections are and the user has an option to use them. Although use of the algorithm consistent tangent improves the convergence rate of global iterations dramatically, there are cases where this tangent can cause divergence or slow convergence of the algorithm. So the user should wisely choose which tangent to use. The proper algorithmic tangent is also calculated for the sub-stepping strategies. This is automatically active whenever the algorithm consistent tangent is used with a sub-stepping method. The tension cut-off surface is implemented to avoid confining pressures turning negative.

5.8 Integration of the constitutive equations under mixed stress-strain loading conditions

In order to integerate the constitutive equations outside a finite element framework a constitutive driver framework is needed. The driver should be able to apply stress paths commonly used in laboratory tests and account for generation of excess pore water pressures for undrained cases. This section describes the integration method developed by Alawaji et al. (1992). This method assumes that the constitutive integration is strain-driven and impose the stress controlled components iteratively. Here $\hat{\boldsymbol{\sigma}}$ denotes the total stress tensor while $\boldsymbol{\sigma}$ represents the effective stress tensor. As before the strains are denoted by $\boldsymbol{\varepsilon}$. $\mathbb{C}$ is the 4^{th} order elastic stiffness tensor and u is used to denote the pore water pressures, hence $\boldsymbol{\sigma} = \hat{\boldsymbol{\sigma}} - u\mathbf{1}$ where $\mathbf{1}$ is the 2^{nd} order identity tensor.

5.8.1 Drained conditions

For a drained case, we can write the incremental constitutive equations as

$$d\boldsymbol{\sigma} = \mathbb{C} : d\boldsymbol{\varepsilon}^e = \mathbb{C}^{ep} : d\boldsymbol{\varepsilon} \quad , \tag{5.66}$$

where $\mathbb{C}^{ep}$ is the elasto-plastic continuum tangent and for sake of notation, the rates are shown as differentials, i.e. $d(\bullet)$ instead of $(\dot{\bullet})$.

In a mixed control test, a combination of stress and strain components are imposed by the testing equipment. For example, in a conventional triaxial test the lateral stresses, σ_2 and σ_3, are controlled by the cell pressure and usually axial strain, ε_1, is applied to shear the sample. In general we can always divide the stress and strain tensors into prescribed components, σ_1^* and ε_2^* , and free components , σ_2 and ε_1 such that

$$\boldsymbol{\sigma} = \left\{ \begin{array}{c} \sigma_1^* \\ \sigma_2 \end{array} \right\}, \quad \boldsymbol{\varepsilon} = \left\{ \begin{array}{c} \varepsilon_1 \\ \varepsilon_2^* \end{array} \right\} \quad . \tag{5.67}$$

In incremental form we can write these quantities as

$$d\boldsymbol{\sigma} = \left\{ \begin{array}{c} d\sigma_1^* \\ d\sigma_2 \end{array} \right\} = \mathbb{C}^{ep} : \left\{ \begin{array}{c} d\varepsilon_1 \\ d\varepsilon_2^* \end{array} \right\} = \left[\begin{array}{cc} C_{11} & C_{12} \\ C_{21} & C_{22} \end{array} \right] \left\{ \begin{array}{c} d\varepsilon_1 \\ d\varepsilon_2^* \end{array} \right\} \quad , \tag{5.68}$$

where $\mathbb{C}^{ep}$ is written in a matrix block form as

$$\mathbb{C}^{ep} = \left[\begin{array}{cc} C_{11} & C_{12} \\ C_{21} & C_{22} \end{array} \right] . \tag{5.69}$$

The completely strain-driven constitutive integration algorithm takes $\boldsymbol{\varepsilon}$ as input and returns the stress tensor, $\boldsymbol{\sigma}$, and the elastoplastic tangent matrix, $\mathbb{C}^{ep}$. In particular the constitutive model returns σ_1 which is the prescribed part of the stress tensor (σ_1^*). We can determine ε_1, so that the returning stress tensor satisfies both the equilibrium conditions and the prescribed stress components. The latter condition, i.e. the out-of-balance effective stress, can be written as

$$\sigma_1 - \sigma_1^* = \mathbf{0} \quad \Rightarrow \quad d\sigma_1 - d\sigma_1^* = \mathbf{0} \quad . \tag{5.70}$$

So, the goal is to determine ε_1 such that $\sigma = \sigma_1(\varepsilon_1)$ satisfies Equation 5.70. Using the Schur complement[2], we can write Equation 5.68 as

$$\left\{ \begin{array}{c} d\varepsilon_1 \\ d\sigma_2 \end{array} \right\} = \left[\begin{array}{cc} C_{11}^{-1} & -C_{11}^{-1} \cdot C_{12} \\ C_{21} \cdot C_{11}^{-1} & \left(C_{22} - C_{21} \cdot C_{11}^{-1} \cdot C_{12}\right) \end{array} \right] \left\{ \begin{array}{c} d\sigma_1^* \\ d\varepsilon_2^* \end{array} \right\} \quad , \tag{5.72}$$

---

[2]In linear algebra, the Schur complement of a matrix block arises from performing Gaussian elimination on this block matrix. Assuming

$$M = \left[\begin{array}{cc} A_{n\times n} & B_{n\times m} \\ C_{m\times n} & D_{m\times m} \end{array} \right] , \tag{5.71}$$

the Shur complement of block A of matrix M is $D - CA^{-1}B$, which is a $m \times m$ matrix.

and we can devise an iterative process such as Newton's method to determine $d\varepsilon_1$. For such iterative method the residual is defined as $\mathcal{R}(\sigma_1) = \sigma_1^* - \sigma_1$. It is easy to show that the Jacobian of the residual function is C_{11}. So the iteration process to find ε_1 can be written as

$$\Delta\varepsilon_1^{i+1} = \Delta\varepsilon_1^i - C_{11}^{-1} \cdot (d\sigma_1^* - d\sigma_1) \quad . \tag{5.73}$$

The starting value, $\Delta\varepsilon_1^0$, for the iterative process can be chosen as the elastic solution that gives $R(\sigma_1) = 0$

$$\Delta\varepsilon_1^0 = \mathbb{C}_{11}^{-1} \cdot (\Delta\sigma_1^* - \mathbb{C}_{12}\Delta\varepsilon_2^*) \quad . \tag{5.74}$$

5.8.2 Undrained conditions

For undrained conditions, the incompressibility condition is enforced by imposing zero change in the volumetric strain, $\Delta\varepsilon_v = 0$. This additional constraint makes the problem over-constrained and strain components are no longer independent. As a result of this condition, pore pressures, u, generate. In contrast to drained conditions where the total and effective stress tensor are identical, in undrained conditions the total stress tensor is different than the effective stresses ($\hat{\boldsymbol{\sigma}} = \boldsymbol{\sigma} + u\mathbf{1}$). However as in the drained case, we can divide the stress and total strain tensors into prescribed components, $\hat{\sigma}_1^*$ and ε_2^*, and free components, $\hat{\sigma}_2$ and ε_1 such that

$$\boldsymbol{\sigma} = \begin{Bmatrix} \hat{\sigma}_1^* \\ \hat{\sigma}_2 \end{Bmatrix} = \begin{Bmatrix} \sigma_1^* + u\delta_1 \\ \sigma_2 + u\delta_2 \end{Bmatrix}, \quad \boldsymbol{\varepsilon} = \begin{Bmatrix} \varepsilon_1 \\ \varepsilon_2^* \end{Bmatrix} \quad , \tag{5.75}$$

where δ_1 and δ_2 are the decomposition of the identity tensor according to the decomposition of the stress tensor. δ_1 corresponds to the prescribed components of the stress tensor while δ_2 corresponds to the free components. In incremental form, we can write these quantities

as

$$d\hat{\boldsymbol{\sigma}} = \left\{ \begin{array}{c} d\hat{\sigma}_1^* \\ d\hat{\sigma}_2 \end{array} \right\} \tag{5.76}$$

$$= \left\{ \begin{array}{c} d\sigma_1 \\ d\sigma_2 \end{array} \right\} + u \left\{ \begin{array}{c} \delta_1 \\ \delta_2 \end{array} \right\} \tag{5.77}$$

$$= \mathbb{C}^{ep} : \left\{ \begin{array}{c} d\varepsilon_1 \\ d\varepsilon_2^* \end{array} \right\} + u \left\{ \begin{array}{c} \delta_1 \\ \delta_2 \end{array} \right\} \tag{5.78}$$

$$= \left[\begin{array}{cc} C_{11} & C_{12} \\ C_{21} & C_{22} \end{array} \right] \left\{ \begin{array}{c} d\varepsilon_1 \\ d\varepsilon_2^* \end{array} \right\} + u \left\{ \begin{array}{c} \delta_1 \\ \delta_2 \end{array} \right\} \quad . \tag{5.79}$$

Since the constitutive equations are completely strain-driven, the imposed stress components must be enforced by the constitutive driver. This translates to

$$\hat{\sigma}_1^* - (\sigma_1 + u\delta_1) = 0 \quad \Rightarrow \quad d\hat{\sigma}_1^* - (d\sigma_1 + du\delta_1) \quad . \tag{5.80}$$

Similarly the incompressibility condition can be written as

$$\varepsilon_v = \boldsymbol{\varepsilon} : \mathbf{1} = 0 \quad \Rightarrow \quad d\boldsymbol{\varepsilon} : \mathbf{1} = 0 \quad \Rightarrow \quad \{d\varepsilon_1 \quad d\varepsilon_2\} \left\{ \begin{array}{c} \delta_1 \\ \delta_2 \end{array} \right\} = 0 \quad . \tag{5.81}$$

For an undrained test, these two conditions, Equations 5.80 and 5.81, have to be satisfied by determining the appropriate values for $d\varepsilon_1$ and du. An iterative solution method is devised here such that both of these equations are enforced. After some algebraic manipulation we

can show that

$$d\hat{\sigma}_2 = (C_{22} - C_{21} \cdot C_{11}^{-1} \cdot C_{12})d\varepsilon_2^* + C_{21} \cdot C_{11}^{-1} d\hat{\sigma}_1^* - du(C_{21} \cdot C_{11}\delta_1 + \delta_2) \tag{5.82}$$

$$d\varepsilon_1 = C_{11}^{-1} d\hat{\sigma}_1^* - C_{11}^{-1} \cdot C_{12} d\varepsilon_2^* - du C_{11}\delta_1 \tag{5.83}$$

$$du = \frac{d\varepsilon_2^* \cdot \delta_2 - C_{11}^{-1} \cdot C_{12} d\varepsilon_2^* \cdot \delta_1 + C_{11}^{-1} d\hat{\sigma}_1^* \cdot \delta_1}{C_{11}\delta_1 \cdot \delta_1} \quad . \tag{5.84}$$

Defining the residual function as

$$\mathcal{R}(d\varepsilon_1, du) = \left\{ \begin{array}{c} d\sigma_1 + du\delta_1 - \hat{\sigma}_1^* \\ \delta_1^{\mathsf{T}} d\varepsilon_1 + \delta_2^{\mathsf{T}} d\varepsilon_2^* \end{array} \right\} \quad , \tag{5.85}$$

we can show that the Jacobian of the residual function with respect to $d\varepsilon_1$ and du is $\begin{bmatrix} C_{11} & \delta_1 \\ \delta_1^{\mathsf{T}} & 0 \end{bmatrix}$. Therefore the iterative process using Newton's method is

$$\Delta\varepsilon_1^{i+1} = \Delta\varepsilon_1^i - \begin{bmatrix} C_{11} & \delta_1 \\ \delta_1^{\mathsf{T}} & 0 \end{bmatrix}^{-1} \cdot \{\mathcal{R}\} \quad . \tag{5.86}$$

The starting value, $\Delta\varepsilon_1^0$ and du for the iteration process can be chosen as the elastic solution when $\mathcal{R} = \{0\}$. That is

$$\Delta u^0 = 0 \tag{5.87}$$

$$\Delta\varepsilon_1^0 = C_{11}^{-1}(\Delta\hat{\sigma}_1^* - C_{21}\Delta\varepsilon_2^*) \quad . \tag{5.88}$$

Both drained and undrained mixed control constitutive driving algorithms are implemented in a program called `MixedDriver` using C++ programming language. This program is used to integrate the Manzari-Dafalias constitutive model also implemented using C++. Using this framework, it is possible to test the constitutive model under different stress

paths and drainage conditions. Also this driver allows for simulating stress-controlled and mixed-controlled loading conditions.

Chapter 6

VERIFICATION AND VALIDATION OF MANZARI-DAFALIAS CONSTITUTIVE MODEL

6.1 Introduction

This chapter presents verification and validation of the implementation of the Manzari-Dafalias model using the integration schemes described in the previous chapters. For this purpose, the MixedDriver tool and OpenSees are used. First, the model is verified using the MixedDriver tool. Several stress paths and loading conditions are used for this purpose. After testing the Manzari-Dafalias model using MixedDriver, a set of single element FE analysis are performed using OpenSees. The configuration of the element model (i.e., loading and boundary conditions) is set up so that the stress path in the element Gauss points follow the same stress path prescribed in the single point MixedDriver program. Then the testing process is extended to multi-element models following the same stress path and the same configuration as in the previous case. Finally, the implementation is tested in the context of specific geotechnical problems. A list of different research projects in which the Manzari-Dafalias model is used to represent material behavior is described as validation of its implementation in the OpenSees computational framework. Details about these projects are published in several papers. The reader is referred to papers authored and coauthored by the author at **Ghofrani** and Arduino (2017); Manzari et al. (2017); Zeghal et al. (2017); Chen et al. (under review); Rgnier et al. (2016, 2018); Ramirez et al. (2018, in press).

6.2 Convergence of different integration schemes

Convergence of different integration schemes are tested with conventional compression tri-axial stress paths. The tests are performed using material parameters for Toyura sand given

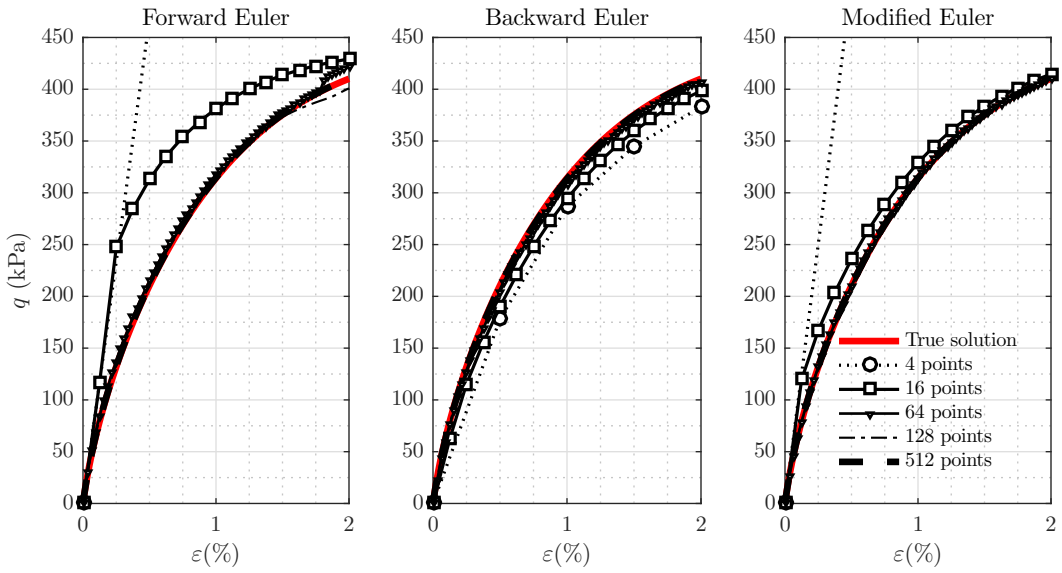

Figure 6.1: Results of triaxial compression test using various integration schemes.

in Dafalias and Manzari (2004) with an initial void ratio of $e = 0.75$ and at an initial isotropic stress state with $p = 160$ kPa. An axial strain of 2% is applied using different strain increments to test the convergence order of each integration scheme. Figure 6.1 shows stress-strain plots comparing these tests for Forward Euler, Modified Euler and Backward Euler methods. This plot confirms that all these integration schemes converge to the same solution. Figure 6.2 shows the order of convergence for these integration schemes. As we expect, Forward and Backward Euler methods show a 1^{st} order accurate convergence rate while the Modified Euler method shows a 2^{nd} order convergence rate. To estimate the error associated with these results, a 4^{th} order Runge-Kutta with 65,536 increments is used as the true solution. It is noteworthy to mention that since the Backward Euler integration scheme is an unconditionally stable scheme, the method gives relatively reasonable results even using large integration steps.

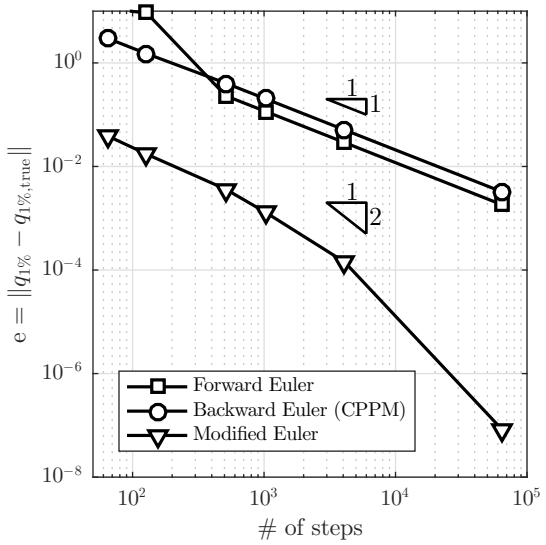

Figure 6.2: Order of convergence for different integration schemes.

6.3 Verification

The response of the Manzari-Dafalias model implemented in OpenSees is verified at different levels including: single point level (using MixedDriver), single element level, and multiple element level. Since MixedDriver uses an implicit Backward Euler scheme, larger strain increments can be used due to the stability characteristics of the integration scheme. However the method is still 1^{st} order accurate. The verification process is performed only for the Backward Euler scheme (CCPM) as other integration schemes were shown in the previous section to be convergent to the same solution.

6.3.1 Verification 1 - Results of various tests with different stress paths

Undrained monotonic CTC test Figures 6.3 and 6.4 show results of single point integration simulations following undrained CTC test stress paths. In this type of test, an initial isotropic consolidation stress state (i.e., $\sigma_1 = \sigma_2 = \sigma_3 = p_0$) is imposed, then the sample is sheared by increasing the axial strain ε_1 while the lateral stress components are kept constant. Drainage is allowed during the consolidation phase of the test. The shearing portion

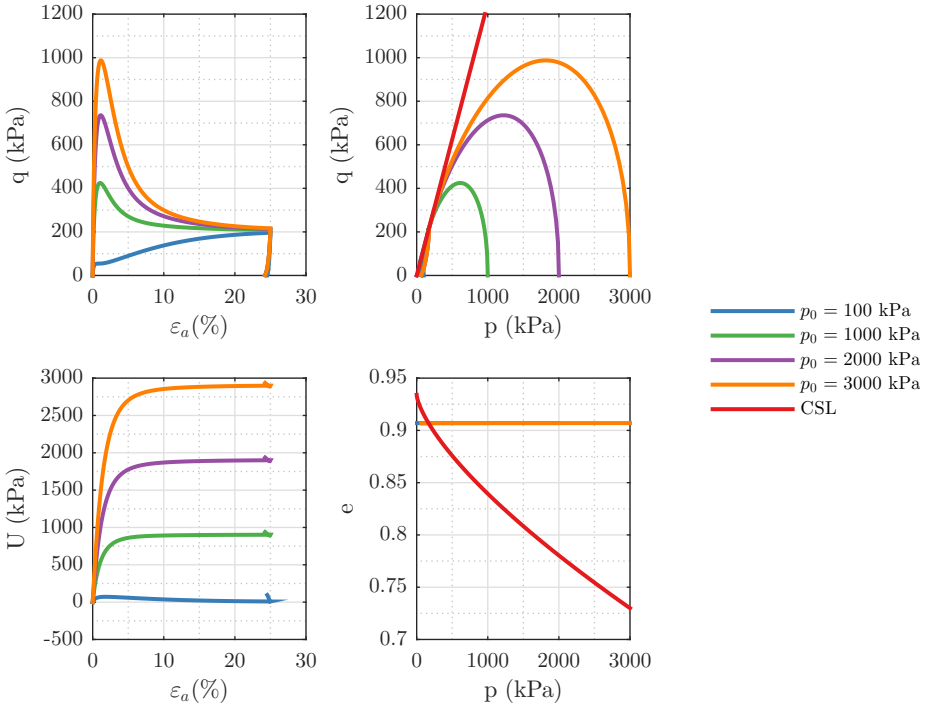

Figure 6.3: Results from single point integration tool, MixedDriver, for undrained CTC loading conditions with initial void ratio $e_i = 0.907$. (top left: stress-strain behavior – top right: stress path – bottom left: pore pressure generation – bottom right: Change in void ratio)

of the test is performed under undrained conditions. Figure 6.3 shows simulation results for a material with an initial void ratio $e_i = 0.907$ at four different initial confining pressures, i.e., $p_0 = 100, 1000, 2000$ and 3000 kPa. As it can be seen in the figure, the constitutive model is capable of capturing typical stress-strain behavior and stress paths for looser-than-critical (cases with $p_o = 1000, 2000$ or 3000 kPa) and denser-than-critical (the $p_0 = 100$ kPa case) sands. This model can also capture softening behavior of looser-than-critical sands.

Figure 6.4 shows the same loading conditions for a material with an initial void ratio $e_i = 0.735$. This material is denser-than-critical under all four initial confining pressures. As shown in this figure, the material model is capable of capturing the contractive/dilative tendency of denser-than-critical sands.

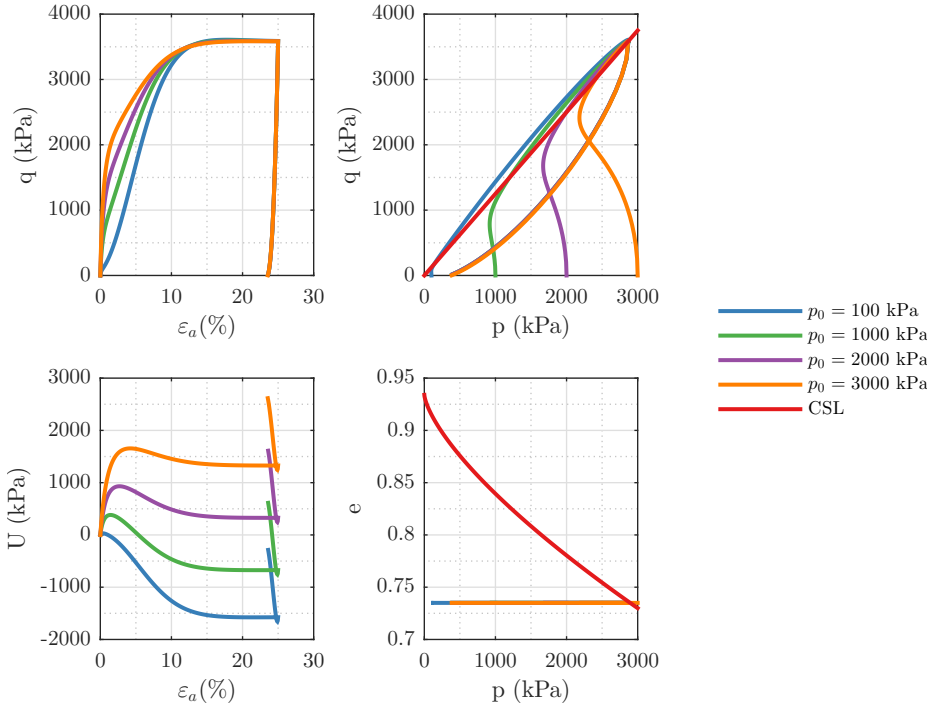

Figure 6.4: Results from single point integration tool, MixedDriver, for undrained CTC loading conditions with initial void ratio $e_i = 0.735$. (top left: stress-strain behavior – top right: stress path – bottom left: pore pressure generation – bottom right: Change in void ratio)

Drained monotonic CTC test Figure 6.5 illustrates results of single point integration simulations for three materials with initial void ratio $e_i = 0.960, 0.886$ and 0.810 under drained monotonic CTC loading conditions. An axial strain of 25% is applied before the material is unloaded. Typical behavior of sands for both looser-than-critical and denser-than-critical are observed in this figure. Specifically, the softening behavior of looser-than-critical materials under drained conditions can be captured using the Manzari-Dafalias constitutive model.

Undrained cyclic CTC test Figure 6.6 shows the material response for an undrained cyclic CTC loading path using the single point integration tool, MixedDriver. The material under test has an initial void ratio $e_i = 0.808$ and initial confining pressure $p_0 = 298$ kPa.

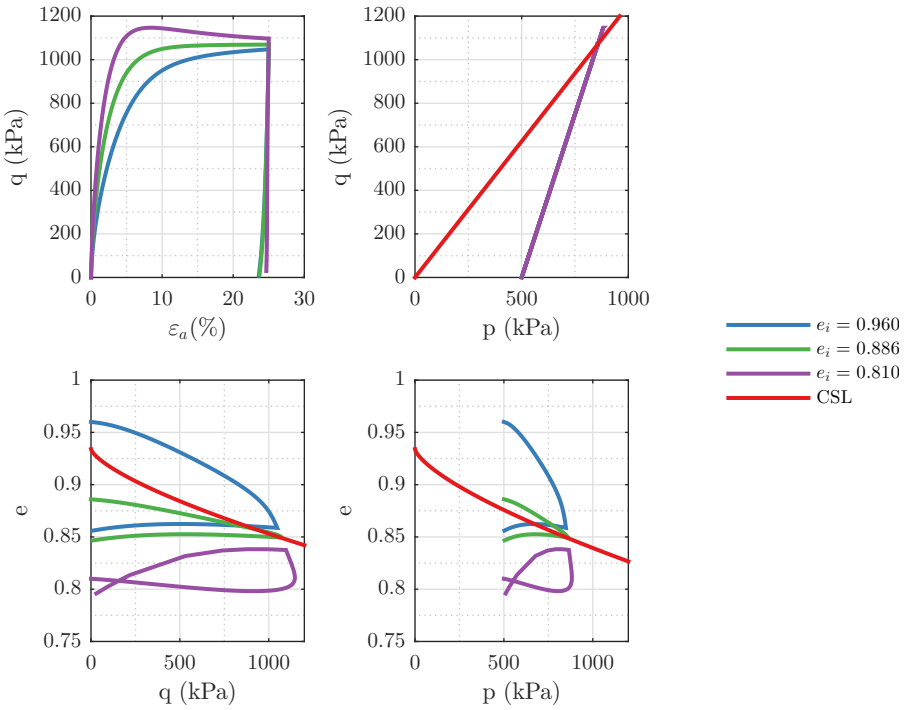

Figure 6.5: Results from single point integration tool, MixedDriver, for drained CTC loading conditions at an initial confining pressure $p = 500$ kPa. (top left: stress-strain behavior – top right: stress path – bottom left: pore pressure generation – bottom right: Change in void ratio)

The test is performed under stress-controlled conditions and an alternating deviatoric stress $q_{max} = 114.2$ kPa is applied. Accumulation of strains in one direction is the result of choosing $c \neq 1$ which means the material behaves differently in compression and extension. The results also show that the constitutive model is capable of capturing cyclic mobility. Notice that the material state is far from a critical state.

6.3.2 Verification 2 - Single-Element Finite Element Model

After verifying the implementation using MixedDriver, a single finite element model is used to evaluate the performance of the model implementation in OpenSees. Figure 6.7 shows the configuration of the OpenSees FE model for a single element test. The element undergoes a stage of pure volumetric consolidation pressure load, followed by a second stage with an

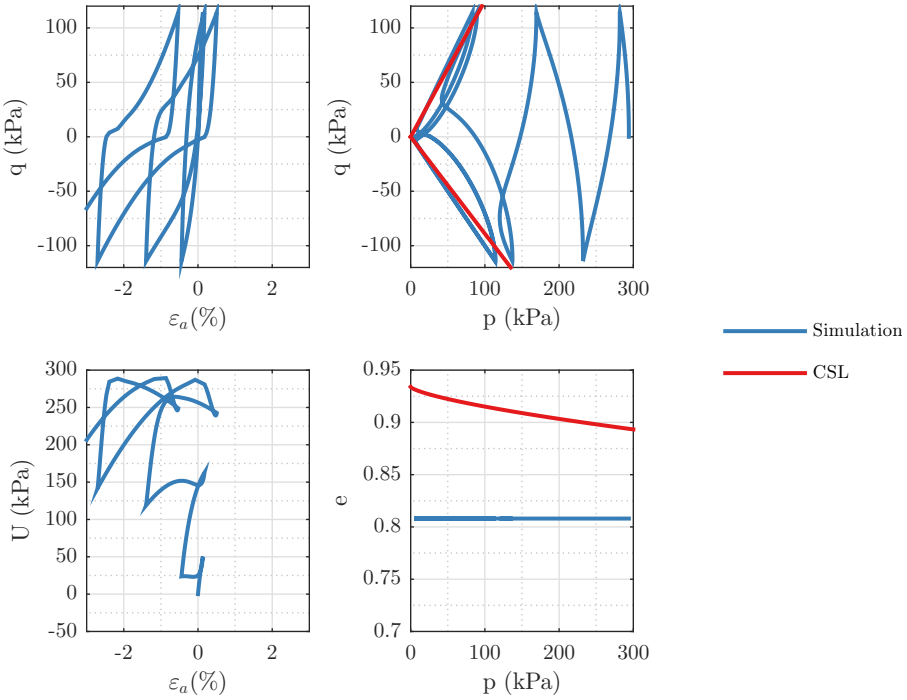

Figure 6.6: Results from single point integration tool, MixedDriver, for cyclic undrained CTC loading conditions at an initial confining pressure $p = 298$ kPa with an initial void ratio $e_i = 0.808$. (top left: stress-strain behavior – top right: stress path – bottom left: pore pressure generation – bottom right: Change in void ratio)

incremental axial load applied such that the loading program represents a CTC test. For this test the SSPbrickUP element (McGann et al., 2015) based on a coupled u-P formulation is used. This element uses a single integration point and an stabilization method to circumvent hour-glass locking modes. The Newmark integration scheme is used to march forward in time with $\beta = \frac{5}{6}$ and $\gamma = \frac{4}{9}$. These values are chosen so that additional numerical damping (resulting from this set of parameters) eradicates any undesirable waves introduced while the loads are applied to the element. Additionally, Rayleigh damping is used to reduce the effects of generated waves in the system[1].

[1]Due to its special formulation, the SSPBrickUP element requires a *transient analysis*. Therefore, damping is required to represent quasi-static cases.

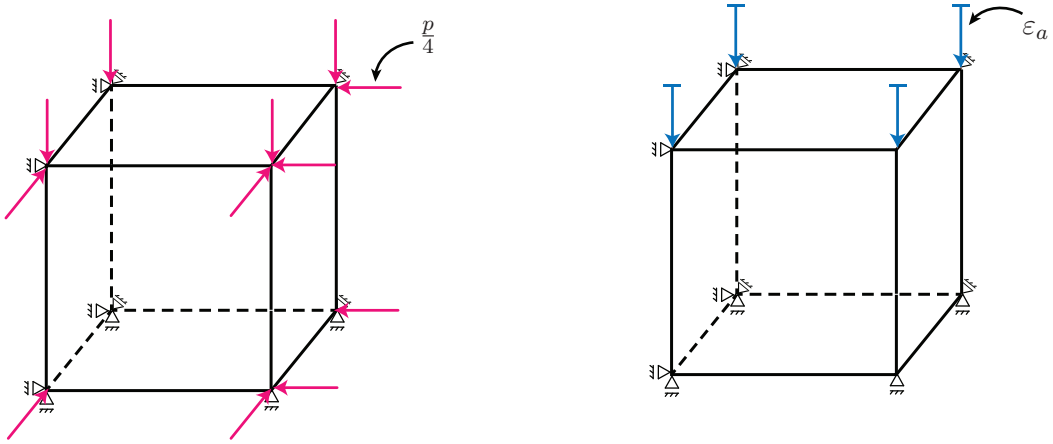

(a) Consolidation (b) Shearing

Figure 6.7: Configuration of single element FE model for CTC test

During the consolidation phase, of the six faces of the element three are fixed in the direction normal to each face. A normal pressure is applied to the faces opposite to the fixed planes hence creating an isotropic consolidation condition. Figure 6.7a depicts the test configuration during the consolidation stage. Normal pressures are incrementally increased until the desired confinement pressure is reached.

Figure 6.7b illustrates the test configuration during the axial shearing stage. During this stage additional axial pressures are applied to the plane perpendicular to the vertical direction. In this way a stress path similar to a CTC test is imposed on the Gauss point. Figure 6.8 compares results from the single element FE model and the corresponding results obtained from MixedDriver. As it can be seen, these results perfectly match verifying the implementation of the constitutive model in OpenSees.

6.3.3 Verification 3 - Multi-Element Finite Element Model

The test configuration described in the previous section is used to create a multi-element test with 3×3 hexahedral elements. Figure 6.9 shows the configuration of the model used

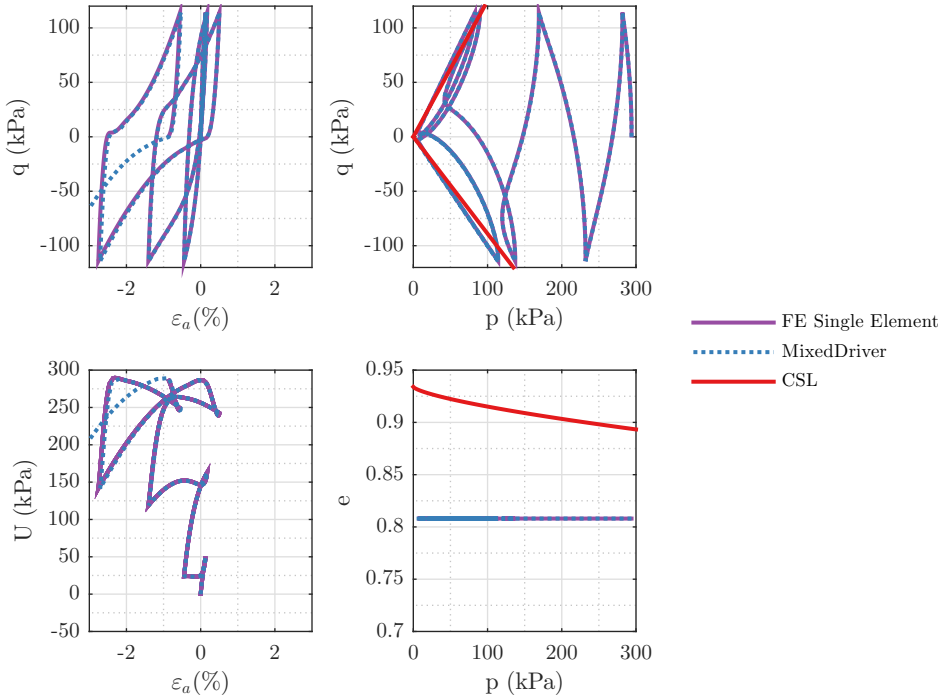

Figure 6.8: FE results for a single element CTC test compared to the results from single point integration scheme using MixedDriver

for verification of Manzari-Dafalias at a multi-element level. As shown in Figure 6.9a, a consistent force system is applied to the nodes to generate the initial confining pressure. Then an axial displacement is applied to the plane perpendicular to the vertical direction in order to simulate the CTC stress paths. Figure 6.10 compares the results from the multi-element FE model and the corresponding results obtained from MixedDriver. As it can be seen from this figure, these results perfectly match, verifying the implementation of the constitutive model in OpenSees.

6.4 Validation

The Manzari-Dafalias constitutive model implemented in OpenSees has been used in several liquefaction related - site response analysis - projects. The objective in most of these projects is to evaluate the performance and practicality of different constitutive models and different

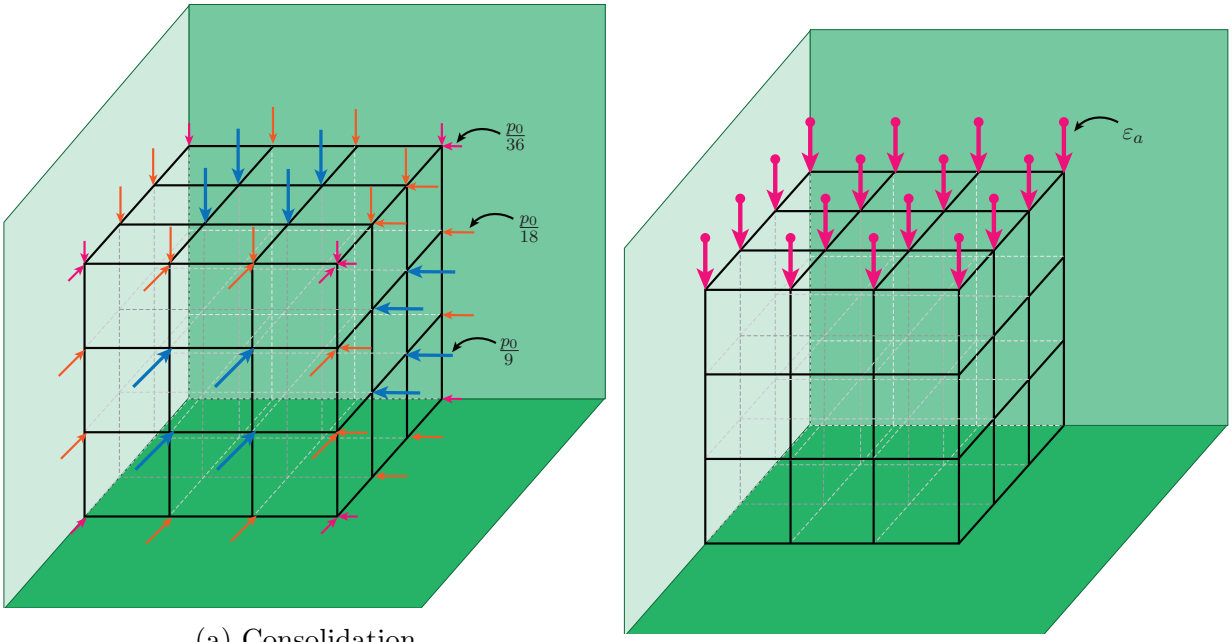

(a) Consolidation

(b) Shearing

Figure 6.9: Configuration of the multi-element FE model for CTC test

numerical analysis platforms by comparing simulation results to actual recordings of motions as well as results of centrifuge tests. A brief description of some of these projects are given below and the reader is referred to the publications related to these projects for further details.

6.4.1 PRENOLIN Project: International benchmark on numerical simulations for 1D nonlinear site response

PRENOLIN or PREdiction of NOnLINear soil behavior was an international benchmarking effort for evaluating various numerical simulation codes and constitutive models in the prediction of nonlinear seismic site response. The project was done in two phases, verification phase and validation phase. In the verification phase simple idealistic cases were used to quantify the uncertainty associated with the numerical framework and the constitutive

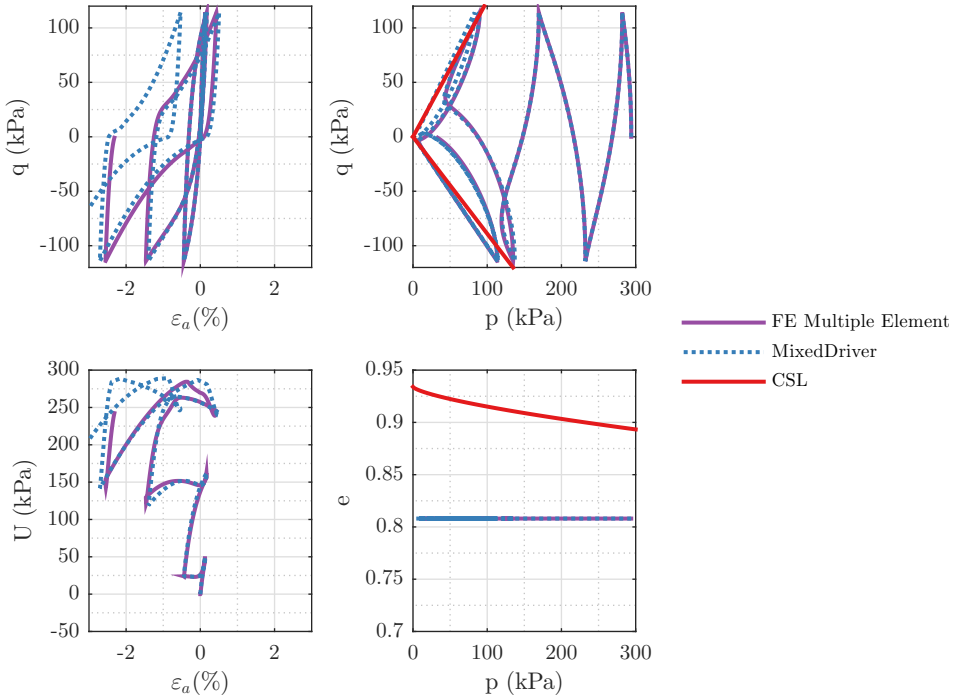

Figure 6.10: FE results for a multi-element CTC test compared to the results from single point integration tool, MixedDriver.

model. Actual strong ground motions were used in the validation phase to compare the numerical frameworks in predicting the ground response at several well-known sites. The outcomes of this project were published and are available in the articles by Rgnier et al. (2016) for the verification phase and Rgnier et al. (2018) for the validation phase.

During the validation phase two sites (Kushiro KSRH10 and Sendai) were chosen from Japanese KiK-net and Port and Airport Research Institute (PARI) strong motion networks: 1) the KSRH10 site, a deep low shear wave velocity soil mainly clayey soils, and 2) the Sendai site, a shallow site composed of sandy soils. Several recorded input motions were chosen and used for the study of these sites.

The Manzari-Dafalias constitutive model implemented in OpenSees was used in this project. The matherial was calibrated for the $G/G_{\max}$ modulus reduction curve. Both effective and total stress analyses of the sites were performed using a soil column model

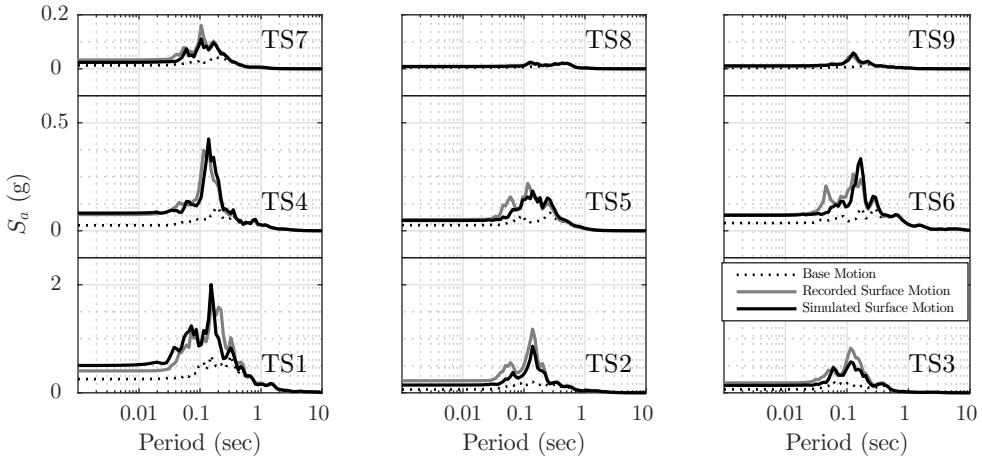

Figure 6.11: Prenolin project; Sendai site; Each plot shows 5% damping acceleration response spectrum for different base acceleration time series.

following the shear beam methodology for site response analysis. Results of the analysis showed that Manzari-Dafalias can capture nonlinearity of ground response reasonably well given a well-chosen set of calibrated parameters. Figures 6.11 and 6.12 show examples of the simulation results obtained for the Prenolin project using Manzari-Dafalias constitutive model. The complete set of results for this project can be found in Rgnier et al. (2016) and Rgnier et al. (2018).

6.4.2 Liquefaction Experiment and Analysis Project (LEAP)

LEAP is an ongoing international effort to generate high quality evaluation process for liquefaction induced geo-hazards. In this project multiple centrifuge facilities around the world perform a standardized test case to provide experimental data for evaluation of numerical frameworks and various constitutive models. Two phases of the project have been completed and two wokshops were held in 2015 and 2017. In these two phases, a 5° sloped layer of Ottawa F-65 sand with a relative density of 65% (target density of 1652 Kg/m^3) was used in the centrifuge experiments. Rigid containers were used to simplify the boundary conditions of the system. Further information about LEAP is available in Manzari et al. (2014),

Kutter et al. (2014) and Kutter et al. (2017). Results of these experiments are published in a special edition volume in the *Soil Dynamics and Earthquake Engineering* journal. Results and outcomes of this project (simulations using Manzari-Dafalias model) are presented in **Ghofrani** et al. (2016), Manzari et al. (2017) and Zeghal et al. (2017).

For loading, a 16 cycle ramped sine wave with a frequency of 1 Hz was scaled to several different peak accelerations to account for non-destructive and destructive motions. The base motion is shown in Figure 6.13.

A 2D plane strain finite element model was created in OpenSees to perform numerical analysis of the centrifuge tests. Figure 6.14 shows the finite element mesh used for this numerical model. This figure shows the boundary conditions as well. Lateral displacements on the lateral boundaries were fixed, displacements of the base were fixed in both directions and the base acceleration was applied to the base, and nodes on the surface were set to have zero pore water pressure to impose drainage at this boundary. Further details of the analysis and results are given in **Ghofrani** and Arduino (2017).

Results of this project showed that Manzari-Dafalias can be calibrated to capture many features of complicated liquefaction analyses. It was also shown, however, that a single set of parameters cannot necessarily represent a specific kind of soil at all relative densities and under all stress paths. Figures 6.15, 6.16 and 6.17 respectively show 5% acceleration response spectra for class-A predictions of the centrifuge tests, class-A excess pore water pressure generation predictions, and class-C prediction of various centrifuge experiments.

This project is an ongoing effort and other phases of the project are being performed at the time of writing this dissertation.

6.4.3 Site Response in a Layered Liquefiable Deposit

In a collaboration between the University of Washington, University of Colorado Boulder and University of British Colombia, two numerical platforms, OpenSees and FLAC (Itasca, 2012) and two constitutive models Manzari-Dafalias and Pressure Dependent Multi-Yield-Surface (Elgamal et al., 2003) were evaluated against centrifuge test data. Again Manzari-Dafalias

showed to be able to capture the behavior reasonably well if calibrated properly. Results of this study are published in Ramirez et al. (2018) and Ramirez et al. (in press).

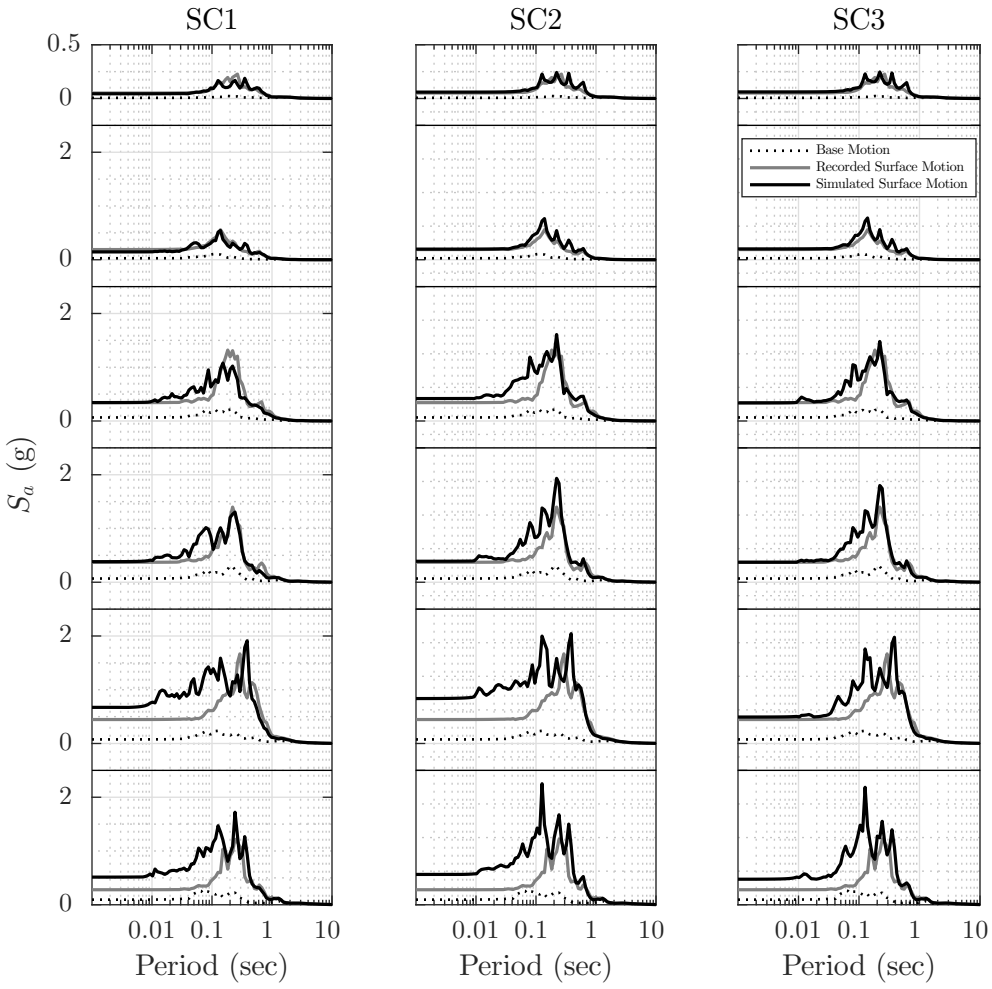

Figure 6.12: Prenolin project; Kushiro site; Each plot shows 5% damping acceleration response spectrum for different base acceleration time series and different soil column configurations.

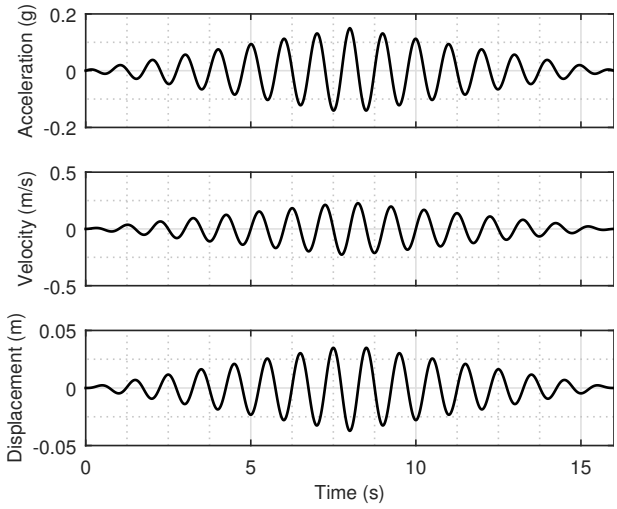

Figure 6.13: LEAP Project; Base motion scaled to 0.15 g (**Ghofrani** and Arduino, 2017)

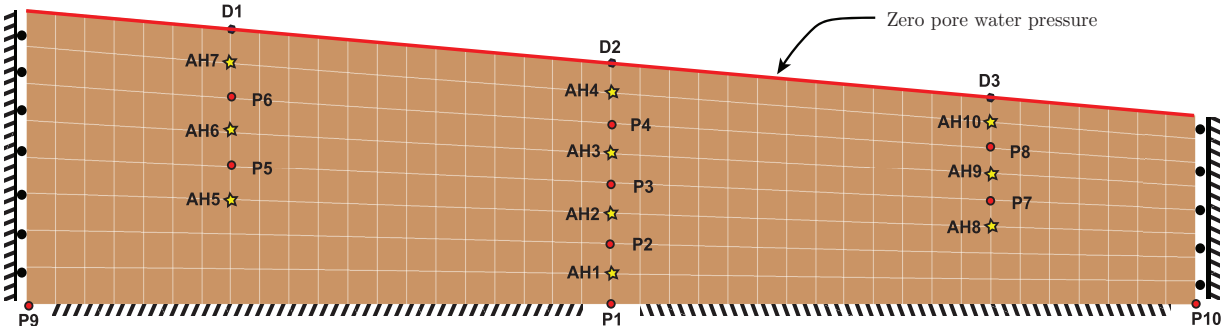

Figure 6.14: LEAP Project; Finite element mesh (**Ghofrani** and Arduino, 2017)

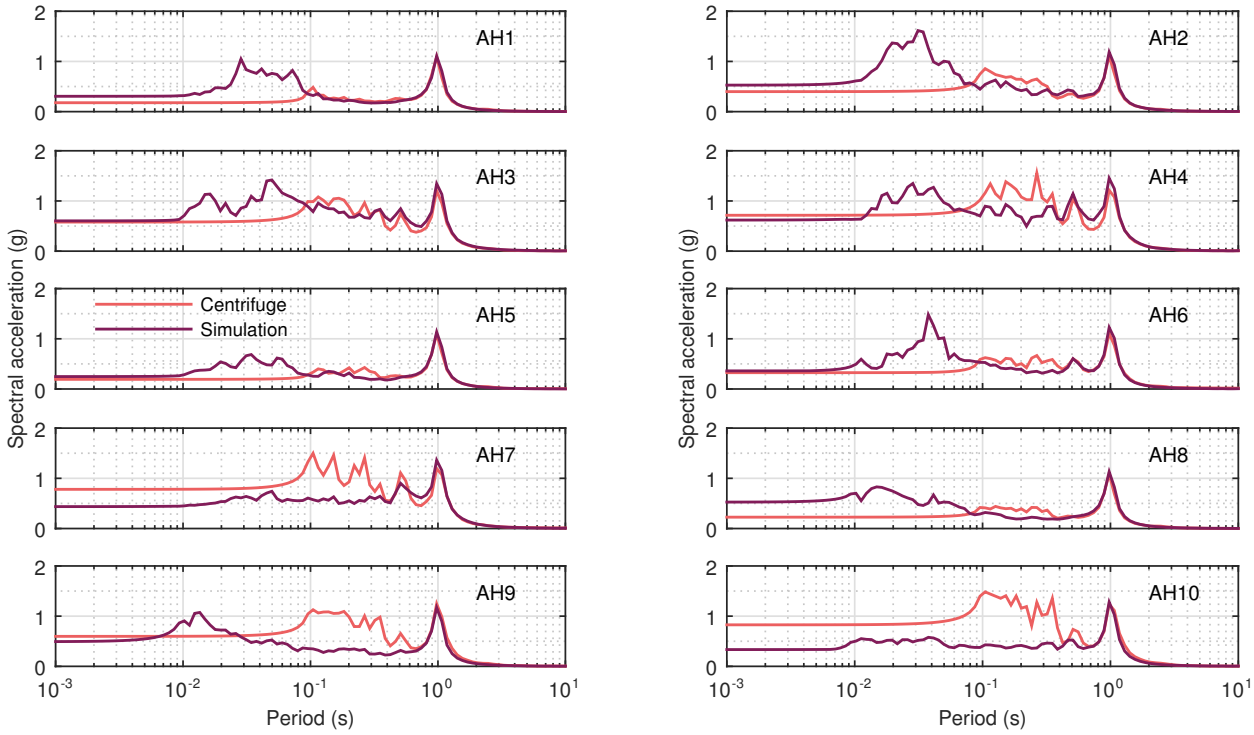

Figure 6.15: LEAP Project; Class-A prediction of RPI centrifuge experiment - 5% damping acceleration response spectrum (**Ghofrani** and Arduino, 2017)

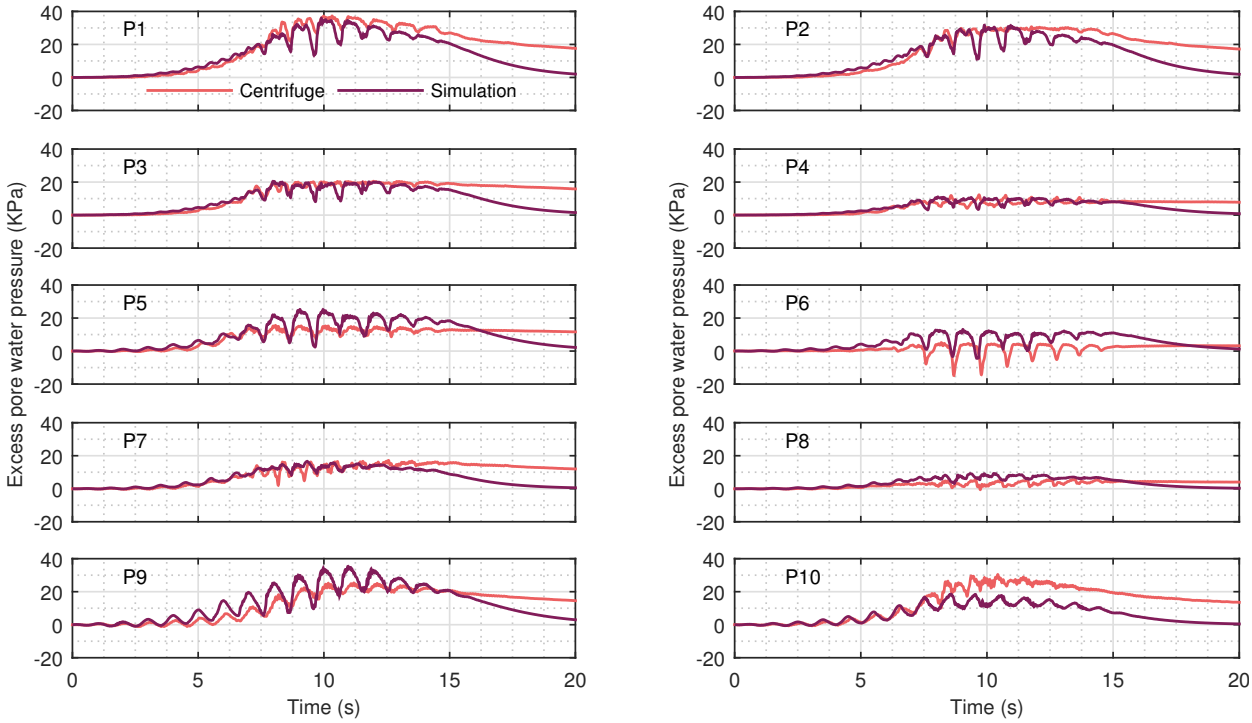

Figure 6.16: LEAP Project; Class-A prediction of RPI centrifuge experiment - excess pore water pressures (**Ghofrani** and Arduino, 2017)

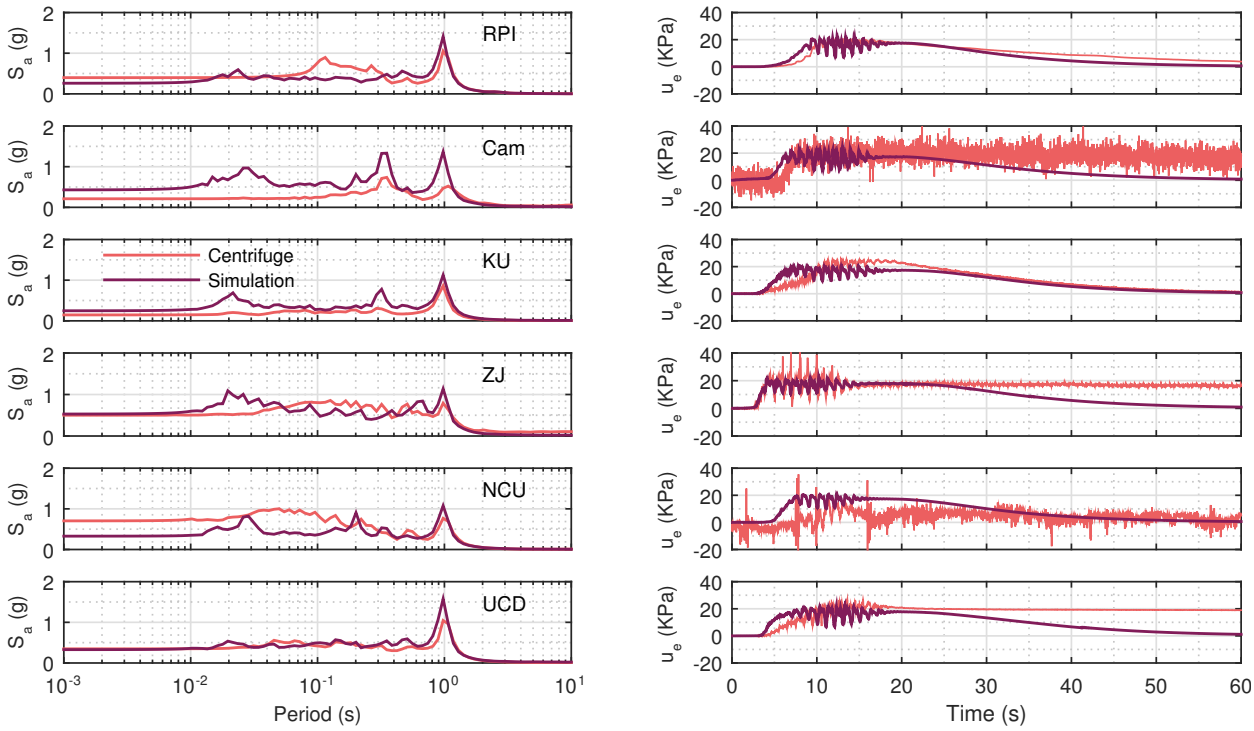

Figure 6.17: LEAP Project; Class-C prediction of centrifuge experiments (**Ghofrani** and Arduino, 2017)

Part III

SOIL-STRUCTURE INTERACTION

The third part of this dissertation addresses the problem of Soil-Structure-Interaction and introduces a mortar formulation to represent the interface behavior between a pile structure and its surrounding soil. To motivate this work, a fiber overlay element using the concept of overlay elements is presented first. Then the formulation of a mortar interface is given and two different implementations of this element are described. In the first implementation a perfect bonding condition is considered, whereas in the second implementation an elasto-plastic behavior is assumed at the interaction surface. These elements are verified later in this part of the dissertation. Various validation examples using these elements are presented in the fourth part of the dissertation.

Chapter 7

EMBEDDED FIBER OVERLAY ELEMENTS

There are four general modes of interface behavior identified in the literature: stick, slip, debonding and rebonding. Of interest in this section is the first mode, i.e. sticking. In this case the contacting bodies are perfectly bonded together and there is no relative movement between them. If stick conditions are assumed true, interface behavior simplifies drastically. This is because the displacement of one of the contacting bodies can be directly calculated knowing the displacement of the other body. For example, Sadek and Shahrour (2004) introduced a macro-element representing an embedded beam within a solid element. Initially they presented the formulation assuming perfect bonding between the beam element and the underlying continuum element, but, eventually the formulation was expanded to consider slipping and separation between the continuum portion of the element and the reinforcing beam element. As expected, this macro-element requires more degrees of freedom to incorporate the relative movement of the beam and solid elements. As an alternative technique, an "overlay" element (Helnwein et al., 1993; Meschke and Helnwein, 1994) is capable of capturing the perfect bonding behavior without introducing extra degrees of freedom; separating the stress state in the beam and the solid and giving the "true" stress as output. The embedded fiber overlay described in this section follows this framework but only axial behavior of the fiber is considered here. As mentioned before, this is done to introduce the concept of embedded elements and also provide an element that can be used in applications where only axial behavior is relevant; e.g. geosynthetics. The fiber overlay element is attractive for its mesh-independent features. In particular, being an overlay element, it brings the freedom to use more than one overlay element to represent reinforcing

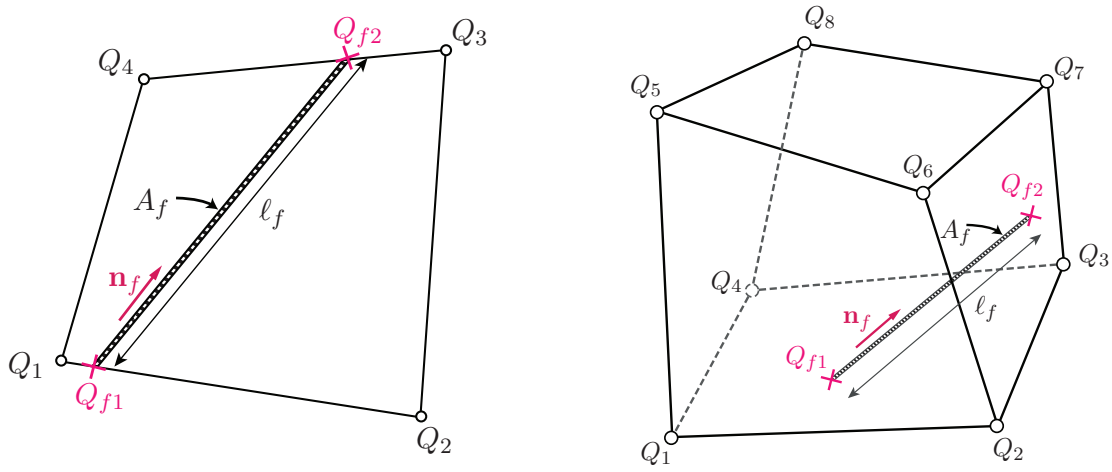

(a) 2D quadrilateral Fiber Overlay element

(b) 3D hexahedral Fiber Overlay element

Figure 7.1: Schematics of 2D and 3D Fiber Overlay elements

fibers in different orientations over a single solid element. The theory behind the fiber overlay element and details about the finite element implementation of this element is given next.

7.1 Theory

Figure 7.1 shows schematics of 2D and 3D fiber overlay elements. In each case the fiber is assumed to have a constant cross-sectional area A_f, initial length ℓ_f, and $\mathbf{n}_f$ representing the orientation of the fiber with $\|\mathbf{n}_f\| = 1$. Assuming perfect bonding between the fiber and the underlying solid element, the strain in the fiber, ε_f, can be calculated using the underlying element strain tensor field at any location along the fiber. That is

$$\varepsilon_f = \mathbf{n}_f \cdot \boldsymbol{\varepsilon} \cdot \mathbf{n}_f = (\mathbf{n}_f \otimes \mathbf{n}_f) : \boldsymbol{\varepsilon} \quad , \tag{7.1}$$

where $\boldsymbol{\varepsilon}$ is the 2$^{\text{nd}}$ order small strain tensor calculated as the symmetric gradient of the displacement field, $\boldsymbol{\varepsilon} = \nabla^{\mathsf{s}}\mathbf{u} = \frac{1}{2}\left(\nabla\mathbf{u} + \nabla^{\mathsf{T}}\mathbf{u}\right)$; where $\mathbf{u}$ defines the displacement field over the solid element.

The internal stress σ_f in the fiber is governed by its constitutive behavior and is a function of the strain ε_f. Given an admissible virtual displacement field, the virtual work of the stress in the fiber element can be expressed as

$$\delta W_f = \int_{\ell_f} \sigma_f(\ell)\ \delta\varepsilon_f(\ell)\ A_f\ \mathrm{d}\ell \quad , \tag{7.2}$$

where $\delta\varepsilon_f(\ell)$ is the virtual strain in the fiber resulting from the admissible virtual displacement field.

The stress-strain behavior of the fiber can be linearized using an appropriate tangential axial stiffness, E_f, and the incremental stress in the fiber can be written as $\mathrm{d}\sigma_f = E_f \mathrm{d}\varepsilon_f$. Assuming negligible change in the length and cross sectional area of the fiber, linearization of the virtual work in Equation 7.2 yields

$$\begin{aligned} \mathrm{d}\delta W_f &= \int_{\ell_f} \delta\varepsilon_f(\ell)\ \mathrm{d}\sigma_f(\ell)\ A_f\ \mathrm{d}\ell \\ &= \int_{\ell_f} \delta\varepsilon_f(\ell)\ E_f(\ell)\ \mathrm{d}\varepsilon_f(\ell)\ A_f\ \mathrm{d}\ell \quad . \end{aligned} \tag{7.3}$$

7.2 Finite Element Formulation

Equations 7.2 and 7.3 provide the basis for calculation of the resisting force vector and tangent stiffness matrix of a fiber overlay element. Using regular finite element shape (interpolation) functions $N_i(\mathbf{x})$, the displacement field inside the solid element is approximated as

$$\mathbf{u}(\mathbf{x}) = \sum_{i=1}^{n_{\mathrm{en}}} N_i(\mathbf{x})\hat{\mathbf{u}}_i \quad , \tag{7.4}$$

where n_{en} is the number of nodes in the element, $\hat{\mathbf{u}}_i$ is the nodal displacement at node i and $\mathbf{x}$ denotes the location of a point inside the solid element. The strain tensor is calculated using the symmetric gradient of the displacement field as

$$\nabla^{\mathsf{s}}\mathbf{u}(\mathbf{x}) = \sum_{i=1}^{n_{\text{en}}} \nabla^{\mathsf{s}} N_i(\mathbf{x})\hat{\mathbf{u}}_i \quad , \tag{7.5}$$

$$\{\boldsymbol{\varepsilon}\} = [\mathbf{B}]\,\{\hat{u}\} \quad , \tag{7.6}$$

where $\{\boldsymbol{\varepsilon}\}$ is the strain tensor written in its vector representation[1] and $[\mathbf{B}]$ is the matrix connecting the strain vector to the vector of nodal displacements $\{\hat{u}\}$. Defining $\mathbb{N} = \mathbf{n}_f \otimes \mathbf{n}_f$ and writing it in the proper vector format[2], $\{\mathbb{N}\}$, the axial strain in the fiber is written as

$$\varepsilon_f = (\mathbf{n}_f \otimes \mathbf{n}_f) : \boldsymbol{\varepsilon} \Rightarrow \varepsilon_f = \{\mathbb{N}\}^{\mathsf{T}}\,[\mathbf{B}]\,\{\hat{u}\} \quad . \tag{7.7}$$

Following the Galerkin method, the nodal virtual displacements are defined as

$$\delta\varepsilon_f = (\mathbf{n}_f \otimes \mathbf{n}_f) : \delta\boldsymbol{\varepsilon} \Rightarrow \{\delta\varepsilon_f\} = \{\delta\hat{u}\}^{\mathsf{T}}\,[\mathbf{B}]^{\mathsf{T}}\,\{\mathbb{N}\} \quad . \tag{7.8}$$

Therefore, Equations 7.2 and 7.3 can be written in terms of $\{\hat{u}\}$ as

---

[1] Voigt representation can be used.

[2] Vector representation of $\mathbb{N}$ depends on how strains and stresses are represented in vector and matrix format. For example, if the strains are written in the 6×1 vector form as $\{\varepsilon_{xx} \quad \varepsilon_{yy} \quad \varepsilon_{zz} \quad \gamma_{xy} \quad \gamma_{yz} \quad \gamma_{zx}\}^{\mathsf{T}}$, then $\mathbb{N} = \{n_x n_x \quad n_y n_y \quad n_z n_z \quad n_x n_y \quad n_y n_z \quad n_z n_x\}^{\mathsf{T}}$.

$$\delta W_f = \int_{\ell_f} \left(\{\delta \hat{u}\}^{\mathsf{T}} [\mathbf{B}]^{\mathsf{T}} \{\mathbb{N}\} \right) \sigma_f \, A_f \, \mathrm{d}\ell \tag{7.9}$$

$$= \{\delta \hat{u}\}^{\mathsf{T}} \int_{\ell_f} [\mathbf{B}]^{\mathsf{T}} \{\mathbb{N}\} \, \sigma_f \, A_f \, \mathrm{d}\ell \tag{7.10}$$

$$= \{\delta \hat{u}\}^{\mathsf{T}} \{F_f\} \quad . \tag{7.11}$$

where $\{F_f\}$ represents the resisting forces vector for the overlay element. Linearization of Equation 7.10 results in the tangent stiffness matrix $[K_f]$. Thus,

$$\mathrm{d}\delta W_f = \int_{\ell_f} \left(\{\delta \hat{u}\}^{\mathsf{T}} [\mathbf{B}]^{\mathsf{T}} \{\mathbb{N}\} \right) E_f \left(\{\mathbb{N}\}^{\mathsf{T}} [\mathbf{B}] \{\mathrm{d}\hat{u}\} \right) \, A_f \, \mathrm{d}\ell \tag{7.12}$$

$$= \{\delta \hat{u}\}^{\mathsf{T}} \int_{\ell_f} [\mathbf{B}]^{\mathsf{T}} \{\mathbb{N}\} \, E_f \, \{\mathbb{N}\}^{\mathsf{T}} [\mathbf{B}] \, A_f \, \mathrm{d}\ell \quad \{\mathrm{d}\hat{u}\} \tag{7.13}$$

$$= \{\delta \hat{u}\}^{\mathsf{T}} [K_f] \{\mathrm{d}\hat{u}\} \quad . \tag{7.14}$$

Here linearization of the fiber constitutive behavior ($\mathrm{d}\sigma_f = E_f \mathrm{d}\varepsilon_f$) is used, where

$$\mathrm{d}\varepsilon_f = (\mathbf{n}_f \otimes \mathbf{n}_f) : \mathrm{d}\boldsymbol{\varepsilon} \Rightarrow \{\mathrm{d}\boldsymbol{\varepsilon}_f\} = \{\mathrm{d}\hat{u}\}^{\mathsf{T}} [\mathbf{B}]^{\mathsf{T}} \{\mathbb{N}\} \quad . \tag{7.15}$$

Following this approach the resisting force vector and tangent stiffness matrix are

$$\{F_f\} = \int_{\ell_f} [\mathbf{B}]^{\mathsf{T}} \{\mathbb{N}\} \, \sigma_f \, A_f \, \mathrm{d}\ell \quad , \tag{7.16}$$

$$[K_f] = \int_{\ell_f} [\mathbf{B}]^{\mathsf{T}} \{\mathbb{N}\} \, E_f \, \{\mathbb{N}\}^{\mathsf{T}} [\mathbf{B}] \, A_f \, \mathrm{d}\ell \quad . \tag{7.17}$$

Evaluation of $[K_f]$ and $\{F_f\}$ requires performing integration over the volume of the fiber. Since a constant cross-sectional area is assumed for the fiber, the integrals over the volume

translate into integrals over the length of the fiber. These integrals can be done numerically using "Gaussian quadrature" techniques. Since in 2D and 3D respectively bi-linear and tri-linear displacement fields are usually chosen for quadrilateral elements, two point Gaussian quadrature integration gives accurate results for not distorted elements. The location and weights for the Gaussian quadrature rule are usually given for a domain ranging from -1 to 1. Therefore, a coordinate transformation must be used to transform the local coordinates of the fiber element to an iso-parametric domain (ζ) where $-1 \leq \zeta \leq 1$ (Figure 7.2). These statements translate mathematically to

$$\int_{V_f} (\bullet)\, \mathrm{d}V = A_f \int_{Q_{f1}}^{Q_{f2}} (\bullet)\, \mathrm{d}\ell \tag{7.18}$$

$$= A_f \int_{-1}^{1} (\bullet)_\zeta J\, \mathrm{d}\zeta \tag{7.19}$$

$$= A_f \sum_{i=1}^{2} (\bullet)_{\zeta_i} J(\zeta_i) w_i \quad , \tag{7.20}$$

where $(\bullet)_\zeta$ is the integrand written in the iso-parametric space in terms of ζ, J is the so-called Jacobian of the transformation ($J = \partial\ell/\partial\zeta = \ell_f/2$) and ζ_i and w_i are the location and the weight factors for the Gaussian quadrature rule.

7.3 Implementation in OpenSees

Three main tasks are identified for proper implementation of the overlay element described above in any FE tool. The first task involves setting up variables such as the fiber location in the solid element, fiber direction and integration points along the fiber. This task is done once the element is created. The second task involves calculating the fiber strain from the nodal displacements of the underlying solid element. The third task involves evaluating the stiffness matrix and the resisting force vector of the element using numerical integration methods as described in the previous section. The strain in the fiber is needed to calculate the stiffness matrix and the resisting force vector, therefore task 2 is actually part of task 3, which

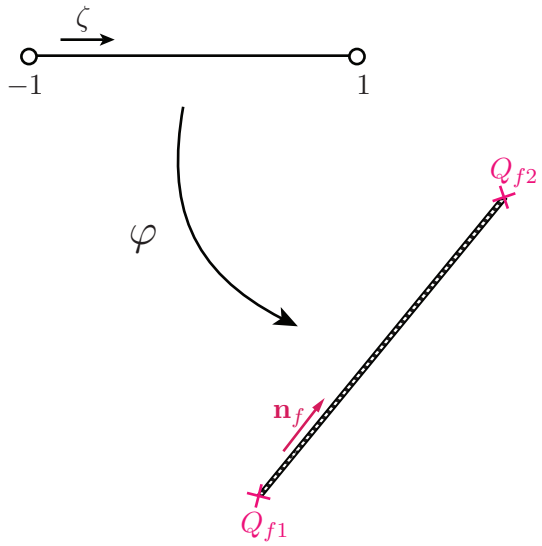

Figure 7.2: Iso-parametric transformation of the 1D fiber

should be performed during each iteration in a nonlinear analysis. The next section describes details of the algorithms used to implement the fiber overlay element in the OpenSees FE framework. These tasks are first described for a 2D case and later extended to 3D.

7.3.1 Task 1: Fiber overlay set-up

2D quadrilateral element In the current implementation of the fiber overlay element, 8 parameters are required for the 2-D quadrilateral element: 4 node tags corresponding to underlying quadrilateral element nodes, 1 'uniaxial' material tag to represent the behavior of the fiber, the cross-sectional area of the fiber and 2 values (noted as β_1 and β_2) specifying the location of the fiber inside the quadrilateral element; β_1 and β_2 specify the location of the two end points of the fiber along the sides of the quadrilateral element. Based on node order, these parameters indicate how far away from the nodes is the location of the fiber points. For example $\beta_1 = 1.5$ indicates that the first point of the fiber lies halfway between nodes 1 and 2, while $\beta_2 = 4.3$ indicates that the second point of the fiber lies three tenth of

the length of the side connecting nodes 4 to 1, away from node 4. Using this approach any configuration of the fiber inside a 2D solid element can be represented.

Given the input parameters for the fiber overlay, the location of the fiber points (Q_{f1} and Q_{f2}) are calculated and used to obtain the fiber unit direction vector as:

$$\mathbf{n}_f = \frac{(Q_{f2} - Q_{f1})}{\|Q_{f2} - Q_{f1}\|} \quad . \tag{7.21}$$

7.3.2 Task 2: Calculating the fiber strain

In order to calculate the fiber strain, one needs to first calculate the strain field in the quadrilateral element; knowing the displacements of the four nodes ($\tilde{\mathbf{u}}_1$—$\tilde{\mathbf{u}}_4$). Bi-linear iso-parametric shape functions

$$N_1 = \frac{1}{4}(1-\xi_1)(1-\xi_2) \quad , \tag{7.22}$$

$$N_2 = \frac{1}{4}(1+\xi_1)(1-\xi_2) \quad , \tag{7.23}$$

$$N_3 = \frac{1}{4}(1+\xi_1)(1+\xi_2) \quad , \tag{7.24}$$

$$N_4 = \frac{1}{4}(1-\xi_1)(1+\xi_2) \quad , \tag{7.25}$$

can be used where $-1 \leq \xi_1, \xi_2 \leq 1$ to approximate the displacement field as

$$\mathbf{u}(\xi_1, \xi_2) = \sum_{i=1}^{4} N_i(\xi_1, \xi_2)\hat{\mathbf{u}}_i \quad . \tag{7.26}$$

The strain field inside the quadrilateral element is the symmetric gradient of the displacement field,

$$\boldsymbol{\varepsilon}(\xi_1, \xi_2) = \nabla^{\mathsf{s}}\mathbf{u}(\xi_1, \xi_2) = \frac{1}{2}\left(\nabla\mathbf{u}(\xi_1, \xi_2) + \nabla^{\mathsf{T}}\mathbf{u}(\xi_1, \xi_2)\right) \quad . \tag{7.27}$$

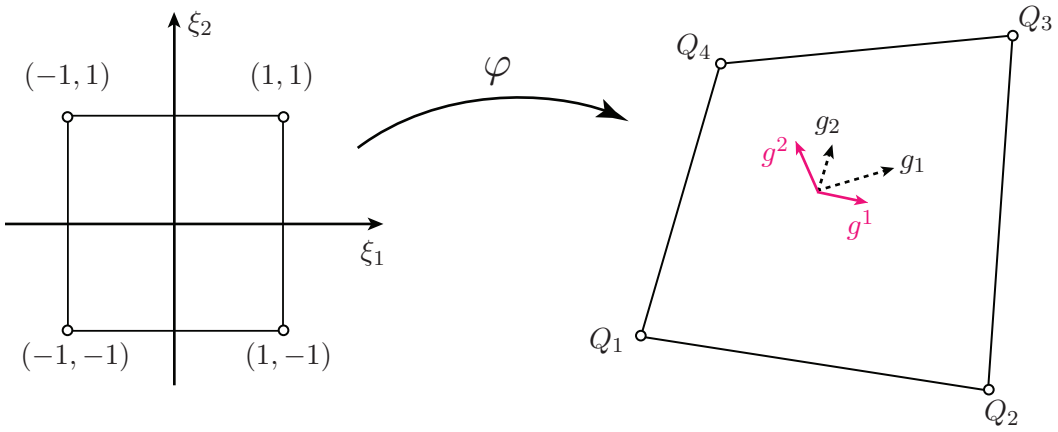

Figure 7.3: Iso-parametric transformation of 2D solid element

The gradient of the displacement field is calculated in the iso-parametric space (Figure 7.3). Suppose Q_i represents the coordinates of the quadrilateral element node i in the original configuration ($\{Q_i\}^T = \{x_i, y_i\}$). Then the transformation from the iso-parametric space ξ_1, ξ_2, to the original configuration $\mathbf{x} = x, y$, can be defined as

$$\mathbf{x} = \varphi(\xi_1, \xi_2) = \sum_{i=1}^{4} N_i(\xi_1, \xi_2) Q_i \quad . \tag{7.28}$$

Therefore we can define the coordinate vectors in the transformed (original) configuration as

$$\mathbf{g}^\alpha = \frac{\partial \varphi(\xi_1, \xi_2)}{\partial \xi_\alpha} \quad . \tag{7.29}$$

Since the basis vectors, $\mathbf{g}^\alpha$, are not necessarily ortho-normal, we define their dual basis as

$$\mathbf{g}_1 = \frac{(\mathbf{g}^1 \wedge \mathbf{g}^2).\mathbf{g}^2}{\mathbf{g}^1.(\mathbf{g}^1 \wedge \mathbf{g}^2).\mathbf{g}^2} \quad , \tag{7.30}$$

$$\mathbf{g}_2 = \frac{(\mathbf{g}^2 \wedge \mathbf{g}^1).\mathbf{g}^1}{\mathbf{g}^2.(\mathbf{g}^2 \wedge \mathbf{g}^1).\mathbf{g}^1} \quad , \tag{7.31}$$

where $(\bullet)\wedge(\circ)$ refers to the so-called "wedge product" defined as $(\bullet)\wedge(\circ) = (\bullet)\otimes(\circ)-(\circ)\otimes(\bullet)$. The displacement field can now be written in terms of the dual basis as $\mathbf{u} = u^{\alpha}\mathbf{g}_{\alpha}$. Hence the displacement field gradient in the iso-parametric space can be written as (note that the Einstein summation rule is used),

$$\nabla\mathbf{u} = \frac{\partial\mathbf{u}}{\partial\xi_i}\mathbf{g}^i = \frac{\partial u_j}{\partial\xi_i}\mathbf{g}^j\otimes\mathbf{g}^i \tag{7.32}$$

$$= \frac{\partial(N_k\hat{\mathbf{u}}_k)_j}{\partial\xi_i}\mathbf{g}^j\otimes\mathbf{g}^i \tag{7.33}$$

$$= (\hat{\mathbf{u}}_k)_j\frac{\partial N_k}{\partial\xi_i}\mathbf{g}^j\otimes\mathbf{g}^i \quad , \tag{7.34}$$

and the strain can be calculated as

$$\boldsymbol{\varepsilon} = \frac{1}{2}(\nabla\mathbf{u} + \nabla^{\mathsf{T}}\mathbf{u}) \tag{7.35}$$

$$= \frac{1}{2}\left((\hat{u}_k)_j\frac{\partial N_k}{\partial\xi_i}(\mathbf{g}^j\otimes\mathbf{g}^i + \mathbf{g}^i\otimes\mathbf{g}^j)\right) \quad . \tag{7.36}$$

With the assumption of perfect bonding between the fiber and the underlying solid element, the axial strain in the fiber can be calculated using the fiber unit direction vector $\mathbf{n}_f$ as

$$\varepsilon_f = \mathbf{n}_f\cdot\boldsymbol{\varepsilon}\cdot\mathbf{n}_f \tag{7.37}$$

$$= \mathbf{n}_f\cdot\left[\frac{1}{2}\left((\hat{u}_k)_j\frac{\partial N_k}{\partial\xi_i}(\mathbf{g}^j\otimes\mathbf{g}^i + \mathbf{g}^i\otimes\mathbf{g}^j)\right)\right]\cdot\mathbf{n}_f \tag{7.38}$$

$$= (\hat{u}_k)_j\frac{\partial N_k}{\partial\xi_i}(\mathbf{n}_f\cdot\mathbf{g}^i)(\mathbf{n}_f\cdot\mathbf{g}^j) \tag{7.39}$$

$$= (\hat{u}_k)_j\frac{\partial N_k}{\partial\xi_i}(n_f)^i(n_f)^j \quad , \tag{7.40}$$

where $(n_f)^i$ and $(n_f)^j$ denote components of $\mathbf{n}_f$ in the direction of $\mathbf{g}_i$ and $\mathbf{g}_j$, i.e., dual base vectors. Notice that in equation 7.40 the metric tensor for the transformation is implicitly used for the inner products of $\mathbf{n}_f$ and $\mathbf{g}^\alpha$. Also ε_f is a function of the position in the original configuration: $\varepsilon_f = \varepsilon_f(\xi_1, \xi_2)$.

7.3.3 Task 3: Calculating the element stiffness matrix and resisting force vector

The element tangent stiffness matrix $[K_f]$ and resisting force vector $\{F_f\}$ are calculated using the strain calculated in Task 2. A uniaxial material object should be created in OpenSees to characterize the fiber's material behavior. This material object is needed to calculate the stress in the fiber for the respective strain ε_f, i.e., $\sigma_f = \sigma_f(\varepsilon_f)$. Here the integration is performed along the fiber element whereas in the previous task, the gradients were calculated in the solid element domain. Therefore in the previous task we were dealing with a 2D bi-linear iso-parametric element whereas in this task we are dealing with a linear 1-D iso-parametric element. Points along the 1D iso-parametric element denoted by ζ correspond to points inside the 2D element with coordinates ξ_1 and ξ_2 and they share the same location in the original configuration.

Using $\mathbb{N} = \mathbf{n}_f \otimes \mathbf{n}_f$, and writing it in the appropriate matrix form, i.e., $\{\mathbb{N}\}$, the resisting force vector is calculated as

$$\{F_f\} = \int_{\ell_f} [\mathbf{B}]^\mathsf{T} \{\mathbb{N}\} \sigma_f \, A_f \, \mathrm{d}\ell \tag{7.41}$$

$$= \int_{-1}^{1} [\mathbf{B}(\zeta)]^\mathsf{T} \{\mathbb{N}\} \sigma_f(\zeta) \, A_f J(\zeta) \, \mathrm{d}\zeta \tag{7.42}$$

$$= \sum_{i=1}^{2} [\mathbf{B}(\zeta_i)]^\mathsf{T} \{\mathbb{N}\} \sigma_f(\zeta_i) \, A_f J(\zeta_i) w_i \quad , \tag{7.43}$$

and the tangent stiffness matrix is calculated as

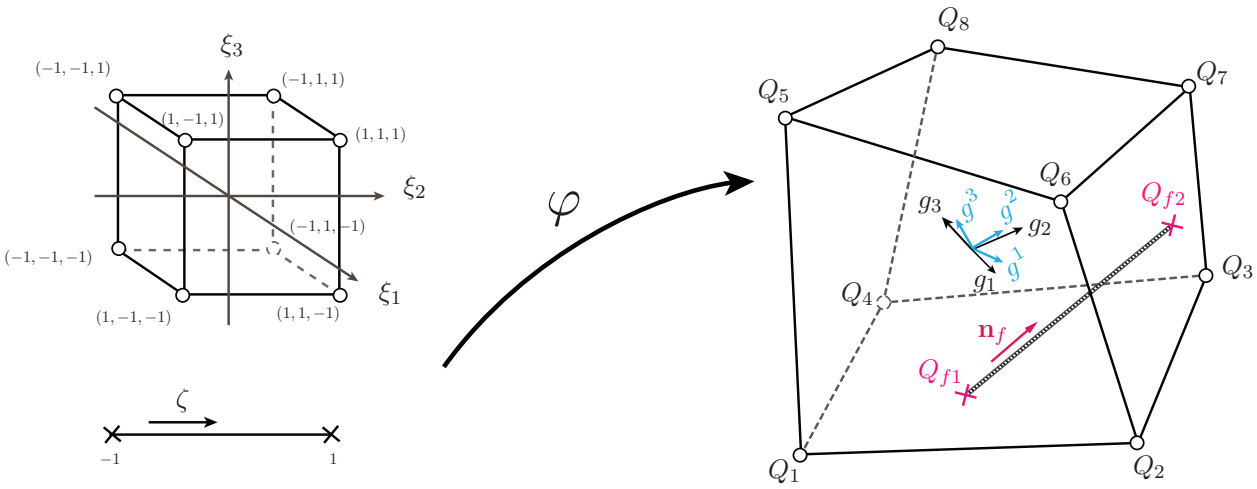

Figure 7.4: Iso-parametric transformation of the 3D fiber overlay element

$$[K_f] = \int_{\ell_f} [\mathbf{B}]^{\mathsf{T}} \{\mathbb{N}\} E_f \{\mathbb{N}\}^{\mathsf{T}} [\mathbf{B}] \; A_f \, \mathrm{d}\ell \tag{7.44}$$

$$= \int_{-1}^{1} [\mathbf{B}(\zeta)]^{\mathsf{T}} \{\mathbb{N}\} E_f(\zeta) \{\mathbb{N}\}^{\mathsf{T}} [\mathbf{B}(\zeta)] \; A_f J(\zeta) \, \mathrm{d}\ell \tag{7.45}$$

$$= \sum_{i=1}^{2} [\mathbf{B}(\zeta_i)]^{\mathsf{T}} \{\mathbb{N}\} E_f(\zeta_i) \{\mathbb{N}\}^{\mathsf{T}} [\mathbf{B}(\zeta_i)] \; A_f J(\zeta_i) w_i \quad , \tag{7.46}$$

where $J(\zeta_i)$ and $[\mathbf{B}(\zeta_i)]$ are the Jacobian of the transformation and the matrix relating strains to displacements, respectively. Using $\{B_f\} = [\mathbf{B}]^{\mathsf{T}} \mathbb{N}$, we can simplify Equations 7.43 and 7.46 as

$$\{F_f\} = \sum_{i=1}^{2} \{B_f(\zeta_i)\} \sigma_f(\zeta_i) \, A_f J(\zeta_i) w_i \quad , \tag{7.47}$$

$$[K_f] = \sum_{i=1}^{2} \{B_f(\zeta_i)\} E_f(\zeta_i) \{B_f(\zeta_i)\}^{\mathsf{T}} \; A_f J(\zeta_i) w_i \quad . \tag{7.48}$$

3D Hexahedral element Implementation details for the 2D quadrilateral element were described above to explain the mechanics of an overlay element. The 3D hexahedral element implementation follows the same process. A major difference in the element definition is the arrangement of the fiber inside the solid element. The starting and ending points of the linear fiber within the hexahedral shape should be expressed in a simple and relatively easy to use manner during pre-processing of the FE model. This requires knowing the hexahedral sides where the fiber intersects, and the intersection point on each side. Knowing the coordinates of the hexahedral element nodes and the fiber starting and ending point coordinates, the intersection points can be found. This process can be done either internally in the implementation of the element when the parameters are initialized, or outside the element as information provided during pre-processing. In the current OpenSees implementation the location parameters of the starting and ending points of the fiber in the iso-parametric space are calculated in the pre-processing phase and passed on to the element. Other details of the element formulation follow very similarly to the 2D quadrilateral implementation.

Chapter 8

NUMERICAL ANALYSIS OF SOIL-STRUCTURE INTERACTION SYSTEMS

8.1 Introduction

The idea of an overlay element described in the previous chapter (by adding the axial stiffness of a fiber to the continuum solid elements) can be used to create coupling between distinct elements. The overlay element can conveniently introduce the interaction between elements without the need to define and implement additional elements. In soil-structure interaction problems we usually assume a kinematic constraint between the structural element and the surrounding soil. For example in the case of deep foundations the kinematic condition could be the impenetrability of the pile surface, meaning the soil cannot penetrate into the pile structure and vice versa. This is the fundamental assumption underlying the contact mechanics formulation. Assuming tied contact between the soil domain and the pile structure simplifies the problem considerably. This assumption could be valid in certain geotechnical problems.

Using this idea, the behavior of a particular body can be embedded in the behavior of another body, forming a new macro-element. In these type of elements two or more mechanical bodies are in direct interaction in such a way that behavior of one can be deduced from the other by considering some kinetic or kinematic conditions. Sadek and Shahrour (2004) developed an embedded element for piles assuming perfect bonding between a beam embedded in its surrounding solid. In their formulation, the bonding condition is kinematically enforced at the beam nodes assuming that the displacement field along the beam can be defined in terms of the solid displacement field expressed by means of standard interpolation functions. Doing so, the beam rotational degrees of freedom are not explicitly expressed in

terms of the solid displacement field, therefore rotational degrees of freedom are added as additional unknowns to the system. Since the compatibility condition is only enforced at the beam nodes, the displacement field along the beam can in general be incompatible to the solid displacement field. This issue can generate non-convergent solutions, specially when the beam and solid nodes are located close to each other.

Turello et al. (2016) addressed this problem by explicitly defining an interaction surface along which the kinematic condition of compatibility is enforced. This is done in a weak sense using the principle of virtual works, meaning that the relative displacements between the beam and the solid produces zero virtual work for any admissible system of virtual interaction forces. In order to do so, mapping functions are developed to map the beam nodal displacements to the interaction surface where perfect bonding (i.e. a rough surface) is assumed between the beam and the solid. By doing so, all beam degrees of freedom (i.e. both rotational and translational) are expressed in terms of the solid nodal displacements. Therefore, no additional unknowns are added to the system of equations for the model under consideration. Turello et al. (2017) expanded this formulation to consider elasto-plastic behavior at the interface between the beam and solid element. Similar to this approach, mortar elements apply the contact conditions between two non-conforming discretizations by mapping the master and slave contact bodies to a well-defined contact boundary in between the bodies and contact conditions are applied over this boundary in a weak sense (Bernardi et al., 1993; Bernardi, 1994).

The embedded element proposed by Turello et al. is suitable for modeling soil-pile systems. This element is also very well suited for dynamic analysis of such problems. Although the gap formation mechanism is not included in their formulation, this type of element can be used in many geotechnical soil-pile problems in which we can assume that the pile is always in contact with its surrounding soil. To address this problem, Turello et al. (2017) extended their embedded formulation to include elasto-plastic behavior at the interface. This elasto-plastic behavior represents the near-field soil-pile interaction. Both these elements (with perfect bonding and with elasto-plastic interface behavior) are described here and

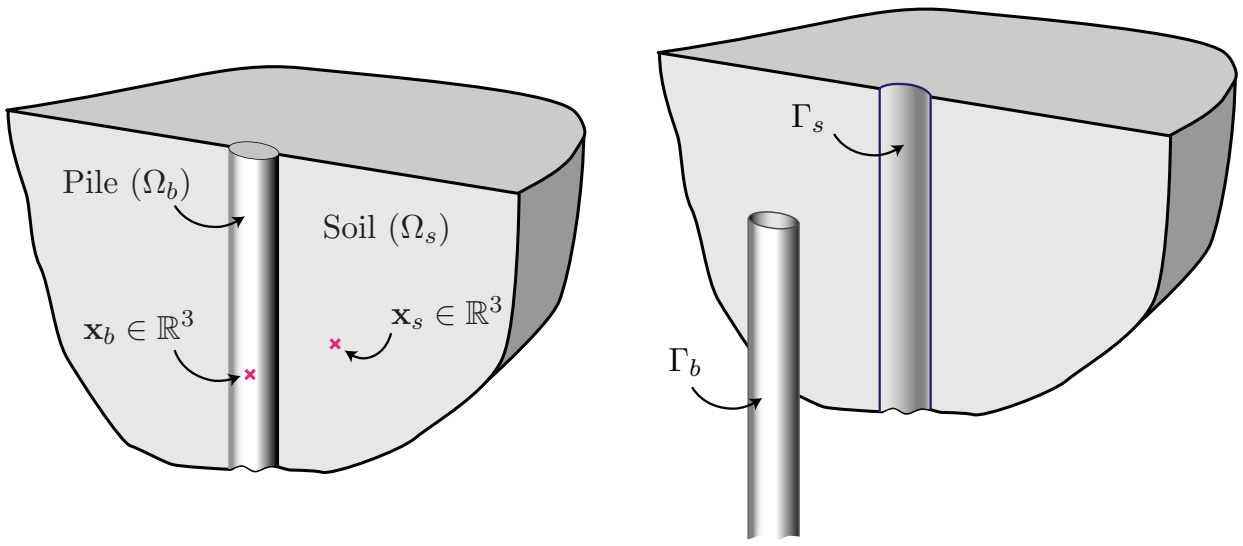

Figure 8.1: Schematic of a pile foundation buried in a soil domain.

implemented in OpenSees. These formulations can be further extended to include contact mechanics and gap formation mechanism.

8.2 Theory

Without loss of generality, we use a pile foundation structure buried in a soil domain to represent the embedded beam in a solid domain formulation. Figure 8.1 depicts such problem where Ω_b represents the pile structure domain and Ω_s denotes the soil domain surrounding the pile. Points locations in Ω_b are denoted by $\mathbf{x}_b \in \mathbb{R}^3$. Similarly $\mathbf{x}_s \in \mathbb{R}^3$ represent the location of points in the soil domain. Using small deformation assumptions, these location vectors are all defined in the undeformed configuration. An exploded view of this problem is shown in Figure 8.1 to illustrate the boundaries of these domains. Γ_b represents the contacting boundary of the pile structure and Γ_s the boundary of soil in contact with the pile.

1D frame elements are frequently used to model pile structures. Here, we also use a 1D beam body ($\bar{\Omega}_b$) to represent the pile domain. As shown in Figure 8.2 points located

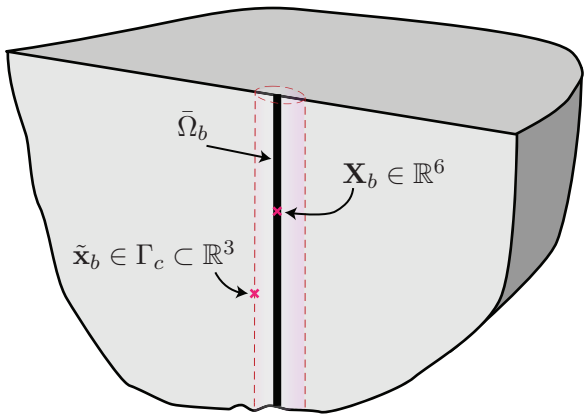

Figure 8.2: Schematic of a 1D pile foundation buried in a 3D soil domain with an explicit interaction surface.

along this 1D line domain are denoted with $\mathbf{X}_b \in \mathbb{R}^3$ representing the centerline of the pile. Doing so, an explicit interaction surface along the pile no longer exists. Therefore, in the formulation under study an outer interaction boundary, Γ_c, is explicitly defined for the pile domain over which the interaction conditions are applied. Points on this boundary are located via a vector $\tilde{\mathbf{x}}_b \in \mathbb{R}^3$.

Point displacements along the 1D pile domain ($\mathbf{X}_b \in \bar{\Omega}_b$) are represented by $\mathbf{U}_b(\mathbf{X}_b) \in \mathbb{R}^6$. Components of $\mathbf{U}_b$ consist of 3 translational and 3 rotational degrees of freedom. Similarly point displacements in the 3D soil body ($\mathbf{x}_s \in \Omega_s$) are defined with 3 degrees of freedom and are represented by $\mathbf{u}_s(\mathbf{x}_s) \in \mathbb{R}^3, \forall \mathbf{x}_s \in \Omega_s$. Compatibility between pile and soil deformation is enforced along the interaction surface, Γ_c. Pile displacements over the 1D body are mapped to the beam surface boundary which are represented with $\tilde{\mathbf{u}}_b(\tilde{\mathbf{x}}_b) \in \mathbb{R}^3, \forall \tilde{\mathbf{x}}_b \in \Gamma_b$. These definitions are shown in Figure 8.3.

Suppose that the soil domain can be parameterized using the parameters ξ, η and ζ all belonging to $\mathbb{R}$ such that $\mathbf{x}_s = \varphi^s(\xi, \eta, \zeta)$, and the 1D beam body using the parameter $\psi \in \mathbb{R}$ such that $\mathbf{X}_b = \varphi^b(\psi)$. By mapping the points from the 1D beam body (beam centerline) to the side surface of the pile, we explicitly define a boundary representing the contacting sides of the pile. Using the well-known Euler-Bernoulli assumption – plane cross sections remain

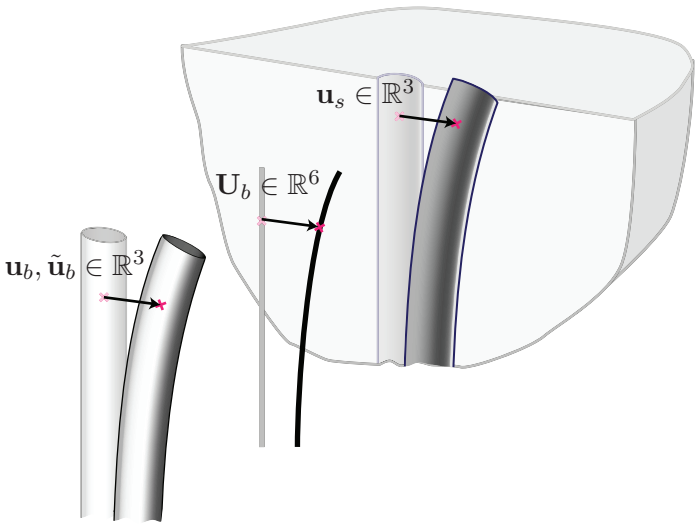

Figure 8.3: Schematic of the original-deformed configuration and definition of displacement vectors.

plane – a mapping $M(\rho, \theta)$ can be defined such that for every point on the centerline, a planar cross section is defined using parameters $\rho \in \mathbb{R}^+$ and $\theta \in [0, 2\pi)$ representing the distance to the centerline and the polar angle respectively. In order to define the outer boundary of the pile, $\tilde{\rho}$ and $\tilde{\theta}$ are used together with this mapping, where $\tilde{\rho}$ defines the distance from centerline to the point on the boundary at the polar angle $\tilde{\theta}$. Therefore, points on the beam boundary, $\tilde{\mathbf{x}}_b$, can be located by parameters ψ, $\tilde{\rho}$ and $\tilde{\theta}$ and the map $\mathcal{H}(\psi, \tilde{\rho}, \tilde{\theta}) = M(\tilde{\rho}, \tilde{\theta}) \circ \varphi^b(\psi)$. Using this approach, a virtual pile boundary, Γ_c, is defined where interaction behavior can be applied. This boundary coincides with the actual pile boundary, Γ_b. Since only points on the boundary of the pile are of interest, we use ρ and θ interchangeably with $\tilde{\rho}$ and $\tilde{\theta}$.

The corresponding soil boundary, Γ_s, is defined by assuming that boundaries of both domains initially occupy the same location in space. This is done by finding the location parameters of points in the soil domain initially sharing the same location as the pile boundary. Unlike the beam domain, points on the soil boundary belong to the interior of the soil domain that can be represented by $\varphi^s(\tilde{\xi}, \tilde{\eta}, \tilde{\zeta})$ where $\tilde{\xi}$, $\tilde{\eta}$ and $\tilde{\zeta}$ represent the parameteriza-

tion of the soil boundary. Soil boundary parameters are found by solving $\tilde{\mathbf{x}}_s^0 = \tilde{\mathbf{x}}_b^0$ for $\tilde{\xi}$, $\tilde{\eta}$ and $\tilde{\zeta}$ where the superscript zero represents the initial conditions.

The interaction behavior is defined over Γ_c. A perfect bonding condition is enforced by applying the condition

$$\tilde{\mathbf{x}}_b(\gamma) - \tilde{\mathbf{x}}_s(\gamma) = 0 \quad \forall \gamma \in \Gamma_c, \forall t \quad , \tag{8.1}$$

where t is a motion parameter (e.g. time). The rate form of this equation follows as

$$\dot{\tilde{\mathbf{x}}}_b(\gamma) - \dot{\tilde{\mathbf{x}}}_s(\gamma) = 0 \quad \forall \gamma \in \Gamma_c, \forall t \quad , \tag{8.2}$$

where $\dot{\bullet} = d\bullet/dt$. One can interpret this equation as enforcing zero relative velocities for points located at the intersecting boundary between the beam and solid.

8.2.1 Point Collocation Method

A point collocation solution of the differential equation 8.2 results in enforcing the perfect bonding condition at specifically chosen points on the boundary which are referred to as *interaction points* henceforth and are denoted by $\bar{\gamma}$.

The interaction points are chosen through discretization of the interaction surface. The condition is then enforced at these points using the Lagrange multipliers or Penalty methods or any other suitable method. For example, when using the Lagrange multipliers method the following term is added to the potential energy of the system,

$$\sum_{\bar{\gamma} \in \bar{\Gamma}_c} \boldsymbol{\lambda}(\bar{\gamma}) \cdot (\tilde{\mathbf{x}}_b(\bar{\gamma}) - \tilde{\mathbf{x}}_s(\bar{\gamma})) \quad , \tag{8.3}$$

where $\bar{\Gamma}_c$ is the discretized Γ_c and $\bar{\gamma}$ represents designated points at which the interaction condition is enforced. $\boldsymbol{\lambda}$ represents the vector of Lagrange multipliers which in this case

represent the interaction forces holding the perfect bonding constraint. Therefore,

$$\Pi = \Pi_{\text{system}} + \sum_{\bar{\gamma}\in\bar{\Gamma}_c} \boldsymbol{\lambda}(\bar{\gamma}_i) \cdot (\tilde{\mathbf{x}}_b(\bar{\gamma}_i) - \tilde{\mathbf{x}}_s(\bar{\gamma}_i)) \,. \tag{8.4}$$

The stationary point of the newly defined potential function can be found by setting its first variation equal to zero. This means

$$\delta\Pi = \delta\Pi_{\text{system}} + \sum_{\bar{\gamma}\in\bar{\Gamma}_c} \delta\boldsymbol{\lambda} \cdot (\tilde{\mathbf{x}}_b - \tilde{\mathbf{x}}_s) + \sum_{\bar{\gamma}\in\bar{\Gamma}_c} \boldsymbol{\lambda} \cdot (\delta\tilde{\mathbf{x}}_b - \delta\tilde{\mathbf{x}}_s) = 0 \quad . \tag{8.5}$$

By considering $\boldsymbol{\lambda}$, $\tilde{\mathbf{x}}_s$ and $\tilde{\mathbf{x}}_b$ as the minimization parameters for the potential function, the interaction condition is satisfied as the energy function is minimized. This analogy will be used in the rest of this chapter.

In the case of non-conservative systems where an energy function does not exist, the condition and the work of resulting reactive forces on the virtual displacements can be added to the virtual work of the system in order to consider the constraint conditions. In mathematical terms, this means

$$\delta W^{\text{internal}} = \delta W^{\text{internal}}_{\text{system}} + \underbrace{\sum_{\bar{\gamma}\in\bar{\Gamma}_c} \boldsymbol{\lambda} \cdot (\delta\tilde{\mathbf{x}}_b - \delta\tilde{\mathbf{x}}_s)}_{\text{Virtual work of interaction forces}} + \underbrace{\sum_{\bar{\gamma}\in\bar{\Gamma}_c} \delta\boldsymbol{\lambda} \cdot (\tilde{\mathbf{x}}_b - \tilde{\mathbf{x}}_s)}_{\text{Constraint enforcement}}$$

$$\forall \text{ admissible } \delta\tilde{\mathbf{x}}_b, \delta\tilde{\mathbf{x}}_s, \delta\boldsymbol{\lambda}. \tag{8.6}$$

The Penalty method can also be used to enforce the interaction condition. In this case a penalty function is used to penalize the relative displacement between the solid and the beam at interaction points. This penalty function is added to the potential of the system. In this case the function

$$\sum_{\bar{\gamma}\in\bar{\Gamma}_c} \frac{1}{2}\epsilon_p \|\tilde{\mathbf{x}}_b(\bar{\gamma}) - \tilde{\mathbf{x}}_s(\bar{\gamma})\|^2 \quad , \tag{8.7}$$

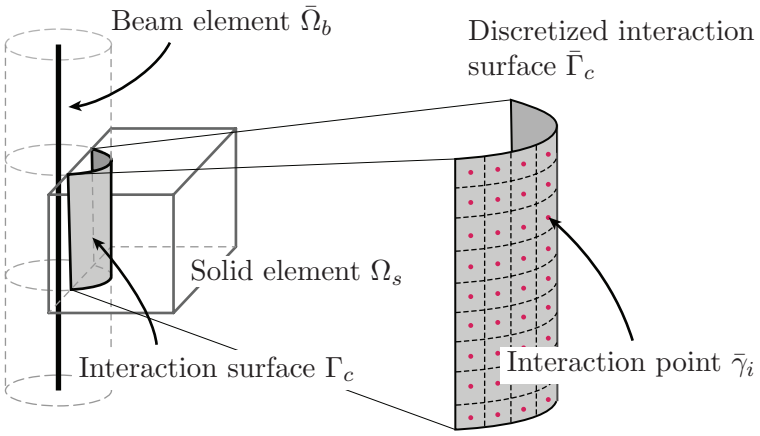

Figure 8.4: Discretization of the interaction surface

is used. Here, ϵ_p is referred to as the *penalty parameter* and is a very large number that is used to penalize the violation of the interaction condition. It can be shown that in the limit, as $\epsilon_p \to \infty$, the condition is exactly enforced. Again the stationary point of the potential energy function is found by setting its variation equal to zero. So,

$$\Pi = \Pi_{\text{system}} + \sum_{\bar{\gamma} \in \bar{\Gamma}_c} \frac{1}{2} \epsilon_p \|\tilde{\mathbf{x}}_b - \tilde{\mathbf{x}}_s\|^2 \quad , \tag{8.8}$$

$$\delta\Pi = \delta\Pi_{\text{system}} + \sum_{\bar{\gamma} \in \bar{\Gamma}_c} \epsilon_p \left(\tilde{\mathbf{x}}_b - \tilde{\mathbf{x}}_s\right) \cdot \left(\delta\tilde{\mathbf{x}}_b - \delta\tilde{\mathbf{x}}_s\right) = 0 \quad . \tag{8.9}$$

We can show that the interaction forces associated with the Penalty method are equal to $\epsilon_p \left(\tilde{\mathbf{x}}_b - \tilde{\mathbf{x}}_s\right)$ at each interaction point. Therefore, if the principle of virtual works is to be used, the work associated with the virtual displacements at the interaction surface is

$$\delta W^{\text{internal}} = \delta W^{\text{internal}}_{\text{system}} + \sum_i \epsilon_p \left(\tilde{\mathbf{x}}_b - \tilde{\mathbf{x}}_s\right) \cdot \left(\delta\tilde{\mathbf{x}}_b - \delta\tilde{\mathbf{x}}_s\right) \quad \forall \text{ admissible } \delta\tilde{\mathbf{x}}_b, \delta\tilde{\mathbf{x}}_s \quad . \tag{8.10}$$

8.2.2 Mortar Method

Another way to apply the condition defined by Equation 8.2 is to use the Lagrange multipliers method and integrate the condition over the interaction surface:

$$\int_{\Gamma_c} \boldsymbol{\lambda}(\gamma) \cdot (\tilde{\mathbf{x}}_b(\gamma) - \tilde{\mathbf{x}}_s(\gamma)) \ \mathrm{d}\gamma = 0 \quad \forall t, \tag{8.11}$$

where $\boldsymbol{\lambda}$ is again the vector of Lagrange multipliers at point γ. This condition can also be interpreted in terms of the principle of virtual forces. For an admissible system of virtual forces $\delta\tilde{f}$, this principle states that

$$\int_{\Gamma_c} \delta\tilde{f} \cdot (\tilde{\mathbf{x}}_b - \tilde{\mathbf{x}}_s) \ \mathrm{d}\Gamma = 0 \quad . \tag{8.12}$$

This equation expresses that any system of admissible virtual forces, $\delta\tilde{f}$, applied on the boundary domain produces zero virtual internal work[1]. Equations 8.11 and 8.12 are the basis for the definition of mortar conditions explained in this section.

The idea behind the *mortar method* is to assume interpolation functions for the Lagrange multipliers field as well as the displacement fields. Doing so, Equation 8.11 results in a geometric condition.

Interpolation of Displacement and Interaction Force Fields

Assume $\{\hat{\mathbf{u}}_s\}$ and $\left\{\hat{\mathbf{U}}_b\right\}$ represent vectors of nodal displacements for the solid and the beam elements, respectively. An interpolation function matrix, $[N_s]$, can be used to estimate the displacement field for the solid, $\mathbf{u}_s$, and a mapping function matrix, $[\mathcal{H}_u]$, can be used to approximate the beam displacement along the interaction surface, $\mathbf{u}_b$[2]. Therefore,

---

[1]For sake of brevity, the integration parameter is omitted from the integrals on the interaction boundary from this point on. These integrals are written as $\int_{\Gamma_c}[\bullet]\,\mathrm{d}\Gamma$ which what really meant is $\int_{\Gamma_c}[\bullet](\gamma)\,\mathrm{d}\gamma$.

[2]Notice the notation change. $\tilde{\mathbf{u}}_b$ denotes the displacements on the boundary of the pile but for the sake of simplicity $\mathbf{u}_b$ will be used henceforth to denote the displacements on the pile boundary.

$$\mathbf{u}_s(\xi,\eta,\zeta) = \sum_{i=1}^{n_{en}^s} N_{si}(\xi,\eta,\zeta)\hat{\mathbf{u}}_{si} = [N_s]\{\hat{\mathbf{u}}_s\} \quad , \tag{8.13}$$

$$\mathbf{u}_b(\psi,\rho,\theta) = \sum_{j=1}^{n_{en}^b} \mathcal{H}_{uj}(\psi,\rho,\theta)\hat{\mathbf{U}}_{bj} = [\mathcal{H}_u]\left\{\hat{\mathbf{U}}_b\right\} \quad , \tag{8.14}$$

where n_{en}^s and n_{en}^b denote the number of nodes per element for the solid and the beam elements respectively, $\hat{\mathbf{u}}_{si}$ is the solid nodal displacements at node i and N_{si} represents the corresponding shape function, similarly $\hat{\mathbf{U}}_{bj}$ is the beam nodal displacements at node j with corresponding mapping function $\mathcal{H}_{uj}$. In the mortar method we assume a structure for the constraint forces (Lagrange multipliers) at the interaction surface by interpolating nodal values. Although a separate discretization can be used for the interaction forces (mortar domain), either beam nodes or solid nodes can be used as well for defining the Lagrange multiplier forces field. For the purpose of this study, constraint forces are interpolated from their values at the beam nodes as this results in a smaller system for the interaction conditions. The mapping function $\mathcal{H}_f$ and interpolation function matrix $[\mathcal{H}_f]$ are developed for this purpose. Therefore,

$$\boldsymbol{\lambda}(\psi,\rho,\theta) = \mathbf{f}_b = \sum_{j=1}^{n_{en}^b} \mathcal{H}_{fj}(\psi,\rho,\theta)\hat{\mathbf{F}}_{bj} = [\mathcal{H}_f]\left\{\hat{\mathbf{F}}_b\right\} \quad , \tag{8.15}$$

where $\mathcal{H}_{fj}$ and $\hat{\mathbf{F}}_{bj}$ denote the mapping function and nodal interaction forces (Lagrange multipliers) at node j and $\hat{\mathbf{F}}_b$ is the vector of nodal interaction forces for the element.

Mortar method

Using the interpolation functions defined above, substituting in Equation 8.11 and simplifying, we have

$$\int_{\Gamma_c} \boldsymbol{\lambda} \cdot (\mathbf{x}_b - \mathbf{x}_s)\, \mathrm{d}\Gamma = \int_{\Gamma_c} \left(\mathcal{H}_f \hat{\mathbf{F}}_b\right) \cdot \left(\mathcal{H}_u \hat{\mathbf{U}}_b - N_s \hat{\mathbf{u}}_s\right) \mathrm{d}\Gamma = 0 \tag{8.16}$$

$$\Rightarrow \left\{\hat{\mathbf{F}}_b\right\}^{\mathsf{T}} \underbrace{\int_{\Gamma_c} [\mathcal{H}_f]^{\mathsf{T}} [\mathcal{H}_u]\, \mathrm{d}\Gamma}_{\left[\mathbb{N}^{fb}\right]^{\mathsf{T}}} \left\{\hat{\mathbf{U}}_b\right\} - \left\{\hat{\mathbf{F}}_b\right\}^{\mathsf{T}} \underbrace{\int_{\Gamma_c} [\mathcal{H}_f]^{\mathsf{T}} [N_s]\, \mathrm{d}\Gamma}_{\left[\mathbb{N}^{fs}\right]^{\mathsf{T}}} \{\hat{\mathbf{u}}_s\} = 0 \quad . \tag{8.17}$$

This results in a geometric condition of the form

$$\mathbb{N}^{fb,\mathsf{T}} \hat{\mathbf{U}}_b - \mathbb{N}^{fs,\mathsf{T}} \hat{\mathbf{u}}_s = \mathbf{0} \quad . \tag{8.18}$$

Equation 8.18 is the fundamental condition that applies perfect bonding between two sides of the mortar domain. If the interpolation functions are independent of the displacement and interaction forces fields, matrices $\mathbb{N}^{fb}$ and $\mathbb{N}^{fs}$ can be computed only once as they are constant. As before, this condition can be applied using Lagrange multipliers or Penalty methods. Using the Lagrange multipliers method we obtain

$$\boldsymbol{\lambda} \cdot \left(\mathbb{N}^{fb,\mathsf{T}} \hat{\mathbf{U}}_b - \mathbb{N}^{fs,\mathsf{T}} \hat{\mathbf{u}}_s\right) = 0 \quad . \tag{8.19}$$

First variation of Equation 8.19 should be added to the variation of the system's potential energy. This results in

$$\delta\Pi = \delta\Pi_{\text{system}} + \delta\boldsymbol{\lambda} \cdot \left(\mathbb{N}^{fb,\mathsf{T}} \hat{\mathbf{U}}_b - \mathbb{N}^{fs,\mathsf{T}} \hat{\mathbf{u}}_s\right) + \boldsymbol{\lambda} \cdot \left(\mathbb{N}^{fb,\mathsf{T}} \delta\hat{\mathbf{U}}_b - \mathbb{N}^{fs,\mathsf{T}} \delta\hat{\mathbf{u}}_s\right) = 0\,. \tag{8.20}$$

For a non-conservative system, the principle of virtual displacements can be used to find a similar solution. Similar to the case of collocation method, we have

$$\delta W^{\text{internal}} = \delta W^{\text{internal}}_{\text{system}} + \delta\boldsymbol{\lambda}\cdot\left(\mathbb{N}^{fb,\mathsf{T}}\hat{\mathbf{U}}_b - \mathbb{N}^{fs,\mathsf{T}}\hat{\mathbf{u}}_s\right) + \boldsymbol{\lambda}\cdot\left(\mathbb{N}^{fb,\mathsf{T}}\delta\hat{\mathbf{U}}_b - \mathbb{N}^{fs,\mathsf{T}}\delta\hat{\mathbf{u}}_s\right) = 0$$
$$\forall \text{ admissible } \delta\hat{\mathbf{U}}_b, \delta\hat{\mathbf{u}}_s, \delta\boldsymbol{\lambda}. \quad (8.21)$$

The Penalty method can be used as well to enforce 8.18. In this case the deviation from the condition is penalized using a quadratic function added to the potential energy of the system as shown below

$$\Pi = \Pi_{\text{system}} + \frac{1}{2}\epsilon_p \left\|\mathbb{N}^{fb,\mathsf{T}}\hat{\mathbf{U}}_b - \mathbb{N}^{fs,\mathsf{T}}\hat{\mathbf{u}}_s\right\|^2 \quad , \quad (8.22)$$

where ϵ_p is the penalty parameter. The stationary point of the potential function is found by solving

$$\delta\Pi = \delta\Pi_{\text{system}} + \epsilon_p \left(\mathbb{N}^{fb,\mathsf{T}}\hat{\mathbf{U}}_b - \mathbb{N}^{fs,\mathsf{T}}\hat{\mathbf{u}}_s\right)\cdot\left(\mathbb{N}^{fb,\mathsf{T}}\delta\hat{\mathbf{U}}_b - \mathbb{N}^{fs,\mathsf{T}}\delta\hat{\mathbf{u}}_s\right) = 0 \quad . \quad (8.23)$$

Again for a non-conservative system we can write

$$\delta W^{\text{internal}} = \delta W^{\text{internal}}_{\text{system}} + \epsilon_p \left(\mathbb{N}^{fb,\mathsf{T}}\hat{\mathbf{U}}_b - \mathbb{N}^{fs,\mathsf{T}}\hat{\mathbf{u}}_s\right)\cdot\left(\mathbb{N}^{fb,\mathsf{T}}\delta\hat{\mathbf{U}}_b - \mathbb{N}^{fs,\mathsf{T}}\delta\hat{\mathbf{u}}_s\right) = 0$$
$$\forall \text{ admissible } \delta\hat{\mathbf{U}}_b, \delta\hat{\mathbf{u}}_s. \quad (8.24)$$

Finite element formulations and linearization of these methods are described in the following chapters.

Chapter 9

EMBEDDED BEAM OVERLAY ELEMENT WITH LOCAL ENFORCEMENT OF PERFECT BONDING INTERFACE

9.1 Finite Element Formulation of Point Collocation Method

This chapter presents a finite element implementation of the embedded beam interaction surface with locally enforced perfect bonding condition in OpenSees. As mentioned in Chapter 8 any constraint enforcement method can be used to apply the interaction condition. Here Lagrange multipliers and Penalty methods are considered.

Lagrange Multipliers Method To apply the perfect bonding condition at designated points on the interaction surface we can use the interpolated displacement fields defined in Equations 8.13 and 8.14. Using Lagrange multipliers to enforce the condition, separate vectors of Lagrange multipliers should be used for each of these points, increasing the size of the model by the size of multipliers vector times number of interaction points. Substituting Equations 8.13 and 8.14 into Equation 8.6 results in

$$\delta W_c = \sum_i \left(\left\{ \delta \hat{\mathbf{U}}_b \right\}_i^{\mathsf{T}} \left[\mathcal{H}_u \right]_i^{\mathsf{T}} \left\{ \boldsymbol{\lambda} \right\}_i - \left\{ \delta \hat{\mathbf{u}}_s \right\}_i^{\mathsf{T}} \left[N^s \right]_i^{\mathsf{T}} \left\{ \boldsymbol{\lambda} \right\}_i \right) + \sum_i \left(\left\{ \delta \boldsymbol{\lambda} \right\}_i^{\mathsf{T}} \left(\left[\mathcal{H}_u \right]_i \left\{ \hat{\mathbf{U}}_b \right\}_i - \left[N^s \right]_i \left\{ \hat{\mathbf{u}}_s \right\}_i \right) \right) \quad , \quad (9.1)$$

or

$$\delta W_c = \sum_i \left\{\delta\hat{\mathbf{U}}_b\right\}_i^{\mathsf{T}} \{F_{cb}\}_i + \sum_i \{\delta\hat{\mathbf{u}}_s\}_i^{\mathsf{T}} \{F_{cs}\}_i + \sum_i \left(\{\delta\boldsymbol{\lambda}\}_i^{\mathsf{T}} \underbrace{\left([\mathcal{H}_u]_i \left\{\hat{\mathbf{U}}_b\right\}_i - [N^s]_i \{\hat{\mathbf{u}}_s\}_i \right)}_{:=\mathbf{0} \text{ by the interaction requirement}} \right) \quad , \quad (9.2)$$

where $\{F_{cb}\}_i = [\mathcal{H}_u]_i^{\mathsf{T}} \{\boldsymbol{\lambda}_i\}$ and $\{F_{cs}\}_i = -[N^s]_i^{\mathsf{T}} \{\boldsymbol{\lambda}_i\}$, represent nodal resisting forces for the beam and the solid respectively at interaction point i. Linearization of Equation 9.1 with respect to nodal displacements and Lagrange multipliers gives the tangent matrix for the constraint application as

$$\mathrm{d}\delta W_c = \sum_i \left(\left\{\delta\hat{\mathbf{U}}_b\right\}_i^{\mathsf{T}} [\mathcal{H}_u]_i^{\mathsf{T}} \{\mathrm{d}\boldsymbol{\lambda}_i\} - \{\delta\hat{\mathbf{u}}_s\}_i^{\mathsf{T}} [N^s]_i^{\mathsf{T}} \{\mathrm{d}\boldsymbol{\lambda}_i\} + \{\delta\boldsymbol{\lambda}\}_i^{\mathsf{T}} [\mathcal{H}_u]_i \left\{\mathrm{d}\hat{\mathbf{U}}_b\right\}_i - \{\delta\boldsymbol{\lambda}\}_i^{\mathsf{T}} [N^s]_i \{\mathrm{d}\hat{\mathbf{u}}_s\}_i \right) \quad . \quad (9.3)$$

Treating each interaction point separately, we can define a nodal resisting forces vector and a tangent matrix for each point which can be assembled into the global system's resisting forces vector and tangent matrix respectively. Doing so, the tangent matrix for point γ_i is

$$K_i^c = \begin{bmatrix} \mathbf{0} & \mathbf{0} & \mathcal{H}_{u_i} \\ \mathbf{0} & \mathbf{0} & -N_i^s \\ \mathcal{H}_{u_i}^{\mathsf{T}} & -N_i^{s,\mathsf{T}} & \mathbf{0} \end{bmatrix} \quad , \quad (9.4)$$

and the nodal resisting forces vector is

$$F_i^c = \begin{Bmatrix} F_{cb_i} \\ F_{cs_i} \\ \mathbf{0} \end{Bmatrix} \quad . \quad (9.5)$$

It is assumed that the nodal information for each interaction point is stored in a vector $\{q_i\}$ as

$$q_i = \left\{ \begin{array}{c} \mathbf{U}_{b_i} \\ \mathbf{u}_{s_i} \\ \boldsymbol{\lambda}_i \end{array} \right\} \quad . \tag{9.6}$$

Penalty Method A different approach for enforcing the perfect bonding condition (Equation 8.3) is to penalize the error due to relative displacement between the beam and the solid domains on the interaction surface. This again, is done at all designated interaction points. As described in the previous chapter one way to penalize the relative displacement is to add the following penalty function to the potential energy of the system as

$$\Pi = \Pi^{\text{system}} + \sum_i \frac{1}{2} \epsilon_p \left\| [\mathcal{H}_u]_i \left\{ \hat{\mathbf{U}}_b \right\}_i - [N^s]_i \left\{ \hat{\mathbf{u}}_s \right\}_i \right\|^2 \tag{9.7}$$

where ϵ_p is a large number called *penalty parameter*. It can be shown that in the limit as $\epsilon_p \to \infty$, the condition is exactly enforced. In this study, the penalty parameter is normalized by the number of interaction points to reduce further ill-conditioning of the problem due to large penalty parameter values.

The first variation of Equation 9.7 is set to zero to find the minimum potential of the system,

$$\delta\Pi = \delta\Pi^{\text{system}} + \delta\Pi^c = \delta\Pi^{\text{system}} + \sum_i \delta\Pi_i^c = 0 \quad , \tag{9.8}$$

where

$$\delta\Pi_i^c = \epsilon_p \left([\mathcal{H}_u]_i \left\{ \delta\hat{\mathbf{U}}_b \right\}_i - [N^s]_i \{\delta\hat{\mathbf{u}}_s\}_i \right)^{\mathsf{T}} \left([\mathcal{H}_u]_i \left\{ \hat{\mathbf{U}}_b \right\}_i - [N^s]_i \{\hat{\mathbf{u}}_s\}_i \right) \tag{9.9}$$

$$= \epsilon_p \left\{ \delta\hat{\mathbf{U}}_b \right\}_i^{\mathsf{T}} \left([\mathcal{H}_u]_i^{\mathsf{T}} [\mathcal{H}_u]_i \left\{ \hat{\mathbf{U}}_b \right\}_i - [\mathcal{H}_u]_i^{\mathsf{T}} [N^s]_i \{\hat{\mathbf{u}}_s\}_i \right)$$

$$+ \epsilon_p \{\delta\hat{\mathbf{u}}_s\}_i^{\mathsf{T}} \left(- [N^s]_i^{\mathsf{T}} [\mathcal{H}_u]_i \left\{ \hat{\mathbf{U}}_b \right\}_i + [N^s]_i^{\mathsf{T}} [N^s]_i \{\hat{\mathbf{u}}_s\}_i \right) \quad . \tag{9.10}$$

Linearization of the virtual work expression with respect to the nodal displacements results in

$$\begin{aligned} \mathrm{d}\delta\Pi_i^c = \quad & \left\{ \delta\hat{\mathbf{U}}_b \right\}_i^{\mathsf{T}} \left(\epsilon_p [\mathcal{H}_u]_i^{\mathsf{T}} [\mathcal{H}_u]_i \right) \left\{ \mathrm{d}\hat{\mathbf{U}}_b \right\}_i \\ & - \left\{ \delta\hat{\mathbf{U}}_b \right\}_i^{\mathsf{T}} \left(\epsilon_p [\mathcal{H}_u]_i^{\mathsf{T}} [N^s]_i \right) \{\mathrm{d}\hat{\mathbf{u}}_s\}_i \\ & - \{\delta\hat{\mathbf{u}}_s\}_i^{\mathsf{T}} \left(\epsilon_p [N^s]_i^{\mathsf{T}} [\mathcal{H}_u]_i \right) \left\{ \mathrm{d}\hat{\mathbf{U}}_b \right\}_i \\ & + \{\delta\hat{\mathbf{u}}_s\}_i^{\mathsf{T}} \left(\epsilon_p [N^s]_i^{\mathsf{T}} [N^s]_i \right) \{\mathrm{d}\hat{\mathbf{u}}_s\}_i \quad . \end{aligned} \tag{9.11}$$

Equations 9.10 and 9.11 are used to derive the nodal resisting force vector, $\{F_i^c\}$, and the element stiffness matrix, $[K_i^c]$, for an interaction point i as

$$F_i^c = \left\{ \begin{array}{c} \epsilon_p [\mathcal{H}_u]_i^{\mathsf{T}} \left([\mathcal{H}_u]_i \left\{ \hat{\mathbf{U}}_b \right\}_i - [N^s]_i \{\hat{\mathbf{u}}_s\}_i \right) \\ -\epsilon_p [N^s]_i^{\mathsf{T}} \left([\mathcal{H}_u]_i \left\{ \hat{\mathbf{U}}_b \right\}_i - [N^s]_i \{\hat{\mathbf{u}}_s\}_i \right) \end{array} \right\} \quad , \tag{9.12}$$

$$K_i^c = \left[\begin{array}{cc} \epsilon_p [\mathcal{H}_u]_i^{\mathsf{T}} [\mathcal{H}_u]_i & -\epsilon_p [\mathcal{H}_u]_i^{\mathsf{T}} [N^s]_i \\ -\epsilon_p [N^s]_i^{\mathsf{T}} [\mathcal{H}_u]_i & \epsilon_p [N^s]_i^{\mathsf{T}} [N^s]_i \end{array} \right] \quad . \tag{9.13}$$

In deriving these equations, it is assumed that the nodal information is stored in a vector $\{q_i\}$ for the interaction point i as

$$q_i = \left\{ \begin{array}{c} \mathbf{U}_{b_i} \\ \mathbf{u}_{s_i} \end{array} \right\} \quad . \tag{9.14}$$

9.2 Definition of the interaction surface

The interaction surface, over which the soil-pile interaction behavior is defined, is a virtual surface. This surface is defined knowing the location of the beam element nodes, nodal tangent vectors and by assuming the Navier-Bernoulli condition which states that a planar cross-section of the beam remains a plane through deformation. Standard cubic Hermite interpolation polynomials are used to define the centerline of the beam. Beam centerline is parameterized as

$$\mathbf{X}^b = \varphi^b(\psi) \quad , \tag{9.15}$$

where

$$\varphi^b(\psi) = H_1(\psi)\mathbf{X}_a^b + H_2(\psi)\mathbf{a}_1 + H_3(\psi)\mathbf{X}_b^b + H_4(\psi)\mathbf{b}_1 \quad -1 \leq \psi \leq 1. \tag{9.16}$$

In this equation $\mathbf{X}_a^b$ and $\mathbf{X}_b^b$ are the coordinates of the beam's starting and ending points, $\mathbf{a}_1$ and $\mathbf{b}_1$ denote the unit tangent vectors at these end-points and

$$H_1 = \frac{1}{4}(1-\psi)^2(2+\psi) \quad , \tag{9.17}$$

$$H_2 = \frac{L}{8}(1-\psi)^2(\psi+1) \quad , \tag{9.18}$$

$$H_3 = \frac{1}{4}(1+\psi)^2(2-\psi) \quad , \tag{9.19}$$

$$H_4 = \frac{L}{8}(1+\psi)^2(\psi-1) \quad , \tag{9.20}$$

where L is the length of the beam. Unit tangent vectors $\mathbf{a}_1$ and $\mathbf{b}_1$ along with two other orthogonal unit vectors for each, define a local frame at each end of the beam. A local orthonormal coordinate system, $\langle \mathbf{c}_1, \mathbf{c}_2, \mathbf{c}_3 \rangle$, is defined at every point along the beam centerline. $\mathbf{Q}_a$, $\mathbf{Q}_b$ and $\mathbf{Q}_c$ denote the transformations from the global coordinate system, $\langle \mathbf{e}_1, \mathbf{e}_2, \mathbf{e}_3 \rangle$, to the local frames. These local coordinate systems are assumed to be initially the same everywhere along the beam with the origin at the corresponding point. This means the beam is assumed to be initially straight and twist-free, thus $\mathbf{Q}_a = \mathbf{Q}_b = \mathbf{Q}_c$ and $\mathbf{c}_1 = (\mathbf{X}_b^2 - \mathbf{X}_b^1)/L$, initially. Kinematics of the beam define the evolution of these local coordinate systems as described in Appendix C. By defining $\mathbf{c}_1$ as the unit tangent vector to the beam centerline, $\mathbf{c}_2$ and $\mathbf{c}_3$ span the beam's cross-sectional plane. For a circular pile with radius ρ, points on the interaction surface are defined as

$$\mathbf{x}_b(\psi, \rho, \theta) = \mathbf{X}_b(\psi) + \rho\cos(\theta)\mathbf{c}_2 + \rho\sin(\theta)\mathbf{c}_3 \quad -1 \leq \psi \leq 1 \text{ and } 0 \leq \theta < 2\pi \quad . \tag{9.21}$$

9.3 Definition of interpolation functions

Solid Element Displacements Although higher order shape functions can be used for the interpolation of nodal results inside the solid elements, standard trilinear shape functions for standard 8-node brick elements are used here for the purpose of this study. Mapping from

an isoparametric space to the actual element space results in

$$N_1^s(\xi,\eta,\zeta) = \frac{1}{8}(1-\xi)(1-\eta)(1-\zeta) \tag{9.22}$$

$$N_2^s(\xi,\eta,\zeta) = \frac{1}{8}(1+\xi)(1-\eta)(1-\zeta) \tag{9.23}$$

$$N_3^s(\xi,\eta,\zeta) = \frac{1}{8}(1+\xi)(1+\eta)(1-\zeta) \tag{9.24}$$

$$N_4^s(\xi,\eta,\zeta) = \frac{1}{8}(1-\xi)(1+\eta)(1-\zeta) \tag{9.25}$$

$$N_5^s(\xi,\eta,\zeta) = \frac{1}{8}(1-\xi)(1-\eta)(1+\zeta) \tag{9.26}$$

$$N_6^s(\xi,\eta,\zeta) = \frac{1}{8}(1+\xi)(1-\eta)(1+\zeta) \tag{9.27}$$

$$N_7^s(\xi,\eta,\zeta) = \frac{1}{8}(1+\xi)(1+\eta)(1+\zeta) \tag{9.28}$$

$$N_8^s(\xi,\eta,\zeta) = \frac{1}{8}(1-\xi)(1+\eta)(1+\zeta) \quad . \tag{9.29}$$

Beam Element Displacement A reference straight beam with a local coordinate system $\langle \mathbf{E}_1, \mathbf{E}_2, \mathbf{E}_3 \rangle$ is used to define the kinematics of the beam. For sake of simplicity the coordinate system $\langle \mathbf{E}_1, \mathbf{E}_2, \mathbf{E}_3 \rangle$ is assumed to be oriented along the global coordinate system. The reference beam is parameterized by $-1 \leq \psi \leq 1$. The deformation vector of the 1D beam, consisting of a displacement vector and a rotation vector, is mapped to the reference straight beam. Then this deformation vector is decomposed into axial and transverse deformations so that we can interpolate these deformations differently. Ultimately the interpolated deformation is mapped back to the global coordinate system. Suppose that $\hat{\mathbf{U}}_a$ ($\hat{\mathbf{U}}_b$) consists of $\hat{\boldsymbol{\omega}}_a^{n+1}$ and $\hat{\boldsymbol{\phi}}_a^{n+1}$ ($\hat{\boldsymbol{\omega}}_b^{n+1}$ and $\hat{\boldsymbol{\phi}}_b^{n+1}$) which respectively denote the nodal displacement and rotation vectors at step $n+1$ for beam nodes a and b. Rotation vectors are used to update $\mathbf{Q}_a$ and $\mathbf{Q}_b$ as

$$\mathbf{Q}_a^{n+1} = \exp\left([\, \hat{\boldsymbol{\phi}}_a^{n+1} - \hat{\boldsymbol{\phi}}_a^{n} \,]_\times \right) \mathbf{Q}_a^n \quad , \tag{9.30}$$

$$\mathbf{Q}_b^{n+1} = \exp\left([\, \hat{\boldsymbol{\phi}}_b^{n+1} - \hat{\boldsymbol{\phi}}_b^{n} \,]_\times \right) \mathbf{Q}_b^n \quad , \tag{9.31}$$

where $[\ \bullet\ ]_\times$ (or as represented later as $[\ \overset{\times}{\bullet}\ ]$ for convenience) is the skew-symmetric matrix representation for cross product with vector $\{\bullet\}$ such that $\bullet \times \mathbf{e} = [\ \bullet\ ]_\times \mathbf{e}$. Knowing $\mathbf{Q}_a$ and $\mathbf{Q}_b$ we can find $\mathbf{Q}_c$ as described in Appendix C. A linear update of $\mathbf{Q}_a$ and $\mathbf{Q}_b$ results in

$$\mathbf{Q}_i^{n+1} \approx \mathbf{Q}_i^n + \left(\hat{\boldsymbol{\phi}}_i^{n+1} - \hat{\boldsymbol{\phi}}_i^n\right) \times \mathbf{Q}_i^n \quad i = a, b. \tag{9.32}$$

These transformations are used to map the deformation vectors to the reference beam space as

$$\boldsymbol{\omega}_A = \mathbf{Q}_a^\mathsf{T} \hat{\boldsymbol{\omega}}_a^{n+1} \quad , \tag{9.33}$$

$$\boldsymbol{\phi}_A = \mathbf{Q}_a^\mathsf{T} \hat{\boldsymbol{\phi}}_a^{n+1} \quad , \tag{9.34}$$

$$\boldsymbol{\omega}_B = \mathbf{Q}_b^\mathsf{T} \hat{\boldsymbol{\omega}}_b^{n+1} \quad , \tag{9.35}$$

$$\boldsymbol{\phi}_B = \mathbf{Q}_b^\mathsf{T} \hat{\boldsymbol{\phi}}_b^{n+1} \quad . \tag{9.36}$$

The deformation vectors are decomposed into axial and transverse components as

$$\boldsymbol{\omega}_A = \mathbb{P}_1^\parallel \boldsymbol{\omega}_A + \mathbb{P}_1^\perp \boldsymbol{\omega}_A = \omega_A^\parallel \mathbf{E}_1 + \boldsymbol{\omega}_A^\perp \quad , \tag{9.37}$$

$$\boldsymbol{\phi}_A = \mathbb{P}_1^\parallel \boldsymbol{\phi}_A + \mathbb{P}_1^\perp \boldsymbol{\phi}_A = \varphi_A^\parallel \mathbf{E}_1 + \boldsymbol{\phi}_A^\perp \quad , \tag{9.38}$$

$$\boldsymbol{\omega}_B = \mathbb{P}_1^\parallel \boldsymbol{\omega}_B + \mathbb{P}_1^\perp \boldsymbol{\omega}_B = \omega_B^\parallel \mathbf{E}_1 + \boldsymbol{\omega}_B^\perp \quad , \tag{9.39}$$

$$\boldsymbol{\phi}_B = \mathbb{P}_1^\parallel \boldsymbol{\phi}_B + \mathbb{P}_1^\perp \boldsymbol{\phi}_B = \varphi_B^\parallel \mathbf{E}_1 + \boldsymbol{\phi}_B^\perp \quad . \tag{9.40}$$

where $\mathbb{P}_1^\parallel = \mathbf{E}_1 \otimes \mathbf{E}_1$ and $\mathbb{P}_1^\perp = \mathbf{1} - \mathbf{E}_1 \otimes \mathbf{E}_1$. The axial component of the displacement vector is interpolated using a linear shape function while the transverse components are interpolated

using cubic Hermite interpolation functions. So,

$$\omega_C^{\parallel} = N_1^b(\psi)\omega_A^{\parallel} + N_2^b(\psi)\omega_B^{\parallel} \quad , \tag{9.41}$$

$$\begin{aligned}\boldsymbol{\omega}_C^{\perp} &= H_1(\psi)\boldsymbol{\omega}_A^{\perp} + H_2(\psi)\left(\exp([\,\boldsymbol{\phi}_A^{\perp}\,]_{\times})\mathbf{E}_1 - \mathbf{E}_1\right) \\ &\quad + H_3(\psi)\boldsymbol{\omega}_B^{\perp} + H_4(\psi)\left(\exp([\,\boldsymbol{\phi}_B^{\perp}\,]_{\times})\mathbf{E}_1 - \mathbf{E}_1\right) \qquad (9.42) \\ &\approx H_1(\psi)\boldsymbol{\omega}_A^{\perp} + H_2(\psi)\left(\boldsymbol{\phi}_A^{\perp} \times \mathbf{E}_1\right) + H_3(\psi)\boldsymbol{\omega}_B^{\perp} + H_4(\psi)\left(\boldsymbol{\phi}_B^{\perp} \times \mathbf{E}_1\right) \quad , \qquad (9.43)\end{aligned}$$

$$\boldsymbol{\omega}_C = \omega_C^{\parallel}\mathbf{E}_1 + \boldsymbol{\omega}_C^{\perp} \quad , \tag{9.44}$$

where

$$N_1^b(\psi) = \frac{1}{2}(1-\psi) \quad \text{and} \tag{9.45}$$

$$N_2^b(\psi) = \frac{1}{2}(1+\psi) \quad . \tag{9.46}$$

The rotation vector is interpolated at point C in the reference frame and mapped back to the global space. The twist angle or the axial component of the rotation vector is linearly interpolated whereas the transverse component of rotation vector is interpolated as described below. From Equation 9.43 the tangent to the beam centerline in the reference configuration is

$$\begin{aligned}\frac{\partial\boldsymbol{\omega}_C(\psi)/\partial\psi}{\|\partial\boldsymbol{\omega}_C(\psi)/\partial\psi\|} = \frac{1}{L}\Bigg(&\frac{dH_1(\psi)}{d\psi}\boldsymbol{\omega}_A^{\perp} + \frac{dH_2(\psi)}{d\psi}\left(\boldsymbol{\phi}_A^{\perp} \times \mathbf{E}_1\right) \\ &+ \frac{dH_3(\psi)}{d\psi}\boldsymbol{\omega}_B^{\perp} + \frac{dH_4(\psi)}{d\psi}\left(\boldsymbol{\phi}_B^{\perp} \times \mathbf{E}_1\right)\Bigg) \quad . \end{aligned} \tag{9.47}$$

This equation represents the change in orientation of $\mathbf{E}_1$, i.e. the tangent to the beam centerline in the undeformed configuration. The objective is to find a unique $\boldsymbol{\phi}_C^{\perp}$ representing the transverse component of rotation vector at point C causing such change in the tangent

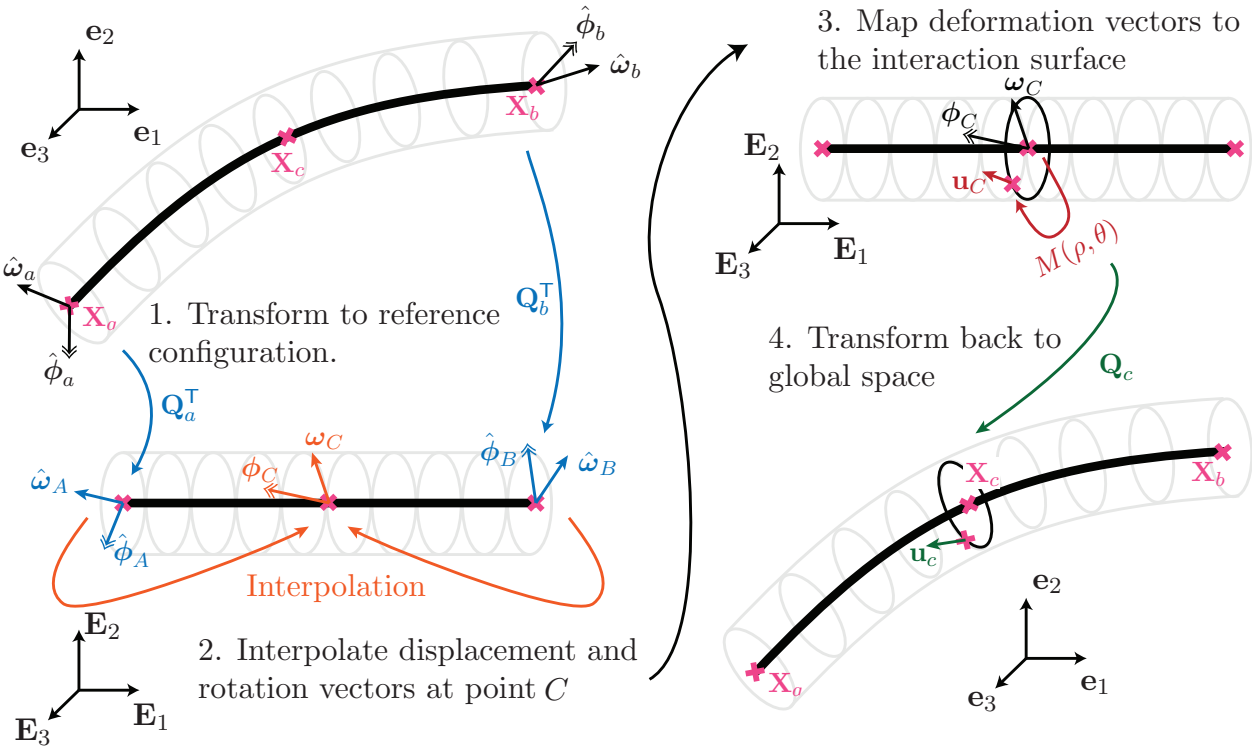

Figure 9.1: Beam surface point displacement interpolation

vector. This means

$$\boldsymbol{\phi}_C^\perp \times \mathbf{E}_1 = \frac{1}{L}\frac{\partial \boldsymbol{\omega}_C(\psi)}{\partial \psi} \quad . \tag{9.48}$$

Consider the vector $\mathbf{E}_1 \times (\boldsymbol{\phi}_C^\perp \times \mathbf{E}_1)$. Using the identity $\mathbf{a} \times (\mathbf{b} \times \mathbf{c}) = (\mathbf{a} \cdot \mathbf{c})\mathbf{b} - (\mathbf{a} \cdot \mathbf{c})\mathbf{b}$, we have

$$\mathbf{E}_1 \times (\boldsymbol{\phi}_C^\perp \times \mathbf{E}_1) = \underbrace{(\mathbf{E}_1 \cdot \mathbf{E}_1)}_{=1} \boldsymbol{\phi}_C^\perp - \underbrace{(\mathbf{E}_1 \cdot \boldsymbol{\phi}_C^\perp)}_{=0, \text{ by definition}} \mathbf{E}_1 = \boldsymbol{\phi}_C^\perp \quad . \tag{9.49}$$

Therefore, we can write

$$\boldsymbol{\phi}_C^\perp = \mathbf{E}_1 \times \left(\frac{1}{L}\frac{\partial \boldsymbol{\omega}_C(\psi)}{\partial \psi} \right) = \frac{1}{L}[\overset{\times}{\mathbf{E}}_1]\frac{\partial \boldsymbol{\omega}_C(\psi)}{\partial \psi} \quad . \tag{9.50}$$

So, the interpolated rotation vector is

$$\varphi_C^{\parallel} = N_1^b(\psi)\varphi_A^{\parallel} + N_2^b(\psi)\varphi_B^{\parallel} \quad , \tag{9.51}$$

$$\boldsymbol{\phi}_C^{\perp} = \frac{1}{L}\left(\frac{dH_1(\psi)}{d\psi}[\overset{\times}{\mathbf{E}}_1]\boldsymbol{\omega}_A^{\perp} + \frac{dH_2(\psi)}{d\psi}\boldsymbol{\phi}_A^{\perp} + \frac{dH_3(\psi)}{d\psi}[\overset{\times}{\mathbf{E}}_1]\boldsymbol{\omega}_B^{\perp} + \frac{dH_4(\psi)}{d\psi}\boldsymbol{\phi}_B^{\perp}\right) \tag{9.52}$$

$$\boldsymbol{\phi}_C = \varphi_C^{\parallel}\mathbf{E}_1 + \boldsymbol{\phi}_C^{\perp} \quad . \tag{9.53}$$

Mapping from the beam centerline to the interaction surface is performed in the reference beam and then transformed back to the global space. Given a point on the centerline designated by parameter ψ, any point on the interaction surface is defined using the polar coordinate system $\langle \rho, \theta \rangle$ where in the local Cartesian system translates to

$$\mathbf{x}_C = \mathbf{X}_C + \rho\cos\theta\,\mathbf{E}_2 + \rho\sin\theta\,\mathbf{E}_3 \quad . \tag{9.54}$$

Displacement at this point is thus calculated as

$$\mathbf{u}_C = \boldsymbol{\omega}_C + \rho\cos\theta\,(\exp([\overset{\times}{\boldsymbol{\phi}}_C])\,\mathbf{E}_2 - \mathbf{E}_2) + \rho\sin\theta\,(\exp([\overset{\times}{\boldsymbol{\phi}}_C])\,\mathbf{E}_3 - \mathbf{E}_3) \tag{9.55}$$

$$\approx \boldsymbol{\omega}_C + \rho\cos\theta\,(\boldsymbol{\phi}_C \times \mathbf{E}_2) + \rho\sin\theta\,(\boldsymbol{\phi}_C \times \mathbf{E}_3) \quad . \tag{9.56}$$

Equation 9.56 can be written in matrix form as $\boldsymbol{\omega}_C = M(\rho,\theta)\,\mathbf{q}_C$, by defining the transformation $M(\rho,\theta)$ as

$$M(\rho,\theta) = \begin{bmatrix} 1 & 0 & 0 & 0 & \rho\sin\theta & -\rho\cos\theta \\ 0 & 1 & 0 & -\rho\sin\theta & 0 & 0 \\ 0 & 0 & 1 & \rho\cos\theta & 0 & 0 \end{bmatrix} \quad , \tag{9.57}$$

and

$$\mathbf{q}_C = \begin{Bmatrix} \boldsymbol{\omega}_C \\ \boldsymbol{\phi}_C \end{Bmatrix} \quad . \tag{9.58}$$

Using the mapping from the reference straight beam to the local coordinate system at point $\mathbf{X}_c$ the displacement vector is mapped back to the global space as

$$\mathbf{u}_c = \mathbf{Q}_c \mathbf{u}_C \quad . \tag{9.59}$$

Putting all these together, we define the vector $\hat{\mathbf{q}}$ and matrix $\mathbb{Q}^{\mathsf{T}}$ as

$$\hat{\mathbf{q}} = \left\{ \begin{array}{c} \hat{\boldsymbol{\omega}}_a \\ \hat{\boldsymbol{\phi}}_a \\ \hat{\boldsymbol{\omega}}_b \\ \hat{\boldsymbol{\phi}}_b \end{array} \right\} \quad \text{and} \quad \mathbb{Q}^{\mathsf{T}} = \left[\begin{array}{cccc} \mathbf{Q}_a^{\mathsf{T}} & & & \\ & \mathbf{Q}_a^{\mathsf{T}} & & \\ & & \mathbf{Q}_b^{\mathsf{T}} & \\ & & & \mathbf{Q}_b^{\mathsf{T}} \end{array} \right] \quad . \tag{9.60}$$

Displacement of point $\mathbf{x}_c$ on the interaction surface defined by parameters ψ, ρ and θ, can be expressed by

$$\mathbf{u}_c = \mathbf{Q}_c \, M(\rho, \theta) \, \varphi^b(\psi) \, \mathbb{Q}^{\mathsf{T}} \, \hat{\mathbf{q}} \quad , \tag{9.61}$$

where

$$\left[\varphi^b(\psi)\right] = \left[\begin{array}{cccc} N_1^b \, \mathbb{P}^{\parallel} + H_1 \, \mathbb{P}^{\perp} & -H_2 \, [\, \overset{\times}{\mathbf{E}}_1 \,] \, \mathbb{P}^{\perp} & N_2^b \, \mathbb{P}^{\parallel} + H_3 \, \mathbb{P}^{\perp} & -H_4 \, [\, \overset{\times}{\mathbf{E}}_1 \,] \, \mathbb{P}^{\perp} \\ \frac{1}{L} \frac{dH_1}{d\psi} [\, \overset{\times}{\mathbf{E}}_1 \,] \mathbb{P}^{\perp} & N_1^b \, \mathbb{P}^{\parallel} + \frac{1}{L} \frac{dH_2}{d\psi} \mathbb{P}^{\perp} & \frac{1}{L} \frac{dH_3}{d\psi} [\, \overset{\times}{\mathbf{E}}_1 \,] \mathbb{P}^{\perp} & N_2^b \, \mathbb{P}^{\parallel} + \frac{1}{L} \frac{dH_4}{d\psi} \mathbb{P}^{\perp} \end{array} \right] \quad . \tag{9.62}$$

This defines the interpolation matrix, $[\mathcal{H}_u]$, used to calculate the interaction point displacement, $\mathbf{u}_b = [\mathcal{H}_u] \, \hat{\mathbf{q}}$, where

$$\mathcal{H}_u = \mathbf{Q}_c \, M \, \varphi^b \, \mathbb{Q}^{\mathsf{T}} \quad . \tag{9.63}$$

9.4 Implementation in OpenSees

Implementing this element in OpenSees consists of two general processes; one is to generate the interaction points at which the bonding condition is applied, the other is to implement the element formulation itself. For this purpose a new command `generateInterfacePoints` is added to OpenSees. This command uses as arguments the beam element tag and associated geometric transformation object tag, radius of the beam (R)[1], number of points in the perimeter of the beam cross section (n_p), number of points in the longitudinal direction of the beam (n_l) and a flag for specifying the method of applying bonding constraint. Optionally a list of tentative solid element tags can also be provided for enhancing the performance of the search algorithm. The command returns a list of generated interaction points. A typical call to `generateInterfacePoints` in Tcl looks like

```
set interfacePointsList [generateInterfacePoints $beam_tag \
        $geomTransf_tag -radius $beam_R -nP $np -nL $nl -penalty \
        <-ele $solid_tags_list>]
```

The `generateInterfacePoints` command gets the position and local coordinate system of the beam element using the beam tag and the geometric transformation tag. Given the location of the beam in space and the required number of points on the interaction surface, interaction points are generated at a distance R from beam's center-line. For each generated point a search is done to find the solid element tag in which the point is located. For this an inverse mapping of the iso-parametric shape functions of solid elements is used. This algorithm is presented in Appendix D. If the local iso-parametric location of the point is within the boundaries of the solid element, the solid tag is assigned to the current point. If the point is not in contact with any solid element, it is discarded. This is done only once during the construction of the FE mesh.

The element is implemented in the `EmbeddedInteractionPoint` class which is inherited from the `Element` class. DOF's of the beam and solid elements in contact define the

[1]Other cross section shapes such as square, rectangle or hexagon can easily be added.

connectivity graph of the `EmbeddedInteractionPoint` element. If the method of Lagrange multipliers is used, additional nodes are created internally to account for the extra equations added to the system. In this case the additional DOF's created by introducing these new nodes are added to the connectivity graph as well. The member function `update()` is called at every iteration. In the case of the Penalty method, trial displacements of the beam and solid nodes, and in the case of Lagrange multipliers method trial displacement of Lagrange nodes, are used to calculate the residual force of the element. This force vector is returned by the `getResistingForce()` member function. The tangent matrix of the element is returned by the `getTangent()` member function. As the global iteration scheme converges the method `commitstate()` is called. Full nonlinear update of the coordinate systems at beam ends is performed as `commitstate()` is called.

Table 9.1: OpenSees recorders for the weak form embedded beam element.

Recorder label	# Output per element	Description
`displacement`	3	Records the displacement of interaction point in the global coordinate system.
`localDisplacement`	3	Records the displacement of interaction point in the local coordinate system of the beam.
`axialDisp`	3	Records the displacement component of interaction point along the beam axis as a vector in the global coordinate system.
`radialDisp`	3	Records the displacement component of interaction point along the radial direction of the beam cross section as a vector in the global coordinate system.
`tangentialDisp`	3	Records the displacement component of interaction point along the tangential direction of the beam cross section as a vector in the global coordinate system.
`globalForce`	3	Records interaction force vector at the interaction point in the global coordinate system.
`localForce`	3	Records interaction force vector at the interaction point in the local coordinate system of the beam.
`axialForce`	3	Records interaction force component at the interaction point along the beam axis as a vector in the global coordinate system.
`radialForce`	3	Records interaction force component at the interaction point along the radial direction of the beam cross section as a vector in the global coordinate system.
`tangentialForce`	3	Records interaction force vector at the interaction point along the tangential direction of the beam cross section as a vector in the global coordinate system.
`solidForce`	3	Records nodal interaction force vector at solid nodes in the global coordinate system.
`beamForce`	12	Records nodal interaction force vector at beam nodes in the global coordinate system.
`beamLocalForce`	12	Records nodal interaction force vector at solid nodes in the local coordinate system of the beam.

Chapter 10

EMBEDDED BEAM OVERLAY ELEMENT WITH GLOBAL ENFORCEMENT OF PERFECT BONDING INTERFACE - MORTAR METHOD

This chapter presents a finite element implementation of the embedded beam interaction surface with globally enforced perfect bonding condition in OpenSees. As mentioned in Chapter 8 any constraint enforcement method can be used to apply the interaction condition. Here Lagrange multipliers and Penalty methods are considered.

Lagrange Multipliers Method Substituting Equations 8.13, 8.14 and 8.15 into Equation 8.11 results in

$$\int_{\Gamma_c} \boldsymbol{\lambda} \cdot (\tilde{\mathbf{x}}_b - \tilde{\mathbf{x}}_s)\, \mathrm{d}\Gamma = \int_{\Gamma_c} \left([\mathcal{H}_f] \left\{ \hat{\mathbf{F}}_b \right\} \right)^{\mathsf{T}} \left([\mathcal{H}_u] \left\{ \hat{\mathbf{U}}_b \right\} - [N^s] \left\{ \hat{\mathbf{u}}_s \right\} \right) \mathrm{d}\Gamma \tag{10.1}$$

$$= \left\{ \hat{\mathbf{F}}_b \right\}^{\mathsf{T}} \left(\underbrace{\int_{\Gamma_c} [\mathcal{H}_f]^{\mathsf{T}} [\mathcal{H}_u] \, \mathrm{d}\Gamma}_{\left[\mathbb{N}^{fb}\right]^{\mathsf{T}}} \left\{ \hat{\mathbf{U}}_b \right\} - \underbrace{\int_{\Gamma_c} [\mathcal{H}_f]^{\mathsf{T}} [N^s] \, \mathrm{d}\Gamma}_{\left[\mathbb{N}^{fs}\right]^{\mathsf{T}}} \left\{ \hat{\mathbf{u}}_s \right\} \right) = 0 \tag{10.2}$$

$$\Rightarrow \left[\mathbb{N}^{fb}\right]^{\mathsf{T}} \left\{ \hat{\mathbf{U}}_b \right\} - \left[\mathbb{N}^{fs}\right]^{\mathsf{T}} \left\{ \hat{\mathbf{u}}_s \right\} = 0 \quad . \tag{10.3}$$

Equation 10.3 defines the discrete geometric condition imposing perfect bonding contact on the boundary between the pile and soil. For the case of small deformations, matrices $\left[\mathbb{N}^{fb}\right]$ and $\left[\mathbb{N}^{fs}\right]$ can be evaluated only once since they only depend on the geometry of the contacting surface and interpolating functions. In case of large deformations one must update the interpolation functions which requires these matrices to be regenerated.

Moreover, Equation 10.3 can be used to write the displacements of one body in terms of the displacements of the other one and therefore embedding the behavior the first body

into the second one. For example, the displacements of the pile can be written as $\left\{\hat{\mathbf{U}}_b\right\} = \left[\mathbb{N}^{fb}\right]^{-\mathsf{T}} \left[\mathbb{N}^{fs}\right]^{\mathsf{T}} \{\hat{\mathbf{u}}_s\}$ which can be substituted in the description of the virtual works of the interaction forces. This would decrease the size of the system by the pile's number of degrees of freedom. However, for the purpose of this study this embedding strategy is not used for practical purposes.

Using the same interpolation functions for the virtual displacements and the interaction forces we can calculate the virtual work of the interaction forces in their discrete form as

$$\delta W_c = \left\{\delta\hat{\mathbf{U}}_b\right\}^{\mathsf{T}} \left[\mathbb{N}^{fb}\right] \left\{\hat{\mathbf{F}}_b\right\} - \{\delta\hat{\mathbf{u}}_s\}^{\mathsf{T}} \left[\mathbb{N}^{fs}\right] \left\{\hat{\mathbf{F}}_b\right\} \tag{10.4}$$

$$= \left\{\delta\hat{\mathbf{U}}_b\right\}^{\mathsf{T}} \{F_{cb}\} + \{\delta\hat{\mathbf{u}}_s\}^{\mathsf{T}} \{F_{cs}\} \quad , \tag{10.5}$$

where $\{F_{cb}\} = \left[\mathbb{N}^{fb}\right] \left\{\hat{\mathbf{F}}_b\right\}$ and $\{F_{cs}\} = -\left[\mathbb{N}^{fs}\right] \left\{\hat{\mathbf{F}}_b\right\}$, represent the nodal resisting force vectors on the beam body and on the solid body respectively. Notice that here it is assumed that matrices $\mathbb{N}^{fb}$ and $\mathbb{N}^{fs}$ are assumed to be independent of the system's deformation and therefore only small strain, linear deformation is considered. Linearization of Equation 10.5 with respect to nodal displacements and constraint forces results in the tangent matrix for the interaction between the soil and the pile. Assuming the nodal information is stored in vector $\{q\}$ as

$$q = \left\{ \begin{array}{c} \mathbf{U}_b \\ \mathbf{u}_s \\ \mathbf{F}_b \end{array} \right\} \tag{10.6}$$

and combining

$$\mathrm{d}\delta W_c = \left\{\delta\hat{\mathbf{U}}_b\right\}^{\mathsf{T}} \left[\mathbb{N}^{fb}\right] \left\{\mathrm{d}\hat{\mathbf{F}}_b\right\} - \{\delta\hat{\mathbf{u}}_s\}^{\mathsf{T}} \left[\mathbb{N}^{fs}\right] \left\{\mathrm{d}\hat{\mathbf{F}}_b\right\} \quad , \tag{10.7}$$

with Equation 10.3, the tangent matrix can be written as

$$K^c = \begin{bmatrix} \mathbf{0} & \mathbf{0} & \mathbb{N}^{fb} \\ \mathbf{0} & \mathbf{0} & -\mathbb{N}^{fs} \\ \mathbb{N}^{fb,\mathsf{T}} & -\mathbb{N}^{fs,\mathsf{T}} & \mathbf{0} \end{bmatrix} \quad , \tag{10.8}$$

and the corresponding resisting nodal force vector can be written as

$$F^c = \begin{Bmatrix} F_{cb} \\ F_{cs} \\ \mathbf{0} \end{Bmatrix} \quad . \tag{10.9}$$

Penalty method The geometric condition imposed by Equation 10.3 can be regularized using the Penalty method. In this case a function that penalizes the residual of the integral in Equation 8.11 is added to the potential energy of the system as

$$\Pi = \Pi^{\text{system}} + \frac{1}{2}\epsilon_p \left\| \left[\mathbb{N}^{fb}\right]^{\mathsf{T}} \left\{\hat{\mathbf{U}}_b\right\} - \left[\mathbb{N}^{fs}\right]^{\mathsf{T}} \{\hat{\mathbf{u}}_s\} \right\|^2 \quad , \tag{10.10}$$

where ϵ_p is a penalty parameter usually several orders of magnitude larger than the stiffness of the system. It can be shown that in the limit as $\epsilon_p \to \infty$, the geometric condition is exactly applied. Also it can be shown that the resulting interaction forces are $\mathbf{f}_b = \epsilon_p \left(\left[\mathbb{N}^{fb}\right]^{\mathsf{T}} \left\{\hat{\mathbf{U}}_b\right\} - \left[\mathbb{N}^{fs}\right]^{\mathsf{T}} \{\hat{\mathbf{u}}_s\} \right)$.

The first variation of Equation 10.10 should be set to zero to find the minimum potential of the system:

$$\delta\Pi = \delta\Pi^{\text{system}} + \epsilon_p \left(\left[\mathbb{N}^{fb}\right]^{\mathsf{T}} \left\{\hat{\mathbf{U}}_b\right\} - \left[\mathbb{N}^{fs}\right]^{\mathsf{T}} \{\hat{\mathbf{u}}_s\} \right)^{\mathsf{T}} \left(\left[\mathbb{N}^{fb}\right]^{\mathsf{T}} \left\{\delta\hat{\mathbf{U}}_b\right\} - \left[\mathbb{N}^{fs}\right]^{\mathsf{T}} \{\delta\hat{\mathbf{u}}_s\} \right) \quad . \tag{10.11}$$

Alternatively, the virtual work of the interaction forces, δW_c, can also be added to the virtual work of the system. The virtual work can be calculated as

$$\delta W_c = \epsilon_p \left(\left[\mathbb{N}^{fb}\right]^{\mathsf{T}} \left\{\hat{\mathbf{U}}_b\right\} - \left[\mathbb{N}^{fs}\right]^{\mathsf{T}} \left\{\hat{\mathbf{u}}_s\right\} \right)^{\mathsf{T}} \left(\left[\mathbb{N}^{fb}\right]^{\mathsf{T}} \left\{\delta\hat{\mathbf{U}}_b\right\} - \left[\mathbb{N}^{fs}\right]^{\mathsf{T}} \left\{\delta\hat{\mathbf{u}}_s\right\} \right) \tag{10.12}$$

$$\begin{aligned} &= \epsilon_p \left\{\delta\hat{\mathbf{U}}_b\right\}^{\mathsf{T}} \left(\left[\mathbb{N}^{fb}\right] \left[\mathbb{N}^{fb}\right]^{\mathsf{T}} \left\{\hat{\mathbf{U}}_b\right\} - \left[\mathbb{N}^{fb}\right] \left[\mathbb{N}^{fs}\right]^{\mathsf{T}} \left\{\hat{\mathbf{u}}_s\right\} \right) \\ &+ \epsilon_p \left\{\delta\hat{\mathbf{u}}_s\right\}^{\mathsf{T}} \left(\left[\mathbb{N}^{fs}\right] \left[\mathbb{N}^{fs}\right]^{\mathsf{T}} \left\{\hat{\mathbf{u}}_s\right\} - \left[\mathbb{N}^{fs}\right] \left[\mathbb{N}^{fb}\right]^{\mathsf{T}} \left\{\hat{\mathbf{U}}_b\right\} \right) \quad . \end{aligned} \tag{10.13}$$

Linearization of the virtual work expression with respect to the nodal displacements results in

$$\begin{aligned} \mathrm{d}\delta W_c = &\left\{\delta\hat{\mathbf{U}}_b\right\}^{\mathsf{T}} \left(\epsilon_p \left[\mathbb{N}^{fb}\right] \left[\mathbb{N}^{fb}\right]^{\mathsf{T}} \right) \left\{\mathrm{d}\hat{\mathbf{U}}_b\right\} - \left\{\delta\hat{\mathbf{U}}_b\right\}^{\mathsf{T}} \left(\epsilon_p \left[\mathbb{N}^{fb}\right] \left[\mathbb{N}^{fs}\right]^{\mathsf{T}} \right) \left\{\mathrm{d}\hat{\mathbf{u}}_s\right\} \\ &- \left\{\delta\hat{\mathbf{u}}_s\right\}^{\mathsf{T}} \left(\epsilon_p \left[\mathbb{N}^{fs}\right] \left[\mathbb{N}^{fb}\right]^{\mathsf{T}} \right) \left\{\mathrm{d}\hat{\mathbf{U}}_b\right\} - \left\{\delta\hat{\mathbf{u}}_s\right\}^{\mathsf{T}} \left(\epsilon_p \left[\mathbb{N}^{fs}\right] \left[\mathbb{N}^{fb}\right]^{\mathsf{T}} \right) \left\{\mathrm{d}\hat{\mathbf{U}}_b\right\} \quad . \end{aligned} \tag{10.14}$$

Assuming the nodal unknowns vector $\{q\}$ is defined as

$$q = \left\{ \begin{array}{c} \mathbf{U}_b \\ \mathbf{u}_s \end{array} \right\} \quad , \tag{10.15}$$

the the resisting force vector, $\{F^c\}$, and the tangent matrix, $[K^c]$, are calculated as

$$F^c = \left\{ \begin{array}{c} \epsilon_p \left[\mathbb{N}^{fb}\right] \left(\left[\mathbb{N}^{fb}\right]^{\mathsf{T}} \left\{\hat{\mathbf{U}}_b\right\} - \left[\mathbb{N}^{fs}\right]^{\mathsf{T}} \left\{\hat{\mathbf{u}}_s\right\} \right) \\ -\epsilon_p \left[\mathbb{N}^{fs}\right] \left(\left[\mathbb{N}^{fb}\right]^{\mathsf{T}} \left\{\hat{\mathbf{U}}_b\right\} - \left[\mathbb{N}^{fs}\right]^{\mathsf{T}} \left\{\hat{\mathbf{u}}_s\right\} \right) \end{array} \right\} \tag{10.16}$$

$$K^c = \left[\begin{array}{cc} \epsilon_p \left[\mathbb{N}^{fb}\right] \left[\mathbb{N}^{fb}\right]^{\mathsf{T}} & -\epsilon_p \left[\mathbb{N}^{fb}\right] \left[\mathbb{N}^{fs}\right]^{\mathsf{T}} \\ -\epsilon_p \left[\mathbb{N}^{fs}\right] \left[\mathbb{N}^{fb}\right]^{\mathsf{T}} & \epsilon_p \left[\mathbb{N}^{fs}\right] \left[\mathbb{N}^{fb}\right]^{\mathsf{T}} \end{array} \right] \quad . \tag{10.17}$$

The formulation presented above is a specific case of *mortar* formulations. In the above formulation the beam boundary is assumed to be the mortar side while the solid boundary in

contact with the beam is the non-mortar side. Therefore, there is no distinct mortar domain defined aside from the beam boundary.

10.1 Interaction Force Interpolation Functions

The interpolation matrix defined in Equations 8.15 and 10.1 is developed here. Suppose that $\hat{\mathbf{F}}_a^{n+1}$ and $\hat{\mathbf{M}}_a^{n+1}$ ($\hat{\mathbf{F}}_b^{n+1}$ and $\hat{\mathbf{M}}_b^{n+1}$) denote the beam nodal force and moment vectors at step $n+1$ respectively, for beam nodes a and b. These vectors are transformed to the reference straight beam configuration using maps $\mathbf{Q}_a$ and $\mathbf{Q}_b$. Although the same approach used for displacements can be used here, these forces and moments are linearly interpolated here for the sake of simplicity,

$$\mathbf{F}_C = N_1^b(\psi)\mathbf{Q}_a^{\mathsf{T}}\hat{\mathbf{F}}_a + N_2^b(\psi)\mathbf{Q}_b^{\mathsf{T}}\hat{\mathbf{F}}_b \tag{10.18}$$

$$\mathbf{M}_C = N_1^b(\psi)\mathbf{Q}_a^{\mathsf{T}}\hat{\mathbf{M}}_a + N_2^b(\psi)\mathbf{Q}_b^{\mathsf{T}}\hat{\mathbf{M}}_b \quad . \tag{10.19}$$

Now the interpolated force and moment vectors are mapped to the interaction surface. As shown in Figure 10.1, the force vector and the twisting moment are distributed over the interaction surface assuming uniform distribution of reaction forces. The bending moment components are distributed assuming a linear distribution of reaction forces. For a circular cross section with radius ρ, we can define a matrix $[M_f(\rho,\theta)]$ which gives the force vector at each point on the interaction surface by solving the equilibrium equation. Therefore, we have $\mathbf{f}_C = M_f\,\bar{\mathbf{q}}$ where

$$M_f = \begin{bmatrix} \frac{1}{2\pi\rho} & 0 & 0 & 0 & \frac{\sin\theta}{2\pi\rho^2} & -\frac{\cos\theta}{2\pi\rho^2} \\ 0 & \frac{1}{2\pi\rho} & 0 & -\frac{\sin\theta}{\pi\rho^2} & 0 & 0 \\ 0 & 0 & \frac{1}{2\pi\rho} & \frac{\cos\theta}{\pi\rho^2} & 0 & 0 \end{bmatrix} \quad \text{and} \quad \bar{\mathbf{q}} = \begin{Bmatrix} \mathbf{F}_C \\ \mathbf{M}_C \end{Bmatrix} \quad . \tag{10.20}$$

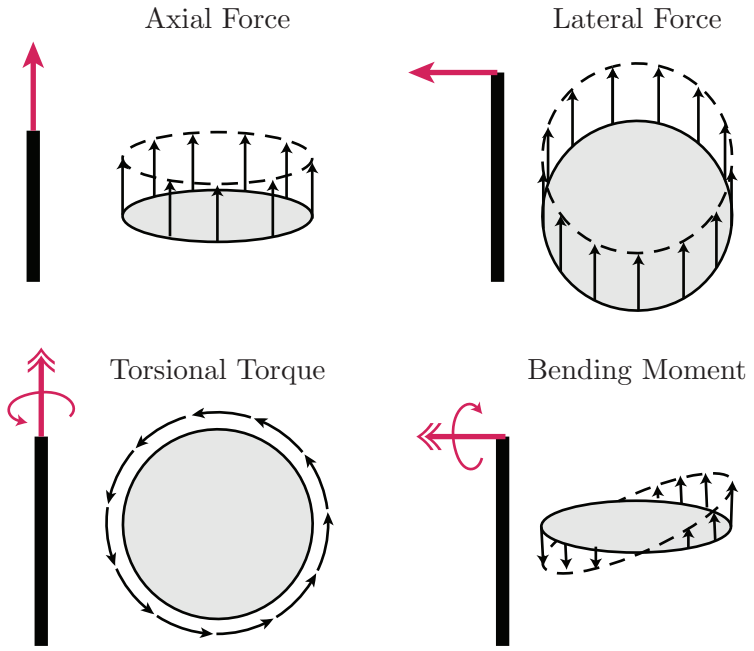

Figure 10.1: Distribution of beam forces on the interaction surface

Finally, the force vector is mapped back to the global space as $\mathbf{f}_c = \mathbf{Q}_c\,\mathbf{f}_C$. Therefore, the interpolating matrix $[\mathcal{H}_f]$ can be written as

$$\mathcal{H}_f = \mathbf{Q}_c\, M_f \begin{bmatrix} N_1^b\,\mathbf{I} & \mathbf{0} & N_2^b\,\mathbf{I} & \mathbf{0} \\ \mathbf{0} & N_1^b\,\mathbf{I} & \mathbf{0} & N_2^b\,\mathbf{I} \end{bmatrix} \mathbb{Q}^{\mathsf{T}} \quad . \tag{10.21}$$

10.2 Evaluation of the integrals over the interaction surface

An analytical solution of the integral equations 8.11 and 10.3 is very tedious if at all possible. Therefore, numerical methods are to be used. For this purpose the interaction surface is discretized into $n_p \times n_L$ surface segments (where n_p is the number of segments along the perimeter of the pile and n_L is the number of longitudinal segments) and use the Gauss-Legendre quadrature method. Using one Gauss point as shown in Figure 10.2 (the center of

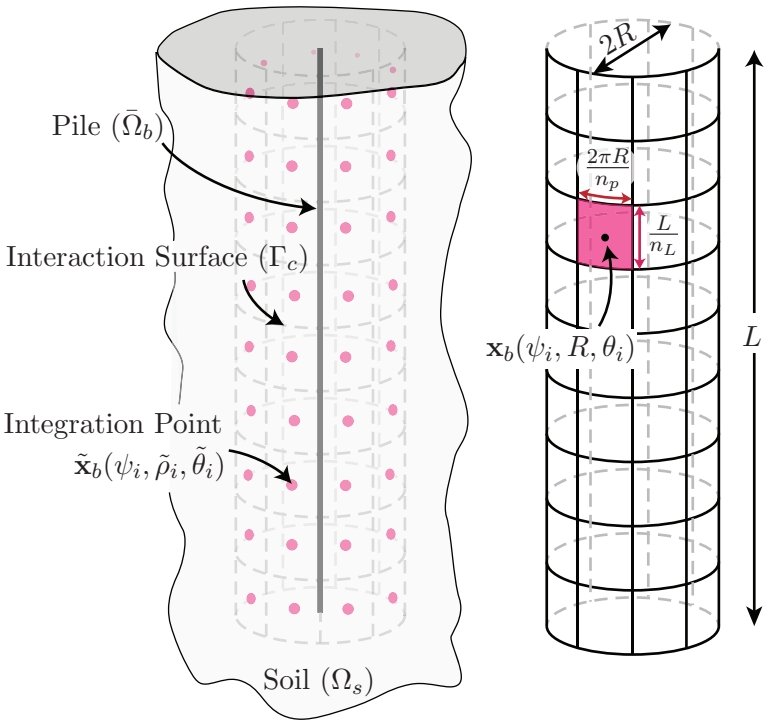

Figure 10.2: Schematic of the interaction boundary and integration points.

area of each segment), we have

$$\int_{\Gamma_c} \bullet \, \mathrm{d}\Gamma = \sum_{i=1}^{n_p \times n_L} \bullet(\psi_i, R, \theta_i) \frac{2\pi R}{n_p} \frac{L}{n_L} \quad . \tag{10.22}$$

10.3 Implementation in OpenSees

The mortar element formulation described above is implemented in the `EmbeddedBeamInterface` class which also inherits from the `Element` class. The same `generateInterfacePoints` function described in section 9.4 is used to generate the integration points (vs interaction points) for the mortar element. In order to compute the matrices $\mathbb{N}^{fb}$ and $\mathbb{N}^{fs}$, a connectivity graph for the element is required. For each mortar element there can be multiple beam elements and multiple solid elements involved. Therefore, the connectivity graph for this element is

more complex than for the strong form. Tag of the solid element and the beam tags associated with each integration point are saved for each mortar element. Then the `set` container, available in the C++ standard library, is used to hold tags of the nodes connected through the mortar element. The `set` container is specifically used to only hold a unique set of node tags. It is used both for the solid node tags and the beam node tags. In order to know the position of each unique tag in the connectivity graph of the mortar element the `map` container, also available in the C++ standard library, is used.

A typical OpenSees command to generate this kind of element (in its Tcl interpreter) looks like

```
set interfacePointsList [generateInterfacePoints $beam_tags_list \
        $geomTransf_tag -radius $beam_R -nP $np -nL $nl -gPenalty \
        <-ele $solid_tags_list>]
```

This command discretizes the beam boundary by generating the Gauss-Legendre supports. Notice that this is very similar to the command used for generating the strong form elements except for the `-gPenalty` argument. This argument tells OpenSees to use weak form elements implemented using the Penalty method. Alternatively, `-gLagrange` can be used instead to use weak form elements implemented using the Lagrange multipliers method. An optional argument `-penaltyParam $e_p` can be used to assign `$e_p` as the penalty parameter. The variable `$beam_tags_list` is a Tcl list container which holds the tags of the connected beam elements forming together a pile. As an alternative, `-beamEleRange $start_tag $end_tag` can be used to give a range of values for the beam element tags. In the current implementation, only one `geomTransf` object can be used to define the geometric transformation matrix for the whole pile. Therefore, piles with breaks in their orientation cannot be modeled currently. Similar to the strong form element generation command, `-ele $solid_tags_list` is an optional argument to make the connectivity search faster. Without this argument, OpenSees checks all solid elements in the model to find any intersection with the list of beam elements. Alternatively, `-solidEleRange $start_tag $end_tag` can be used to provide a range of values for the solid element tags.

For post-processing convenience, location of the Gauss-Legendre points can be written to a file named `$filename` using the argument `-file $filename`. In addition, if the optional argument `-connectivity $filename` is passed to the command, the connectivity graph of the element is written to the file `$filename`. The information written to this file contains the number of solid nodes and beam nodes in contact, a list of solid node tags followed by a list of beam node tags. This information is necessary for interpreting the information recorded by the element.

Several recorders are defined for the weak form embedded beam elements. These recorders are listed in Table 10.1.

Table 10.1: OpenSees recorders for the weak form embedded beam element.

Recorder label	# Output per element	Description
`displacement`	3 × `$numPts`	Records displacement of each integration point in the global coordinate system.
`localDisplacement`	3 × `$numPts`	Records displacement of each integration point in the local coordinate system of the beam.
`axialDisp`	3 × `$numPts`	Records displacement component of each integration point along the beam axis as a vector in the global coordinate system.
`radialDisp`	3 × `$numPts`	Records displacement component of each integration point along the radial direction of the beam cross section as a vector in the global coordinate system.
`tangentialDisp`	3 × `$numPts`	Records displacement component of each integration point along the tangential direction of the beam cross section as a vector in the global coordinate system.
`globalForce`	3 × `$numPts`	Records interaction force vector at each integration point in the global coordinate system.
`localForce`	3 × `$numPts`	Records interaction force vector at each integration point in the local coordinate system of the beam.
`axialForce`	3 × `$numPts`	Records interaction force component at each integration point along the beam axis as a vector in the global coordinate system.
`radialForce`	3 × `$numPts`	Records interaction force component at each integration point along the radial direction of the beam cross section as a vector in the global coordinate system.
`tangentialForce`	3 × `$numPts`	Records interaction force vector at each integration point along the tangential direction of the beam cross section as a vector in the global coordinate system.
`solidForce`	3 × `$numSnodes`	Records nodal interaction force vector at solid nodes in the global coordinate system.
`beamForce`	12 × `$numBnodes`	Records nodal interaction force vector at beam nodes in the global coordinate system.
`beamLocalForce`	12 × `$numBnodes`	Records nodal interaction force vector at solid nodes in the local coordinate system of the beam.

`$numPts` is the number of Gauss-Legendre integration points.
`$numSnodes` is the number of solid nodes in contact.
`$numBnodes` is the number of beam nodes in contact.

Chapter 11

EMBEDDED BEAM WITH ELASTO-PLASTIC INTERFACE OVERLAY ELEMENT

Following the idea presented in the previous section, the embedded beam element with weakly enforced bonding condition is augmented with an elasto-plastic behavior at the interface. This is based on the work by Turello et al. (2017). A constitutive behavior is used to establish a relationship between the reaction forces at the interaction surface and the relative movement between the soil and the pile. Therefore, Equation 8.12 is written as

$$\int_{\Gamma_c} \delta\tilde{f} \cdot (\tilde{\mathbf{u}}_b - \tilde{\mathbf{u}}_s - \mathbf{u}_{\text{rel}})\, \mathrm{d}\Gamma = 0 \quad \forall \text{ admissible } \delta\tilde{f}, \tag{11.1}$$

where $\mathbf{u}_{\text{rel}}$ is the relative displacement between the solid and the beam at the interaction surface. For the purpose of this work, let us denote the reactive forces at the interaction surface by $\tilde{\mathbf{t}}_{\text{rel}}$. These are the forces that impose the condition noted in Equation 11.1. By assigning an elasto-plastic constitutive behavior to these forces, the relative displacement between the solid and the beam dissipates some of the internal energy of the system. Virtual work of these forces equal to

$$\delta W_{c,\text{rel}} = \int_{\Gamma_c} \mathbf{t}_{\text{rel}} \cdot (\delta\tilde{\mathbf{u}}_b - \delta\tilde{\mathbf{u}}_s)\, \mathrm{d}\Gamma = \int_{\Gamma_c} \mathbf{t}_{\text{rel}} \cdot \delta\mathbf{u}_{\text{rel}}\, \mathrm{d}\Gamma \quad . \tag{11.2}$$

In order to define a constitutive relationship between $\mathbf{u}_{\text{rel}}$ and $\mathbf{t}_{\text{rel}}$, we assume there is a region around the pile with thickness h where the interaction behavior is constituted. The outer side of this region is assumed to be non-moving so that we can define a strain tensor

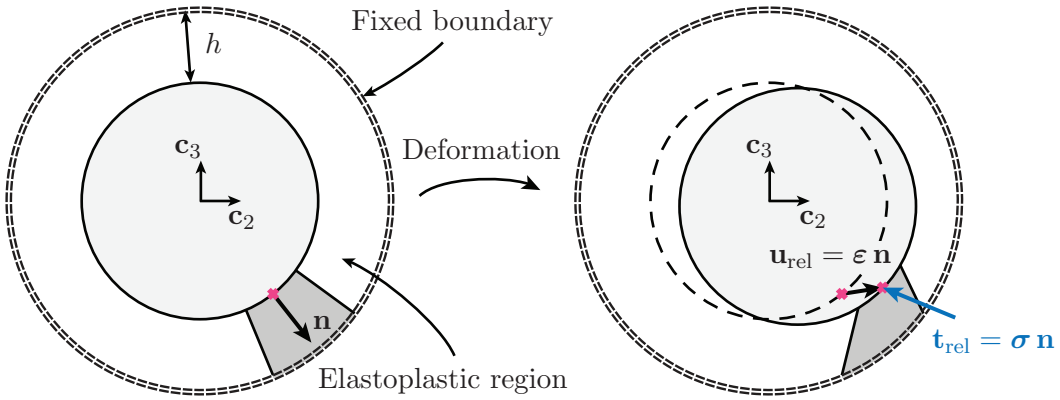

Figure 11.1: Definition of the elastoplastic region around the pile.

which is used for the constitutive behavior (see Figure 11.1). The strain tensor is

$$\boldsymbol{\varepsilon}_{\text{rel}} = \frac{1}{2h}\left(\mathbf{u}_{\text{rel}} \otimes \mathbf{n} + \mathbf{n} \otimes \mathbf{u}_{\text{rel}}\right) \quad , \tag{11.3}$$

where $\mathbf{n}$ is the unit normal vector to the interaction surface. A constitutive behavior for the interaction between the pile and the soil (representing the near field frictional contact) is defined for the stress tensor, $\boldsymbol{\sigma}_{\text{rel}}$, through $\boldsymbol{\varepsilon}_{\text{rel}}$ such that $\boldsymbol{\sigma}_{\text{rel}} = \hat{\boldsymbol{\sigma}}(\boldsymbol{\varepsilon}_{\text{rel}})$. Knowing the stress tensor at the interaction surface, $\mathbf{t}_{\text{rel}}$ is calculated as

$$\mathbf{t}_{\text{rel}} = \boldsymbol{\sigma}_{\text{rel}}\,\mathbf{n} \quad . \tag{11.4}$$

Expanding Equation 11.1 in terms of finite element interpolation functions as defined in the previous section, we have

$$\int_{\Gamma_c} \delta\tilde{f} \cdot \left(\tilde{\mathbf{u}}_b - \tilde{\mathbf{u}}_s - \mathbf{u}_{\text{rel}}\right) \mathrm{d}\Gamma = 0 \tag{11.5}$$

$$\Rightarrow \left[\mathbb{N}^{fb}\right]^{\mathsf{T}} \left\{\hat{\mathbf{U}}_b\right\} - \left[\mathbb{N}^{fs}\right]^{\mathsf{T}} \left\{\hat{\mathbf{u}}_s\right\} - \left[\mathbb{N}^{fb}\right]^{\mathsf{T}} \left\{\hat{\mathbf{U}}_{\text{rel}}\right\} = 0 \quad , \tag{11.6}$$

$$\text{or } \left\{\hat{\mathbf{U}}_{\text{rel}}\right\} = \left\{\hat{\mathbf{U}}_b\right\} - \left[\mathbb{N}^{fb}\right]^{-\mathsf{T}} \left[\mathbb{N}^{fs}\right]^{\mathsf{T}} \left\{\hat{\mathbf{u}}_s\right\} \quad . \tag{11.7}$$

Contribution of the interaction surface to the internal virtual work of the system is

$$\delta W_{c,\text{rel}} = \int_{\Gamma_c} \left([\mathcal{H}_u] \left\{ \delta \hat{\mathbf{U}}_{\text{rel}} \right\} \right)^{\mathsf{T}} \mathbf{t}_{\text{rel}} \, \mathrm{d}\Gamma \tag{11.8}$$

$$= \left\{ \delta \hat{\mathbf{U}}_b \right\}^{\mathsf{T}} \left\{ \hat{\mathbf{T}}_{\text{rel}} \right\} - \{ \delta \hat{\mathbf{u}}_s \}^{\mathsf{T}} \left[\mathbb{N}^{fs} \right] \left[\mathbb{N}^{fb} \right]^{-1} \left\{ \hat{\mathbf{T}}_{\text{rel}} \right\} \quad , \tag{11.9}$$

where $\left\{ \hat{\mathbf{T}}_{\text{rel}} \right\} = \int_{\Gamma_c} [\mathcal{H}_u]^{\mathsf{T}} \mathbf{t}_{\text{rel}} \, \mathrm{d}\Gamma$ and the nodal resisting force vectors for the solid and the beam elements are $\{F_{cb}\} = \left\{ \hat{\mathbf{T}}_{\text{rel}} \right\}$ and $\{F_{cs}\} = - \left[\mathbb{N}^{fs} \right] \left[\mathbb{N}^{fs} \right]^{-1} \left\{ \hat{\mathbf{T}}_{\text{rel}} \right\}$. Linearization of Equation 11.9 with respect to nodal unknowns results in

$$\mathrm{d}\delta W_{c,\text{rel}} = \left\{ \delta \hat{\mathbf{U}}_b \right\}^{\mathsf{T}} \left\{ \mathrm{d}\hat{\mathbf{T}}_{\text{rel}} \right\} - \{ \delta \hat{\mathbf{u}}_s \}^{\mathsf{T}} \left[\mathbb{N}^{fs} \right] \left[\mathbb{N}^{fb} \right]^{-1} \left\{ \mathrm{d}\hat{\mathbf{T}}_{\text{rel}} \right\} \quad , \tag{11.10}$$

where

$$\mathrm{d}\hat{\mathbf{T}}_{\text{rel}} = \frac{\partial \hat{\mathbf{T}}_{\text{rel}}}{\partial \hat{\mathbf{U}}_b} \mathrm{d}\hat{\mathbf{U}}_b + \frac{\partial \hat{\mathbf{T}}_{\text{rel}}}{\partial \hat{\mathbf{u}}_s} \mathrm{d}\hat{\mathbf{u}}_s \quad . \tag{11.11}$$

Terms $\partial \hat{\mathbf{T}}_{\text{rel}} / \partial \hat{\mathbf{U}}_b$ and $\partial \hat{\mathbf{T}}_{\text{rel}} / \partial \hat{\mathbf{u}}_s$ are expanded as

$$\frac{\partial \hat{\mathbf{T}}_{\text{rel}}}{\partial \hat{\mathbf{U}}_b} = \frac{\partial}{\partial \hat{\mathbf{U}}_b} \left(\int_{\Gamma_c} [\mathcal{H}_u]^{\mathsf{T}} \mathbf{t}_{\text{rel}} \, \mathrm{d}\Gamma \right) \tag{11.12}$$

$$= \int_{\Gamma_c} [\mathcal{H}_u]^{\mathsf{T}} \frac{\partial \mathbf{t}_{\text{rel}}}{\partial \mathbf{u}_{\text{rel}}} \frac{\partial \mathbf{u}_{\text{rel}}}{\partial \hat{\mathbf{U}}_{\text{rel}}} \cancelto{\mathbf{I}}{\frac{\partial \hat{\mathbf{U}}_{\text{rel}}}{\partial \hat{\mathbf{U}}_b}} \, \mathrm{d}\Gamma \tag{11.13}$$

$$= \int_{\Gamma_c} [\mathcal{H}_u]^{\mathsf{T}} \frac{\partial \mathbf{t}_{\text{rel}}}{\partial \mathbf{u}_{\text{rel}}} [\mathcal{H}_u] \, \mathrm{d}\Gamma \quad , \tag{11.14}$$

and

$$\frac{\partial \hat{\mathbf{T}}_{\text{rel}}}{\partial \hat{\mathbf{u}}_s} = \frac{\partial}{\partial \hat{\mathbf{u}}_s}\left(\int_{\Gamma_c} [\mathcal{H}_u]^{\mathsf{T}}\, \mathbf{t}_{\text{rel}}\, \mathrm{d}\Gamma\right) \tag{11.15}$$

$$= \int_{\Gamma_c} [\mathcal{H}_u]^{\mathsf{T}}\, \frac{\partial \mathbf{t}_{\text{rel}}}{\partial \mathbf{u}_{\text{rel}}} \frac{\partial \mathbf{u}_{\text{rel}}}{\partial \hat{\mathbf{U}}_{\text{rel}}} \frac{\partial \hat{\mathbf{U}}_{\text{rel}}}{\partial \hat{\mathbf{u}}_s}\, \mathrm{d}\Gamma \tag{11.16}$$

$$= -\int_{\Gamma_c} [\mathcal{H}_u]^{\mathsf{T}}\, \frac{\partial \mathbf{t}_{\text{rel}}}{\partial \mathbf{u}_{\text{rel}}} [\mathcal{H}_u]\ \mathrm{d}\Gamma\ \left(\left[\mathbb{N}^{fb}\right]^{-\mathsf{T}} \left[\mathbb{N}^{fs}\right]^{\mathsf{T}}\right) \quad . \tag{11.17}$$

The term $\partial \mathbf{t}_{\text{rel}}/\partial \mathbf{u}_{\text{rel}}$, written in indicial form, is worked out as

$$\frac{\partial \mathbf{t}_{\text{rel}}}{\partial \mathbf{u}_{\text{rel}}} = \frac{\partial(\boldsymbol{\sigma}_{\text{rel}}\mathbf{n})}{\partial \mathbf{u}_{\text{rel}}} = \mathbb{C}^{ep}_{ikrs}(\delta_{sj}\frac{n_r}{2h} + \delta_{rj}\frac{n_s}{2h}) n_k\, \mathbf{e}_i \otimes \mathbf{e}_j \quad , \tag{11.18}$$

where $\mathbb{C}^{ep} = \partial \boldsymbol{\sigma}_{\text{rel}}/\partial \boldsymbol{\varepsilon}_{\text{rel}}$, is the continuum tangent of the constitutive model representing the interaction between the solid and the beam.

Defining $\mathbf{K}_{\text{rel}}$ as

$$\mathbf{K}_{\text{rel}} = \int_{\Gamma_c} [\mathcal{H}_u]^{\mathsf{T}}\, \frac{\partial \mathbf{t}_{\text{rel}}}{\partial \mathbf{u}_{\text{rel}}} [\mathcal{H}_u]\ \mathrm{d}\Gamma \quad , \tag{11.19}$$

we have

$$\mathrm{d}\delta W_{c,\text{rel}} = \left\{\delta \hat{\mathbf{U}}_b\right\}^{\mathsf{T}} \mathbf{K}_{\text{rel}} \left\{\mathrm{d}\hat{\mathbf{U}}_b\right\} \tag{11.20}$$

$$- \left\{\delta \hat{\mathbf{U}}_b\right\}^{\mathsf{T}} \mathbf{K}_{\text{rel}} \left[\mathbb{N}^{fb}\right]^{-\mathsf{T}} \left[\mathbb{N}^{fs}\right]^{\mathsf{T}} \{\mathrm{d}\hat{\mathbf{u}}_s\} \tag{11.21}$$

$$- \{\delta \hat{\mathbf{u}}_s\}^{\mathsf{T}} \left[\mathbb{N}^{fs}\right] \left[\mathbb{N}^{fb}\right]^{-1} \mathbf{K}_{\text{rel}} \left\{\mathrm{d}\hat{\mathbf{U}}_b\right\} \tag{11.22}$$

$$+ \{\delta \hat{\mathbf{u}}_s\}^{\mathsf{T}} \left[\mathbb{N}^{fs}\right] \left[\mathbb{N}^{fb}\right]^{-1} \mathbf{K}_{\text{rel}} \left[\mathbb{N}^{fb}\right]^{-\mathsf{T}} \left[\mathbb{N}^{fs}\right]^{\mathsf{T}} \{\mathrm{d}\hat{\mathbf{u}}_s\} \quad , \tag{11.23}$$

which written in matrix form gives the stiffness matrix of this overlay element as

$$\mathbf{K} = \begin{bmatrix} \mathbf{K}_{\text{rel}} & -\mathbf{K}_{\text{rel}} \left[\mathbb{N}^{fb}\right]^{-\mathsf{T}} \left[\mathbb{N}^{fs}\right]^{\mathsf{T}} \\ -\left[\mathbb{N}^{fs}\right] \left[\mathbb{N}^{fb}\right]^{-1} \mathbf{K}_{\text{rel}} & \left[\mathbb{N}^{fs}\right] \left[\mathbb{N}^{fb}\right]^{-1} \mathbf{K}_{\text{rel}} \left[\mathbb{N}^{fb}\right]^{-\mathsf{T}} \left[\mathbb{N}^{fs}\right]^{\mathsf{T}} \end{bmatrix} \quad . \tag{11.24}$$

11.1 Implementation in OpenSees

Implementation of `EmbeddedEPBeamInterface` class follows the same methodology defined in section 10.3. An additional argument is required in the definition of the elastoplastic interface element to define the `nDMaterial` object tag associated with the interface behavior.

A typical OpenSees command to generate this kind of element (in its Tcl interpreter) looks like

```
set interfacePointsList [generateInterfacePoints $beam_tags_list \
        $geomTransf_tag -radius $beam_R -nP $np -nL $nl \
        -ElastoPlastic -mat $mat_tag <-ele $solid_tags_list>]
```

This is very similar to the command used to generate perfect bonding weak form embedded elements except for the arguments `-ElastoPlastic` and `-mat $mat_tag`. The `$mat_tag` is the tag of a `nDMaterial` object that defines the constitutive behavior of the elastoplastic interaction surface. The recorders defined for this element are similar to the ones defined for the perfect bonding weak form embedded elements listed in Table 10.1.

Chapter 12

VERIFICATION OF EMBEDDED OVERLAY ELEMENTS

This chapter presents verification of the fiber overlay element and the strong and weak form of the embedded beam interface elements. Simple examples are used for this purpose. A convergence study is also included for these elements.

12.1 Verification of Fiber Overlay Element

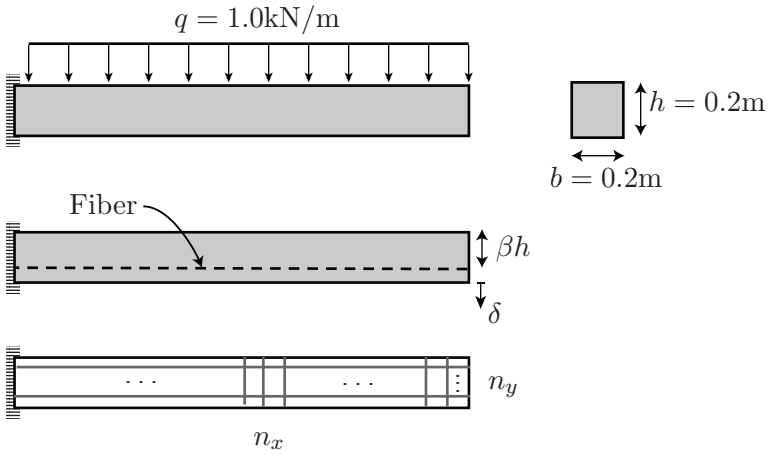

Figure 12.1: Test configuration and parameter definition for fiber element evaluation test

A simple elastic cantilever beam reinforced with elastic fibers is considered here to verify the fiber element implementation. Figure 12.1 shows a schematic of the configuration of the test. The 2 m long beam has a rectangular cross section with $b = 0.2$ m and $h = 0.2$ m. The fiber is located at a distance βh from the top of the section. A uniformly distributed lateral load, $q = 1.0$ kN/m , is applied over the length of the beam. For verification purposes, the maximum deflection of the beam at its free end is recorded. Cross sectional area of the fiber

is 5×10^{-4} m^2 and an elastic material with $E_f = 200,000$ kPa is assigned to the fiber. An elastic isotropic material with $E = 20,000$ kPa and $\nu = 0.3$ is used for the beam. A simple analysis of the beam gives the maximum deflection as

$$\delta_{\max} = \frac{1}{8}\frac{qL^4}{EI}\,, \tag{12.1}$$

where I is the second moment of area about the neutral axis for this beam. To calculate the deflection of the composite beam, the effective bending stiffness of the beam, $(EI)_{\text{eq}}$ is used. Given the perfect bonding condition between the beam material and the fiber, we can calculate the effective bending stiffness as

$$(EI)_{\text{eq}} = (EI)_{\text{beam}} + (EI)_{\text{fiber}} = (EI)_{\text{beam}} + E_f A_f d^2\,, \tag{12.2}$$

where d is the distance to the fiber from the neutral axis. In order to calculate the location of the neutral axis an equivalent section with area adjusted for the difference in material stiffness is considered. The center of area for the equivalent section is the position of the neutral axis. Additional deflection due to shearing deformation of the beam is calculated and added as

$$\delta_{\text{shear}} = \frac{\alpha q_{\text{beam}} L^2}{2AG}\,, \tag{12.3}$$

where $\alpha = \frac{3}{2}$ for a rectangular cross section and G is the shear modulus of the beam material. q_{beam} is the portion of q that is resisted by the beam which is calculated from the bending stiffness of the beam compared to the equivalent stiffness.

Figure 12.2 shows the deflection of the reinforced beam for various β values. Both analytical and numerical solutions are shown in the figure. The maximum deviation from analytical solution in this test is at most 2%.

In order to evaluate the convergence of the element, number of elements in both x and y directions are consistently increased and the convergence error is calculated as the absolute

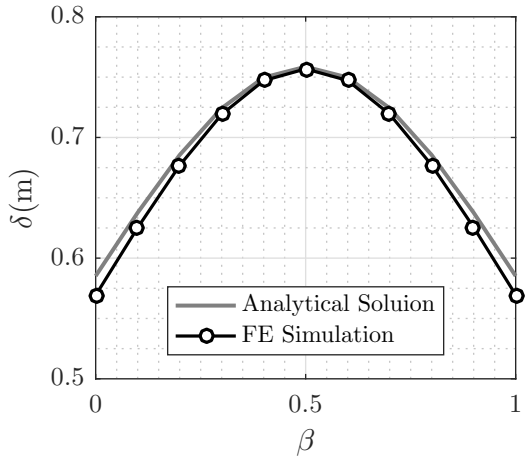

Figure 12.2: Fiber overlay element performance compared to the analytical solution

difference between the deflection of the beam and the deflection of the beam with finest mesh. Figure 12.3 shows the results of this convergence analysis. The element shows a consistent convergence behavior to a value very close to an analytical solution based on the assumptions described above.

12.2 Verification of Embedded Beam Interface element - Strong and Weak Forms

For verification of embedded beam-solid interface elements, a single 11 m long circular elastic pile with a diameter of $D = 1$ m and elastic properties $E = 2 \times 10^6$ kPa and $\nu = 0.2$ is embedded in an elastic soil medium with $E = 40000$ kPa and $\nu = 0.33$. Figure 12.4 shows a schematic of the problem. These properties were chosen to represent typical elastic properties for a pile and soil. The pile head is located 1 m above ground. The soil domain extends 15 m on each side of the pile centerline and the height of the soil domain is chosen 25 m to reduce boundary effects. The pile is loaded at its head with a concentrated load applied in a diagonal direction with respect to the solid block faces. For comparison, a fully 3D model is developed with the same configuration. The load in the 3D case is applied as a concentrated point load as well but the nodes on the pile head surface are tied together to move the same

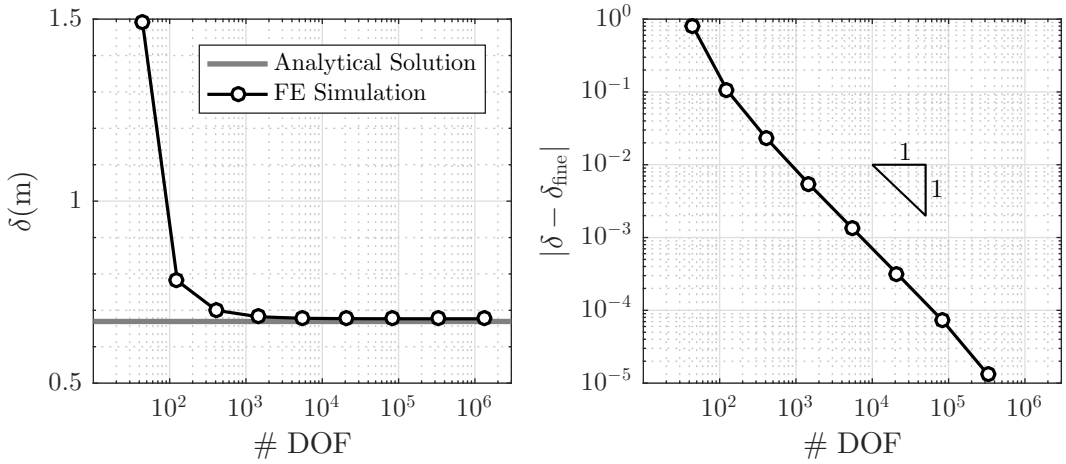

Figure 12.3: Convergence test for the fiber overlay element

amount in the horizontal direction. Both strong and weak forms of the embedded interface formulation are used to evaluate the performance of these elements.

This simple test emphasizes the dramatic advantage of using embedded elements in generating meshes for 3D analysis over fully discretized 3D models. Figure 12.5 shows close-ups of two meshes, one discretizing the pile using solid elements and another one using a linear element for the beam with the embedded interface elements. The figure clearly shows using embedded interface elements allows creating simpler regular solid continuum meshes maintaining the same geometry, and still incorporating the presence of the pile.

Figure 12.6 shows model dimensions as well as the mesh discretization used for the full 3D model. A finer mesh is used in the vicinity of the pile while it gets coarser away from the pile. A lateral force of $F = 23500$ kN is applied to the pile head. Figures 12.7 and 12.8 show contours of the horizontal displacement and shear stress respectively, on the deformed shape of the model. Although displacements obtained using the weak form model shows softer behavior in the beam element, we will see later that the strong form formulation causes locking in the element and results in artificial stiffness. When comparing the contour plots, relatively similar patterns is observed as expected.

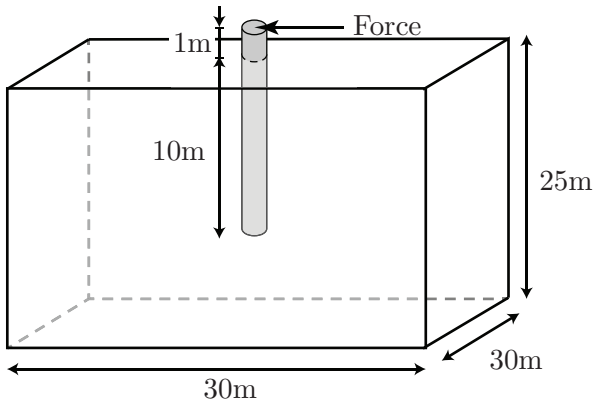

Figure 12.4: Schematic of the laterally loaded pile problem.

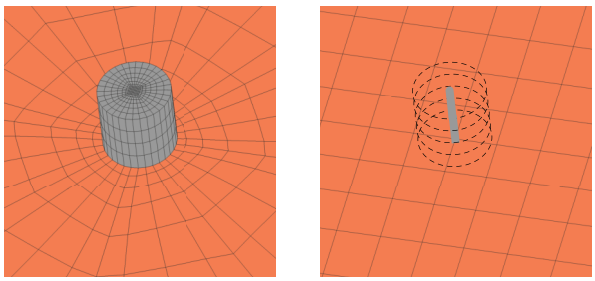

3D Solid Embedded Interface

Figure 12.5: Finite element discretization for a full 3D model versus using embedded interface element.

In order to extract shear force and bending moment diagrams from the 3D model, cuts along the length of the pile are made and the stresses on this plane are integrated. For a cut at a depth z the shear force in the x direction is calculated as

$$V_x(z) = \int_A \sigma_{xz} \, \mathrm{d}A \quad . \tag{12.4}$$

The bending moment about the y axis is then calculated using

$$M_y(z) = \int_A \sigma_{zz} x \, \mathrm{d}A \quad . \tag{12.5}$$

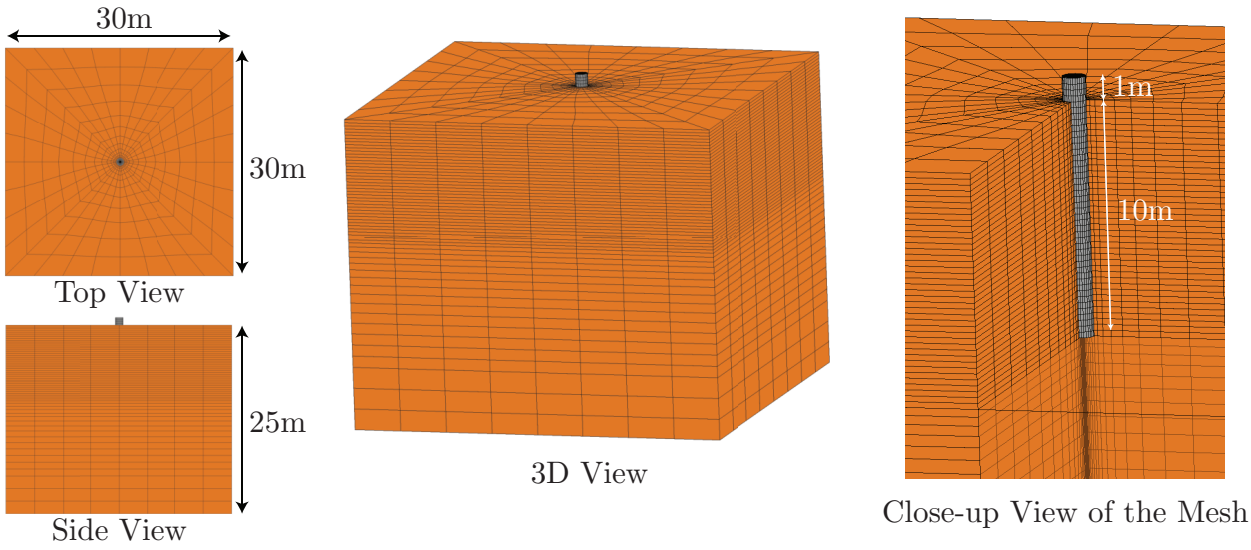

Figure 12.6: Full 3D finite element mesh.

Figure 12.9 shows contours of shear stress along the length of the pile. Contours of shear stresses at three sections at various depths along the pile are also shown in this figure. Using this technique to extract shear force and bending moment demands from 3D structure simulations we can compare the internal forces estimated from 1D linear beam elements to the full 3D model response. Figure 12.10 shows comparison of results from the three models; full 3D model, strong form embedded interface element and weak form embedded element. As indicated earlier, the weak form element does not follow the displacement behavior as close but it captures the shear force diagram as well as the moment diagram very well. The strong form elements perform poorly in the internal digrams, although they capture the displacement relatively well.

Figure 12.11 shows comparisons of results from three cases with different interface behavior, keeping all other properties and dimensions identical. The model configuration is the same as defined for the previous problem except for that two new cases are considered here. The first one includes an elastoplastic behavior using a J2 plasticity material, to represent the interface, with a Young's modulus of $E = 1.0 \times 10^4$ kPa and a yield stress of $\sigma_y = 20$ kPa.

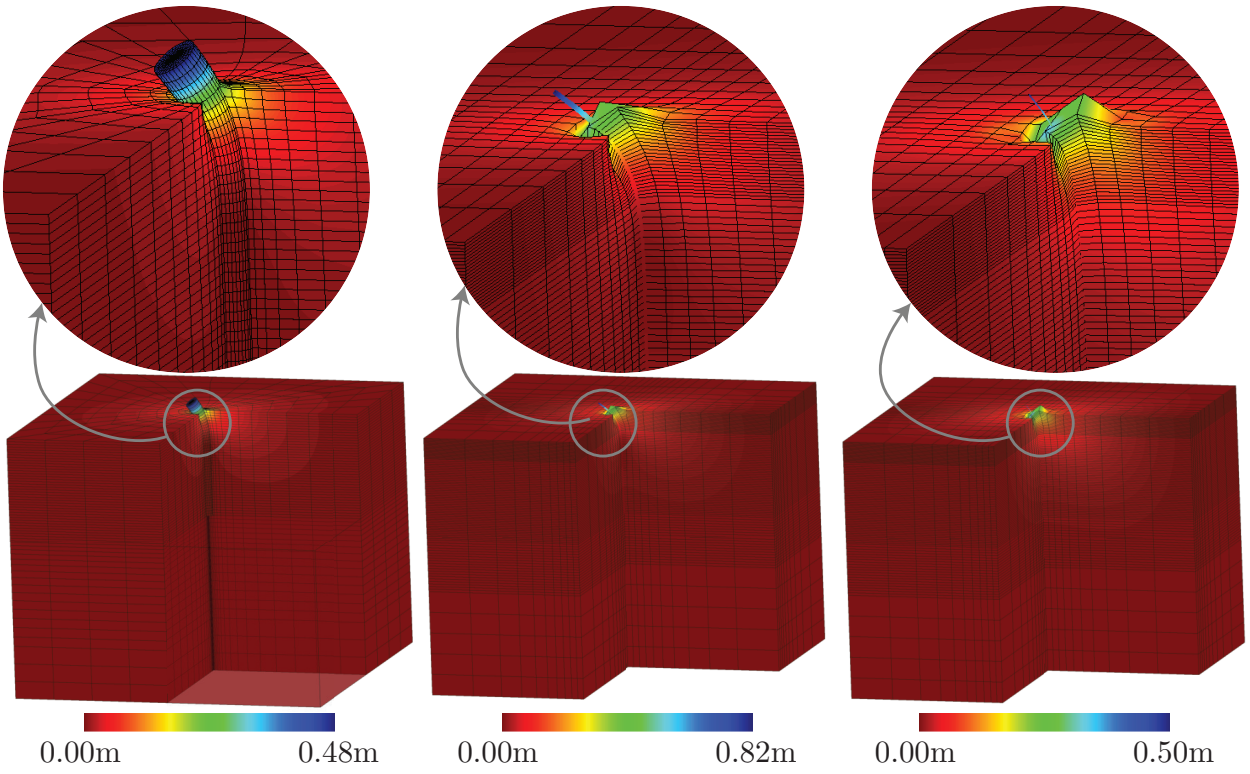

Figure 12.7: Contour plots of horizontal displacement for all three models.

In the other case an elastic isotropic material with a Young's modulus of $E = 1.0 \times 10^4$ kPa is considered. It is obvious from this figure that the case with an elastic interface behavior allows for some additional relative displacement at the interface surface between the beam and the soil, resulting in greater displacements. This is also true for the elastoplastic case but due to yielding of the interface behavior, more relative displacement is allowed and structural demands are redistributed.

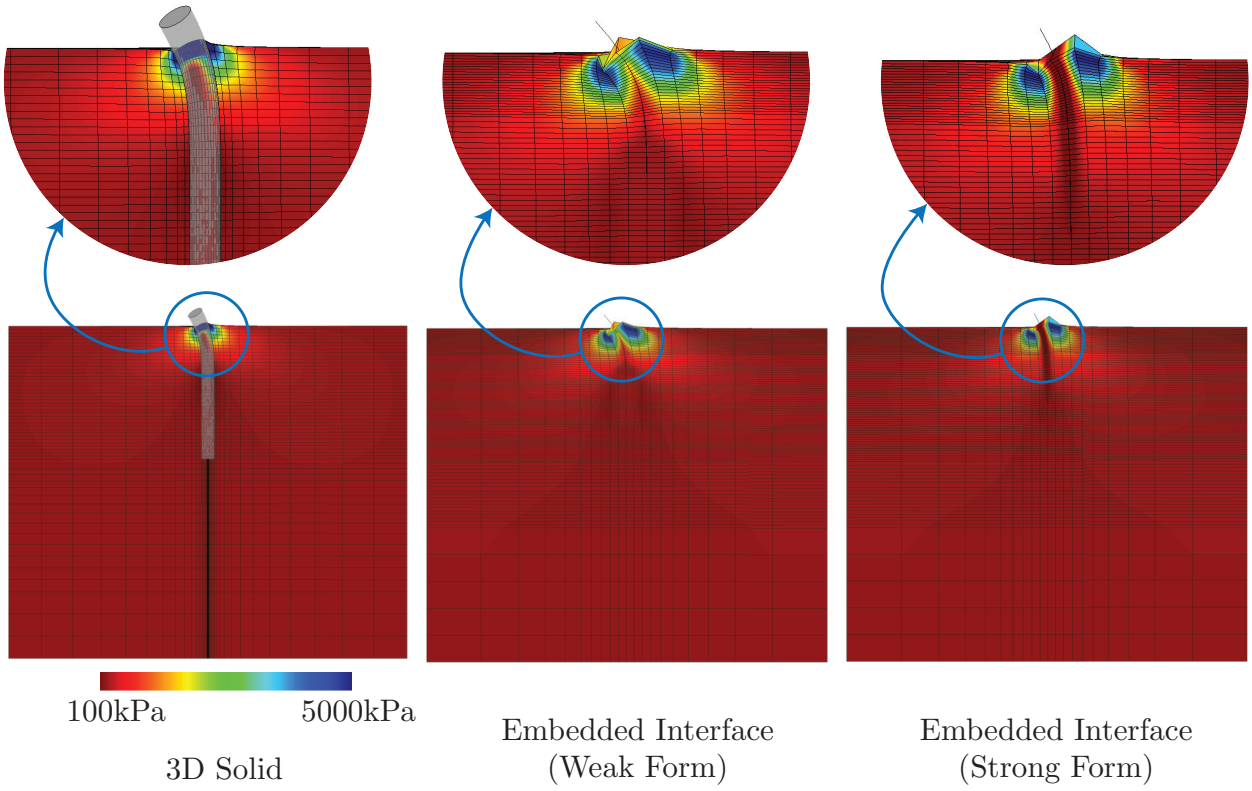

Figure 12.8: Contour plots of shear stress (σ_{xz}) for all three models.

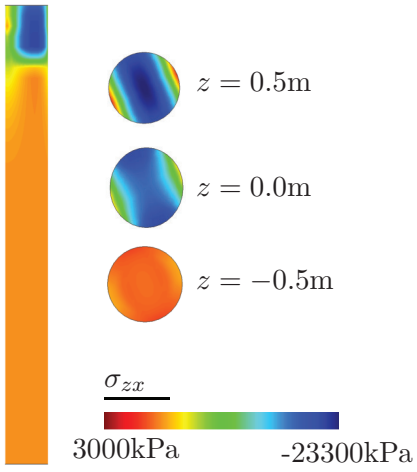

Figure 12.9: Shear Stress along the length of the pile as well as 3 sections at various depths.

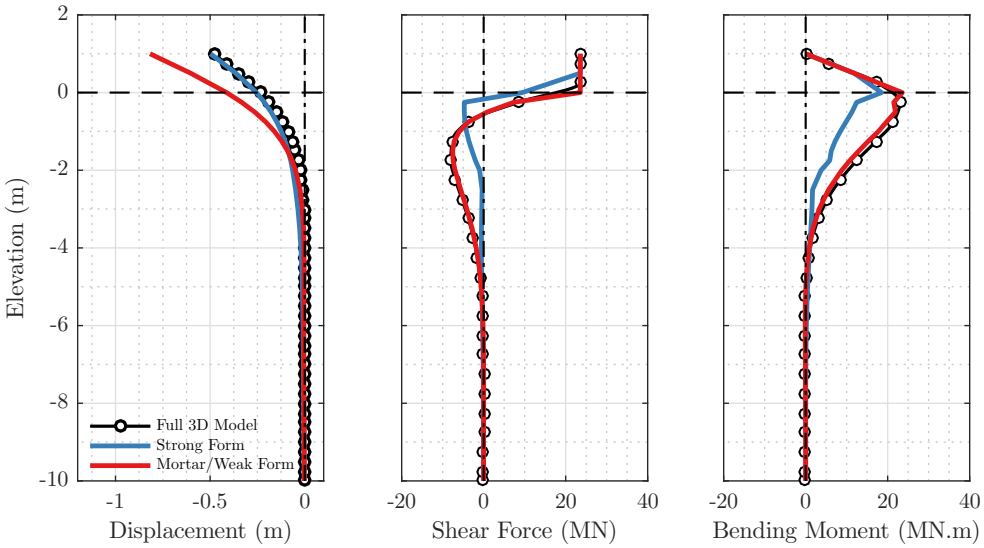

Figure 12.10: Profile plots of displacement, shear force diagram and bending moment diagram for all three models.

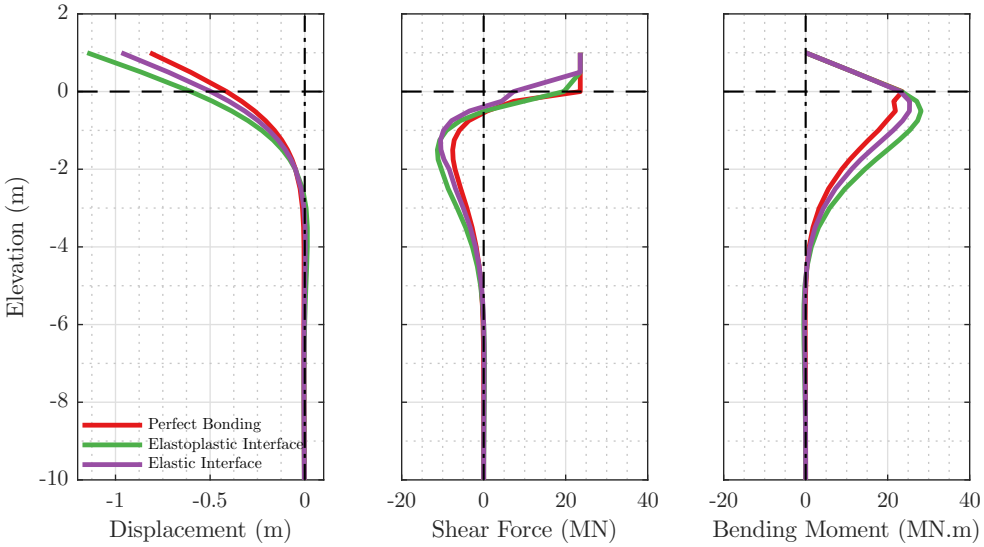

Figure 12.11: Profile plots of displacement, shear force diagram and bending moment diagram; Comparison between the perfect bonding element and the element with elastoplastic interface behavior.

12.2.1 Convergence

To evaluate the performance of the embedded interface elements a convergence study is done using a similar model described in the previous section. The only difference is the portion of the pile above the ground surface is discarded here and the lateral force is applied directly to the pile head located at the ground surface. Several aspects of convergence are considered here. One is the performance of the element as the discretization size is reduced. This can be done by varying the solid mesh size, as well as, the beam mesh size or both at the same time. In this study a consistent refinement of the mesh is utilized to experiment the convergence behavior. The other aspect of convergence to consider is the number of embedded interaction/integration points. In the case of strong form embedded interface elements, the number of interaction points along the perimeter of the pile (n_p) and along the length of the pile (n_l) are consistently increased to evaluate convergence. Similarly, since the integration over the interface area for the weak form formulation is applied using a single point support Gauss-Legendre quadrature numerical approach, this is the other aspect of convergence that is studied here by consistently increasing the number of integration points (consistently refining the area of each integration patch).

Convergence of the Strong Form Embedded Interface Elements - Locking Problem

Figure 12.12 shows the displacement of the pile head when the number of interaction/integration points is increased for embedded interface elements. The figure shows that when using embedded elements based on the strong form formulation, increasing the number of interaction points produces results that tend to zero. This is caused by the locking effect in these elements and is due to incompatibility of the displacement fields in the beam and solid elements. In these elements. the assumed cubic polynomial displacement field in the beam domain follows from using Hermite interpolation functions and the displacement field inside the solid is assumed to be linear in the three directions of the isoparametric element. By applying the interaction condition in the strong form, the problem is over constrained and

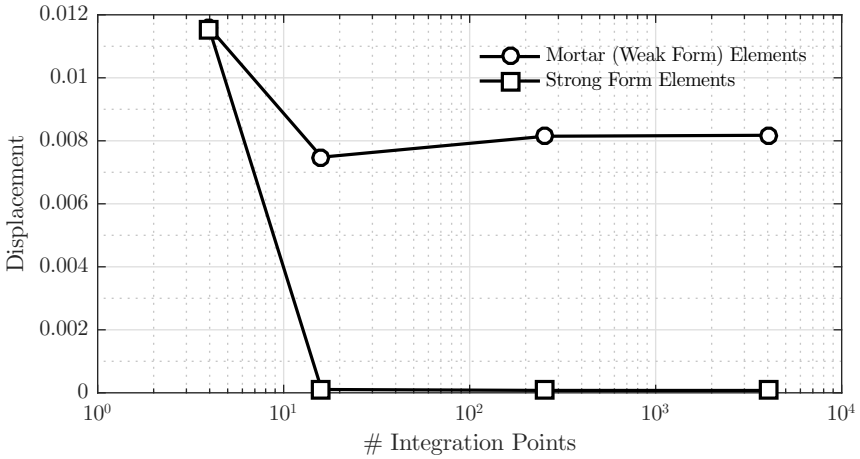

Figure 12.12: Convergence of the results as the number of integration patches (for the weak form elements) as well as interaction points (for the strong form elements) are increased.

the only acceptable solution is the null solution. As discussed in the next section, this problem is weakened in the mortar element formulation by applying the condition in an average sense and releasing the additional constraints. Figure 12.12 clearly shows that by consistently increasing the number of integration points, the pile head displacement converges to a non-zero value when weak form embedded interface elements are used.

Convergence of the Weak Form Embedded Interface Elements

The same model is used to evaluate the convergence of weak form embedded interface elements by consistently reducing the size of the mesh. Due to the three dimensional aspect of the model, consistent refinement in the solid domain increases the computational cost dramatically, therefore extremely fine models cannot be devised and used for this purpose.

Figure 12.13 shows the error, measured as the difference in pile head displacement between the considered case and the displacement obtained from the finest mesh, u_{fine}, as the mesh size is refined in either beam or solid domain or both at the same time. The figure shows that the elements exhibit acceptable convergence behavior. Although the convergence rate drops dramatically in the beam domain refinement as shown in Figure 12.13(c), a consistent

refinement in the solid domain does not show the same trend. This is not seen in the consistent refinement of both domains either. This can be explained by considering the fact that the displacement field in the beam domain is of higher order and the errors in the coarser solid mesh can dominate the error, hence the reduction in convergence rate. All in all, the weak form element demonstrates acceptable convergence behavior.

Convergence of the Numerical Integration Method

The numerical integration method used in the weak form elements is evaluated for convergence behavior here. Figure 12.14 shows the same error estimate discussed in the previous section as the number of integration points are consistently increased both along the beam centerline and its perimeter. As the integration technique is very similar to the trapezoidal integration method, we expect to achieve a 2^{nd} order convergence rate. Figure 12.14 confirms that the integration technique used for the weak form elements follow a 2^{nd} order convergence rate.

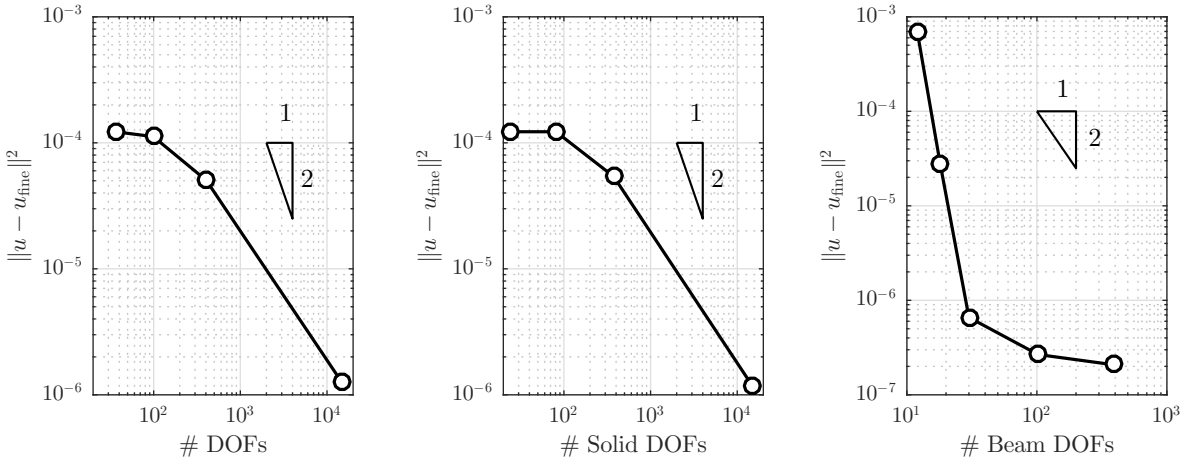

(a) both Solid and Beam (b) Solid (c) Beam

Figure 12.13: Convergence study of weak form elements.

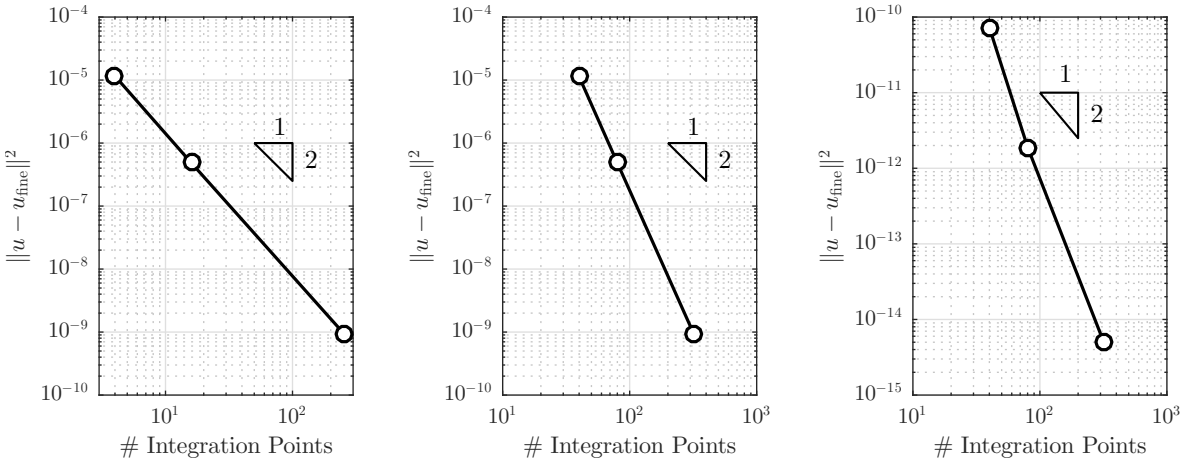

(a) $nP \times nL$ (b) nP (c) nL

Figure 12.14: Convergence study of weak form element numerical integration method.

Part IV

STATIC AND DYNAMIC EXAMPLES

The constitutive model and embedded elements introduced in parts II and III of this dissertation are used here to examine the response of several geotechnical engineering problems. These examples are divided into two chapters. The first chapter presents several static/quasi-static cases while the second chapter presents dynamic test cases.

Chapter 13

STATIC AND QUASI-STATIC TESTS

Tests presented in this chapter intend to show the effectiveness of the tools described in previous chapters and implemented in OpenSees for different aspects of geotechnical earthquake engineering purposes. Results of numerical analyses in this chapter are only representative of the capabilities of the numerical tools and are not intended to completely validate the models against experimental results or real world case histories. Therefore, all test configurations presented in this chapter are arbitrarily chosen.

In this context, a simple slope is considered first to perform a factor of safety analysis. The fiber overlay element is used in this model to show the effectiveness of reinforcing a slope. A batter pile subject to a lateral force is considered next. Given the locking issue that arises when using the strong form embedded interface elements, only weak form mortar elements are used for the batter pile problem as well as all other studies presented here and in the next chapter. Finally, a single pile model and a pile group model are used in a pseudo-static analysis of lateral spreading similar to the 3D FE model presented in Chapter 3.

13.1 Factor of Safety of Reinforced Soil

The simplest geotechnical engineering problem that can be used to demonstrate the effectiveness of the fiber element is a reinforced slope problem. Although the assumption of perfect bonding between the fiber and the soil is restrictive, the numerical model can be used to verify calculations of factor of safety against failure. In this example a typical 2H:1V slope with a height of $h = 2$ m is considered. Depth to a stiff layer is assumed to be $D = 5$ m and only a cohesive soil material is considered. In the analysis, the strength of the soil is reduced until a specific number of iterations (in this case 100) is reached and the displacements in-

creased rapidly. The stresses at this point in the analysis are used to estimate the factor of safety for the slope. To examine the improvement obtained in the behavior of the slope when using such elements, fiber overlay elements are used as reinforcing material. Two different reinforcing configurations are considered; one with short length reinforcing elements and the other with the reinforcing elements that stretch all the way to the boundaries of the soil domain. Figure 13.1 depicts the geometry and configuration of the model and finite element discretization used for this problem. During the analysis, the strength of the soil (σ_y in this case) is reduced in successive steps until failure occurs.

The material response is modeled using a J2 plasticity model with elastic properties $G = 1.0 \times 10^7$ kPa and $\nu = 0.48$ and a yield stress of $\sigma_y = 15$ kPa. This yield stress corresponds to a cohesion $c = 8.66$ kPa. The density of the material is $\rho = 1.7$ Mg/m^3. Using the slope stability charts prepared by Taylor (1948), a factor of safety for this slope without any reinforcement is calculated to be 1.44.

Figure 13.2 shows the deformed shape as well as displacement contours for the strength reduction model after failure. The re-gridding method described by Griffiths and Kidger (1995) is used to generate the deformed meshes. In this method the difference in nodal displacements between two steps just prior to failure is used as the deformation. This displacement is interpolated over a regular grid and shown over the undeformed grid.

A deep seated failure surface is observed as expected for the unreinforced cohesive (J2 type) material. With the addition of reinforcing fibers, the failure mechanism changes when using 9 m long fibers. The failure surface extends to the end of the fibers in this case with displacements smaller than the unreinforced case. When long fibers extending to the boundaries of model are used, no distinct failure surface is observed and the permanent deformations are much smaller than the previous cases. Figure 13.3 shows the displacement of the slope crest as the strength of the soil is reduced. Also included in this plot is the reduction factor obtained from Taylor charts as the reciprocal of the factor of safety. The figure shows that drastic change in displacement pattern starts almost exactly at the reduction factor obtained from the design chart. Figure 13.4 shows displacement contours for a reduction

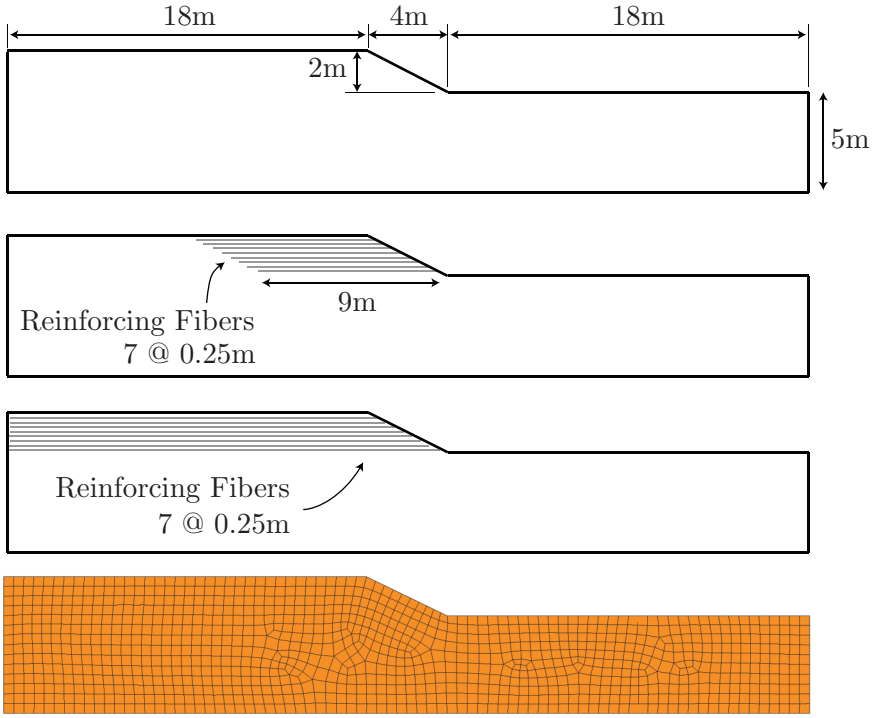

Figure 13.1: Geometry and FE mesh used for strength reduction model.

factor equal to 0.65. The figure shows much less displacements in the reinforced cases than the unreinforced one. Reinforcing the slope results in a more ductile failure and increase in factor of safety.

13.2 Batter Pile Analysis

The evaluation case discussed in Section 12.2 is used here with a pile rotated $\beta = 30°$ about the y-axis on the ground surface to emphasize the benefit of using embedded interface elements. The pile and soil properties are described in Section 12.2. A fully 3D discretization of this model with hexahedral elements would be extremely difficult to create and would prevent using a regular grid. However this is easily achieved using the embedded beam interface elements presented in Part III of this dissertation. Figure 13.5 shows the configuration and finite element mesh used for the batter pile examined here. In all cases a concentrated lateral

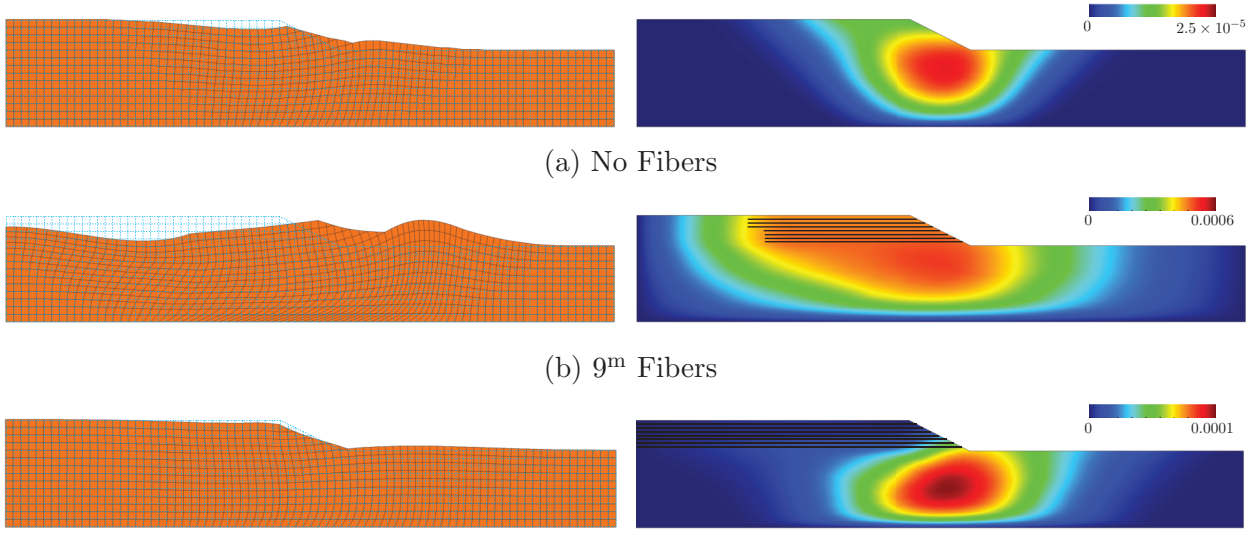

(a) No Fibers

(b) 9^{m} Fibers

(c) Long Fibers

Figure 13.2: Deformed mesh and displacement contours at slope failure for a J2 material. Contour plots are in "m" and deformation is exaggerated several times on the deformed shape for enhanced visualization.

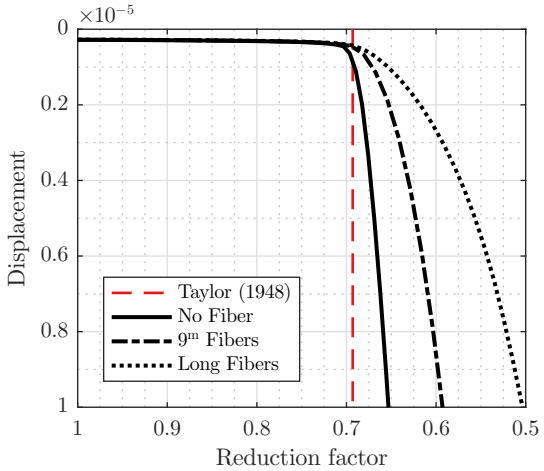

Figure 13.3: Crest displacement versus reduction factor obtained from the strength reduction models for a J2 material.

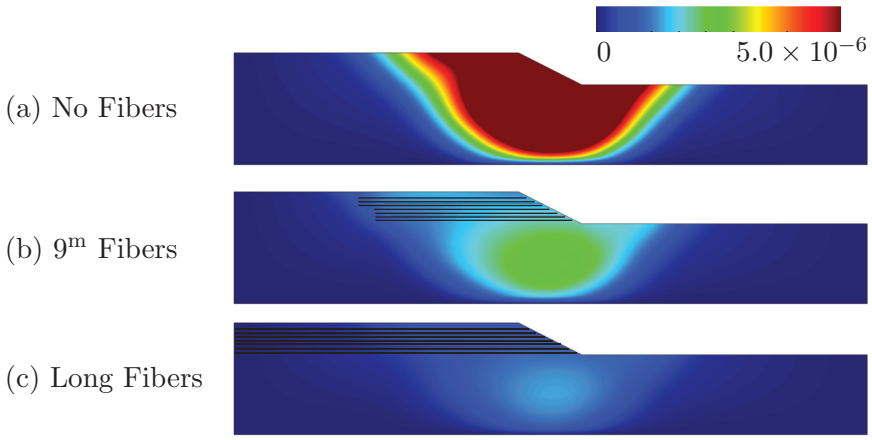

Figure 13.4: Displacement contour plots at strength reduction factor equal to 0.65 for unreinforced model, reinforced model with 9 m long fiber and reinforced model with fibers extending all the way to the boundaries.

load, $F = 23500$ kN, is applied to the pile head. Contour plots of displacement and various stress components in a cross section of the mesh coinciding with the centerline of the pile are shown in Figure 13.6. Displacement profiles in horizontal and vertical directions as well as shear force and bending diagrams along the beam in the beam local coordinate system are shown in Figure 13.7. Also included in this figure are results for cases where the pile batter angle about the y-axis is $\beta = 15°$ and $\beta = 0°$. As expected increasing the batter angle causes less lateral displacement but more vertical displacement. Also shown in the figure is that increasing batter angle results in less structural demands in the lateral direction for the same loading. Not shown here are the axial response of the pile which increases with the batter angle.

13.3 Lateral Spreading Pushover Analysis - Single Pile and Pile Group Models

A challenging task in geotechnical earthquake engineering is to evaluate the forces exerted on a pile by liquefaction-induced lateral spreading of the surrounding soil. A simplified quasi-static method for modeling such case is to apply a kinematic displacement profile on the

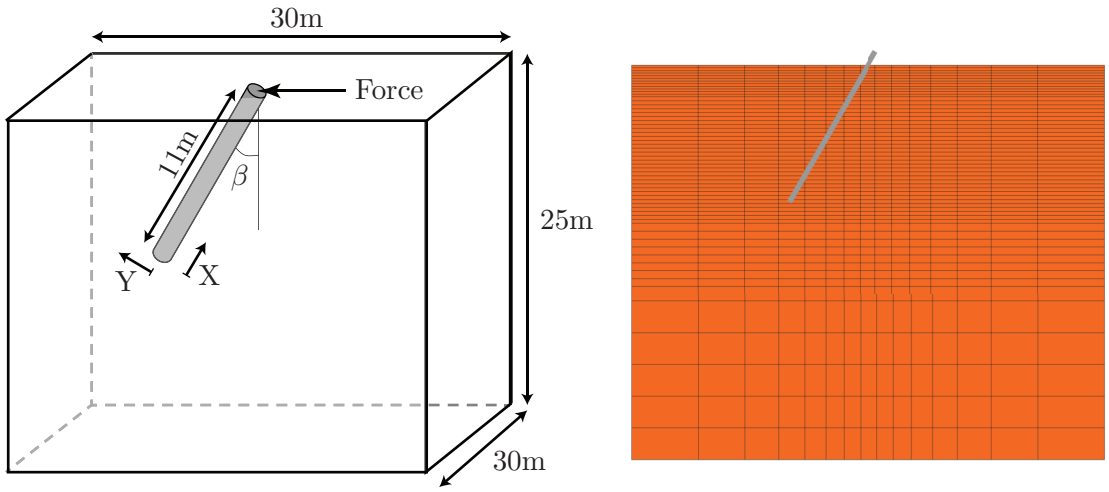

Figure 13.5: Configuration and discretization of the model used for the batter pile example.

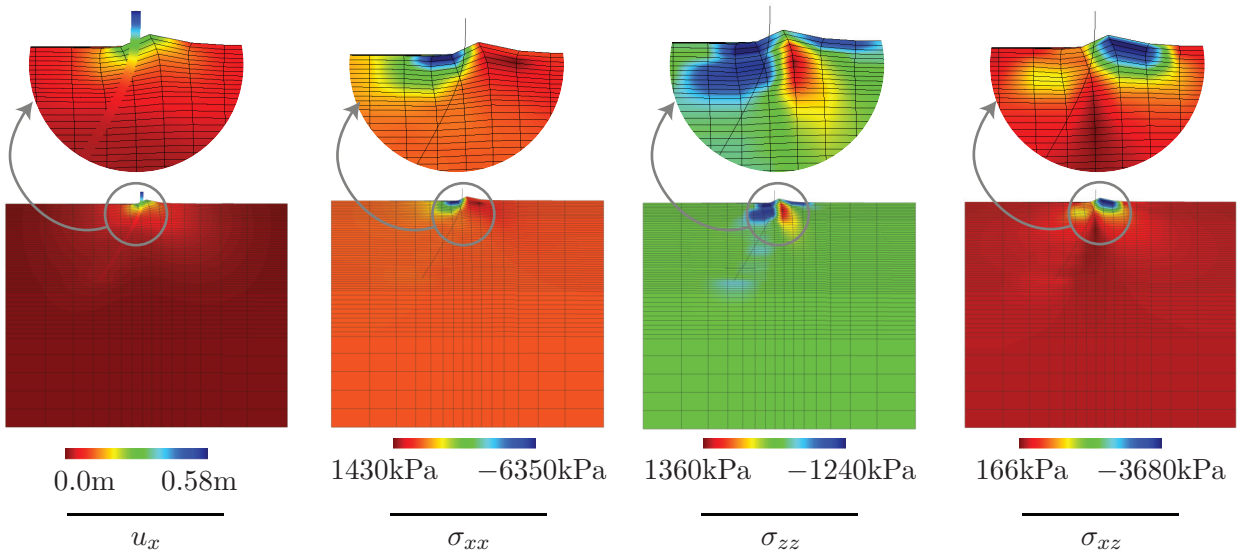

Figure 13.6: Contour plots of soil displacement and stress components for batter pile model.

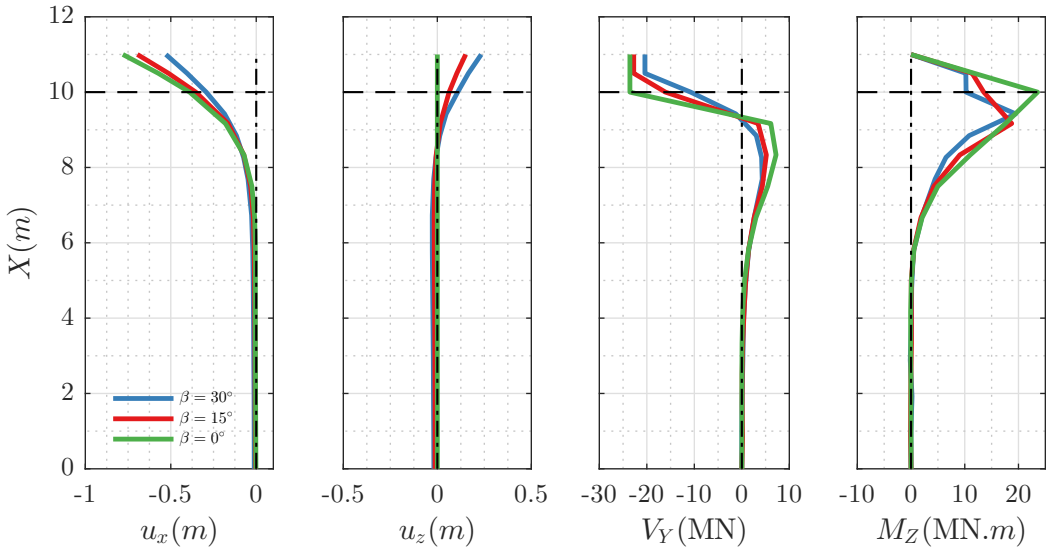

Figure 13.7: Result profiles along the batter pile. Note that x and z denote the horizontal and vertical directions in the global coordinate system and X, Y and Z define the local coordinate system of the beam. X is oriented along the longitudinal direction of the beam and Y lies in the x-z plane. y and Z both denote the out-of-plane direction in this figure.

boundaries of the model. The kinematic profile is an approximation to the lateral spreading pattern estimated to happen underground. For this mater, it is customary to estimate the amount of lateral spreading at the surface and use a trilinear displacement profile with a linear transition in the liquefiable layer from zero displacements to the estimated lateral spreading demand in the crustal soil. In this section we first analyze a single pile subjected to lateral spreading and then a configuration close to the model used for the Llacolén bridge presented in Chapter 3.

13.3.1 Single Pile

For the single pile case, the kinematic displacement profile shown in Figure 13.8 is applied to a single pile configuration similar to the configuration used in section 12.2. The non-liquefiable soil is modeled using a J2 plasticity model with $s_u = 100$ kPa. For the purpose of modeling liquefied soil behavior, a very low shear stiffness, $G = 20.5$ kPa, and a Poisson's

ratio close to 0.5 is chosen ($K = 506.0$ kPa), and the strength is also modeled with a J2 type plasticity model with an estimated residual undrained shear strength, $s_u = 37.0$ kPa. The soil and pile properties are summarized in Table 13.1. Figure 13.8 also shows the deformed shape of the mesh as well as the contour plot of shear strains after application of 10 cm lateral spreading. The Euler-Bernoulli assumption of planes remaining plane can be verified using this plot.

Table 13.1: Soil and pile properties used in the lateral spreading problem.

Non-liquefiable Soil Layers	G	60,000.0 kPa
	K	300,000.0 kPa
	ρ	1.7 Mg/m^3
	s_u	100.0 kPa
Liquefiable Soil Layer	G	20.5 kPa
	K	506.0 kPa
	ρ	1.7 Mg/m^3
	s_u	37.0 kPa
Beam	r	0.25 m
	E	2,500,000.0 kPa
	ν	0.2
	ρ	0.0 Mg/m^3

The displacement profile as well as shear force and bending moment diagrams are shown in Figure 13.9. The displacement profile in this figure shows the behavior one expects for such loading. Due to symmetry of the problem in the vertical direction, it is expected the curvature of the pile should be zero at the middle of the liquefiable layer resulting in zero internal moment response at this location which is observed in the figure. As the liquefied soil does not provide much resistance, it is expected that the shear demand remains nearly constant in the liquefiable soil layer. This is also confirmed in this figure with the expected transition in shear forces close to the layer top and bottom boundaries. Figure 13.10 shows displacement profiles for various locations along the soil domain at regular intervals away

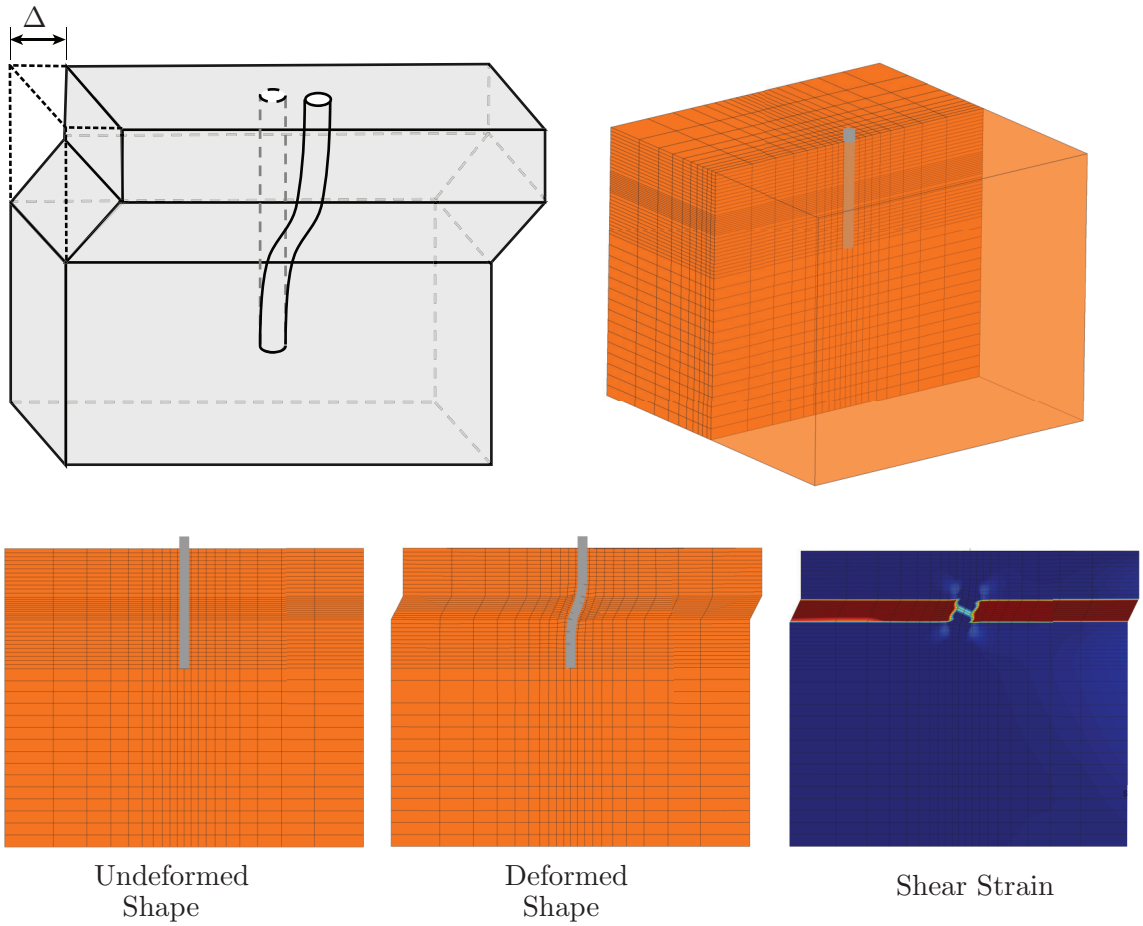

Figure 13.8: Schematic of lateral spreading problem. 3D view of the FE mesh as well as 2D deformed and undeformed meshes. Contour plot of shear strains after application of profile displacements is also shown.

from the pile. This figure shows the "pinning effect" as the pile resistance impedes the soil to move as much as it would in the absence of the pile.

13.3.2 Pile Group

A quasi-static evaluation of lateral spreading demands is performed on a group of piles similar to the Llacolén bridge's southeast bent described in Chapter 3. The bridge bent is duplicated exactly here except for the pile cap beam which is omitted for simplicity. Instead

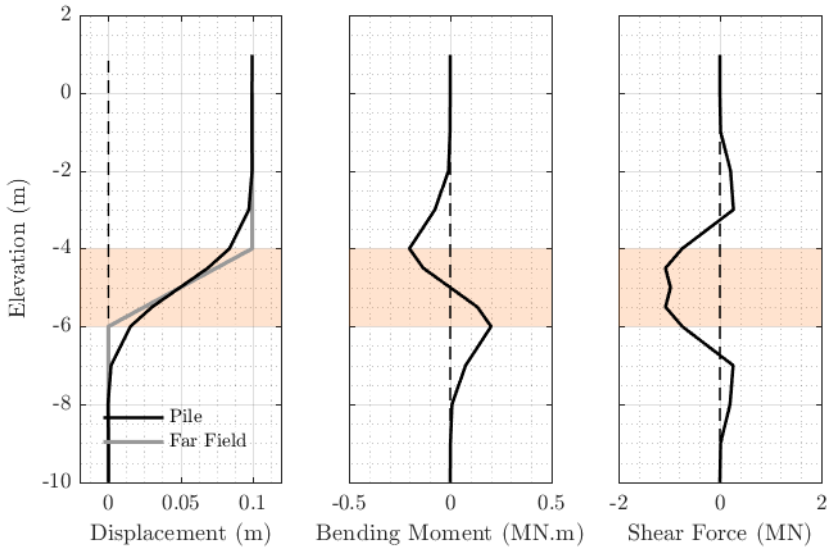

Figure 13.9: Profile of pile response (structural demand) to the kinematic loading of lateral spreading.

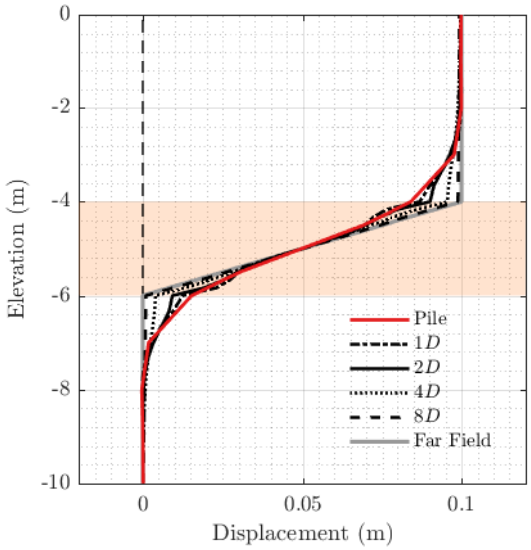

Figure 13.10: Profile of soil displacement at various distances from the pile centerline.

of a pressure dependent Drucker-Prager type constitutive model, a pressure independent J2 type plasticity model is used for all soils to remove difficulties related to the tensile strength of the soil due to pulling forces by the piles. The material parameters are chosen to be as close as possible to the ones used in Chapter 3. Mesh generation for this model is considerably easier and faster than for the model presented in Chapter 3. As a result, refining the mesh is simpler to do. In the model presented here, 123,872 nodes and 116,065 elements are used compared to 50,350 nodes and 44,955 elements used in the model presented in Chapter 3. As mentioned above refining the model presented in Chapter 3 would be a complicated task. The loading is applied with a tri-linear deformation pattern applied to the boundaries of the model, keeping the displacement of the underlying layers at zero and using a linear variation over the liquefiable layer from zero to estimated lateral spreading displacement at the dry crust layer. In this problem a lateral spreading displacement of 40 cm is applied.

Figure 13.11 illustrates the finite element mesh used for this example and contour plots of displacement and shear strains after application of the loading. The top view of the displacement contour plot clearly shows the pile pinning effect which is comparable to results presented in Chapter 3. Figure 13.12 depicts contour plots of the interaction forces on the interaction surface in the local coordinate system of the pile. Three-dimensional effects due to asymmetry in the geometry of the bent is seen in this figure. Structural demand profiles on the piles are shown in Figure 13.13. The shaded areas show the range of demands for all piles and the solid line shows results for one of the middle piles. Color blue represents the results for piles with elastic behavior while red stands for results from piles with elastoplastic behavior. Figure 13.13a shows results from the WSDOT study and described in Chapter 3 for similar loading conditions. Figure 13.13b depicts results for a similar model using embedded interface elements. The differences in results, when these two models are compared, are due to (1) difference in the constitutive models used to represent soil behavior, (2) absence of the pile cap beam in the embedded interface model and (3) different interface conditions. Point (3) refers to perfect bonding between the soil and pile surface in the embedded interface model, where in the WSDOT model a contact formulation was used and gaps were allowed

to form between the soil and the pile surface. As shown in Figure 13.13 although these models are different in several aspects, the results are comparable nonetheless, showing that aspects of interest in the results, e.g. maximum structural demands, may be insensitive to certain modeling aspects, e.g. material back-bone curve, gap formation, etc.

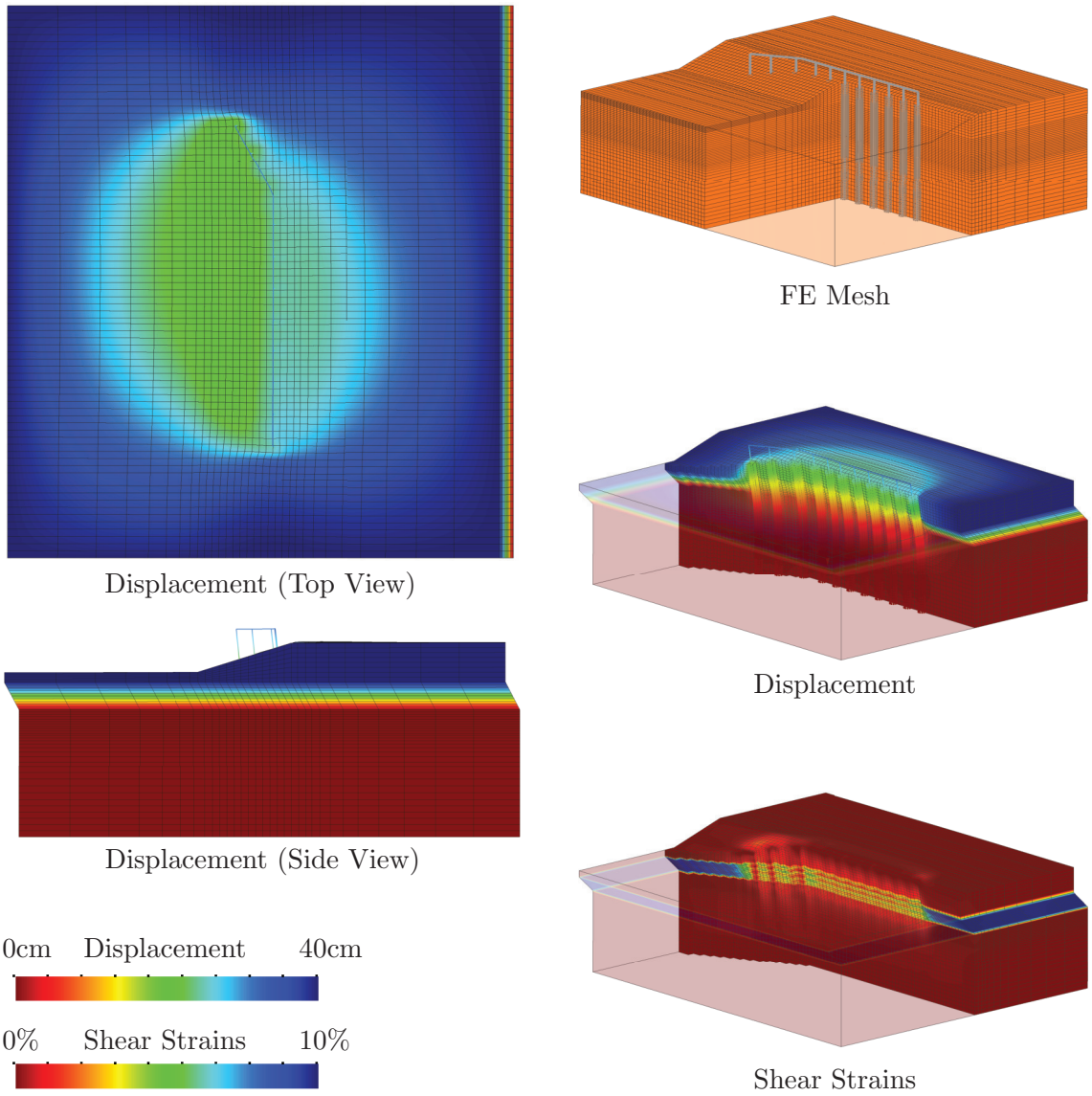

Figure 13.11: Finite element mesh and contour plots of displacement as well as shear strains.

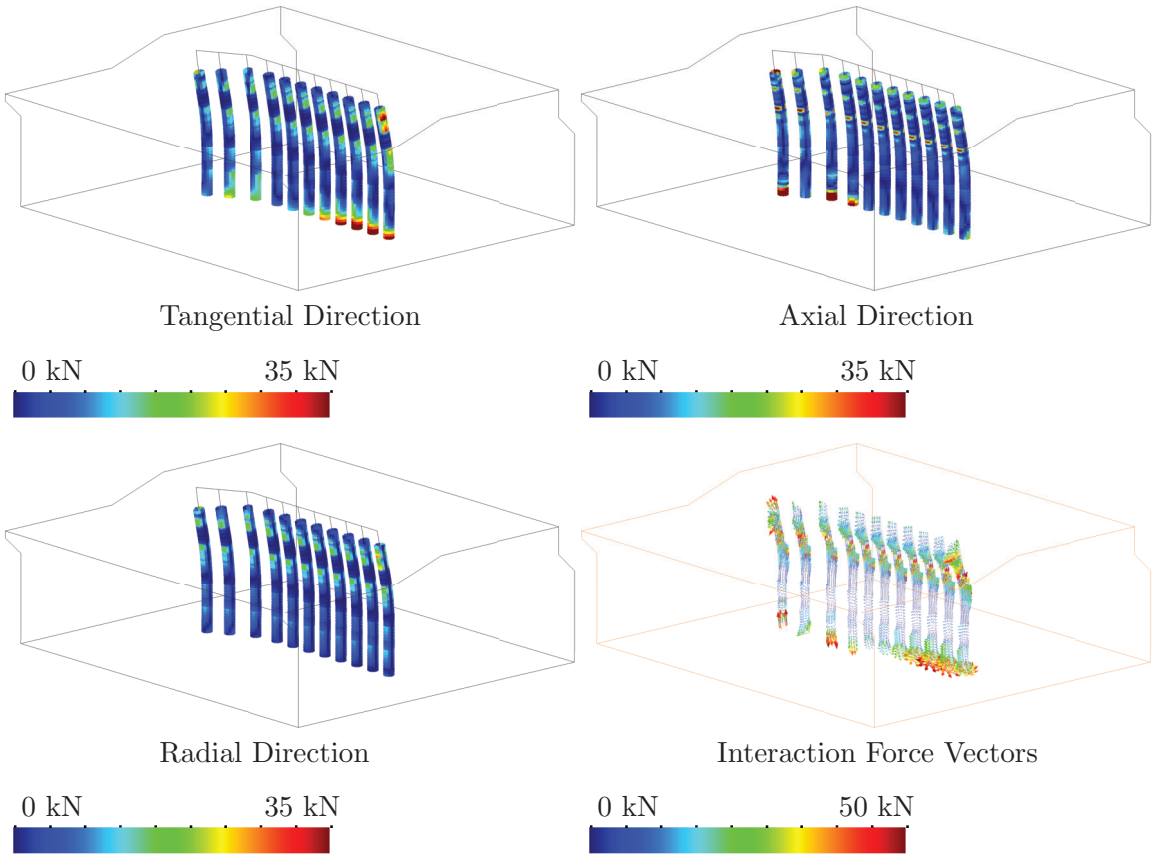

Figure 13.12: Interaction force components in the local coordinate system of the interaction surface on the deformed shape. The bottom left plot shows force vectors color coded with their magnitude.

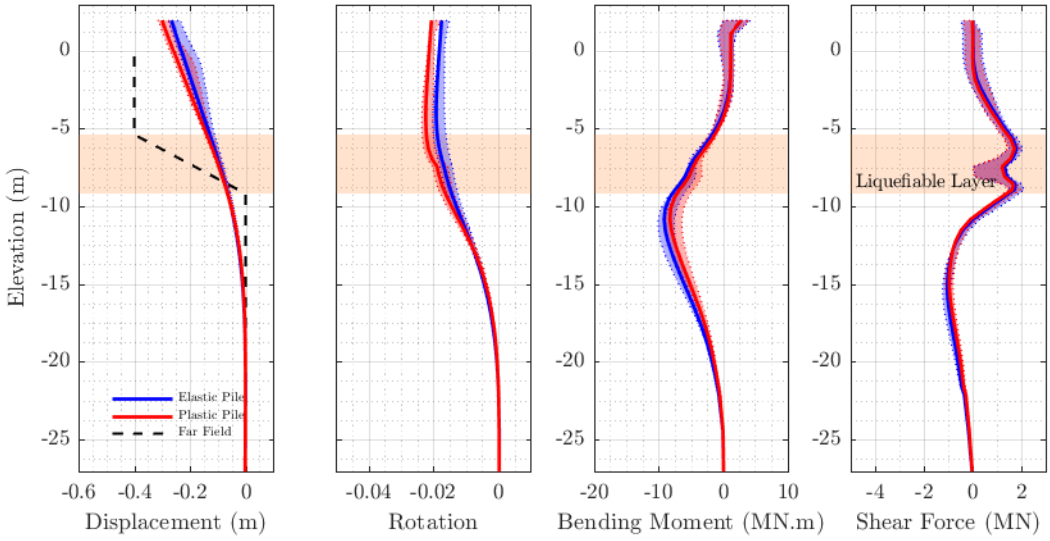

(a) Results obtained from the model described in Chapter 3 for far-field displacement of 40 cm

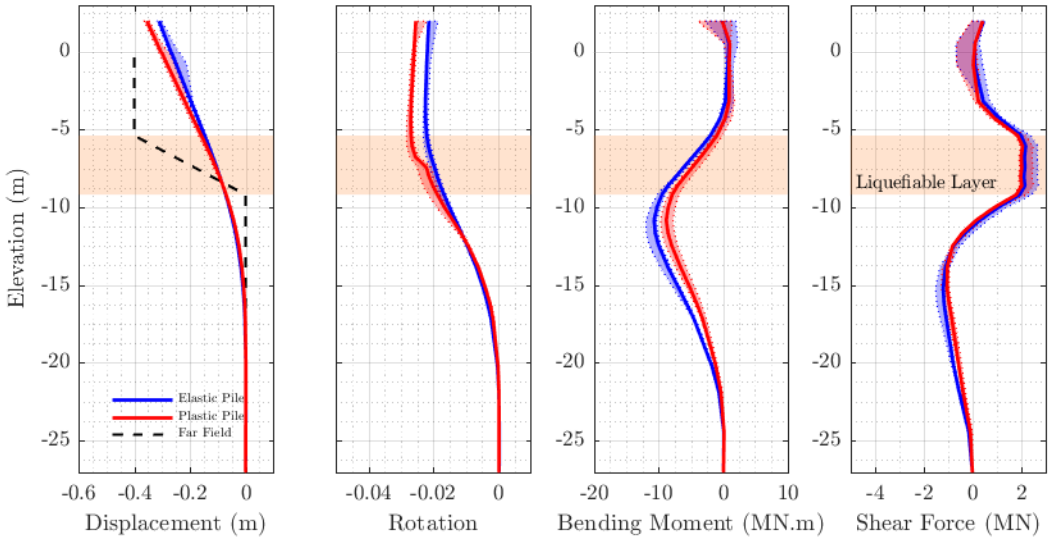

(b) Results obtained from the model using weak form embedded interface elements for far-field displacement of 40 cm.

Figure 13.13: Displacement, rotation (nodal values), bending moment and shear force profiles for bridge bent piles subject to lateral spreading.

Chapter 14

DYNAMIC TESTS

This chapter presents three dynamic 3D numerical analyses of typical geotechnical earthquake engineering problems. Results of these simulations are presented here as a proof of concept and as a first validation phase in support of the finite element tools discussed in this document. A few important aspects of 3D dynamic analyses are discussed here. A soil-water coupled formulation for considering multiple soil phases is probably the most relevant aspect in this regard; especially, when effects of pore water pressures are significant. In this study the u-P fully coupled formulation (Zienkiewicz and Shiomi, 1984) is used. Another important aspect in dynamic analysis is the integration of the wave equation in time. This is a very well studied subject and is addressed using conventional methods.

In all the examples presented in this chapter, the Newmark integration method with $\beta = 0.25$ and $\gamma = 0.5$ is used. Different Newmark parameters can lead to excessive numerical damping, significantly altering results. Kinematic boundary conditions are highly important and are addressed here using a very simplistic approach. For this purpose, a massive soil column assuming a shear beam behavior is used in all cases and it is tied to the boundaries of the model. In this way the far-field behavior is captured reasonably well. However, reflection of waves trapped in the model are not addressed. By putting the boundaries at relatively large distances from the superstructure and applying some reasonable damping to the system, the effect of such trapped energy is reduced. A more refined boundary representation is outside the scope of this study and it is suggested as a future study. The earthquake excitation can be applied to the model using various methods. In this study we use the East-West component of the Gilroy No. 1 motion and apply it as an acceleration to the rigid base of the model. Other alternatives allow to consider a compliant rock base.

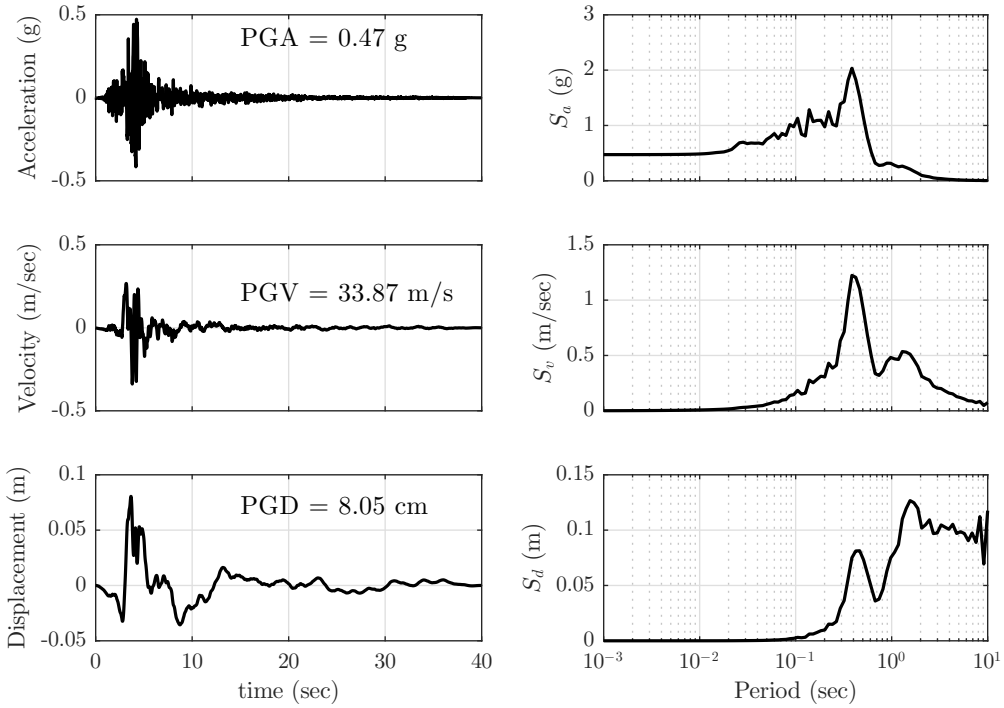

Figure 14.1: Time history and response spectra of motion Gilroy No. 1.

Although this is an easy modification to the models used in this study, the rock base is not included here. Figure 14.1 illustrates time histories of acceleration, velocity and displacement as well as the response spectra of the motion used here.

Another important aspect to consider when addressing geotechnical earthquake engineering problems, in particular liquefaction, is the constitutive model. In general this requires the use of advanced constitutive models. The constitutive model presented in Chapter 4 is used here to capture liquefaction of the soil. In cases where soil liquefaction is not desired, an isotropic elastic model is used for sake of simplicity. Finally, to capture soil-structure interaction, the mortar embedded finite elements introduced in Chapter 8 and its following chapters are used here.

This chapter presents three examples with increasing levels of complexity to showcase the capabilities of the tools developed in this dissertation. First, a single pile model embedded in a soil medium is used to examine kinematic interaction effects by changing the stiffness of

the pile. Then a simple bridge bent, with two orthogonal loading orientations and different superstructure masses, is considered and lastly a liquefiable soil profile with an embedded pile is used to investigate lateral spreading effects induced by a dynamic load.

14.1 Kinematic Soil-Structure Interaction

In the soil-structure interaction (SSI) field of geotechnical earthquake engineering, kinematic interaction is one of the influential factors in determining the response of the system to an input motion. In the example presented here we try to investigate the effectiveness of the mortar embedded interface elements in capturing such effects. The single pile embedded in a soil domain depicted in Chapter 12 and Figure 12.4 is considered here. Three different stiffness values, 2,500 kPa, 250,000.0 kPa and 25,000,000.0 kPa are chosen for the pile material. Table 14.1 summarizes the soil and pile material properties used in this study. For simplicity linear elastic properties are considered for the soil.

Table 14.1: Properties used for analysis of kinematic soil-structure interaction.

Soil	E	40,000.0 kPa
	ν	0.3
	ρ	1.7 Mg/m^3
Pile	r	0.5 m
	E	Variable
	ν	0.2
	ρ	0.0 Mg/m^3

Four single-frequency motions with frequencies equal to 0.5 Hz, 1 Hz, 2 Hz and 4 Hz and an amplitude of 0.15 g (shown in Figure 14.2) are applied to the base of the model. Figure 14.3a shows the 5% damping acceleration response spectra for the input motions and corresponding free field response recorded in the soil column. The figure shows that the soil amplifies the motions with frequencies closer to the natural period of the soil ($T_n = \frac{4H}{V_s} = \frac{4\times 25 \text{ m}}{95.15 \text{ m/s}} = 1.05$ s). Figure 14.3b shows the 5% damping acceleration response spectra of the

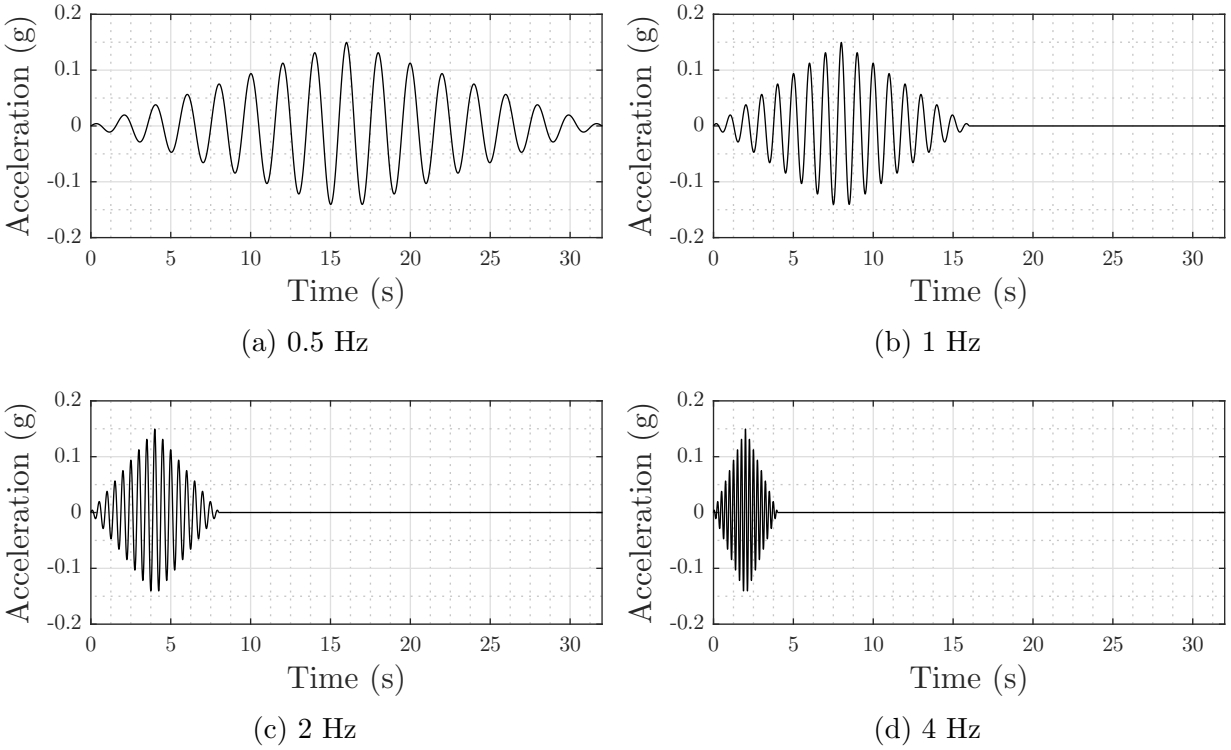

(a) 0.5 Hz (b) 1 Hz

(c) 2 Hz (d) 4 Hz

Figure 14.2: Acceleration time histories used in the kinematic interaction example.

pile head as well as its magnification factor when compared to the free field response. The figure includes results obtained for all four motions and three pile stiffness values. In the case of the softest pile, $E = 2,500$ kPa, since the soil is stiffer than the pile, it is expected that the effect of pile presence to be small which is confirmed in these figures. Figure 14.4 shows the magnification factor, defined as the ratio between the peak acceleration at the pile head and the peak acceleration at the free field ground surface, versus frequency. The figure shows that the motion with higher frequencies result in greater magnifications. However, it is important to mention that the frequencies used in this study may not cover a full range of frequencies required to resolve the complete frequency-dependent kinematic interaction behavior. Nevertheless, based on the results obtained from these analyses, the stronger pile under the high frequency shows greater response.

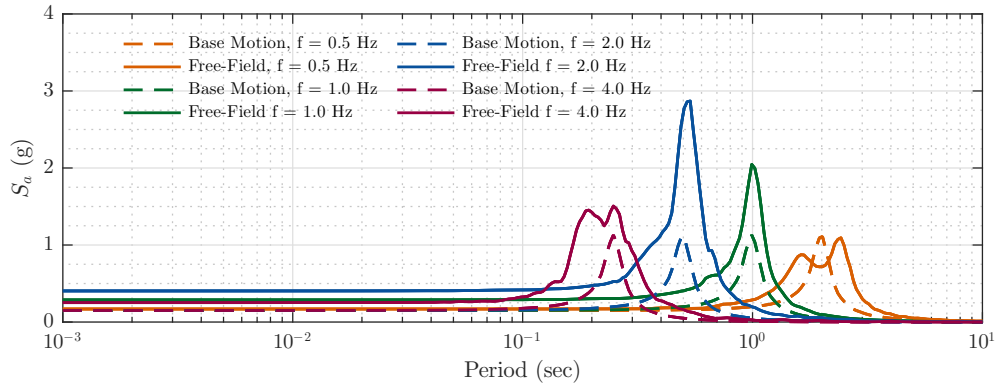

(a) Input motion and free field surface 5% damping acceleration response spectra for various motion frequencies.

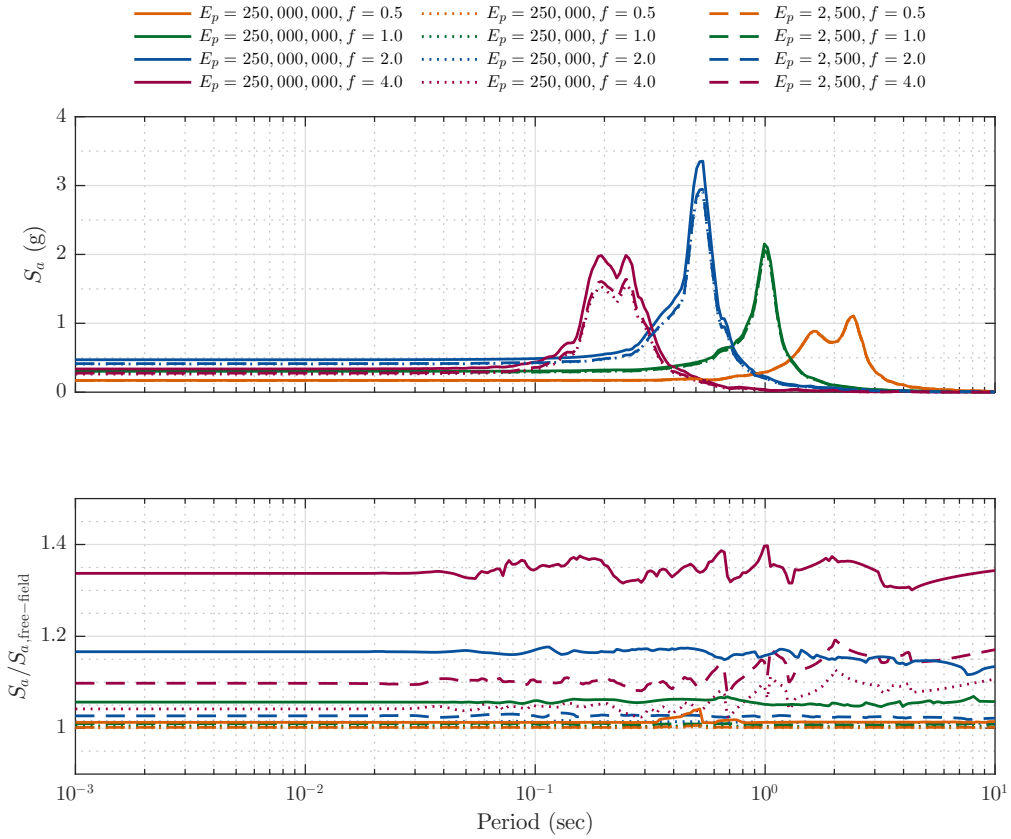

(b) Top: Pile head 5% damping acceleration response spectra for various pile stiffness values and motion frequencies. Bottom: Pile head spectral acceleration magnification compared to the free field.

Figure 14.3: Kinematic interaction results for various pile stiffnesses and different motion frequencies.

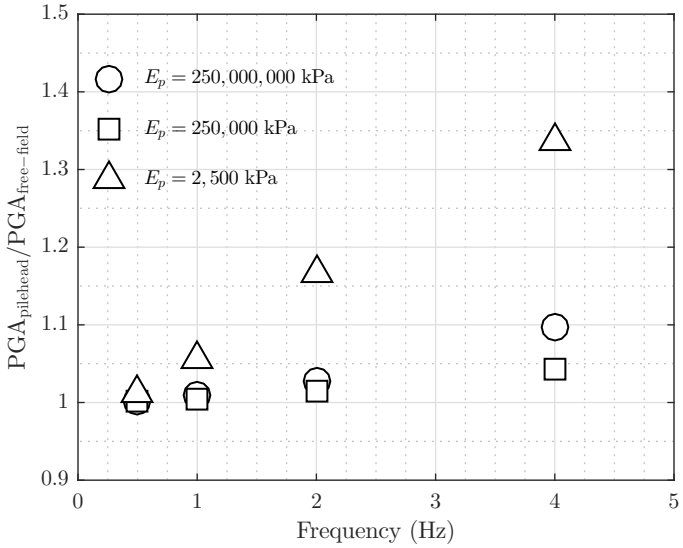

Figure 14.4: Peak acceleration magnification factor for various pile stiffnesses.

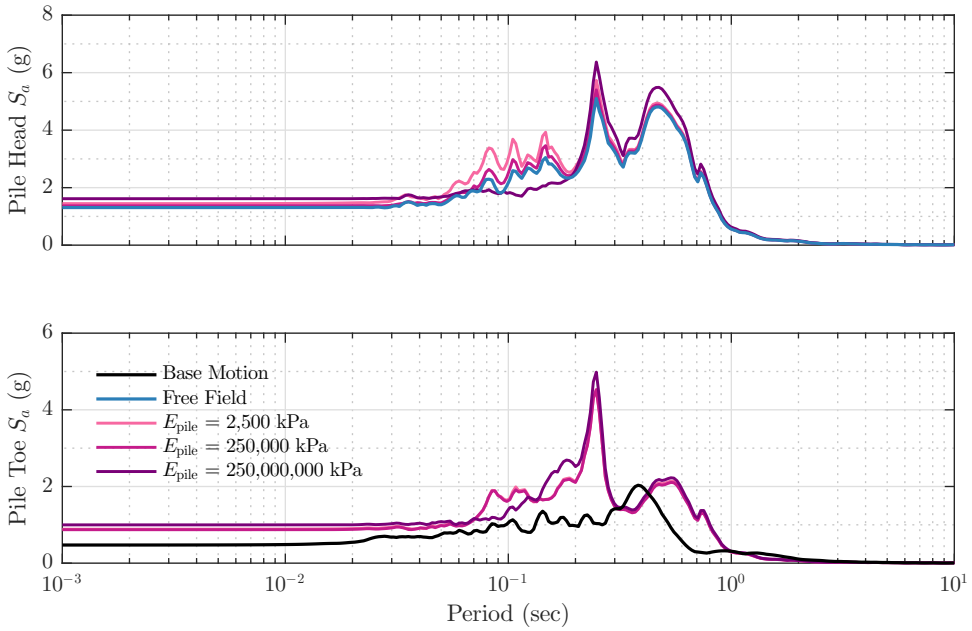

Figure 14.5: Pile head and toe 5% damping acceleration response spectra for various pile stiffnesses.

To further investigate kinematic interaction effects, the Gilroy No. 1 motion (Figure 14.1) is applied to the base of the model. The same set of pile stiffnesses described above are used here. Figure 14.5 shows the 5% damping response spectra of the pile head and the pile toe recordings. The response spectra of the base input motion and the free field accelerations are also plotted for comparison. The effect of kinematic interaction is clearly observed at periods between 0.05 s to 0.3 s. A better manifestation of kinematic interaction due to pile stiffness can be seen in the soil surface response close to the pile head and is examined next. The top plot in Figure 14.6 shows the 5% damping response spectrum of the surface motion at one pile diameter away from the centerline of the pile. For reference the response spectra for the input motion and the free field accelerations are also included in the plot. The middle and bottom plots in the figure show the ratio of these values with the base input motion response spectrum and with the free field motion response spectrum, respectively. The kinematic interaction effect due to the pile presence is clearly visible at periods between 0.05 s to 0.3 s.

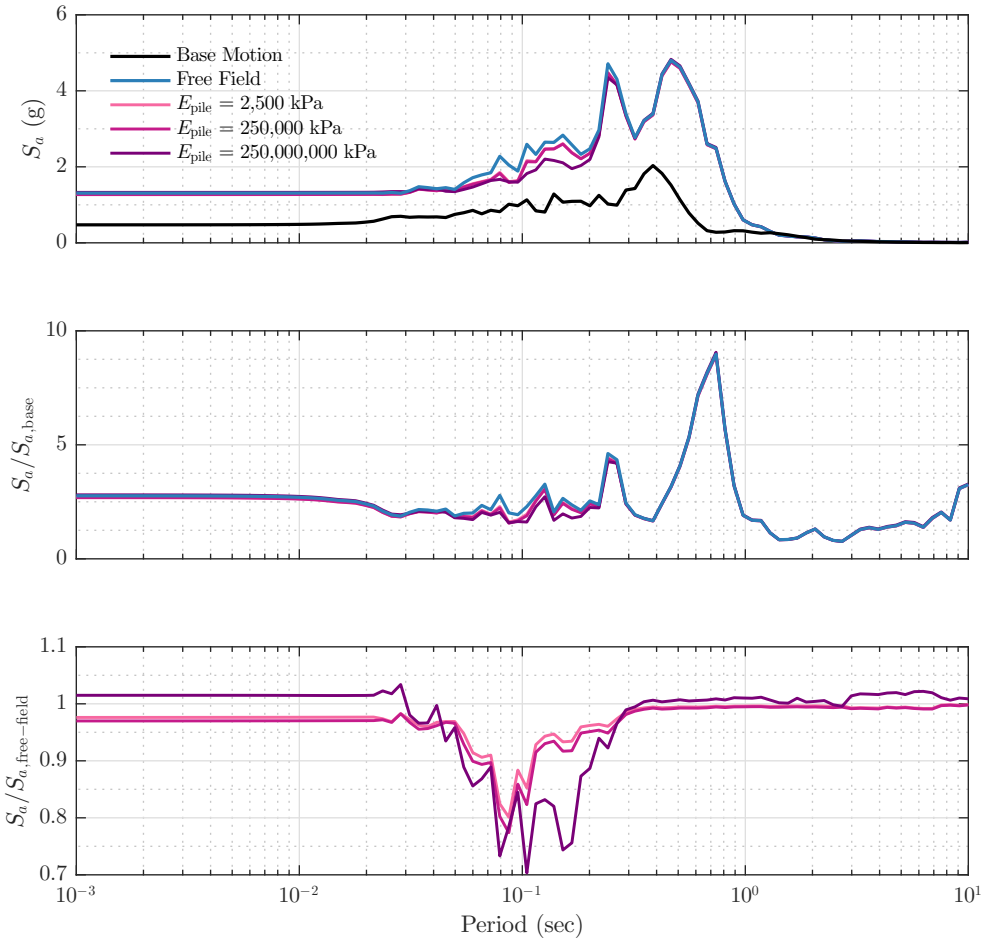

Figure 14.6: 5% damping acceleration response spectra at the soil surface $1D$ away from the pile head. The amplification ratio (surface to the base motion) as well as the ratio between the surface motion spectrum next to the pile and the free field motion spectrum are presented as well.

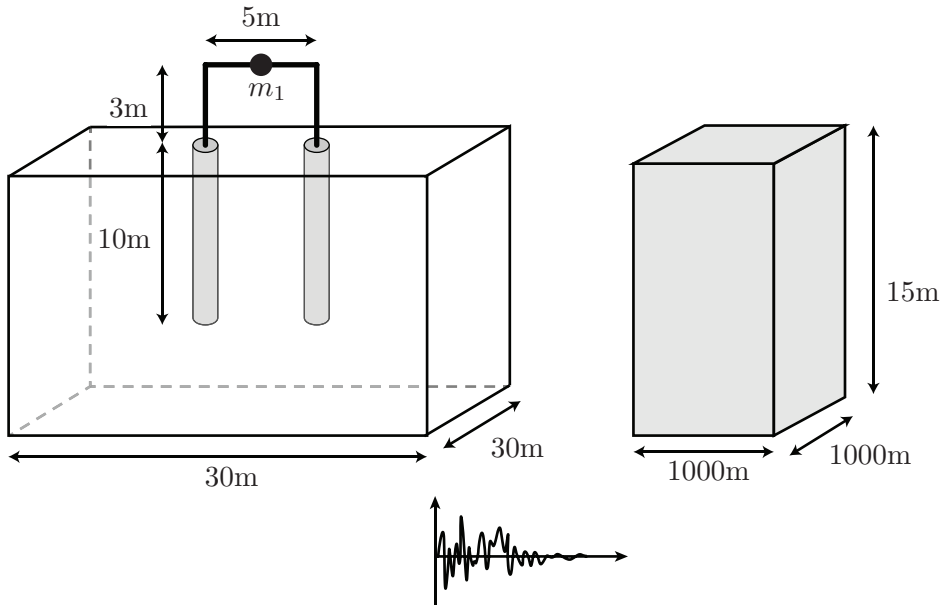

Figure 14.7: Bridge bent configuration.

14.2 Analysis of a Simple Bridge Bent

In this section the dynamic response of a bridge bent supported on deep foundations is investigated. Figure 14.7 shows a schematic of the bent and soil domain configuration. As shown in the figure, a massive soil column is used to impose the free field response. All boundaries of the model are tied to this column. This soil column is modeled as a shear

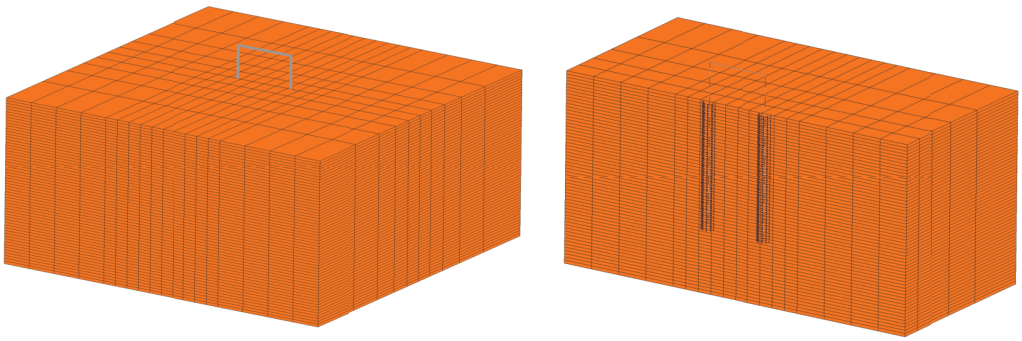

Figure 14.8: Finite element mesh used for the simple bridge bent model.

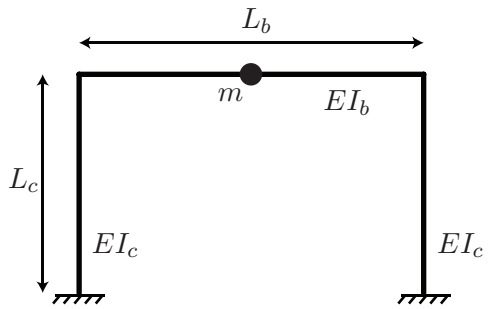

Figure 14.9: A simplified model of the bridge bent problem.

beam and the input motion is applied to the base. The Gilroy No. 1 motion shown in Figure 14.1 is used in this example. Table 14.2 summarizes the material properties used for the soil and the pile domain, as well as, the superstructure mass concentrated in the middle of the beam. A linear elastic soil is used in this example. Figure 14.8 illustrates the finite element mesh created for the model. The figure also shows a section cut of the model to illustrate the embedment of the pile foundations. Two cases are considered in the analysis. One with a mass representing a massive super-structure and one without the mass. Furthermore, the input motion is applied in two perpendicular directions; parallel to the plane of the bridge bent and perpendicular to this plane.

Table 14.2: Properties used for simple bridge bent analysis.

Soil	E	40,000.0 kPa
	ν	0.33
	ρ	1.7 Mg/m^3
Pile	r	0.25 m
	E	2,500,000.0 kPa
	ν	0.2
	ρ	0.0 Mg/m^3
Mass	m	40.0 Mg

Figure 14.10 shows pile and column response profiles of displacement, nodal rotation, bending moment and shear force for all cases. Shaded areas in the plots illustrate the range of results obtained during the earthquake shaking. The figure shows the results for both the massless bent and the case in which the superstructure mass is considered. Figure 14.10a shows the results for the case where motion is applied in the out-of-plane direction of the bent. Figure 14.10b on the other hand, shows the results for the case where the motion is applied in the in-plane direction of the bent. The displacements and shear forces are recorded in the direction parallel to the direction of motion while nodal rotations and bending moments are recorded in the perpendicular direction to the direction of motion.

As expected the superstructure swings more above the ground in the cases where a superstructure mass is considered. As a result more bending moment and shear force demands are observed in both input motions. However the effect of the superstructure mass on the behavior of the embedded part of the pile is small, nonetheless not zero.

It is also noticeable that when using an in-plane motion, the bent displacements are larger than for the out-of-plane motion. This is a counter-intuitive result that deserves further analysis. For this purpose the bent in-plane and out-of-plane natural frequencies are evaluated and a final analysis considering a single-frequency motion with a frequency $f = 1$ Hz is considered. An approximate to the natural frequency of the bridge bent can be calculated for the simple case shown in Figure 14.9. Natural frequencies of such system in both in-plane and out-of-plane directions are

$$\omega_{\text{in-plane}} = \sqrt{\frac{24EI_c}{mL_c^3}\left(\frac{7\gamma + 6\beta}{4\gamma + 6\beta}\right)}, \tag{14.1}$$

$$\omega_{\text{out-of-plane}} = \sqrt{\frac{6EI_c}{mL_c^3}}, \tag{14.2}$$

where $\gamma = \dfrac{L_b}{L_c}$ and $\beta = \dfrac{EI_b}{EI_c}$. For the case considered here, these equations yield a natural frequency of 1.04 Hz, corresponding to a natural period of 0.96 s in the out-of-plane direction and 2.45 Hz and 0.41 s for the in-plane direction. Examination of the input motion accel-

eration response spectrum shown in Figure 14.1 shows that the Gilroy No. 1 motion will result in a greater response when applied to a system with the latter natural frequency than the former. This explains the greater displacement for the case where the motion is applied parallel to the bridge bent plane even though the system has higher stiffness considering the resistance caused by the frame. To further investigate this, the single-frequency, 1 Hz motion shown in Figure 14.2b is applied in both directions and results are shown in Figures 14.11 and 14.12. Since the frequency of this motion is closer to the out-of-plane natural frequency of the system, greater response is observed in the out-of-plane model. Figure 14.11 shows the structural demand profiles along the pile structure and Figure14.12 shows the displacement of the superstructure mass, confirming that the out-of-plane response is generally larger, particularly the displacement of the superstructure mass shows considerably greater response.

Returning to the Gilroy motion response, Figure 14.13 shows displacement response time histories for the superstructure. Figure 14.13a shows the response for the case where motion is applied in the perpendicular direction to the plane of bridge bent while Figure 14.13b shows the response for the case where motion is applied in the parallel direction to the bridge bent plane. As expected when the inertial forces of the superstructure are present, the superstructure oscillates at a different amplitude and frequency compared to the case when these inertial forces do not exist. Careful inspection of this figure confirms the simple calculation of the natural frequencies performed above where coincidence of the natural frequency of one case resonates more with the input motion compared to the other case. Figure 14.13a also shows that the mass oscillates at a frequency close to 1.04 Hz when the motion is applied perpendicular to the plane of the bridge bent whereas Figure 14.13b shows the mass oscillates at a higher frequency, close to 2.45 Hz, and at a greater amplitude when motion is applied parallel to the bridge bent plane.

Figures 14.14 and 14.15 show 5% damping acceleration response spectra for two points in the model. Figure 14.14 shows results for a point on the ground surface, exactly midway between the pile heads and Figure14.15 shows results for a point at the top of the super-

structure. Effects of the superstructure mass on the ground surface response are very small. Figure 14.14a and 14.14b show very small effect on the recorded ground motion due to presence of the pile. This could be due to the contrast between the superstructure natural period and the natural period of the soil block and the foundation system.

The contrast between the response of the bridge bent to motions in two directions is more visible in Figures 14.15a and 14.15b. These figures show superstructure mass 5% damping acceleration response spectra for both input motions. Both cases show amplification at periods close to the natural period of the superstructure for both directions of application of input motion. A connection can be made between Figures 14.14 and 14.15 by assuming the former approximates the input motion applied to a superstructure configuration with a fixed base as depicted in Figure 14.9 and the latter representing the response of such configuration when undergone the input motion. For this case we expect the spectral acceleration at the natural period of the superstructure obtained from Figure 14.14 to be equal to the peak acceleration of the superstructure mass obtained from Figure 14.15. Marked with a circle in Figure 14.14a and 14.14b are the spectral acceleration at the natural frequency of the system corresponding to the direction of input motion. Superstructure peak acceleration is marked with a circle in Figures 14.15a and 14.15b. Although not the same, we can see that values obtained from Figure 14.14 present a first order approximation to the more elaborate model shown in Figure 14.15.

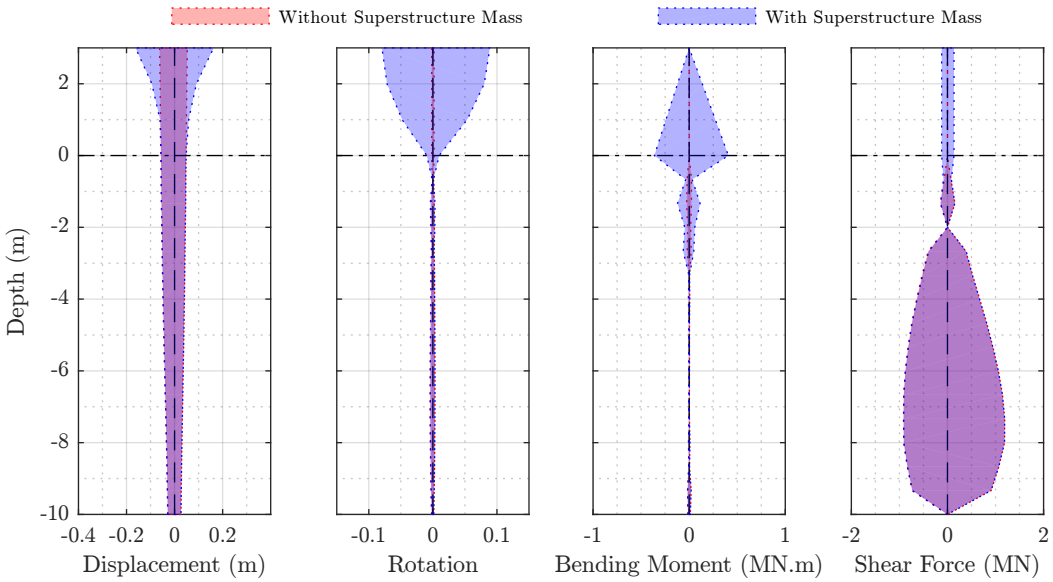

(a) Motion applied perpendicular to the bent in-plane horizontal direction.

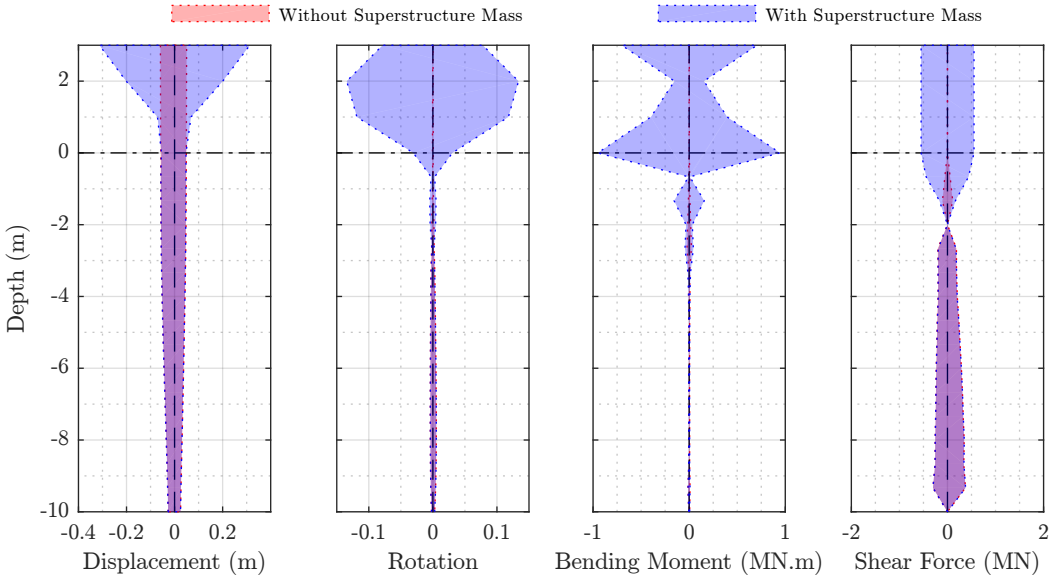

(b) Motion applied parallel to the bent in-plane horizontal direction.

Figure 14.10: Profile of pile response to Gilroy motion. The shaded area represents the range of values.

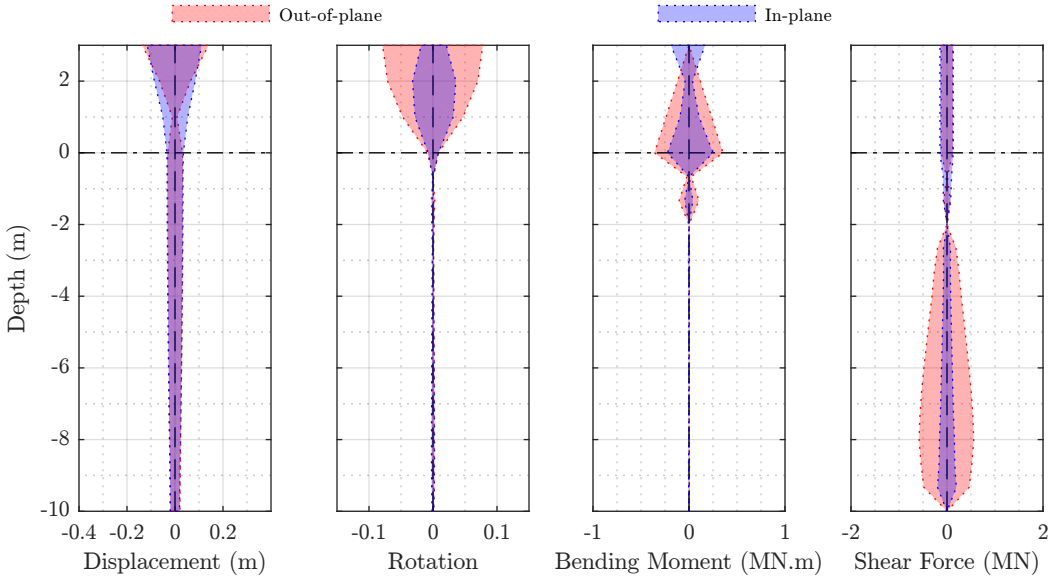

Figure 14.11: Profile of pile response to a 1 Hz motion applied in directions parallel and perpendicular to the plane of the bridge bent. The displacement and shear forces are recorded in the direction of applied motion while nodal rotation and bending moments are recorded in the perpendicular direction. Shaded areas represent the range of values.

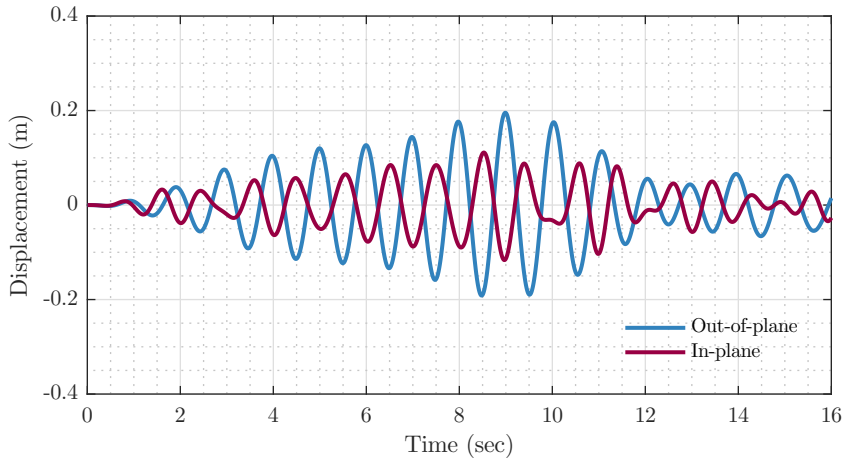

Figure 14.12: Pile head displacement response to a 1 Hz motion applied in directions parallel and perpendicular to the plane of the bridge bent.

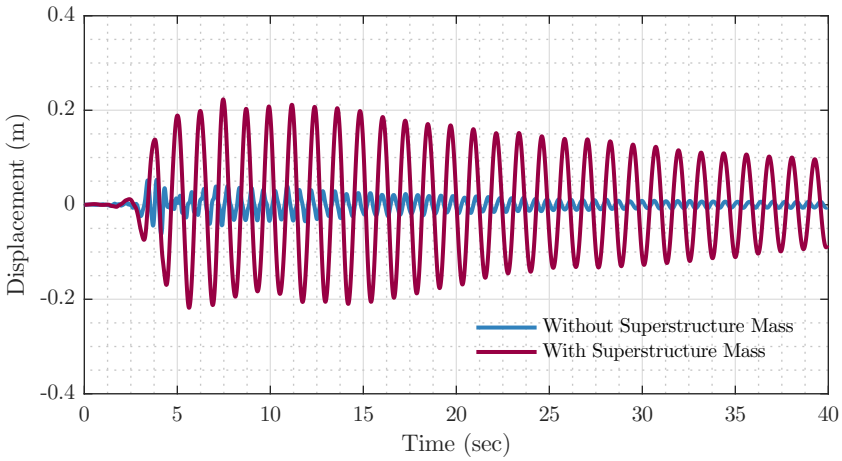

(a) Motion applied perpendicular to the bent in-plane horizontal direction.

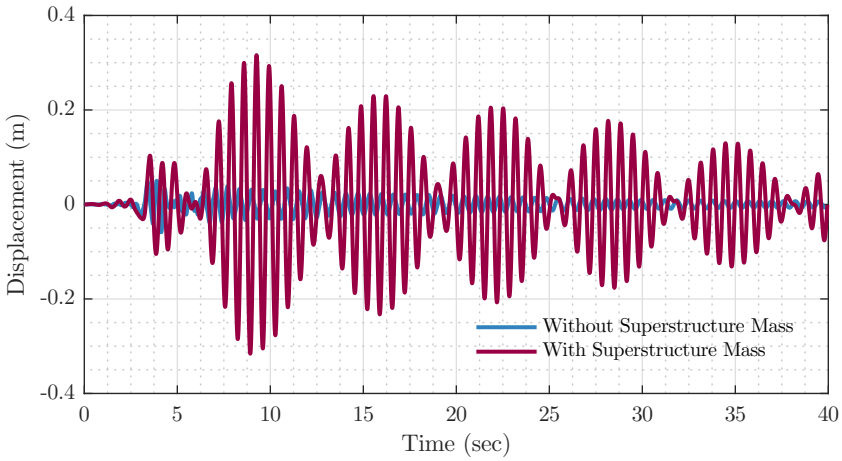

(b) Motion applied parallel to the bent in-plane horizontal direction.

Figure 14.13: Superstructure displacement response time history to Gilroy motion.

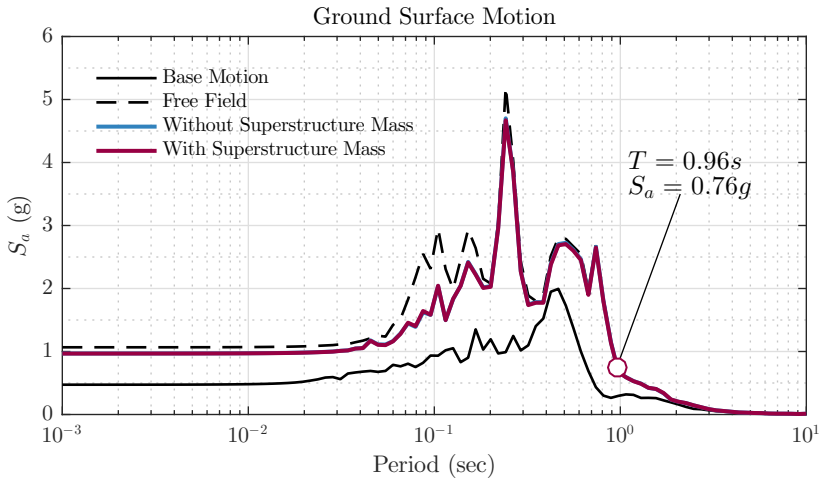

(a) Motion applied perpendicular to the bent in-plane horizontal direction.

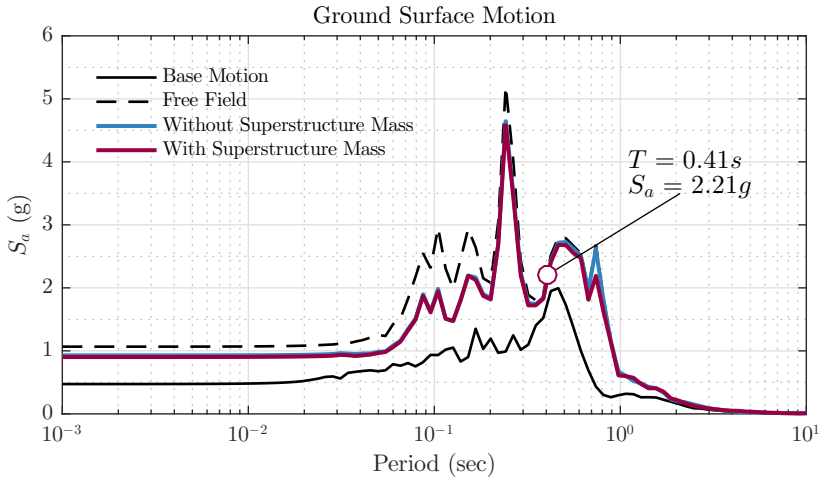

(b) Motion applied parallel to the bent in-plane horizontal direction.

Figure 14.14: Ground surface (soil) acceleration response spectrum (5% damping) at a point midway between pile heads (Gilroy motion).

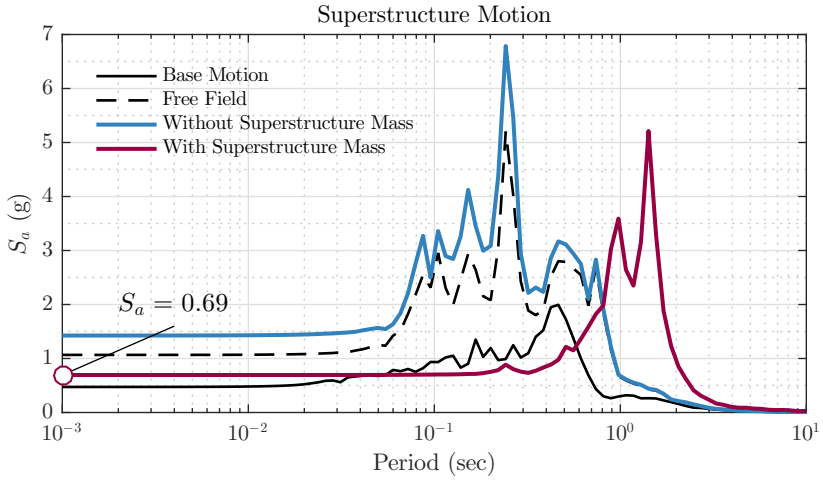

(a) Motion applied perpendicular to the bent in-plane horizontal direction.

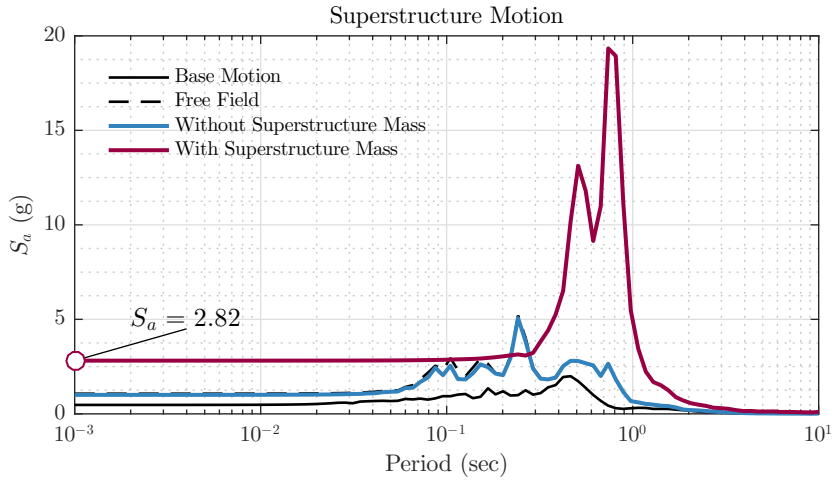

(b) Motion applied parallel to the bent horizontal in-plane direction.

Figure 14.15: Superstructure acceleration response spectrum (5% damping) for Gilroy motion.

14.3 Dynamic Analysis of Lateral Spreading

In this example the constitutive model and mortar embedded interface elements introduced in this study are combined to perform a 3D analysis of a pile embedded in a soil medium with a layer of liquefiable material. Two geometries are considered here: 1) a flat 2% sloping ground surface, and 2) a geometry similar to the Llacolén bridge northeastern approach considered in Chapter 3. In both cases massive soil columns assuming shear beam behavior are used to model the far field response. In the second model two massive soil columns are used to represent the up-slope and the down-slope far field behavior and the side boundaries are fixed against movement in the lateral direction. The pore water pressures on the crustal layer are set to zero in order to prevent excess pore water pressures to build up in that layer. The ground water table is assumed to be at a depth 5.4 m below ground surface (below the up-slope ground surface in the second model). Figures 14.16 and 14.17 show schematics of these two models.

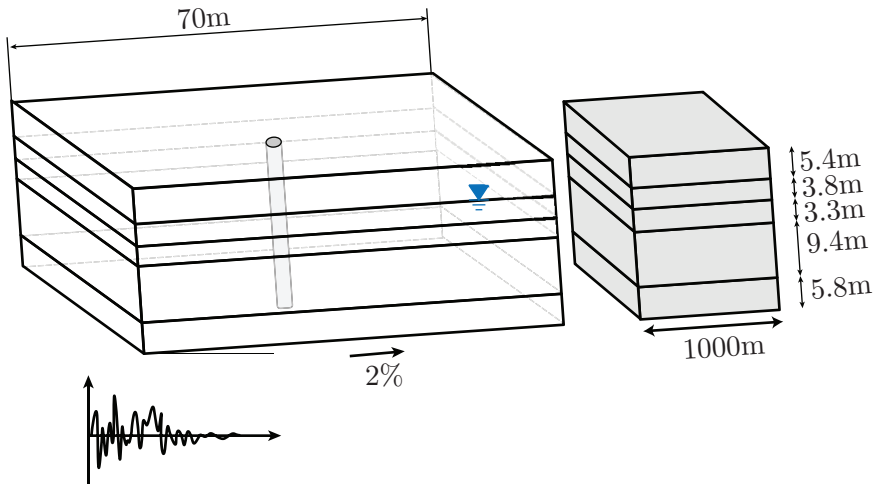

Figure 14.16: Configuration of the model used for dynamic analysis of lateral spreading.

Tables 14.3 and 14.4 summarize the material properties used in this study. Other model parameters for the Manzari-Dafalias constitutive model used for this problem are tabulated

Table 14.3: Pile structure properties used in the lateral spreading problem.

Property	r (m)	E (kPa)	G (kPa)
Value	0.75	19,000,000.0	7,600,000.0

Table 14.4: Soil material properties used for dynamic analysis of lateral spreading.

Layer	G_0	ν	e	ρ (Mg/m^3)	k (m/s)
Loose Sand	37.67	0.35	0.77	1.7	1.0×10^{-5}
Dense Sand	63.77	0.3	0.66	2.0	1.0×10^{-4}
Medium Dense Sand	37.67	0.33	0.77	1.8	1.0×10^{-3}
Gravel	108.51	0.28	0.55	2.1	1.0×10^{-3}

in Table 14.5 and correspond to the calibrated values for the Toyura sand (Dafalias and Manzari, 2004).

Figure 14.18 shows the finite element mesh used for modeling the flat ground case. A section cut is also included in the figure to depict the embedment of the pile. Two cases are considered here. In each case, the Gilroy No. 1 motion is applied to the base of the model in one of the horizontal directions; parallel to the 2% slope and perpendicular to the slope.

Permanent horizontal displacement contour plots at the end of shaking for both motion directions on the deformed configuration of the system are shown in Figure 14.19. The figure shows a lateral spreading displacement profile which is slightly different from the tri-linear profile used in the quasi-static lateral spreading models presented in Chapter 3. Also the figure shows more displacements in the case motion is applied parallel to the slope direction, than in the case motion is applied perpendicular to the slope direction.

Figure 14.20 shows structural demand profiles for the sloping flat ground model. Displacement, nodal rotation, bending moment and shear force profiles for both excitation directions are included in the figure. Shaded areas show the range of structural demand whereas the

Table 14.5: Calibrated parameters for Manzari-Dafalias constitutive model for Toyura sand (Dafalias and Manzari, 2004).

Parameter		Value
Critical State	M	1.25
	c	0.712
	λ_c	0.019
	e_0	0.934
	ξ	0.7
Yield Surface	m	0.01
Plastic Modulus	h_0	7.05
	c_h	0.968
	n^b	1.1
Dilatancy	A_0	0.704
	n^d	3.5
Fabric Tensor	$z_{\max}$	4
	c_z	600

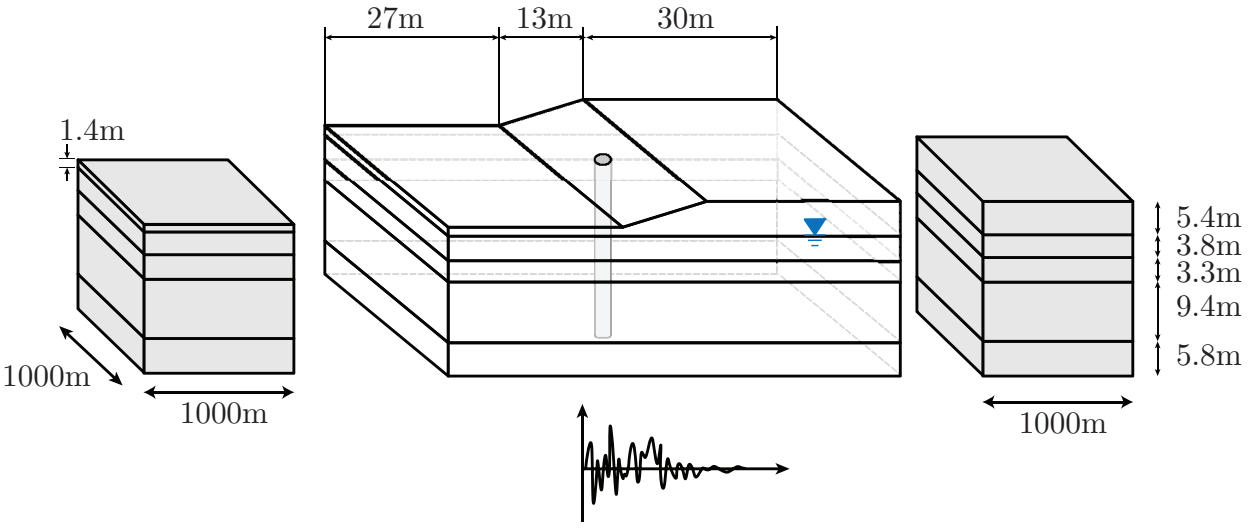

Figure 14.17: Configuration of the model used for dynamic analysis of lateral spreading.

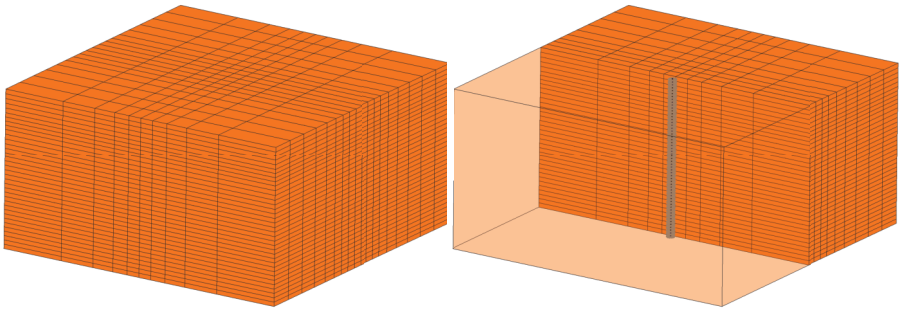

Figure 14.18: Finite element mesh used for dynamic analysis of lateral spreading.

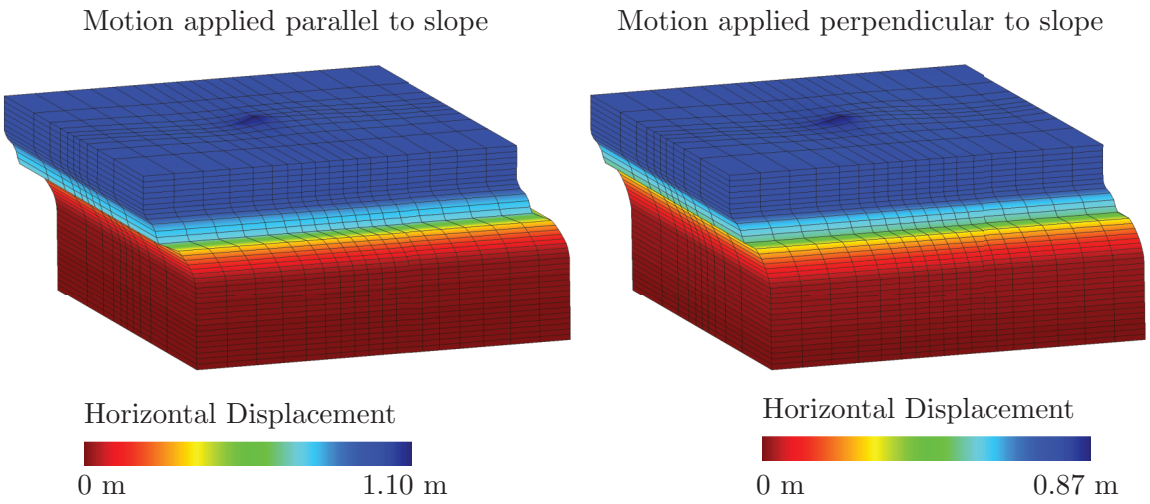

Figure 14.19: Permanent deformation of the model after application of the motion.

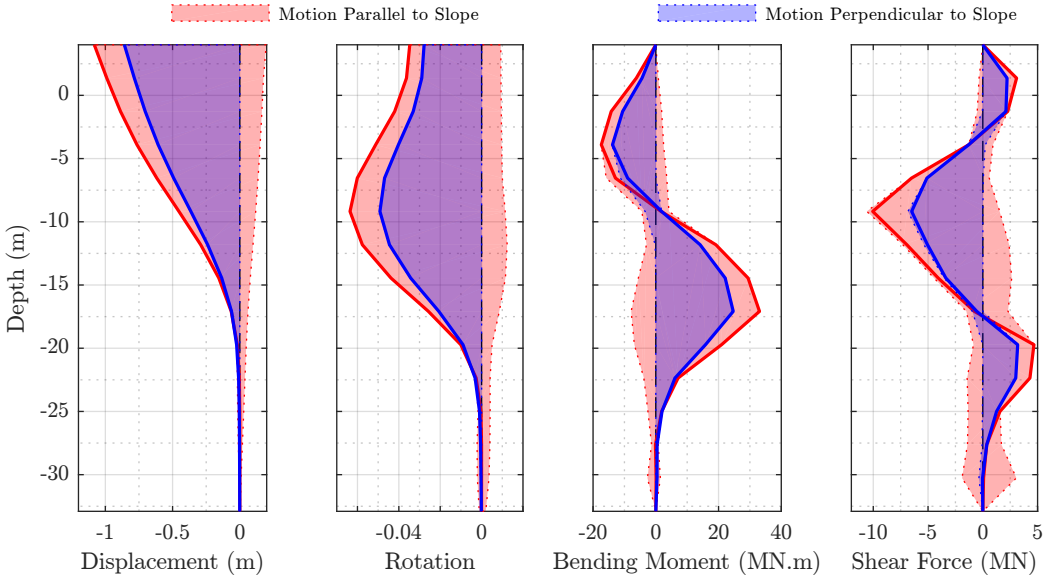

Figure 14.20: Pile response profile for two motion directions. Shaded areas show the range of values for each parameter and the solid line shows the permanent (residual) values.

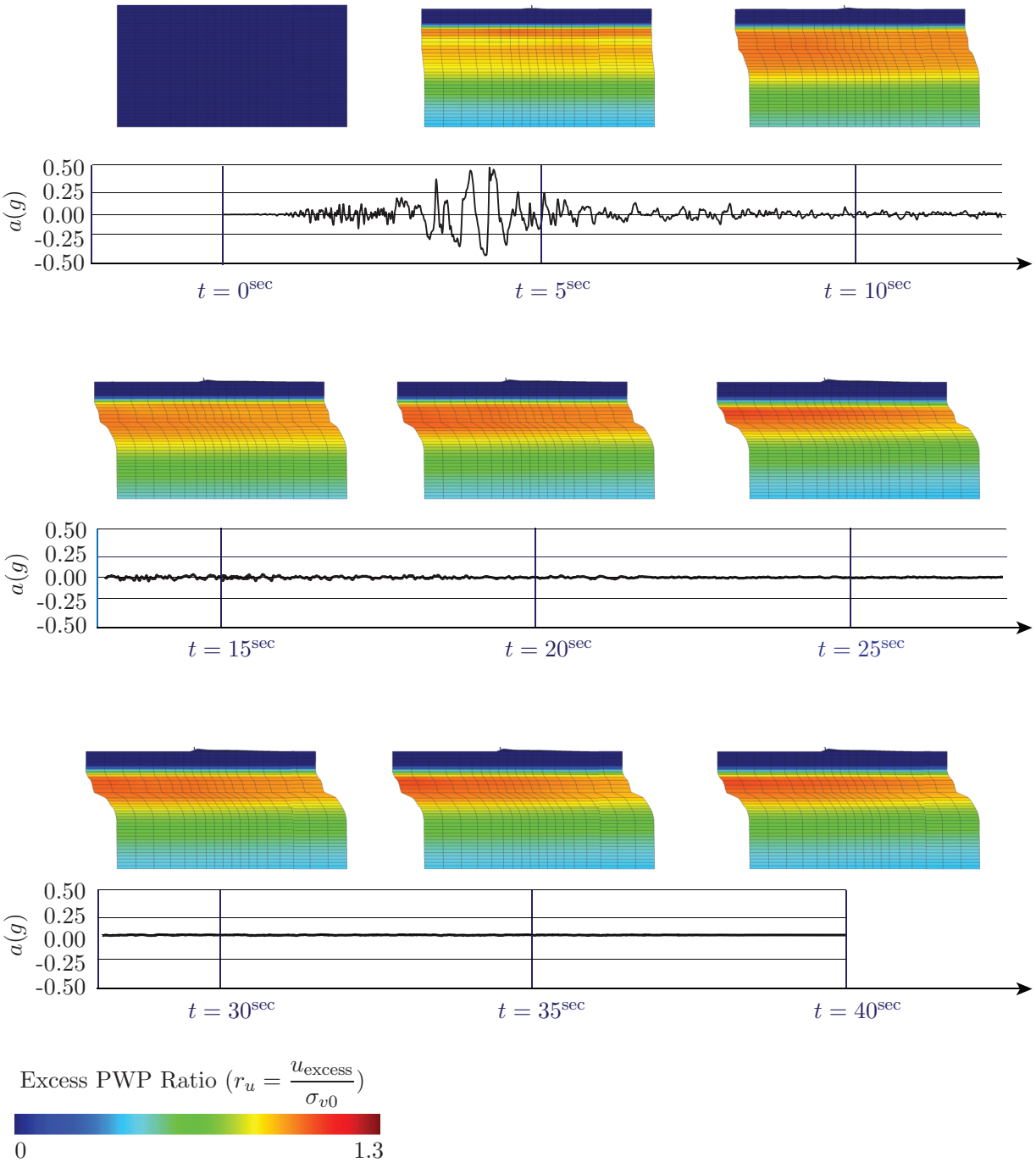

Figure 14.21: Contour plot of the excess pore water pressure ratios at different times during the earthquake excitation (deformation exaggerated 10 times).

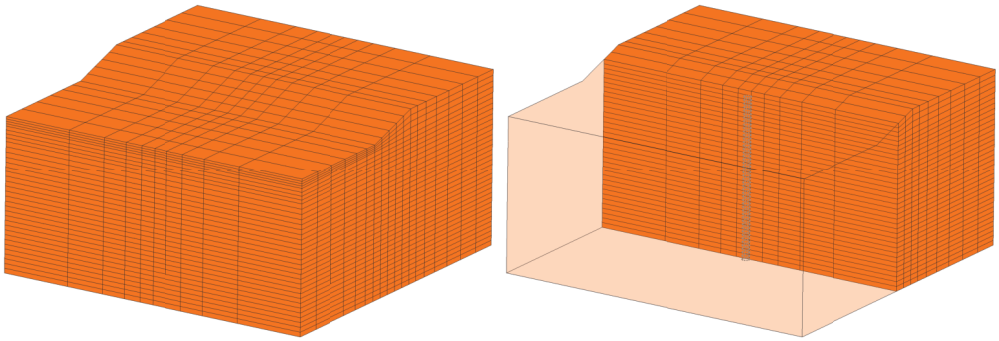

Figure 14.22: Finite element mesh used for dynamic analysis of lateral spreading.

solid lines show permanent (locked in) structural demands in the pile. Again, the figure shows that structural demands are greater for the case where the motion is applied parallel to the slope.

The development of excess pore water pressures in the system during the earthquake excitation is shown in Figure 14.21. The figure shows the excess pore water pressure ratio, r_u, defined as $u_{\text{excess}}/\sigma'_{v0}$ where u_{excess} denotes the excess pore water pressures and σ'_{v0} represents the initial vertical effective stress. The time history of the base acceleration is shown for reference and contour plots are located near representative times. The figure shows that as the motion progresses, the excess pore water pressures build up causing liquefaction in the soil. With loss of strength in liquefied soil the crust moves in the slope direction as expected. Dissipation of excess pore water pressures require performing the analysis for longer duration which in this case is very time consuming due to the size of the model.

The finite element mesh used for the second case is shown in Figure 14.22. A section cut is also included in the figure to show the embedment of the foundation. The Gilroy No. 1 motion is also used in this case. Instead of applying the motion in two directions, two soil permeability values are considered in this case. In the first case, a very large permeability of $k = 1.0$ m/s is assigned to all soil layers whereas in the second case values presented in Table 14.4 are used. A large permeability avoids generation of excess pore water pressure which prevents liquefaction of the soil.

Figure 14.23 shows contours of permanent deformation after application of the motion, for both cases with different soil permeability values. The case with large permeability shows a displacement pattern indicative of a slope failure without much of far field lateral displacements. On the other hand, the case with less permeable soil layers show deformation pattern indicative of a combination of slope failure and lateral spreading. The lateral spreading is more visible in the down-slope far field results. This is because the liquefaction in the layers under the down-slope region happens earlier than elsewhere due to lower confining pressures.

Figure 14.24 shows the structural demand profiles for both cases with different permeability values. Shaded areas in the figure show the range of structural demands in terms of displacement, nodal rotation, bending moment and shear force. As expected, demands are considerably higher in the case with smaller soil permeabilities involving lateral spreading. The solid lines represent the permanent structural demands at the end of shaking.

Figure 14.25 illustrates contours of excess pore water pressure ratio on the deformed mesh over time for the case with smaller soil permeabilities. The time history of the base acceleration is shown for reference and contour plots are located near representative times. As expected the excess pore water pressures increase over time resulting in liquefaction of the underlying layers. This is more prominent in the layers under the down-slope region due to lower confining pressures there. As a result of liquefaction, the upper dry layers slide towards the down-slope direction causing lateral spreading. Dissipation of the excess pore water pressures require performing the analysis for longer duration which is computationally expensive in this case.

Figure 14.26 shows the soil response at four locations in the model with smaller soil permability as described below. The first column presents stress-strain plots, the second column shows stress path plots, the third column shows excess pore water pressure ratio plots and the fourth column shows time history of volumetric strain plots. Plots labeled with (a) are for a point in the up-slope part of the main mesh 6 m below the reference elevation, (b) corresponds to a point at the same elevation in the up-slope boundary soil column, (c) shows the results for a point at the same elevation but in the down-slope part

of the main mesh and (d) corresponds to a point at the same elevation in the down-slope boundary soil column. The reference elevation is at the ground surface at the down-slope of the model. Complete liquefaction can be inferred from the excess pore water pressure ratio plots. The stress path plots clearly show the cyclic mobility behavior and liquefaction of this particular point in the soil domain. Large loss of stiffness is observed in the stress-strain plots.

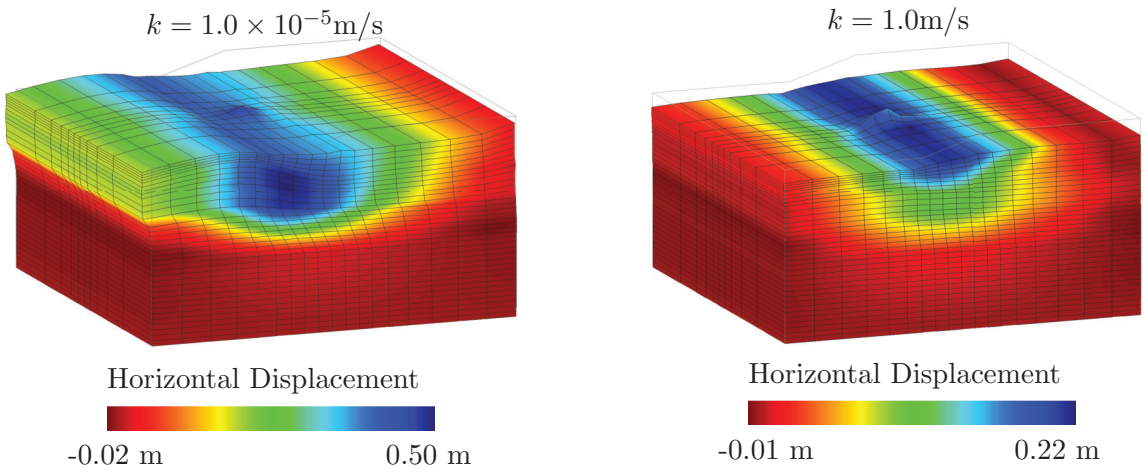

Figure 14.23: Ultimate deformation of the model after application of the motion.

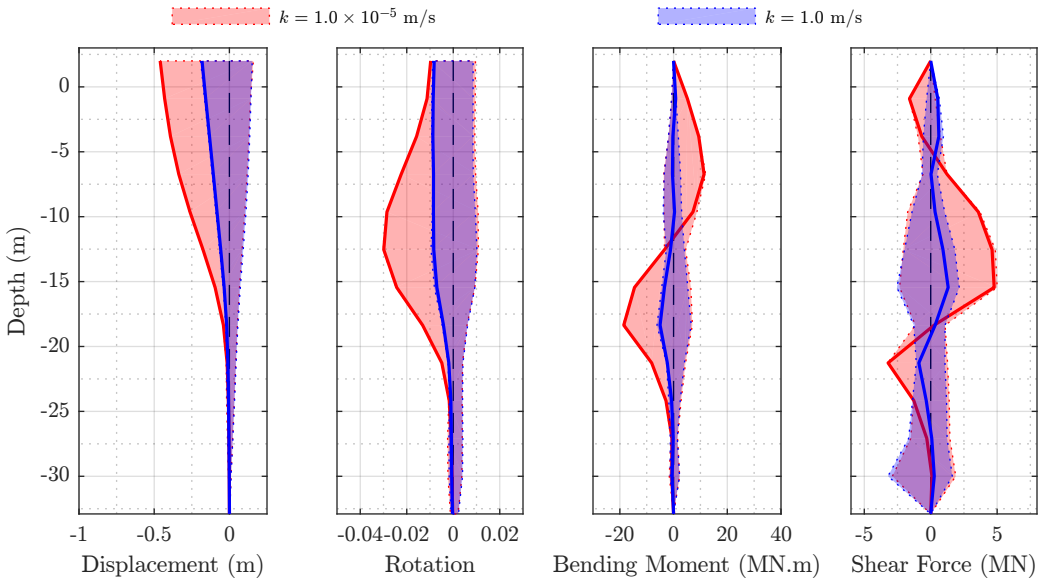

Figure 14.24: Pile response profile for two soils with different permeability values. Shaded areas show the range of values for each parameter and the solid line shows the permanent (residual) values.

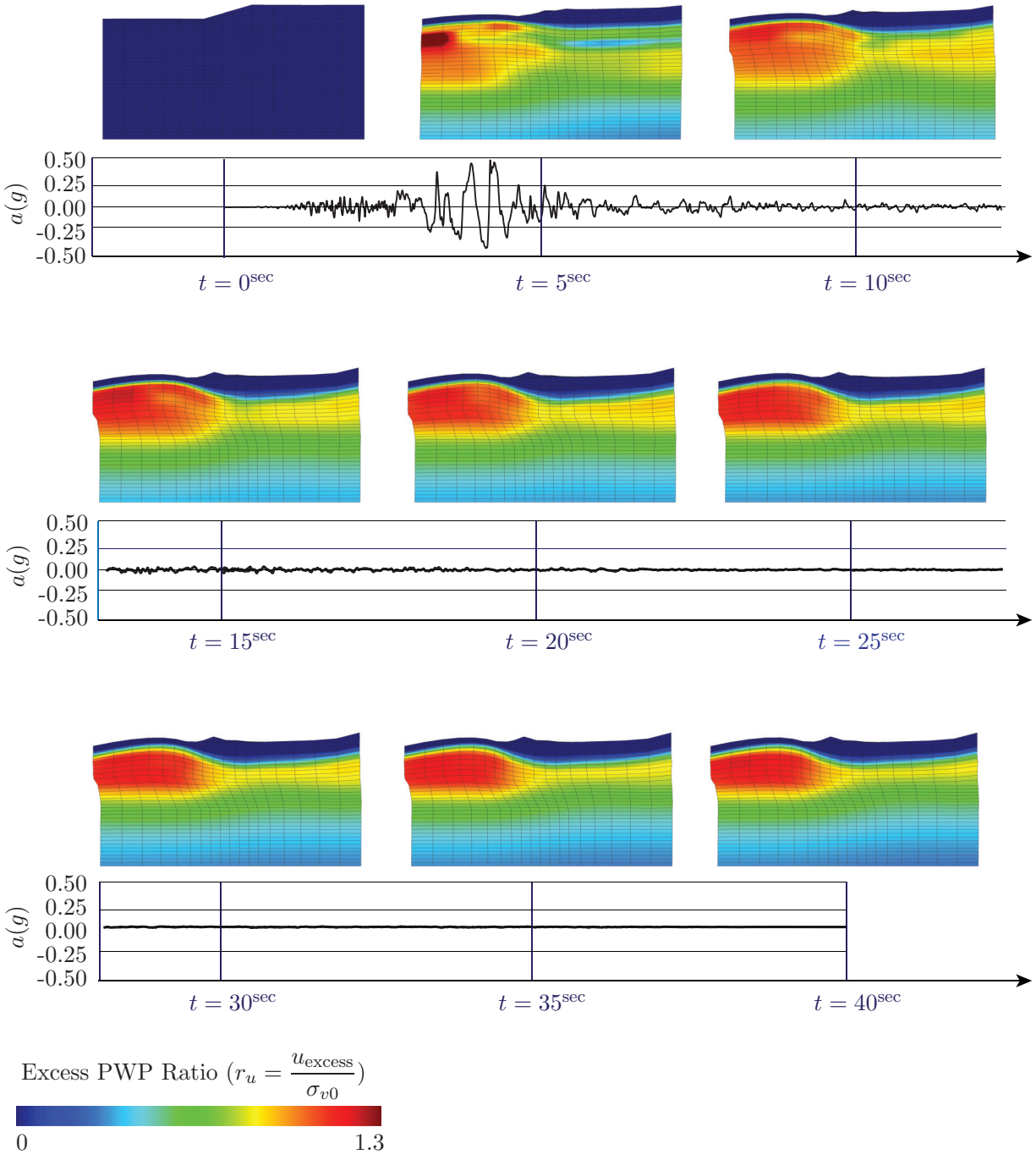

Figure 14.25: Contour plot of the excess pore water pressure ratios at different times during the earthquake excitation (deformation exaggerated 10 times).

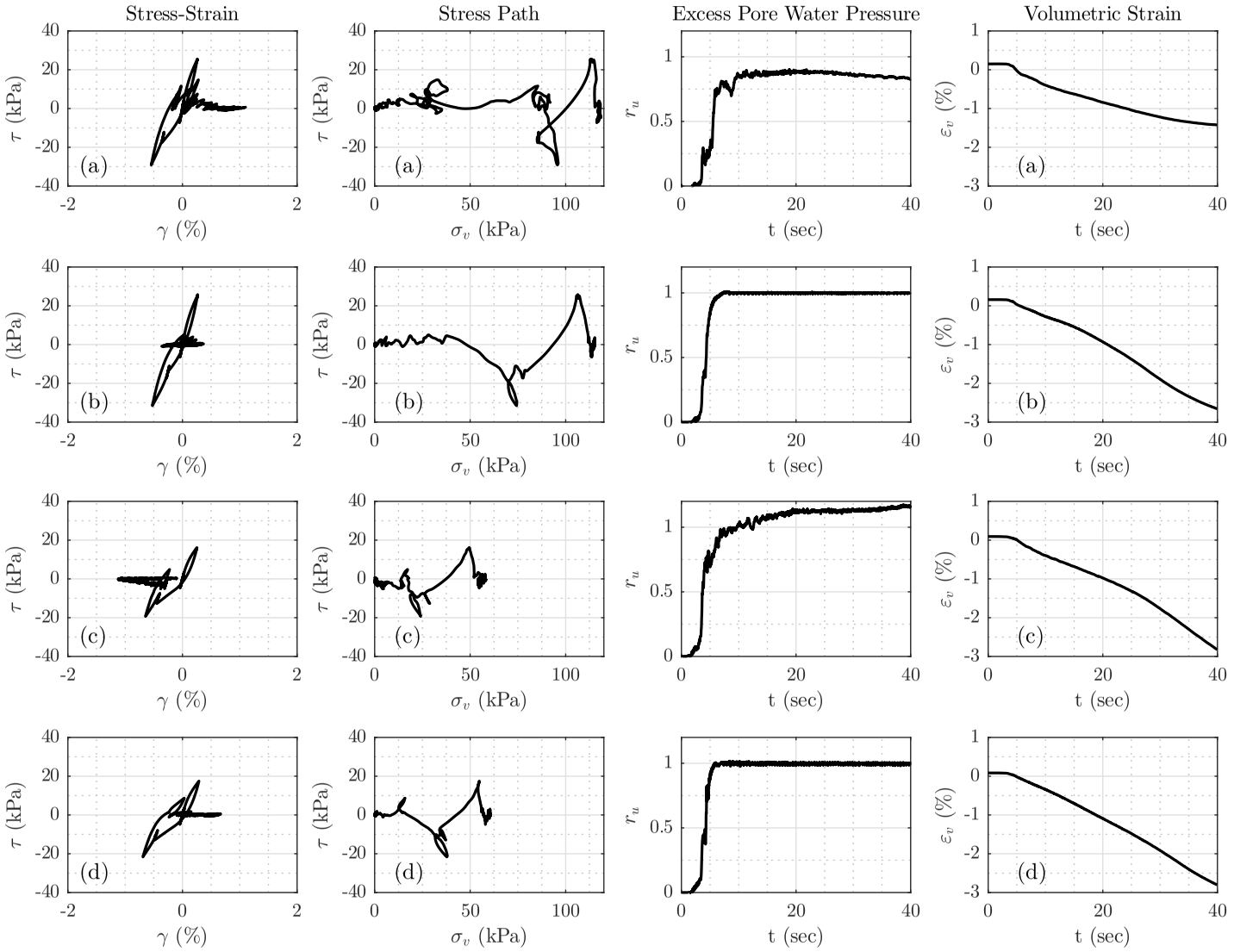

Figure 14.26: Plots of stress-strain behavior, stress path, excess pore water pressure built-up and time history of the volumetric strain at 4 different locations. Read page 285 for details about this figure.

Chapter 15

RESEARCH OUTCOMES AND SUGGESTIONS FOR FUTURE STUDIES

This dissertation presents numerical tools for the analysis of bridge foundations subject to liquefaction and lateral spreading. Specifically, constitutive modeling and soil structure interaction aspects of such geotechnical earthquake engineering problems are considered. This is done in the pursuit of performing 3D dynamic analysis of pile foundations buried in liquefiable soils subject to lateral spreading. This research includes a brief review of pile design methodologies for lateral spreading loading cases, development and analysis of an appropriate case history bridge, development and implementation of an appropriate constitutive model and an embedded interface element, and several examples presenting the applicability of these tools.

15.1 Summary and Conclusions

This section presents a summary of the work completed as part of this research. Basic aspects of each part are reiterated and conclusions drawn from these studies are emphasized.

15.1.1 Design and modeling of piles in laterally spreading ground

The Washington State Department of Transportation (WSDOT) recently changed the design procedure for design of bridge foundations subject to liquefaction-induced lateral spreading to include the effects of foundation pinning resistance. The procedure is used by the California department of transportation (Caltrans) as well. The procedure makes a distinction between cases where the mobilized soil mass is too large and the bridge foundation does not provide

much resistance to soil mass movement (unrestrained case) and the case where the foundation can provide enough resistance to impede soil mass movement to some extent (restrained case).

For the "unrestrained case" the method uses a Beam on Nonlinear Winkler Foundation (BNWF) model to analyze the pile (or equivalent single pile in the case of a pile group) and assumes the soil displacement is large enough to mobilize the full passive resistance of the soil. On the other hand, the restrained case uses the "pile pinning" analysis methods (Martin et al., 2002; Boulanger et al., 2006; Ashford et al., 2011) to estimate the near-field soil movement and uses the assumption of compatibility between the foundation resistance and embankment deformation during lateral spreading.

15.1.2 Llacolén bridge

In continuing the research performed by the University of Washington Geotechnical Modelling research group for the Washington State Department of Transportation started by McGann et al. (2015), the Llacolén bridge located in Chile was chosen as a case history for a bridge bent that was subject to loads from liquefaction-induced lateral spreading. The case history bridge foundation considered by McGann et al. (2015) included unique features in terms of three-dimensional site geometry. The Llacolén bridge provided a different aspect, having a peculiar structural geometry. In this analysis constitutive models and interface elements available in OpenSees were used.

3D finite element models

A Quasi-static 3D finite element analysis of the Northeastern Llacolén bridge approach bent was performed to identify and evaluate mechanisms leading to foundation failure in such cases. The quasi-static model was based on the assumption that liquefaction had already happened and inertial effects were ignored. As a result of these assumptions the lateral spreading kinematic loading was applied through a tri-linear deformation profile applied to the boundaries of the model. Reduction in soil strength due to liquefaction was considered by assigning post-liquefaction properties to a pressure-independent J2-plasticity type material

model. Fiber cross sections were used to account for the nonlinearity of pile structural elements. Existence of the expansion gap in the bridge deck was also accounted for using a compression-only spring including a gap.

Overall, observations from the bridge site matched to results obtained from the 3D FE model. It was found that the nonlinear behavior of the pile structural elements can be very important as their behavior may change the overall failure mechanism. The closure of the expansion gap effectively impeded further movement of pile heads due to the resistance provided by the deck axial stiffness. It was shown that in the case of the Llacolén bridge, structural demands in the transverse direction (perpendicular to the direction of lateral spreading) played an important role and must not be ignored. Such effects cannot be captured using simplified one-dimensional BNWF models. These three-dimensional effects also resulted in a range of structural demands in different piles whereas in one-dimensional models this could not be observed.

Simplified BNWF models

A series of BNWF models were conducted following the procedure elaborated by WSDOT and Caltrans geotechnical design manuals and based on the *pile pinning* procedure (Martin et al., 2002; Boulanger et al., 2006; Ashford et al., 2011). A comparison between the 3D and 1D numerical model results revealed that if full passive resistance is mobilized (like flow failure cases) 1D model results fall within the range of results obtained from the 3D models. However, if soil passive resistance is not fully mobilized, pile pinning analyses generally result in conservative estimation of demands. Although the WSDOT and Caltrans design procedures try to account for this by performing pile pinning analysis for the *restrained* case, such results were also seen in the *unrestrained* case which these procedures do not account for.

15.1.3 Constitutive modeling of granular soils

An advanced constitutive model based on bounding surface plasticity and critical state soil mechanics was presented and implemented in OpenSees. The Manzari-Dafalias material model was first introduced by Manzari and Dafalias (1997) and later enhanced by Dafalias and Manzari (2004). Several integration methods for nonlinear constitutive equations were explored and evaluated. A constitutive driver for integrating these equations outside a finite element framework was developed and implemented. This driver is capable of integrating equations under drained and undrained conditions and mixed stress-strain controlled loading paths. Different aspects of the nonlinear equation solver such as the tangent matrices were considered. It seems a 2^{nd} order explicit integration method (modified Euler method) is more efficient and accurate than 1^{st} order forward and backward Euler methods.

The Manzari-Dafalias model was used in several projects to evaluate its effectiveness in predicting ground response as the earthquake waves travel through layers of liquefiable soils. The *Prenolin* project was an international effort to benchmark numerical site response analysis against available recorded data at several sites in Japan. The Manzari-Dafalias material model implemented in the OpenSees finite element framework was used as one of the many numerical approaches considered by different teams in this project. Other projects such as *LEAP*, which is an ongoing project, was an effort to generate reliable centrifuge test data for evaluation of constitutive models. At the time of writing this dissertation two workshops had been held for the LEAP project and there are more under consideration.

Overall, the material model proved to be capable of capturing the behavior of granular soil subject to cyclic mobility and liquefaction. Results such as surface acceleration, excess pore water generation and dissipation and surface displacement, both in the vertical and lateral directions, were shown to be preperly simulated using the Manzari-Dafalias material model. Even though the material formulation is inherently capable of capturing soil behavior at different relative densities and under different confining pressures, in one stage of the LEAP project it proved to be difficult, if at all possible, to calibrate the model such that it

captured the behavior under different conditions using only a single set of parameters. In another project which was conducted to evaluate the effect of several modeling aspects, such as the numerical framework, constitutive model as well as the operator, it was shown that the material model should be calibrated for the conditions of the soil used in the centrifuge test, i.e. relative density and cyclic stress ratio, in order to reasonably predict the outcome.

15.1.4 Soil-structure interaction

A fiber overlay element formulation was implemented in OpenSees to motivate the idea of overlay elements. These elements either augment the underlying element with additional stiffness due to the existence of an additional element (e.g. stiffness of reinforcement elements added to a solid element representing the concrete matrix) or create the coupling between two or more elements usually occupying the same location in space (e.g. coupling between a pile surface and the surrounding soil by the interface behavior). The fiber overlay element can be used for modeling reinforced soil slopes in the context of geotechnical engineering. A convergence study performed on this element using a reinforced elastic beam model showed that the element converges to an analytical solution.

To simplify modeling the interaction between a pile represented by a linear 1D element with 6 nodal degrees of freedom and the surrounding soil represented by solid elements with 3 nodal degrees of freedom, an interaction surface around the pile representing the actual pile side boundaries was defined and interaction elements enforcing the bonding condition in a strong sense were developed and implemented. These elements were shown to lock and results tend to zero as finer discretizations were used.

The idea of mortar elements was applied to the interaction surface between a pile boundary and the surrounding soil. Perfect bonding conditions were applied using this formulation in a weak sense and was shown that these elements do not suffer from the locking issue as their strong form counterparts. A convergence study showed that these elements converge to a solution close to a solution obtained from a 3D model with the pile modeled using solid elements. Several examples of models using such elements were presented in this dissertation;

including a single pile under lateral loads, a single pile under lateral spreading kinematic profile, a group of piles under lateral spreading kinematic profile and finally dynamic analysis of a single pile under laterally spreading ground conditions.

15.1.5 3D dynamic analyses of piles in laterally spreading ground

Using the tools developed and implemented in this research, a 3D dynamic analysis of a pile embedded in a soil mass consisting of liquefiable layers of soil was performed and it was shown that the tools implemented in this study facilitate such analysis dramatically.

15.2 Suggestions for Future Research

The research performed in this dissertation opens up several paths for future research. Suggestions for future developments include but are not limited to: (1) perform additional 3D modeling and analysis of case history bridge foundations to evaluate and fine tune the current design methodologies; (2) investigate the validity of 3D quasi-static analyses by performing dynamic analyses; (3) expand and refine the Manzari-Dafalias model to eradicate its deficiencies; (4) expand and refine the embedded elastoplastic beam interface elements by developing appropriate constitutive behavior to represent the nonlinear response of the pile-soil interface; (5) add a contact formulation to the mortar elements; (6) perform parameter studies using these tools to inform and evaluate design methodologies.

15.2.1 Additional case study evaluations

The Llacolén bridge in Chile provides a case history with important three dimensional effects due to the peculiar bridge bent geometry. Other case histories can be evaluated using the same approach to investigate different geometries or parameters not included in this research. There are several aspects of the model that can be refined such as considerations for the bridge deck, considerations for the expansion gap, connections or other sections of the bridge.

In addition, it seems appropriate to evaluate the pile pinning procedure using similar types of 3D finite element analyses. Especially for cases considered to be “unrestrained” in

the terminology of WSDOT and Caltrans methods, it is reasonable to analyze the validity of considering flow failure for the design of pile foundations.

15.2.2 Constitutive modeling

Several aspects of the Manzari-Dafalias model can be improved. There has been several attempts to improve its formulation to better capture the response of granular materials subject to cyclic loads. Probably the most promising and practical of them being the work done by Ziotopoulou and Boulanger (2013) who improved the formulation such that the model would be applicable to general trends of soil behavior. The issue with this improvement is that it was done only for 2D plane strain cases and extension of this model to 3D multiaxial cases would be very difficult.

The nonlinear integration of constitutive equations is another avenue in which researchers can step foot into and evaluate other methods to get a more robust and stable integration methods. The general family of geometric integration methods, of which the 4^{th} order Runge-Kutta is a member of, seems to be an appropriate place to start investigating more.

15.2.3 Soil-structure interaction

There are several aspects of the elements implemented in this research that can be a subject of future work. Refinements to the implementation can include adding different cross section geometry of the pile, improving the numerical area integration method and improving the algorithm for finding the interaction surface between the pile and the surrounding soil. The formulation can be even extended to the point that these elements could be used for simpler analyses of embedded walls and retaining structures.

The constitutive behavior at the interaction surface is another path for future improvements. A properly developed and implemented constitutive model for this surface can capture frictional behavior and provide a more realistic behavior. Using a more general view, the mortar elements can be augmented with contact mechanics to included the gap-forming behavior as well as frictional behavior at the surface.

The mortar formulation can be applied to evaluate the interaction between shell or plate elements and solid elements for a more realistic, and at the same time efficient, analysis of retaining walls and embedded structures. If augmented with contact mechanics, a solid-solid mortar formulation could be developed for non-conforming meshes where someone may need to model interfaces between soil and foundations (whether deep or shallow) by releasing underlying assumptions in the 1D or 2D simplified elements.

15.2.4 Parameter study using tools implemented in this research

The tools implemented in this research provide building blocks for certain problems in geotechnical earthquake engineering. A parameter study over these problems can be done to inform or evaluate current design methodologies and their underlying assumptions. With the power of parallel computation these days, parameter study using 3D finite element models are not far-reaching anymore.

Part V

APPENDICES

Appendix A

MITIGATION OF CONVERGENCE PROBLEMS USING SUB-STEPPING

A.1 Sub-stepping for Backward Euler Method (CPPM Method)

Due to nonlinearity of the constitutive equations and as a result of inherited drawbacks of Newton's iterative solution method, the implicit integration process from step n to step $n+1$ may not converge at all the time. One way to facilitate the convergence is to start the Newton iterations with an initial guess (initial starting point for iteration process) closer to the actual solution (e.g. Macari et al., 1997). Another way of getting around this problem is to improve convergence of Newton's method by using "Line Search" algorithms (e.g. Armero and Pérez-Foguet, 2002; Pérez-Foguet and Armero, 2002). If none of these methods prove effective in improving the convergence of integration step, smaller increments may be used. By performing the integration process over a set of smaller sub-steps, we can reduce the nonlinearity of the model behavior and therefore improve the convergence. A recursive algorithm can be used to locally divide a failed step into two equally sized sub-steps and if any of the sub-steps fail to converge further divide them into two smaller sub-steps. The sub-stepping process will be done for finite number of times before the integration step is declared divergent and integration process stops. This way an adaptive sub-stepping scheme is achieved but if the algorithm consistent tangent operator for the local integration method is not supplied to the global level solution iterations, the convergence rate of the global iterations will be jeopardized. The process to get the consistent tangent operator for a CPPM method with sub-stepping is described here (Pérez-Foguet et al., 2001).

Suppose the solution at step n (i.e. $\{\boldsymbol{\sigma}_n, \boldsymbol{\alpha}_n, \mathbf{z}_n, \dot{\gamma}_n\}^{\mathsf{T}}$) is known. In order to step forward to $n+1$ the following system of nonlinear equations is needed to be solved:

$$\begin{cases} \boldsymbol{\varepsilon}^{e}_{n+1} + \Delta\gamma_{n+1}\mathbf{R}_{n+1} - \boldsymbol{\varepsilon}^{e,\mathrm{tr}}_{n+1} = 0 & 6 \text{ equations} \\ \boldsymbol{\alpha}_{n+1} - \boldsymbol{\alpha}_{n} - \Delta\gamma_{n+1}\hat{\boldsymbol{\alpha}}_{n+1} = 0 & 6 \text{ equations} \\ \mathbf{z}_{n+1} - \mathbf{z}_{n} - \Delta\gamma_{n+1}\hat{\mathbf{z}}_{n+1} = 0 & 6 \text{ equations} \\ f_{n+1} = \|\mathbf{s}_{n+1} - p_{n+1}\boldsymbol{\alpha}_{n+1}\| - \sqrt{\frac{2}{3}}mp_{n+1} = 0 & 1 \text{ equation} \end{cases} . \tag{A.1}$$

We can linearize these equations with respect to the vector of unknowns

$$\{\boldsymbol{\sigma}_{n+1}, \boldsymbol{\alpha}_{n+1}, \mathbf{z}_{n+1}, \dot{\gamma}_{n+1}\}^{\mathsf{T}} \quad , \tag{A.2}$$

and use a Newton-like method to solve these nonlinear equations. Notice that in the equations above, the tensor valued functions are written in their compact symmetric vector form with 6 entries. For the sake of simplicity and clarity, these equations are represented by separating the known parameters and take them to the other side of the equation. This form of representation helps with the future algebraic manipulation and is shown below.

$$\underbrace{\begin{Bmatrix} \boldsymbol{\varepsilon}^{e}_{n+1} + \Delta\gamma_{n+1}\mathbf{R}_{n+1} \\ \boldsymbol{\alpha}_{n+1} - \Delta\gamma_{n+1}\hat{\boldsymbol{\alpha}}_{n+1} \\ \mathbf{z}_{n+1} - \Delta\gamma_{n+1}\hat{\mathbf{z}}_{n+1} \\ f_{n+1} \end{Bmatrix}}_{\mathcal{R}_{n+1}} = \begin{bmatrix} \mathbf{I} & & & 0 \\ & \mathbf{I} & & \\ & & \mathbf{I} & \\ 0 & & & 0 \end{bmatrix} \cdot \begin{Bmatrix} \boldsymbol{\varepsilon}^{e}_{n} \\ \boldsymbol{\alpha}_{n} \\ \mathbf{z}_{n} \\ \Delta\gamma_{n} \end{Bmatrix} + \begin{Bmatrix} \Delta\boldsymbol{\varepsilon} \\ \mathbf{0} \\ \mathbf{0} \\ 0 \end{Bmatrix} \quad , \tag{A.3}$$

where $\mathbf{I}$ is the 6×6 identity matrix and $\Delta\gamma$ is added to the equation for simplicity in later algebraic manipulations.

The global solution method iterates over $\Delta\boldsymbol{\varepsilon}$ to satisfy the equilibrium conditions. As a result of linearizing equilibrium equations with respect to $\Delta\boldsymbol{\varepsilon}$, the constitutive equations need to be linearized with respect to $\Delta\boldsymbol{\varepsilon}$ as well. Therefore, linearizing both sides of Equation A.3

with respect to $\Delta\boldsymbol{\varepsilon}$ we get

$$\frac{\mathrm{d}\,\mathcal{R}_{n+1}}{\mathrm{d}\,\Delta\boldsymbol{\varepsilon}} = \begin{bmatrix} \mathbf{I} & & 0 \\ & \mathbf{I} & \\ & & \mathbf{I} \\ 0 & & 0 \end{bmatrix} \frac{\mathrm{d}\,\{\boldsymbol{\varepsilon}^e_n, \boldsymbol{\alpha}_n, \mathbf{z}_n, \Delta\gamma_n\}^{\mathsf{T}}}{\mathrm{d}\,\Delta\boldsymbol{\varepsilon}} + \frac{\mathrm{d}}{\mathrm{d}\,\Delta\boldsymbol{\varepsilon}} \begin{Bmatrix} \Delta\boldsymbol{\varepsilon} \\ \mathbf{0} \\ \mathbf{0} \\ 0 \end{Bmatrix} \quad , \tag{A.4}$$

where

$$\frac{\mathrm{d}\,\{\boldsymbol{\varepsilon}^e, \boldsymbol{\alpha}, \mathbf{z}, \Delta\gamma\}^{\mathsf{T}}}{\mathrm{d}\,\Delta\boldsymbol{\varepsilon}} = \begin{bmatrix} d\boldsymbol{\varepsilon}^e/d\Delta\boldsymbol{\varepsilon} \\ d\boldsymbol{\alpha}/d\Delta\boldsymbol{\varepsilon} \\ d\mathbf{z}/d\Delta\boldsymbol{\varepsilon} \\ d\Delta\gamma/d\Delta\boldsymbol{\varepsilon} \end{bmatrix}_{19\times 6} \quad . \tag{A.5}$$

The left hand side of Equation A.4 can be written as

$$\frac{\mathrm{d}\,\mathcal{R}_{n+1}}{\mathrm{d}\,\Delta\boldsymbol{\varepsilon}} = \frac{\mathrm{d}\,\mathcal{R}_{n+1}}{\mathrm{d}\,\{\boldsymbol{\sigma}_{n+1}, \boldsymbol{\alpha}_{n+1}, \mathbf{z}_{n+1}, \Delta\gamma_{n+1}\}^{\mathsf{T}}} \cdot \frac{\mathrm{d}\,\{\boldsymbol{\sigma}_{n+1}, \boldsymbol{\alpha}_{n+1}, \mathbf{z}_{n+1}, \Delta\gamma_{n+1}\}^{\mathsf{T}}}{\mathrm{d}\,\Delta\boldsymbol{\varepsilon}} \quad . \tag{A.6}$$

Notice that the term $\dfrac{\mathrm{d}\,\mathcal{R}_{n+1}}{\mathrm{d}\,\{\boldsymbol{\sigma}_{n+1}, \boldsymbol{\alpha}_{n+1}, \mathbf{z}_{n+1}, \Delta\gamma_{n+1}\}^{\mathsf{T}}}$ is the Jacobian matrix of the aforementioned equations, $[J\,]$, and the first term on the right hand side of Equation A.4 will be zero. So Equation A.4 can be written as

$$\frac{\mathrm{d}\,\{\boldsymbol{\sigma}_{n+1}, \boldsymbol{\alpha}_{n+1}, \mathbf{z}_{n+1}, \Delta\gamma_{n+1}\}^{\mathsf{T}}}{\mathrm{d}\,\Delta\boldsymbol{\varepsilon}} = [J^{-1}_{n+1}] \cdot \begin{bmatrix} \mathbf{I} \\ \mathbf{0} \\ \mathbf{0} \\ 0 \end{bmatrix} \quad . \tag{A.7}$$

By defining the projection operator P as $P = \{[\mathbf{I}]_{6\times 6} \quad [\mathbf{0}]_{6\times 13}\}^{\mathsf{T}}$, the consistent tangent operator, $[C^{\sigma}_{n+1}]$, can be written as

$$[C^{\sigma}_{n+1}] = \frac{\mathrm{d}\,\boldsymbol{\sigma}_{n+1}}{\mathrm{d}\,\Delta\boldsymbol{\varepsilon}} = P^{\mathsf{T}} \cdot [J^{-1}_{n+1}] \cdot P \quad , \tag{A.8}$$

which is the 6×6 upper left block of the $[J^{-1}_{n+1}]$ matrix.

Now suppose due to sub-stepping, the strain increment is divided into two portions, $\beta\Delta\boldsymbol{\varepsilon}$ and $(1-\beta)\Delta\boldsymbol{\varepsilon}$. The consistent tangent operator for the first sub-step is calculated from the method described above. The only modification needed would be the size of integration step over this sub-step for which we have $\dfrac{\mathrm{d}\,\{\beta\Delta\boldsymbol{\varepsilon}, \mathbf{0}, \mathbf{0}, 0\}^{\mathsf{T}}}{\mathrm{d}\,\Delta\boldsymbol{\varepsilon}} = \beta P$. Therefore the consistent tangent operator for the initial sub-step (the one right after the previous converged step, n) is $\beta[J^{-1}_{n+\beta}] \cdot P$.

The nonlinear equations for the following portion of the integration can be written as

$$\begin{cases} \boldsymbol{\varepsilon}^{e}_{n+1} + \Delta\gamma_{n+1}\mathbf{R}_{n+1} - \boldsymbol{\varepsilon}^{e,\mathrm{tr}}_{n+1} = 0 \\ \boldsymbol{\alpha}_{n+1} - \boldsymbol{\alpha}_{n+\beta} - \Delta\gamma_{n+1}\hat{\boldsymbol{\alpha}}_{n+1} = 0 \\ \mathbf{z}_{n+1} - \mathbf{z}_{n+\beta} - \Delta\gamma_{n+1}\hat{\mathbf{z}}_{n+1} = 0 \\ f_{n+1} = \|\mathbf{s}_{n+1} - p_{n+1}\boldsymbol{\alpha}_{n+1}\| - \sqrt{\frac{2}{3}}mp_{n+1} = 0 \end{cases} , \tag{A.9}$$

or

$$\underbrace{\begin{Bmatrix} \boldsymbol{\varepsilon}^{e}_{n+1} + \Delta\gamma_{n+1}\mathbf{R}_{n+1} \\ \boldsymbol{\alpha}_{n+1} - \Delta\gamma_{n+1}\hat{\boldsymbol{\alpha}}_{n+1} \\ \mathbf{z}_{n+1} - \Delta\gamma_{n+1}\hat{\mathbf{z}}_{n+1} \\ f_{n+1} \end{Bmatrix}}_{\mathcal{R}_{n+1}} = \begin{bmatrix} \mathbf{I} & & 0 \\ & \mathbf{I} & \\ & & \mathbf{I} \\ 0 & & 0 \end{bmatrix} \cdot \begin{Bmatrix} \boldsymbol{\varepsilon}^{e}_{n+\beta} \\ \boldsymbol{\alpha}_{n+\beta} \\ \mathbf{z}_{n+\beta} \\ \Delta\gamma_{n+\beta} \end{Bmatrix} + \begin{Bmatrix} (1-\beta)\Delta\boldsymbol{\varepsilon} \\ \mathbf{0} \\ \mathbf{0} \\ 0 \end{Bmatrix} \quad . \tag{A.10}$$

Linearization of this equation gives

$$\frac{\mathrm{d}\,\mathcal{R}_{n+1}}{\mathrm{d}\,\Delta\boldsymbol{\varepsilon}} = \begin{bmatrix} \mathbf{I} & & 0 \\ & \mathbf{I} & \\ & & \mathbf{I} \\ 0 & & 0 \end{bmatrix} \frac{\mathrm{d}\left\{\boldsymbol{\varepsilon}^e_{n+\beta}, \boldsymbol{\alpha}_{n+\beta}, \mathbf{z}_{n+\beta}, \Delta\gamma_{n+\beta}\right\}^{\mathsf{T}}}{\mathrm{d}\,\Delta\boldsymbol{\varepsilon}} + \frac{\mathrm{d}}{\mathrm{d}\,\Delta\boldsymbol{\varepsilon}} \begin{Bmatrix} (1-\beta)\Delta\boldsymbol{\varepsilon} \\ \mathbf{0} \\ \mathbf{0} \\ 0 \end{Bmatrix} \quad . \tag{A.11}$$

The left hand side of this equation can be written as

$$\frac{\mathrm{d}\,\mathcal{R}_{n+1}}{\mathrm{d}\,\Delta\boldsymbol{\varepsilon}} = \underbrace{\frac{\mathrm{d}\,\mathcal{R}_{n+1}}{\mathrm{d}\left\{\boldsymbol{\sigma}_{n+1}, \boldsymbol{\alpha}_{n+1}, \mathbf{z}_{n+1}, \Delta\gamma_{n+1}\right\}^{\mathsf{T}}}}_{[J_{n+1}]} \cdot \frac{\mathrm{d}\left\{\boldsymbol{\sigma}_{n+1}, \boldsymbol{\alpha}_{n+1}, \mathbf{z}_{n+1}, \Delta\gamma_{n+1}\right\}^{\mathsf{T}}}{\mathrm{d}\,\Delta\boldsymbol{\varepsilon}} \quad , \tag{A.12}$$

therefore,

$$\frac{\mathrm{d}\left\{\boldsymbol{\sigma}_{n+1}, \boldsymbol{\alpha}_{n+1}, \mathbf{z}_{n+1}, \Delta\gamma_{n+1}\right\}^{\mathsf{T}}}{\mathrm{d}\,\Delta\boldsymbol{\varepsilon}} =$$

$$[J^{-1}_{n+1}] \cdot \left(\begin{bmatrix} \mathbf{I} & & 0 \\ & \mathbf{I} & \\ & & \mathbf{I} \\ 0 & & 0 \end{bmatrix} \frac{\mathrm{d}\left\{\boldsymbol{\varepsilon}^e_{n+\beta}, \boldsymbol{\alpha}_{n+\beta}, \mathbf{z}_{n+\beta}, \Delta\gamma_{n+\beta}\right\}^{\mathsf{T}}}{\mathrm{d}\,\Delta\boldsymbol{\varepsilon}} + (1-\beta) \begin{bmatrix} \mathbf{I} \\ \mathbf{0} \\ \mathbf{0} \\ 0 \end{bmatrix} \right) \quad . \tag{A.13}$$

The term $\dfrac{\mathrm{d}\left\{\boldsymbol{\varepsilon}^e_{n+\beta}, \boldsymbol{\alpha}_{n+\beta}, \mathbf{z}_{n+\beta}, \Delta\gamma_{n+\beta}\right\}^{\mathsf{T}}}{\mathrm{d}\,\Delta\boldsymbol{\varepsilon}}$ is to be calculated. We can use the chain rule and write

$$\frac{\mathrm{d}\left\{\boldsymbol{\varepsilon}^e_{n+\beta}, \boldsymbol{\alpha}_{n+\beta}, \mathbf{z}_{n+\beta}, \Delta\gamma_{n+\beta}\right\}^{\mathsf{T}}}{\mathrm{d}\,\Delta\boldsymbol{\varepsilon}} =$$

$$\frac{\mathrm{d}\left\{\boldsymbol{\varepsilon}^e_{n+\beta}, \boldsymbol{\alpha}_{n+\beta}, \mathbf{z}_{n+\beta}, \Delta\gamma_{n+\beta}\right\}^{\mathsf{T}}}{\mathrm{d}\left\{\boldsymbol{\sigma}_{n+\beta}, \boldsymbol{\alpha}_{n+\beta}, \mathbf{z}_{n+\beta}, \Delta\gamma_{n+\beta}\right\}^{\mathsf{T}}} \cdot \frac{\mathrm{d}\left\{\boldsymbol{\sigma}_{n+\beta}, \boldsymbol{\alpha}_{n+\beta}, \mathbf{z}_{n+\beta}, \Delta\gamma_{n+\beta}\right\}^{\mathsf{T}}}{\mathrm{d}\,\Delta\boldsymbol{\varepsilon}} \quad . \tag{A.14}$$

In this equation $\frac{\mathrm{d}\left\{\boldsymbol{\sigma}_{n+\beta}, \boldsymbol{\alpha}_{n+\beta}, \mathbf{z}_{n+\beta}, \Delta\gamma_{n+\beta}\right\}^{\mathsf{T}}}{\mathrm{d}\,\Delta\boldsymbol{\varepsilon}}$ is calculated during the calculation process for consistent tangent operator of the first portion of the integration sub-stepping and is equal to $\beta[J^{-1}_{n+\beta}]\cdot P$. The first term on the right hand side of this equation can be analytically calculated as

$$\frac{\mathrm{d}\left\{\boldsymbol{\varepsilon}^{e}_{n+\beta}, \boldsymbol{\alpha}_{n+\beta}, \mathbf{z}_{n+\beta}, \Delta\gamma_{n+\beta}\right\}^{\mathsf{T}}}{\mathrm{d}\left\{\boldsymbol{\sigma}_{n+\beta}, \boldsymbol{\alpha}_{n+\beta}, \mathbf{z}_{n+\beta}, \Delta\gamma_{n+\beta}\right\}^{\mathsf{T}}} = \begin{bmatrix} \mathbb{C}^{-1} & & & 0 \\ & \mathbf{I} & & \\ & & \mathbf{I} & \\ 0 & & & 1 \end{bmatrix} \quad . \tag{A.15}$$

Therefore, the consistent tangent operator for the whole integration step will be

$$\frac{\mathrm{d}\,\boldsymbol{\sigma}_{n+1}}{\mathrm{d}\,\Delta\boldsymbol{\varepsilon}} = P^{\mathsf{T}}\cdot[J^{-1}_{n+1}]\left(\begin{bmatrix} \mathbf{I} & & & 0 \\ & \mathbf{I} & & \\ & & \mathbf{I} & \\ 0 & & & 0 \end{bmatrix}\cdot\begin{bmatrix} \mathbb{C}^{-1} & & & 0 \\ & \mathbf{I} & & \\ & & \mathbf{I} & \\ 0 & & & 1 \end{bmatrix}\cdot\beta[J^{-1}_{n+\beta}]\cdot P + (1-\beta)\cdot P\right) \quad . \tag{A.16}$$

If we represent the inverse Jacobian matrix as

$$[J^{-1}] = \begin{bmatrix} [J^{-1}]_{11} & [J^{-1}]_{12} & [J^{-1}]_{13} & {J^{-1}}_{14} \\ [J^{-1}]_{21} & [J^{-1}]_{22} & [J^{-1}]_{23} & {J^{-1}}_{24} \\ [J^{-1}]_{31} & [J^{-1}]_{32} & [J^{-1}]_{33} & {J^{-1}}_{34} \\ {J^{-1}}_{41} & {J^{-1}}_{42} & {J^{-1}}_{43} & {J^{-1}}_{44} \end{bmatrix} \quad , \tag{A.17}$$

where each of the matric blocks shown are 6×6 matrices, we can simplify Equation A.16 as follows. First we can see that the term in the parenthesis in Equation A.16 can be written

as

$$\begin{aligned}
&\begin{bmatrix} \mathbf{I} & & & 0 \\ & \mathbf{I} & & \\ & & \mathbf{I} & \\ 0 & & & 0 \end{bmatrix} \cdot \begin{bmatrix} \mathbb{C}^{-1} & & & 0 \\ & \mathbf{I} & & \\ & & \mathbf{I} & \\ 0 & & & 1 \end{bmatrix} \cdot \beta[J^{-1}_{n+\beta}] \cdot P + (1-\beta) \cdot P \\
&= \begin{Bmatrix} \beta\mathbb{C}^{-1} \cdot [J^{-1}_{n+\beta}]_{11} + (1-\beta)\mathbf{I} \\ [J^{-1}_{n+\beta}]_{21} \\ [J^{-1}_{n+\beta}]_{31} \\ 0 \end{Bmatrix} = \begin{Bmatrix} \mathbb{C}^{-1} \cdot [C^{\sigma}_{n+\beta}] + (1-\beta)\mathbf{I} \\ [J^{-1}_{n+\beta}]_{21} \\ [J^{-1}_{n+\beta}]_{31} \\ 0 \end{Bmatrix} \quad .
\end{aligned} \tag{A.18}$$

Using this and multiplying $P^{\mathsf{T}} \cdot [J^{-1}_{n+1}]$ from left, we get

$$\frac{\mathrm{d}\,\boldsymbol{\sigma}_{n+1}}{\mathrm{d}\,\Delta\boldsymbol{\varepsilon}} = P^{\mathsf{T}} \cdot [J^{-1}_{n+1}] \cdot \begin{Bmatrix} \mathbb{C}^{-1} \cdot [C^{\sigma}_{n+\beta}] + (1-\beta)\mathbf{I} \\ [J^{-1}_{n+\beta}]_{21} \\ [J^{-1}_{n+\beta}]_{31} \\ 0 \end{Bmatrix} \tag{A.19}$$

$$= \begin{Bmatrix} \underbrace{[J^{-1}_{n+1}]_{11}}_{[C^{\sigma}_{n+1}]} & [J^{-1}_{n+1}]_{12} & [J^{-1}_{n+1}]_{13} & J^{-1}_{n+1}{}_{14} \end{Bmatrix} \cdot \begin{Bmatrix} \mathbb{C}^{-1} \cdot [C^{\sigma}_{n+\beta}] + (1-\beta)\mathbf{I} \\ [J^{-1}_{n+\beta}]_{21} \\ [J^{-1}_{n+\beta}]_{31} \\ 0 \end{Bmatrix} \tag{A.20}$$

$$= [C^{\sigma}_{n+1}] \cdot \mathbb{C}^{-1} \cdot [C^{\sigma}_{n+\beta}] + (1-\beta)[C^{\sigma}_{n+1}] + [J^{-1}_{n+1}]_{12} \cdot [J^{-1}_{n+\beta}]_{21} + [J^{-1}_{n+1}]_{13} \cdot [J^{-1}_{n+\beta}]_{31} \quad . \tag{A.21}$$

A.2 Extension to the general sub-stepping process

Suppose a particular integration step is divided into k sub-steps with step lengths $\beta_1, \beta_2, \cdots$ and β_k. The first sub-step with step length β_1 follows Equation A.8 with the only difference

that $\dfrac{\mathrm{d}\left\{\beta_1\Delta\boldsymbol{\varepsilon},\mathbf{0},\mathbf{0},0\right\}^{\mathsf{T}}}{\mathrm{d}\,\Delta\boldsymbol{\varepsilon}}=\beta_1 P$. Therefore, we have

$$\frac{\mathrm{d}\left\{\boldsymbol{\sigma}_{n+\beta_1},\boldsymbol{\alpha}_{n+\beta_1},\mathbf{z}_{n+\beta_1},\Delta\gamma_{n+\beta_1}\right\}^{\mathsf{T}}}{\mathrm{d}\,\Delta\boldsymbol{\varepsilon}}=\beta_1[J^{-1}_{n+\beta_1}]\cdot P \quad . \tag{A.22}$$

For step $i=2\cdots k$ the following equations are to be satisfied:

$$\begin{cases} \boldsymbol{\varepsilon}^{e}_{n+\beta_i}+\Delta\gamma_{n+\beta_i}\mathbf{R}_{n+\beta_i}-\boldsymbol{\varepsilon}^{e,\mathrm{tr}}_{n+\beta_i}=0 \\ \boldsymbol{\alpha}_{n+\beta_i}-\boldsymbol{\alpha}_{n+\beta_{i-1}}-\Delta\gamma_{n+\beta_i}\hat{\boldsymbol{\alpha}}_{n+\beta_i}=0 \\ \mathbf{z}_{n+\beta_i}-\mathbf{z}_{n+\beta_{i-1}}-\Delta\gamma_{n+\beta_i}\hat{\mathbf{z}}_{n+\beta_i}=0 \\ f_{n+\beta_i}=\|\mathbf{s}_{n+\beta_i}-p_{n+\beta_i}\boldsymbol{\alpha}_{n+\beta_i}\|-\sqrt{\frac{2}{3}}mp_{n+\beta_i}=0 \end{cases} . \tag{A.23}$$

These equations can be otherwise written as

$$\underbrace{\begin{Bmatrix} \boldsymbol{\varepsilon}^{e}_{n+\beta_i}+\Delta\gamma_{n+\beta_i}\mathbf{R}_{n+\beta_i} \\ \boldsymbol{\alpha}_{n+\beta_i}-\Delta\gamma_{n+\beta_i}\hat{\boldsymbol{\alpha}}_{n+\beta_i} \\ \mathbf{z}_{n+\beta_i}-\Delta\gamma_{n+\beta_i}\hat{\mathbf{z}}_{n+\beta_i} \\ f_{n+\beta_i} \end{Bmatrix}}_{\mathcal{R}_{n+\beta_i}} = \begin{bmatrix} \mathbf{I} & & 0 \\ & \mathbf{I} & \\ & & \mathbf{I} \\ 0 & & 0 \end{bmatrix} \cdot \begin{Bmatrix} \boldsymbol{\varepsilon}^{e}_{n+\beta_{i-1}} \\ \boldsymbol{\alpha}_{n+\beta_{i-1}} \\ \mathbf{z}_{n+\beta_{i-1}} \\ \Delta\gamma_{n+\beta_{i-1}} \end{Bmatrix} + \begin{Bmatrix} \beta_i\Delta\boldsymbol{\varepsilon} \\ \mathbf{0} \\ \mathbf{0} \\ 0 \end{Bmatrix} \quad . \tag{A.24}$$

Using the chain rule and following the same process from Equation A.11 to A.19 with little modification gives

$$\frac{\mathrm{d}\,\mathcal{R}_{n+1}}{\mathrm{d}\,\Delta\boldsymbol{\varepsilon}}=\underbrace{\frac{\mathrm{d}\,\mathcal{R}_{n+1}}{\mathrm{d}\left\{\boldsymbol{\sigma},\boldsymbol{\alpha},\mathbf{z},\Delta\gamma\right\}^{\mathsf{T}}}}_{[J_{n+1}]}\cdot\frac{\mathrm{d}\left\{\boldsymbol{\sigma},\boldsymbol{\alpha},\mathbf{z},\Delta\gamma\right\}^{\mathsf{T}}}{\mathrm{d}\,\Delta\boldsymbol{\varepsilon}} \quad , \tag{A.25}$$

therefore,

$$\frac{\mathrm{d}\left\{\boldsymbol{\sigma}_{n+\beta_i}, \boldsymbol{\alpha}_{n+\beta_i}, \mathbf{z}_{n+\beta_i}, \Delta\gamma_{n+\beta_i}\right\}^{\mathsf{T}}}{\mathrm{d}\,\Delta\boldsymbol{\varepsilon}} =$$

$$[J^{-1}_{n+\beta_i}] \cdot \left(\begin{bmatrix} \mathbf{I} & & & 0 \\ & \mathbf{I} & & \\ & & \mathbf{I} & \\ 0 & & & 0 \end{bmatrix} \cdot \begin{bmatrix} \mathbb{C}^{-1} & & & 0 \\ & \mathbf{I} & & \\ & & \mathbf{I} & \\ 0 & & & 1 \end{bmatrix} \frac{\mathrm{d}\left\{\boldsymbol{\sigma}^{e}_{n+\beta_{i-1}}, \boldsymbol{\alpha}_{n+\beta_{i-1}}, \mathbf{z}_{n+\beta_{i-1}}, \Delta\gamma_{n+\beta_{i-1}}\right\}^{\mathsf{T}}}{\mathrm{d}\,\Delta\boldsymbol{\varepsilon}} + \beta_i \begin{bmatrix} \mathbf{I} \\ \mathbf{0} \\ \mathbf{0} \\ 0 \end{bmatrix} \right) \quad . \tag{A.26}$$

The term $\frac{\mathrm{d}\left\{\boldsymbol{\sigma}^{e}_{n+\beta_{i-1}}, \boldsymbol{\alpha}_{n+\beta_{i-1}}, \mathbf{z}_{n+\beta_{i-1}}, \Delta\gamma_{n+\beta_{i-1}}\right\}^{\mathsf{T}}}{\mathrm{d}\,\Delta\boldsymbol{\varepsilon}}$ is calculated in the previous sub-step and therefore is known at sub-step i. Equation A.26 gives a recursive algorithm for explicitly defining the consistent tangent operator for the whole integration step. Given the notation used in the process above, the consistent tangent operator for the whole step is

$$\frac{\mathrm{d}\,\boldsymbol{\sigma}_{n+1}}{\mathrm{d}\,\Delta\boldsymbol{\varepsilon}} = P^{\mathsf{T}} \cdot \frac{\mathrm{d}\left\{\boldsymbol{\sigma}_{n+\beta_k}, \boldsymbol{\alpha}_{n+\beta_k}, \mathbf{z}_{n+\beta_k}, \Delta\gamma_{n+\beta_k}\right\}^{\mathsf{T}}}{\mathrm{d}\,\Delta\boldsymbol{\varepsilon}} \quad . \tag{A.27}$$

Appendix B

CALCULATION OF NECESSARY DERIVATIVES FOR MANZARI-DAFALIAS CONSTITUTIVE MODEL

In order to calculate the Jacobian of the system of equations, in this appendix derivatives of necessary parameters in Manzari-Dafalias constitutive model are calculated. Here $\mathbb{1}$ denotes the 4^{th} order identity tensor, $\mathbb{1}_{dev}$ denotes the 4^{th} order deviatoric operator and $\mathbf{1}$ denotes the 2^{nd} order identity tensor. Also $\boldsymbol{r} = \boldsymbol{s} - p\,\boldsymbol{\alpha}$ is defined as the tensor pointing from the center of yield surface to the stress state. Several useful identities are used in this chapter such as

$$\mathrm{tr}(\boldsymbol{a}\cdot\boldsymbol{b}) = \mathrm{tr}(\boldsymbol{a}\cdot\boldsymbol{b}) \quad , \tag{B.1}$$

$$\mathbb{1}_{dev} = \mathbb{1} - \frac{1}{3}(\mathbf{1}\otimes\mathbf{1}) \quad , \tag{B.2}$$

$$(\boldsymbol{a}\otimes\boldsymbol{a}) : \mathbb{1}_{dev} = \boldsymbol{a}\otimes\boldsymbol{a} \quad \forall \boldsymbol{a}, tr(\boldsymbol{a}) = 0 \quad , \tag{B.3}$$

$$(\boldsymbol{n}\otimes\boldsymbol{n}) : (\boldsymbol{\alpha}\otimes\mathbf{1}) = (\boldsymbol{n}:\boldsymbol{\alpha})(\boldsymbol{n}\otimes\mathbf{1}) \quad , \tag{B.4}$$

$$\mathrm{d}(\|\boldsymbol{r}\|) = \frac{\boldsymbol{r}}{\|\boldsymbol{r}\|} : \mathbf{d}\boldsymbol{r} \quad . \tag{B.5}$$

Equation B.5 is proven by writing the definition of the tensorial norm as a double-dot product:

$$\begin{aligned} \|\boldsymbol{r}\| =& (\boldsymbol{r}:\boldsymbol{r})^{\frac{1}{2}} \\ \Rightarrow \mathrm{d}(\|\boldsymbol{r}\|) =& \frac{1}{2}(\boldsymbol{r}:\boldsymbol{r})^{-\frac{1}{2}}(\mathbf{d}\boldsymbol{r}:\boldsymbol{r}+\boldsymbol{r}:\mathbf{d}\boldsymbol{r}) \\ =& \frac{\boldsymbol{r}}{\|\boldsymbol{r}\|} : \mathbf{d}\boldsymbol{r} \quad . \end{aligned} \tag{B.6}$$

Some of the fundamental derivatives used in the following sections are

$$p = \frac{1}{3}\left(\mathbf{1} : \boldsymbol{\sigma}\right) \Rightarrow \mathrm{d}p = \frac{1}{3}\left(\mathbf{1} : \mathbf{d}\boldsymbol{\sigma}\right) \quad , \tag{B.7}$$

$$\boldsymbol{s} = \mathbb{1}_{dev} : \boldsymbol{\sigma} \Rightarrow \mathbf{d}\boldsymbol{s} = \mathbb{1}_{dev} : \mathbf{d}\boldsymbol{\sigma} \quad , \tag{B.8}$$

$$\boldsymbol{r} = \boldsymbol{s} - p\,\boldsymbol{\alpha} \Rightarrow \mathbf{d}\boldsymbol{r} = \mathbf{d}\boldsymbol{s} - \mathrm{d}p\,\boldsymbol{\alpha} - p\,\mathbf{d}\boldsymbol{\alpha} \quad . \tag{B.9}$$

Therefore we have

$$\frac{\partial p}{\partial \boldsymbol{\sigma}} = \frac{1}{3}\mathbf{1} \quad , \tag{B.10}$$

$$\frac{\partial \boldsymbol{s}}{\partial \boldsymbol{\sigma}} = \mathbb{1}_{dev} \quad , \tag{B.11}$$

$$\frac{\partial \boldsymbol{r}}{\partial \boldsymbol{\sigma}} = \mathbb{1}_{dev} - \frac{1}{3}(\boldsymbol{\alpha} \otimes \mathbf{1}) \quad , \tag{B.12}$$

$$\frac{\partial \boldsymbol{r}}{\partial \boldsymbol{\alpha}} = -p\mathbb{1} \quad . \tag{B.13}$$

Derivatives of other parameters follow next.

Differentials of $\boldsymbol{n}$

$$\boldsymbol{n} = \frac{\boldsymbol{r}}{\|\boldsymbol{r}\|} \tag{B.14}$$

$$\Rightarrow \mathbf{d}\boldsymbol{n} = \frac{\mathbf{d}\boldsymbol{r}\left(\|\boldsymbol{r}\|\right) - \mathrm{d}(\|\boldsymbol{r}\|)\,\boldsymbol{r}}{\|\boldsymbol{r}\|^2} \tag{B.15}$$

$$= \frac{1}{\|\boldsymbol{r}\|}\left(\mathbf{d}\boldsymbol{r} - \left(\frac{\boldsymbol{r}}{\|\boldsymbol{r}\|} \otimes \frac{\boldsymbol{r}}{\|\boldsymbol{r}\|}\right) : \mathbf{d}\boldsymbol{r}\right) \tag{B.16}$$

$$= \frac{1}{\|\boldsymbol{r}\|}\left(\mathbb{1} - \boldsymbol{n} \otimes \boldsymbol{n}\right) : \mathbf{d}\boldsymbol{r} \tag{B.17}$$

Therefore we have

$$\mathbf{d}\boldsymbol{n} = \frac{1}{\|\boldsymbol{r}\|}\left(\mathbb{1}_{dev} - \frac{1}{3}\boldsymbol{\alpha}\otimes\mathbf{1} - \boldsymbol{n}\otimes\boldsymbol{n} + \frac{1}{3}(\boldsymbol{n}:\boldsymbol{\alpha})(\boldsymbol{n}\otimes\mathbf{1}) : \mathbf{d}\boldsymbol{\sigma} - p\,(\mathbb{1} - \boldsymbol{n}\otimes\boldsymbol{n}) : \mathbf{d}\boldsymbol{\alpha}\right) \quad , \tag{B.18}$$

which gives

$$\begin{cases} \dfrac{\partial \boldsymbol{n}}{\partial \boldsymbol{\sigma}} = \dfrac{1}{\|\boldsymbol{r}\|}\left(\mathbb{1}_{dev} - \dfrac{1}{3}\boldsymbol{\alpha}\otimes\mathbf{1} - \boldsymbol{n}\otimes\boldsymbol{n} + \dfrac{1}{3}(\boldsymbol{n}:\boldsymbol{\alpha})(\boldsymbol{n}\otimes\mathbf{1})\right) \\ \dfrac{\partial \boldsymbol{n}}{\partial \boldsymbol{\alpha}} = \dfrac{p}{\|\boldsymbol{r}\|}\left((\boldsymbol{n}\otimes\boldsymbol{n}) - \mathbb{1}\right) \\ \dfrac{\partial \boldsymbol{n}}{\partial \boldsymbol{z}} = \mathbf{0} \end{cases} . \tag{B.19}$$

Differentials of b_0

$$b_0 = G_0 h_0 (1 - c_h e)(\frac{p}{p_{atm}})^{-\frac{1}{2}} \tag{B.20}$$

$$\Rightarrow \mathrm{d}b_0 = G_0 h_0 (1 - c_h e)(-\frac{1}{2}(\frac{\mathrm{d}p}{p_{atm}})(\frac{p}{p_{atm}})^{-\frac{3}{2}}) \tag{B.21}$$

$$= \underbrace{G_0 h_0 (1 - c_h e)(\frac{p}{p_{atm}})^{-\frac{1}{2}}}_{b_0}(-\frac{1}{2}(\frac{1}{3}\mathbf{1} : \mathbf{d}\boldsymbol{\sigma})\frac{\cancel{p_{atm}}}{p\ \cancel{p_{atm}}}) \tag{B.22}$$

Therefore we have

$$\mathrm{d}b_0 = -\frac{b_0}{6p} \quad \mathbf{1} : \mathbf{d}\boldsymbol{\sigma} \quad , \tag{B.23}$$

which gives

$$\begin{cases} \dfrac{\partial b_0}{\partial \boldsymbol{\sigma}} = -\dfrac{b_0}{6p}\,\mathbf{1} \\ \dfrac{\partial b_0}{\partial \boldsymbol{\alpha}} = \mathbf{0} \\ \dfrac{\partial b_0}{\partial \boldsymbol{z}} = \mathbf{0} \end{cases} . \tag{B.24}$$

Differentials of ψ

$$\psi = e - \left(e_0 - \lambda_c (\frac{p}{p_{atm}})^{\xi} \right) \tag{B.25}$$

$$\Rightarrow \mathrm{d}\psi = \lambda_c \xi \frac{\mathrm{d}p}{p_{atm}} (\frac{p}{p_{atm}})^{\xi - 1} \tag{B.26}$$

Therefore we have

$$\mathrm{d}\psi = \frac{\lambda_c\, \xi}{3\, p_{atm}} (\frac{p}{p_{atm}})^{\xi - 1}\, (\mathbf{1} : \mathbf{d}\boldsymbol{\sigma}) \tag{B.27}$$

which gives

$$\begin{cases} \dfrac{\partial \psi}{\partial \boldsymbol{\sigma}} = \dfrac{\lambda_c\, \xi}{3\, p_{atm}} (\dfrac{p}{p_{atm}})^{\xi - 1}\, \mathbf{1} \\ \dfrac{\partial \psi}{\partial \boldsymbol{\alpha}} = \mathbf{0} \\ \dfrac{\partial \psi}{\partial \boldsymbol{z}} = \mathbf{0} \end{cases} \tag{B.28}$$

Differentials of A_d

$$A_d = A_0 (1 + < \boldsymbol{z} : \boldsymbol{n} >) \tag{B.29}$$

$$\Rightarrow \mathrm{d}A_d = A_0 \overline{\{\boldsymbol{z} : \boldsymbol{n}\}} (\mathbf{d}\boldsymbol{z} : \boldsymbol{n} + \boldsymbol{z} : \mathbf{d}\boldsymbol{n}) \tag{B.30}$$

Therefore we have

$$\mathrm{d}A_d = A_0\overline{\{\boldsymbol{z}:\boldsymbol{n}\}}(\boldsymbol{n}:\mathbf{d}\boldsymbol{z}+\boldsymbol{z}:\frac{\partial \boldsymbol{n}}{\partial \boldsymbol{\sigma}}:\mathbf{d}\boldsymbol{\sigma}+\boldsymbol{z}:\frac{\partial \boldsymbol{n}}{\partial \boldsymbol{\alpha}}:\mathbf{d}\boldsymbol{\alpha}) \tag{B.31}$$

which gives

$$\begin{cases} \dfrac{\partial A_d}{\partial \boldsymbol{\sigma}} = A_0\overline{\{\boldsymbol{z}:\boldsymbol{n}\}}(\boldsymbol{z}:\dfrac{\partial \boldsymbol{n}}{\partial \boldsymbol{\sigma}}) \\ \dfrac{\partial A_d}{\partial \boldsymbol{\alpha}} = A_0\overline{\{\boldsymbol{z}:\boldsymbol{n}\}}(\boldsymbol{z}:\dfrac{\partial \boldsymbol{n}}{\partial \boldsymbol{\alpha}}) \\ \dfrac{\partial A_d}{\partial \boldsymbol{z}} = A_0\overline{\{\boldsymbol{z}:\boldsymbol{n}\}}\boldsymbol{n} \end{cases} \tag{B.32}$$

Differentials of h

$$h = \frac{b_0}{(\boldsymbol{\alpha}-\boldsymbol{\alpha}_{in}):\boldsymbol{n}} \tag{B.33}$$

$$\Rightarrow \mathrm{d}h = \frac{\mathrm{d}b_0\,((\boldsymbol{\alpha}-\boldsymbol{\alpha}_{in}):\boldsymbol{n}) - \mathrm{d}((\boldsymbol{\alpha}-\boldsymbol{\alpha}_{in}):\boldsymbol{n})\,b_0}{((\boldsymbol{\alpha}-\boldsymbol{\alpha}_{in}):\boldsymbol{n})^2} \tag{B.34}$$

$$\begin{aligned} = &\frac{1}{(\boldsymbol{\alpha}-\boldsymbol{\alpha}_{in}):\boldsymbol{n}}\left(\frac{\partial b_0}{\partial \boldsymbol{\sigma}} - \underbrace{\frac{b_0}{(\boldsymbol{\alpha}-\boldsymbol{\alpha}_{in}):\boldsymbol{n}}}_{h}(\boldsymbol{\alpha}-\boldsymbol{\alpha}_{in}):\frac{\partial \boldsymbol{n}}{\partial \boldsymbol{\sigma}}\right):\mathbf{d}\boldsymbol{\sigma} - \\ &\underbrace{\frac{b_0}{(\boldsymbol{\alpha}-\boldsymbol{\alpha}_{in}):\boldsymbol{n}}}_{h}\left(\frac{\boldsymbol{n}+(\boldsymbol{\alpha}-\boldsymbol{\alpha}_{in}):\dfrac{\partial \boldsymbol{n}}{\partial \boldsymbol{\alpha}}}{(\boldsymbol{\alpha}-\boldsymbol{\alpha}_{in}):\boldsymbol{n}}\right):\mathbf{d}\boldsymbol{\alpha} \end{aligned} \tag{B.35}$$

Therefore we have

$$\mathrm{d}h = \frac{1}{(\boldsymbol{\alpha}-\boldsymbol{\alpha}_{in}):\boldsymbol{n}}\left(\frac{\partial b_0}{\partial \boldsymbol{\sigma}} - h(\boldsymbol{\alpha}-\boldsymbol{\alpha}_{in}):\frac{\partial \boldsymbol{n}}{\partial \boldsymbol{\sigma}}\right):\mathbf{d}\boldsymbol{\sigma} - h\left(\frac{\boldsymbol{n}+(\boldsymbol{\alpha}-\boldsymbol{\alpha}_{in}):\dfrac{\partial \boldsymbol{n}}{\partial \boldsymbol{\alpha}}}{(\boldsymbol{\alpha}-\boldsymbol{\alpha}_{in}):\boldsymbol{n}}\right):\mathbf{d}\boldsymbol{\alpha} \tag{B.36}$$

which gives

$$\begin{cases} \dfrac{\partial h}{\partial \boldsymbol{\sigma}} = \dfrac{1}{(\boldsymbol{\alpha}-\boldsymbol{\alpha}_{in}):\boldsymbol{n}}\left(\dfrac{\partial b_0}{\partial \boldsymbol{\sigma}} - h(\boldsymbol{\alpha}-\boldsymbol{\alpha}_{in}):\dfrac{\partial \boldsymbol{n}}{\partial \boldsymbol{\sigma}}\right) \\ \dfrac{\partial h}{\partial \boldsymbol{\alpha}} = \dfrac{-h}{(\boldsymbol{\alpha}-\boldsymbol{\alpha}_{in}):\boldsymbol{n}}\left(\boldsymbol{n} + (\boldsymbol{\alpha}-\boldsymbol{\alpha}_{in}):\dfrac{\partial \boldsymbol{n}}{\partial \boldsymbol{\alpha}}\right) \\ \dfrac{\partial h}{\partial \boldsymbol{z}} = \mathbf{0} \end{cases} \tag{B.37}$$

Differentials of $\cos 3\theta$

$$\cos(3\theta) = \sqrt{6}\,\mathbf{1} : \boldsymbol{n}^3 \tag{B.38}$$

$$\Rightarrow \mathrm{d}\cos(3\theta) = \sqrt{6}\,\mathbf{1} : \mathbf{d}(\boldsymbol{n^3}) \tag{B.39}$$

$$= \sqrt{6}\,\mathbf{1} : (\mathbf{d}\boldsymbol{n}.\boldsymbol{n}^2 + \boldsymbol{n}.\mathbf{d}\boldsymbol{n}.\boldsymbol{n} + \boldsymbol{n}^2.\mathbf{d}\boldsymbol{n}) \tag{B.40}$$

$$= 3\sqrt{6}\,\boldsymbol{n}^2 : \mathbf{d}\boldsymbol{n} \tag{B.41}$$

Therefore we have

$$\mathrm{d}\cos(3\theta) = 3\sqrt{6}\,\boldsymbol{n}^2 : \left(\frac{\partial \boldsymbol{n}}{\partial \boldsymbol{\sigma}} : \mathbf{d}\boldsymbol{\sigma} + \frac{\partial \boldsymbol{n}}{\partial \boldsymbol{\alpha}} : \mathbf{d}\boldsymbol{\alpha}\right) \tag{B.42}$$

which gives

$$\begin{cases} \dfrac{\partial \cos(3\theta)}{\partial \boldsymbol{\sigma}} = 3\sqrt{6}\,\boldsymbol{n}^2 : \dfrac{\partial \boldsymbol{n}}{\partial \boldsymbol{\sigma}} \\ \dfrac{\partial \cos(3\theta)}{\partial \boldsymbol{\alpha}} = 3\sqrt{6}\,\boldsymbol{n}^2 : \dfrac{\partial \boldsymbol{n}}{\partial \boldsymbol{\alpha}} \\ \dfrac{\partial \cos(3\theta)}{\partial \boldsymbol{z}} = \mathbf{0} \end{cases} \tag{B.43}$$

Differentials of g

$$g(\theta, c) = \frac{2c}{(1+c) - (1-c)\cos 3\theta} \tag{B.44}$$

$$\Rightarrow \mathrm{d}g = \frac{(2c)(1-c)}{((1+c) - (1-c)\cos 3\theta)^2}\mathrm{d}(\cos 3\theta) \tag{B.45}$$

$$= \frac{g^2\,(1-c)}{2c}\mathrm{d}(\cos 3\theta) \tag{B.46}$$

Therefore we have

$$\mathrm{d}g = g^2\,\frac{1-c}{2c}\left(\frac{\partial(\cos 3\theta)}{\partial \boldsymbol{\sigma}} : \mathbf{d}\boldsymbol{\sigma} + \frac{\partial(\cos 3\theta)}{\partial \boldsymbol{\alpha}} : \mathbf{d}\boldsymbol{\alpha}\right) \tag{B.47}$$

which gives

$$\begin{cases} \dfrac{\partial g}{\partial \boldsymbol{\sigma}} = g^2\,\dfrac{1-c}{2c}\dfrac{\partial(\cos 3\theta)}{\partial \boldsymbol{\sigma}} \\ \dfrac{\partial g}{\partial \boldsymbol{\alpha}} = g^2\,\dfrac{1-c}{2c}\dfrac{\partial(\cos 3\theta)}{\partial \boldsymbol{\alpha}} \\ \dfrac{\partial g}{\partial \boldsymbol{z}} = \mathbf{0} \end{cases} \tag{B.48}$$

Differentials of α_θ^d

$$\alpha_\theta^d = g\,M_c\,e^{(n^d\,\psi)} - m \tag{B.49}$$

$$\Rightarrow \mathrm{d}\alpha_\theta^d = \mathrm{d}g\,M_c\,e^{(n^d\,\psi)} + g\,M_c\,n^d\mathrm{d}\psi\,e^{(n^d\,\psi)} \tag{B.50}$$

$$= M_c\,e^{(n^d\,\psi)}\,\left[\left(\frac{\partial g}{\partial \boldsymbol{\sigma}} + g\;n^d\,\frac{\partial \psi}{\partial \boldsymbol{\sigma}}\right) : \mathbf{d}\boldsymbol{\sigma} + \frac{\partial g}{\partial \boldsymbol{\alpha}} : \mathbf{d}\boldsymbol{\alpha}\right] \tag{B.51}$$

Therefore we have

$$\mathrm{d}\alpha_\theta^d = M_c\,e^{(n^d\,\psi)}\,\left[\left(\frac{\partial g}{\partial \boldsymbol{\sigma}} + g\;n^d\,\frac{\partial \psi}{\partial \boldsymbol{\sigma}}\right) : \mathbf{d}\boldsymbol{\sigma} + \frac{\partial g}{\partial \boldsymbol{\alpha}} : \mathbf{d}\boldsymbol{\alpha}\right] \tag{B.52}$$

which gives

$$\begin{cases} \dfrac{\partial \alpha_\theta^d}{\partial \boldsymbol{\sigma}} = M_c\, e^{(n^d\,\psi)}\, \left(\dfrac{\partial g}{\partial \boldsymbol{\sigma}} + g\; n^d\, \dfrac{\partial \psi}{\partial \boldsymbol{\sigma}} \right) \\ \dfrac{\partial \alpha_\theta^d}{\partial \boldsymbol{\alpha}} = M_c\, e^{(n^d\,\psi)}\, \dfrac{\partial g}{\partial \boldsymbol{\alpha}} \\ \dfrac{\partial \alpha_\theta^d}{\partial \boldsymbol{z}} = \mathbf{0} \end{cases} \tag{B.53}$$

Differentials of α_θ^b

$$\alpha_\theta^b = g\, M_c\, e^{-(n^b\,\psi)} - m \tag{B.54}$$

$$\Rightarrow \mathrm{d}\alpha_\theta^b = \mathrm{d}g\, M_c\, e^{-(n^b\,\psi)} - g\, M_c\, n^b \mathrm{d}\psi\, e^{-(n^b\,\psi)} \tag{B.55}$$

Therefore we have

$$\mathrm{d}\alpha_\theta^b = M_c\, e^{-(n^b\,\psi)}\, \left[\left(\frac{\partial g}{\partial \boldsymbol{\sigma}} - g\; n^b\, \frac{\partial \psi}{\partial \boldsymbol{\sigma}} \right) : \mathbf{d}\boldsymbol{\sigma} + \frac{\partial g}{\partial \boldsymbol{\alpha}} : \mathbf{d}\boldsymbol{\alpha} \right] \tag{B.56}$$

which gives

$$\begin{cases} \dfrac{\partial \alpha_\theta^b}{\partial \boldsymbol{\sigma}} = M_c\, e^{-(n^b\,\psi)}\, \left(\dfrac{\partial g}{\partial \boldsymbol{\sigma}} - g\; n^b\, \dfrac{\partial \psi}{\partial \boldsymbol{\sigma}} \right) \\ \dfrac{\partial \alpha_\theta^b}{\partial \boldsymbol{\alpha}} = M_c\, e^{-(n^b\,\psi)}\, \dfrac{\partial g}{\partial \boldsymbol{\alpha}} \\ \dfrac{\partial \alpha_\theta^b}{\partial \boldsymbol{z}} = \mathbf{0} \end{cases} \tag{B.57}$$

Differentials of D

$$D = A_d(\boldsymbol{\alpha}^{\boldsymbol{d}}_{\boldsymbol{\theta}} - \boldsymbol{\alpha}) : \boldsymbol{n} = A_d(\sqrt{\frac{2}{3}}\alpha^d_\theta \underbrace{\boldsymbol{n} : \boldsymbol{n}}_{1} - \boldsymbol{\alpha} : \boldsymbol{n}) \tag{B.58}$$

$$\Rightarrow \mathrm{d}D = \mathrm{d}A_d\,(\sqrt{\frac{2}{3}}\alpha^d_\theta - \boldsymbol{\alpha} : \boldsymbol{n}) + A_d(\sqrt{\frac{2}{3}}\mathrm{d}\alpha^d_\theta - \mathbf{d}\boldsymbol{\alpha} : \boldsymbol{n} - \boldsymbol{\alpha} : \mathbf{d}\boldsymbol{n}) \tag{B.59}$$

Therefore we have

$$\begin{aligned}\mathrm{d}D = &\left[(\sqrt{\frac{2}{3}}\alpha^d_\theta - \boldsymbol{\alpha} : \boldsymbol{n})\frac{\partial A_d}{\partial \boldsymbol{\sigma}} + A_d(\sqrt{\frac{2}{3}}\frac{\partial \alpha^d_\theta}{\partial \boldsymbol{\sigma}} - \boldsymbol{\alpha} : \frac{\partial \boldsymbol{n}}{\partial \boldsymbol{\sigma}})\right] : \mathbf{d}\boldsymbol{\sigma} \\ &+ \left[(\sqrt{\frac{2}{3}}\alpha^d_\theta - \boldsymbol{\alpha} : \boldsymbol{n})\frac{\partial A_d}{\partial \boldsymbol{\alpha}} + A_d(\sqrt{\frac{2}{3}}\frac{\partial \alpha^d_\theta}{\partial \boldsymbol{\alpha}} - \boldsymbol{\alpha} : \frac{\partial \boldsymbol{n}}{\partial \boldsymbol{\alpha}} - \boldsymbol{n})\right] : \mathbf{d}\boldsymbol{\alpha} \\ &+ (\sqrt{\frac{2}{3}}\alpha^d_\theta - \boldsymbol{\alpha} : \boldsymbol{n})\frac{\partial A_d}{\partial \boldsymbol{z}} : \mathbf{d}\boldsymbol{z}\end{aligned} \tag{B.60}$$

which gives

$$\begin{cases} \dfrac{\partial D}{\partial \boldsymbol{\sigma}} = (\sqrt{\dfrac{2}{3}}\alpha^d_\theta - \boldsymbol{\alpha} : \boldsymbol{n})\dfrac{\partial A_d}{\partial \boldsymbol{\sigma}} + A_d(\sqrt{\dfrac{2}{3}}\dfrac{\partial \alpha^d_\theta}{\partial \boldsymbol{\sigma}} - \boldsymbol{\alpha} : \dfrac{\partial \boldsymbol{n}}{\partial \boldsymbol{\sigma}}) \\ \dfrac{\partial D}{\partial \boldsymbol{\alpha}} = (\sqrt{\dfrac{2}{3}}\alpha^d_\theta - \boldsymbol{\alpha} : \boldsymbol{n})\dfrac{\partial A_d}{\partial \boldsymbol{\alpha}} + A_d(\sqrt{\dfrac{2}{3}}\dfrac{\partial \alpha^d_\theta}{\partial \boldsymbol{\alpha}} - \boldsymbol{\alpha} : \dfrac{\partial \boldsymbol{n}}{\partial \boldsymbol{\alpha}} - \boldsymbol{n}) \\ \dfrac{\partial D}{\partial \boldsymbol{z}} = (\sqrt{\dfrac{2}{3}}\alpha^d_\theta - \boldsymbol{\alpha} : \boldsymbol{n})\dfrac{\partial A_d}{\partial \boldsymbol{z}} \end{cases} \tag{B.61}$$

Differentials of B

$$B = 1 + \frac{3}{2}\,\frac{1-c}{c}\,g\,\cos(3\theta) \tag{B.62}$$

$$\Rightarrow \mathrm{d}B = \frac{3}{2}\,\frac{1-c}{c}\,(\mathrm{d}g\cos(3\theta) + g\,\mathrm{d}\cos(3\theta)) \tag{B.63}$$

Therefore we have

$$\mathrm{d}B = \frac{3}{2}\frac{1-c}{c}\left[\left(\cos(3\theta)\frac{\partial g}{\partial \boldsymbol{\sigma}} + g\frac{\partial \cos(3\theta)}{\partial \boldsymbol{\sigma}}\right) : \mathbf{d}\boldsymbol{\sigma} + \left(\cos(3\theta)\frac{\partial g}{\partial \boldsymbol{\alpha}} + g\frac{\partial \cos(3\theta)}{\partial \boldsymbol{\alpha}}\right) : \mathbf{d}\boldsymbol{\alpha}\right] \tag{B.64}$$

which gives

$$\begin{cases} \dfrac{\partial B}{\partial \boldsymbol{\sigma}} = \dfrac{3}{2}\dfrac{1-c}{c}\left(\cos(3\theta)\dfrac{\partial g}{\partial \boldsymbol{\sigma}} + g\dfrac{\partial \cos(3\theta)}{\partial \boldsymbol{\sigma}}\right) \\ \dfrac{\partial B}{\partial \boldsymbol{\alpha}} = \dfrac{3}{2}\dfrac{1-c}{c}\left(\cos(3\theta)\dfrac{\partial g}{\partial \boldsymbol{\alpha}} + g\dfrac{\partial \cos(3\theta)}{\partial \boldsymbol{\alpha}}\right) \\ \dfrac{\partial B}{\partial \boldsymbol{z}} = \mathbf{0} \end{cases} \tag{B.65}$$

Differentials of C

$$\begin{aligned} C = 3\sqrt{\frac{3}{2}}\frac{1-c}{c}g \;\Rightarrow\; \mathrm{d}C &= 3\sqrt{\frac{3}{2}}\frac{1-c}{c}\mathrm{d}g \\ &= 3\sqrt{\frac{3}{2}}\frac{1-c}{c}\left(\frac{\partial g}{\partial \boldsymbol{\sigma}} : \mathbf{d}\boldsymbol{\sigma} + \frac{\partial g}{\partial \boldsymbol{\alpha}} : \mathbf{d}\boldsymbol{\alpha}\right) \end{aligned}$$

Therefore we have

$$\mathrm{d}C = 3\sqrt{\frac{3}{2}}\frac{1-c}{c}\left(\frac{\partial g}{\partial \boldsymbol{\sigma}} : \mathbf{d}\boldsymbol{\sigma} + \frac{\partial g}{\partial \boldsymbol{\alpha}} : \mathbf{d}\boldsymbol{\alpha}\right) \tag{B.66}$$

which gives

$$\begin{cases} \dfrac{\partial C}{\partial \boldsymbol{\sigma}} = 3\sqrt{\dfrac{3}{2}}\dfrac{1-c}{c}\dfrac{\partial g}{\partial \boldsymbol{\sigma}} \\ \dfrac{\partial C}{\partial \boldsymbol{\alpha}} = 3\sqrt{\dfrac{3}{2}}\dfrac{1-c}{c}\dfrac{\partial g}{\partial \boldsymbol{\alpha}} \\ \dfrac{\partial C}{\partial \boldsymbol{z}} = \mathbf{0} \end{cases} \tag{B.67}$$

Differentials of $\boldsymbol{R}$

$$\boldsymbol{R} = B\boldsymbol{n} - C(\boldsymbol{n}^2 - \frac{1}{3}\mathbf{1}) + \frac{1}{3}D\mathbf{1} \tag{B.68}$$

$$\Rightarrow \mathrm{d}\boldsymbol{R} = \mathrm{d}B\boldsymbol{n} + B\mathbf{d}\boldsymbol{n} - \mathrm{d}C(\boldsymbol{n}^2 - \frac{1}{3}\mathbf{1}) - C\overbrace{\mathbf{d}\boldsymbol{n}.\boldsymbol{n}+\boldsymbol{n}.\mathbf{d}\boldsymbol{n}}^{\mathbf{d}\boldsymbol{n}^2} + \frac{1}{3}\mathrm{d}D\mathbf{1} \tag{B.69}$$

Therefore we have

$$\begin{aligned}\mathbf{d}\boldsymbol{R} = &\left(\frac{\partial B}{\partial \boldsymbol{\sigma}} : \mathbf{d}\boldsymbol{\sigma} + \frac{\partial B}{\partial \boldsymbol{\alpha}} : \mathbf{d}\boldsymbol{\alpha}\right)\boldsymbol{n} + B\left(\frac{\partial \boldsymbol{n}}{\partial \boldsymbol{\sigma}} : \mathbf{d}\boldsymbol{\sigma} + \frac{\partial \boldsymbol{n}}{\partial \boldsymbol{\alpha}} : \mathbf{d}\boldsymbol{\alpha}\right) - \\ &\left(\frac{\partial C}{\partial \boldsymbol{\sigma}} : \mathbf{d}\boldsymbol{\sigma} + \frac{\partial C}{\partial \boldsymbol{\alpha}} : \mathbf{d}\boldsymbol{\alpha}\right)(\boldsymbol{n}^2 - \frac{1}{3}\mathbf{1}) - \\ &C\left[\left(\frac{\partial \boldsymbol{n}}{\partial \boldsymbol{\sigma}} : \mathbf{d}\boldsymbol{\sigma} + \frac{\partial \boldsymbol{n}}{\partial \boldsymbol{\alpha}} : \mathbf{d}\boldsymbol{\alpha}\right).\boldsymbol{n} + \boldsymbol{n}.\left(\frac{\partial \boldsymbol{n}}{\partial \boldsymbol{\sigma}} : \mathbf{d}\boldsymbol{\sigma} + \frac{\partial \boldsymbol{n}}{\partial \boldsymbol{\alpha}} : \mathbf{d}\boldsymbol{\alpha}\right)\right] + \\ &\frac{1}{3}\left[\frac{\partial D}{\partial \boldsymbol{\sigma}} : \mathbf{d}\boldsymbol{\sigma} + \frac{\partial D}{\partial \boldsymbol{\alpha}} : \mathbf{d}\boldsymbol{\alpha} + \frac{\partial D}{\partial \boldsymbol{z}} : \mathbf{d}\boldsymbol{z}\right]\mathbf{1}\end{aligned} \tag{B.70}$$

which gives

$$\begin{cases} \dfrac{\partial \boldsymbol{R}}{\partial \boldsymbol{\sigma}} = \boldsymbol{n} \otimes \dfrac{\partial B}{\partial \boldsymbol{\sigma}} + B\dfrac{\partial \boldsymbol{n}}{\partial \boldsymbol{\sigma}} - (\boldsymbol{n}^2 - \dfrac{1}{3}\mathbf{1}) \otimes \dfrac{\partial C}{\partial \boldsymbol{\sigma}} - C\left(\left(\left(\dfrac{\partial \boldsymbol{n}}{\partial \boldsymbol{\sigma}}\right)^T.\boldsymbol{n}\right)^T + \boldsymbol{n}.\dfrac{\partial \boldsymbol{n}}{\partial \boldsymbol{\sigma}}\right) + \dfrac{1}{3}\left(\mathbf{1} \otimes \dfrac{\partial D}{\partial \boldsymbol{\sigma}}\right) \\ \dfrac{\partial \boldsymbol{R}}{\partial \boldsymbol{\alpha}} = \boldsymbol{n} \otimes \dfrac{\partial B}{\partial \boldsymbol{\alpha}} + B\dfrac{\partial \boldsymbol{n}}{\partial \boldsymbol{\alpha}} - (\boldsymbol{n}^2 - \dfrac{1}{3}\mathbf{1}) \otimes \dfrac{\partial C}{\partial \boldsymbol{\alpha}} - C\left(\left(\left(\dfrac{\partial \boldsymbol{n}}{\partial \boldsymbol{\alpha}}\right)^T.\boldsymbol{n}\right)^T + \boldsymbol{n}.\dfrac{\partial \boldsymbol{n}}{\partial \boldsymbol{\alpha}}\right) + \dfrac{1}{3}\left(\mathbf{1} \otimes \dfrac{\partial D}{\partial \boldsymbol{\alpha}}\right) \\ \dfrac{\partial \boldsymbol{R}}{\partial \boldsymbol{z}} = \dfrac{1}{3}\left(\mathbf{1} \otimes \dfrac{\partial D}{\partial \boldsymbol{z}}\right) \end{cases} \tag{B.71}$$

Differentials of $\bar{\boldsymbol{\alpha}}$

$$\overline{\boldsymbol{\alpha}} = \frac{2}{3}\, h\, \left(\sqrt{\frac{2}{3}}\alpha_\theta^b\, \boldsymbol{n} - \boldsymbol{\alpha}\right) \tag{B.72}$$

$$\Rightarrow \mathbf{d}\overline{\boldsymbol{\alpha}} = \frac{2}{3}\mathrm{d}h\left(\sqrt{\frac{2}{3}}\alpha_\theta^b\boldsymbol{n} - \boldsymbol{\alpha}\right) + \frac{2}{3}\, h\, \left(\sqrt{\frac{2}{3}}(\mathrm{d}\alpha_\theta^b\boldsymbol{n} + \alpha_\theta^b\mathbf{d}\boldsymbol{n}) - \mathbf{d}\boldsymbol{\alpha}\right) \tag{B.73}$$

Therefore we have

$$\begin{aligned}\mathbf{d}\overline{\boldsymbol{\alpha}} =& \frac{2}{3}\left(\frac{\partial h}{\partial \boldsymbol{\sigma}} : \mathbf{d}\boldsymbol{\sigma} + \frac{\partial h}{\partial \boldsymbol{\alpha}} : \mathbf{d}\boldsymbol{\alpha}\right)\left(\sqrt{\frac{2}{3}}\alpha_\theta^b\, \boldsymbol{n} - \boldsymbol{\alpha}\right) + \\ & \frac{2}{3}\, h\, \left(\sqrt{\frac{2}{3}}\left(\frac{\partial \alpha_\theta^b}{\partial \boldsymbol{\sigma}} : \mathbf{d}\boldsymbol{\sigma} + \frac{\partial \alpha_\theta^b}{\partial \boldsymbol{\alpha}} : \mathbf{d}\boldsymbol{\alpha}\right)\boldsymbol{n} + \right. \\ & \left. \alpha_\theta^b\left(\frac{\partial \boldsymbol{n}}{\partial \boldsymbol{\sigma}} : \mathbf{d}\boldsymbol{\sigma} + \frac{\partial \boldsymbol{n}}{\partial \boldsymbol{\alpha}} : \mathbf{d}\boldsymbol{\alpha}\right) - \mathbf{d}\boldsymbol{\alpha}\right)\end{aligned} \tag{B.74}$$

which gives

$$\begin{cases} \dfrac{\partial \overline{\boldsymbol{\alpha}}}{\partial \boldsymbol{\sigma}} = \dfrac{2}{3}\left(\sqrt{\dfrac{2}{3}}\alpha_\theta^b\, \boldsymbol{n} - \boldsymbol{\alpha}\right) \otimes \dfrac{\partial h}{\partial \boldsymbol{\sigma}} + \dfrac{2}{3}\, h\, \left(\sqrt{\dfrac{2}{3}}\boldsymbol{n} \otimes \dfrac{\partial \alpha_\theta^b}{\partial \boldsymbol{\sigma}} + \alpha_\theta^b\, \dfrac{\partial \boldsymbol{n}}{\partial \boldsymbol{\sigma}}\right) \\ \dfrac{\partial \overline{\boldsymbol{\alpha}}}{\partial \boldsymbol{\alpha}} = \dfrac{2}{3}\left(\sqrt{\dfrac{2}{3}}\alpha_\theta^b\, \boldsymbol{n} - \boldsymbol{\alpha}\right) \otimes \dfrac{\partial h}{\partial \boldsymbol{\alpha}} + \dfrac{2}{3}\, h\, \left(\sqrt{\dfrac{2}{3}}\boldsymbol{n} \otimes \dfrac{\partial \alpha_\theta^b}{\partial \boldsymbol{\alpha}} + \alpha_\theta^b\, \dfrac{\partial \boldsymbol{n}}{\partial \boldsymbol{\alpha}} - \mathbb{1}\right) \\ \dfrac{\partial \overline{\boldsymbol{\alpha}}}{\partial \boldsymbol{z}} = \mathbf{0} \end{cases} \tag{B.75}$$

Differentials of $\bar{\boldsymbol{z}}$

$$\overline{\boldsymbol{z}} = -\, c_z\langle -D\rangle(z_{max}\boldsymbol{n} + \boldsymbol{z}) \tag{B.76}$$

$$\Rightarrow \mathbf{d}\boldsymbol{z} = c_z\overline{\{-D\}}\mathrm{d}D(z_{max}\boldsymbol{n} + \boldsymbol{z}) - c_z\langle -D\rangle(z_{max}\mathbf{d}\boldsymbol{n} + \mathbf{d}\boldsymbol{z}) \tag{B.77}$$

Therefore we have

$$\mathbf{d}\overline{\boldsymbol{z}} = c_z\overline{\{-D\}}\left(\frac{\partial D}{\partial \boldsymbol{\sigma}} : \mathbf{d}\boldsymbol{\sigma} + \frac{\partial D}{\partial \boldsymbol{\alpha}} : \mathbf{d}\boldsymbol{\alpha} + \frac{\partial D}{\partial \boldsymbol{z}} : \mathbf{d}\boldsymbol{z}\right)(z_{max}\boldsymbol{n} + \boldsymbol{z}) - c_z\langle -D\rangle(z_{max}\left(\frac{\partial \boldsymbol{n}}{\partial \boldsymbol{\sigma}} : \mathbf{d}\boldsymbol{\sigma} + \frac{\partial \boldsymbol{n}}{\partial \boldsymbol{\alpha}} : \mathbf{d}\boldsymbol{\alpha}\right) + \mathbf{d}\boldsymbol{z}) \tag{B.78}$$

which gives

$$\begin{cases} \dfrac{\partial \overline{\boldsymbol{z}}}{\partial \boldsymbol{\sigma}} = c_z\,\overline{\{-D\}}(z_{max}\boldsymbol{n} + \boldsymbol{z}) \otimes \dfrac{\partial D}{\partial \boldsymbol{\sigma}} - c_z\,\langle -D\rangle z_{max}\dfrac{\partial \boldsymbol{n}}{\partial \boldsymbol{\sigma}} \\ \dfrac{\partial \overline{\boldsymbol{z}}}{\partial \boldsymbol{\alpha}} = c_z\,\overline{\{-D\}}(z_{max}\boldsymbol{n} + \boldsymbol{z}) \otimes \dfrac{\partial D}{\partial \boldsymbol{\alpha}} - c_z\,\langle -D\rangle z_{max}\dfrac{\partial \boldsymbol{n}}{\partial \boldsymbol{\alpha}} \\ \dfrac{\partial \overline{\boldsymbol{z}}}{\partial \boldsymbol{z}} = c_z\,\overline{\{-D\}}(z_{max}\boldsymbol{n} + \boldsymbol{z}) \otimes \dfrac{\partial D}{\partial \boldsymbol{z}} - c_z\,\langle -D\rangle \mathbb{1} \end{cases} \tag{B.79}$$

B.1 Differentials of the Residuals

Differentials of $\boldsymbol{\mathcal{R}_1}$

$$\boldsymbol{\mathcal{R}_1} = \boldsymbol{\varepsilon^e} + \dot{\gamma}\boldsymbol{R} - \boldsymbol{\varepsilon}^{\boldsymbol{e},trial} \tag{B.80}$$

$$\Rightarrow \mathbf{d}\boldsymbol{R_1} = \mathbf{d}\boldsymbol{\varepsilon^e} + \mathrm{d}\dot{\gamma}\boldsymbol{R} + \dot{\gamma}\mathbf{d}\boldsymbol{R} \tag{B.81}$$

Therefore we have

$$\mathbf{d}\boldsymbol{\mathcal{R}_1} = \frac{\partial \boldsymbol{\varepsilon^e}}{\partial \boldsymbol{\sigma}} : \mathbf{d}\boldsymbol{\sigma} + \boldsymbol{R}\mathrm{d}\dot{\gamma} + \dot{\gamma}\left(\frac{\partial \boldsymbol{R}}{\partial \boldsymbol{\sigma}} : \mathbf{d}\boldsymbol{\sigma} + \frac{\partial \boldsymbol{R}}{\partial \boldsymbol{\alpha}} : \mathbf{d}\boldsymbol{\alpha} + \frac{\partial \boldsymbol{R}}{\partial \boldsymbol{z}} : \mathbf{d}\boldsymbol{z}\right) \tag{B.82}$$

which gives

$$\begin{cases} \dfrac{\partial \boldsymbol{\mathcal{R}_1}}{\partial \boldsymbol{\sigma}} = \dfrac{\partial \boldsymbol{\varepsilon}^{\boldsymbol{e}}}{\partial \boldsymbol{\sigma}} + \dot{\gamma}\dfrac{\partial \boldsymbol{R}}{\partial \boldsymbol{\sigma}} = \mathbb{D}^e + \dot{\gamma}\dfrac{\partial \boldsymbol{R}}{\partial \boldsymbol{\sigma}} \\ \dfrac{\partial \boldsymbol{\mathcal{R}_1}}{\partial \boldsymbol{\alpha}} = \dot{\gamma}\dfrac{\partial \boldsymbol{R}}{\partial \boldsymbol{\alpha}} \\ \dfrac{\partial \boldsymbol{\mathcal{R}_1}}{\partial \boldsymbol{z}} = \dot{\gamma}\dfrac{\partial \boldsymbol{R}}{\partial \boldsymbol{z}} \\ \dfrac{\partial \boldsymbol{\mathcal{R}_1}}{\partial \dot{\gamma}} = \boldsymbol{R} \end{cases} \tag{B.83}$$

Differentials of $\boldsymbol{\mathcal{R}_2}$

$$\boldsymbol{\mathcal{R}_2} = \boldsymbol{\alpha}^{(n+1)} - \boldsymbol{\alpha}^{(n)} - \dot{\gamma}\overline{\boldsymbol{\alpha}} \tag{B.84}$$

$$\Rightarrow \mathbf{d}\boldsymbol{R_2} = \mathbf{d}\boldsymbol{\alpha} - \mathrm{d}\dot{\gamma}\overline{\boldsymbol{\alpha}} - \dot{\gamma}\mathbf{d}\overline{\boldsymbol{\alpha}} \tag{B.85}$$

Therefore we have

$$\mathbf{d}\boldsymbol{\mathcal{R}_2} = \mathbf{d}\boldsymbol{\alpha} - \mathrm{d}\dot{\gamma}\overline{\boldsymbol{\alpha}} - \dot{\gamma}\left(\frac{\partial \overline{\boldsymbol{\alpha}}}{\partial \boldsymbol{\sigma}} : \mathbf{d}\boldsymbol{\sigma} + \frac{\partial \overline{\boldsymbol{\alpha}}}{\partial \boldsymbol{\alpha}} : \mathbf{d}\boldsymbol{\alpha}\right) \tag{B.86}$$

which gives

$$\begin{cases} \dfrac{\partial \boldsymbol{\mathcal{R}_2}}{\partial \boldsymbol{\sigma}} = -\dot{\gamma}\dfrac{\partial \overline{\boldsymbol{\alpha}}}{\partial \boldsymbol{\sigma}} \\ \dfrac{\partial \boldsymbol{\mathcal{R}_2}}{\partial \boldsymbol{\alpha}} = \mathbb{1} - \dot{\gamma}\dfrac{\partial \overline{\boldsymbol{\alpha}}}{\partial \boldsymbol{\alpha}} \\ \dfrac{\partial \boldsymbol{\mathcal{R}_2}}{\partial \boldsymbol{z}} = \mathbf{0} \\ \dfrac{\partial \boldsymbol{\mathcal{R}_2}}{\partial \dot{\gamma}} = -\overline{\boldsymbol{\alpha}} \end{cases} \tag{B.87}$$

Differentials of $\boldsymbol{\mathcal{R}_3}$

$$\boldsymbol{\mathcal{R}_3} = \boldsymbol{z}^{(n+1)} - \boldsymbol{z}^{(n)} - \dot{\gamma}\overline{\boldsymbol{z}} \tag{B.88}$$

$$\Rightarrow \mathbf{d}\boldsymbol{R_3} = \mathbf{d}\boldsymbol{z} - \mathrm{d}\dot{\gamma}\overline{\boldsymbol{z}} - \dot{\gamma}\mathbf{d}\overline{\boldsymbol{z}} \tag{B.89}$$

Therefore we have

$$\mathbf{d}\boldsymbol{\mathcal{R}_3} = \mathbf{d}\boldsymbol{z} - \mathrm{d}\dot{\gamma}\overline{\boldsymbol{z}} - \dot{\gamma}\left(\frac{\partial\overline{\boldsymbol{z}}}{\partial\boldsymbol{\sigma}} : \mathbf{d}\boldsymbol{\sigma} + \frac{\partial\overline{\boldsymbol{z}}}{\partial\boldsymbol{\alpha}} : \mathbf{d}\boldsymbol{\alpha} + \frac{\partial\overline{\boldsymbol{z}}}{\partial\boldsymbol{z}} : \mathbf{d}\boldsymbol{z}\right) \tag{B.90}$$

which gives

$$\begin{cases} \dfrac{\partial\boldsymbol{\mathcal{R}_3}}{\partial\boldsymbol{\sigma}} = -\dot{\gamma}\dfrac{\partial\overline{\boldsymbol{z}}}{\partial\boldsymbol{\sigma}} \\ \dfrac{\partial\boldsymbol{\mathcal{R}_3}}{\partial\boldsymbol{\alpha}} = -\dot{\gamma}\dfrac{\partial\overline{\boldsymbol{z}}}{\partial\boldsymbol{\alpha}} \\ \dfrac{\partial\boldsymbol{\mathcal{R}_3}}{\partial\boldsymbol{z}} = \mathbb{1} - \dot{\gamma}\dfrac{\partial\overline{\boldsymbol{z}}}{\partial\boldsymbol{z}} \\ \dfrac{\partial\boldsymbol{\mathcal{R}_3}}{\partial\dot{\gamma}} = -\overline{\boldsymbol{z}} \end{cases} \tag{B.91}$$

Differentials of $\mathcal{R}_4$

$$\mathcal{R}_4 = \|\boldsymbol{s} - p\boldsymbol{\alpha}\| - \sqrt{\frac{2}{3}}mp = \|\boldsymbol{r}\| - \sqrt{\frac{2}{3}}mp \tag{B.92}$$

$$\Rightarrow \mathrm{d}R_4 = \mathrm{d}(\|\boldsymbol{r}\|) - \sqrt{\frac{2}{3}}m\mathrm{d}p \tag{B.93}$$

$$= \frac{\boldsymbol{r}}{\|\boldsymbol{r}\|} : \mathbf{d}\boldsymbol{r} - \frac{1}{3}\sqrt{\frac{2}{3}}m\mathbf{1} : \mathbf{d}\boldsymbol{\sigma} \tag{B.94}$$

Therefore we have

$$\mathrm{d}\mathcal{R}_4 = \boldsymbol{n} : \left(\mathbb{1}_{dev} : \mathbf{d}\boldsymbol{\sigma} - \frac{1}{3}(\boldsymbol{\alpha}\otimes\mathbf{1}) : \mathbf{d}\boldsymbol{\sigma} - p\mathbf{d}\boldsymbol{\alpha}\right) - \frac{1}{3}\sqrt{\frac{2}{3}}m\mathbf{1} : \mathbf{d}\boldsymbol{\sigma} \tag{B.95}$$

which gives

$$\begin{cases} \dfrac{\partial \mathcal{R}_4}{\partial \boldsymbol{\sigma}} = \boldsymbol{n} - \dfrac{1}{3}\left(\boldsymbol{n} : \boldsymbol{\alpha} + \sqrt{\dfrac{2}{3}} m\right) \mathbf{1} \\ \dfrac{\partial \mathcal{R}_4}{\partial \boldsymbol{\alpha}} = -p\boldsymbol{n} \\ \dfrac{\partial \mathcal{R}_4}{\partial \boldsymbol{z}} = \mathbf{0} \\ \dfrac{\partial \mathcal{R}_4}{\partial \dot{\gamma}} = 0 \end{cases} \tag{B.96}$$

Appendix C

BEAM FRAME UPDATE AND THEORY OF ROTATION

In order to define the interaction surface, over which the interaction between the soil and the pile is defined, a local coordinate system is defined at every point along the 1D beam element. Evolution of this local coordinate system is defined through kinematics of the beam. Although the beam is assumed to be initially straight and twist-free, the theory explained here can be extended to a more general case. For this the reader can refer to the dissertation by Petek (2006) and the article by Cardona and Geradin (1988).

C.1 Definition of the beam's local coordinate system

As shown in Figure C.1 let $\langle \mathbf{e}_1, \mathbf{e}_2, \mathbf{e}_3 \rangle$ define an orthonormal Cartesian coordinate system in the global space. Local Cartesian systems are defined at each end of the beam, namely $\langle \mathbf{a}_1, \mathbf{a}_2, \mathbf{a}_3 \rangle$ at the starting point, $\mathbf{X}_a$, and $\langle \mathbf{b}_1, \mathbf{b}_2, \mathbf{b}_3 \rangle$ at the ending point, $\mathbf{X}_b$, in such a way that $\mathbf{a}_1$ and $\mathbf{b}_1$ are the unit tangent vectors to the beam centerline at corresponding points. Therefore, $\mathbf{a}_2$ and $\mathbf{a}_3$ ($\mathbf{b}_2$ and $\mathbf{b}_3$) span the cross sectional plane of the beam at the starting (ending) point. We also define a mapping, $\Phi^b(\psi)$, from a straight beam aligned with the $\mathbf{e}_1$ axis of the global system and parameterized with $-1 \leq \psi \leq 1$ to the beam in the global space. A local coordinate system, $\langle \mathbf{E}_1, \mathbf{E}_2, \mathbf{E}_3 \rangle$, can also be defined for this reference beam for sake of generality. However, for the purposes of current document it is assumed that this local coordinate system coincides with the global system, so $\mathbf{E}_i = \mathbf{e}_i$. Let's denote the transformation from the global system to each of these local systems as $\mathbf{Q}_a$ and $\mathbf{Q}_b$. Thus,

$$\mathbf{a}_i = \mathbf{Q}_a \cdot \mathbf{e}_i \quad \text{and} \tag{C.1}$$

$$\mathbf{b}_i = \mathbf{Q}_b \cdot \mathbf{e}_i \quad i = 1, 2, 3. \tag{C.2}$$

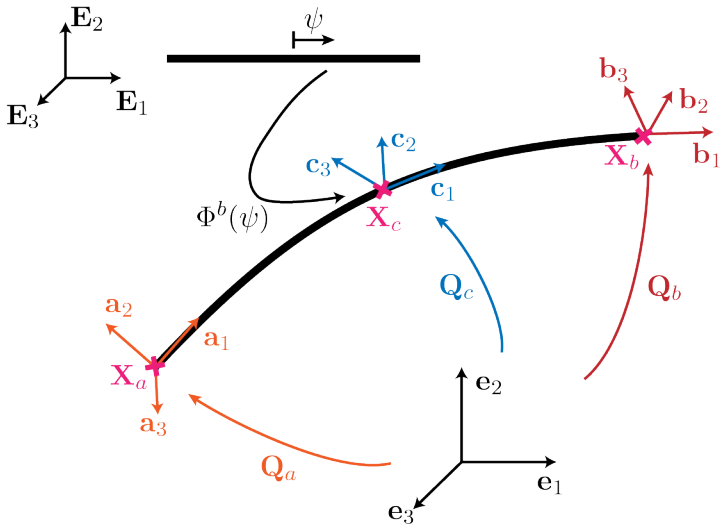

Figure C.1: Definition of the mappings used for updating the frame of reference at each point along the beam

Given the coordinate systems at end points of the beam, an interpolation scheme is defined to define the local coordinate system at point $\mathbf{X}_c$ mapped by $\Phi^b(\psi)$. First, the unit tangent vector at this point, $\mathbf{c}_1$, is calculated as

$$\mathbf{c}_1 = \frac{\partial \Phi^b(\psi)/\partial \psi}{\|\partial \Phi^b(\psi)/\partial \psi\|} \quad . \tag{C.3}$$

Knowing $\mathbf{c}_1$ a drill-free transformation, $\mathbf{Q}_{ac}^{df}$, from the coordinate system at $\mathbf{X}_a$ can be defined. The angle of twist at point $\mathbf{X}_c$ needs to be known in order to fully define the coordinate system at this point. To find this angle, a drill-free transformation, $\mathbf{Q}_{ab}^{df}$, from point $\mathbf{X}_a$ to $\mathbf{X}_b$ is calculated. The rotation angle, χ, between the actual coordinate system at $\mathbf{X}_b$ and the drill-free transformation of the frame at point $\mathbf{X}_a$ is assumed to be the total twist angle of the beam. Angle of twist at point $\mathbf{X}_c$ is linearly interpolated from the total

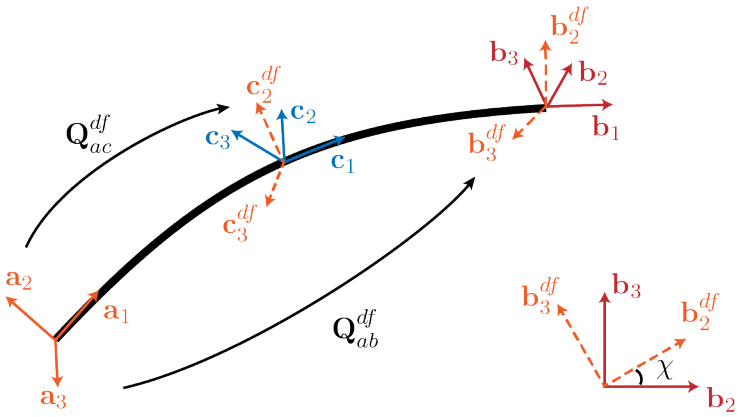

Figure C.2: Schematic of the drill-free transformations and total angle of twist

twist angle. Figure C.2 illustrates a schematic showing these transformations. Therefore,

$$\mathbf{b}_2^{df} = \mathbf{Q}_{ab}^{df} \cdot \mathbf{a}_2 \quad \text{and} \tag{C.4}$$

$$\chi = \cos^{-1}\left(\mathbf{b}_2^{df} \cdot \mathbf{b}_2\right) \quad . \tag{C.5}$$

Angle of twist at point $\mathbf{X}_c$ is $\chi_c = \frac{1+\psi}{2}\chi$. Using the rotation theory we can now fully define the evolution of the coordinate system at every point along the beam.

C.2 Theory of Rotation

Suppose we want to rotate a vector $\mathbf{v}$ about an axis represented by a unit vector, $\mathbf{e}$, at an angle θ. Vector $\mathbf{v}$ is decomposed into a part parallel to $\mathbf{e}$ and a part perpendicular to this axis.

$$\mathbf{v} = \mathbf{v}^{\parallel} + \mathbf{v}^{\perp} \quad , \tag{C.6}$$

where

$$\mathbf{v}^{\parallel} = (\mathbf{e}\cdot\mathbf{v})\,\mathbf{e} \quad \text{and} \tag{C.7}$$

$$\mathbf{v}^{\perp} = \mathbf{v} - (\mathbf{e}\cdot\mathbf{v})\,\mathbf{e} = -\mathbf{e}\times\mathbf{e}\times\mathbf{v} \quad . \tag{C.8}$$

Rotation of the parallel part of vector $\mathbf{v}$ about $\mathbf{e}$ results in the same vector meaning $\mathbf{v}^{\mathrm{rot},\parallel} = \mathbf{v}^{\parallel}$. It is possible to show that rotation of $\mathbf{v}^{\perp}$ about $\mathbf{e}$ is equal to

$$\mathbf{v}^{\mathrm{rot},\perp} = \cos\theta\,\mathbf{v}^{\perp} + \sin\theta\,\mathbf{e}\times\mathbf{v}^{\perp} \quad . \tag{C.9}$$

Notice that $\mathbf{e}\times\mathbf{v} = \mathbf{e}\times\mathbf{v}^{\perp}$. Therefore,

$$\mathbf{v}^{\mathrm{rot}} = \mathbf{v}^{\mathrm{rot},\parallel} + \mathbf{v}^{\mathrm{rot},\perp} \tag{C.10}$$

$$= (\mathbf{e}\cdot\mathbf{v})\,\mathbf{e} - \cos\theta\,\mathbf{e}\times\mathbf{e}\times\mathbf{v} + \sin\theta\,\mathbf{e}\times\mathbf{v} \tag{C.11}$$

$$= \cos\theta\,\mathbf{v} + (1-\cos\theta)\,(\mathbf{e}\cdot\mathbf{v})\,\mathbf{e} + \sin\theta\,\mathbf{e}\times\mathbf{v} \quad . \tag{C.12}$$

The cross product can be written in terms of a skew-symmetric matrix multiplication as $\mathbf{e}\times\mathbf{v} = [\,\overset{\times}{\mathbf{e}}\,]\mathbf{v}$ where,

$$\mathbf{e} = \left\{ \begin{array}{c} e_1 \\ e_2 \\ e_3 \end{array} \right\} \quad \text{and} \quad [\,\overset{\times}{\mathbf{e}}\,] = \left[\begin{array}{ccc} 0 & -e_3 & e_2 \\ e_3 & 0 & -e_1 \\ -e_2 & e_1 & 0 \end{array} \right] \quad . \tag{C.13}$$

It can be shown that

$$\mathbf{v}^{\mathrm{rot}} = \left(\cos\theta\,\mathbf{I} + \sin\theta\,[\,\overset{\times}{\mathbf{e}}\,] + (1-\cos\theta)\mathbf{e}\mathbf{e}^{\mathsf{T}}\right)\mathbf{v} \quad \text{or} \tag{C.14}$$

$$\mathbf{v}^{\mathrm{rot}} = \underbrace{\left(\mathbf{I} + \sin\theta\,[\,\overset{\times}{\mathbf{e}}\,] + (1-\cos\theta)[\,\overset{\times}{\mathbf{e}}\,]^2\right)}_{:=R}\mathbf{v} \quad . \tag{C.15}$$

Equation C.15 is known as Rodrigues' rotation formula. Using Cayley-Hamilton theorem we can show that the exponential map of matrix $\theta[\overset{\times}{\mathbf{e}}]$ is equal to matrix R,

$$\exp(\theta[\overset{\times}{\mathbf{e}}]) = \left(\mathbf{I} + \sin\theta\,[\overset{\times}{\mathbf{e}}] + (1-\cos\theta)[\overset{\times}{\mathbf{e}}]^2\right) = R \quad . \tag{C.16}$$

Expanding C.16 in Taylor series, linear approximation of matrix R is equal to

$$R \approx \mathbf{I} + \theta[\overset{\times}{\mathbf{e}}] \quad , \tag{C.17}$$

which translates into

$$\mathbf{v}^{\text{rot}} \approx \mathbf{v} + \boldsymbol{\theta} \times \mathbf{v} \quad , \tag{C.18}$$

where $\boldsymbol{\theta} = \theta\,\mathbf{e}$.

C.3 Calculation of drill-free transformations

Knowing vectors $\mathbf{a}$ and $\mathbf{b}$ our objective is to calculate the rotation matrix that transforms vector $\mathbf{a}$ to vector $\mathbf{b}$. We can use cross product of these two vectors to calculate the axis of rotation as

$$\mathbf{e} = \frac{\mathbf{b} \times \mathbf{a}}{\|\mathbf{b} \times \mathbf{a}\|} \quad . \tag{C.19}$$

Also as $\|\mathbf{b} \times \mathbf{a}\| = \|\mathbf{b}\|\|\mathbf{a}\| \sin\theta$, θ being the angle between two vectors, we can calculate the rotation angle as

$$\theta = \sin^{-1}\left(\frac{\|\mathbf{b} \times \mathbf{a}\|}{\|\mathbf{b}\|\|\mathbf{a}\|}\right) \quad , \tag{C.20}$$

therefore the rotation matrix, R, transforming vector $\mathbf{a}$ to vector $\mathbf{b}$ is [1]

$$R = \exp\left(\sin^{-1}\left(\frac{\|\mathbf{b}\times\mathbf{a}\|}{\|\mathbf{b}\|\|\mathbf{a}\|}\right)\left[\ \frac{\mathbf{b}\times\mathbf{a}}{\|\mathbf{b}\times\mathbf{a}\|}\ \right]_{\times}\right) \quad . \tag{C.21}$$

If both $\mathbf{a}$ and $\mathbf{b}$ are unit vectors and the rotation angle between them is small enough to assume $\sin\theta \approx \theta$, we can write the rotation matrix as

$$R = \exp\left([\ \mathbf{b}\times\mathbf{a}\ ]_{\times}\right) \tag{C.22}$$

Assuming small deformations, drill-free transformations $\mathbf{Q}_{ab}^{df}$ and $\mathbf{Q}_{ac}^{df}$ are calculated as

$$\mathbf{Q}_{ab}^{df} = \exp\left([\ \mathbf{b}_1\times\mathbf{a}_1\ ]_{\times}\right) \tag{C.23}$$

$$\mathbf{Q}_{ac}^{df} = \exp\left([\ \mathbf{c}_1\times\mathbf{a}_1\ ]_{\times}\right) \quad . \tag{C.24}$$

Knowing the angle of twist at point $\mathbf{X}_c$, the rotation matrix for the twist is written as

$$\mathbf{Q}_c^{\chi} = \exp\left(\chi_c[\ \overset{\times}{\mathbf{c}_1}\ ]\right) \tag{C.25}$$

Therefore, the complete transformation from the global coordinate space to the local coordinate space at point $\mathbf{X}_c$ is

$$\mathbf{Q}_c = \mathbf{Q}_c^{\chi}\,\mathbf{Q}_{ac}^{df}\,\mathbf{Q}_a \quad . \tag{C.26}$$

---

[1] Notice change of notation: $[\ \bullet\ ]_{\times} = [\ \overset{\times}{\bullet}\ ]$.

Appendix D

THE INVERSE MAPPING OF TRI-LINEAR INTERPOLATION OF SOLID ELEMENTS

Location of points in a solid body is defined through a tri-linear interpolation function as defined in set of Equations 9.23-9.29. The inverse of this mapping is needed in order to calculate the parameters defining a point in the global space. As the inverse of this mapping cannot be explicitly derived, we use a Newton-Raphson method to solve a system of nonlinear equations. Suppose point $\mathbf{x}$ is located in the global space with coordinates (x, y, z). The objective is to find (ξ, η, ζ) so that,

$$\mathbf{x} = \sum_{i=1}^{8} N_i(\xi, \eta, \zeta)\hat{\mathbf{x}}_i \quad , \tag{D.1}$$

where $\hat{\mathbf{x}}_i$ denote the location vector of each of 8 nodes. The residual vector $\{R\}$ is generated as $R = \mathbf{x} - \sum_{i=1}^{8} N_i(\xi, \eta, \zeta)\hat{\mathbf{x}}_i$. Therefore, the residual can be written as

$$R_1 = a + a_\xi\ \xi + a_\eta\ \eta + a_\zeta\ \zeta + a_{\xi\eta}\ \xi\eta + a_{\xi\zeta}\ \xi\zeta + a_{\eta\zeta}\ \eta\zeta + a_{\xi\eta\zeta}\ \xi\eta\zeta \tag{D.2}$$

$$R_2 = b + b_\xi\ \xi + b_\eta\ \eta + b_\zeta\ \zeta + b_{\xi\eta}\ \xi\eta + b_{\xi\zeta}\ \xi\zeta + b_{\eta\zeta}\ \eta\zeta + b_{\xi\eta\zeta}\ \xi\eta\zeta \tag{D.3}$$

$$R_3 = c + c_\xi\ \xi + c_\eta\ \eta + c_\zeta\ \zeta + c_{\xi\eta}\ \xi\eta + c_{\xi\zeta}\ \xi\zeta + c_{\eta\zeta}\ \eta\zeta + c_{\xi\eta\zeta}\ \xi\eta\zeta \quad . \tag{D.4}$$

Starting the iterations with $\xi = \eta = \zeta = 0$, the initial residual is equal to

$$R = \left\{ \begin{array}{c} a \\ b \\ c \end{array} \right\} = \left\{ \begin{array}{c} \hat{x}_1 + \hat{x}_2 + \hat{x}_3 + \hat{x}_4 + \hat{x}_5 + \hat{x}_6 + \hat{x}_7 + \hat{x}_8 - 8x \\ \hat{y}_1 + \hat{y}_2 + \hat{y}_3 + \hat{y}_4 + \hat{y}_5 + \hat{y}_6 + \hat{y}_7 + \hat{y}_8 - 8y \\ \hat{z}_1 + \hat{z}_2 + \hat{z}_3 + \hat{z}_4 + \hat{z}_5 + \hat{z}_6 + \hat{z}_7 + \hat{z}_8 - 8z \end{array} \right\} \tag{D.5}$$

The initial tangent matrix for Newton-like iterations is formed as

$$K = \begin{bmatrix} a_\xi & a_\eta & a_\zeta \\ b_\xi & b_\eta & b_\zeta \\ c_\xi & c_\eta & c_\zeta \end{bmatrix} \quad , \tag{D.6}$$

where

$$a_\xi = -\hat{x}_1 + \hat{x}_2 + \hat{x}_3 - \hat{x}_4 - \hat{x}_5 + \hat{x}_6 + \hat{x}_7 - \hat{x}_8 \tag{D.7}$$

$$a_\eta = -\hat{x}_1 - \hat{x}_2 + \hat{x}_3 + \hat{x}_4 - \hat{x}_5 - \hat{x}_6 + \hat{x}_7 + \hat{x}_8 \tag{D.8}$$

$$a_\zeta = -\hat{x}_1 - \hat{x}_2 - \hat{x}_3 - \hat{x}_4 + \hat{x}_5 + \hat{x}_6 + \hat{x}_7 + \hat{x}_8 \tag{D.9}$$

$$b_\xi = -\hat{y}_1 + \hat{y}_2 + \hat{y}_3 - \hat{y}_4 - \hat{y}_5 + \hat{y}_6 + \hat{y}_7 - \hat{y}_8 \tag{D.10}$$

$$b_\eta = -\hat{y}_1 - \hat{y}_2 + \hat{y}_3 + \hat{y}_4 - \hat{y}_5 - \hat{y}_6 + \hat{y}_7 + \hat{y}_8 \tag{D.11}$$

$$b_\zeta = -\hat{y}_1 - \hat{y}_2 - \hat{y}_3 - \hat{y}_4 + \hat{y}_5 + \hat{y}_6 + \hat{y}_7 + \hat{y}_8 \tag{D.12}$$

$$c_\xi = -\hat{z}_1 + \hat{z}_2 + \hat{z}_3 - \hat{z}_4 - \hat{z}_5 + \hat{z}_6 + \hat{z}_7 - \hat{z}_8 \tag{D.13}$$

$$c_\eta = -\hat{z}_1 - \hat{z}_2 + \hat{z}_3 + \hat{z}_4 - \hat{z}_5 - \hat{z}_6 + \hat{z}_7 + \hat{z}_8 \tag{D.14}$$

$$c_\zeta = -\hat{z}_1 - \hat{z}_2 - \hat{z}_3 - \hat{z}_4 + \hat{z}_5 + \hat{z}_6 + \hat{z}_7 + \hat{z}_8 \quad . \tag{D.15}$$

Therefore, first estimation of ξ, η and ζ are

$$\begin{Bmatrix} \xi^1 \\ \eta^1 \\ \zeta^1 \end{Bmatrix} = -\left[K\right]^{-1} \{R\} \quad . \tag{D.16}$$

From this point on the vector of residuals can be formed using Equations D.3 through D.4. The iteration tangent matrix is calculated from

$$K_{11}^k = a_\xi + a_{\xi\eta}\eta^k + a_{\xi\zeta}\zeta^k + a_{\xi\eta\zeta}\eta^k\zeta^k \tag{D.17}$$

$$K_{12}^k = a_\eta + a_{\xi\eta}\xi^k + a_{\eta\zeta}\zeta^k + a_{\xi\eta\zeta}\xi^k\zeta^k \tag{D.18}$$

$$K_{13}^k = a_\zeta + a_{\xi\zeta}\xi^k + a_{\eta\zeta}\eta^k + a_{\xi\eta\zeta}\xi^k\eta^k \tag{D.19}$$

$$K_{21}^k = b_\xi + b_{\xi\eta}\eta^k + b_{\xi\zeta}\zeta^k + b_{\xi\eta\zeta}\eta^k\zeta^k \tag{D.20}$$

$$K_{22}^k = b_e ta + b_{\xi\eta}\xi^k + b_{\eta\zeta}\zeta^k + b_{\xi\eta\zeta}\xi^k\zeta^k \tag{D.21}$$

$$K_{23}^k = b_\zeta + b_{\xi\zeta}\xi^k + b_{\eta\zeta}\eta^k + b_{\xi\eta\zeta}\xi^k\eta^k \tag{D.22}$$

$$K_{31}^k = c_\xi + c_{\xi\eta}\eta^k + c_{\xi\zeta}\zeta^k + c_{\xi\eta\zeta}\eta^k\zeta^k \tag{D.23}$$

$$K_{32}^k = c_e ta + c_{\xi\eta}\xi^k + c_{\eta\zeta}\zeta^k + c_{\xi\eta\zeta}\xi^k\zeta^k \tag{D.24}$$

$$K_{33}^k = c_\zeta + c_{\xi\zeta}\xi^k + c_{\eta\zeta}\eta^k + c_{\xi\eta\zeta}\xi^k\eta^k \quad , \tag{D.25}$$

where

$$a_{\xi\eta} = \quad x_1 - x_2 + x_3 - x_4 + x_5 - x_6 + x_7 - x_8 \tag{D.26}$$

$$a_{\xi\zeta} = \quad x_1 - x_2 - x_3 + x_4 - x_5 + x_6 + x_7 - x_8 \tag{D.27}$$

$$a_{\eta\zeta} = \quad x_1 + x_2 - x_3 - x_4 - x_5 - x_6 + x_7 + x_8 \tag{D.28}$$

$$a_{\xi\eta\zeta} = -x_1 + x_2 - x_3 + x_4 + x_5 - x_6 + x_7 - x_8 \tag{D.29}$$

$$b_{\xi\eta} = \quad y_1 - y_2 + y_3 - y_4 + y_5 - y_6 + y_7 - y_8 \tag{D.30}$$

$$b_{\xi\zeta} = \quad y_1 - y_2 - y_3 + y_4 - y_5 + y_6 + y_7 - y_8 \tag{D.31}$$

$$b_{\eta\zeta} = \quad y_1 + y_2 - y_3 - y_4 - y_5 - y_6 + y_7 + y_8 \tag{D.32}$$

$$b_{\xi\eta\zeta} = -y_1 + y_2 - y_3 + y_4 + y_5 - y_6 + y_7 - y_8 \tag{D.33}$$

$$c_{\xi\eta} = \quad z_1 - z_2 + z_3 - z_4 + z_5 - z_6 + z_7 - z_8 \tag{D.34}$$

$$c_{\xi\zeta} = \quad z_1 - z_2 - z_3 + z_4 - z_5 + z_6 + z_7 - z_8 \tag{D.35}$$

$$c_{\eta\zeta} = \quad z_1 + z_2 - z_3 - z_4 - z_5 - z_6 + z_7 + z_8 \tag{D.36}$$

$$c_{\xi\eta\zeta} = -z_1 + z_2 - z_3 + z_4 + z_5 - z_6 + z_7 - z_8 \quad . \tag{D.37}$$

Convergence is checked by the norm of the residual vector at each step. The iterations continue until convergence is reached. The calculated values of ξ, η and ζ are used to decide if the interaction point falls inside an element or not. If $-1 \leq \xi, \eta, \zeta \leq 1$, the point falls in the inside region of the element otherwise the element is not in contact with the pile surface.

Appendix E

SAMPLE OPENSEES INPUT FILES FOR VARIOUS TESTS

This appendix includes sample `tcl` input files used for a few of the simple models performed in this dissertation using OpenSees. These models include a single element conventional triaxial compression test (both drained and undrained) and a laterally loaded pile embedded in an elastic medium.

E.1 Drained Conventional Triaxial Test

```
# start from a clean state
wipe

# test Specific parameters
# ========================

# confinement Stress
set pConf   -300.0

# deviatoric strain
set devDisp -0.7

# initial void ratio
set vR      0.886

# create a 3D domain with 3 DOFs at each node
model BasicBuilder -ndm 3 -ndf 3

# create nodes
node 1  1.0     0.0     0.0
node 2  1.0     1.0     0.0
node 3  0.0     1.0     0.0
node 4  0.0     0.0     0.0
node 5  1.0     0.0     1.0
node 6  1.0     1.0     1.0
node 7  0.0     1.0     1.0
node 8  0.0     0.0     1.0

# apply fixities
```

```
fix 1    0 1 1
fix 2    0 0 1
fix 3    1 0 1
fix 4    1 1 1
fix 5    0 1 0
fix 6    0 0 0
fix 7    1 0 0
fix 8    1 1 0

# create the soil material and elements
nDMaterial ManzariDafalias  1 125 0.05 $vR 1.25 0.712 0.019 0.934 0.7 1\
          00 0.01 7.05 0.968 1.1 0.704 3.5 4 600 1.42 2 2 1 1.0e-8 1.0e\
          -8

element SSPbrick   1    1 2 3 4 5 6 7 8    1

# create the output directory
if [catch { set retstr [file mkdir Output] } errmsg] {

    puts "Cannot create directory 'Output'. due to error: $errmsg"
    puts "Exiting...."
    exit
}

# create recorders
recorder Node    -file ./output/DMdisp.out   -time -nodeRange 1 8 -dof \
          1 2 3 disp
recorder Element -file ./output/DMstress.out -time stress
recorder Element -file ./output/DMstrain.out -time strain

# confinement pressure load pattern
set pNode [expr $pConf / 4.0]
pattern Plain 1 {Series -time {0 10 1e10} -values {0 1 1} -factor 1} {
    load 1  $pNode  0.0    0.0
    load 2  $pNode  $pNode 0.0
    load 3  0.0     $pNode 0.0
    load 4  0.0     0.0    0.0
    load 5  $pNode  0.0    $pNode
    load 6  $pNode  $pNode $pNode
    load 7  0.0     $pNode $pNode
    load 8  0.0     0.0    $pNode
}

# create analysis
integrator  LoadControl 0.1
numberer    RCM
system      BandGeneral
constraints Transformation
test        NormDispIncr 1e-5 50 1
algorithm   Newton
```

```
analysis    Static

# apply confinement
analyze 100

# read vertical displacement of top plane
set delta0 [nodeDisp 5 3]
set delta [expr $delta0 + $devDisp]
set ratio [expr $delta/$delta0]
# apply deviatoric strain
set lValues [list 1 $ratio $ratio]
set ts "{Series -time {10 100 10000} -values {$lValues} -factor 1}"

# shear load pattern
eval "pattern Plain 2 $ts {
        sp 5  3         $delta0
        sp 6  3         $delta0
        sp 7  3         $delta0
        sp 8  3         $delta0
}"
puts "starting analysis..."
set startT [clock seconds]

# run the analysis
analyze 900

set endT [clock seconds]
puts "loading analysis execution time: [expr $endT-$startT] seconds."

# clear up
wipe
```

E.2 Unrained Conventional Triaxial Test

```
# start from a clean state
wipe

# test Specific parameters
# ========================

# confinement Stress
set pConf   -300.0

# deviatoric strain
set devDisp -0.7

# permeablity
set perm    1.0e-9

```

```
# Initial void ratio
set vR      0.735

# rayleigh damping parameter
set damp   0.1
set omega1 0.0157
set omega2 64.123
set a1 [expr 2.0*$damp/($omega1+$omega2)]
set a0 [expr $a1*$omega1*$omega2]

# create a 3D domain with 3 DOFs at each node
model BasicBuilder -ndm 3 -ndf 4

# create nodes
node 1  1.0     0.0     0.0
node 2  1.0     1.0     0.0
node 3  0.0     1.0     0.0
node 4  0.0     0.0     0.0
node 5  1.0     0.0     1.0
node 6  1.0     1.0     1.0
node 7  0.0     1.0     1.0
node 8  0.0     0.0     1.0

# apply fixities
fix 1   0 1 1 1
fix 2   0 0 1 1
fix 3   1 0 1 1
fix 4   1 1 1 1
fix 5   0 1 0 1
fix 6   0 0 0 1
fix 7   1 0 0 1
fix 8   1 1 0 1

# create the soil material and elements
nDMaterial ManzariDafalias  1 125 0.05 $vR 1.25 0.712 0.019 0.934 0.7 1\
          00 0.01 7.05 0.968 1.1 0.704 3.5 4 600 1.42 2 2 1 1.0e-8 1.0e\
          -8

# create element
element SSPbrickUP   1  1 2 3 4 5 6 7 8  1 2.2e8 1.0 $perm $perm $perm \
          $vR 1.5e-5

# create the output directory
if [catch { set retstr [file mkdir Output] } errmsg] {

    puts "Cannot create directory 'Output'. due to error: $errmsg"
    puts "Exiting...."
    exit
}

```

```
# create recorders
recorder Node    -file ./output/UDLdisp.out   -time -nodeRange 1 8 \
         -dof 1 2 3 disp
recorder Node    -file ./output/UDLpress.out  -time -nodeRange 1 8 \
         -dof 4 vel
recorder Element -file ./output/UDLstress.out -time stress
recorder Element -file ./output/UDLstrain.out -time strain

# confinement pressure load pattern
set pNode [expr $pConf / 4.0]
pattern Plain 1 {Series -time {0 10000 1e10} -values {0 1 1} -factor 1\
         } {
    load 1  $pNode  0.0    0.0    0.0
    load 2  $pNode  $pNode 0.0    0.0
    load 3  0.0     $pNode 0.0    0.0
    load 4  0.0     0.0    0.0    0.0
    load 5  $pNode  0.0    $pNode 0.0
    load 6  $pNode  $pNode $pNode 0.0
    load 7  0.0     $pNode $pNode 0.0
    load 8  0.0     0.0    $pNode 0.0
}

# create analysis
constraints Penalty 1.0e15 1.0e15
test        NormDispIncr 1.0e-5 20 1
algorithm   Newton
numberer    RCM
system      BandGeneral
integrator  Newmark 0.5 0.25
rayleigh    $a0 0.0 $a1 0.0
analysis    Transient

# apply confinement
analyze 100 100

# let the model rest and waves damp out
analyze 50  100

# close drainage valves
for {set x 1} {$x<9} {incr x} {
   remove sp $x 4
}
analyze 50 100

# read vertical displacement of top plane
set vertDisp [nodeDisp 5 3]
# apply deviatoric strain
set lValues [list 1 [expr 1+$devDisp/$vertDisp] [expr 1\
         +$devDisp/$vertDisp]]
```

```
set ts "{Series -time {20000 50000 1.0e10} -values {$lValues} -factor \
        1}"

# shear load pattern
eval "pattern Plain 2 $ts {
        sp 5  3 $vertDisp
        sp 6  3 $vertDisp
        sp 7  3 $vertDisp
        sp 8  3 $vertDisp
}"

# set number and length of (pseudo)time steps
set dT      100
set numStep 300

set startT [clock seconds]

# run the analysis
analyze $numStep  $dT

set endT [clock seconds]
puts "loading analysis execution time: [expr $endT-$startT] seconds."

# clear up
wipe
```

E.3 A Single Pile Under Lateral Loads

```
# start from a clean state
wipe

# create a 3D domain with 3 DOFs at each node
model BasicBuilder -ndm 3 -ndf 3

# define the domain
set x_min -5.0
set x_max  5.0
set y_min -5.0
set y_max  5.0
set z_min  0.0
set z_max  20.0

# define meshing parameters
set numEle_x 10
set numEle_y 10
set numEle_z 20

# define beam location
set b_x1  0.0
```

```
22 set b_y1  0.0
23 set b_z1  10.0
24 set b_x2  0.0
25 set b_y2  0.0
26 set b_z2  20.0
27
28 # define beam meshing parameter
29 set b_numEle 10
30
31 # define number of descritization points
32 set nP 8
33 set nL 8
34
35 # create the soil geometry
36 set dx [expr ($x_max-$x_min)/$numEle_x]
37 set dy [expr ($y_max-$y_min)/$numEle_y]
38 set dz [expr ($z_max-$z_min)/$numEle_z]
39
40 set nodeInfo [open nodeInfo.dat w]
41 for {set ii 0} {$ii <= $numEle_x} {incr ii} {
42   for {set jj 0} {$jj <= $numEle_y} {incr jj} {
43     for {set kk 0} {$kk <= $numEle_z} {incr kk}  {
44       set nodeTag [expr ($numEle_y+1)*($numEle_z+1)*$ii + \
          ($numEle_z+1)*$jj + $kk + 1]
45       set nodeX   [expr $x_min + $ii * $dx]
46       set nodeY   [expr $y_min + $jj  * $dy]
47       set nodeZ   [expr $z_min + $kk * $dz]
48
49 # create soil nodes and write info to file
50       node    $nodeTag $nodeX $nodeY $nodeZ
51       puts $nodeInfo "$nodeTag $nodeX $nodeY $nodeZ"
52     }
53   }
54 }
55 close $nodeInfo
56
57 # fix the boundaries of the mesh
58 fixX $x_min 1 0 0
59 fixX $x_max 1 0 0
60 fixY $y_min 0 1 0
61 fixY $y_max 0 1 0
62 fixZ $z_min 1 1 1
63
64
65 # create the soil material and elements
66 set E       1.0e8
67 set nu      0.33
68 set density 1.7
69 nDMaterial ElasticIsotropic 1 $E $nu $density
70
```

```
set elemInfo [open elementInfo.dat w]
for {set ii 0} {$ii < $numEle_x} {incr ii} {
  for {set jj 0} {$jj < $numEle_y} {incr jj} {
    for {set kk 0} {$kk < $numEle_z} {incr kk}  {
      set sNode1  [expr ($numEle_y+1)*($numEle_z+1)*$ii + \
          ($numEle_z+1)*$jj + $kk + 1]
      set sNode2  [expr ($numEle_y+1)*($numEle_z+1)*($ii+1) + \
          ($numEle_z+1)*$jj + $kk + 1]
      set sNode3  [expr ($numEle_y+1)*($numEle_z+1)*($ii+1) + \
          ($numEle_z+1)*($jj+1) + $kk + 1]
      set sNode4  [expr ($numEle_y+1)*($numEle_z+1)*$ii + \
          ($numEle_z+1)*($jj+1) + $kk + 1]
      set sNode5  [expr $node1 + 1]
      set sNode6  [expr $node2 + 1]
      set sNode7  [expr $node3 + 1]
      set sNode8  [expr $node4 + 1]
      set eleTag [expr $numEle_y*$numEle_z*$ii + $numEle_z*$jj + $kk + \
          1]
      set eleWgt [expr -1.0 * $density * 9.81]

# create soil elements and write info to file
      element SSPbrick  $eleTag $sNode1 $sNode2 $node3 $sNode4 $sNode5 \
          $sNode6 $sNode7 $sNode8 1 0.0 0.0 $eleWgt
      puts $elemInfo "$eleTag $sNode1 $sNode2 $sNode3 $sNode4 $sNode5 \
          $sNode6 $sNode7 $sNode8 1"
    }
  }
}
close $elemInfo

# analysis details
set dt       0.1
set numSteps 5
set maxIter  20
set tol      1.0e-20
set printOpt 1

# Create analysis
constraints Transformation
numberer    RCM
test        EnergyIncr $tol $maxIter $printOpt
algorithm   Newton
system      SparseGeneral
integrator  LoadControl $dt
analysis    Static

# create a 3D domain with 6 DOFs at each node
model BasicBuilder -ndm 3 -ndf 6

# create the beams
```

```
114 set b_dx [expr ($b_x2 - $b_x1)/($b_numEle + 0.0)]
115 set b_dy [expr ($b_y2 - $b_y1)/($b_numEle + 0.0)]
116 set b_dz [expr ($b_z2 - $b_z1)/($b_numEle + 0.0)]
117
118 set nodeInfo [open nodeInfoB.dat w]
119 for {set ii 0} {$ii <= $b_numEle} {incr ii} {
120     set nodeTag [expr 100000 + $ii + 1]
121     set nodeX   [expr $b_x1 + $ii * $b_dx]
122     set nodeY   [expr $b_y1 + $ii * $b_dy]
123     set nodeZ   [expr $b_z1 + $ii * $b_dz]
124
125 # create beam nodes and write info to file
126     node  $nodeTag $nodeX $nodeY $nodeZ
127     puts $nodeInfo "$nodeTag $nodeX $nodeY $nodeZ"
128 }
129 close $nodeInfo
130
131 # geomTransf Linear $tag $xz1 $xz2 $xz3
132 geomTransf Linear 1   0.0 1.0 0.0
133
134 # beam element properties
135 set radius 0.25
136 set area   [expr 3.14159 * $radius * $radius]
137 set E      20.0e6
138 set G      [expr $E/ (2.0 * (1.0 + 0.3))]
139 set I      [expr $area * $area / 3.14159 / 4.0]
140 set J      [expr 2.0 * $I]
141
142 set elemInfo [open elementInfoB.dat w]
143 for {set ii 0} {$ii < $b_numEle} {incr ii}  {
144   set bNode1 [expr 100000 + $ii + 1]
145   set bNode2 [expr $node1 + 1]
146
147 # create beam elements and write info to file
148   element elasticBeamColumn $bNode1 $bNode1 $bNode2 $area $E $G $J $I \
          $I 1
149   puts $elemInfo "$bNode1 $bNode1 $bNode2 1"
150 }
151 close $elemInfo
152
153 # generate interface elements
154 set interfaceElemsFile "interfaceInfo.dat"
155 if {[file exists $interfaceElemsFile] == 1} { file delete \
          $interfaceElemsFile }
156
157 set interfaceElems {}
158 for {set ii 0} {$ii < $b_numEle} {incr ii}  {
159   set elem [expr 100000 + $ii + 1]
```

```
160   set interfaceElems [concat $interfaceElems [generateInterfacePoints \
          $elem 1  -gPenalty -shape circle -nP $nP -nL $nL -radius \
          $radius -file $interfaceElemsFile ]]
161 }
162
163 # beam uniform loads
164 pattern Plain 1 {Series -time {0 1 2 1e10} -values {0 0 1 1} -factor 1\
          } {
165   eleLoad -range [expr 100000 + 1] [expr 100000 + $b_numEle] -type \
          -beamUniform  0.0 0.0 [expr -1.0*$area*20.5*9.81]
166 }
167
168 # beam nodal loads
169 pattern Plain 2 {Series -time {0 4.0 5.0 1e10} -values {0 0 1 1} \
          -factor 1} {
170     load [expr 100000 + $b_numEle + 1]  1000  0.0    0.0   0.0 0.0 0.0
171 }
172
173 # create recorders
174 recorder Element -time -file contactDisp.out   -ele        \
          $interfaceElems disp
175 recorder Element -time -file contactBeamCL.out -ele        \
          $interfaceElems force
176 recorder Node    -time -file beamDisp.out      -nodeRange  100001 \
          [expr 100001 + $b_numEle] -dof 1 2 3 4 5 6  disp
177 recorder Node    -time -file displacement.out  -nodeRange  1 [expr \
          ($numEle_y+1)*($numEle_z+1)*($numEle_z+1)]  -dof 1 2 3 disp
178 recorder Element -time -file stress.out        -eleRange   1 [expr \
          $numEle_x*$numEle_y*$numEle_z] stress
179 recorder Element -time -file strain.out        -eleRange   1 [expr \
          $numEle_x*$numEle_y*$numEle_z] strain
180
181 # run the analysis
182 analyze $numSteps
183
184 # clear up
185 wipe
```

BIBLIOGRAPHY

Abdoun, T. and Dobry, R. (2002). "Evaluation of pile foundation response to lateral spreading." *Soil Dynamics and Earthquake Engineering*, 22(9-12), 1051–1058.

Adachi, N., Miyamoto, Y., and Koyamada, K. (1998). "Shaking table test and lateral loading test for pile foundation in saturated sand." *Proc. Intl. Conf. Centrifuge98*, Tokyo, Japan, Sept, 23–25.

Alawaji, H., Runesson, K., Sture, S., and Axelsson, K. (1992). "Implicit integration in soil plasticity under mixed control for drained and undrained response." *International journal for numerical and analytical methods in geomechanics*, 16(10), 737–756.

American Association of State Highway and Transportation Officials (AASHTO) (2010a). *Guide Specifications for LRFD Seismic Bridge Design*. Washington, D.C., 1st edition.

American Association of State Highway and Transportation Officials (AASHTO) (2010b). *LRFD Bridge Design Specifications*. Washington, D.C., 5th edition.

American Petroleum Institute (API) (1987). *Recommended Practice for Planning, Designing and Constructing Fixed Offshore Platforms*. American Petroleum Institute, Washington, D.C., 17th edition.

American Petroleum Institute (API) (2007). *Recommended Practice for Planning, Designing and Constructing Fixed Offshore Platforms–Working Stress Design*. American Petroleum Institute, 21st edition. Errata and Supplement 3, October 2007.

Anandarajah, A. (2011). *Computational methods in elasticity and plasticity: solids and porous media*. Springer-Verlag New York, New York.

Arduino, P., Kramer, S. L., Li, P., and Horne, J. C. (2006). "Stiffness of piles in liquefiable soils." *Seismic Performance and Simulation of Pile Foundations in Liquefied and Laterally Spreading Ground*, R. W. Boulanger and K. Tokimatsu, eds., GSP 145, ASCE, 134–148.

Arduino, P., McGann, C., **Ghofrani**, A., et al. (2017a). "Numerical evaluation of forces on piled bridge foundations in laterally spreading soil." *Report No. WA-RD 874.1*, Washington (State) Dept. of Transportation. Research Office.

Arduino, P., McGann, C. R., and **Ghofrani**, A. (2017b). "Design procedure for bridge foundations subject to liquefaction-induced lateral spreading." *Report No. WA-RD 874.2*, Washington (State) Dept. of Transportation. Research Office.

Armero, F. and Pérez-Foguet, A. (2002). "On the formulation of closest-point projection algorithms in elastoplasticity part i: The variational structure." *International Journal for Numerical Methods in Engineering*, 53(2), 297–329.

Armstrong, R. J. (2010). *Evaluation of the Performance of Piled Bridge Abutments Affected by Liquefaction-Induced Ground Deformations Through Centrifuge Tests and Numerical Analysis Tools*. Ph.D. Dissertation, University of California at Davis.

Armstrong, R. J., Boulanger, R. W., Galerce, U., Kutter, B. L., and Wilson, D. W. (2008). "Centrifuge modeling of pile pinning effects." *Geotechnical Earthquake Engineering and Soil Dynamics IV*, D. Zeng, M. T. Manzari, and D. R. Hiltunen, eds., GSP 181, ASCE, 1–12.

Ashford, S. A., Boulanger, R. W., and Brandenberg, S. J. (2011). "Recommended design practice for pile foundations in laterally spreading ground." *PEER Report No. 2011/04*, Pacific Earthquake Engineering Research Center, University of California, Berkeley.

Ashford, S. A. and Juirnarongrit, T. (2006). "Push-over analyses of piles in laterally spreading soil." *Seismic Performance and Simulation of Pile Foundations in Liquefied and Lat-*

erally Spreading Ground, R. W. Boulanger and K. Tokimatsu, eds., GSP 145, ASCE, 109–120.

Ashour, M. and Ardalan, H. (2011). "Piles in fully liquefied soils with lateral spread." *Computers and Geotechnics*, 38(6), 821–833.

Ates, S. and Constantinou, M. C. (2011). "Example of application of response history analysis for seismically isolated curved bridges on drilled shaft with springs representing soil." *Soil Dynamics and Earthquake Engineering*, 31(3), 334–350.

Basha, B. M. and Babu, G. S. (2009). "Computation of sliding displacements of bridge abutments by pseudo-dynamic method." *Soil Dynamics and Earthquake Engineering*, 29(1), 103–120.

Been, K. and Jefferies, M. G. (1985). "A state parameter for sands." *Géotechnique*, 35(2), 99–112.

Bernardi, C. (1994). "A new nonconforming approach to domain decomposition: the mortar element method." *Nonliner Partial Differential Equations and Their Applications*.

Bernardi, C., Maday, Y., and Patera, A. T. (1993). "Domain decomposition by the mortar element method." *Asymptotic and numerical methods for partial differential equations with critical parameters*, Vol. 384, Dordrecht, Springer, 269–286.

Bhattacharya, S., Bolton, M. D., and Madabhushi, S. P. G. (2005). "A reconsideration of the safety of piled bridge foundations in liquefiable soils." *Soils and Foundations*, 45(4), 13–25.

Boroschek, R., Soto, P., and León, R. (2010). *Registros del Terremoto del Maule, Mw=8.8, 27 de Febrero de 2010*. RENADIC Report 10/05.

Boroschek, R. L., Contreras, V., Kwak, D. Y., and Stewart, J. P. (2012). "Strong ground motion attributes of the 2010 mw 8.8 maule, chile, earthquake." *Earthquake Spectra*, 28(S1), S19–S38.

Boulanger, R. W., Chang, D., Gulerce, U., Brandenberg, S. J., and Kutter, B. L. (2006). "Evaluating pile pinning effects on abutments over liquefied ground." *Seismic Performance and Simulation of Pile Foundations in Liquefied and Laterally Spreading Ground*, R. W. Boulanger and K. Tokimatsu, eds., GSP 145, ASCE, 306–318.

Boulanger, R. W., Curras, C. J., Kutter, B. L., Wilson, D. W., and Abghari, A. (1999). "Seismic soil-pile-structure interaction experiments and analyses." *Journal of Geotechnical and Geoenvironmental Engineering, ASCE*, 125(9), 750–759.

Boulanger, R. W., Kutter, B. L., Brandenberg, S. J., Singh, P., and Chang, D. (2003). *Pile Foundations in liquefied and laterally spreading ground during earthquakes: Centrifuge experiments and analyses*. Center for Geotechnical Modeling, University of California at Davis, Davis, CA. Rep. UCD/CGM-03/01.

Bozorgzadeh, A., Ashford, S. A., and Restrepo, J. I. (2008). "Effect of backfill soil type on stiffness and ultimate capacity of bridge abutments." *Geotechnical Earthquake Engineering and Soil Dynamics IV*, D. Zeng, M. T. Manzari, and D. R. Hiltunen, eds., GSP 181, ASCE, 1–10.

Bradley, B. A., Cubrinovski, M., Dhakal, R. P., and MacRae, G. A. (2009). "Intensity measures for the seismic response of pile foundations." *Soil Dynamics and Earthquake Engineering*, 29(6), 1046–1058.

Bradley, B. A., Cubrinovski, M., Dhakal, R. P., and MacRae, G. A. (2010). "Probabilistic seismic performance and loss assessment of a bridge–foundation–soil system." *Soil Dynamics and Earthquake Engineering*, 30(5), 395–411.

Bradley, B. A., Cubrinovski, M., and Haskell, J. J. (2011). "Probabilistic pseudo-static analysis of pile foundations in liquefiable soils." *Soil Dynamics and Earthquake Engineering*, 31(10), 1414–1425.

Brandenberg, S. J. (2005). *Behavior of pile foundations in liquefied and laterally spreading ground*. Ph.D. Dissertation, University of California at Davis.

Brandenberg, S. J., Boulanger, R. W., Kutter, B. L., and Chang, D. (2005). "Behavior of pile foundations in laterally spreading ground during centrifuge tests." *Journal of Geotechnical and Geoenvironmental Engineering*, 131(11), 1378–1391.

Brandenberg, S. J., Boulanger, R. W., Kutter, B. L., and Chang, D. (2007a). "Liqufaction induced softening of load transfer between pile groups and laterally spreading crusts." *Journal of Geotechnical and Geoenvironmental Engineering, ASCE*, 133(1), 91–103.

Brandenberg, S. J., Boulanger, R. W., Kutter, B. L., and Chang, D. (2007b). "Static pushover analyses of pile groups in liquefied and laterally spreading ground in centrifuge tests." *Journal of Geotechnical and Geoenvironmental Engineering, ASCE*, 133(9), 1055–1066.

Brandenberg, S. J., Zhang, J., Kashighandi, P., Huo, Y., and Zhao, M. (2011). "Demand fragility surfaces for bridges in liquefied and laterally spreading ground." *PEER Report No. 2011/01*, Pacific Earthquake Engineering Research Center, University of California, Berkeley.

Bray, J. D. and Travasarou, T. (2007). "Simplified procedure for estimating earthquake-induced deviatoric slope displacements." *Journal of Geotechnical and Geoenvironmental Engineering, ASCE*, 133(4), 381–392.

Brinch Hansen, J. (1961). "The ultimate resistance of rigid piles against transversal forces." *Bulletin No. 12*, Geoteknisk Institute, Copenhagen, 5–9.

Broms, B. B. (1964). "Lateral resistance of piles in cohesionless soils." *Journal of the Soil Mechanics and Foundations Division, ASCE*, 90(SM3), 123–156.

Brown, D. A. and Shie, C. F. (1990). "Three-dimensional finite element model of laterally loaded piles." *Computers and Geotechnics*, 10(1), 59–79.

Brown, D. A. and Shie, C.-F. (1991). "Some numerical experiments with a three dimensional finite element model of a laterally loaded pile." *Computers and Geotechnics*, 12(2), 149–162.

Brown, D. A., Shie, C. F., and Kumar, M. (1989). "*p-y* curves for laterally loaded piles derived from three-dimensional finite element model." *Proceedings of the III International Symposium, Numerical Models in Geomechanics (NUMOG III) 8-11 May 1989*, Niagara Falls, Canada, Elsevier Applied Sciences, 683–690.

California Department of Transportation (Caltrans) (2011). *Guidelines on Foundation Loading and Deformation Due to Liquefaction Induced Lateral Spreading.* Internal Policy Proposal, February 2011.

Cardona, A. and Geradin, M. (1988). "A beam finite element non-linear theory with finite rotations." *International journal for numerical methods in engineering*, 26(11), 2403–2438.

Chang, D., Boulanger, R. W., Brandenberg, S. J., and Boulanger, R. W. (2006). "Dynamic analyses of soil-pile-structure interaction in laterally spreading ground during earthquake shaking." *Seismic Performance and Simulation of Pile Foundations in Liquefied and Laterally Spreading Ground*, R. W. Boulanger and K. Tokimatsu, eds., GSP 145, ASCE, 218–229.

Chang, D. W., Lin, B. S., Yeh, C. H., and Cheng, S. H. (2008). "FD solutions for static and dynamic winkler models with lateral spread induced earth pressures on piles." *Geotechnical Earthquake Engineering and Soil Dynamics IV*, D. Zeng, M. T. Manzari, and D. R. Hiltunen, eds., GSP 181, ASCE.

Chen, L., **Ghofrani**, A., and Arduino, P. (under review). "Prediction of leap-ucd-2017 centrifuge test results using two advanced plasticity sand models." *Centrifuge Experiments and Numerical Simulations of Lateral Spreading due to Soil Liquefaction: Proceedings of the LEAP-UCD-2017 Workshop – 14-15 Dec 2017*, M. Zeghal, B. Kutter, and M. Manzari, eds., Davis, CA.

Cubrinovski, M. and Ishihara, K. (2004). "Simplified method for analysis of piles undergoing lateral spreading in liquefied soils." *Soils and Foundations*, 44(5), 119–133.

Cubrinovski, M. and Ishihara, K. (2006). "Assessment of pile group response to lateral spreading by single pile analysis." *Seismic Performance and Simulation of Pile Foundations in Liquefied and Laterally Spreading Ground*, R. W. Boulanger and K. Tokimatsu, eds., GSP 145, ASCE, 242–254.

Cubrinovski, M., Kokusho, T., and Ishihara, K. (2006). "Interpretation from large-scale shake table tests on piles undergoing lateral spreading in liquefied soils." *Soil Dynamics and earthquake engineering*, 26(2-4), 275–286.

Dafalias, Y. and Taiebat, M. (2013). "Anatomy of rotational hardening in clay plasticity." *Géotechnique*, 63(16), 1406.

Dafalias, Y. F. (1986). "Bounding surface plasticity i: Mathematical foundation and hypoplasticity." *Journal of Engineering Mechanics*, 112(9), 966–987.

Dafalias, Y. F. and Manzari, M. T. (2004). "Simple plasticity sand model accounting for fabric change effects." *Journal of Engineering Mechanics*, 130(6), 622–634.

Desai, C. S. and Appel, G. C. (1976). "3D analysis of laterally loaded structures." *Proceedings of the 2nd International Conference on Numerical Methods in Geomechanics - June 1976*, Blacksburg, VA, 405–418.

Dicleli, M. (2005). "Integral abutment-backfill behavior on sand soil-pushover analysis approach." *Journal of Bridge Engineering, ASCE*, 10(3), 354–364.

Dungca, J. R., Kuwano, J., Takahashi, A., Saruwatari, T., Izawa, J., Suzuki, H., and Tokimatsu, K. (2006). "Shaking table tests on the lateral response of a pile buried in liquefied sand." *Soil Dynamics and Earthquake Engineering*, 26, 287–295.

Durran, D. R. (2013). *Numerical methods for wave equations in geophysical fluid dynamics*, Vol. 32. Springer Science & Business Media.

Elgamal, A., Yang, Z., Parra, E., and Ragheb, A. (2003). "Modeling of cyclic mobility in saturated cohesionless soils." *International Journal of Plasticity*, 19(6), 883–905.

Faraji, S., Ting, J. M., Crovo, D. S., and Ernst, H. (2001). "Nonlinear analysis of integral bridges: Finite element model." *Journal of Geotechnical and Geoenvironmental Engineering, ASCE*, 127(5), 454–461.

Faris, A. T., Seed, R. B., Kayen, R. E., and Wu, J. (2006). "A semi-empirical model for the estimation of maximum horizontal displacement due to liquefaction-induced lateral spreading." *Proceedings, 8th U.S. National Conference on Earthquake Engineering*, San Franciso, CA, April 18-22, Paper No. 1323.

Faruque, M. O. and Desai, C. S. (1982). "3D material and geometric nonlinear analysis of piles." *Proceedings of the 2nd International Conference on Numerical Methods in Offshore Piling – April 29-30, 1982*, University of Texas at Austin, 553–576.

Federal Highway Administration (FHWA) (2011). *Post-Earthquake Reconnaissance Report on Transportation Infrastructure: Impact of the February 27, 2010, Offshore Maule Earthquake in Chile*. W.-H. P. Yen, G. Chen, I. Buckle, T. Allen, D. Alzamora, J. Ger, and J. G. Arias, Publication No. FHWA-HRT-11-030, U.S. Department of Transportation, McLean, VA.

Fleming, W. G. K., Weltman, A. J., Randolph, M. F., and Elson, W. K. (1985). *Piling Engineering*. Surrey University Press, London.

Fujii, S., Cubrinovski, M., Tokimatsu, K., and Hayashi, T. (1998a). "Analyses of damaged and undamaged pile foundations in liquefied soils during the 1995 kobe earthquake." *Geotechnical Earthquake Engineering and Soil Dynamics III*, ASCE, 1187–1198.

Fujii, S., Isemoto, N., Satou, Y., Kaneko, O., Funahara, H., Arai, T., and Tokimatsu, K. (1998b). "Investigation and analysis of a pile foundation damaged by liquefaction during the 1995 hyogoken-nambu earthquake." *Soils and Foundations*, 38(Special), 179–192.

Geo-Engineering Extreme Events Reconnaissance (GEER) Association (2010). *Geo-engineering Reconnaissance of the 2010 Maule, Chile Earthquake*. J. Bray and D. Frost, eds., Report No. GEER-022.

Goodman, R. E., Taylor, R. L., and Brekke, T. L. (1968). "A model for the mechanics of jointed rocks." *Journal of Soil Mechanics & Foundations Div.*

Griffiths, D. and Kidger, D. (1995). "Enhanced visualization of failure mechanisms by finite elements." *Computers & structures*, 55(2), 265–268.

Hamada, M. (1996). "Liquefaction, graound deformation and their caused damage to structures." *Special Report on the Hyogoken-nanbu Earthquake, Committee of Earthquake Engineering, Japan Society of Civil Engineers*, 45–92.

Hara, T., Yu, Y., and Ugai, K. (2004). "Behavior of piled bridge abutments on soft ground: A design method proposal based on 2D elasto-plastic-consolidation coupled FEM." *Computers and Geotechnics*, 31, 339–355.

Helnwein, P., Liu, C. H., Meschke, G., and Mang, H. A. (1993). "A new 3-d finite element model for cord-reinforced rubber composites application to analysis of automobile tires." *Finite elements in analysis and design*, 14(1), 1–16.

Hofstetter, G. and Taylor, R. (1990). "Non-associative drucker-prager plasticity at finite strains." *Communications in Applied Numerical Methods*, 6(8), 583–589.

Ishihara, K., Tatsuoka, F., and Yasuda, S. (1975). "Undarined deformation and liquefaction of sand under cyclic stresses." *Soils and Foundations*, 15(1), 29–44.

Itasca, F. (2012). "Fast lagrangian analysis of continua, version 7.0." *Itasca Consulting Group Inc., Minneapolis, MN*.

Karube, D. and Kimura, M. (1996). "Damage to foundations of railway structures." *Soils and foundations*, 36(Special), 201–210.

Khalili-Tehrani, P., Ahlberg, E., Rha, C., Lemnitzer, A., Salamanca, A., Nigbor, R., Stewart, J. P., Wallace, J., and Taciroglu, E. (2007). "Field-testing and modeling of soil-structure interaction for highway support structures." *Proceedings of the 2007 Structures Congress*, R. Lyons, J. W. Wallace, and E. Stovner, eds., Long Beach, CA, ASCE.

Khosrojerdi, M. and Pak, A. (2015). "Numerical investigation on the behavior of the gravity waterfront structures under earthquake loading." *Ocean Engineering*, 106, 152–160.

Knappett, J. A., Mohammadi, S., and Griffin, C. (2010). "Lateral spreading forces on bridge piers and pile caps in laterally spreading soil: Effect of angle of incidence." *Journal of Geotechnical and Geoenvironmental Engineering, ASCE*, 136(12), 1589–1599.

Kondoh, M. and Tamura, K. (2003). "Experimental study on liquefaction-induced earth pressure on bridge abutment." *Proceedings of the 19th U.S.-Japan Bridge Engineering Workshop*, Tsukuba, Japan, October 27-30.

Kotsoglou, A. N. and Pantazopoulou, S. J. (2009). "Assessment and modeling of embankment participation in the seismic response of integral abutment bridges." *Bulletin of Earthquake Engineering*, 7(2), 343–361.

Kraft, L. M., Ray, R. P., and Kagawa, T. (1981). "Theoretical *t-z* curves." *Journal of the Geotechnical Engineering Division, ASCE*, 107(11), 1543–1561.

Kramer, S. L. (1996). *Geotechnical earthquake engineering*. Prentice Hall, Upper Saddle River, NJ.

Kramer, S. L. (2008). *Evaluation of Liquefaction Hazards in Washington State*. Washington State Department of Transportation (WSDOT), WA-RD 668.1.

Kulhawy, F. H. and Mayne, P. W. (1990). "Manual on estimating soil properties for foundation design." *Report no.*, Electric Power Research Inst., Palo Alto, CA (USA); Cornell Univ., Ithaca, NY (USA). Geotechnical Engineering Group. EPRI EL-6800, Project 1493-6 Final Report.

Kutter, B., Manzari, M., Zeghal, M., Zhou, Y., and Armstrong, R. (2014). "Proposed outline for LEAP verification and validation processes." *Geotechnics for Catastrophic Flooding Events*, Informa UK Limited, 99–108.

Kutter, B. L., Carey, T. J., Hashimoto, T., Zeghal, M., Abdoun, T., Kokkali, P., Madabhushi, G., Haigh, S. K., d'Arezzo, F. B., Madabhushi, S., Hung, W.-Y., Lee, C.-J., Cheng, H.-C., Iai, S., Tobita, T., Ashino, T., Ren, J., Zhou, Y.-G., Chen, Y.-M., Sun, Z.-B., and Manzari, M. T. (2017). "LEAP-GWU-2015 experiment specifications, results, and comparisons." *Soil Dynamics and Earthquake Engineering*.

Laursen, T. A. (2002). *Computational Contact and Impact Mechanics: Fundamentals of Modelling Interfacial Phenomena in Nonlinear Finite Element Analysis*. Springer, Berlin.

Lax, P. D. and Richtmyer, R. D. (1956). "Survey of the stability of linear finite difference equations." *Communications on Pure and Applied Mathematics*, 9(2), 267–293.

Lemitzer, A., Ahlberg, E. R., Nigbor, R. L., Wallace, A. S. J. W., and Stewart, J. P. (2009). "Lateral performance of full-scale bridge abutment wall with granular backfill." *Journal of Geotechnical and Geoenvironmental Engineering*, 135(4), 506–514.

Lemitzer, A., Khalili-Tehrani, P., Ahlberg, E. R., Rha, C., Taciroglu, E., Wallace, J. W., and Stewart, J. P. (2010). "Nonlinear efficiency of bored pile group under lateral loading." *Journal of Geotechnical and Geoenvironmental Engineering*, 136(12), 1673–1685.

Li, X. and Dafalias, Y. (2000). "Dilatancy for cohesionless soils." *Geotechnique*, 50(4), 449–460.

Li, X.-S. and Wang, Y. (1998). "Linear representation of steady-state line for sand." *Journal of geotechnical and geoenvironmental engineering*, 124(12), 1215–1217.

Macari, E. J., Weihe, S., and Arduino, P. (1997). "Implicit integration of elastoplastic constitutive models for frictional materials with highly non-linear hardening functions." *Mechanics of Cohesive-frictional Materials*, 2(1), 1–29.

Manzari, M., Kutter, B., Zeghal, M., Iai, S., Tobita, T., Madabhushi, S., Haigh, S., Mejia, L., Gutierrez, D., Armstrong, R., Sharp, M., Chen, Y., and Zhou, Y. (2014). "LEAP projects: Concept and challenges." *Geotechnics for Catastrophic Flooding Events*, Informa UK Limited, 109–116.

Manzari, M. T. and Dafalias, Y. F. (1997). "A critical state two-surface plasticity model for sands." *Géotechnique*, 47(2), 255–272.

Manzari, M. T., Ghoraiby, M. E., Kutter, B. L., Zeghal, M., Abdoun, T., Arduino, P., Armstrong, R. J., Beaty, M., Carey, T., Chen, Y., **Ghofrani**, A., Gutierrez, D., Goswami, N., Haigh, S. K., Hung, W.-Y., Iai, S., Kokkali, P., Lee, C.-J., Madabhushi, S. G., Mejia, L., Sharp, M., Tobita, T., Ueda, K., Zhou, Y., and Ziotopoulou, K. (2017). "Liquefaction experiment and analysis projects (LEAP): Summary of observations from the planning phase." *Soil Dynamics and Earthquake Engineering*.

Martin, G. R., March, M. L., Anderson, D. G., Mayes, R. L., and Power, M. S. (2002). "Recommended design approach for liquefaction induced lateral spreads." *Proc., 3rd Natl. Seismic Conf. and Workshop on Bridges and Highways*, MCEER-02-SP04, Buffalo, NY.

Matsui, T. (1993). "Case studies on cast-in-place bored piles and some considerations for design." *Proceedings of the 2nd International Geotechnical Seminar on Deep Foundations on Bored and Auger Piles, Ghent, Belgium, 1-4 June 1993*, 77–102.

Matsui, T., Kitazawa, M., Nanjo, A., and Yasuda, F. (1997). *Investigation of damaged foundations in the Great Hanshin earthquake disaster*. Balkema.

Matsui, T. and Oda, K. (1996). "Foundation damage of structures." *Soils and foundations*, 36(Special), 189–200.

McClelland, B. and Focht, J. (1958). "Soil modulus for laterally loaded piles." *Transactions, ASCE*, 123, 1049–1086.

McGann, C. R. (2013). "Numerical evaluation of forces on piled bridge foundations in laterally spreading soil." Ph.D. dissertation, University of Washington, Seattle, WA.

McGann, C. R., Arduino, P., and Mackenzie-Helnwein, P. (2012). "Development of simplified analysis procedure for piles in laterally spreading layered soils." *PEER Report No. 2012/05*, Pacific Earthquake Engineering Research Center, University of California, Berkeley.

McGann, C. R., Arduino, P., and Mackenzie-Helnwein, P. (2015). "A stabilized single-point finite element formulation for three-dimensional dynamic analysis of saturated soils." *Computers and Geotechnics*, 66, 126–141.

McKenna, F., Scott, M. H., and Fenves, G. L. (2010). "Nonlinear finite element analysis software architecture using object composition." *Journal of Computing in Civil Engineering*, 24(1), 95–107.

McKenna, F. T. (1997). "Object-oriented finite element programming: Frameworks for analysis, algorithms and parallel computing." Ph.D. thesis, University of California, Berkeley, Berkeley, California.

Meera, R. S., Shanker, K., and Basudhar, P. K. (2007). "Flexural response of piles under liquefied soil conditions." *Geotechnical and Geological Engineering*, 25(4), 409–422.

Meschke, G. and Helnwein, P. (1994). "Large-strain 3d-analysis of fibre-reinforced composites using rebar elements: hyperelastic formulations for cords." *Computational Mechanics*, 13(4), 241–254.

Meyerhof, G. G. (1976). "Bearing capacity and settlement of pile foundations." *Journal of the Soil Mechanics and Foundations Division, ASCE*, 102, 197–228.

Miwa, S., Ikeda, T., and Sato, T. (2006). "Damage process of pile foundation in liquefied ground during strong ground motion." *Soil Dynamics and Earthquake Engineering*, 26(2-4), 325–336.

Moehle, J., Riddel, R., and Boroschek, R. (2010). "Learning from earthquakes: the M_w 8.8 chile earthquake of february 27, 2010." *Earthquake Engineering Research Institute, Oakland*.

Mokwa, R. L. and Duncan, J. M. (2001). "Laterally loaded pile groups and *p-y* multipliers." *Foundations and Ground Improvement: Proceedings of a specialty conference: June 9-13, Blacksburg, VA*, T. L. Brandon, ed., Geotechnical Special Publication No. 113, ASCE, 728–742.

Muqtadir, A. and Desai, C. S. (1986). "Three-dimensional analysis of a pile-group foundation." *International journal for numerical and analytical methods in geomechanics*, 10(1), 41–58.

Nishizawa, S., Hashimoto, M., Sakata, Y., and Sonoi, K. (1998). "Investigation and analysis of a landing pier of steel pipe piles damaged by the 1995 hyogoken-nambu earthquake." *Soils and Foundations*, 38(Special), 133–145.

Oh-Oka, H., Fukui, M., Hatanaka, M., Ohara, J., and Honda, S. (1998). "Permanent deformation of steel pipe piles penetrating compacted fill at wharf on port island." *Soils and Foundations*, 38(Special), 147–162.

Oh-Oka, H., Onishi, K., Nanba, S., Mori, T., Ishikawa, K., Koyama, S., and Shimazu, S.-i. (1997). "Liquefaction induced failure of piles in the 1995 kobe earthquake." *Proceedings of the Third Kansai International Geotechnical Forum (KIG-Forum'97), January 1997, Kobe, Japan*, 265–274.

Ooi, P. S. K., Lin, X., and Hamada, H. S. (2010). "Numerical study of an integral abutment bridge supported on drilled shafts." *Journal of Bridge Engineering, ASCE*, 15(1), 19–31.

OpenSees (2007). *Open System for Earthquake Engineering Simulation*. `http://opensees.berkeley.edu`. Pacific Earthquake Engineering Research Center (PEER), University of California, Berkeley.

Pérez-Foguet, A. and Armero, F. (2002). "On the formulation of closest-point projection algorithms in elastoplasticity part ii: Globally convergent schemes." *International Journal for numerical Methods in Engineering*, 53(2), 331–374.

Pérez-Foguet, A., Rodríguez-Ferran, A., and Huerta, A. (2001). "Consistent tangent matrices for substepping schemes." *Computer methods in applied mechanics and engineering*, 190(35), 4627–4647.

Petek, K. A. (2006). *Development and Application of Mixed Beam-Solid Models for Analysis of Soil-Pile Interaction Problems*. Ph.D. Dissertation, University of Washington.

Potts, D. and Gens, A. (1985). "A critical assessment of methods of correcting for drift from the yield surface in elasto-plastic finite element analysis." *International Journal for Numerical and Analytical Methods in Geomechanics*, 9(2), 149–159.

Ramirez, J., Barrero, A., Chen, L., Dashti, S., **Ghofrani**, A., Taiebat, M., and Arduino, P. (in press). "Site response in a layered liquefiable deposit: Evaluation of different numerical

tools and methodologies with centrifuge experimental results." *Journal of Geotechnical and Geoenvironmental Engineering*.

Ramirez, J., Barrero, A. R., Chen, L., **Ghofrani**, A., Dashti, S., Taiebat, M., and Arduino, P. (2018). "Capabilities and limitations of different numerical tools in capturing seismic site performance in a layered liquefiable site." *Geotechnical Earthquake Engineering and Soil Dynamics V, June 10-13, 2018 – Austin, Texas*.

Ramos, R., Abdoun, T., and Dobry, R. (1999). "Centrifuge modeling effects of superstructure stiffness on pile bending moments due to lateral spreading." *Proceedings of the Seventh U.S.-Japan Workshop on Earthquake Resistant Design of Lifeline Facilities and Countermeasures Against Soil Liquefaction, August 15-17, 1999, Seattle Washington*, 599–608.

Reese, L. C., Isenhower, W. M., and Wang, S.-T. (2006). *Analysis and Design of Shallow and Deep Foundations*. John Wiley & Sons, Inc., Hoboken, New Jersey.

Reese, L. C. and Matlock, H. (1956). *Non-dimensional solutions for laterally-loaded piles with soil modulus assumed proportional to depth*. Association of Drilled Shaft Contractors.

Reese, L. C. and Van Impe, W. F. (2001). *Single Piles and Pile Groups Under Lateral Loading*. A.A. Balkema, Rotterdam, Netherlands.

Reese, L. C. and Van Impe, W. F. (2010). *Single piles and pile groups under lateral loading*. CRC Press, Boca Raton, FL.

Richard, F., Woods, R., and Hall Jr, J. (1970). *Vibration of soils and foundations*. International Series in Theoretical and Applied Mechanics. Prentice-Hall, Englewood Cliffs, NJ.

Robins, P., Tarin, R., Thompson, D., Higuchi, S., Mori, T., and Kutter, B. (1999). "Centrifuge modeling of the seismic response of lng production facility structures: Phase III."

Report no., Report No. UCD/CGM-99/02, Center for Geotechnical Modeling, Department of Civil and Environmental Engineering, University of California, Davis.

Rollins, K. M., Gerber, T. M., Lane, J. D., and Ashford, S. A. (2005). "Lateral resistance of a full-scale pile group in liquefied sand." *Journal of Geotechnical and Geoenvironmental Engineering, ASCE*, 131(1), 115–125.

Romstad, K., Kutter, B., Maroney, B., Vanderbilt, E., Griggs, M., and Chai, Y. H. (1995). "Experimental measurements of bridge abutment behavior." *Report No. UCD-STR-95-1*, Dept. of Civil and Environmental Engineering, University of California, Davis, CA.

Rowe, P. W. (1962). "The stress-dilatancy relation for static equilibrium of an assembly of particles in contact." *Proceedings of the royal society of London a: mathematical, physical and engineering sciences*, Vol. 269, The Royal Society, 500–527.

Ruegg, J., Rudloff, A., Vigny, C., Madariaga, R., De Chabalier, J., Campos, J., Kausel, E., Barrientos, S., and Dimitrov, D. (2009). "Interseismic strain accumulation measured by gps in the seismic gap between constitución and concepción in chile." *Physics of the Earth and Planetary Interiors*, 175(1), 78–85.

Rgnier, J., Bonilla, L., Bard, P., Bertrand, E., Hollender, F., Kawase, H., Sicilia, D., Arduino, P., Amorosi, A., Asimaki, D., Boldini, D., Chen, L., Chiaradonna, A., DeMartin, F., Ebrille, M., Elgamal, A., Falcone, G., Foerster, E., Foti, S., Garini, E., Gazetas, G., Glis, C., **Ghofrani**, A., Giannakou, A., Gingery, J. R., Glinsky, N., Harmon, J., Hashash, Y., Iai, S., Jeremi, B., Kramer, S., Kontoe, S., Kristek, J., Lanzo, G., Lernia, A. d., LopezCaballero, F., Marot, M., McAllister, G., Diego Mercerat, E., Moczo, P., MontoyaNoguera, S., Musgrove, M., NietoFerro, A., Pagliaroli, A., Pisan, F., Richterova, A., Sajana, S., Santisi d'Avila, M. P., Shi, J., Silvestri, F., Taiebat, M., Tropeano, G., Verrucci, L., and Watanabe, K. (2016). "International benchmark on numerical simulations for 1d, nonlinear site response (prenolin): Verification phase based on canonical casesinternational

benchmark on numerical simulations for 1d, nonlinear site response (prenolin)." *Bulletin of the Seismological Society of America*, 106(5), 2112.

Rgnier, J., Bonilla, L., Bard, P., Bertrand, E., Hollender, F., Kawase, H., Sicilia, D., Arduino, P., Amorosi, A., Asimaki, D., Boldini, D., Chen, L., Chiaradonna, A., DeMartin, F., Elgamal, A., Falcone, G., Foerster, E., Foti, S., Garini, E., Gazetas, G., Glis, C., **Ghofrani**, A., Giannakou, A., Gingery, J., Glinsky, N., Harmon, J., Hashash, Y., Iai, S., Kramer, S., Kontoe, S., Kristek, J., Lanzo, G., Lernia, A. d., LopezCaballero, F., Marot, M., McAllister, G., Diego Mercerat, E., Moczo, P., MontoyaNoguera, S., Musgrove, M., NietoFerro, A., Pagliaroli, A., Passeri, F., Richterova, A., Sajana, S., Santisi dAvila, M. P., Shi, J., Silvestri, F., Taiebat, M., Tropeano, G., Vandeputte, D., and Verrucci, L. (2018). "Prenolin: International benchmark on 1d nonlinear siteresponse analysisvalidation phase exerciseprenolin: International benchmark on 1d nonlinear siteresponse analysisvalidation phase exercise." *Bulletin of the Seismological Society of America*, 108(2), 876.

Sadek, M. and Shahrour, I. (2004). "A three dimensional embedded beam element for reinforced geomaterials." *International journal for numerical and analytical methods in geomechanics*, 28(9), 931–946.

Schofield, A. N. and Wroth, C. P. (1968). *Critical state soil mechanics*. European civil engineering series. McGraw-Hill, New York.

Seed, H. B. and Reese, L. C. (1957). "The action of soft clay along friction piles." *Transactions, ASCE*, 122, 731–754.

Sekiguchi, H. (1977). "Induced anisotropy and time dependency in clays." *Proceedings of 9th Intemational Conference on Soil Mechanics and Foundation Engineering, Specialty Session 9, Tokyo, Japan*, 229–237.

Sextos, A. G. and Taskari, O. (2008). "Comparative assessment of advanced computational tools for embankment-abutment-bridge superstructure interaction." *Proceedings of the 14th World Conference on Earthquake Engineering*, Beijing, China, October 12-17.

Shamsabadi, A., Ashour, M., and Norris, G. (2005). "Bridge abutment nonlinear force-displacement-capacity prediction for seismic design." *Journal of Geotechnical and Geoenvironmental Engineering*, 131(2), 151–161.

Shamsabadi, A., Khalili-Tehrani, P., Stewart, J. P., and Taciroglu, E. (2010). "Validated simulation models for lateral response of bridge abutments with typical backfills." *Journal of Bridge Engineering, ASCE*, 15(3), 302–311.

Shamsabadi, A., Rollins, K. M., and Kapuskar, M. (2007). "Nonlinear soil-abutment-bridge structure interaction for seismic performance-based design." *Journal of Geotechnical and Geoenvironmental Engineering, ASCE*, 133(6), 707–720.

Shin, H., Arduino, P., Kramer, S. L., and Mackie, K. (2008). "Seismic response of a typical highway bridge in liquefiable soil." *Geotechnical Earthquake Engineering and Soil Dynamics IV*, D. Zeng, M. T. Manzari, and D. R. Hiltunen, eds., GSP 181, ASCE.

Silva, P. F. and Manzari, M. T. (2008). "Soil-structure interaction analysis of bridge columns supported on CISS piles." *Geotechnical Earthquake Engineering and Soil Dynamics IV*, D. Zeng, M. T. Manzari, and D. R. Hiltunen, eds., GSP 181, ASCE, 1–11.

Simo, J. C. and Hughes, T. J. R. (1998). *Computational Inelasticity*. Springer, New York.

Sloan, S. W., Abbo, A. J., and Sheng, D. (2001). "Refined explicit integration of elastoplastic models with automatic error control." *Engineering Computations*, 18(1/2), 121–194.

Stewart, J. P., Taciroglu, E., Wallace, J. W., Ahlberg, E. R., Lemnitzer, A., Rha, C., and Khalili-Tehrani, P. (2007). "Full scale cyclic large deflection testing of foundation support systems for highway bridges. Part I: Drilled shaft foundations." *UCLA - SGEL Report*

2007/01, Department of Civil and Environmental Engineering, University of California, Los Angeles.

Suzuki, H., Tokimatsu, K., Sato, M., and Abe, A. (2006). "Factor affecting horizontal subgrade reaction of piles during soil liquefaction and lateral spreading." *Seismic Performance and Simulation of Pile Foundations in Liquefied and Laterally Spreading Ground*, R. W. Boulanger and K. Tokimatsu, eds., GSP 145, ASCE, 1–10.

Taciroglu, E., Rha, C., and Wallace, J. W. (2006). "A robust macroelement model for soil–pile interaction under cyclic loads." *Journal of geotechnical and geoenvironmental engineering*, 132(10), 1304–1314.

Taji, Y. (1998). "Modeling of a prototype soil-pile-structure system during seismic ground liquefaction." *Proc. Centrifuge 98*, 283–288.

Takahashi, A., Sugita, H., and Tanimoto, S. (2006). "Permanent deformation of bridge abutment on liquefiable soils." *Technical Memorandum of Public Works Research Institute*, 4009, 411–424.

Taylor, D. (1948). *Fundamentals of soil mechanics*. Chapman And Hall, Limited.; New York.

Ghofrani, A. and Arduino, P. (2017). "Prediction of leap centrifuge test results using a pressure-dependent bounding surface constitutive model." *Soil Dynamics and Earthquake Engineering*.

Ghofrani, A., McGann, C. R., and Arduino, P. (2016). "Influence of modeling decisions on three-dimensional finite element analysis of two existing highway bridges subjected to lateral spreading." *Transportation Research Record: Journal of the Transportation Research Board*, 2592, 143–150.

Tobita, T., Iai, S., Sugaya, M., and Kaneko, H. (2006). "Analysis of group pile behavior under lateral spreading." *Seismic Performance and Simulation of Pile Foundations in*

Liquefied and Laterally Spreading Ground, R. W. Boulanger and K. Tokimatsu, eds., GSP 145, ASCE, 294–305.

Tokimatsu, K. and Asaka, Y. (1998). "Effects of liquefaction-induced ground displacements on pile performance in the 1995 hyogoken-nambu earthquake." *Soils and Foundations*, 38(2), 163–177.

Tokimatsu, K., Mizuno, H., and Kakurai, M. (1996). "Building damage associated with geotechnical problems." *Soils and foundations*, 36(Special), 219–234.

Tokimatsu, K., Oh-oka, H., Satake, K., Shamoto, Y., and Asaka, Y. (1997). "Failure and deformation modes of piles due to liquefaction-induced lateral spreading in the 1995 hyogoken-nambu earthquake." *J Struct Eng AIJ, Jpn*, 495, 95–100.

Tokimatsu, K., Suzuki, H., and Sato, M. (2005). "Effects of inertial and kinematic interaction on seismic behavior of pile with embedded foundation." *Soil Dynamics and Earthquake Engineering*, 25, 753–762.

Turello, D. F., Pinto, F., and Sánchez, P. J. (2016). "Embedded beam element with interaction surface for lateral loading of piles." *International Journal for Numerical and Analytical Methods in Geomechanics*, 40(4), 568–582.

Turello, D. F., Pinto, F., and Sánchez, P. J. (2017). "Three dimensional elasto-plastic interface for embedded beam elements with interaction surface for the analysis of lateral loading of piles." *International Journal for Numerical and Analytical Methods in Geomechanics*, 41(6), 859–879.

Valsamis, A., Bouckovalas, G., and Chaloulos, Y. (2011). "Simplified design of single piles under liquefaction induced lateral spreading." *Proceedings of the 5th International Conference on Earthquake Geotechnical Engineering*, Santiago, Chile, January 10-13, Paper No. SDOVA.

Vijayvergiya, V. N. (1977). "Load movement characteristics of piles." *Proceedings of the Ports '77 Conference, ASCE, Vol II*, 269–284.

Wallace, J. W., Fox, P. J., Stewart, J. P., Janoyan, K., Qiu, T., and Lermitte, S. (2001). "Cyclic large deflection testing of shaft bridges Part I: Background and field test results." *Report to California Department of Transportation.*

Washington State Department of Transportation (WSDOT) (2011a). *Bridge Design Manual (LRFD).* Technical Manual M 23-50.05, May 2011.

Washington State Department of Transportation (WSDOT) (2011b). *Geotechnical Design Manual (LRFD).* Technical Manual M 46-03.04, April 2011.

Wriggers, P. (2002). *Computational Contact Mechanics.* John Wiley & Sons, Ltd, West Sussex, England.

Wu, J. (2002). *Liquefaction triggering and post-liquefaction deformation of Monterey 0/30 sand under uni-directional cyclic simple shear loading*, Vol. 1. University of California, Berkeley.

Yoshida, N. and Hamada, M. (1990). "Analysis of damages of foundation piles due to liquefaction-induced permanent ground displacements." *Proc. 8th Japan Earthquake Engineering Symposium*, Vol. 1, 55–60.

Youd, T. L., Hansen, C. M., and Bartlett, S. F. (2002). "Revised multilinear regression equations for prediction of lateral spread displacement." *Journal of Geotechnical and Geoenvironmental Engineering, ASCE*, 128(12), 1007–1017.

Zeghal, M., Goswami, N., Kutter, B. L., Manzari, M. T., Abdoun, T., Arduino, P., Armstrong, R., Beaty, M., Chen, Y.-M., **Ghofrani**, A., Haigh, S., Hung, W.-Y., Iai, S., Kokkali, P., Lee, C.-J., Madabhushi, G., Tobita, T., Ueda, K., Zhou, Y.-G., and Ziotopoulou, K. (2017). "Stress-strain response of the LEAP-2015 centrifuge tests and numerical predictions." *Soil Dynamics and Earthquake Engineering.*

Zha, J. (2004). "Lateral spreading forces on bridge abutment walls/piles." *Geotechnical Engineering for Transportation Projects*, M. K. Yegian and E. Kavazanjian, eds., GSP 126, ASCE, 1711–1720.

Zha, J. (2006). "Lateral spreading forces on bridge piles." *Seismic Performance and Simulation of Pile Foundations in Liquefied and Laterally Spreading Ground*, R. W. Boulanger and K. Tokimatsu, eds., GSP 145, ASCE, 71–82.

Zienkiewicz, O., Best, B., Dullage, C., and Stagg, K. (1970). "Analysis of nonlinear problems in rock mechanics with particular reference to jointed rock systems." *Report No. 364*, International Society for Rock Mechanics.

Zienkiewicz, O. and Shiomi, T. (1984). "Dynamic behaviour of saturated porous media; the generalized biot formulation and its numerical solution." *International journal for numerical and analytical methods in geomechanics*, 8(1), 71–96.

Ziotopoulou, K. and Boulanger, R. (2013). "Calibration and implementation of a sand plasticity plane-strain model for earthquake engineering applications." *Soil Dynamics and Earthquake Engineering*, (53), 268–280.